INTERNATIONAL DOCTORAL
SCHOOL OF THE USC

Francisco
Rey Tarrío

PhD Thesis

Photoreactivity and Novel Designs in Smart Chiral Materials

Santiago de Compostela, 2022

Doctoral Programme in Chemical Science and Technology

TESE DE DOUTORAMENTO

Photoreactivity and Novel Designs in Smart Chiral Materials

Francisco Rey Tarrío

ESCOLA DE DOUTORAMENTO INTERNACIONAL DA UNIVERSIDADE DE SANTIAGO DE COMPOSTELA
PROGRAMA DE DOUTORAMENTO EN CIENCIA E TECNOLOXÍA QUÍMICA

SANTIAGO DE COMPOSTELA
2022

DECLARACIÓN DEL AUTOR/A DE LA TESIS

D./Dña. **Francisco Rey Tarrío**

Título da tese: **Photoreactivity and Novel Designs in Smart Chiral Materials**

Presento mi tesis, siguiendo el procedimiento adecuado al Reglamento y declaro que:

1) La tesis abarca los resultados de la elaboración de mi trabajo.
2) De ser el caso, en la tesis se hace referencia a las colaboraciones que tuvo este trabajo.
3) Confirmo que la tesis no incurre en ningún tipo de plagio de otros autores ni de trabajos presentados por mí para la obtención de otros títulos.
4) La tesis es la versión definitiva presentada para su defensa y coincide la versión impresa con la presentada en formato electrónico.

Y me comprometo a presentar el Compromiso Documental de Supervisión en el caso que el original no esté depositado en la Escuela.

En **Santiago de Compostela**, **27 de septiembre de 2022**.

Firma electrónica

AUTORIZACIÓN DEL DIRECTOR / TUTOR DE LA TESIS

Photoreactivity and Novel Designs in Smart Chiral Materials

D./Dª. Emilio Quiñoá Cabana
D./Dª. Félix Manuel Freire Iribarne

INFORMAN:

Que la presente tesis, se corresponde con el trabajo realizado por D/Dª. Francisco Rey Tarrío, bajo nuestra dirección/tutorización, y autorizamos su presentación, considerando que reúne los requisitos exigidos en el Reglamento de Estudios de Doctorado de la USC, y que como directores de esta no incurre en las causas de abstención establecidas en la Ley 40/2015.

De acuerdo con lo indicado en el Reglamento de Estudios de Doctorado, declaran también que la presente tesis doctoral es idónea para ser defendida en base a la modalidad de Monográfica con reproducción de publicaciones, en los que la participación del doctorando/a fue decisiva para su elaboración y las publicaciones se ajustan al Plan de Investigación.

En Santiago de Compostela, 27 de septiembre de 2022

Contents

Abbreviations and Acronyms

AFM	Atomic Force Microscopy
Aib	α-aminoisobutyric acid
anti	Antiperiplanar
ap	Antiperiplanar
BTA	1,3,5-benzenetricarboxamide
c-c	*Cis-cisoidal*
c-t	*Cis-transoidal*
CD	Circular Dichroism
CIP	Cahn–Ingold–Prelog
cod	*Cis-cis*-1,5-cyclooctadiene
CPL	Circular Polarized Luminescence
CSP	Chiral Stationary Phase
d	Doblet
D	Diameter
DCM	Dichloromethane
DIPEA	Diisopropylethylamine
DLS	Dynamic Light Scattering
DMF	*N,N*-Dimethylformamide
DMSO	Dimethyl sulfoxide
DSC	Differential Scanning Calorimetry
EPR	Electronic Paramagnetic Resonance
equiv	Equivalents
et al.	Latin expression "*et Alii*", and others
e.g.,	Latin expression "*exempli gratia*", for example
g	Gram
GPC	Gel Permeation Chromatography
H	Hour
HA	Hyaluronic acid
HOAt	1-hydroxy-7-azabenzotriazole
HOPG	Highly Oriented Pyrolytic Graphite

HPLC	High-Performance Liquid Chromatography
Hz	Hertz
IR	Infrared
LB	Langmuir-Blodgett
LBL	Layer-by-Layer
LS	Langmuir-Schaefer
m	Multiplet
M helix	Counterclockwise helix
mg	Milligram
min	Minute
mL	Milliliter
mM	Millimolar
MMFF	Molecular Modeling Force Field
mmol	Millimol
MPA	α-methoxy-α-phenylacetic acid
MS	Mass spectroscopy
MTPA	α-methoxy-α-trifluoromethyl-α-phenylacetic acid
M_w	Molecular weight
nbd	2,5-norbornadiene
nm	Nanometer
NMR	Nuclear Magnetic Resonance
OPV	oligo(phenylenevinylene)
PAA	Poly(acrylic acid)
PAH	Hydrochloride of Poly(Allylamine)
PDI	Polydispersity index
PGME	Phenylglycine methyl ester
POM	Polarizing Optical Microscope
PPA	Poly(phenylacetylene)
Prof.	Professor
s	Singlet
sa	Broad signal
SCAT	Highly Selective Photocyclic Aromatization

SEM	Scanning Electron Microscopy
sp	Synperiplanar
syn	Synperiplanar
TEM	Transmission Electron Microscopy
TGA	Thermogravimetric Analysis
THF	Tetrahydrofuran
TMS	Trimethylsilane
UV-Vis	Ultraviolet-Visible Spectroscopy
VCD	Vibrational Circular Dichroism
XPS	X-ray Photoelectron spectroscopy
δ	Chemical shift
°C	Celsius degree
$[\alpha]$	Specific Optical Rotation

List of publications

During the development of this Thesis, the following articles have been published in scientific journals. Furthermore, the results of these articles have been included within this manuscript.

1) **Francisco Rey-Tarrío**, Rafael Rodríguez, Emilio Quiñoá, Ricardo Riguera and Félix Freire. *Angew. Chem. Int. Ed.*, **2021**, *60*, 8095-8103.
Impact factor: 15.336 (2020)
Category: Chemistry (Q1).

F. R.-T. has contributed in the experimental part (synthesis and characterization) discussion of results and preparation of the manuscript.

License number for the reproduction of the article: 5387130545320

2) **Francisco Rey-Tarrío**, Santiago Guisán-Ceinos, Juan M. Cuerva, Delia Miguel, Maria Ribagorda, Emilio Quiñoá and Félix Freire. *Angew. Chem. Int. Ed.*, **2022**, *61*, e202207623.
Impact factor: 16.823 (2021)
Category: Chemistry (Q1).

F. R.-T. has contributed in the experimental part (synthesis and characterization) discussion of results and preparation of the manuscript.

License number for the reproduction of the article: 5387131395698

Chapter I

Introduction

INTRODUCTION

Macromolecules are high molecular weight species whose discovery dates to the 19th century, but it was not until the early of 1920 when Hermann Staudinger presented a series of reactions that form high molecular weight species by joining large numbers of small molecules. He proposed that these high molecular weight structures were linked by covalent bonds, thus giving rise to the concept of macromolecules.[1]

In this field, biological macromolecules such as proteins, sugars or DNA quickly reach great relevance for the relationship between their biological functions and their secondary structure (Figure 1), responsible of their functions. This relationship gave the idea of generating synthetic macromolecules that can imitate properties of the natural ones. In this line, some of the most relevant discoveries was the α-helix[2] of proteins (Pauling, 1950) and the double helix of the DNA (Watson and crick, 1953).[3]

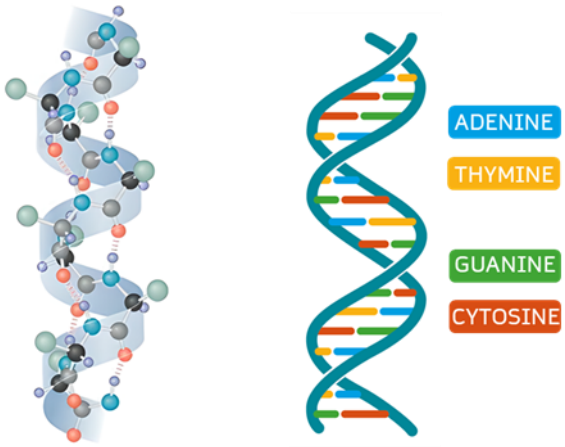

Figure 1. Examples of fragments of an α-helix and double helix of DNA.

Shortly after, Natta reported the first example of a synthetic helical polymer. The helical structure of the isotactic poly(propylene), constituted by a racemic mixture of left-handed and right-handed helices in solid state that is lost when the polymer is dissolved.[4]

Continuing in this line, Pino *et al.* reported the preparation of a series of poly(vinyl) polymers with excess of one helical sense, that was achieved by polymerization of

[1] (a) H. Staudinger, J. Fritschi, *Helv. Chim. Acta,* **1922**, *5,* 785-806. (b) Hierarchical Macromolecular Structures: 60 years after the Staudinger Nobel Prize I; V. Percec; Ed.; *Advances in Polymer Science*, Vol. *261*; Springer: New York, **2013.**

[2] L. Pauling, R. B. Corey, H. R. Branson, *Proc. Natl. Acad. Sci., U.S.A*. **1951**, *37*, 205-211.

[3] J. D. Watson, F. H. C. Crick, *Nature*, **1953**, *171*, 737-738.

[4] G. Natta, P. Pino, P. Corradini, F. Danusso, E. Mantica, G. Mazzanti, G. Moraglio, *J. Am. Chem. Soc.,* **1955**, *77*, 1708-1710.

monomers with the presence of a chiral center that induce a preference helical sense in the polymer. The excess of one of helices was determined by optical rotation.[5]

Important advances were produced in the 70's for the important contribution of several groups in this field, especially the groups of Okamoto, Nolte and Green. Highlighting the preparation of the first helical polymer by polymerization of achiral monomers (Okamoto, 1968), promoting the helicity using a chiral catalyst.[6]

Later, in 1988 Green *et al.* reported the synthesis and properties of a new class of helical polymers, the poly(isocyanate)s. Constituted by a mixture of left-handed and right-handed conformations connected by reversals in the same propeller. Moreover, population of both helical senses can be modified by use of external stimuli, giving rise to the first example of dynamic helical polymers.[7]

1. Classification of helical polymers

Helical polymers can be classified as static or dynamic based on the energy barrier for the interconversion between both helical senses (*M* and *P*).[8]

1.1 Static helical polymers

These polymers, present one preferred helical sense defined during the polymerization for the use of optically active monomers or a chiral initiator/catalyst. Subsequently, the left-handed or right-handed helices obtained cannot be modified due to the high energy barrier between both helical senses. In this group, polymers generally present bulky substituents. Some examples are poly(methacrylate)s (poly-**1**), poly(methylacrylamide)s (poly-**2**) poly(quinoxaline-2,3-dyl)s (poly-**3**) or poly(guanidine)s (poly-**4**) (Figure 2).[9]

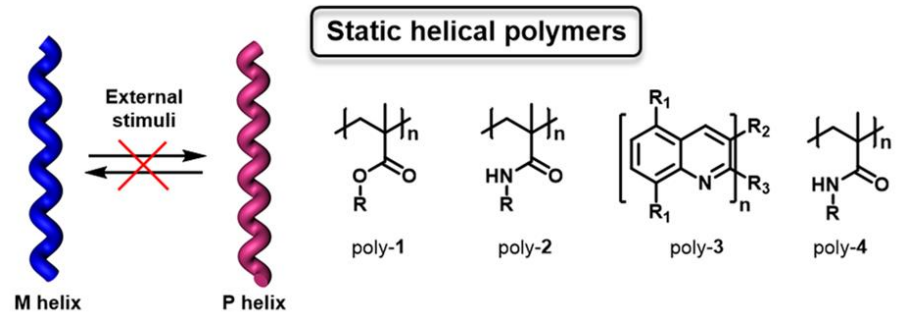

Figure 2. Conceptual representation and some scaffolds of static helical polymers.

[5] P. Pino, G. P. Lorenzi, *J. Am. Chem. Soc.,* **1960**, *82*, 4745-4747.

[6] Y. Okamoto, K. Suzuki, K. Ohta, K. Hatada, H. Yuki, *J. Am. Chem. Soc.,* **1979**, *101*, 4763-4765.

[7] M. M. Green, C. Andreola, B. Munoz, M. P. Reidy, K. Zero, *J. Am. Chem. Soc.,* **1988**, *110*, 4063-4065.

[8] (a) E. Yashima, K. Maeda, H. Iida, Y. Furusho, K. Nagai, *Chem. Rev.,* **2009**, *109*, 6102-6111. (b) J. J. L. Cornelissen, A. E. Rowan, R. J. M. Nolte, N. A. J. M. Sommerdijk, *Chem. Rev.,* **2001**, *101*, 4039-4070.

[9] Y. Okamoto, T. Nakano, *Chem. Rev.,* **1994**, *94*, 349-372.

1.2 Dynamic helical polymers

These polymers can present two helical senses (*M* and *P*) after the polymerization due to the low energy barrier for the interconversion between them. Obtained, by polymerization of optically active monomers or achiral monomers with a chiral stimulus (e.g., chiral solvents or additives), generating an excess of preferred helical in an equilibrium that can be easy tuned by external stimuli (e.g., solvent polarity, temperature, metal ions, etc). Some representative examples of this group are poly(isocyanate)s (poly-**5**), poly(silane)s (poly-**6**), or poly(acetylene)s (poly-**7**) (Figure 3).[10]

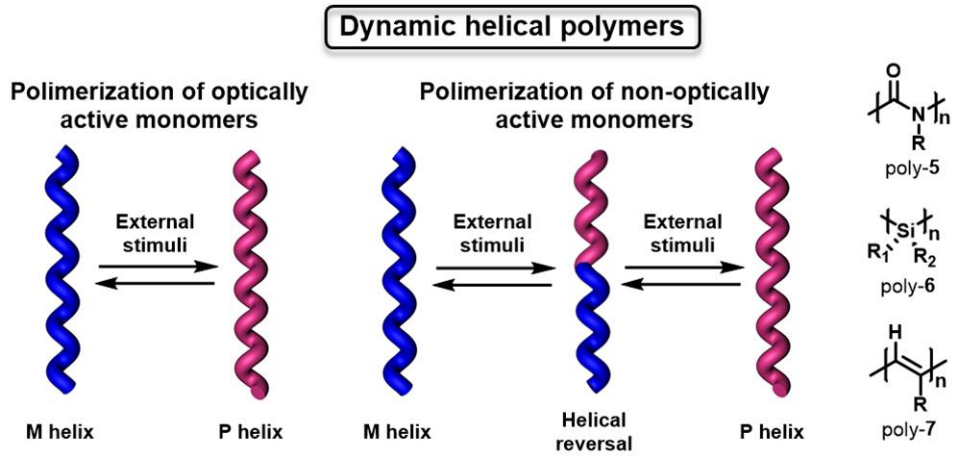

Figure 3. Conceptual representation and some scaffolds of dynamic helical polymers.

1.3 Foldamers

There are oligomers that present a strong tendency to a adopt a conformationally ordered state in solution, stabilized by non-covalent interactions between nonadjacent monomers. This results in a balance between the helical conformation and the unfolded structures, being for these excellent materials for supramolecular chemistry. Some examples of these compounds are oligo(meta-phenyleneethynylene)s (poly-**8**) or oligo(pyridinecarboxyamide)s (poly-**9**) (Figure 4).[11]

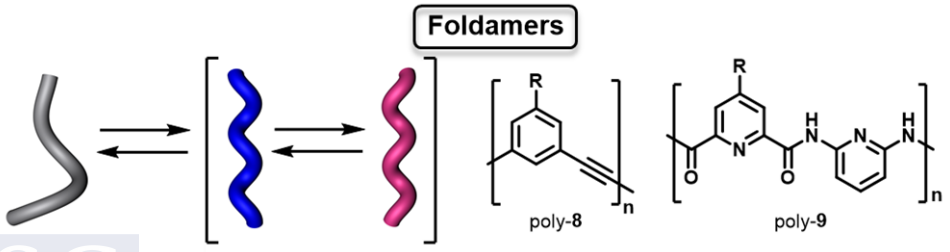

Figure 4. Conceptual representation and some examples of foldamers.

[10] I. Louzao, J. M. Seco, E. Quiñoá, R. Riguera, *Angew. Chem. Int. Ed.*, **2010**, *49*, 1430-1433.

[11] (a) D. J. Hill, M. J. Mio, R. B. Prince, T. S. Hughes, J. S. Moore, *Chem. Rev.*, **2001**, *101*, 3893-4012. (b) D. H. Appella, L. A. Christianson, I. L. Karle, D. R. Powell, S. H. Gellman, *J. Am. Chem. Soc.*, **1996**, *118*, 13071-13072.

2. Poly(acetylene)s and Poly(phenylacetylene)s

Poly(acetylene)s (PAs) are a family of dynamic helical polymers with π-conjugated double bonds that are obtained from polymerization of acetylene monomers (Figure 5). For their stability in solid state and solution, and their simple handling has been extensively studied in the last decades. Moreover, for their optical and chiroptical properties, these present potential applications as Chiral Stationary Phases (CSPs) for HPLC, in asymmetric catalyst, as sensors, etc.[12]

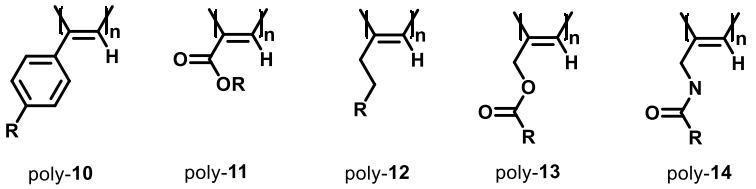

Figure 5. Representative examples of the PA family.

Poly(phenylacetylene)s (PPAs) are one of the most studied polymers derived from poly(acetylene)s. First time reported by Yashima in 1995, they are characterized for being able to adopt four possible configurations of the polyene conjugated double bonds —*cis*-*cisoidal* (*c*-*c*), *cis*-*transoidal* (*c*-*t*), *trans*-*cisoidal* (*t*-*c*) and *trans*-*transoidal* (*t*-*t*)—.[13] However, a *cis* configuration of double bonds is structurally required to get a helical structure. This is achievable using catalysts as Rh(I) (e.g. $[Rh(nbd)Cl]_2$ (nbd: 2,5-norbornadiene), $[Rh(cod)Cl]_2$ (cod: *cis*,*cis*-1,5-cyclooctadiene)) in a process called living polymerization, that is also characterized for produce high molecular weight polymers and low polydispersity. Mechanistically, polymerization is a process stereospecific and regioselective based on a head to tail 2,1-insertion, controlled by the steric repulsion generated between adjacent monomers inserted (Figure 6). Moreover, another strong advantage of Rh (I) catalysts is that it tolerates many polar functional groups and solvents (organic solvents or even water with suitable ligands), allowing a high versatility catalyst and preparation of a wide range of polymers.[14]

[12] (a) Y. Zhou, C. Zhang, Q. Geng, L. Liu, H. Dong, T. Satoh, Y. Okamoto, *Polymer*, **2017**, *131*, 17-24. (b) L. Liu, Y. Wang, F. Wang, C. Zhang, Y. Zhou, Z. Zhou, X. Liu, R. Zhu, H. Dong, T. Satoh, *React. Funct. Polym.,* **2020**, *146*, 104392. (c) Suárez-Picado, E.; Quiñoá, E.; Riguera, R.; Freire, F.; *Chem. Mater.,* **2018**, *30*, 6908-6914.

[13] K. Maeda, E. Yashima, *Top. Curr. Chem.,* **2006**, *265*, 47-88.

[14] (a) Z. Ke, S. Abe, T. Ueno, K. Morokuma, *J. Am. Chem. Soc.,* **2011**, *133*, 7926-7941. (b) K. Hirao, Y. Ishii, T. Terao, Y. Kishimoto, T. Miyatake, T. Ikariya, R. Noyori, *Macromolecules,* **1998**, *31*, 3405-3408. (c) Y. Kishimoto, P. Eckerle, T. Miyatake, T. Ikariya, T. Noyori, *J. Am. Chem. Soc.,* **1994**, *116*, 12131-12132. (d) N. S. L. Tan, A. B. Lowe, *Angew. Chem. Int. Ed.,* **2020**, *59*, 2-16.

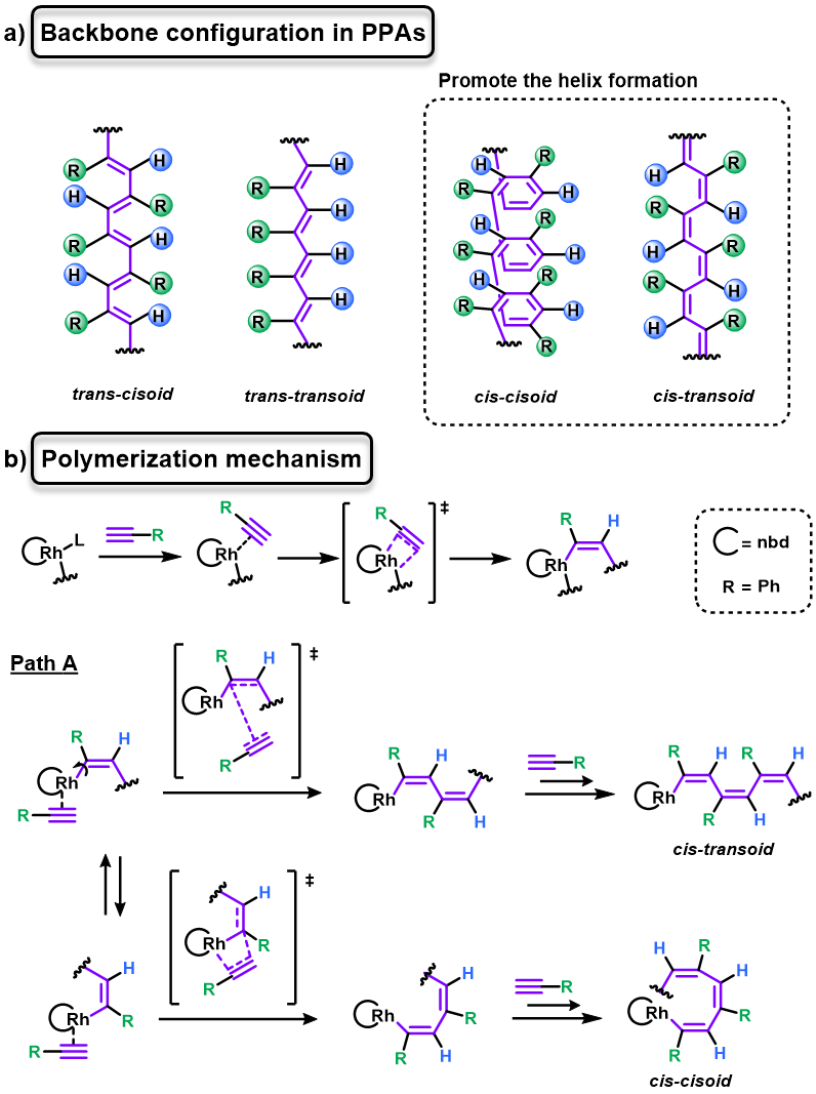

Figure 6. a) Possible configurations of the polyene backbone of PPAs**.** b) Proposed polymerization mechanism of PPAs with Rh(I).

3. Structure and characterization of PPAs

A deep characterization of the secondary structure of the PPA is key to work on potential applications for the structure-function relationship. To get it, a combination of the information from multiple techniques is required.

3.1 Architecture of PPAs

Independently of its sense or elongation, all PPAs are constituted by two coaxial helices (internal and external).

The internal helix is constituted by the conjugated polyene backbone. As result, this is rigid and lacks supramolecular interactions inside. If it presents a preferred helical sense (*M* or *P)* this can be determine by Circular dichroism (CD). This technique determines the

sense of the internal helix. Furthermore, helical sense and elongation is determined by the dihedral angle (ω_1) that depends on the interactions among pendant groups.[15]

The external helix is oriented around the internal one and constituted by the pendant groups, whose conformation depends on the supramolecular interactions among them. Its preferred helical sense can only be determined by Atomic Force Microscopy (AFM).

Internal and external helices can rotate in the same or opposite direction depends on the helical scaffold adopted. When ω_1 is lower than 90°, the polymer adopts a compressed *c-c* structure, with three residues per turn (3/1 helix), and both helices rotate in the same direction. In the other case (ω_1>90°), a more stretched conformation (*c-t*) is adopted, with two residues per turn (2/1 helix) and helices rotating in opposite directions (Figure 7).[16]

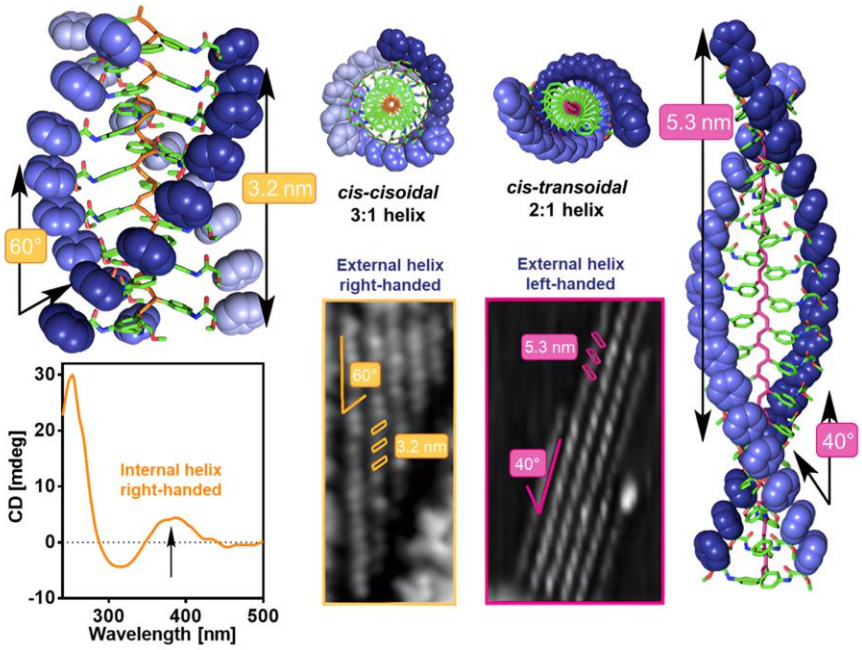

Figure 7. *Cis-cisoidal* and *cis-transoidal* 3D models of poly-(*S*)-**15** in combination of their CD and AFM images.

3.2 Determination of the polyene backbone configuration

The polyene backbone, internal helix, can adopt four possible configurations *cis-cisoidal*, *cis-transoidal*, *trans-cisoidal* and *trans-transoidal*. From among them, the *cis* configuration —the one that adopt a helical conformation— can be distinguish from *trans* configuration for the resonation of the vinyl proton.

Thus, theorical and experimental studies demonstrated that for the *trans* configurations the vinyl proton resonates between 6.20-7.20. Furthermore, the *t-c* and *t-t* scaffolds can be

[15] B. Fernández, R. Rodríguez, E. Quiñoá, R. Riguera, F. Freire, *ACS omega*, **2019**, *4,* 5233-5240.

[16] R. Rodríguez, E. Quiñoá, R. Riguera, F. Freire, *J. Am. Chem. Soc.,* **2016**, *138*, 9620-9628.

distinguished between them for the resonation of the aromatic protons in the ^{1}H-NMR spectra. Due to in the *t-t* backbones two aromatic protons resonates at higher chemical shift while for *t-c* backbones all protons resonate together.

Similarly, *cis* configurations —*c-c* and *c-t*— are distinguished by resonance of a vinyl proton around 5.60-5.80 ppm.[17] Again, resonation of aromatic protons distinguishes between scaffolds. Thus, in *c-c* one aromatic proton is shifted upfield while in *c-t* two are shifted upfield. Moreover, for *cis* polyenes the chemical shift of the vinylic proton indicates the aromatic substitution pattern para- (5.80 ppm), meta- (6.85 ppm) and ortho-substituted (6.70 ppm), being just possible a *c-t* scaffolds for meta- and ortho-substitution.[16] With this information is also possible estimates the *cis* content of double bonds based on the equation 1 (where A_{cis} is the peak area of the vinyl proton at 5.6-5.8 ppm, A_{total} is the total area of the ^{1}H NMR spectrum and H_{total} is the number of protons corresponding to the pendant).

$$\%_{cis} = [A_{cis}/(A_{total} \cdot H_{total})] \cdot 100$$

Equation 1. Mathematical statement to calculate the *cis* content of double bonds in PPAs.

Usually, is difficult interpretate ^{1}H NMR spectra for distinguishing *c-c* from *c-t* scaffolds. For these cases Different Scanning Calorimetry (DSC) is a powerful technique to elucidate the secondary structure of PPAs in solid phase. Characteristic exothermic peaks differentiate thermograms of *c-c* from *c-t* scaffolds. Thus, thermograms of *c-c* scaffolds present one isomerization peak around 240 °C, *c-c* to *t-t* isomerization process. While *c-t* scaffolds, exhibit another peak around 140 °C, *c-t* to *c-c* isomerization (Figure 8).[18]

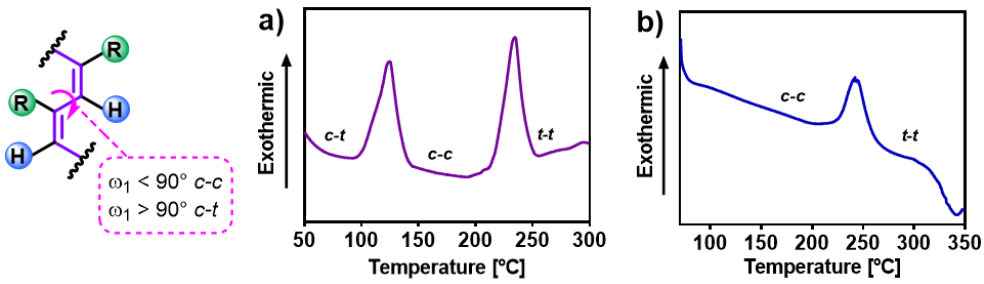

Figure 8. Examples of DSC thermograms of a) *c-t* and b) *c-c* scaffolds.

[17] (a) C. I. Simionescu, V. Percec, J. *Polym. Sci., Polym. Chem. Ed.,* **1980**, *18*, 147-155. (b) C. I. Simionescu, V. Percec, *J. Polym. Sci., Polym. Lett. Ed.,* **1979**, *17*, 421-429. (c) C. I. Simionescu, V. Percec, S. Dumitrescu, *J. Polym. Sci., Polym. Chem. Ed.,* **1977**, *15*, 2497-2509.

[16] R. Rodríguez, E. Quiñoá, R. Riguera, F. Freire, *J. Am. Chem. Soc.,* **2016**, *138*, 9620-9628

[18] (a) A. Motoshige, Y. Mawatari, Y. Yoshida, R. Motoshige, M. Tabata, *Polym. Chem.,* **2014**, *5*, 971-978. (b) A. Motoshige, Y. Mawatari, R. Motoshige, Y. Yoshida, M. Tabata, *J. Polym. Sci., Part A: Polym. Chem.*, **2013**, *51*, 5177-5183. (c) Y. Yoshida, Y. Mawatari, A. Motoshige, R. Motoshige, T. Hiraoki, M. Wagner, K. Müllen, M. Tabata, *J. Am. Chem. Soc.,* **2013**, *135*, 4110-4116.

Moreover, Raman spectroscopy is an additional technique to characterize the configuration of the conjugated polyene. Three characteristic resonance bands are active in Raman, for PPAs with configuration *cis*- C=C_{cis} (ca. 1580 cm^{-1}), C-C_{cis} (ca. 1335 cm^{-1}) and C-H_{cis} (965 cm^{-1}). While for the *trans*- configuration the position of the bands is C=C_{trans} (ca. 1475 cm^{-1}), C-C_{trans} (ca. 1200 cm^{-1}) and C-H_{trans} (740 cm^{-1}).[19] Moreover, the deformation bands of C-H_{trans} (1015 cm^{-1}) and C-H_{cis} (1015 cm^{-1}) are active in infrared spectroscopy.[20]

Additionally, Ultraviolet-visible spectroscopy (UV-Vis) provide information about the degree of elongation of the double bonds, and consequently the polymer. Thus, bathochromic shifts on the absorption (usually around 400 nm) indicates elongation of the helical structure and increase of the conjugation of double bonds. In the opposite case, hypsochromic shifts result on a decrease of conjugation and a compression of the polymer.[21]

3.3 Determination of the helical sense of the polymer

In this section several techniques that are useful to determine the helical sense will be describe.

3.3.1 Optical rotation

Optical rotation (α) measures the degree of variation of a polarized light beam when interacts with a chiral molecule in solution. Due to the technique depends on the solvent, temperature, concentration and cell length, the measurement is standardized with the equation 2. Thus, the specific rotation [α] is calculated as the quotient of the observed optical rotation (α) with the product of the length of the cuvette with concentration of the sample (c). Also, the temperature of the measurement (T) and the wavelength (λ) must be indicated.[22]

$$[\alpha]_{\lambda}^{t} = \frac{\alpha}{l \cdot c}$$

Equation 2. Mathematical statement to calculate specific optical rotation [α].

---

[19] (a) A. Misayaka, T. Sone, Y. Mawatari, S. Setauesh, K. Müllen, M. Tabata, *Macromol. Chem. Phys.,* **2006**, *207*, 1938-1944. (b) K. Huang, Y. Mawatari, A. Miyasaka, Y. Sadahiro, M. Tabata, Y. Kashiwaya, *Polymer,* **2007**, *48*, 6366-6373. (c) A. Miyasaka, Y. Mawatari, T. Sone, M. Tabata, *Polym. Degrad. Stab.,* **2007**, *92*, 253-259.

[20] (a) T. Ito, H. Shirakawa, S. Ikeda, *J. Polym. Sci., Part A: Polym. Chem.,* **1974**, *12*, 11-20. (b) H. Shirakawa, S. Ikeda, *Polym. J.,* **1971**, *2,* 231-244.

[21] (a) V. Percec, M. Peterca, J. G. Rudick, E. Aqad, M. R. Imam, P. A. Heiney, *Chem. Eur. J*., **2007**, *13*, 9572-9581. (b) V. Percec, J. G. Rudick, M. Peterca, E. Aqad, M. R. Imam, P. A. Heiney, *J. Polym. Sci., Part A: Polym. Chem.,* **2007**, *45*, 4974-4987. (c) V. Percec, E. Aqd, M. Peterca, J. G. Rudick, L. Lemon, J. C. Ronda, B. B. De, P. A. Heiney, E. W. Meijer, *J. Am. Chem. Soc., **2006**, 128*, 16365-16372. (d) V. Percec, J. G. Rudick, M. Peterca, M. Wagner, M. Obata, C. M. Mitchell, W. D. Cho, V. S. K. Balagurusamy, P. A. Heiney.; *J. Am. Chem. Soc*., **2005**, *127*, 15257-15264.

[22] P. Vollhardt, N. Schore, *Organic Chemistry: Structure and Function.;* 5nd ed., Omega, **2008**, p 174.

The main disadvantage of the technique is its low sensitivity. Moreover, in the case of macromolecules such as PPAS, [α] value is between one and ten orders of magnitude higher than for the corresponding monomer.

3.3.2 Circular Dichroism

Circular dichroism is the most powerful technique for determine the helical sense of polymers due to the large amount of information that provides and its operational simplicity. Thus, it allows to determine the presence of a preferred helical sense on macromolecules. Moreover, is useful to analyze the variation in the absorption when a Circularly Polarized Light (CPL) beam interacts with the sample. For this case, when the sample contains chiral molecules with at least one chromophore group, a difference is generated in the absorption of left- and right-handed circularly polarized light (*S*- and *R*-CPL respectively).

Moreover, CD can be monitored with small amount of sample and under different conditions, detecting conformational changes that allows to obtain kinetic and thermodynamic parameters.[23,24]

Specifically, for PPAs it allows detecting the presence of a helical excess analyzing the Cotton effect of the vinylic region (usually around 380 nm), where the negative/positive Cotton effect corresponds to *M/P* internal helix respectively. Moreover, the effect of variations on the vinylic CD signal promoted by external stimuli (e.g., temperature, solvents polarity, pH, etc) can be easily monitored.[25]

3.3.3 Theoretically Calculated Circular Dichroism

To complement CD measurements, theoretical calculations are a powerful tool to discern helical structures. For PPAs, it is common to use Molecular Modeling Force Field developed in 1994 (MMFF94) for energy minimization followed by Time-Dependent Density Function Theory (TD-DFT) to calculated CD spectra. In our group 3-21G, 6-31G, 6-31G* and 6-31G** bases were analyzed in combination with the hybrid functions CAM-B3LYP and rCAM-B3LYP, selecting the 3-21G basis with rCAM-B3LYP functional as the more accurate for calculate CD spectra. Moreover, this work demonstrates for several PPAs a

---

[23] (a) G. G. Hammes, *Circular Dichroism, Optical Rotatory Dispersion, and Fluorescence Polarization, In Spectroscopy for the Biological Sciences*, John Wiley & Sons, Inc. **2005**, p 63. (b) N. Bereova, K. Nakanishi, R. W. Woody, *Circular Dichroism: Principles and Applications*, 2nd ed., Wiley-VCH: New York, **2000**, p 912.

[24] (a) K. Nakanishi, N. Berona, *Circular Dichroism: Principles and Applications*; ed por N. Berova, K. Nakanishi, W. R Woody, **2000**, *Wiley-VCH,* 2nd ed, p 361. (b) N. Harada, K. Nakanishi, *Circular Dichroic Spectroscopy-Exciton Coupling in Organic Stereochemistry*, 2nd ed., University Science Books: Mill Valley, CA, **1983**.

[25] M. Alzubi, S. Arias, I. Louzao, E. Quiñoá, R. Riguera, F. Freire. *Chem. Commun*, **2017**, *53*, 8573-8576.

correlation between sign of measured CD spectra and the helical sense of the internal helix (*M* or *P* for negative and positive Cotton effect in the vinylic region respectively). This correlation is found thanks to the relationship of experimental polymer CD with calculated CD for short oligomers employing this set (3-21G with RCAM-B3LYP after MMFF94 energy minimization).[26]

3.3.4 Vibrational Circular Dichroism

Vibrational Circular Dichroism (VCD) is a spectroscopy technique that measure differences in attenuation of left and right circularly polarized light in the infrared region. This technique present strong sensitivity in the detection of the formation of protein fibril structures in solution and allows the direct monitoring and control of supramolecular chirality. [27] Furthermore, is useful to distinguish between different conformations of pendant groups in PPAs.[28]

3.3.5 X-ray diffraction

X-ray diffraction is a phenomenon in which the atoms of a crystal generate an interference pattern of the waves present in an incident beam of X rays. In PPAs, it provides information related to their secondary structures (helical pitch, helix length and interpendant distances). However, the large limitation of this technique is the difficult for preparation of the sample, that required well oriented films of polymer.[29]

3.3.6 Atomic Force Microscopy

AFM is a highly sensitive type of scanning probe microscopy that gathered the information by sweeping the surface of the sample with a sharp AFM tip to generate a three-dimensional topographic image of the surface. According of the type of movement of the tip, AFM can work in three modes: contact mode, tapping mode and non-contact mode.

In PPAS, it allows to determine several parameters of the secondary structure (helical pitch, packing angle and especially helical sense of the external helix). The limitation of the

[26] (a) B. Fernández, R. Rodríguez, A. Rizzo, E. Quiñoá, R. Riguera, F. Freire, *Angew. Chem. Int. Ed.*, **2018**, *57*, 3666-3670. (b) L. Palomo, R. Rodríguez, S. Medina, E. Quiñoá, J. Casado, F. Freire, F. J. Ramírez, *Angew. Chem. Int. Ed.*, **2020** *132*, 9165-9172.

[27] (a) S. Ma, X. Cao, M. Mak, A. Sadik, C. Walkner, T. B. Freedman, I. K. Lednev, R. K. Dukor, L. A. Nafie, *J. Am. Chem. Soc*., **2007**, *129*, 12364-12365. (b) D. Kurouski, R. A. Lombardi, R. K. Dukor, I. K. Lednev, L. A. Nafie, *Chem. Commun.*, **2010**, *46*, 7154-7156.

[28] B. Nieto-Ortega, R. Rodríguez, S. Medina, E. Quiñoá, R. Riguera, J. Casado, F. Freire, F. J. Ramírez, *J. Phys. Chem. Lett.,* **2018**, *9*, 2266-2670.

[29] E. Yashima, *Polym. J.,* **2010**, *42*, 3-16.

technique is determined by the sample preparation. Only with well-ordered monolayers is possible to discern structural parameters from AFM images.[30,31]

Two factors are crucial for the preparation of monolayers. In the first place, the selection of adequate substrate since this can influence the intramolecular interactions between chains and the helical conformation. Secondly, the sample deposition methodology, where several methods are available:

DROP CASTING

Drop casting technique consists in the deposition of a small amount of solution over a substrate, where the solvent is evaporated leaving the polymer on the surface. Moreover, substrate selection is based on the polarity of the polymers, the influence of the surface in the morphology of PPAs monolayers was demonstrated by Yashima and co-workers. They deposited by drop casting a copolymer based on two pendants groups —an achiral C_{60}-bound and an optically active amine— over mica and highly oriented pyrolytic graphite (HOPG). AFM results over mica substrate showed spherical aggregates based on the repulsion between hydrophobic C_{60} and hydrophilic mica (poly-**16**, Figure 9), while for HOPG substrate, extended copolymers chains and isolated particles were recovered in the AFM images for the attractive interactions between C_{60} pendants and the HOPG.[32]

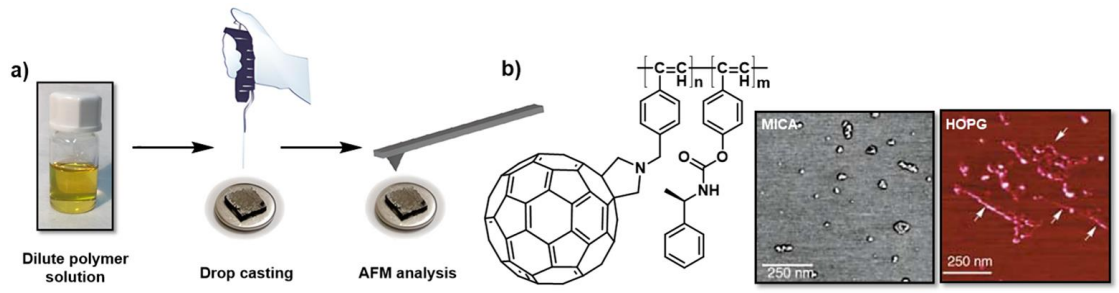

Figure 9. a) Schematic representation of drop casting deposition technique. b) Structure of poly-**16** and its AFM images by drop casting deposition over MICA and HOPG.

SPIN COATING

Spin coating is a deposition technique for the obtention of uniform monolayers with controlled thickness. The procedure consists in four steps: deposition, spin up, spin off, and evaporation (Figure 10a). Moreover, solvent evaporation of the polymer solution take place

[30] J. Kumaki, S. -I. Sakurai, E. Yashima, *Chem. Soc. Rev.*, **2009**, *38*, 737-746.

[31] F. Freire, E. Quiñoá, R. Riguera, *Chem. Rev.*, **2016**, *116*, 1242-1271.

[32] T. Nishimura, K. Takatani, S. Sakurai, K. Maeda, E. Yashima, *Angew. Chem. Int. Ed.*, **2002**, *114*, 3754-3756.

in an air/solid interphase, doing the polymer-surface interactions and the evaporation rate of the solvent critical for the obtention of monolayers.

Yashima *et al.* analyze the technique introducing long alkyl chains as pendants on PPAs to promote the self-assembly by interdigitation of pendants. A dilute solution of polymer was deposited by spin coating on HOPG. After this, it was remained overnight under a solvent atmosphere to promote the formation of ordered monolayers. Thus, poly-(*S*)-**17** and poly-(*R*)-**17** images showed a helical pitch of 2.34, a packing angle of 40° and an external *M/P* helix (from *L* and *R* alanine decyl ester respectively) (Figure 10b).[33]

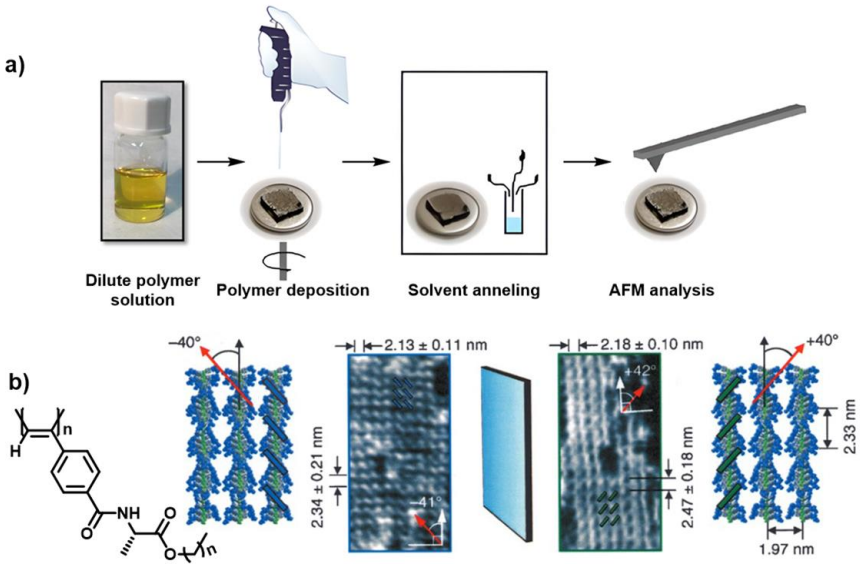

Figure 10. a) Schematic representation of spin coating deposition technique. b) Structure of poly-(*S*)-**17** and for both enantiomers 3D model and AFM images.

Alternative methodology developed by Percec *et al.* consists in apply thermal annealing instead of vapor solvent atmosphere after spin coating over HOPG and mica substrates.[34] Moreover, it was demonstrated that long alkyl chains in pendants are not essential for the obtention of 2D crystals of PPAs. Thus, in our research group, axially racemic poly-(*S*)-**18** (the anilide of (*S*)-α-methoxy-α-phenylacetic acid (MPA)) was deposited using Yashima methodology does not generate ordered monolayers due to the high dynamism of the PPA, based on the presence of two different conformations in a 1:1 equilibrium (*ap*: carbonyl and

[33] (a) S. -I. Sakurai, K. Okoshi, J. Kumaki, E. Yashima, *Angew. Chem. Int. Ed.,* **2006**, *45*, 1245-1248. (b) S. -I. Sakurai, K. Okoshi, J. Kumaki, E. Yashima, *J. Am. Chem. Soc.,* **2006**, *128*, 5650-5651.

[34] (a) V. Percec, M. Obata, J. G. Rudick, B. B. De, M. Glodde, T. K. Bera, S. N. Magonov, V. S. K. Balagurusamy, P. A. Heiney, *J. Polym. Sci., Part A: Polym. Chem.,* **2002**, *40*, 3509-3533. (b) V. Percec, J. G. Rudick, M. Peterca, S. R. Staley, M. Wagner, M. Obata, C. M. Mitchell, W. -D. Cho, V. S. K. Balagurusamy, J. N. Lowe, M. Glodde, O. Weichold, K. J. Chung, N. Ghionni, S. N. Magonov, P. A. Heiney, *Chem. Eur. J.,* **2006**, *12*, 5731-5746. (c) V. Percec, J. G. Rudick, M. Wagner, M. Obata, C. M. Mitchell, W. -D. Cho, S. N. Magonov, *Macromolecules,* **2006**, *39,* 7342-7351.

methoxy groups antiperiplanar oriented and *sp*: carbonyl and methoxy groups synperiplanar oriented) on the pendants that is transmitted to the helix.[35]

Generation of 2D crystals was promoted by addition of metal ions (M^+ for *ap* conformation and M^{2+} for *sp* conformation) to a dilute solution of polymer. Spin coating samples from these solutions was remained under a THF atmosphere overnight. Resulting AFM images show 2D crystals of polymers with helical pitch of 3.2 nm, packing angle of 60° and *M/P* helical sense based on the metal ion added (M^+ and M^{+2} respectively).

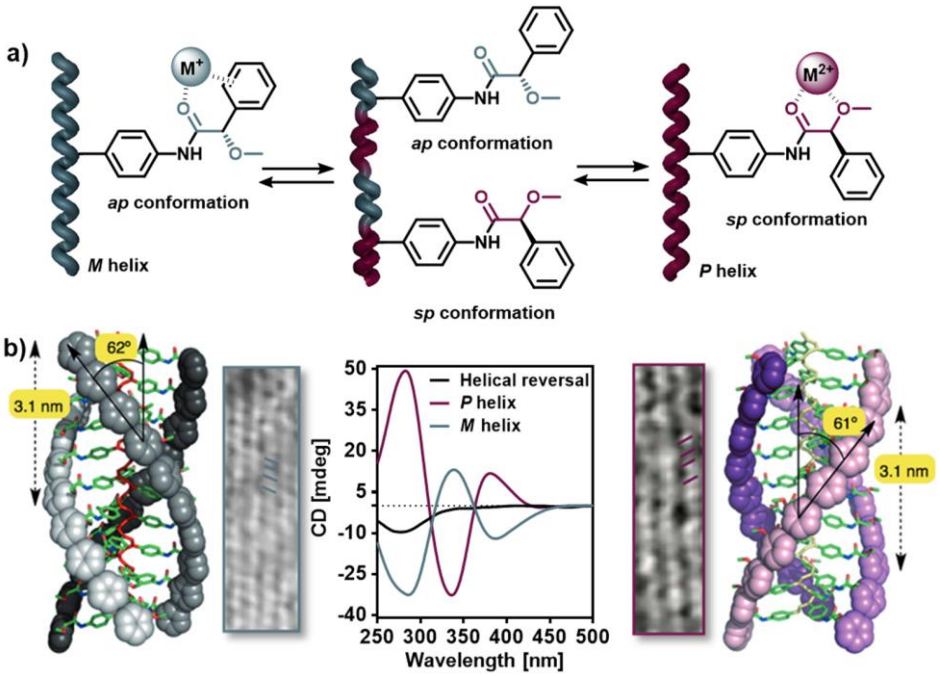

Figure 11. a) Representation of the conformational *ap/sp* equilibrium of poly-(*S*)-**18**. b) 3D model, AFM images and CD spectra of both conformations of poly-(*S*)-**18**.

LANGMUIR-BLODGETT (LB)

In this methodology, monolayers are formed by transference of the organic material deposited on the surface of a liquid to the solid support by immersion or emersion. Thus, as monolayer is formed at an air/water interphase, the hydrophobic/hydrophilic interaction between polymer and the surface is key in the monolayer formation.[36]

For PPAs, a diluted polymer solution in $CHCl_3$ (0.1 mg/mL, 200 μL) is spread dropwise via Hamilton syringe over the water surface homogeneously. After $CHCl_3$ evaporation (10 minutes), barriers are slowly closed increasing the surface pressure on a controlled way.

[35] F. Freire, J. M. Seco, E. Quiñoá, R. Riguera, *Angew. Chem. Int. Ed.,* **2011**, *50*, 11692-11696.

[36] (a) G. G. Roberts, *Langmuir-Blodgett Films*, Plenum, New York, **1990**. (b) T. Kawauchi, J. Kumaki, A. Kitaura, K. Okoshi, H. Kusanagi, K. Kobayashi, T. Sugai, H. Shinohara, E. Yashima, *Angew. Chem. Int. Ed.,* **2008**, *47*, 515-519.

Finally, the substrate is removed from water taking away the monolayer formed over the water surface (Figure 12).

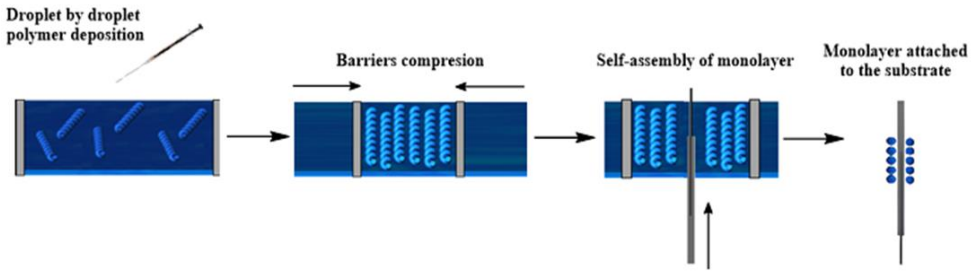

Figure 12. Schematic illustration of Langmuir-Blodgett deposition technique.

LANGMUIR-SCHAEFER (LS)

Langmuir-Schaefer methodology is a variation of Langmuir-Blodgett technique that allow the use of HOPG as substrate (better for interact with PPAs for being more hydrophobic than mica). In this methodology, monolayer is exfoliated from surface to HOPG instead to be extracted from water layer, that is not possible due to the hydrophobic properties of HOPG.[25]

The procedure is similar than for LB. The main difference is that monolayer is attached to solid support by attractive interactions when the HOPG is approached to the surface, instead of immersion the solid support (mica) in the water as happen in the LB methodology (Figure 13a).[37]

With this protocol, in our group successful results were obtained in the preparation of several monolayers. As example, great monolayers showing left- and right-handed regions of helices were obtained for poly-**18**, allowing to determine important structural parameters, confirming a *c-c* polymer with helical pitch of 3.2 nm and packing angle of 60°. Results are in concordance with the previous studies for this PPA with metal ions by spin coating deposition technique (Figure 13b). [38]

[25] M. Alzubi, S. Arias, I. Louzao, E. Quiñoá, R. Riguera, F. Freire, *Chem. Commun*., **2017**, *53*, 8573-8576.

[37] (a) A. Ulman, *An introduction to Ultrathin, Organic films –From Langmuir-Blodgett To Self-Assembly,* Academic Press, **2013**. (b) R. Rodríguez, J. Ignés-Mullol, F. Sagués, E. Quiñoá, R. Riguera, F. Freire, *Nanoscale,* **2016**, *8*, 3362-3667.

[38] (a) S. Sakurai, K. Kuroyanagi, R. Nunokawa, E. Yashima, *J. Polym. Sci., Part A: Polym. Chem.,* **2004**, *42*, 5838-5844. (b) S. Matsushita, K. Akagi, *J. Am. Chem. Soc.,* **2015**, *137*, 9077-9087. (c) K. Akagi, *Chem. Rev.,* **2009**, *109*, 5354-5401.

[16] R. Rodríguez, E. Quiñoá, R. Riguera, F. Freire, *J. Am. Chem. Soc.,* **2016**, *138*, 9620-9628.

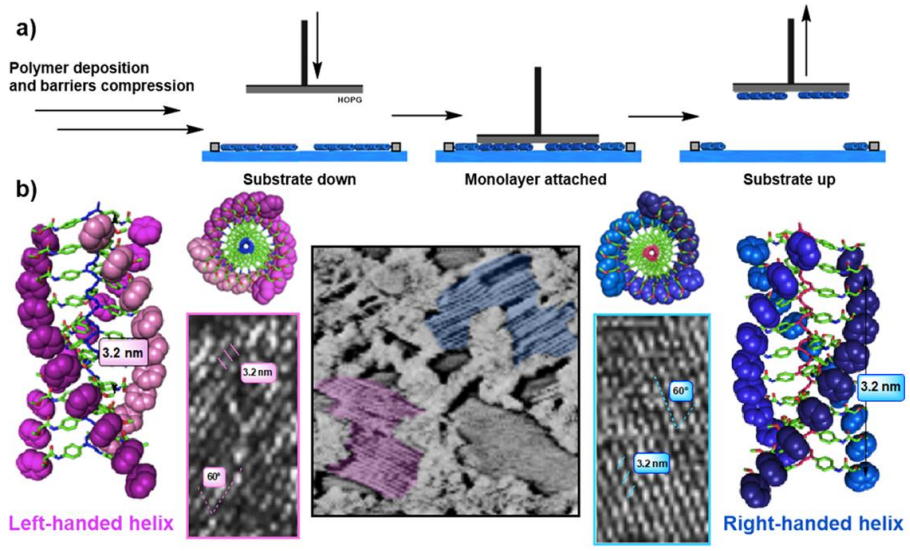

Figure 13. a) Conceptual representation of Langmuir-Blodgett methodology. b) AFM images and 3D models of *M* and *P* helices of poly-(S)-**18**.

Similarly, several *meta* substituted PPAs were analyzed with this methodology in our group. Among these studies, as interesting example the poly-(*S*)-**15** was determined as an equilibrium of *c-c* and *c-t* helices. A compressed *c-c* with 3.2 nm of helical pitch, 60° of packing angle and internal and external *P* helices, rotating in the same direction. The second, a stretched *c-t* backbone with 5.3 nm of helical pitch, 40° of packing angle and helices rotating in opposite directions, internal *P* helix and external *M* helix (Figure 7, section 2.1).[16]

4. Properties of PPAs

Diverse properties related to the secondary structure of PPAs, mainly helical sense and elongation, have been deeply studied for the structure-function relationship of these polymers and the resulting potential applications in drug delivery, as sensors, etc.

4.1 Helix induction

PPAs prepared from achiral monomers presents a 1:1 mixture of *M* and *P* helices. Helical induction results of the non-covalent interaction with chiral external stimuli (e.g., chiral molecules or chiral solvents) that induce a preferred helical sense, resulting in optically active helical polymers.

First example of this phenomenon was reported by Yashima and co-workers. An optically inactive poly(carboxy)phenylacetylene (poly-**19**) dissolved in DMSO was mixture with chiral amines. Interaction between achiral carboxylic functional groups as pendants and chiral amine results in an acid-base interaction inducing a preferred helical sense

confirmed by CD. Moreover, this process is reversible by acid addition (e.g., trifluoracetic acid) and it was demonstrated also in gel and solid state (Figure 14a).[39]

4.2 Memory effect

Memory effect is a phenomenon that consists in the remaining of the helical sense after removing the chiral external stimuli. Prof. Yashima report this phenomenon replacing a chiral amine by an achiral one, monitoring CD signal demonstrate that no variations on helical sense happen when the chiral external stimuli was removed. The helical sense after chiral amine removed is stabilized by electrostatic repulsions between carboxylic groups on the pendant and the achiral amine (Figure 14b).[40]

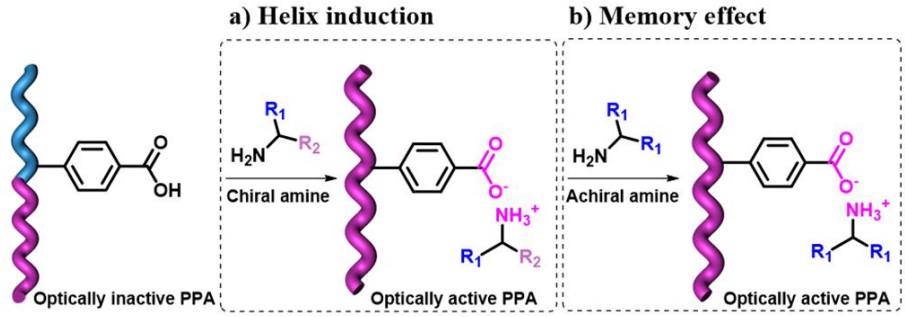

Figure 14. Schematic illustration of a) Helix induction and b) Memory Effect.

4.3 Chiral amplification

Chiral amplification consists in the addition of chiral or achiral external stimuli to an axially racemic helical polymer, increasing the chiral content by formation of covalent or non-covalent interactions.

An interesting example of this phenomenon was described in our research group, poly-(*S*)-**18** derived from the anilide of α-methoxy-α-phenylacetic acid (MPA) presents a null CD on the vinylic region (1:1 equilibrium of left- and right-handed helices) despite presents a chiral center on the pendant group. This polymer is axially racemic due to the equilibrium between *ap* conformation (dihedral angle [C=O-C-OMe] ca. 180°) and *sp* conformation (dihedral angle [C=O-C-OMe] ca. 0°) on the pendant groups.[35] However, addition of small amount of metal ions (e.g., Li^+ or Ba^{2+}) shifts the equilibrium generating and optically active polymer whose helical sense (*M/P*) can be controlled with the metal valence. Thus, monovalent metal ions (e.g., Ag^+ or Li^+) stabilizes the *ap* conformation (*M* helix) by

[39] (a) E. Yashima, T. Matsushima, Y. Okamoto, *J. Am. Chem. Soc.,* **1995**, *117*, 11596-11597. (b) Y. Hase, K. Nagai, H. Iida, K. Maeda, N. Ochi, K. Sawabe, K. Sakajiri, K. Okoshi, E. Yashima, *J. Am. Chem. Soc.,* **2009**, *131*, 10719.

[40] E. Yashima, K. Maeda, Y. Okamoto, *Nature*, **1999**, *399*, 449-451.

[35] F. Freire, J. M. Seco, E. Quiñoá, R. Riguera, *Angew. Chem. Int. Ed.* **2011**, *50*, 11692-11696.

coordination to carbonyl group and phenyl group of the pendant. While divalent metal ions (e.g., Ba^{2+} or Ni^{2+}) stabilizes the *sp* conformation (*P* helix) for coordination to both carbonyl groups of the pendant (Figure 11a, section 2.3.5). Besides, the amount added of a donor cosolvent (e.g., MeOH) can disrupt the cation-π interaction (metal ion-aryl ring interaction) —without disturb the chelation between carbonyl group and metal ion—, turning the *ap* to *sp* conformation and consequently *M* to *P* helix.[41]

Moreover, since the reported of the chiral amplification phenomenon, several processes were studies such as Sergeants and Soldiers Effect, Chiral Coalition, Chiral Conflict, Majority Rules or Domino effect. Some of these are described below.

4.3.1 Sergeants and Soldiers Effect

The Sergeants and Soldiers Effect is a particular case of chiral amplification where a copolymer is prepared by combination of a small amount of a chiral monomer (sergeant) with an achiral one (soldier).

This phenomenon was reported by Green *et al. in* 1988 with poly(isocyanate)s.[42] Later, was studied for several static and dynamic helical polymers (e.g., poly(methacrylate)s (poly-**1**, Figure 2), poly(silane)s (poly-**6**, Figure 3), or poly(acetylene)s (poly-**7**, Figure 3) (Figures 2 and 3 in section 1.1).

As limitation, the helical sense is determined by the chirality of the Sergeant. Interestingly, our research group report a Sergeant and Soldiers effect without this restriction. As it's described in detail at the beginning of this subsection (3.3) poly-**18** presents and axially racemic mixture of left- and right-handed helices as result of its conformational equilibrium between *ap* and *sp* conformation at the pendant. Therefore, copolymerization of an achiral monomer (Soldier) with a small percentage of monomers derived from anilide of MPA (Sergeant) generates an optically inactive copolymer. However, when a small amount of metal ion is added the *ap/sp* conformational equilibrium of the MPA moiety shifts towards *ap* (M^+) or *sp* (M^{2+}) conformation inducing and *M* or *P* helix respectively. Then, this chiral amplification on the MPA moiety is transferred by Sergeant and Soldier Effect to achiral monomers and as result to all helix (Figure 15).[43]

[41] S. Arias, F. Freire, E. Quiñoá, R. Riguera, *Polym. Chem*., **2015**, *6*, 4725-4733.

[42] (a) M .M. Green, J. -W. Park, T. Sato, A. Teramoto, S. Lifson, R. L. B. Selinger, J. V. Selinger, *Angew. Chem. Int. Ed.*, **1999**, *38*, 3138-3154. (b) M. M. Green, N. C. Peterson, T. Sato, A. Teramoto, R. Cook, S. Lifson, *Science*, **1995**, *268*, 1860-1866. (c) M. M. Green, B. A. Garetz, B. Munoz, H. P. Chang, S. Hoke, R. G. Cooks, *J. Am. Chem. Soc.,* **1995**, *117*, 4181-4182.

[43] K. Cobos, E. Quiñoá, R. Riguera, F. Freire, *J. Am. Chem. Soc.,* **2018**, *38*, 12239-12246.

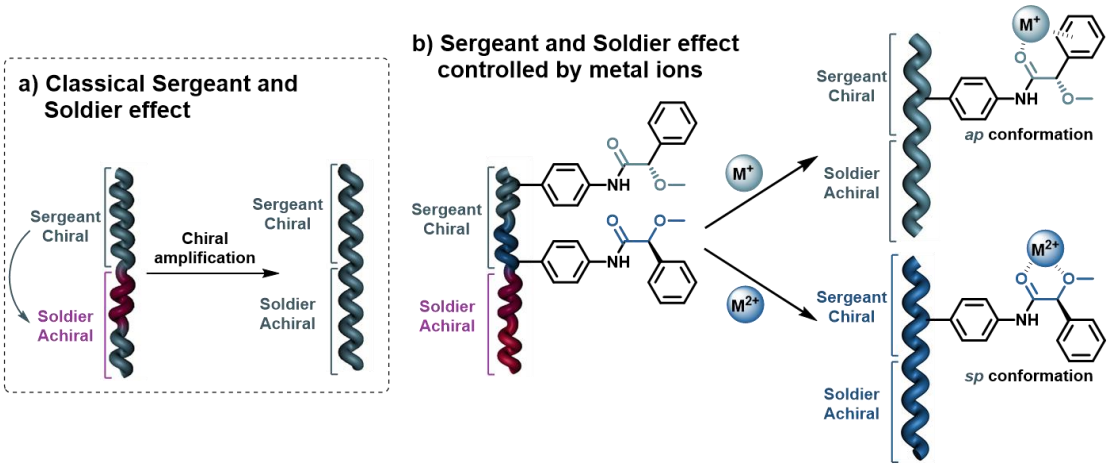

Figure 15. a) Schematic representation of the classical Sergeants and Soldiers Effect. b) Sergeant and Soldiers Effect controlled by metal ion coordination over the ap/sp equilibrium of poly-(*S*)-**18**.

4.3.2 Majority Rules

Majority Rules is a phenomenon based on a cooperative effect. When two monomers are copolymerized in similar proportion (e.g., 51%-49%) the one found in minor proportion adopts the helical sense of the majority to avoid the formation of reversals (Figure 16a).

Moreover, this effect is also observed in helical polymers by non-covalent interactions. As example, Yashima and co-workers prepared a PPA (poly-**20**) bearing an aza-18-crown ether as pendant. This achiral polymer (CD=0) was mixture with a chiral amino acid generating an optically active supramolecular complex, with a preferred helical sense determined by the enantiomeric excess of the amino acid with a strong sensitivity (0.005% of excess is enough to adopt a single helical sense).[44]

4.3.3 Domino Effect

Domino effect consists in the incorporation of chiral residues by covalent or non-covalent interactions at the terminal positions of achiral polymer/oligomers chains, inducing a preferred helical sense (Figure 16b) in the main chain.

An interesting work on this effect was reported by Inai *et al*. They prepared optically inactive oligopeptides, with unprotected N-terminal positions, based on α-aminoisobutiric acid (Aib) and (Z)-α,β-didehydrophenylalanine (ΔᶻPhe) (poly-**21**) or Aib and (Z)-β-(4,4'-

[44] R. Nonokawa, E. Yashima, *J. Am. Chem. Soc.*, **2003**, *125*, 1278-1283.

biphenyl)- α,β-didehydropalanine (ΔᶻBip) (poly-**22**). The helical induction is transferred by covalent attach to the N-terminal position promoting the complete folding of the helix.[45]

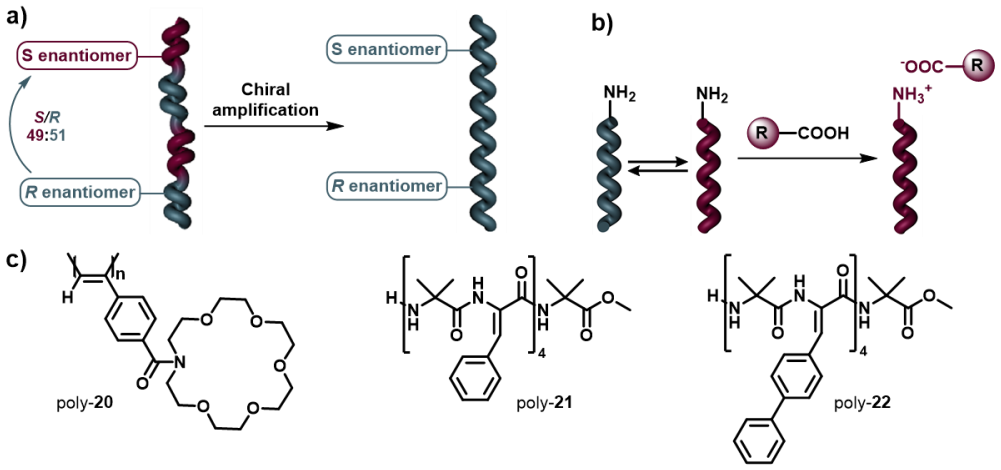

Figure 16. Schematic representation of a) Majority rules and b) Domino effect. c) Structures of the cited compounds.

4.4 Helical inversion

Helical inversion is a phenomenon of dynamic helical polymers that consists in the reversible interconversion between *M* to *P* or *P* to *M* helices, that can be promoted by several external stimuli (e.g., solvents polarity, temperature, metal ions, light irradiation, etc).

Several works about this phenomenon were reported in our research group. As example, a group of PPAs bearing *L*-amino acids methyl ester (e.g., *L*-Alanine methyl ester, *L*-Valine methyl ester, *L*-Leucine methyl ester, etc) were prepared. The helical sense of these *cis-transoidal* polymers (2:1 helix, with internal and external helices rotating in opposite sense), was studied by monitoring the vinylic CD signal showing a *M* internal helix in non-donor solvents (e.g., $CHCl_3$) and a *P* internal helix in more donor solvents (e.g., THF) (Figure 17a).

Furthermore, by addition of metal ions (e.g., Ba^{+2}, Ni^{+2}, Ag^{+}) helical inversion from *M* to *P* helix was also promoted. Infrared studies demonstrates that *P* helix is stabilized by the syn conformation induced by complexation of both carbonyl groups with the metal ion (dihedral angle between carbonyl groups close to 0°). Also, a second helical inversion, recovering starting *M* internal helix, was demonstrated increasing the ratio of donor cosolvent (MeOH), that induce the anti conformation (dihedral angle between carbonyl groups close to 180°) by solvation of metal ions (Figure 17b).[46]

[45] (a) Y. Inai, H. Komori, N. Ousaka, *Chem. Rec.*, **2007**, *7*, 191-202. (b) N. Ousaka, Y. Inai, *J. Org. Chem.*, **2009**, *74*, 1429-1439.

[46] S. Arias, M. Núñez-Martínez, E. Quiñoá, R. Riguera, F. Freire, *Polym. Chem.*, **2017**, *8*, 3740-3745.

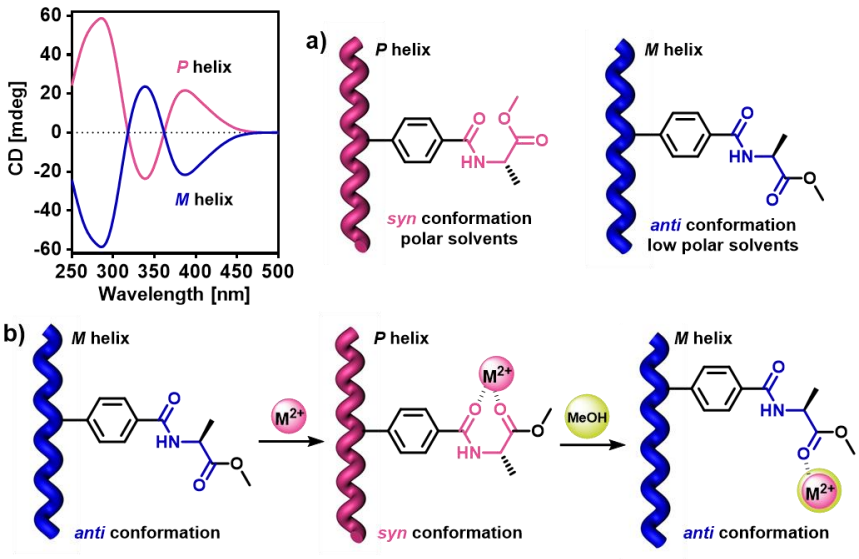

Figure 17. A PPA bearing *L*-Alanine methyl ester as pendant group (poly-(*S*)-**23**) as example of helical inversion due to a) solvents polarity and b) metal ions.

4.5 Control of chain length in PPAs

Together with the helical sense, the elongation of the polymer is the other structurally key factor. The degree of compression of the helical scaffold is controlled by the structure and the interactions of the pendant groups. Moreover, changes in the length (compression/stretching) can be promoted by external stimuli (e.g., temperature, solvents polarity, etc.) and can be monitored by UV-Vis absorption of the polyene backbone.[47]

Interesting research in this topic was reported by Tabata's group. They presented a PA in which coexists three scaffolds at the same time (one compressed and two stretched). Moreover, population among helices was modified using external stimulus. Temperature dependent studies demonstrate that a low temperature increases the population of the compressed helix, reaching an approximated population of 1:1:1 at 0 °C.[19]

Our research group, reported a PPA as example of the elongation control, the anilide from (*R)*-α-methoxy-α-trifluoromethyl-α-phenylacetic acid (MTPA)(poly-(*R*)-**24**). This can modulate at the same time the elongation and the helical sense by interaction with solvents properties (solvent polarity and donor ability).

First, solvent polarity allows to control the *ap/sp* equilibrium between carbonyl and methoxy group modifying the helical sense. In low polar solvents (e.g., $CHCl_3$) an *ap*

[47] M. Núñez-Martínez, S. Arias, E. Quiñoá, R. Riguera, F. Freire, *Chem. Mater.*, **2021**, *33*, 4805-4812.

[18] (c) Y. Yoshida, Y. Mawatari, A. Motoshige, R. Motoshige, T. Hiraoki, M. Wagner, K. Müllen, M. Tabata, *J. Am. Chem. Soc.*, **2013**, 135, 4110-4116.

conformation of carbonyl and methoxy groups is adopted inducing a left-handed helical sense. While, in more polar solvents (e.g., THF) a *sp* conformation between carbonyl and methoxy groups induces a right-handed helical sense.

Besides, donor ability of the mentioned solvent can control the elongation of the helix at the same time. Thus, in $CHCl_3$ —a non-donor solvent—, amide group adopts a *trans* conformation, that has been reported as the most common conformation due to the stabilization promoted by intramolecular hydrogen bonds between vicinal pendants. On the other hand, in THF —a donor solvent—, amide group adopts a *cis* conformation due to the interaction with the donor solvent resulting in a stretching of the helix. As result, this polymer can adopt four possible conformations that modulate sense and elongation (Figure 18).[48]

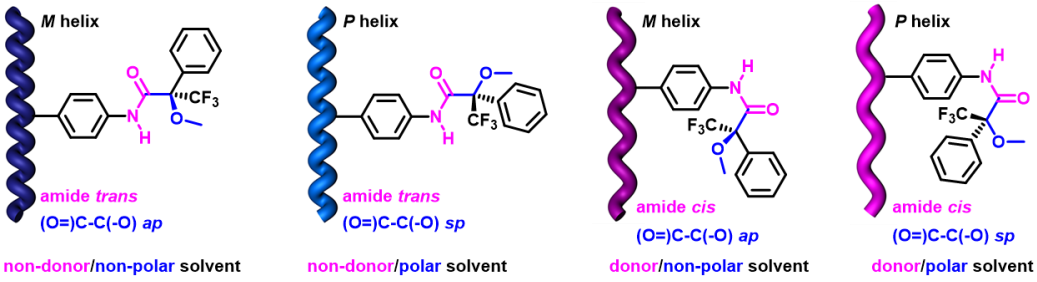

Figure 18. Representation of the four possible conformations of poly-(*R*)-**24** based on donor and polar character of the solvent and its influences on the sense and elongation of the helix.

Another more recent work in our group describes the influence of the substitution pattern of the aryl ring (*para*, *meta* and *ortho*) over the elongation. *Para*, *meta* and *ortho* PPA bearing MPA pendants (described in detail in section 3.3) (poly-**18**, poly-**15** and poly-**25** respectively) were prepared and differences in elongation and also dynamic behavior were found. The *para*-substituted *(*poly-**18**) presents a compressed *cis-cisoidal* and highly dynamic helix. *Meta*-substituted (poly-**15**) presents a less dynamic behaviour and was found as a mixture of a compressed *cis-cisoidal* and a stretched *cis-transoidal* helix. Finally, *ortho*-substituted (poly-**25**) was characterized as extremely stretched *cis-transoidal* polymer, that generates helical fibers instead individual helices and shows a poor solubility in common organic solvents and a static behavior (Figure 19).[16]

[48] S. Leiras, F. Freire. J. M. Seco, E. Quiñoá, R. Riguera, *Chem. Sci.,* **2013**, *4*, 2735-2743.

[16] R. Rodríguez, E. Quiñoá, R. Riguera, F. Freire, *J. Am. Chem. Soc.,* **2016**, *138*, 9620-9628.

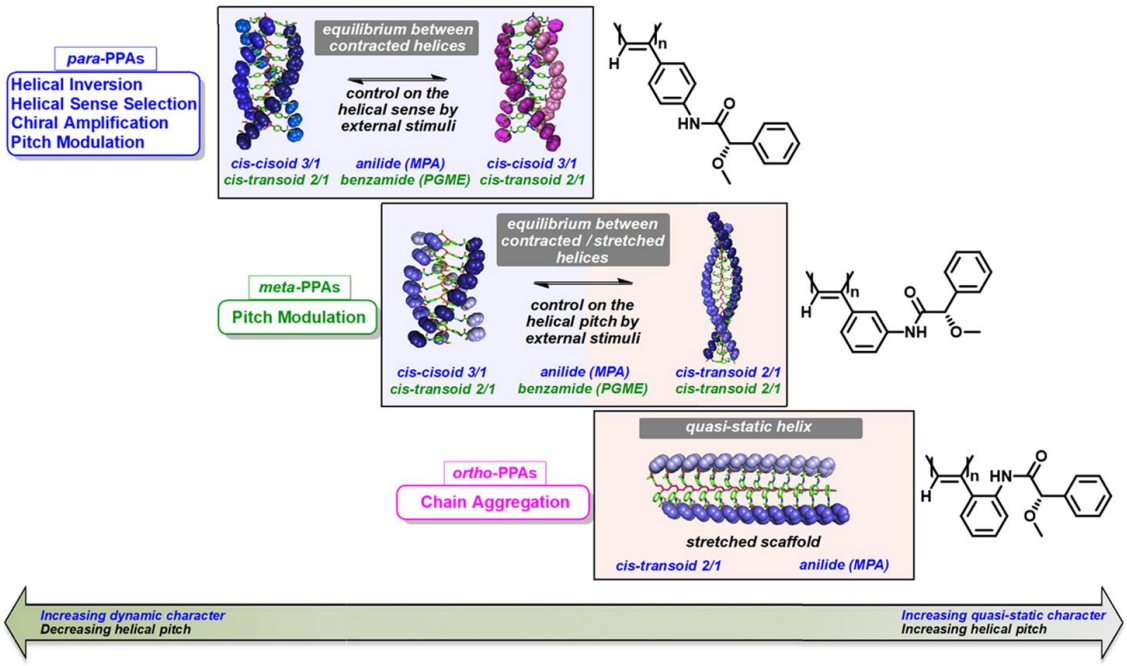

Figure 19. Schematic representation of the effect on aromatic substitution pattern in PPAs.

5. Stability of PPAs

Stability of poly(phenylacetylene)s is strong linked to the polyene backbone reactivity. Several mechanisms of polyene degradation have been described.

5.1 Thermal and oxidative degradation

During decades the mechanism of thermal degradation of the polyene backbone was object of study due to the contradictory experimental reports of several groups under different temperature and atmosphere conditions.[49] Finally, Percec and co-workers demonstrate that mechanism in solution and solid phase is the same. This consists in an intramolecular cyclization followed by a chain cleavage of the polyene chain, resulting in the formation of 1,3,5-trisubstituted benzene ring under inert atmosphere or vacuum. Moreover, they found that different proposed mechanisms are the result of the interference of a parallel oxidation process under air conditions.

For this result, they monitored the *cis* content evolution with time by NMR under different conditions. First, several polymer samples on $CDCl_3$ at 45 °C and under ambient atmosphere or N_2 was analyzed. Results show that in all cases the formation of 1,3,5-

[49] (a) J. Sedlacek, J. Vohlidal, Z. Grubisic-Gallot, *Makromol. Chem. Rapid. Commun.*, **1993**, *14*, 51-53. (b) T. Masuda, B. -Z. Tang, T. Higashimura, H. Yamaoka, *Macromolecules,* **1985**, *18*, 2369-2373. (c) S. M. A. Karim, R. Nomura, T. Masuda, *J. Polym. Sci. Part. A: Polym. Phys.,* **2001**, *39*, 3130-3136 (c) Kong, X.; Lam, J. W. Y.; Tang, B. Z.; *Macromolecules,* **1999**, *32*, 1722-1730.

triphenylbenzene was found. However, they found that under air the degradation is accelerated and, if the exposition to air is prolonged, a parallel oxidative process was found.[50]

Therefore, thermal reactivity of poly(phenylacetylene)s can be analyzed as a two steps reaction:

First step, formation of 1,3-cyclohexadiene repeating units via cyclization of triene sequences along the polyene backbone. It is proposed that the reaction is a 6π electrocyclic ring closures both in solid phase and solution. Moreover, this step is independent of the solvent (under vacuum or inert atmosphere) and in presence of air or light a small decrease in the molecular weight take place. In presence of O_2 or light in $CHCl_3$, cyclization rate is much faster due to the HCl formed by the decomposition of $CHCl_3$. Simultaneous presence of O_2 and light induce an oxidative parallel process to the cyclization whose mechanism is not clear. However, it is proposed a [2+2] cycloaddition of singlet O2 with a backbone alkene generating a transient 1,2-dioxetane that decomposes generating several aldehyde products.[51]

Second step consists on the aromatization of 1,3-cyclohexadiene units generated in the step one. High temperatures are necessary for the activation of this step. However, the aromatization takes place in random positions of the polyene backbone, generating the 1,3,5-triphenylbenzene in low yield.[52] As result, by-products are generated due to the aromatization requires 3 acetylene units and the random character of the thermal cyclization promotes the generation of fragments mismatched (Figure 20).

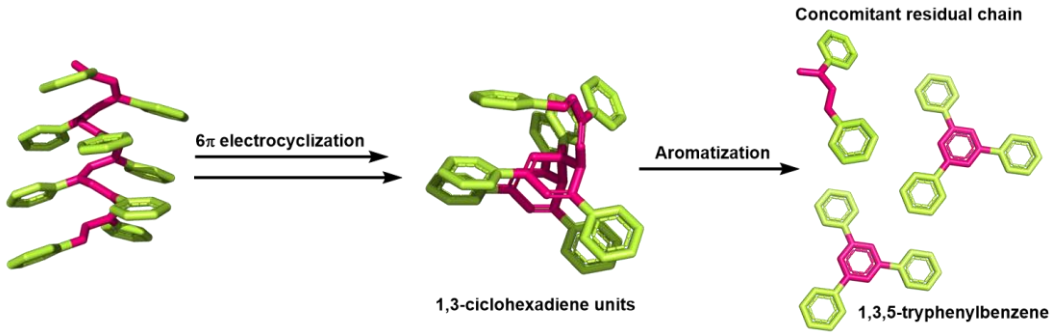

Figure 20. Representation of the degradation mechanism by intramolecular electrocyclization.

[50] V. Percec, J. Rudick, P. Nomber, W. Buchowicz, J. *Polym. Sci., Part A: Polym. Chem.,* **2002**, *40*, 3212-3220.

[51] (a) V. Percec, J. G. Rudick, *Macromolecules,* **2005**, *38*, 7241-7250. b) J. Vohlídal, D. Rédrová, M. Pacovská, J. Sedlácek, *Collect. Czech. Chem. Commun.,* **1993**, *58*, 2651-2662.

[52] S. Matsunami, T. Watanabe, H. Kamimura, T. Kakuchi, F. Ishii, K. Tsude, *Polymer,* **1996**, *37*, 4853-4855.

5.2 Radical *cis-trans* isomerization

Tabata's group has reported a *cis-trans* isomerization of *cis-transoid* PPAs induced by pressure. The compression of the polymer enhance the more stable trans configuration by a radical mechanism (Figure 21) confirmed by Electronic Paramagnetic Resonance (EPR).[53, 19b] Alternatively, polymers can be isomerized since *cis* to *trans* polyene by mechanochemically grinding treatment at 77 K.[19]

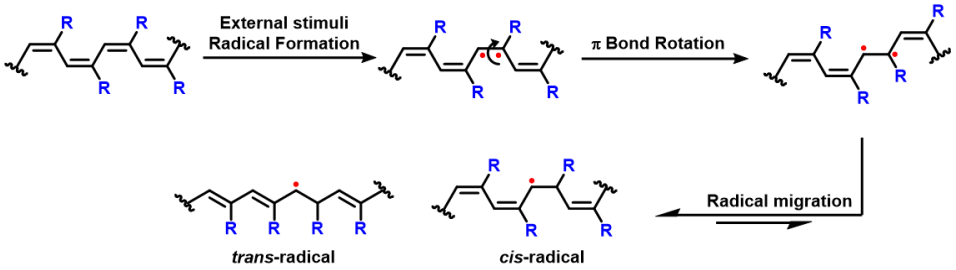

Figure 21. Schematic representation of the radical isomerization mechanism of PPAs.

5.3 Photochemical reactivity

More recently, Liu and co-workers reported a new reaction, highly selective photocyclic aromatization (SCAT), to prepare 1,3,5-trisubstitued benzene derivatives from polyene reactivity. Unlike the thermal reactivity, photocyclic aromatization is highly selective under specific conditions, the characteristics of the reactions are: [54]

1. It is a quantitative reaction, only the corresponding 1,3,5-trisubstitud benzene derivative is formed under the appropriate conditions.
2. It is intramolecular, only take place between three adjacent monomer units in one macromolecule.
3. It is stereospecific and topochemical, the reactivity depends on the conformation and configuration of the polymer in the reaction conditions.
4. Highly selectivity (100 %) under controlled conditions and visible light without heating.
5. It is a solid state reaction, in solution process was described as a non-selective degradation.
6. The resulting cyclic trimers could form a supramolecular polymer.

[53] M. Tabata, Y. Tanaka, Y. Sadahiro, T. Sone, K. Yokota, I. Miura, *Macromolecules,* **1997**, *30*, 5200-5204.

[19] (b) K. Huang, Y. Mawatari, A. Miyasaka, Y. Sadahiro, M. Tabata, Y. Kashiwaya, *Polymer,* **2007**, *48*, 6366-6373.

[19] (c) A. Miyasaka, Y. Mawatari, T. Sone, M. Tabata, *Polym. Degrad. Stab.,* **2007**, *92*, 253-259.

[54] (a) L. Liu, T. Namikoshi, Y. Zang, T. Aoki, S. Hadano, Y. Abe, T. Kaneko, *J. Am. Chem. Soc.*, **2013**, *135,* 602-605. (b) M. Miyata, T. Masahiro, E. Hiromichi, K. Takashi, A. Toshiki, *Chem. Lett.,* **2014**, *43*, 1476-1477.

The reaction takes place in two steps. First, a photochemical 6π electrocyclic ring-closing reaction (conrotatory process) that limits the reaction. After this, a fast aromatization generates the corresponding 1,3,5-trisubstitued benzene derivatives (Figure 22). Furthermore, for the structurally requirements the reaction only happens for *cis-cisoidal* PPAs (more compressed than *cis-transoid*) and even and even among these, it is estimated that the distance between the carbons that will form the covalent bond must be lower than 4 Å. While, selective is based on domino effect, reaction starts at the end of the polymers and extend orderly along the chain, avoiding formation of byproducts as happen in the thermal degradation due to the random positions on which cyclization occurs.

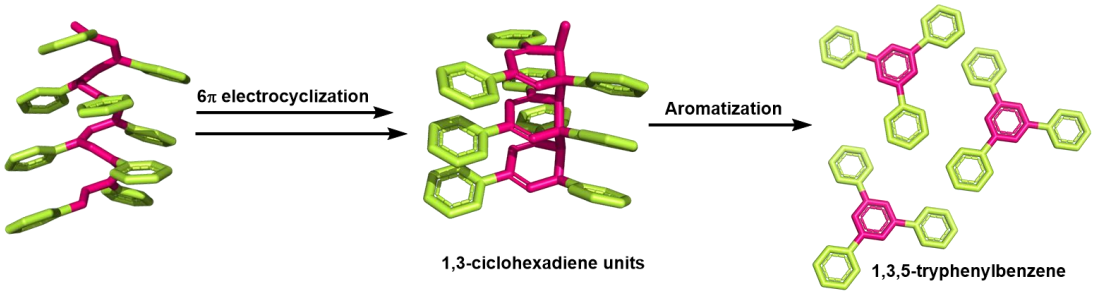

Figure 22. Representation of two steps mechanism of SCAT reaction.

6. PPAs response modulation

We have seen several examples for modulate classical pendant design for PPAs with external stimuli that acts on the equilibrium in the pendant group both in anilides (*ap/sp* equilibrium between carbonyl and methoxy groups) as in benzamides (*anti/syn* equilibrium between two carbonyl groups). In addition, there are some examples to modulate new materials based on the combination of this equilibrium with other functional groups. As an example, preparation of chiral gold-PPA nanocomposites was recently achieved in our group, introducing a thiol functional group on the pendant for link the polymer to the gold nanoparticles. [55] In this line, we will describe in this section the properties and functionalities of several functional groups that we will combine to PPAs in later chapters to create new polymeric materials.

6.1 Photoresponse in PPAs

In the section 4.3 we have seen the reported photoreactivity of PPAs. This focused on non-reversible reactions on the polyene backbone under visible light while the classical pendant groups are inert to light stimuli. However, this process is irreversible, as alternative

[55] J. Bergueiro, M. Núñez-Martínez, S. Arias, E. Quiñoá, R. Riguera, F. Freire, *Nanoscale Horiz.*, **2020**, *5,* 495-500.

an interesting functional group to combine with PPAs is the azo group, since depending on the substituents that present, its absorption wavelength can be tuned and its isomerization is reversible by light or temperature.[56]

Organic azo compounds are a subtype of azo group derived from the diazene (HN=NH), within which there are subgroups depending on the residues attached to the azo (aliphatic, aromatic or mixture). Spectroscopically, azo group is characterized by an ethenic π-electron system with antisymmetric wavefunctions relative to the molecular plane and a unique n-electron system. The state of the n-orbital determines the photochemical behavior, and the aromatic azo compounds present a π-system more extended than the aliphatic, resulting in increasing photostability with the n-π* transition in the UV-Vis region (colorless compounds) and lower energy barriers for the photoisomerization that can be easy tuned by the character of the substitution group or groups.[57]

In aromatic azo compounds, azobenzenes are classify based on the UV-Vis spectrum as azobenzene-type molecules, aminoazobenzene-type molecules (substituents as amino, a donor group) that promote a red shift of the UV-Vis spectrum and lower half-lives and *pseudo*-estilbene (substituents as an amino and a nitro group, a donor and an acceptor group respectively) that promote a greater red shift with very short half-lives (Figure 23a).[58]

Absorption bands can be easily assigned using the azobenzene molecule as example. For this case, the *E* isomer have in the UV spectrum the weak n–π* transition at 440 nm and a strong π–π* transition close to 320 nm while the *Z* isomer have a stronger n–π* transition at 440 nm and other two transitions in the UV region (280 nm and 250 nm) (Figure 23b). Moreover, the *E* conformation of azobenzene is almost planar while the *Z* adopt a bent conformation with the phenyl ring twisted close to 55° in relation to the plane of the azo. For the *E*-*Z* isomerization, four possible mechanisms of isomerization are proposed (rotation, inversion, concerted inversion and inversion-assisted rotation, Figure 23c). For each case the pathway of the isomerization and the behavior of the azobenzene in the medium is dependent of electronic transition involved in the photochemistry excitation, number and type of substituents, environment (solvent, presence of metal ions,

[56] H. Durr, H. Bouas-Laurent, *Photochromism: molecules and systems*, *Elsevier*, **2003**.

[57] L. M. Blinov, T. Kawai, M. V. Kozlovsky, Y. Kawata, K. Ichimura, T. Seki, S. Kawata, *Photoreactive organic thin films*, Elsevier, **2002**.

[58] Z. Mahimwalla, K. G. Yager, J. I. Mamiya, A. Shishido, A. Priimagi, C. J. Barrett, *Polym. Bull.,* **2012**, *69*, 967-1006.

temperature and pressure) and its position in the case of macromolecules (in chain, side chain or acting as cross-linker).[59]

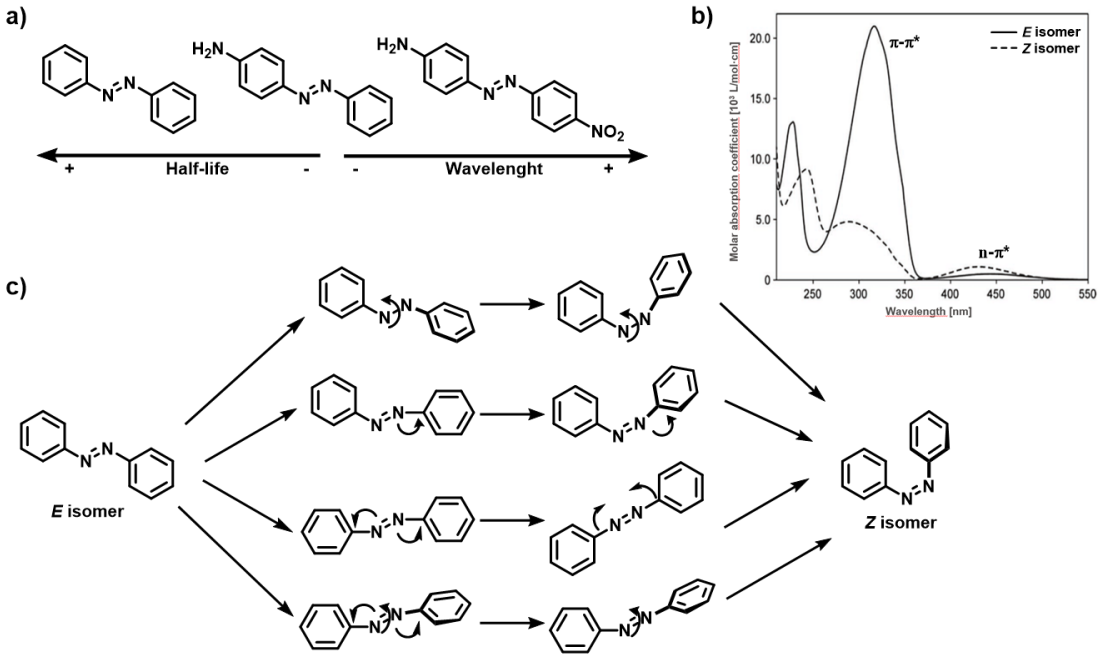

Figure 23. a) Representative examples of different types of azobenzenes. b) UV-Vis spectrum of *E* and *Z* isomers of azobenzene. c) Proposed mechanisms for *E*-*Z* isomerization of azobenzenes.

In the azobenzene molecule, and the majority of substituted azo aromatic compounds the more stable *E* isomer can be isomerized to *Z* irradiating with UV light (on the π–π* transition). While the reversible process (*cis* to *trans* isomerization) can be promoted by light (irradiation on n–π* transition), darkness or temperature. For discrete molecules the photochemical conversion is usually of seconds while thermal relaxation can consume hours or days. Moreover, in the substituted aromatic azo compounds in *ortho*- and *para*-positions, a second photochromism reaction is possible when the functional group attached is a hydroxy- or amino- group. Interesting example of this phenomenon was reported by Watchtveitl and co-workers. They analyze the behavior after photoexcitation of *trans*-(phenyldiazenyl)phenol substituted in *ortho*-, *meta*-, and *para*-. Results demonstrate that deactivation of *trans*-4-(phenyldiazenyl)phenol can go by a enol/keto tautomerism, modulating the energy barrier of this way, instead go by the *trans*-*cis* isomerization (Figure 24a).[60]

[59] (a) V. Marturano, V. Ambrogi, N. A. G. Bandeira, B. Tylkowski, M. Giamberini, P. Cerruti, *Phys. Sci. Rev.,* **2017**, *2*. (b) H. D. Bandara, S. C. Burdette, *Chem. Soc. Rev.,* **2012**, *41*, 1809-1825. (c) G. S. Kumar, D. C. Neckers, *Chem. Rev.,* **1989**, *89,* 1915-1925.

[60] S. Steinwand, T. Halbritter, D. Rastädter, J. M. Ortiz-Sánchez, I. Burghardt, A. Heckel, J. Wachtveitl, *Chem. Eur. J.*, **2015**, *21,* 15720-15731.

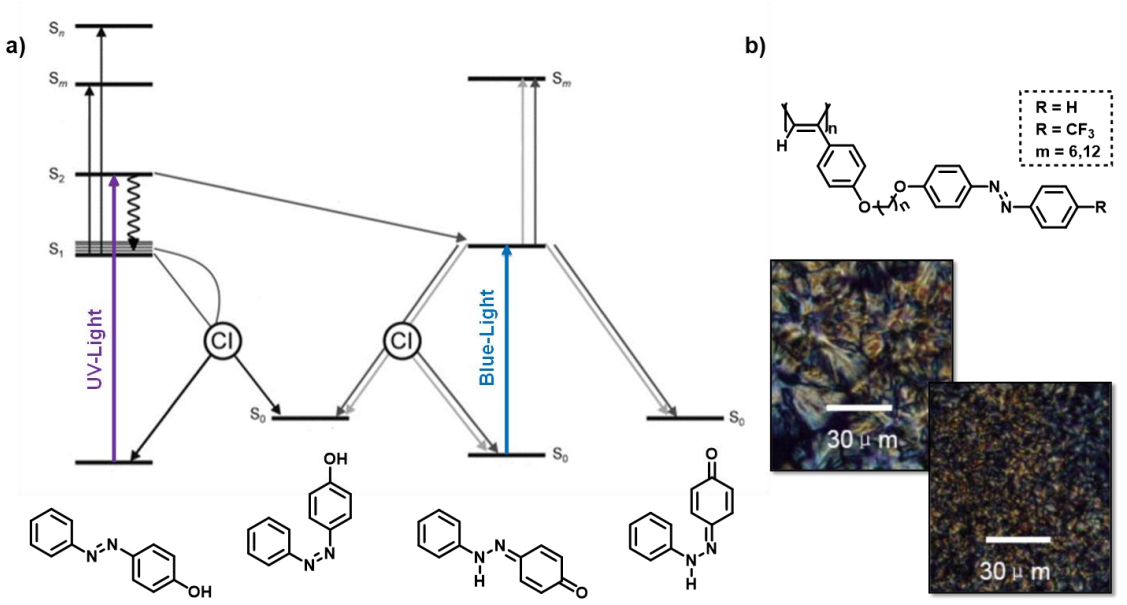

Figure 24. a) Enol/keto tautomerism as deactivation mechanism in competition with the cis/trans isomerization of the *trans*-4-(phenyldiazenyl)phenol. b) Structure of the reported examples of PPAs bearing azobenzene derivatives and their liquid crystalline properties revealed with polarizing optical microscope (POM) images.

In polymers, functionalization with azobenzenes has been extensively studied due to their potential applications for liquid crystallinity,[61] optical nonlinearity,[62] self-assembly,[63] etc. In the case of poly(acetylene)s several works describe the synthesis, characterization and some optical properties,[64] while for PPAs only some achiral polymers were prepared by Tang *et al.* introducing azobenzenes in the pendant to promote liquid-crystalline properties (Figure 24b).[65]

6.2 Chirality inducers in helical polymers

In chiral PPAs watched up to now, the pendant groups are connected to the phenylacetylene by an anilide or benzamide group. This is the simplest and most efficient way to introduce groups that can act as chiral inducers (e.g., MTPA, amino acids, etc.) to generate a preferred helical sense. However, some interesting alternatives have been analyzed, thus Yashima *et al*. reported a comparison between four possible functional

[61] I. Zebger, M. Rutloh, U. Hoffmann, J. Stumpe, H. W. Siesler, S. Hvilsted, *Macromolecules,* **2003**, *36*, 9373-9382.

[62] H. El Ouazzani, K. Iliopoulos, M. Pranaitis, O. Krupka, V. Smokal, A. Kolendo, B. Sahraoui, *J. Phys. Chem. B,* **2011**, *115*, 1944-1949.

[63] I. Tomatsu, A. Hashidzume, A. Harada, *J. Am. Chem. Soc.,* **2006**, *128*, 2226-2227.

[64] (a) Q. Zeng, Z. A. Li, Z. Li, C. Ye, J. Qin, B. Z. Tang, *Macromolecules*, **2007**, *40*, 5634-5637. (b) Z. Q. Yan, Y. F. Chen, S. Y. Guang, H. Y. Xu, L. F. Li, *Polym. Sci. Ser. B*, **2011**, *53*, 535-539. (c) G. Zhao, G. Wei, W. Zhu, F. Ke, S. Guang, F. Zhang, H. Xu, *J. Appl. Polym. Sci.*, **2018**, *135,* 46100.

[65] A. Xiao, H. Zhao, Y. Gao, J. Tong, L. Shan, Y. Chen, B. Z. Tang, *Polymer*, **2011**, *52,* 5290-5301.

groups connected to the phenylacetylene that generate *cis-transoidal* PPAs (poly-**26** to poly-**29**, Figure 25).[66] However, the main research with this functional groups focus on generate achiral PPAs and promote helicity through interaction with external stimuli (e.g., amines, fullerenes, etc.).[67]

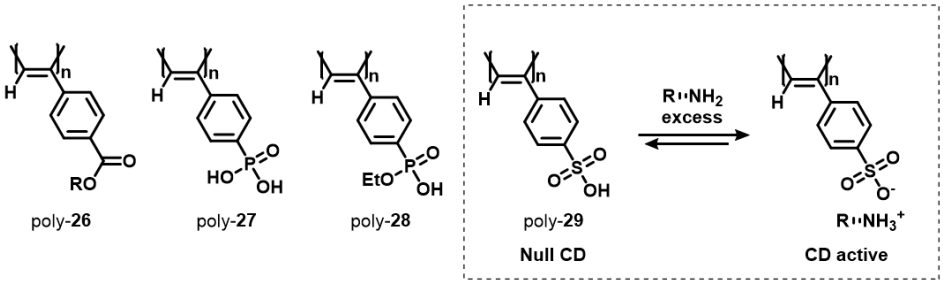

Figure 25. Structures of poly-**26** to poly-**29** and poly-**29** as example of helicity induction in this optically inactive PPAs.

Furthermore, other PPAs substituted with ester and hydroxy groups,[68] nitro groups,[69] sulfonamide groups,[70] etc. attached to the phenylacetylene has been extensively studied. However, sulfoxide group has gone practically unnoticed in PPAs chemistry, only Tabata and co-workers synthesized a PPA bearing a *n*-butylsulfoxide as pendant (poly-**30**). They found that this polymer adopts a *cis-transoidal* structure and showed that under a pressure induced a *cis-trans* isomerization of the backbone occurs, and the unpaired electron created by the rotational scission of the *cis* *C*=C bond can migrate on the alkyl sulfoxide moiety in the *cis*-radical (Figure 26, see Figure 21 in section 4.2 for radical formation).[19] Thus, a radical sulfoxide is generated by radical migration only in the *cis*-radical.

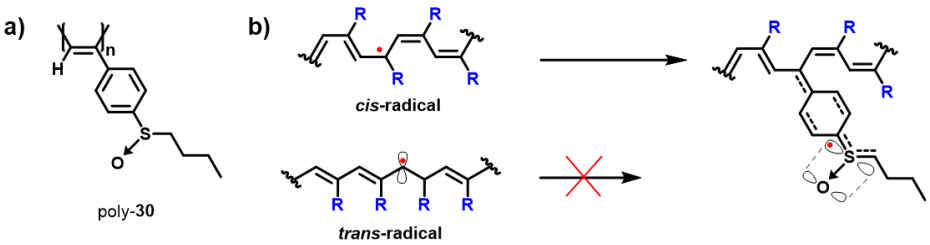

Figure 26. a) Structure of poly-**30**. b) *cis*-radical and *trans*-radical generated under pressure and radical migration to sulfoxide moiety in the *cis*-radical.

---

[66] T. Hasegawa, K. Maeda, H. Ishiguro, E. Yashima, *Polym. J.,* **2006**, *38,* 912-919.

[67] (a) H. Onouchi, D. Kashiwagi, K. Hayashi, K. Maeda, E. Yashima, *Macromolecules*, **2004**, *37,* 5495-5503. (b) T. Nishimura, K. Tsuchiya, S. Ohsawa, K. Maeda, E. Yashima, Y. Nakamura, J. Nishimura, *J. Am. Chem. Soc.*, **2004**, *126*, 11711-11717. (c) M. Morimoto, K. Tamura, K. Nagai, E. Yashima, *J. Polym. Sci. A: Polym. Chem.,* **2010**, *48,* 1383-1390.

[68] (a) Y. Gu, L. Liu, Y. Wang, C. Zhang, H. Dong, T. Aoki, *Macromolecules*, **2021**, *54*, 10216-10223. (b) M. Tabata, Y. Mawatari, *Polym. Rev.,* **2017**, *57*, 65-88. (c) Y. Zang, Y. Lun, M. Teraguchi, T. Kaneko, H. Jia, F. Miao, T. Aoki, *Membranes*, **2020**, *10*, 199.

[69] T. Sone, R. D'Amato, Y. Mawatari, M. Tabata, A. Furlani, M. V. Russo, *J. Polym. Sci. A: Polym. Chem.,* **2004**, *42,* 2365-2376.

[70] R. Sakai, E. B. Barasa, N. Sakai, S. I. Sato, T. Satoh, T. Kakuchi, *Macromolecules*, **2012**, *45,* 8221-8227.

On the other hand, Tabata and co-workers omits any information about the helical sense of the polymer, so its synthetic route probably results in a racemic mixture. Thus, one of the great advantages of the sulfoxides, the aforementioned intrinsic chirality when their carbonated substituents are different, has not yet been analyzed in PPAs. This could induce helicity without have to apply external stimuli or introduce another functional group in the pendant. Since sulfoxides have been widely and successfully used as chiral inductors, so similar behavior is expected in PPAs.[71]

These works reveal the most influence characteristics of this functional group. In the S-O bond that characterize it, oxygen does not form a p bond with the sulfur as is usual, a d_p–p_p bond is generated by overlapping of the d orbital of the sulfur and a p orbital of the oxygen. Thus, it presents a pyramidal geometry with a large energy barrier for the inversion when the carbonated substituents are different, allowing the stabilization of enantiomers. The chirality in this pyramidal structure is defined using *R/S* nomenclature by the Cahn–Ingold–Prelog (CIP) system applying convention b, *"contributions by d orbitals to bonds of quadriligant atoms are neglected'*. As result S-O bond is considered as a single bond, and the lone electron pair is assigned atomic number zero (lowest priority).[72]

Moreover, the rigid conformation, the large stereoelectronic differences between both faces (electron pair and oxygen) and the carbonated substituents of the sulfoxide, explain its effectiveness as a chiral transfer agent.[73] Finally, another interesting property that involves the sulfur bond are that the oxygen operates as acceptor of Lewis acids in the S-O bond, going fast to well-ordered states with an effective transfer of chiral information.[74]

6.3 Teleinduction in PPAs

The control of the helical induction in PPAs has been extensively studied. Thus, it is known that the capability of helical induction decreases when the distance of the chiral center to the backbone increases.[75] However, effective chiral teleinduction in PPAs has been reported in our research group, introducing flexible achiral linker (one or two glycines,

---

[19] (b) K. Huang, Y. Mawatari, A. Miyasaka, Y. Sadahiro, M. Tabata, Y. Kashiwaya, *Polymer,* **2007**, *48*, 6366-6373.

[71] (a) X. Salom-Roig, C. Bauder, *Synthesis*, **2020**, *52,* 964-978. (b) S. Resa, P. Reiné, L. Á. de Cienfuegos, S. Guisán-Ceinos, M. Ribagorda, G. Longhi, G. Mazzeo, S. Abbate, S. J. Mota, D. Miguel, J. M. Cuerva, *Org. Biomol. Chem.* **2019**, *17,* 8425-8434. (c) S. Resa, D. Miguel, S. Guisán-Ceinos, G. Mazzeo, D. Choquesillo-Lazarte, S. Abbate, L. Crovetto, D. J. Cárdenas, C. Carreño, M. Ribagorda, G. Longhi, A. Mota, L. Á. de Cienfuegos, J. M. Cuerva, *Chem. Eur. J.* **2018**, *24,* 2653-2662.

[72] R. Bentley, *Chem. Soc. Rev.*, **2005**, *34,* 609-624.

[73] M. C. Carreño, G. Hernández-Torres, M. Ribagorda, A. Urbano, *Chem. Commun.,* **2009**, 6129-6144.

[74] (a) L. F. Tietze, A. Schuffenhauer, P. R. Schreiner, *J. Am. Chem. Soc.*, **1998**, *120*, 7952-7958. (b) I. Fernandez, N. Khiar, *Chem. Rev.,* **2003**, *103,* 3651-3706.

[75] D. B. Amabilino, E. Ramos, J. L. Serrano, T. Sierra, J. Veciana, *J. Am. Chem. Soc.,* **1998**, *120*, 9126–9134.

poly-**31** and poly-**32** respectively) between backbone and the chiral center. Teleinduction result of the formation of an organized β-sheet orientation on the glycine spacers and even can be switched acting on the interactions between spacers (Figure 27).[76] In the same line, more recently another phenomenon of remote chiral induction was demonstrated introducing a rigid spacer, a oligo(p-phenyleneethynylene)s (OPEs) (poly-**33** and poly-**34** respectively). In this case, helical induction is based on a chiral harvesting phenomenon where the orientation of the chiral center induces the specific tilting on the OPE unit that is harvested to the polyene orienting the internal helix.[77]

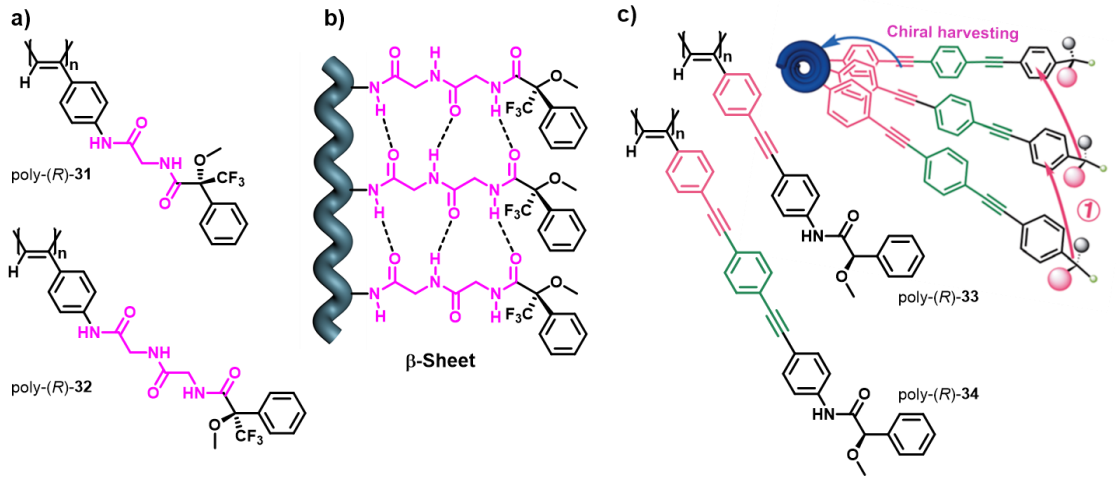

Figure 27. a) Structures of PPAs introducing flexible spacers, poly-(*R*)-**31** and poly-(*R*)-**32**. b) Representation of an organized β-sheet for poly-(*R*)-**32**. c) Structure of PPAs introducing rigid spacers, poly-(*R*)-**33** and poly-(*R*)-**34**, and their chiral harvesting transmission mechanism.

As new approach of rigid spacer, we have valued the generation of a metal complex, an untested system in PPAs. For this idea, based on their properties an interesting metal center could be the platinum. Structurally, Pt(II) is a d^8 complex that present a square planar geometry (usually low spin and strong field complexes due to their greatest crystal field splitting energy) where metal center is linked to four ligands in the x-y plane (Figure 28a). As result, this spatial arrangement allows two possible stereoisomers (*cis/trans*). Moreover, ligands can be classified by function of several parameters: number of coordination sites (mono-, di- or polydentate ligands) and chemical nature (inorganic and neutral, cationic and anionic organic ligands), among others. For the general formula PtL_2X_2 we will define them based on the type of their covalent bonds:[78]

[76] R. Rodríguez, E. Quiñoá, R. Riguera, F. Freire, *Chem. Mater.,* **2018**, *30*, 2493-2497.

[77] Z. Fernández, B. Fernández, E. Quiñoá, R. Riguera, F. Freire, *Chem. Sci.*, **2020**, *11*, 7182-7187.

[78] M. L. H. Green, *J. Organomet. Chem.,* **1995**, *500*, 127-148.

-L ligands, derived from neutral molecules: amines, pyridines, tertiary phosphines (PR_3), alkenes, etc.

-X ligands, derived from anionic molecules: halides (e.g., Cl^-, Br^-), alkoxy-alkyl molecules (ligands neutral as one electron but anionic as two, e.g., $EDTA^{4-}$), etc.

-Z ligands, a particular case in that ligands are two electrons acceptor (generally are borum center molecules as BX_3/BR_3, other examples are $AlCl_3$, Ag^+, H^+)

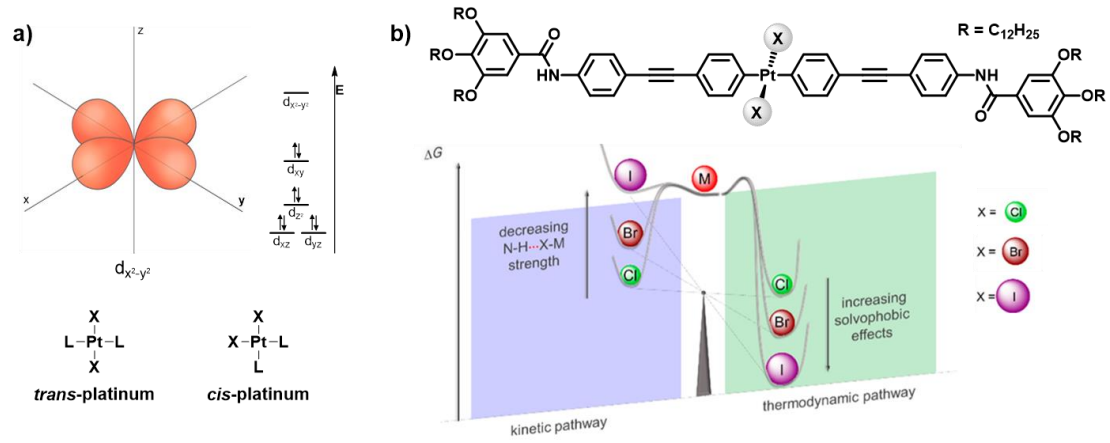

Figure 28. a) Cristal field splitting of square planar complex and *cis/trans* isomers for a platinum metal center. b) Effect of the halide on supramolecular polymerization involving platinum complexes.

Furthermore, for their use as lineal spacers in PPA only *trans* isomers are suitable. This distribution leaves two X ligands on the structure perpendicular to the backbone. The influence of this ligands was analyzed by Fernández and co-workers, they reported the effect of different halides (Cl-, Br-, I-) on Pt(II) complexes involved on supramolecular polymerization. Thus, the size of the halide destabilizes kinetic pathway on the supramolecular polymerization due to the disruption of attractive forces, driving the structure in the thermodynamic pathway to promote conformational rearrangement to compensate the steric hindrance (Figure 28b).[79]

As conclusion, Pt(II) complexes have shown interesting physicochemical, redox and catalytic properties. In this line, remarks the introduction of Pt···Pt interactions as driving force, its emission properties (e.g., Circularly Polarized Luminiscence) in combination with appropriated ligands and a synthetic route via ligand displacement that provides an easy and wide range of ligands.[80]

[79] J. Matern, N. Bäumer, G. Fernández, *J. Am. Chem. Soc.*, **2021**, *143*, 7164-7175.

[80] (a) X. P. Zhang, V. Y. Chang, J. Liu, X. L. Yang, W. Huang, Y. Li, C. H. Li, G. Muller, X. Z. You, *Inorg. Chem.*, **2015**, *54*, 143-152. (b) J. O. Edwards, *Inorganic Reaction Mechanisms, Part 1*, Vol. 26, John Wiley & Sons, **2009**. (c) N.

7. Supramolecular assemblies of PPAs

Supramolecular assembly is the combination of two or more molecules by non-covalent bonds. Generally, the term is used to refers to the combination of a large number of molecules that are linked by self-assembly. In this process self-organization could happen, leaving the assemblies to generate higher-order structures.

The size of the assembly can range since nanometers to micrometers and the architecture (films, layers, spheres, membranes, etc.) depends on the type of interaction (hydrogen bonding, π-π aromatic stacking, ionic interactions, charged electrostatic interactions or combinations of two or more of them) and the spatially disposition of the interactions. Moreover, the hydrogen bond constitutes a special interesting interaction for its directionality, reversibility and high strength of the bonding.[81]

Finally, supramolecular chirality is a remarkable case resulted of the spatial arrangements of the molecules and depends on the chirality of the molecule.[82]

7.1 Fibers and superhelices

Helical polymers can establish supramolecular arrangements by intermolecular interaction between pendant groups. This interaction requires complementary functional groups in the pendants with enough space to stabilize interactions between helices.

As example, our group reported the formation of the first example of a reversible stereocomplex with PPAs. When the polymer bearing the α-methoxy-α-trifluoromethyl-α-phenylacetamide pendant group (MTPA group) is solubilized in THF, the pendant groups present a *cis* amide conformation by competition of the solvent with the intramolecular interaction that promote usually the *trans* amide conformation.[48] As result of this conformation, when both enantiomeric polymers (poly-(*R*)-**24** and poly-(*S*)-**24**) are mixed it is produced the formation of this fiber-like aggregate by supramolecular interactions of the enantiomeric pendants. Moreover, high concentrations leave to the formation of a gel

Bäumer, K. K. Kartha, S. Buss, I. Maisuls, J. P. Palakkal, C. A. Strassert, G. Fernández, *Chem. Sci.*, **2021**, *12*, 5236-5245.

[81] (a) J. -M. Lehn, *Supramolecular Chemistry: Concepts and Perspectives*; Wiley-VCH: Weinheim, Germany, **1995**. (b) J. W. Steed, J. L. Atwood, J. *Supramolecular Chemistry*, John Wiley & Sons: West Sussex, U.K., **2005.**

[82] (a) M. Liu, L. Zhang, T. Wang, *Chem. Rev.,* **2015**, *115,* 7304-7397. (b) E. Yashima, N. Ousaka, D. Taura, K. Shimomura, T. Ikai, K. Maeda, *Chem. Rev.,* **2016**, *116,* 13752-13990. (c) X. Yan, J. Cao, Y. Zhang, P. Weng, D. Miao, Z. Zhao, Z. Li, Y. B. Jiang, *Chem. Commun.*, **2021**, *57,* 1802-1805. (d) P. Duan, H. Cao, L. Zhang, M. Liu, *Soft. Matter,* **2014**, *10*, 5428-5448. (e) L. Zhang, L. Qin, X. Wang, H. Cao, M. Liu, *Adv. Mater.,* **2014**, *26*, 6959-6964. (f) Y. Yang, Y. Zhang, Z. Wei, *Adv. Mater.,* **2013**, *25*, 6039-6049.

[48] S. Leiras, F. Freire. J. M. Seco, E. Quiñoá, R. Riguera, *Chem. Sci.,* **2013**, *4*, 2735-2743.

and the stereocomplex formation is reversible. Addition of high polar solvents (e.g., MeOH), high temperature or solvents that promote the *trans* amide (e.g., $CHCl_3$) inducing the cleavage of the stereocomplex through the disruption of the intermolecular hydrogen bonds between *cis* amides (Figure 29).[83]

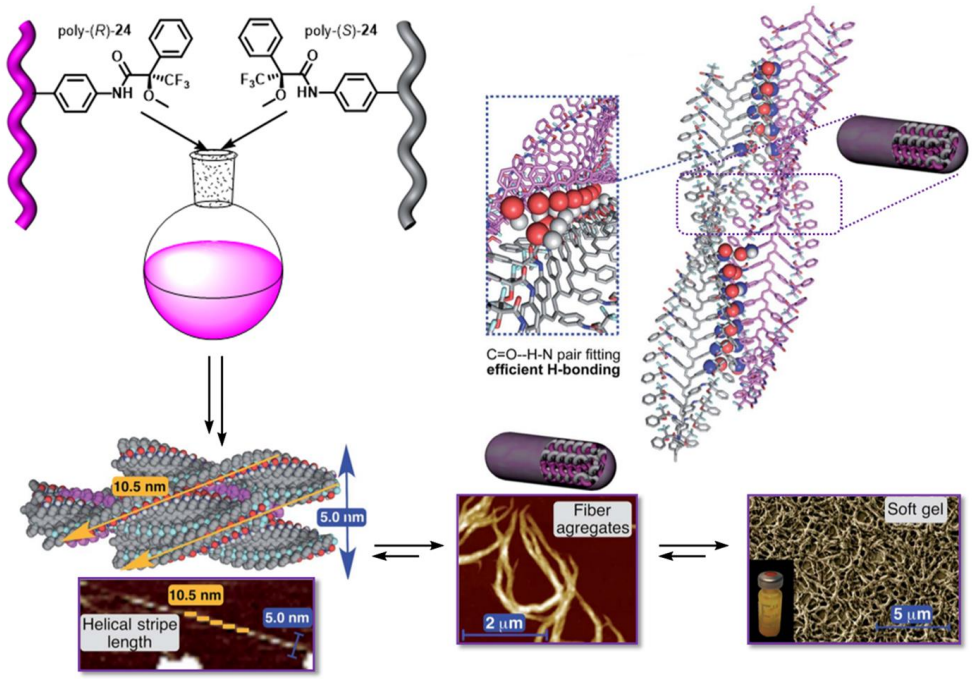

Figure 29. Structure of the *R* and *S* enantiomers of poly-**24** and conceptual representation of their interaction, accompanied of AFM (helical strip and fibers) and SEM (soft gel) images of some steps of the stereocomplexation.

Another interesting example was reported by Yashima and co-workers. They reported several PPAs bearing β-CyDs that promotes hierarchical superstructured helical assemblies on a micrometer scale with controlled helical sense. Interestingly gelation of the supramolecular aggregate of 2β-CyD (poly-**35**) is obtained in presence of the mixture of chiral amine ((*S*) and (*R*)-1-phenylethylamine) with selective interaction with the (*S*)-1-phenylethylamine. Thus, the specific gelation was the result of a preferred-handed helical array between β-CyD units and polar ester or amide (Figure 30a).[84]

Another interesting example reported a PPA bearing *L*-alanine methyl ester as pendant (poly-(*S*)-**23**), This spontaneously forms supramolecular assemblies by evaporation of the solvent (methanol) on the mica surface to promote cables with right-handed twists. Due to the strong solvation power of methanol, polymer chains take an extended conformation in solution during the solvent evaporation. This promotes non-covalent interchain

[83] S. Leiras, F. Freire, E. Quiñoá, R. Riguera, *Chem. Sci.,* **2015**, *6*, 246-253.

[84] K. Maeda, H. Mochizuki, K. Osato, E. Yashima, *Macromolecules,* **2011**, *44*, 3217-3226.

interactions such as hydrogen bonds, side-by-side interaction that give thick to nanofibers. Also, head-to-tail aggregation extends the length of the fibers. In the other hand, in a non-polar solvent as $CHCl_3$, spherical vesicles are formed. In this solvent, polymer chain forms micelles with the alanine methyl ester pendants group in the core, that can grow in size and stick by intermicellar hydrogen bond to minimize the interfacial surface area (Figure 30b).[85]

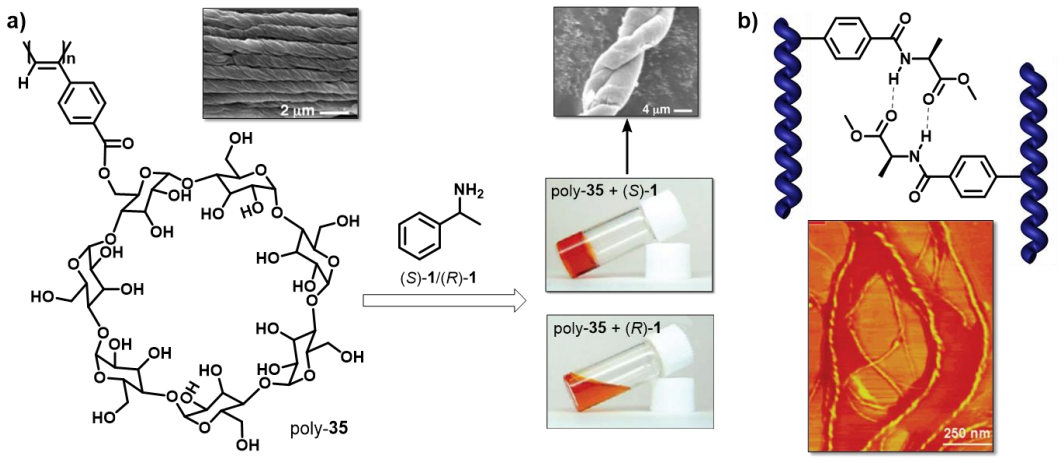

Figure 30. a) Structure of poly-**35** and SEM images in absence and presence of (*S*)-**1**. b) Schematic illustration of intermolecular hydrogen bonds in poly-(*S*)-**23** and phase images of their fibers.

7.2 Layer-by-layer assembly

Yashima *et al.* reported an interesting assembly of optically active multilayers using macromolecular helicity memory in water. For this, two achiral polyelectrolytes were prepared (PPAs bearing a phosphonate or an ammonium group as pendant, poly-**36** and poly-**37** respectively) that was complexed with chiral molecules that induce a preferred helical sense ((*S*)-phenylalaninol and (*S*)-phenyllactic acid for (*S*)-**2** and (*S*)-**3** respectively). The layers assembly was successful achieved by alternative deposition of the helical induced PPAs and polyelectrolytes with opposite charge (hydrochloride of poly(allylamine) (PAH) and the sodium salt of poly(acrylic acid) (PAA)) that displace chiral molecules.[86]

[85] K. K. Cheuk, B. S. Li, J. W. Lam, Y. Xie, B. Z. Tang, *Macromolecules,* **2008**, *41,* 5997-6005.

[86] K. Maeda, Y. Matsushita, M. Ezaka, E. Yashima, *Chem. Commun.,* **2005**, 4152-4154.

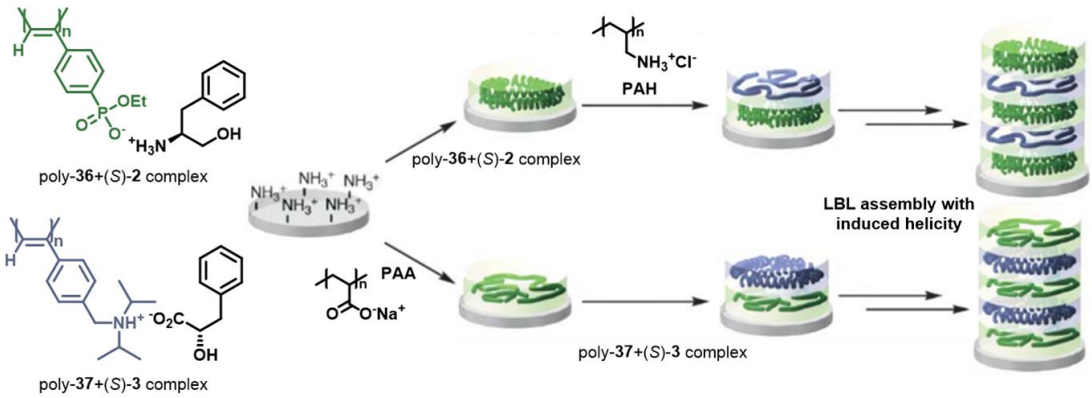

Figure 31. LbL self-assembly of charged PPAs with induced macromolecular helicity.

8. Applications of PPAs

The dynamism and the control of elongation and helical sense of PPAs provide a high versatility of PPAs to manipulate this polymer for several potential applications. In this section will be comment some of the more important applications.

8.1 Sensors

The response to external stimuli is widely studied in PPAs based on the ability of these polymers to interact specifically with monovalent and divalent metal ions,[41, 87] solvent properties,[48,88] temperature,[89] etc.

An interesting colorimetric sensor was recently reported in our research group. A PPA bearing the MPA pendant group was linked to the polyene backbone by a glycine spacer (poly-(*R*)-**38**) and the control over the amide bonds that gives the glycine group promote the colorimetric response.[90]

In polar solvents (e.g., TFE), polymer solution is yellow and present the classical CD pattern. This is due to polymer adopts the extended form of the pendant, hydrogen bonds between neighbor pendants, thus steric hindrance among pendant is low and the chiral MPA units induces a preferred helical sense in the backbone by chiral teleinduction. For the other

[41] S. Arias, F. Freire, E. Quiñoá, R. Riguera, *Polym. Chem.*, **2015**, *6,* 4725-4733.

[87] M. Alzubi, S. Arias, R. Rodríguez, E. Quiñoá, R. Riguera, F. Freire, *Angew. Chem., Int. Ed.*, **2019**, *131,* 13499-13503.

[48] S. Leiras, F. Freire, J. M. Seco, E. Quiñoá, R. Riguera, *Chem. Sci.,* **2013**, *4,* 2735-2743.

[88] S. Wang, X. Feng, J. Zhang, P. Yu, Z. Guo, Z. Li, X. Wan, *Macromolecules*, **2017**, *50,* 3489-3499.

[89] (a) S. Li, K. Liu, G. Kuang, T. Masuda, A. Zhang, *Macromolecules*, **2014**, *47,* 3288-3296. (b) F. Wang, C. Zhou, K. Liu, J. Yan, W. Li, T. Masuda, A. Zhang, *Macromolecules*, **2019**, *52*, 8631-8642.

[90] R. Rodríguez, E. Quiñoá, R. Riguera, F. Freire, *Small*, **2019**, *15*, 1805413.

hand, in low polar solvents (e.g., $CHCl_3$) the solutions shows an intense red color due to bathochromic shift of the polyene and null CD region. This is the result of a bent form in the pendant, intramolecular hydrogen bond in each pendant, that avoid chiral teleinduction from MPA moiety (Figure 32). Moreover, interconversion between structures with the associated colorimetric change is a reversible process.

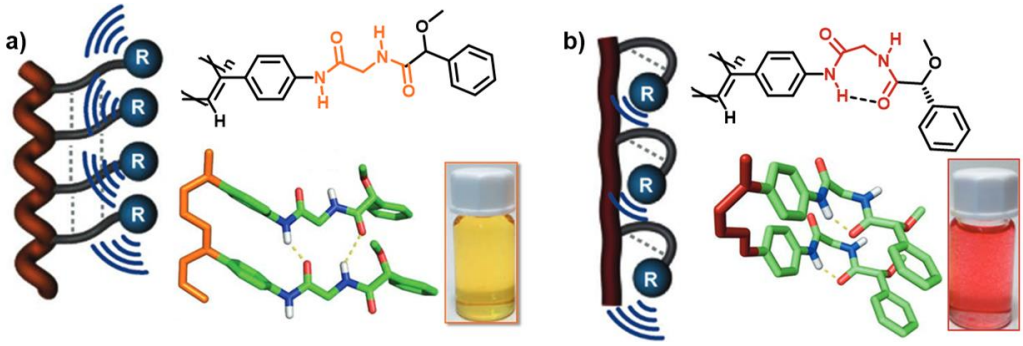

Figure 32. Conceptual representation of a) extended form of (poly-(*R*)-**38**) in polar solvents and b) bent form of (poly-(*R*)-**3**) in low polar solvents.

8.2 Asymmetric Catalysis

Asymmetric catalyst is one of the best application goals of PPAs for its recyclability, kinetic advantages of catalyzing in a homogeneous phase, etc. In this field of application, with the asymmetric induction, other phenomena can be expected related to the macromolecular optically activity of the PPAs (cooperativity, chiral amplification, etc.). Thus, Reggelin *et al.* described the first example of asymmetric catalysis in PPAs, a C-C bond formation reaction. For this result, a polymer bearing methacrylate derivatives as pendants (poly-**39 and** poly-**40**) were polymerized using a chiral initiator to promote a preferred helical sense. Thus, when poly-**39** is complexed as monodentate ligand to the palladium catalyst, the enantiomeric excess on the allylic substitution reactions is consequence of the helicity of the polymer ligand (Figure 33a).[91]

Recently, Maeda and co-workers achieved the asymmetric catalytic ability with dynamically racemic helical polymers by transformation in polymers with a preferred helical sense, for this they combined several properties related with the secondary structure of PPAs such as helical induction, chiral amplification and memory effect. To do this, they synthesized a new poly-(biarylylacetylene) (PBA)-based asymmetric catalyst composed of axially chiral, but racemic 2-arylpyridyl-N-oxide monomer units, with N-oxide moieties close to the polymer backbone. The resulting PPA (poly-**41**) is enantioselective deracemize with a chiral alcohol (*(R)*- or *(S)*-1-phenylethane-1,2-diol) that induces a

[91] M. Reggelin, M. Schultz, M. Holbach, *Angew. Chem., Int. Ed.*, **2002**, *41*, 1614-1617.

preferred helical sense. This remains by memory effect after removing the stimulus and also is accompanied by a chiral enhancement phenomenon. Finally, the resulting helicity-memorized of poly-**41** is high enantioselectivity for the asymmetric allylation of benzaldehyde (Figure 33b).[92]

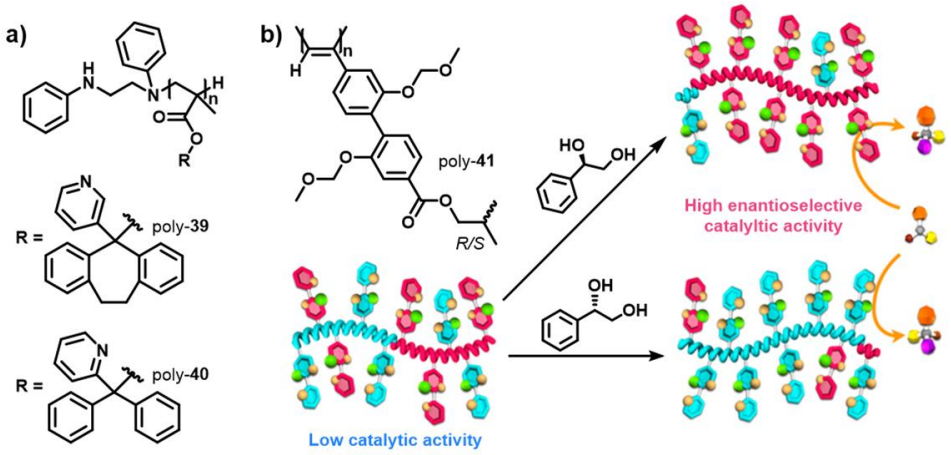

Figure 33. a) Structures of poly-**39** and poly-**40**. b) Structure of racemic poly-**41** and schematic illustration of its emergent highly enantioselective catalytic activity.

8.3 Chiral Recognition

Combination of High-Performance Liquid Chromatography (HPLC) with chiral stationary phases (CSP) is one of the more powerful techniques to separate enantiomeric racemic mixtures. The effectiveness of this technique is highly dependent to the chiral recognition capability of the chiral stationary phase. Moreover, CSP can be since small molecules to bigger polymer, and even if some CSP are commercial is necessary to synthesize and to study new materials to resolve many racemates yet.[93]

Several CSP were reported employing the helical structure of PPAs.[94] An interesting example of chiral recognition was reported by the groups of Yashima and Maeda. They synthesized a PPA bearing a bisphenol derivative as pendant (axially racemic) (poly-**42**). The polymer is introduced in a HPLC column as CSP. A preferred helical sense accompanied by a chiral amplification phenomenon is obtained by a treatment with a chiral alcohol (*(R)*- or (*S*)-1-phenylethanol to get right- and left-handed helices respectively). After removing the chiral alcohol, macromolecular helicity remains and the system is successfully applied

[92] T. Ikai, M. Ando, M. Ito, R. Ishidate, N. Suzuki, K. Maeda, Yashima, E.; *J. Am. Chem. Soc.*, **2021**, *143,* 12725-12735.

[93] Y. Okamoto, T. Ikai, *Chem. Soc. Rev.*, **2008**, *37*, 2593-2608.

[94] (a) C. Zhang, H. Wang, Q. Geng, T. Yang, L. Liu, R. Sakai, T. Satoh, T. Kakuchi, Y. Okamoto, *Macromolecules*, **2013**, *46,* 8406-8415. (b) C. Zhang, F. Liu, Y. Li, X. Shen, X. Xu, R. Sakai, T. Satoh, T. Kakuchi, Y. Okamoto, *J. Polym. Sci., Part A: Polym. Chem.*, **2013**, *51,* 2271-2278.

to separate *trans*-stilbene oxide. Moreover, the inversion of the helical sense of the polymer results in a reversed elution order (Figure 34a).[95]

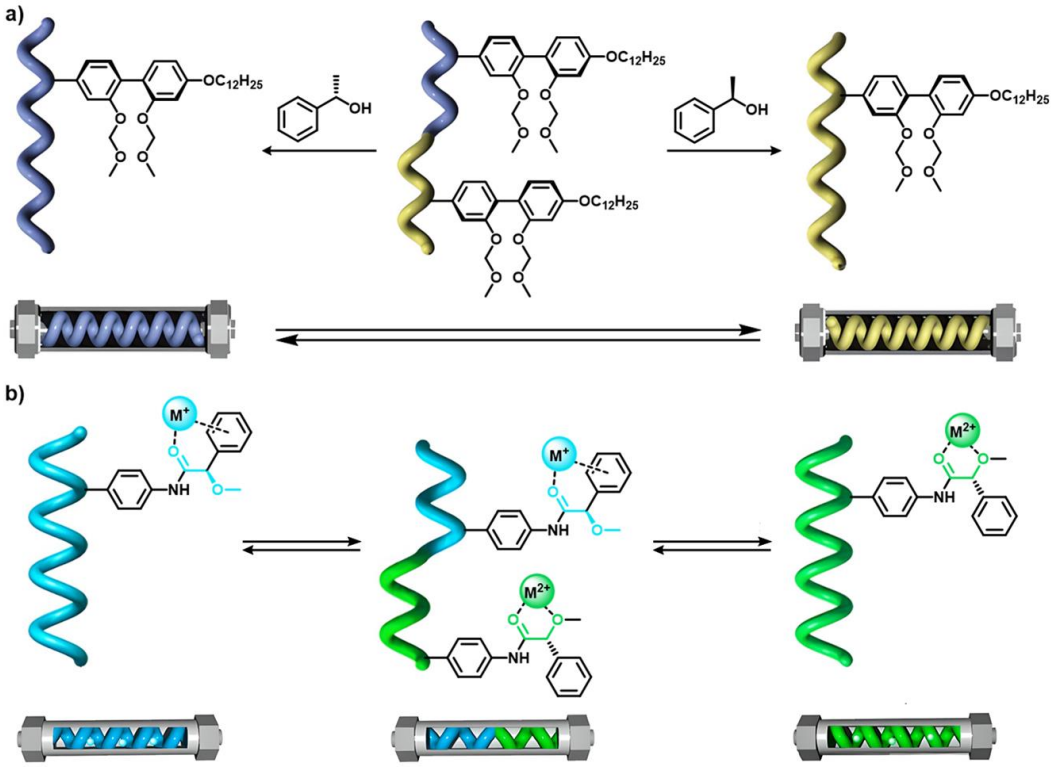

Figure 34. Schematic representation of macromolecular helicity modulation and its application as CSP in HPLC columns for a) poly-**42** and b) poly-(*R*)-**18**.

More recently, Maeda´s group in collaboration with our group prepared a CSP phase coated with a PPA bearing MPA units as pendant (poly-(*R*)-**18**). This polymer, as was fully explained in section 3.3, is axially racemic and can adopt selectively *M* or *P* helix using external stimuli. Therefore, addition of catalytic amount of sodium or cesium tetrakis[3,5-bis(trifluromethyl)phenyl]borate salts(NaBArF and CsBArF respectively) in HPLC system results in the *M* and *P* helix respectively, this reversible macromolecular helicity is used to select the order of elution of an enantiomeric racemic mixtures. Thus, poly-**18** is the first example of a CSP for HPLC capable of switching reversibly its chiral recognition ability between three different states using external achiral stimuli.[96]

[95] K. Shimomura, T. Ikai, S. Kanoh, E. Yashima, *Nat. Chem.,* **2014**, *6*, 429-434.

[96] D. Hirose, A. Isobe, E. Quiñoá, F. Freire, K. Maeda, *J. Am. Chem. Soc*., **2019**, *141*, 8592-8598.

9. Supramolecular helical polymers

As was described at the beginning, PPAs are prepared by catalytic polymerization generating a polyene skeleton. Thus, the preparation of these polymers is irreversible. They are linked by covalent bonds and separation of monomeric units is only possible via degradation reactions on the polyene backbone (e.g., light, temperature, etc.).

Alternative, supramolecular polymers emerge as an alternative characterized by their high reversibility because they are stabilizing only by non-covalent interactions (e.g., Van der Waal's forces, hydrogen bonding and π- π stacking), forces relatively weak that can be broken under several stimulus (e.g., temperature, pressure, solvent polarity, etc). As result, supramolecular polymers occur through several equilibriums whose parameters and properties will be explained in the next sections.

9.1 Thermodynamic Parameters

Based on the mechanism by which each monomer is added, supramolecular polymers can be obtained by cooperative or isodesmic polymerization.

In the cooperative case, polymerization occurs under thermodynamic control and in two steps. First, an unfavoured nucleation phase (K_{nuc}) followed by a favoured polymerization stage (K_{elo}). This mechanism results in a sharp transition since a state dominated by small aggregates to other composed by large polymers, where the size of polymer chains depends on the monomer concentration and temperature.

In the other hand, in the isodesmic polymerization process each addition of monomers is independent. Interactions between pendants are unaffected for the length of the chain, and as result they are equivalent (equal equilibrium constant, Knuc = Kelo). Moreover, the chain growth can be favoured increasing the monomers concentration or decreasing the polymerization temperature.

These self-assembly processes can be easily recognized by several techniques as CD or UV-Vis spectroscopy, which have been widely applied to discern between both cases. Thus, monitoring an intrinsic property, such as the wavelength, in relation with the temperature in a cooling the resulting graphic is reveal the self-assembly mechanism. If the shape of the curve is as hyperbole in a slope without angle the polymerization is a cooperative process. While if the curve is sigmoidal, polymerization is an isodesmic process (Figure 35). Moreover, the rate of the cooling curve is crucial to avoid hysteresis and remain thermodynamic control.

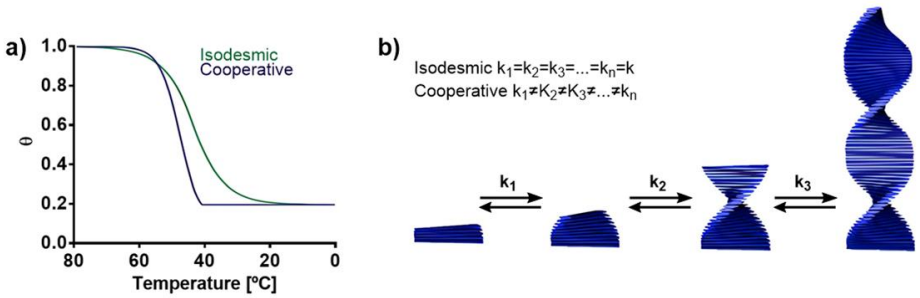

Figure 35. a) Schematic illustration of cooling curves for isodesmic and cooperative processes. b) Conceptual representation of mechanisms of supramolecular polymerization.

9.2 Cooperative polymerization

During the self-assembly, first monomers aggregate into kinetically preferred structure for later desegregate and polymerize into the thermodynamic aggregate. This makes that generally exist more than one single structure, especially if the mechanism of polymerization is cooperative, and as result, it exists a kinetic contribution in the polymerization.

THERMODYNAMICALLY CONTROLLED POLYMERIZATION

Cooperative self-assembly was large studied in several systems. As example, supramolecular polymers derived from the 1,3,5-benzenetricarboxamides (BTAs) has been widely reported, these molecules present three amide groups in the core forming a triple array of hydrogen bonds, placing the adjacent molecules one on top of the other with a rotation angle of 60º, which allows the effective π stacking of aromatic units. As example, Meijer *et al.* recently synthesized new supramolecular polymers based on BTAs bearing tetra(ethylene glycol) (BTA-OEG_4) (poly-**43**) that are water soluble. These are assembled in presence of hyaluronic acid (HA) at different ratios, showing strong interactions that led to the formation of small fibers and even heterogeneous hydrogels. Moreover, in a second approach HA was covalently functionalized with BTAs (HA-BTA) and coassembly with BTA-OEG_4 in different ratios resulting in 1D supramolecular fibers (poly-**44**). Moreover, hydrogels from this coassembly show a stronger resilient than BTA-OEG_4 analogues and present self-healing properties (Figure 36).[97]

[97] S. Varela-Aramburu, L. Su, J. Mosquera, G. Morgese, S. M. Schoenmakers, R. Cardinaels, A. R. A. Palmans, E. W. Meijer, *Biomacromolecules*, **2021**, *22*, 4633-4641.

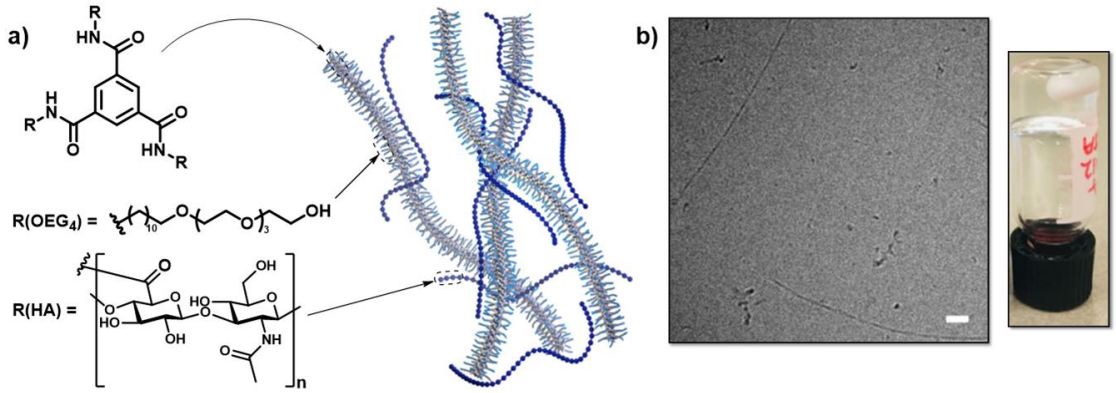

Figure 36. a) General structure of a BTA and schematic representation of BTA with groups OEG_4 and HA that generate poly-**44**. b) CryoTEM and gel images of HA-BTA coassembled with BTA-OEG_4 (poly-**44**).

As alternative of the hydrogen bonding in combination with π–π and/or hydrophobic interactions, other strategies as using dipolar interactions,[98] metal-ligand coordination,[99] etc. are possible. In this line, assembly of small molecules by metal-metal interactions is a recent approach described for first time for Fernández and co-workers. In this work, they achieved cooperative self-assembly of an OPE-based pyridyl complexed to Pd(II) (mono-**45**) controlled by metallophilic interactions (Pd···Pd). Temperature UV-Vis studies demonstrate the metallophilic interactions for the appearance of a red-shifted band when temperature is slow cooling since 50 °C (monomers dissolved) to room temperature (aggregate state). Moreover, this absorption is also assigned to additional π-π interactions between OPEs (Figure 37). This was corroborated by theorical studies and supramolecular polymerization of the equivalent system in absence of Pd(II), demonstrating that methallophilic Pd···Pd interactions are the origin of the cooperativity.[100]

[98] G. Fernández, M. Stolte, V. Stepanenko, F. Würthner, *Chem. Eur. J.*, **2013**, *19*, 206-217.

[99] J. W. Wackerly, J. S. Moore, *Macromolecules*, **2006**, *39*, 7269-7276.

[100] M. J. Mayoral, C. Rest, V. Stepanenko, J. Schellheimer, R. Q. Albuquerque, G. Fernández, *J. Am. Chem. Soc.*, **2013**, *135*, 2148-2151.

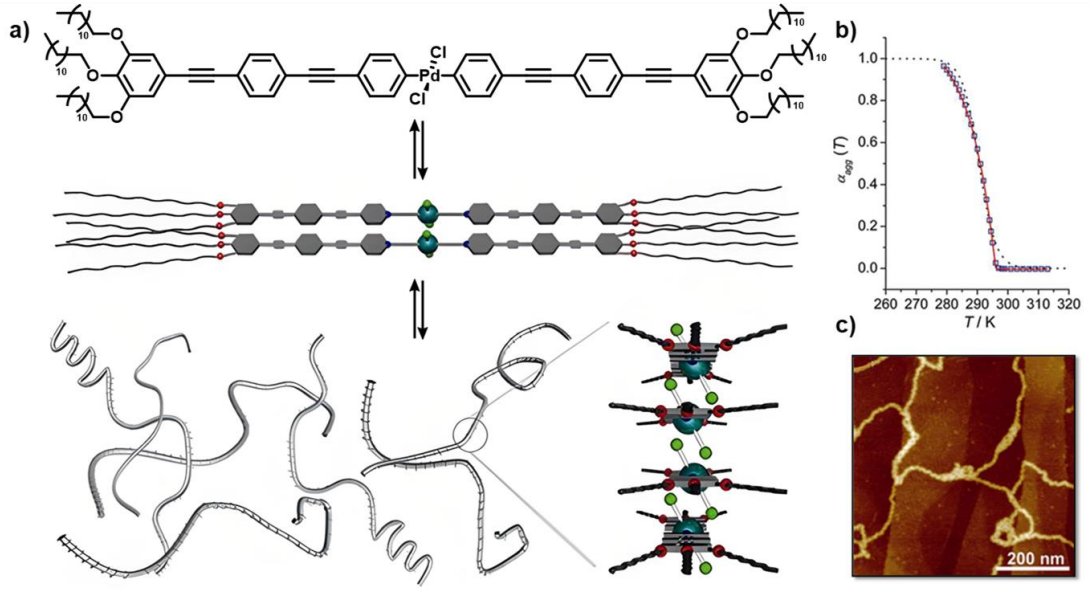

Figure 37. a) Structure of mono-**45** and schematic illustration of the proposed self-assembly pathway. b) Cooling curve of the polymerization that follow a cooperative process. C) AFM image of the resulting supramolecular polymer deposited by spin coating on HOPG.

KINETICALLY CONTROLED POLYMERIZATION

The influence of kinetics result in the obtention of more than one type of aggregate, hindering the experimental studies, generating assemblies very dependent of several variables such as temperature range and rate, preparation method, different kinds of solvent processing and the application of external stimuli.[101]

A representative example of this behavior was reported by Meijer and co-workers. They prepared a linear π-conjugated oligo(phenylenevinylene) (OPV) that self-assembly by π-π stacking into dimers generating a lef0.t-handed helical aggregate (poly-**46**). Moreover, quenching a monomer solution in an ice bath the aggregates exhibit a right-handed helix. Furthermore, the right-handed helical aggregates evolve with the time towards the thermodynamically more stable left-handed ones (Figure 38a).[102]

Another interesting example was recently reported by Fernández and co-workers. They prepared a chiral OPE-based bispyridyldichlorido Pd(II) complex (mono-**47**) and discovered a hidden kinetic pathway alternative to the thermodynamic previously reported. This cooperative pathway incorporates two consecutive species (Agg I and Agg II) that present a high kinetic stability and it is produced by solvophobic quenching (injecting monomer into a large volume of an aggregating solvent as MCH). Moreover, this kinetic

[101] M. Wehner, F. Würthner, *Nat. Rev. Chem.*, **2020**, *4*, 38-53

[102] P. A. Korevaar, S. J. George, A. J. Markvoort, M. M. J. Smulders, P. A. J. Hilbers, A. P. H. J. Schenning, T. F. A. De Greef, E. W. Meijer, *Nature*, **2012**, *481*, 492-496.

pathway evolves rapidly to clustered superstructures (Agg IIc) preserving the packing mode and avoiding the coupled polymerization equilibria in solution by the rapid clustering step. As result, redirection of the polymerization to the thermodynamic pathway is avoided (Figure 38b).[103]

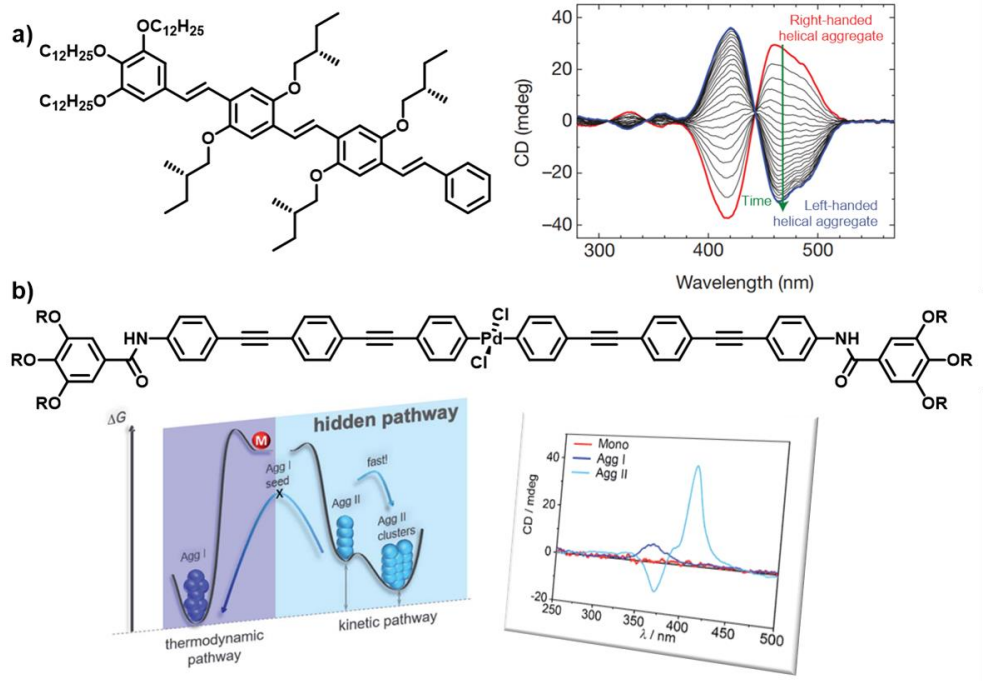

Figure 38. a) Molecular structure of mono-**46** and CD spectra of left-handed and right-handed helical aggregates of poly-**46**. b) Molecular structure of mono-**47**, schematic illustration of its polymerization pathways and CD spectra of their species.

9.3 Supramolecular polymerization of phenylacetylene monomers

In our group Z. Fernández and co-workers recently reported the first example of supramolecular polymerization using an OPE unit (mono-**34**) previously reported in covalent polymerization for preparation of a PPA (poly-**34**).[77] Thus, this work demonstrates the potential application of phenylacetylene monomers for supramolecular polymerization. Furthermore, they found that polymerization takes place in this system by two possible isodesmic mechanisms in competition, controlled by solvents and temperature. Which also depend on the size of the aggregate, generating short oligomers that result in twisted sheets or large supramolecular polymers forming helical columns (Figure 39).[104]

[103] J. Matern, K. K. Kartha, L. Sánchez, G. Fernández, *Chem. Sci.*, **2020**, *11*, 6780-6788.

[77] Z. Fernández, B. Fernández, E. Quiñoá, R. Riguera, F. Freire, *Chem. Sci.*, **2020**, *11*, 7182-7187.

[104] Z. Fernández, B. Fernández, E. Quiñoá, F. Freire, *Angew. Chem., Int. Ed.*, **2021**, *60*, 9919-9924.

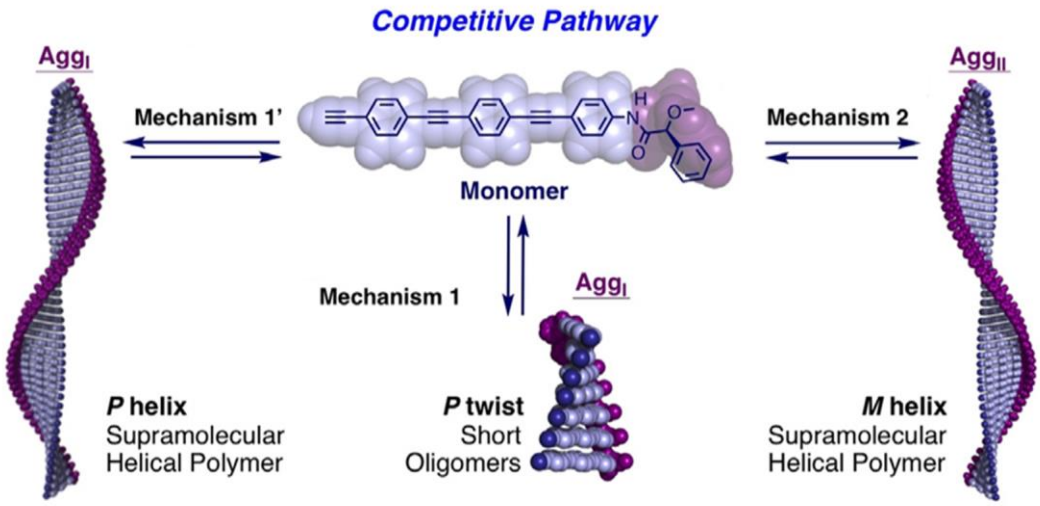

Figure 39. Schematic representation of the competitive pathway for mono-**34**.

METALLOSUPRAPHENYLACETYLENE POLYMERS

Unlike catalytic polymerization that generates a polyene backbone, the reported supramolecular polymerization of phenylacetylene monomers leaves the terminal acetylene group free. This difference provides a versatile connection point that paves the way for interesting supramolecular proposes.

In this line, metallosupramolecular polymers based on metal–ligand coordination has attracted much attention as a significant class of organic/inorganic hybrid supramolecular materials.[105] Thus, in previous examples was comment an interesting new approach controlling self-assembly by metallophilic interactions. Among all possibilities, Ag(I) present a strong affinity to acetylene group, capability to promote Ag···Ag interactions and possibility to adopt a lineal structure. Making these complexes very interesting for supramolecular chemistry.

Focusing on Ag(I) characteristics, its complexes present an interesting geometrical flexibility for its d^{10} sphere, being able to be found generating supramolecular aggregates in one, two or three dimensions. For linear complexes (e.g., fibers), these present coordination index of two and are usually found when ligands are rigid, which can be partial distorted to Zigzag type by coordinating anions or solvents. Moreover, the metallophilic Ag···Ag interactions usually are at lower distance than the van der Waals radio of two silver atoms (3.44 Å).[106] A fact that has been shown to be key in diversity Ag(I) polymeric complexes, a

[105] (a) S. Ogi, C. Grzeszkiewicz, F. Wurthner, *Chem. Sci.*, **2018**, *9*, 2768-2773. (b) K. Y. Kim, J. Kim, C. J. Moon, J. Liu, S. S. Lee, M. Y. Choi, C. Feng, J. H. Jung, *Angew. Chem. Int. Ed.*, **2019**, *58*, 11709-11714.

[106] (a) A. Bellusci, A. Crispini, D. Pucci, E. I. Szerb, M. Ghedini, *Cryst. Growth Des.*, **2008**, *8*, 3114-3122. (b) C. L. Chen, B. S. Kang, C. Y. Su, *Aust. J. Chem.*, **2006**, *59*, 3-18.

research line in growth for their potential applications in chirality[107], luminescence,[108] conductivity,[109] etc.

The main research in silver polymers is focused on their coordination to a N-donor groups. As example, Oliver and co-workers prepared a lineal N-donor Ag-based cationic 1D polymer (poly-**48**) that selective trap oxo-anions (Figure 40a).[110] Moreover, as an interesting supramolecular polymerization example Lee *et al.* report a kinetically controlled chiral supramolecular polymerization based on a ligand-silver complex. This structure allows a reversible transformation between *M*- and *P*-type helices, where the complex play a key role in chiral inversion. Moreover, the coordination anion (NO_3-) play a crucial role on the formation of the supramolecular polymer and also the helical inversion.[111]

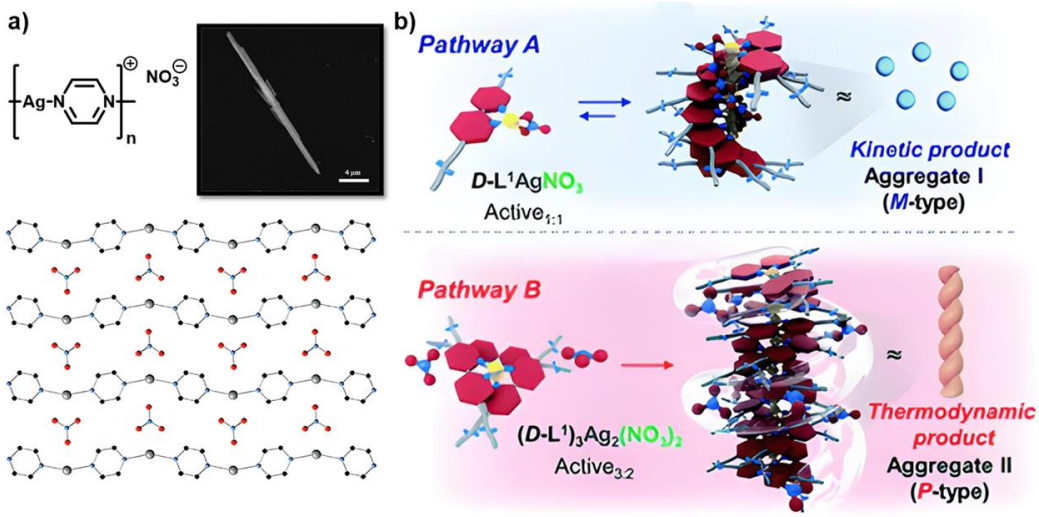

Figure 40. a) Structure and SEM image of a crystal of poly-**48**. b) Left- and Right-handed supramolecular helices of poly-**49**.

Finally, some research emerges recently applying acetylenes linked to silver in supramolecular polymerization. As example, Zao and co-workers prepared chiral silver clusters by intramolecular cyclization reaction of *o*-ethynylaniline derivatives. These

[107] P. Reiné, A. M. Ortuño, S. Resa, L. Á. de Cienfuegos, M. Ribagorda, A. J. Mota, S. Abatte, G. Longhi, D. Miguel, J. M. Cuerva, *ChemPhotoChem*, **2022**, *6*, e202100160.

[108] C. Seward, W. L. Jia, R. Y. Wang, G. D. Enright, S. Wang, *Angew. Chem. Int. Ed.*, **2004**, *116*, 2993-2996.

[109] K. G. Liu, F. Rouhani, H. Moghanni-Bavil-Olyaei, X. W. Wei, X. M. Gao, J. Z. Li, X. W. Yan, M. L. Hu, A. Morsali, *J. Mater. Chem. A*, **2020**, *8*, 12975-12983.

[110] E. Soe, B. Ehlke, S. R. Oliver, *Environ. Sci. Technol.*, **2019**, *53*, 7663-7672.

[111] H. Choi, S. Heo, S. Lee, K. Y. Kim, J. H. Lim, S. H. Jung, S. S. Lee, H. Miyake, J. Y. Lee, J. H. Jung, *Chem. Sci.*, **2020**, *11*, 721-730.

materials exhibit versatile photoluminescence and chiroptical behavior under different methanol/water mixtures, with formation of micrometer helical nanofibers (Figure 41).[112]

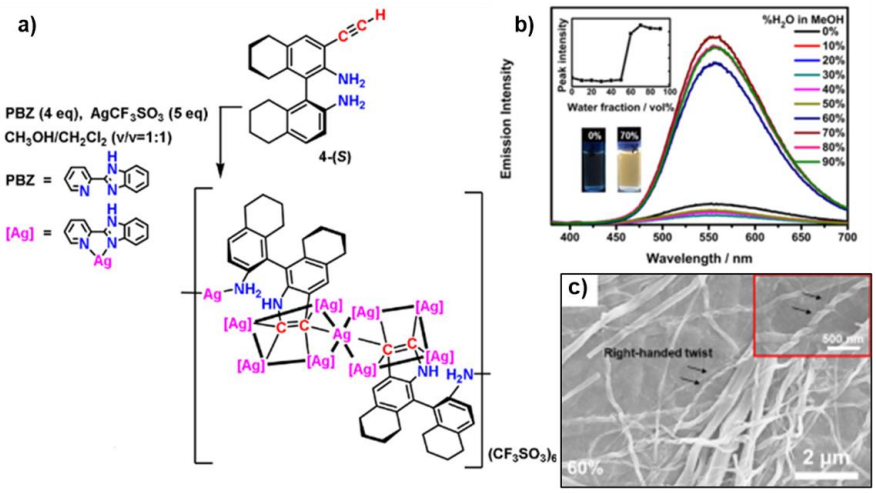

Figure 40. a) Preparation of the spirocyclic cluster and its b) photoluminescence spectra and c) SEM images for 60% of water in the methanol/water mixture.

[112] H. Wu, X. He, B. Yang, C. C. Li, L. Zhao, *Angew. Chem., Int. Ed.*, **2021**, *60*, 1535-1539.

Chapter II

Objectives

OBJECTIVES

Helical polymers —covalent and supramolecular— have been widely studied in the last years due to their promising properties related to their helical structures. In both cases, the knowledge of the helical secondary structure and its reactivity is key for their potential applications.

This thesis is focused on the synthesis and study of the properties of helical polymers. From the study of the photoreactivity of poly(phenylacetylene)s (PPAs), through the generation of PPAs with controlled photoresponse, to finally create new metallopolymers —covalent and supramolecular—. Considering this information, the detailed objectives of this Doctoral Thesis will be depicted below in six chapters.

Chapter III. Photochemical Electrocyclization of Poly(phenylacetylene)s: Unwinding Helices to Elucidate their 3D-Structure in Solution

The secondary structure of PPAs is composed of two coaxial helices. An internal helix, determined by the conformation adopted by the polyene backbone, and the external one described by the pendant groups. Furthermore, depending on if the skeleton of the PPA adopts a *cis-cisoidal* or a *cis-transoidal* conformation around the dihedral angle (ω_1) of the conjugated double bonds (*cisoidal* $\omega_1 > 90°$; *transoidal* $\omega_1 < 90°$), the sense of both helices is the same or opposite respectively.

The determination of the *cis/trans* structure is key to understand the secondary structure of the polymer. Typically, this information can be obtained from Differential Scanning Calorimetry (DSC) or Atomic Force Microscopy (AFM) in combination with other techniques by building a 3D model. Nevertheless, on occasions, a correct assignment is difficult based on this information. As a result, the main objective of this chapter was the preparation of a library of PPAs with a well-known secondary structure and by the photoreactivity under visible light, to implement a protocol that identifies in solution the presence of a *cis-cisoidal* or *cis-transoidal* PPA with an approximate value of ω_1.

Publication associated with this objective: Francisco Rey-Tarrío, Rafael Rodríguez, Emilio Quiñoá, Ricardo Riguera and Félix Freire. *Angew. Chem., Int. Ed.*, **2021**, *60*, 8095-8103.

Chapter IV. Helix Reversals in Poly(phenylacetylene)s: More than Structural Motifs

Due to their structure-function relationship, the helical scaffold in PPAs is responsible for their applications. Nevertheless, although from a combination of different techniques we can determine several parameters of the secondary structure (e.g., *cis/trans* conformation of the double bonds, *M/P* helical sense of both helices, dihedral angle (ω_1), etc.) it is not possible to obtain information about the excess of the screw sense excess in solution.

The decrease in the screw sense excess is a result of the appearance of regions with a helical sense opposite to the majority due to the generation of reversals. Taking this into account, based on the relationship between the secondary structure and the photoreactivity under visible light in PPAs, this chapter addressed for the first time the development of a methodology to identify and quantify reversals in solution in helical polymers.

Chapter V. Photostability and Dynamic Helical Behavior in Chiral Poly(phenylacetylene)s with a Preferred Screw-Sense

Recent studies in photoreactivity in helical polymers allowed us to determine that the stability of PPAs is directly related to the elongation degree of the helix. Furthermore, the dynamic behaviour of a helical polymer is known to decrease as the helix is stretched.

This general lack of light stability limits the applications of PPAs in the industry. Due to the importance of photostability for certain applications, as well as its general durability in all possible fields of application, the main goal of this project was the development of a photostable PPA by tuning the dynamic behaviour of the material.

Publication associated with this objective: Francisco Rey-Tarrío, Santiago Guisán-Ceinos, Juan M. Cuerva, Delia Miguel, Maria Ribagorda, Emilio Quiñoá and Félix Freire. *Angew. Chem. Int. Ed.*, **2022**, *61*, e202207623.

Chapter VI. Photostable Multi-Switches Based on Azo-Poly(phenylacetylene)s with three different chiral motifs (***Helix$_{int}$/Helix$_{ext}$/Helix$_{Azo}$***)

In the literature there are only a few examples of dynamic helical polymers that employed light as external stimulus. In the case of PPAs, no related studies were found, probably due to the reported poor photostability of the PPA backbone.

Prompted by these studies, in this chapter azobenzene groups were introduced in the pendant of PPAs. With these, we searched the obtention of multi-switch materials that respond to different stimuli (e.g., light, temperature, metal ions, solvents, etc.), and with improved photostability thanks to the light absorption by a new chromophore that prevents the incidence of radiation on the polyene backbone.

Chapter VII. Multi-helical Materials by combining Metallo-Supramolecular and Covalent Helical Polymers: Five Axially Motifs within a Helical Polymer

Supramolecular and covalent helical polymers share many characteristics, such as responsiveness to stimuli or communications mechanisms. As result, it is possible prepare materials combining both approaches, generating helical polymers stabilized with a helical supramolecular arrangement in the periphery of the helix, as in chapter VI.

Furthermore, from the literature, we know that in helical polymers introduction of rigid spacers between the polyene and the chiral moiety, such as OPE units, adopts a chiral arrangement resulting in multi-helical scaffolds with the formation of up to four different helices. Inspired by these results, we wanted to do a step forward in the preparation of multi-helical materials. For this task, we combine bispyridyldichloride Pt^{II} complexes — which have been widely and successfully employed in supramolecular chemistry— with polyacetylenes to prepare multi-helical materials.

Chapter VIII. Metallo-Supramolecular Fibers from Phenylacetylene Monomers: Cation Induced Self-Assembly

Supramolecular polymers arise from the assembly of monomeric units through intermolecular non-covalent interactions. Considering the main driving force that promotes self-assembly, there is a wide range of alternatives with applications in asymmetric synthesis, circularly polarized light emissive materials, sensing, etc.

Taking advantage of this versatility, the main goal of this project was the development of a new chiral supramolecular aggregate by mix and shake, for which metal ions (Ag^+) were employed to generate an organic-metal complex that aggregates spontaneously through a simple aggregation pathway thanks, mainly, to the $Ag^+\cdots Ag^+$ and $Ag^+\cdots\pi$ interactions.

Chapter III

Photochemical Electrocyclization of Poly(phenylacetylene)s: Unwinding Helices to Elucidate their 3D-Structure in Solution

CHAPTER III: Photochemical Electrocyclization of Poly(phenylacetylene)s: Unwinding Helices to Elucidate their 3D-Structure in Solution

Adapted from:

Francisco Rey-Tarrío, Rafael Rodríguez, Emilio Quiñoá, Ricardo Riguera and Félix Freire*

[*] Francisco Rey-Tarrío, Dr. Rafael Rodríguez, Prof. Dr. Emilio Quiñoá, Prof. Dr. Ricardo Riguera, Prof. Dr. Félix Freire

Centro Singular de Investigación en Química Biolóxica e Materiais Moleculares (CiQUS) and Departamento de Química Orgánica. Universidade de Santiago de Compostela, 15782, Santiago de Compostela (Spain)

Angew. Chem. Int. Ed. **2021**, *60*, 8095-8103.

Abstract

Photochemical electrocyclization of poly(phenylacetylene)s (PPAs) is used for the structural elucidation of a polyene backbone. This method not only allows classification of PPAs in cis-cisoidal (ω_1< 90°) or cis-transoidal structures (ω_1> 90°), but also approximating ω_1. A PPA solution is illuminated with visible light and monitoring the photochemical electrocyclization of the PPA helix by measuring the ECD spectra at different times. PPAs with a cis-cisoidal structure show a reduction of the ECD signal of at least 50 % before 30 min of irradiation, while cis-transoidal helices need much longer time because the transoidal bond must be isomerized. The different cis-cisoidal and cis-transoidal helices require different times to decrease their ECD signal by 50% ($t_{1/2}$), depending on the degree of compression or stretching of the helix, establishing a relationship between the secondary structure adopted by PPA (ω_1) and the time required to lose the ECD vinylic signal by light irradiation.

1. Introduction

The helix is a structural motif responsible of the function of biomolecules such as peptides, proteins, polysaccharides or DNA. This structure-function relationship has prompted the scientific community to study other non-natural helical materials such as helical polymers.[1-6] The importance of these materials lies in their wide applications in fields such as sensing,[7-15] asymmetric synthesis,[15-17] chiral recognition[18] and separation.[19-22] Among helical polymers, poly(phenylacetylene)s constitute a very interesting family due to their dynamic structure[23,25] where the flexibility of the polyenic backbone allows to tune the elongation[26-32] and the helical sense[33-43] of the polymer. These changes are triggered when an external stimulus interacts with the substituents modifying their steric and/or supramolecular interactions.[27-33,44] In such a way that the backbone prefers to adopt a different helix by changing the dihedral angle between conjugated double bonds.

The skeleton of Poly(phenylacetylene)s (PPAs) can adopt four possible configurations, *cis-cisoidal, cis-transoidal*, *trans-cisoidal* and *trans-transoidal*, depending on the *cis/trans* structure of the double bond and the *cisoidal/transoidal* conformation around the dihedral angle between conjugated double bonds [*cisoidal* ($\omega_1 < 90°$); *transoidal* ($\omega_1 > 90°$)].[24]

Pleasantly, Rh(I) catalysts allows the formation of PPAs with *cis* configuration of double bonds.[45-47] A major problem emerges in the ω_1 dihedral angle control by monomer design,[48] where the balance between the steric and supramolecular interactions involved in the structure stabilization frequently allow for a single polymer to be constituted by an equilibrium mixture of several helices with different pitches and/or sense.[47-50]

Moreover, an important feature of PPAs is that the macromolecular helix is described by two coaxial helices. An internal helix determined by the conformation adopted by the polyene backbone, and the external one described by the pendant groups, which are arranged describing a helical structure, coaxial to the internal one. The *P*/*M* sense of the internal helix depends on the sign of the (ω_1) dihedral angle, that also influences the external helical direction. Thus, in *cis-cisoidal* helices ($\omega_1 < 90°$), the two helices rotate in the same sense [P_{int}/P_{ext} or M_{int}/M_{ext}], while in *cis-transoidal* ($\omega_1 > 90°$) polymers, both helices rotate in opposite directions [P_{int}/M_{ext} or M_{int}/P_{ext}].[51]

Hence, to build up the 3D-structure of a PPA, it is necessary to combine the information extracted by different techniques in solution and in the solid state —Nuclear Magnetic Resonance (NMR),[26,52-56] Differential Scanning Calorimetry (DSC),[56] Raman,[57] Raman Optical Activity (ROA),[58] Vibrational Circular Dichroism (VCD),[59] Electronic

Circular Dichroism (ECD),[60-62] Atomic Force Microscopy (AFM),[50,63-72] X-Ray[73-82] as well as Time Dependent-Density Functional Theory (TD-DFT) calculations (Figure 1).[83-85] Nevertheless, a correct assignment of the *cis-cisoidal* (*c-c*) or *cis-transoidal* (*c-t*) configuration of the polyene backbone is far from solved because the DSC thermogram is affected by the pendant groups or even by the dynamic behavior of the polymer,[56] rendering the technique useless in many cases. Searching for a more robust technique to distinguish *cis-cisoidal* ($\omega_1 < 90°$) from *cis-transoidal* ($\omega_1 > 90°$) structures,[79,86-91] we turned our attention to some stimuli-triggered transformations that linked to the polymer structure, such as those produced by light, temperature or pressure. Thus, while high-pressure induces a *cis*-to-*trans* isomerization of double bonds by generation of radical species in the backbone, thermal treatment of poly(phenylacetylene) results in an intramolecular cyclization and subsequent chain cleavage of 1,3,5-triphenylbenzene derivatives. The reaction can be carried out in solution or in the solid state and stimulated with air, pressure or electric fields, but nevertheless, the reaction is not very effective and occurs partially.[79,86-93]

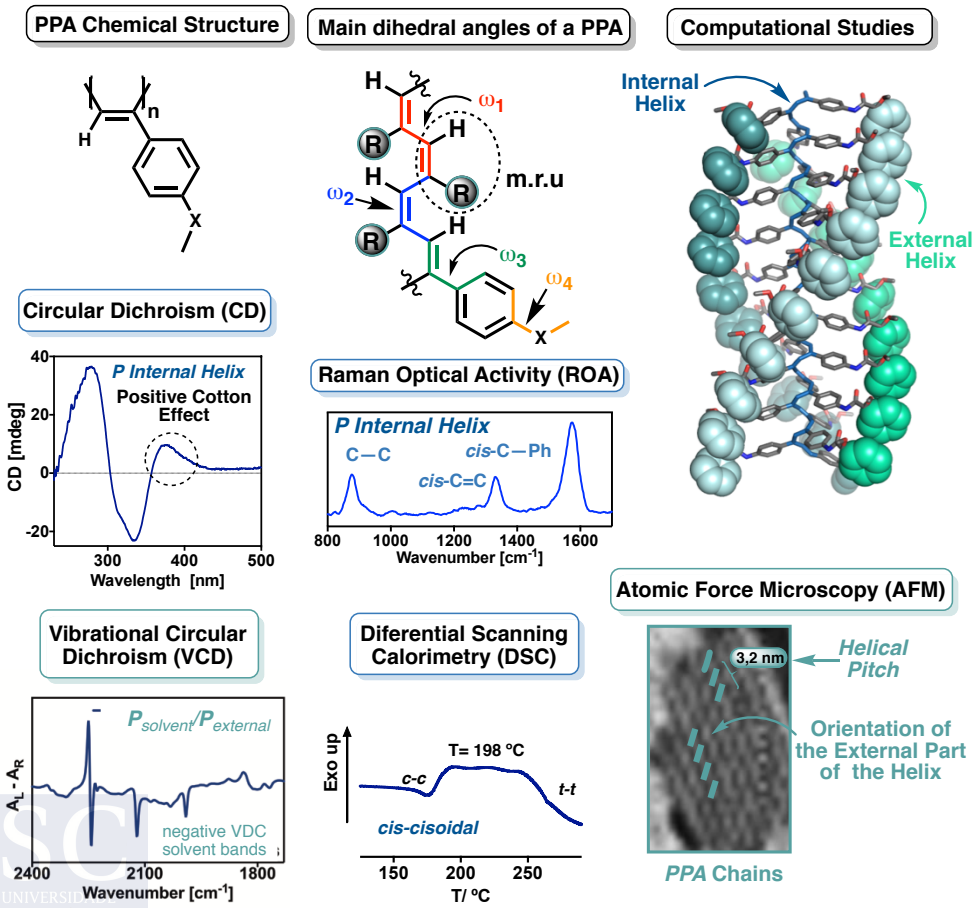

Figure 1. Chemical structure and main dihedral angles of PPAs. Combination of structural techniques —AFM, X-ray, DSC, computational studies, DFT, ECD, VCD, ROA— used to elucidate the 3D structures in PPAs.

In contrast, the controlled irradiation of PPAs under visible light leads to 1,3,5-triphenyl substituted benzenes in a highly selective intramolecular process.[56] From literature it is known that this photocyclic aromatization process takes place in the solid state, while in solution the reaction proceeds in small yields.[56] Interestingly, the reactivity of the polymer backbone depends directly on the configuration of the starting polyene —only those *cis-cisoidal* scaffolds with a short distance between double bonds (< 4Å) were found to react—, and it was used for the formation of self-supporting supramolecular polymeric membranes.[94,95]

Herein, we will show that visible light photochemistry can be implemented as a unique structural tool to identify in solution not only the presence of a *cis-cisoidal* or *cis-transoidal* skeleton of a PPA, but also to provide an approximated dihedral angle for ω_1. The process involves irradiating a dilute PPA solution with visible light (λ> 350 nm) and monitoring the CD decay of the polymer after a short period of time (40-200 min). Moreover, this irradiation protocol and consequent photochemical electrocyclization[78] of the PPA helix is also useful to identify different helices coexisting in a polymer in solution.

2. Results and Discussion

To perform these studies, we selected the PPA that bears the para-ethynylanilide of the (*R*)-α-methoxy-α-trifluoromethylphenylacetic acid (MTPA) [poly-(*R*)-**1**], because this polymer adopts a *cis-cisoidal* scaffold in non-donor solvents and a *cis-transoidal* one in donor solvents.[31] For instance, poly-(*R*)-**1** in chloroform, (non-donor/low polar; classification of solvents based on a combination of donor/acceptor properties and polarities together with their dielectric constants and Gutmann's values),[31] shows a compressed *cis-cisoidal* polyene scaffold (3 nm helical pitch, ω_1= 70° aprox.), with a *P* orientation of both the internal [positive CD at 377 nm] and the external (AFM) helices (Figure 2a). For its part, when poly-(*R*)-**1** is dissolved in THF, (donor/low-polar), the polyene backbone adopts a stretched *cis-transoidal* structure (3.9 nm helical pitch, ω_1 c.a. -155°), where the internal and the external helices are opposite oriented. Thus, while the internal helix has a *M* [CD(-) at 377 nm] helical orientation, the external one rotates in the opposite *P* direction (AFM) (Figure 2b).[31] Therefore, from a single polymer, two different structures (*c-c* and *c-t*) can be generated and submitted to photochemical studies.

Thus, two vials containing 2.1 mg/7·mL ($9.00 \cdot 10^{-4}$ M) of poly-(*R*)-**1** dissolved in chloroform (vial 1) or in THF (vial 2) under an argon atmosphere were irradiated with visible light (ω_1> 350 nm). 200 μL of these two poly-(*R*)-**1** solutions were extracted at different irradiation times and introduced in a 0.1 cm quartz cuvette. ECD studies show

that the ECD spectra of the polymer at the vinylic region decreases with time in both solutions, leading to a null CD although at different rates (Figure 2b-c). Adjusting the CD signal decay of the vinyl band —photochemical electrocyclization process— to a first order reaction showed that the reduction of the 377 nm band to a half height, requires for poly-(*R*)-**1** in chloroform, 27 min of irradiation —half-life [$t_{1/2\,(377\ nm)}$ = 27 min]—, with a rate constant K= $2.507 \cdot 10^{-2}$ min^{-1} (Figure 2d), while when poly-(*R*)-**1** is dissolved in THF the kinetic parameters are $t_{1/2\,(377\ nm)}$= 78 min, and K= $8.825 \cdot 10^{-3}$ min^{-1} (Figure 2d). GPC monitoring of both experiments shows the disappearance of the well-folded poly-(*R*)-**1** chain and its conversion by photochemical electrocyclization process, which evolve after continuously irradiation with visible light to the corresponding 1,3,5-trisubstituted benzene —1,3,5-(*R*)-**1**— unambiguously identified by mass spectroscopy (See figures S21 and S22). However, the main goal of this work is not the generation of the 1,3,5-trisubstituted benzene by a photocyclic aromatization process, which has already been described by Aoki and coworkers.[56] Herein, we look for the time consumed in the photochemical electrocyclization process to reach a null ECD signal in the vinylic region, specific for each secondary structure of a PPA. Thus, to study the photochemical electrocyclization of the polymer, we must monitor the complete disappearance of the polyene ECD band, which is indicative of the loss of its secondary structure. At this stage, no rearomatization with chain cleavage takes place yet and therefore UV-vis studies cannot be used to monitor the photochemical electrocyclization process, due to the presence of polyenes together with the cyclohexadiene units formed (see Figures S20-S27).

Interestingly, irradiation of samples of poly-(*R*)-**1** with different chain lengths produce, at the same concentration and temperature, identical ECD decay patterns, which indicates that the PPA photochemical electrocyclization process is independent of the polymer size (see Figure S30) being only dependent on the secondary structure of the polymer.

Hence, the different kinetic parameters obtained for the photochemical electrocyclization of poly-(*R*)-**1** in $CHCl_3$ and THF (*c-c* and *c-t* structures respectively) indicate that there is a direct relationship between the helical scaffold —secondary structure— adopted by the polyene skeleton and its sensitivity to light irradiation (Figure 3).

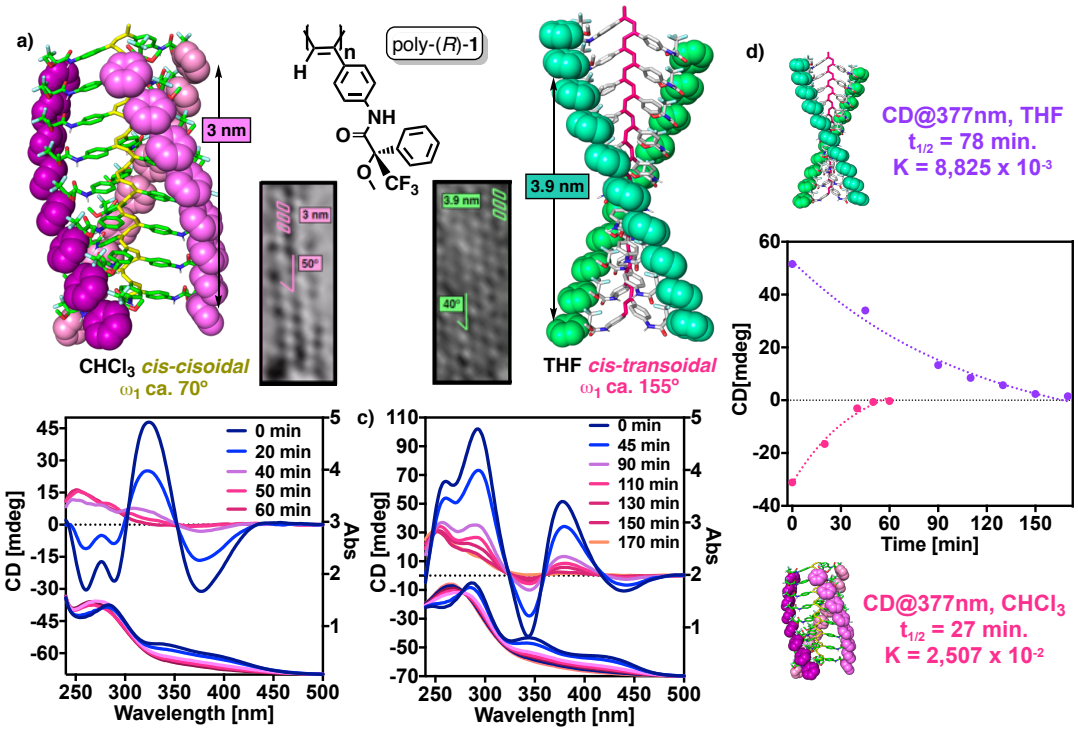

Figure 2. (a) 3D structures of poly-(*R*)-**1** in non-donor ($CHCl_3$, *cis-cisoidal*) and donor (THF, *cis-transoidal*) solvents. ECD and UV-vis spectra of poly-(*R*)-**1** after irradiation with visible light in (b) $CHCl_3$ and (c) THF. (d) ECD signal decay vs time for poly-(*R*)-**1** after irradiation with visible light. [poly-(*R*)-**1**] = $9.00 \cdot 10^{-4}$ M (0.3 $mg \cdot mL^{-1}$ THF or $CHCl_3$). ECD and UV-vis studies were performed in a 0.1 cm quartz cuvette.

In order to evaluate the scope of this process, the generality of those conclusions, and its potential application as a tool to unequivocally determine the *cis-transoidal* or *cis-cisoidal* scaffold of PPAs, we repeated the visible light irradiation experiments with a series of other PPAs with well-known *c-c* or *c-t* helical structure, as described next.

Poly-(*R*)-**2** bearing the para-ethynylbenzamide of (*R*)-phenylglycine methyl ester as substituent was selected as model compound because adopts a well-known *cis-transoidal* helix (3.8 nm, ω_1 c.a. 148°) in $CHCl_3$,[43] with its internal helix *M* oriented [CD(-) at 380 nm], and the external one describing a *P* helix [determined by AFM] (Figure 4a).

Visible light (λ> 350 nm) irradiation studies of [poly-(*R*)-**2**] dissolved in $CHCl_3$ (2.1 mg/7·mL,$1.02 \cdot 10^{-3}$ M) showed a ECD decay that fits to a first order reaction with kinetic parameters: $t_{1/2\,(368\,nm)}$= 63 min and K = $1.088.10^{-2}$ min^{-1}— (figure 4b-c).

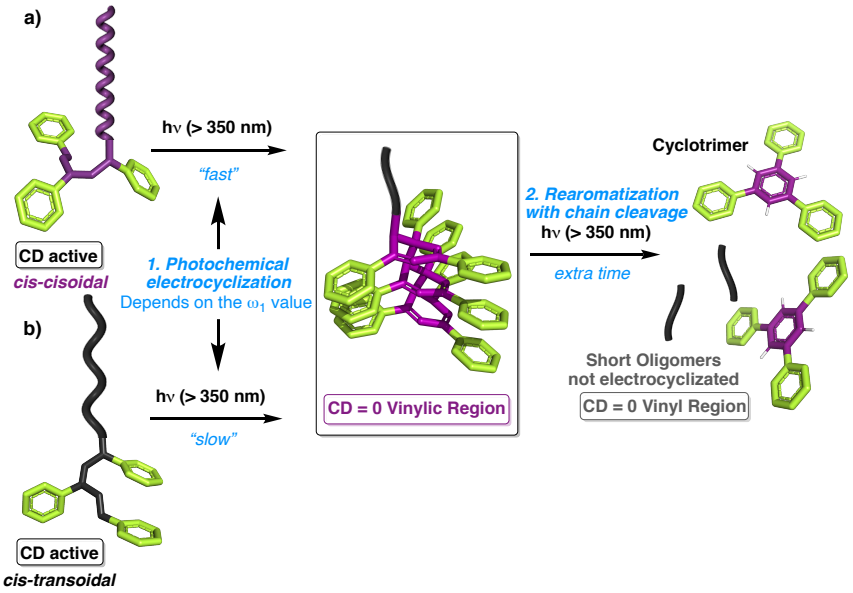

Figure 3. Schematic illustration of the two-step photocyclic aromatization reaction —photochemical electrocyclization (formation of cyclohexadiene units in the main chain) + rearomatization with chain cleavage (formation of 1,3,5-trisubstituted benzenes)— in (a) *cis-cisoidal* and (b) *cis-transoidal* polyene scaffolds.

Comparison of the kinetic parameters obtained for poly-(*R*)-**2** and poly-(*R*)-**1** show the values obtained for poly-(*R*)-**2** are similar to those generated for a THF solution of poly-(*R*)-**1**, and therefore for a *cis-transoidal* helix (poly-(*R*)-**1** $t_{1/2\,(THF)}$ = 78 min; poly-(*R*)-**2** $t_{1/2}$ = 63min), which are clearly different to those obtained when poly-(*R*)-**1** is dissolved in chloroform and corresponds to a *cis-cisoidal helix* (poly-(*R*)-**1** $t_{1/2\,(CHCl3)}$= 27 min; poly-(*R*)-**2** $t_{1/2}$= 63 min). Therefore, the photochemical electrocyclization data suggests that poly-(*R*)-**2** in $CHCl_3$ has a *cis-transoidal* backbone (Figure 4d), needing an extra time for the electrocyclization reaction due to a prior *transoidal to cisoidal* photoinduction reaction.

These data also indicate that there is a correlation between the elongation of the helix (ω_1) and the time needed for the photochemical electrocyclization data suggests that, the one produced before the photocyclic aromatization reaction. Thus, while poly-(*R*)-**2** with ω_1 c.a. 148° needs 63 min for the photochemical electrocyclization, poly-(*R*)-**1** with ω_1 c.a. 155° consumes 15 min. of extra time, due to the presence of a more elongated structure (ω_1 poly-(*R*)-**2** < ω_1 poly-(*R*)-**1**).

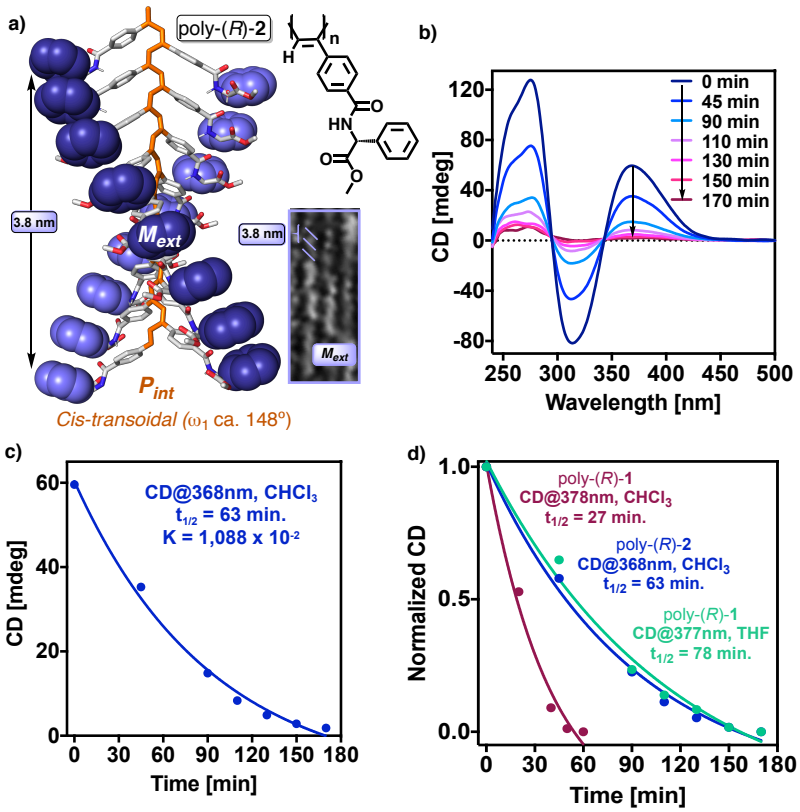

Figure 4. (a) Chemical structure and representative helical scaffold adopted by poly-(*R*)-**2**. (b) CD spectra of poly-(*R*)-**2** in $CHCl_3$ at different irradiation times with visible light (λ> 350 nm) [poly-(*R*)-**2**]= $1.02 \cdot 10^{-3}$ M. (c) First order reaction fit of the $ECD_{(368\ nm)}$ signal decay vs time obtained for the photochemical electrocyclization data suggests that of poly-(*R*)-**2**. (d) Comparison of the first order reaction fit obtained for the normalized ECD signal decay vs time corresponding to the photochemical electrocyclization data suggests that of poly-(*R*)-**1** in $CHCl_3$ and THF and poly-(*R*)-**2** in $CHCl_3$. [poly-(*R*)-**1**]= $9.00 \cdot 10^{-4}$ M; [poly-(*R*)-**2**]= $1.02 \cdot 10^{-3}$ M. ECD studies were performed in a 0.1 cm quartz cuvette.

Another example used to test the correlation between the PPA helical structure and the kinetic parameters of the photochemical electrocyclization process was poly-(*S*)-**3**, that bears the para-ethynylanilide of (*S*)-mandelic acid as substituent.[48] This polymer adopts in $CHCl_3$ a compressed *cis-cisoidal* helix (3.1 nm, ω_1 c.a. 70°), where the internal and the external helices are *P* oriented [CD_{380nm}(-) at 368 nm, ω_1 ca. 70°] (Figure 5a).[48]

Irradiation of a chloroform solution of poly-(*S*)-**3** (2.1 mg·/ 7 mL, $1.19 \cdot 10^{-3}$ M) showed the expected evolution of the CD signal, which fits to a first order decay —kinetic parameters: $t_{1/2\ (386\ nm)}$= 26 min and K= $2.68 \cdot 10^{-2}$ min^{-1}— (figure 5b-c). In this case, the half-time value obtained for poly-(*S*)-**3** is close to the one obtained for a chloroform solution of poly-(*R*)-**1** ($t_{1/2}$ = 27 min figure 5d) and coherent with a similar *cis-cisoidal* scaffold (ω_1 c.a. 70°).

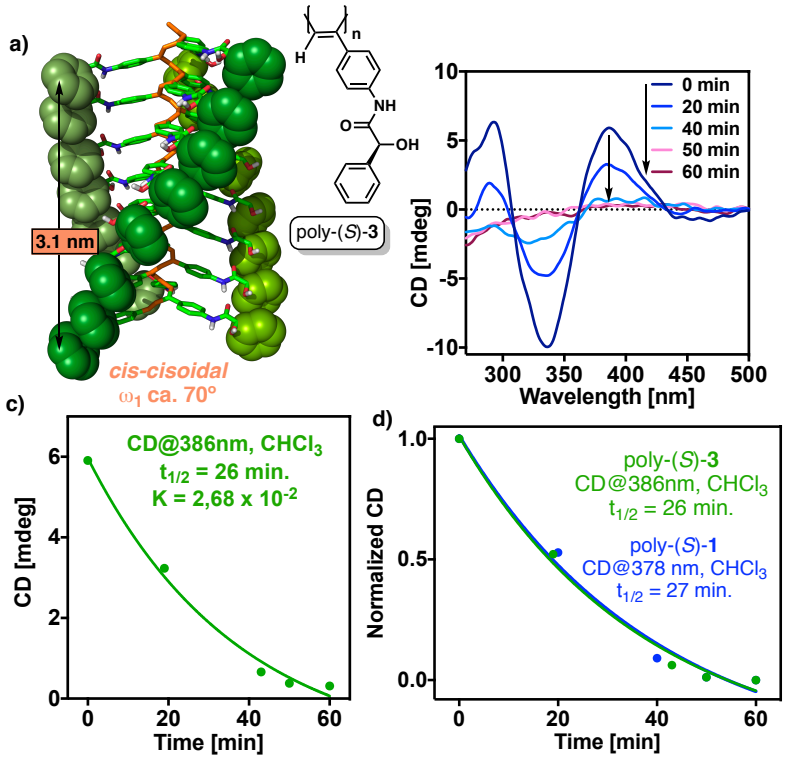

Figure 5. (a) Chemical structure and 3D structure of poly-(*S*)-**3** in THF (*cis-cisoidal*). (b) ECD spectra of poly-(*S*)-**3** after irradiation with visible light in THF. (c) ECD and (d) normalized ECD signal decay vs time for poly-(*S*)-**3** after irradiation with visible light. [poly-(*S*)-**3**] = $1.19 \cdot 10^{-3}$ M. ECD studies were performed in a 0.1 cm quartz cuvette.

To further explore the $t_{1/2}/\omega_1$ relationship, we chose as useful example poly-(*S*)-**4**. This PPA bears the ortho-ethynylanilide of (*S*)-α-methoxy-α-phenylacetic acid as pendant (Figure 6a) and adopts a very stretched -almost flat- helical structure —ω_1 c.a. 170°; P_{int} CD_{484}(+); M_{ext} (AFM)— (Figure 6a).[49]

Irradiation of poly-(*S*)-**4** in $CHCl_3$ (0.3 mg·mL^{-1}, $1.13 \cdot 10^{-3}$ M) showed a very slow CD_{484} signal decay that fits to a first order reaction with a $t_{1/2\,(386\,nm)}$= 1513 min and K= $4.581 \cdot 10^{-4}$ min^{-1}, data that is in full agreement with the presence of an elongated *cis-transoidal* helical structure (Figure 6b-c).

In this case, the photochemical electrocyclization time needed for poly-(*S*)-**4** is much higher than those found for other PPAs with *cis-transoidal* skeletons (poly-(*S*)-**4** $t_{1/2}$= 1513 min vs. poly-(*R*)-**1** $t_{1/2\,(THF)}$= 78 min; poly-(*R*)-**2** $t_{1/2}$= 63 min). This is due to the presence of a highly stretched almost planar helix (poly-(*S*)-**4** ω_1 c.a. 170° vs. poly-(*R*)-**1** ω_1 c.a. 155° (THF); poly-(*R*)-**2** ω_1 c.a. 148°) and coherent with the structure previously reported (figure 6c).

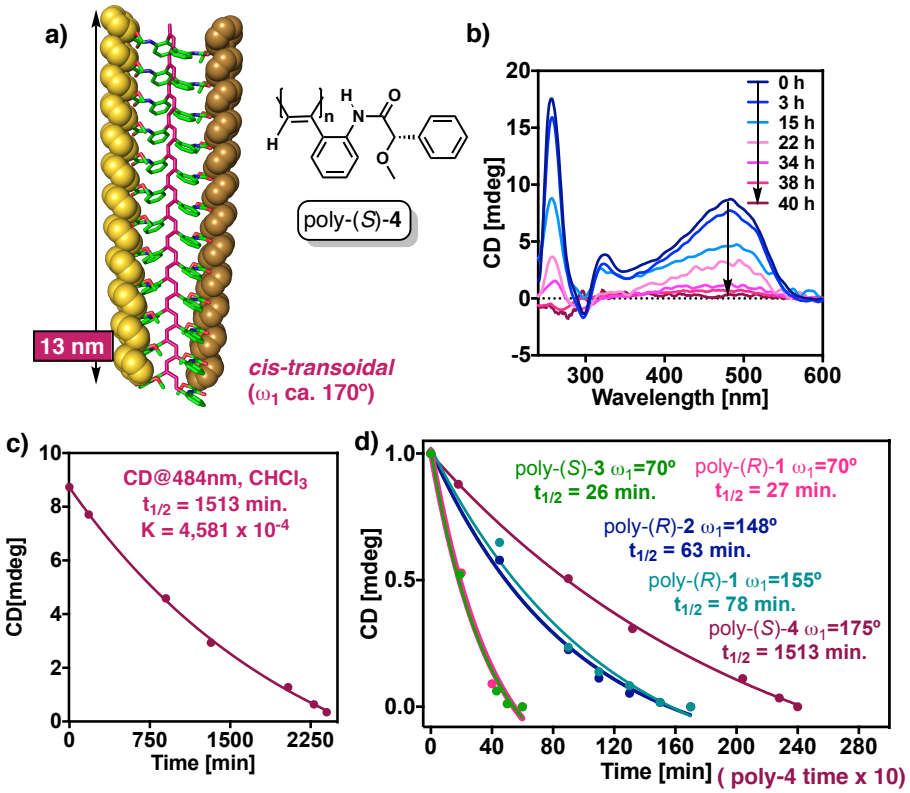

Figure 6. (a) Chemical structure and representative *cis-transoidal* helical scaffold adopted by poly-(*S*)-**4**. (b) CD spectra of poly-(*S*)-**6** at different irradiation times under visible light. (c) ECD and (d) normalized ECD signal decay *vs* time for poly-(*S*)-**4** after irradiation with visible light. [poly-(*S*)-**4**]= $1.13 \cdot 10^{-3}$ M, $CHCl_3$. ECD studies were performed in a 0.1 cm quartz cuvette.

Next, we decided to test the merits of this correlation in more complex systems, namely those PPAs that are constituted by two different scaffolds in equilibrium. Two representative examples are poly-(*S*)-**5**, that bears the meta-ethynylanilide of (*S*)-α-methoxy-α-phenylacetic acid as substituent and poly-(*R*)-**6** with the meta-ethynylbenzamide of (*R*)-phenylglycine methyl ester as pendant.[49] Poly-(*S*)-**5** in chloroform is constituted by an equilibrium mixture of a compressed *cis-cisoidal* —ω_1 c.a. 70°; P_{int} CD_{380}(+); P_{ext} (AFM)— and a streched *cis-transoidal* — ω_1 c.a. 155°; P_{int} CD_{380}(+); M_{ext} (AFM)— helices (Figure 7a), while poly-(*R*)-**6** in the same solvent is formed by a mixture of two *cis-transoidal* helices with different elongation—helix 1: ω_1 c.a. 160°, P_{int} CD_{380}(+), M_{ext} (AFM); helix 2: ω_1 c.a. 165°; P_{int} CD_{380}(+), M_{ext} (AFM)— (Figure 8a).[49] In both cases, poly-(*S*)-**5** and poly-(*R*)-**6,** the polyene band at the CD spectra is constituted by a contribution of the two helical structures, clearly observed in poly-(*R*)-**6** by the presence of a CD band with two peaks. Thus, irradiation studies with visible light (520 nm) of chloroform solutions of poly-(*S*)-**5** (2.1 mg/ 7 mL; $1.13 \cdot 10^{-3}$ M) and poly-(*R*)-**6** (2.1 mg/ 7 mL; $1.02 \cdot 10^{-3}$ M) were followed by studying the CD signal decay at two different

wavelengths for each polymer, one at the beginning of the Cotton band, and the second at the end —poly-(*S*)-**5** CD at 370 and 398 nm; poly-(*R*)-**6** CD at 373 and 428 nm—. In the case of poly-(*S*)-**5**, the ECD spectrum obtained in a 0.1 cm quartz cuvette is too weak to analyze the ECD signal decay during the photochemical electrocyclization process. Thus, to improve the ECD signal, a 1 cm quartz cuvette was used to register the ECD spectrum (Figure 7b). The results showed similar kinetic parameters ($t_{1/2}$) for both quartz cuvettes (Figure S35). To corroborate these results, photochemical electrocyclization studies of poly-(*R*)-**6** were carried out in 1 cm and 0.1 cm quartz cuvettes under the same protocols applied to poly-(*S*)-**5**. As expected, the kinetic parameters ($t_{1/2}$) obtained were almost identical (Figure S36).

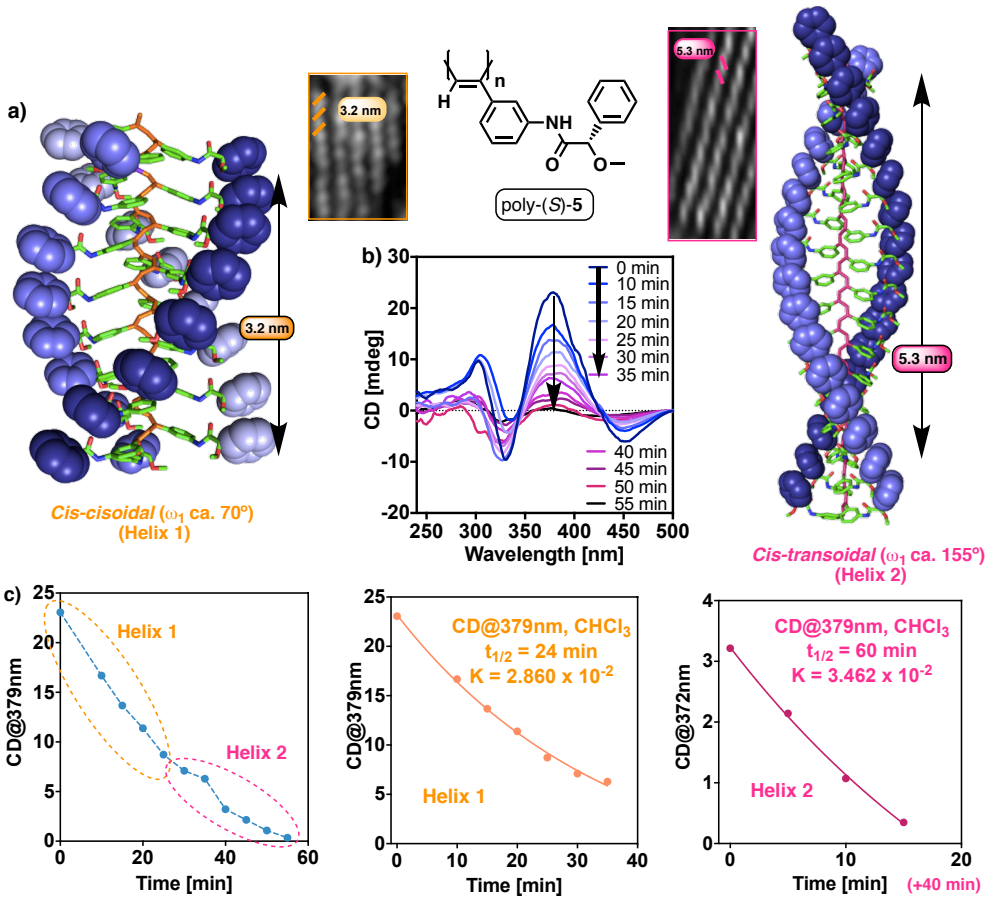

Figure 7. (a) Chemical structure and representative *cis-cisoidal* and *cis-transoidal* helical scaffolds adopted by poly-(*S*)-**5**. (b) ECD spectra of poly-(*S*)-**5** at different times of irradiation under visible light. (c) ECD signal decay *vs* time for poly-(*S*)-**5** after irradiation with visible light. [poly-(*S*)-**5**]= $1.13 \cdot 10^{-3}$ M, $CHCl_3$.

The CD signal decay measured at the two wavelengths showed two different slopes for both polymers that correspond to the photochemical electrocyclization processes followed by the existence of two helices in solution (Figure 7c and Figures S35 and S36). For instance, in poly-(*S*)-**5** the photocyclic process takes place between 0 and 60 min for helix

1, while for helix 2 goes from 40 to 90 min. Both curves —helix 1 and helix 2—can be fitted to a first order reaction, obtaining the following kinetic parameters —$t_{1/2\,(379nm)}$ = 24 min, K = $2.860 \cdot 10^{-2}$ min^{-1} for helix 1, and $t_{1/2\,(379nm)}$ = 60 min, K = $3.462 \cdot 10^{-2}$ min^{-1} for helix 2). The data obtained at a different wavelength, 398 nm, provided similar results (Figure S32). Therefore, helix 1 has a half time (25 min) similar to those obtained for poly-(*R*)-**1** (27 min.) and poly-(*S*)-**3** (26 min) that correspond to a *cis-cisoidal* skeleton (ω_1 c.a. 70°), while helix 2 has a half time (65 min), close to the one obtained for poly-(*R*)-**2** and that corresponds to a *cis-transoidal* polyene structure (ω_1 c.a. 150°).

In the case of poly-(*R*)-**6**, the photochemical electrocyclization of helix 1 takes place between 0 and 180 min, while for helix 2 it goes from 180 to 370 min either at 373 or 428 nm (Figure 8b). Data fitting measured at 373 nm gave the following kinetic parameters —$t_{1/2\,(373nm)}$= 188 min, K= $3.671 \cdot 10^{-3}$ min^{-1} for helix 1, and $t_{1/2\,(373nm)}$= 280 min, K= $2.475 \cdot 10^{-3}$ min^{-1} for helix 2. Similar data was obtained by fitting the data collected at 428 nm (Figure S26). These results indicate that poly-(*R*)-**6** is composed by two *cis-transoidal* helices, with ω_1 value in a range of 150°-170° —poly-(*R*)-**1** ω_1 c.a. 155°, $t_{1/2}$ = 78 min; poly-(*S*)-**4** ω_1 c.a. 170°, $t_{1/2}$= 1513 min—. The ω_1 value deduced from these irradiation studies for each helical structure of poly-(*S*)-**5** and poly-(*R*)-**6** are coincident with the information reported in the literature,[49] demonstrating again the robustness of the PPA photochemical electrocyclization as structural tool.

Finally, to illustrate the relationship between the ω_1 and the half-time $t_{1/2}$ of the photochemical electrocyclization, we plotted the normalized CD signal decay *vs.* time for all the structures (Figures 9a) and the $t_{1/2}$ versus their ω_1 values, taken as a stretching indicator (Figure 9b). This graph not only shows the correlation between $t_{1/2}$ and ω_1 values, but also serves to illustrate the dependence of the photochemical electrocyclization process with the *cis-cisoidal* or *cis-transoidal* structure of the original helix, where a *transoidal* to *cisoidal* conformational change is required before the photocyclic reaction to takes place.

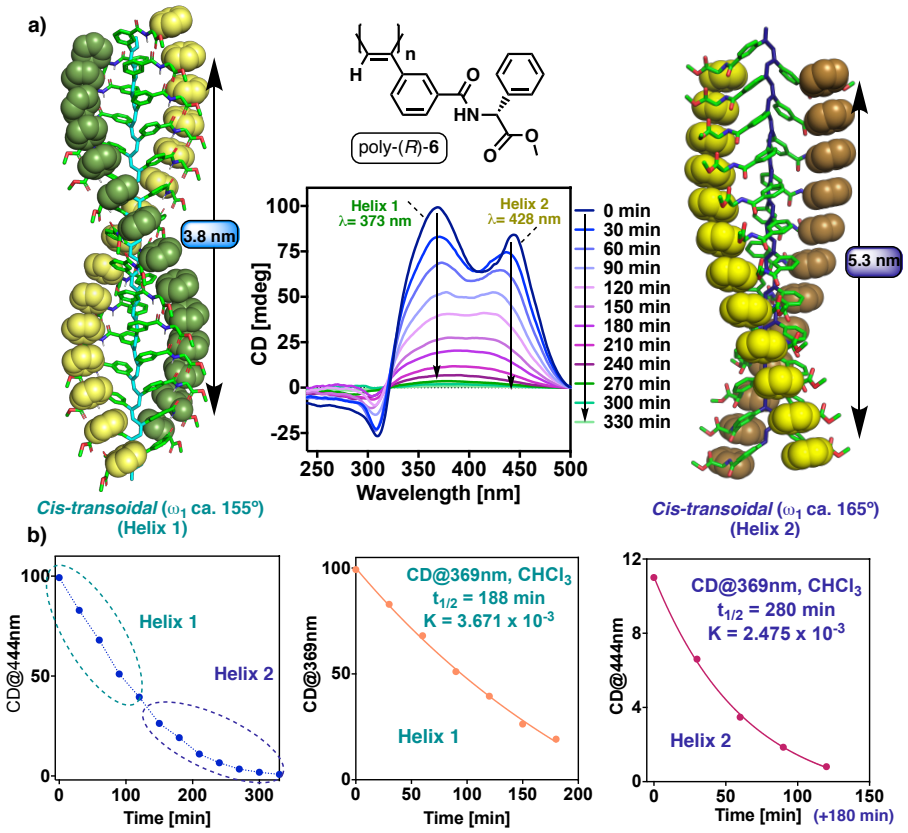

Figure 8. (a) Chemical structure and representative *cis-transoidal* helical scaffolds adopted by poly-(*R*)-**6** and CD spectra of poly-(*R*)-**6** at different times of irradiation under visible light. (b) ECD signal decay *vs* time for poly-(*R*)-**6** after irradiation with visible light. [poly-(*R*)-**6**]= $1.02 \cdot 10^{-3}$ M, $CHCl_3$. ECD studies were performed in a 1 cm quartz cuvette for poly-(S)-**5** and poly-(*R*)-**6.**

This relationship responds to equation (1)

$$Y=Y0 + (Plateau-Y0)*(1-\exp(-K*x)) \quad (1)$$

where Y is ω_1, Plateau is the ω_1 value at infinite time, K is the photochemical electrocyclization rate and x is $t_{1/2}$.

Our data were fitted to equation (1), to obtain equation (2) (R square 0.993), useful to determine the approximated ω_1 from the $t_{1/2}$.

$$\omega_1 = -147.5 + 312.6*(1-\exp(-4.659 \cdot 10^{-2}*t_{1/2})) \quad (2)$$

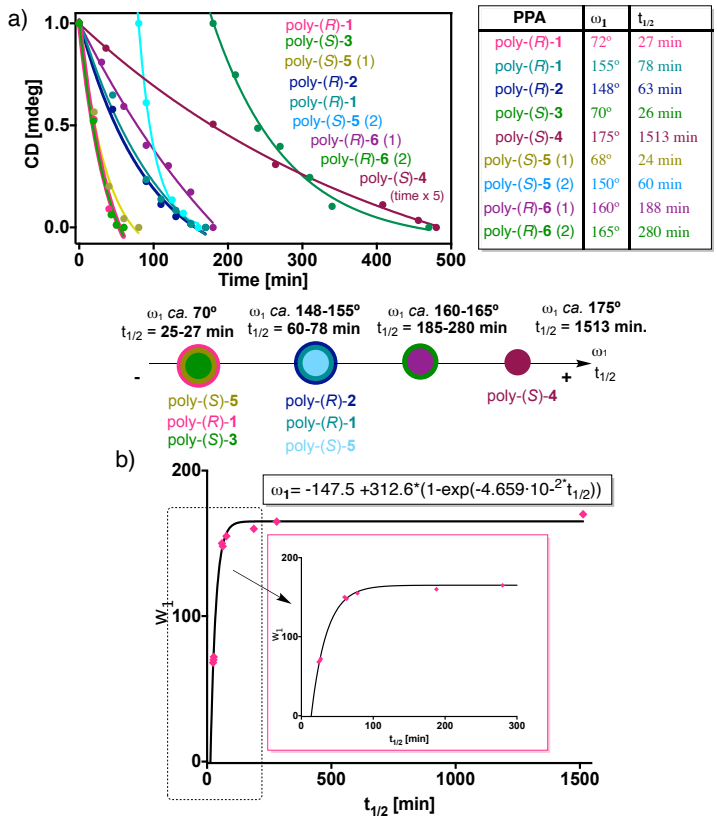

Figure 9. a) Normalized CD signal decay of poly-(**1**-**6**) during photochemical electrocyclization of the different PPA backbones. b) Variation of the PPA ω_1 vs $t_{1/2}$ of the backbone photochemical electrocyclization process and the corresponding fit to an exponential equation.

As a proof of this concept, we decided to test it with a novel PPA designed to be folded into a compressed (helix 1) and a stretched (helix 2) helix. To this end, we prepared poly-(*R*)-**7** PPA that bears a *meta* substituted (*R*)-MTPA group as pendant— (Figure 10a for synthetic and characterization details).[96] Poly-(*R*)-**7** is an isomer of poly-(*R*)-**1**, which has the MTPA group in the *para* position.

Next, poly-(*R*)-**7** was submitted to light irradiation in $CHCl_3$ and THF ([Poly-(*R*)-**7**]= 2.1 mg/ 7 mL; $9.00 \cdot 10^{-4}$ M).

Again, the ECD signal obtained for poly-(*R*)-**7** in both solvents was weak when using the 0.1 cm quartz cuvette. Because of this, we present the photochemical electrocyclization studies of this polymer in a 1 cm quartz cuvette (Figure 10) (see Figures S36 and S37 for 0.1 cm quartz cuvette studies).

In both cases, the CD signal showed in coherence with the previous results, the expected decay of the polyene band associated to the photochemical electrocyclization (Figure 7b-c). Plotting the CD_{370} signal versus time, in both solvents, gave CD curves with two different slopes corresponding to a mixture of two helices in solution. The following

kinetic parameters were obtained after independent first order decay fits of the data in the two solvents.

Poly-(*R*)-**7** dissolved in chloroform showed $t_{1/2\,(381nm)}$= 32 min, K= 2.131·10^{-2} min^{-1} for helix 1, and $t_{1/2\,(381nm)}$ = 61 min, K = 4.425·10^{-2} min^{-1} for helix 2. Application of equation 2 to those data gives for helix 1, ω_1= 89°, which corresponds to a *cis-cisoidal structur*e and ω_1= 146° for helix 2, that corresponds to a stretched *cis-transoidal* scaffold.

The same study for poly-(*R*)-**7** dissolved in THF, afforded $t_{1/2\,(362nm)}$= 24 min, K= 2.863·10^{-2} min^{-1} for helix 1, and $t_{1/2\,(362nm)}$= 76 min, K = 9.110·10^{-3} min^{-1} for helix 2. These kinetic values correspond to a mixture of a *cis-cisoidal* (helix 1, ω_1= 60°) and a *cis-transoidal* (helix 2, ω_1= 156°) helices, in good agreement with the expected ω_1 value for poly-(*R*)-**7**.

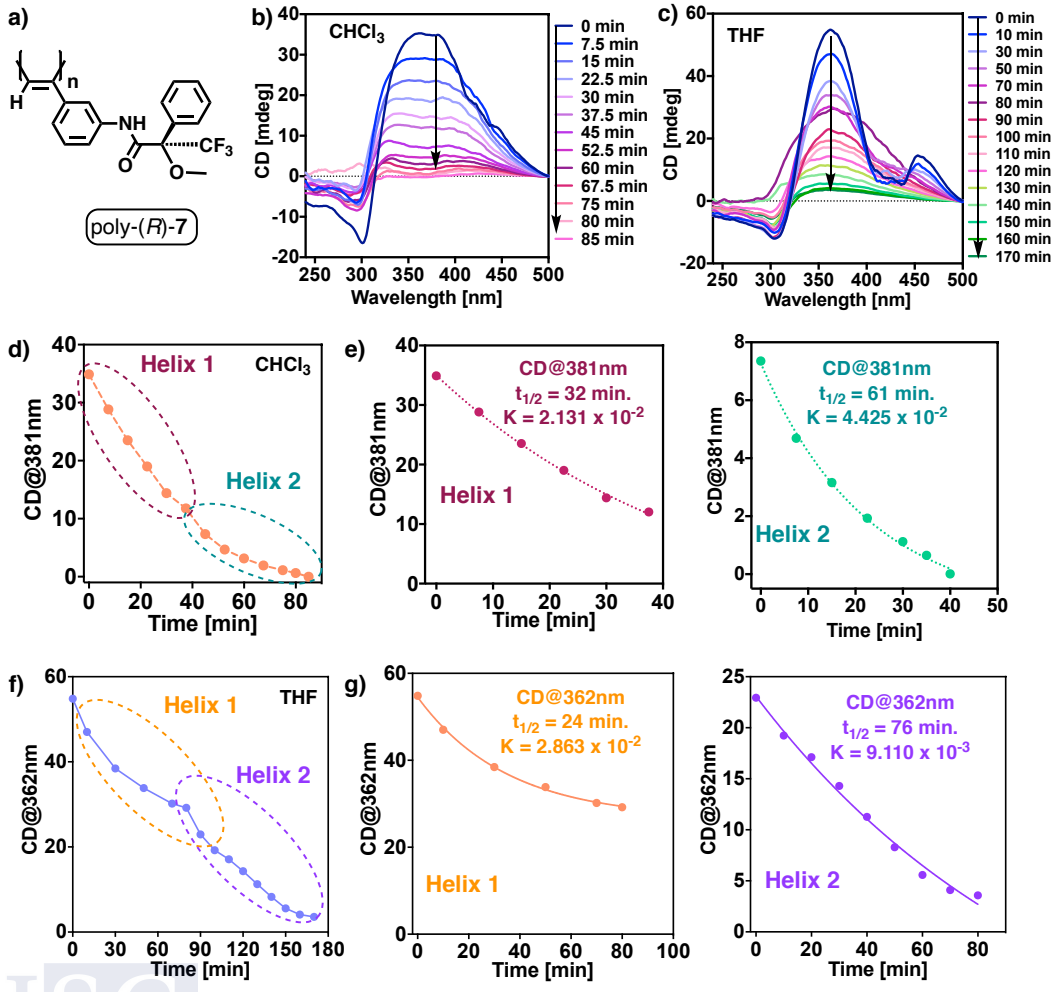

Figure 10. (a) Structure of poly-(*R*)-**7**. (b) CD spectra of poly-(*R*)-**7** in $CHCl_3$, at different times of irradiation under visible light (c) CD spectra of poly-(*R*)-**7**, in THF, at different times of irradiation under visible light. (d), (e) ECD signal decay *vs* time for poly-(*R*)-**7** after irradiation with visible light in $CHCl_3$. [poly-(*R*)-**7**] = 9.00·10^{-4} M, $CHCl_3$. (f), (g) ECD signal decay *vs* time for poly-(*R*)-**7** after irradiation with visible light in THF. [poly-(*R*)-**7**] = 9.00·10^{-4} M, THF. ECD studies were performed in a 0.1 cm quartz cuvette.

3. Conclusion

In conclusion, it has been demonstrated through a good number of PPAs with different well-known helical structures —6 polymers, 9 helical scaffolds— that visible light irradiation can be introduced as a powerful technique to determine the secondary structure of polyacetylenes. The basis of the method lies on the quite different rate observed for the photochemical electrocyclization depending on the scaffold (*cis-cisoidal*, *cis-transoidal*) of the helical polymer.

To perform these studies, vials containing a dilute solution of a PPA [(poly-(**1**-**6**)]= 2.1 mg/ 7 mL; c.a. $1 \cdot 10^{-3}$ M] was irradiated with visible light (ω_1> 350 nm) and the CD signal decay monitored versus time to afford the photochemical electrocyclization rate and the $t_{1/2}$ as the relevant parameters.

The results show that there is a direct relationship between the elongation of a PPA (ω_1) and its $t_{1/2}$. For instance, $t_{1/2}$= 26 min corresponds to a *cis-cisoidal* PPA with ω_1 c.a. 70°. such as poly-(*R*)-**1** ($CHCl_3$), poly-(*S*)-**3** or poly-(*S*)-**5** (helix 1). For their part, PPAs with more elongated chain (larger ω_1) show higher $t_{1/2}$ values —poly-(*R*)-**1** (THF) (ω_1= 155°, $t_{1/2}$= 78 min.); poly-(*R*)-**2** (ω_1= 148°, $t_{1/2}$= 63 min); poly-(*S*)-**4** (ω_1= 170°, $t_{1/2}$= 1513 min)—. The kinetic data for all the polymers used in this study, fit well into equation 2 that therefore can be used to predict the scaffold of a PPA (ω_1) from its $t_{1/2}$ kinetic value. The use of the visible light for the photochemical electrocyclization of PPAs as a tool to determine their helical structure by using a $t_{1/2}$/ ω_1 relationship, is exceptionally important in this field because no other techniques can provide an approximated value for ω_1 in solution. This value is necessary to build up an approximated helical structure of the PPA, where important helical parameters such as relative helical sense of the internal and external helices of a PPA depends on this value —*cis-cisoidal* structures (ω_1< 90°) both helices rotate in the same direction, while in *cis-transoidal* scaffolds (ω_1< 90°) both helices rotate in opposite directions

Although the studies in this work are limited to PPAs substituted by amide groups (anilide, benzamide), no doubt similar investigations can be carried out with other PPAs that bear other connecting groups (ester, ether...). To do this, it will be essential to have a solid base of structural information on these polymers, including AFM images and theoretical calculations, in order to know if the results would be comparable to those of the anilide/benzamide PPAs.

4. References

[1] E. Yashima, N. Ousaka, D. Taura, K. Shimomura, T. Ikai, K. Maeda. *Chem. Rev.,* **2016**, *116*, 13752-13990.

[2] E. Yashima, K. Maeda, H. Iida, Y. Furusho, K. Nagai. Helical Polymers: Synthesis, Structures, and Functions. *Chem. Rev.,* **2009**, *109*, 6102-6211.

[3] T. Nakano, Y. Okamoto. Synthetic Helical Polymers: Conformation and Function. *Chem. Rev.*, **2001**, *101*, 4013-4038.

[4] E. Schwartz, M. Koepf, H. J. Kitto, R. J. M. Nolte, A. E. Rowan. *Polym. Chem.,* **2011**, *2*, 33-47.

[5] K. Maeda, M. Nozaki, K. Hashimoto, K. Shimomura, D. Hirose, T. Nishimura, G. Watanabe, E. Yashima. *J. Am. Chem. Soc*., **2020**, *142*, 7668-7682.

[6] E. Yashima, K. Maeda, Y. Furusho. *Acc. Chem. Res.,* **2008**, *41*, 1166-1180.

[7] R. Ishidate, A. J. Markvoort, K. Maeda, E. Yashima. *J. Am. Chem. Soc.*, **2019**, *141*, 7605-7614.

[8] K. Maeda, D Hirose, N. Okoshi, K. Shimomura, Y. Wada, T. Ikai, S. Kanoh, E. Yashima. *J. Am. Chem. Soc.,* **2018**, *140*, 3270−3276.

[9] R. Sakai, E. B. Barasa, N. Sakai, S. -I. Sato, T. Satoh, T. Kakuchi. *Macromolecules*, **2012**, *45*, 8221-8227.

[10] E. Yashima, K. Maeda. *Macromolecules*, **2008**, *41*, 3-12.

[11] K. Maeda, E. Yashima. *Top. Curr. Chem.* **2006**, *265*, 47-88.

[12] R. Nonokawa, E. Yashima. *J. Am. Chem. Soc.*, **2003**, *125*, 1278-1283.

[13] E. Yashima, K. Maeda, Y. Okamoto. *Nature*, **1999**, *399*, 449-451.

[14] E. Yashima, K. Maeda, T. Matsushima, Y. Okamoto, Y. *Chirality*, **1997**, *9*, 593-600.

[15] M. Ando, R. Ishidate, T. Ikai, K. Maeda, E. Yashima. *J. Polym. Sci., Part A: Polym. Chem.* **2019**, *57*, 2481-2490.

[16] C. Zhang, Y. Qiu, S. Bo, F. Wang, Y. Wang, L. Liu, Y. Zhou, H. Niu, H Dong, T. Satoh. *J. Polym. Sci., Part A: Polym. Chem.* **2019**, *57*, 1024-1031.

[17] R. P. Megens, G. Roelfes. *Chem. Eur. J.* **2011**, *17*, 8514-8523.

[18] E. Anger, H. Iida, T. Yamaguchi, K. Hayashi, D. Kumano, J. Crassous, N. Vanthuyne, C. Roussel, E. Yashima. *Polym. Chem*. **2014**, *5*, 4909-4914.

[19] R. Ishidate, T. Sato, T. Ikai, S. Kanoh, E. Yashima, K. Maeda. *Polym. Chem.*, **2019**, *10*, 6260-6268.

[20] D. Hirose, A. Isobe, E. Quiñoá, F. Freire, K. Maeda. *J. Am. Chem. Soc.* **2019**, *141*, 8592-8598.

[21] J. Shen, Y. Okamoto. *Chem. Rev*., **2016**, *116*, 1094-1138.

[22] K. Shimomura, T. Ikai, S. Kanoh, E. Yashima, K. Maeda. *Nat. Chem.* **2014**, *6*, 429-434.

[23] J. Liu, J. W. Y. Lam, B. Z. Tang. *Chem. Rev.*, **2009**, *109*, 5799-5867.

[24] C. I. Simionescu, V. Percec. *Prog. Polym. Sci.*, **1982**, *8*, 133-214.

[25] V. Percec. *Israel J. Chem*. **2020**, *60*, 48-66.

[26] R. Rodríguez, E. Suárez-Picado, E. Quiñoá, R. Riguera, F. Freire. *Angew. Chem. Int. Ed.* **2020**, *59*, 8616-8 622.

[27] R. Rodríguez, E. Quiñoá, R. Riguera, F. Freire. *Small,* **2019**, *15*, 1805413.

[28] F. Ishiwari, K. Nakazono, Y. Koyama, T. Takata. *Angew. Chem. Int. Ed.,* **2017**, *56*, 14858-14862.

[29] R. Rodríguez, S. Arias, E. Quiñoá, R. Riguera, F. Freire. *Nanoscale*, **2017**, *9*, 17752-17757.

[30] N. Zhu, K. Nakazono, T. Takata. *Chem. Commun.,* **2016**, *52*, 3647-3649.

[31] S. Leiras, F. Freire, J. M. Seco, E. Quiñoá, R. Riguera. *Chem. Sci.*, **2013**, *4*, 2735-2743.

[32] K. Maeda, H. Mochizuki, M. Watanabe, E. Yashima. *J. Am. Chem. Soc*., **2006**, *128,* 7639-7650.

[33] K. Maeda, N. Kamiya, E. Yashima. *Chem.Eur. J.,* **2004**, *10*, 4000-4010.

[34] T. Ikai, R. Ishidate, K. Inoue, K. Kaygisiz, K. Maeda, E. Yashima. *Macromolecules*, **2020**, *53*, 973-981.

[35] M. Alzubi, S. Arias, R. Rodríguez, E. Quiñoá, R. Riguera, F. Freire. *Angew. Chem. Int. Ed.*, **2019**, *58*, 13365-13369.

[36] R. Rodríguez, E. Quiñoá, R. Riguera, F. Freire. *Chem. Mater.* **2018**, *30*, 2493-2497.

[37] T. Van Leeuwen, G. H. Heideman, D. Zhao, S. J. Wezenberg, B. L. Feringa. *Chem. Commun.* **2017**, *53*, 6393-6396.

[38] S. Arias, M. Núñez-Martínez, E. Quiñoá, R. Riguera, F. Freire. *Polym. Chem*., **2017**, *8*, 3740-3745.

[39] M. Alzubi, S. Arias, I. Louzao, E. Quiñoá, R. Riguera, F. Freire. *Chem. Commun*., **2017**, *53*, 8573-8576.

[40] S. Arias, J. Bergueiro, F. Freire, E. Quiñoá, R. Riguera. *Small*, **2016**, *12*, 238-244.

[41] S. Arias, F. Freire, E. Quiñoá, R. Riguera. *Polym. Chem*., **2015**, *6*, 4725-4733.

[42] F. Freire, J. M. Seco, E. Quiñoá, R. Riguera. *Angew. Chem. Int. Ed.*, **2011**, *50*, 11692-11696.

[43] I. Louzao, J. M. Seco, E. Quiñoá, R. Riguera. *Angew. Chem. Int. Ed.* **2010**, *49*, 1430-1433.

[44] V. Percec, E. Aqad, M. Peterca, J. G. Rudick, L. Lemon, J. C. Ronda, B. B. De, P. A. Heiney, E. W. Meijer. *J. Am. Chem. Soc.*, **2006**, *128*, 16365-16372.

[45] T. Taniguchi, T. Yoshida, K. Echizen, K. Takayama, T. Nishimura, K. Maeda. *Angew. Chem. Int. Ed.*, **2020**, *59*, 8670-8680.

[46] N. S. L. Tan, A. B. Lowe. *Angew. Chem. Int. Ed.*, **2020**, *59*, 5008-5021.

[47] Z. Ke, S. Abe, T. Ueno, K. Morokuma. *J. Am. Chem. Soc*., **2011**, *133*, 7926-7941.

[48] K. Cobos, R. Rodríguez, O. Domarco, B. Fernández, E. Quiñoá, R. Riguera, F. Freire. *Macromolecules*, **2020**, *53*, 3182-3193.

[49] R. Rodríguez, E. Quiñoá, R. Riguera, F. Freire. *J. Am. Chem. Soc.* **2016**, *138*, 9620-9628.

[50] Y. Yoshida, Y Matawari, A. Motoshige, R. Motoshige, T. Hiraoki, M. Wagner, K. Müllen, M. Tabata. *J. Am. Chem. Soc.*, **2013**, *135*, 4110-4116.

[51] K. Morino, K. Maeda, Y. Okamoto, E. Yashima, T. Sato. *Chem. Eur. J*., **2002**, *8*, 5112-5120.

[52] F. Freire, E. Quiñoá, R. Riguera. *Chem. Commun.*, **2017**, *53*, 481-492.

[53] C. I. Simionescu, V. Percec, S. Dumitrescu. *J. Polym. Sci., Polym. Chem. Ed.* **1977**, *15*, 2497-2509.

[54] C. I. Simionescu, V. Percec. *J. Polym. Sci. B Polym. Lett. Ed.* **1979**, *17*, 421-429.

[55] V. Percec. *Polym. Bull.* **1983**, *10*, 1–7.

[56] L. Liu, T. Namikoshi, Y. Zang, T. Aoki, S. Hadano, Y. Abe, I. Wasuzu, T. Tsutsuba, M. Teraguchi, T. Kaneko. *J. Am. Chem. Soc.***, 2013**, *135*, 602-605.

[57] H. Shirakawa, T. Ito, S. Ikeda. *Polym. J.* **1973**, *4,* 460-462.

[58] L. Palomo, R. Rodríguez, S. Medina, E. Quiñoá, J. Casado, F. Freire, F.J. Ramírez. *Angew. Chem. Int. Ed*., **2020**, *59*, 9080-9087.

[59] B. Nieto-Ortega, R. Rodríguez, S. Medina, E. Quiñoá, R. Riguera, J. Casado, F. Freire, F. J. Ramírez. *J. Phys. Chem. Lett.*, **2018**, *9*, 2266-2270.

[60] Tabei, J.; Shiotsuki, M.; Sanda, F.; Masuda, T. *Macromolecules* **2005**, *38*, 9448-9454.

[61] T. Kaneko, Y. Umeda, T. Yamamoto, M. Tereguchi, T. Aoki. *Macromolecules* **2005**, *38*, 9420-9426.

[62] F. Takei, H. Hayashi, K. Onitsuka, N. Kobayashi, S. Takahashi. *Angew. Chem. Int. Ed.* **2001**, *40*, 4092-4094.

[63] R. Rodríguez, J. Ignés-Mullol, F. Sagués, E. Quiñoá, R. Riguera, F. Freire. *Nanoscale*, **2016**, *8*, 3362-3367.

[64] J. Kumaki. *Polym. J.*, **2016**, *48*, 3-14.

[65] J. Kumaki, S.-I. Sakurai, E. Yashima. *Chem. Soc. Rev.*, **2009**, *38*, 737-746.

[66] S.-I. Sakurai, K. Okoshi, J. Kumaki, E. Yashima. *J. Am. Chem. Soc.* **2006**, *128*, 5650-5651.

[67] K. Okoshi, S.-I. Sakurai, S. Ohsawa, J. Kumaki, E. Yashima. *Angew. Chem. Int. Ed.* **2006**, *45*, 8173-8176.

[68] S.-I. Sakurai, K. Okoshi, J. Kumaki, E. Yashima. *Angew. Chem. Int. Ed.*, **2006**, *45*, 1245-1248.

[69] V. Percec, J. G. Rudick, M. Peterca, S. R. Staley, M. Wagner, M. Obata, C. M. Mitchell, W.-D. Cho, V. S. K. Balagurusamy, J. N. Lowe, M. Glodde, O. Weichold, K. J. Chung, N. Ghionni, S. N. Magonov, P. A. Heiney. *Chem. Eur. J.,* **2006**, *12*, 5731-5746.

[70] V. Percec, J. G. Rudick, M. Wagner, M. Obata, C. M. Mitchell, W.-D. Cho, S. N. Magonov. *Macromolecules,* **2006**, *39*, 7342-7351.

[71] J. G. Rudick and V. Percec. *Macromol. Chem. Phys.*, **2008**, *209,* 1759-1768.

[72] V. Percec, M. Obata, J. G. Rudick, B. B. De, M. Glodde, T. K. Bera, S. N. Magonov, V. S. K. Balagurusamy, P. A. Heiney. *J. Polym. Sci. Part A Polym. Chem.,* **2002**, *40*, 3509–3533.

[73] A. Motoshige, Y. Mawatari, R. Motoshige, Y. Yoshida, M. Tabata. *J. Polym. Sci., Part A: Polym. Chem.*, **2013**, *51*, 5177-5183.

[74] X.-Q. Liu, J. Wang, S. Yang, E.-Q. Chen. *ACS Macro Lett.*, **2014**, *3*, 834-838.

[75] V. Percec, J. G. Rudick, M. Peterca, E. Aqad, M. R. Imam, P. A. Heiney. *J. Polym. Sci., Part A: Polym. Chem.*, **2007**, *45*, 4974-4987.

[76] V. Percec, M. Peterca, J. G. Rudick, E. Aqad, M. R. Imam, P. A. Heiney. *Chem.–Eur. J.*, **2007**, *13*, 9572-9581.

[77] V. Percec, J. G. Rudick, M. Peterca, P. A. Heiney. *J. Am. Chem. Soc.*, **2008**, *130*, 7503-7508.

[78] V. Percec, J. G. Rudick, M. Peterca, M. Wagner, M. Obata, C. M. Mitchell, W. D. Cho, V. S. K. Balagurusamy, P. A. Heiney. *J. Am. Chem. Soc.,* **2005**, *127*, 15257-15264.

[79] J. G. Rudick, V. Percec. *Acc. Chem. Res.,* **2008**, *41*, 1641-1652.

[80] B. L. Feringa, W. R. Browne. *Nature Nanotech*., **2008**, *3* 383-384.

[81] A. Miyasaka, T. Sone, Y. Mawatari, S. Setayesh, K. Müllen, M. Tabata. *Macromol. Chem. Phys.,* **2006**, *207*, 1938-1944.

[82] T. Ito, H. Shirakawa, S. Ikeda. *J. Polym. Sci., Part A: Polym. Chem.,* **1996**, *34*, 2533-2542.

[83] B. Fernández, R. Rodríguez, E. Quiñoá, R. Riguera, F. Freire. *ACS Omega*, **2019**, *4*, 5233-5240.

[84] B. Fernández, R. Rodríguez, A. Rizzo, E. Quiñoá, R. Riguera, F. Freire. *Angew. Chem. Int. Ed.,* **2018**, *57*, 3666-3670.

[85] E. Yashima. *Polymer Journal*, **2010**, *42*, 3-16

[86] V. Percec, J. G. Rudick, M. Peterca, M. Wagner, M. Obata, C. M. Mitchell, W. D. Cho, V. S. K. Balagurusamy, P. A. Heiney. *J. Am. Chem. Soc.*, **2005**, *127*, 1527-15264.

[87] B. L. Feringa, W. R. Browne. Nature Nanotechnology, **2008**, *3*, 383-383,

[88] M. Tabata, Y. Tanaka, Y. Sadahiro, T. Sone, K. Yokota, I. Miura. *Macromolecules*, **1997**, *30*, 5200-5204.

[89] M. Tabata, T. Sone, Y. Sadahiro, K. Yokota. *Macromol. Chem. Phys.*, **1998**, *199*, 1161-1166.

[90] C. I. Simionescu, V. Percec. *J. Pol. Science: Polymer Chemistry Edition*, **1980**, *18*, 147-155.

[91] V. Percec, J. G. Rudick. *Macromolecules*, **2005**, *38*, 7241-7250.

[92] C. I. Simionescu, V. Percec. *J. Pol. Science: Polymer symposia*. **1980**, *67*, 43-71

[93] V. Percec, J. Rudick, P. Nomber, W. Buchowicz. *J. Polym. Sci.*, *Part A: Polym. Chem.* **2002**, *40*, 3212-3220.

[94] M. Miyamata, T. Namikoshi, L. Liu, L. Zang, Y. Zang, T. Aoki, Y. Abe, Y. Onimayama, T. Tsutsuba, M. Teraguchi, T. Kaneko. *Polymer*, **2013**, *54*, 4431-4435.

[95] L. Liu, G. Zhang, T. Aoki, Y. Wang, T. Kaneko, M. Teraguchi, C. Zhang, H. Dong. *ACS Macro Lett.* **2016**, *5*, 1381–1385.

[96] Literature show that *meta*- substituted PPAs are usually formed by an equilibrium between a compressed helix, coincident with the one adopted in the *para*-substituted form, and another more elongated one (see references 49 and 50).

Chapter IV

Helix Reversals in Poly(phenylacetylene)s: More than Structural Motifs

CHAPTER IV: Helix Reversals in Poly(phenylacetylene)s: More than Structural Motifs

Abstract

The secondary structure and folding of dynamic helical polymers such as poly(phenylacetylene)s (PPAs) have been scarcely studied during the last decades due to the complexity of the systems. Important parameters such as the helical folding, or the presence of helix reversals along a polymer chain in solution were no addressed until now. Herein, photo-chemical electrocyclization (PE) of PPAs will be used as a tool to determine not only the presence of a cis-cisoidal or cis-transoidal polyene backbone by performing the experiments at different temperatures (room temperature and 4°C), but also to obtain an approximate value of the percentage of helix reversals along a chain. To perform these studies, a library of well folded PPAs —homopolymers and copolymers showing chiral conflict effect— were used to stablish a relationship between the PE rate and the percentage of reversals along a certain helix scaffold (%r). The PE of a dynamic PPA depends only on the helical scaffold adopted by the polymer and the number of reversals, without being affected by the chemical structure of the pendant group. Four different equations were obtained from these studies to determine the %r in a PPA. The application of one equation or the other will depend on the helical scaffold adopted by the PPA —c-c (ω_1 ca. 65-80°); c-t (ω_1 ca. 145-150°); c-t (ω_1 ca. 155-160°); c-t (ω_1 ca. 165°)—. These studies are of great interest because allow us also to determine from a group of ECD active PPAs, which are the best folded, without looking only at the intensity of the ECD trace.

1. Introduction

Dynamic helical polymers have attracted the attention of the scientific community during the last decades due to their stimuli responsive properties and the functionality attributed to the helical scaffold. Thus, while helical sense and elongation of dynamic helical polymers can be altered by their interaction with external stimuli,[1-21] the helical scaffolds adopted by the polymers are responsible of their applications in different fields such as asymmetric synthesis,[22-24] chiral recognition,[25] or chiral stationary phases in HPLC.[26-28] Importantly, to create a dynamic helical polymer with a good performance in certain applications it is necessary to know its secondary structure, which also allows establishing a structure/function relationship in this kind of materials. Among dynamic helical polymers, poly(phenylacetylene)s (PPAs) has been extensively studied due to the robustness of the polymerization reaction with Rh(I) catalysts, which can be done in polar and non-polar solvents, with phenylacetylene monomers bearing different polar and non-polar functional groups.[29-31] In all cases, polymers with high stereoregularity, *cis* configuration of double bonds, and in high yield are obtained. The large library of PPAs found in literature allows stablishing that depending on the size and position of the pendant group in the phenylacetylene monomer it is possible to create PPAs with different elongations or ω_1 (dihedral angle between conjugated double bonds).[32,33] To determine an approximate value for ω_1, combination of the information obtained from different structural techniques —UV-vis, circular dichroism (CD),[34-36] vibrational circular dichroism (VCD),[37] Raman,[38] Raman optical activity (ROA),[39] differential scanning calorimetry (DSC)[40] and atomic force microscopy (AFM)—[41-49] is needed. This fact is due to the complexity of the helical scaffolds found in PPAs, which are made by two coaxial helices: an internal helix described by the polyene backbone and an external one described by the pendants, which, depending on the stereoregularity of the polyene backbone, can rotate in the same (*cis-cisoidal*, $\omega_1 < 90°$) or opposite directions (*cis-transoidal*, $\omega_1 > 90°$).[50-52] Recently, our group reported another approach to get information about the secondary structure of PPAs.[53] In such a case, photochemical electrocyclization (PE) of the polyene backbone is used,[54-55] where the half-time $t_{1/2}$ of the process to reach a null ECD signal in the vinylic region in solution depends directly on the ω_1 adopted by the PPA. Thus, a dilute solution of a PPA [c.a. $1 \cdot 10^{-3}$ M] is irradiated with visible light ($\lambda > 350$ nm) and the CD signal decay monitored versus time to afford the PE rate constant and the $t_{1/2}$ as the relevant parameters using a first order reaction fitting. Next, by applying equation (1) is possible to obtain an approximate value for ω_1.

$$\omega_1 = -147.5 + 312.6*(1-\exp(-4.659 \cdot 10^{-2} * t_{1/2})) \quad (1)$$

Interestingly, although these studies allow to model an approximate secondary structure of the PPA, no information about the presence of reversals within a helical scaffold can be extracted. Reversals are structural motifs found in helical polymers that induce helical inversions along polymer chains. In PPAs, Prof. Yashima visualized this structural motif by AFM studies of a PPA bearing α-aminoisobutyric acid (Aib) n-decyl esters as achiral pendant.[56] This motif was also visualized by AFM in chiral PPAs possessing a screw sense excess.[57] Curiously, although the existence of helix reversals was evidenced in the solid state through high-resolution AFM images, the study of this structural motif is solution has not yet been addressed. This fact is due to the complexity of the polymers and the absence of robust structural tools that allows determining the secondary structure of polymers in solution.

Herein, we want to address the identification of helix reversals in solution using the PE of PPAs. As it was mentioned above, the rate of the PE of PPAs depends on the elongation (ω_1) of the polymer and on its dynamic behavior. Therefore, the presence of mismatches such as helix reversals within a helical scaffold should have effects on the PE of PPAs. To perform these studies, we have chosen a combination of polymers and copolymers with different folding propensities induced by solvents or by chiral-to-chiral communication produced between comonomers.

2. Results and Discussion

As homopolymers with known secondary structure, we have chosen PPAs with well-known *cis-cisoidal* (*c-c*) and *cis-transoidal* (*c-t*) scaffolds and with different benzamide and anilide pendant groups. For instance, poly-(*R*)-**1** bears the *para*-ethynylbenzamide of (*R*)-phenylglycine methyl ester as pendant. This polymer adopts a *c-t* scaffold —ω_1 c.a. 148°, helical pitch 3.8 nm— with a P_{int}/M_{ext} screw sense excess in low-polar solvents such as THF and $CHCl_3$ (Figure 1a,b). Although the folding degree is different based on the intensity of the ECD trace, which is attributed to the presence of reversals along the helix, that could alter the rate of the PE process. Therefore, two vials containing 7 mL of poly-(*R*)-**1** (c= $1.02 \cdot 10^{-3}$ M) in THF and $CHCl_3$ were irradiated with visible light, and the PE process was monitored by plotting the ECD signal decay versus time (Figure 1c). The half-life ($t_{1/2}$= ln2/k) was obtained for each solution —poly-(*R*)-**1** ($CHCl_3$) $t_{1/2}$= 63 min, poly-(*R*)-**1** (THF)— indicating the presence of a *c-t* scaffold in $CHCl_3$ (ω_1 c.a. 148°) and a *c-c* helix in THF (ω_1 c.a. 88°) when fitted to equation 1. As expected, the ω_1 obtained from irradiation studies of poly-(*R*)-**1** in $CHCl_3$ (well folded), is in good agreement with the value obtained experimentally from other structural techniques. While the value obtained for this polymer in THF (poorly folded) is far from the admissible, based in the expected $t_{1/2}$ rates

for a *c-t* scaffold in the photochemical electrocyclization process. This result indicates that there is a strong relationship between the photochemical electrocyclization process and the folding of the helical polymer.

Therefore, two structural parameters are closely related in the PE studies, the helical scaffold, and the folding degree. Thus, a poorly folded PPA will produce small half-life values of the PE process that will led to a wrong ω_1 value. Therefore, to avoid wrong ω_1 assignment based on the folding degree of the PPA, it is necessary to determine first if the polymer adopts a *c-c* or a *c-t* scaffold. From previous studies, it is known that PE highly depends on the helical scaffold adopted by the PPA, being fast for *c-c* and slow for *c-t* PPAs. We believe that this effect is produced by the different orientations of conjugated double bonds in both scaffolds, that are well oriented in *c-c* to promote the PE, while in *c-t* PPAs, the polyene backbone needs to reorient the conjugated double bonds to promote the PE. These conformational changes should be affected by temperature, being the PE delayed at low temperatures.

To corroborate this hypothesis, PE studies at room temperature (rt) and 4°C were carried out for poly-(*R*)-**1** and for poly-(*R*)-**2**, that bears the *para*-ethynylanilide of the (*R*)-α-methoxy-α-trifluoromethylphenylacetic acid as pendant. This polymer adopts a compressed helix in $CHCl_3$ (3.0 nm helical pitch, ω_1 c.a. 70°), while a stretched helix is induced in poly-(*R*)-**2** when dissolved in THF (3.9 nm helical pitch, ω_1 c.a. 155°; Figure 1e).

Moreover, PE studies indicate a good folding for poly-(*R*)-**2** in both solvents providing an ω_1 value that matches the one obtained from the combination of other structural techniques —poly-(*R*)-**2** $\omega_{1(THF)}$ c.a. 155°, $\omega_{1(CHCl3)}$ c.a. 72°)—.

Thus, vials containing 7 mL of poly-(*R*)-**1** and poly-(*R*)-**2** prepared in THF and $CHCl_3$, respectively, were irradiated with visible light at rt and 4°C. These studies show how temperature affects *c-c* and *c-t* scaffolds differently. Thus, while the PE of poly-(*R*)-**2** dissolved in $CHCl_3$ is not affected by temperature changes —*c-c* scaffold—, the PE of poly-(*R*)-**2** in THF and the PE of poly-(*R*)-**1** in $CHCl_3$ and THF are delayed at low temperatures —*c-t* helix— (Figure 1d,f).

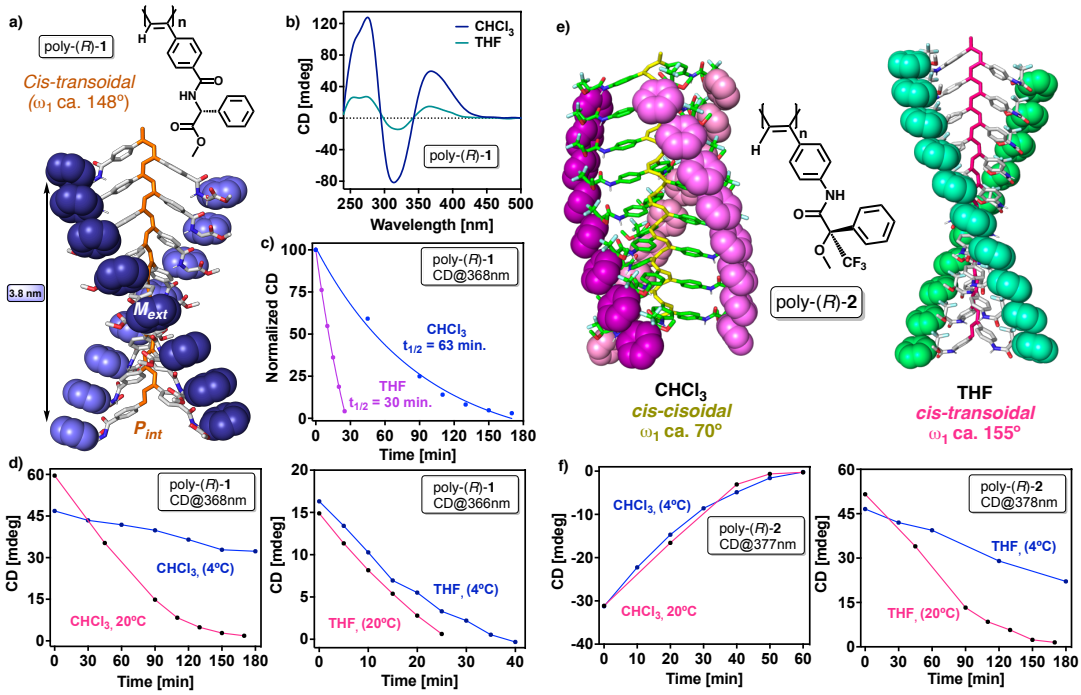

Figure 1. a) Chemical and 3D structure of poly-(*R*)-**1**. b) ECD spectra of poly-(*R*)-**1** in $CHCl_3$ and THF. c) Normalized CD signal decay vs. time for poly-(*R*)-**1** at different irradiation times under visible light. d) ECD signal decay vs. time for poly-(*R*)-**1**, in $CHCl_3$ and THF, at different irradiation times under visible light at two temperatures. e) Chemical and 3D models of poly-(*R*)-**2**. f) ECD signal decay vs. time for poly-(*R*)-**2**, in $CHCl_3$ and THF, at different irradiation times under visible light at two temperatures. [poly-(*R*)-**1**]= $1.02 \cdot 10^{-3}$ M, [poly-(*R*)-**2**]= $9.00 \cdot 10^{-4}$ M.

To extrapolate this observation to all PPAs, we performed PE studies at rt and 4°C for other PPAs with well-known *c-c* and *c-t* secondary structures. These studies show that in the case of PPAs possessing a *c-c* helical scaffold such as poly-(*S*)-**3** and poly-(*R*)-**4** that bear the *para*-ethynylanilide of (*S*)-mandelic acid as pendant and the *para*-ethynylanilide of (*S*)-α-methoxy-α-phenylacetic acid as substituent respectively, the ECD signal decay produced during the studies reach an ECD= 0 at the same time for both temperatures, rt and 4°C (Figure 2a,b). On the other hand, in *c-t* PPAs —poly-(S)-**5**, poly-(S)-**6** and poly-(*S*)-**7**, bearing the para-ethynylbenzamide of (*L*)-alanine methyl ester, (*L*)-valine methyl ester and (*L*)-phenylalanine methyl ester respectively—, the ECD signal decay produced by PE of the polyene backbone is largely affected by temperature reaching an ECD= 0 to longer times (Figure 2a,c).

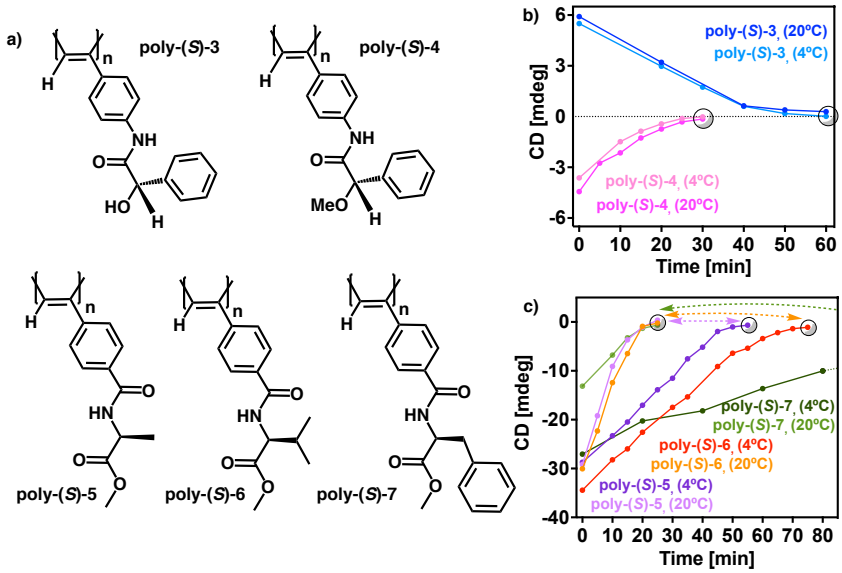

Figure 2. a) Chemical structure of poly-(*S*)-**3**, poly-(*R*)-**4**, poly-(*S*)-**5**, poly-(*S*)-**6** and poly-(*S*)-**7**. b) ECD signal decay vs. time for poly-(*S*)-**3** (CD@386nm), poly-(*R*)-**4** (CD@383nm), poly-(*S*)-**5** (CD@368nm), poly-(*S*)-**6** (CD@367nm) and poly-(*S*)-**7** (CD@368nm) at different irradiation times under visible light at two temperatures. [poly-(*S*)-**3**]= $1.19 \cdot 10^{-3}$ M, [poly-(*R*)-**4**]= $1.13 \cdot 10^{-3}$ M, [poly-(*S*)-**5**]= $1.30 \cdot 10^{-3}$ M, [poly-(*S*)-**6**]= $1.16 \cdot 10^{-3}$ M, [poly-(*S*)-**7**]= $9.76 \cdot 10^{-4}$ M.

Next, we aimed to explore the role of the reversals in the PE studies of random copolymer series containing the two enantiomers of monomer-**1**— poly[(*R*)-**1**$_r$-co-(*S*)-**1**$_{(1-r)}$]—. ECD studies show a chiral conflict between the two enantiomeric comonomers, which induces opposite helical senses within the copolymer chain. Therefore, on this copolymer series, a controlled number of reversals is introduced along the chain when a mismatch of absolute configuration —*R/S*— is present.

PE studies of poly[(*R*)-**1**$_r$-co-(*S*)-**1**$_{(1-r)}$] copolymer series in $CHCl_3$ — c= $1.02 \cdot 10^{-3}$ M, 7 mL— show a strong dependence between the copolymer photostability and the percentage of reversals —$t_{ECD50\%}$ or $t_{ECD20\%}$ *vs* percentage of reversals (*r*)— where the decay can be fitted to a first order reaction (2).

$$Y=(Y_0\text{-Plateau}) \cdot \exp^{(-K \cdot X)}+\text{Plateau} \quad (2)$$

Where Y is the time needed to reduce the ECD signal to the 50% or 20%. Y_0 is the time needed to reach a CD= 50% or 20% in the homopolymer (0% reversals), Plateau is the minimum time need to unfold the copolymer if it has a 100% of reversals, K is the rate constant and X is the percentage of reversals.

(c-$t_{145\text{-}150}$) $t_{ECD50\%}=59.84 \cdot \exp^{(-0.03812 \cdot \%r)}-4.530$ ($R^2=0.979$) (3)

(c-$t_{145\text{-}150}$) $t_{ECD20\%}=102.5 \cdot \exp^{(-0.05553 \cdot \%r)}+7.857$ ($R^2=0.985$) (3)

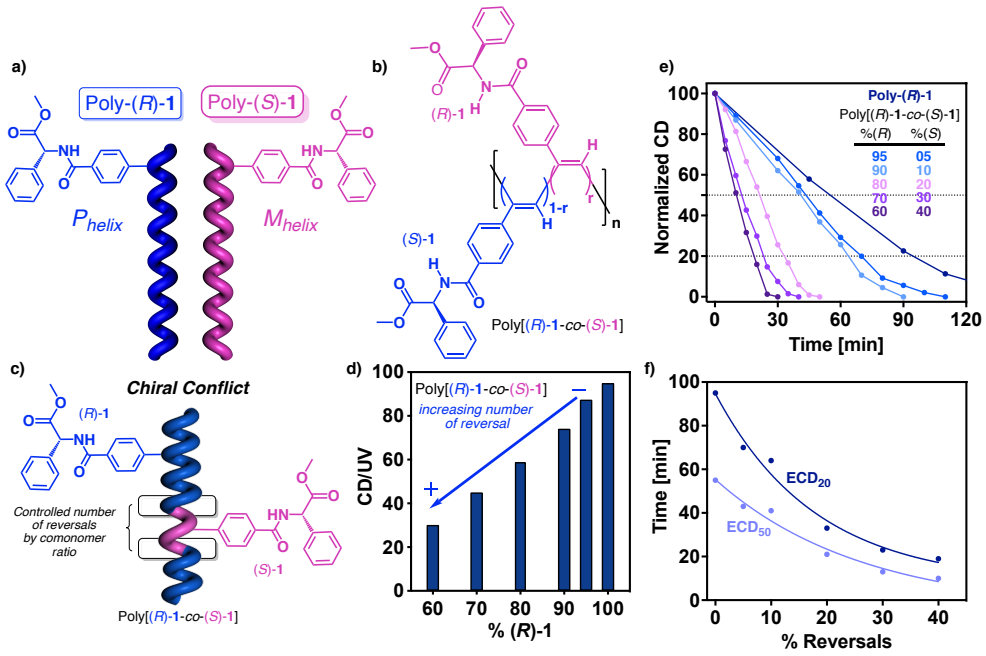

Figure 3. a) Chemical structure and helix sense representation of poly-(*R*)-**1** and poly-(*S*)-**1**. b) Chemical structure of the copolymer poly[(*R*)-**1**-co-(*S*)-**1**]. c) Conceptual representation of the chiral conflict phenomenon. d) Variation of the CD/UV signal (CD@368nm) vs percentage of (*R*)-**1** in the poly[(*R*)-**1**-co-(*S*)-**1**] series. e) Normalized CD signal decay (CD@368nm) vs. time for poly[(*R*)-**1**-co-(*S*)-**1**] series at different irradiation times under visible light. f) Time consumed for reach ECD signal 50% and 20% during the photochemical electrocyclization vs percentage of reversals in the poly[(*R*)-**1**-co-(*S*)-**1**] series. [poly[(*R*)-**1**-co-(*S*)-**1**]]= $1.02 \cdot 10^{-3}$ M.

Using this equation, it is possible to extract an approximate value for the percentage of reversals of poly-(*R*)-**1** when dissolved in THF. In this case, the $t_{ECD50\%}$ and $t_{ECD20\%}$ values obtained during the PE studies are 11 min and 19 min respectively, which corresponds to the presence of ca. 35% and 40% of reversals within the polymer chain.

To further confirm the robustness of this protocol that allows determining an approximated value of the percentage of reversals within a PPA, a random copolymer series containing the two enantiomers of monomer-**2** was prepared —poly[(*R*)-**2**$_r$-co-(*S*)-**2**$_{(1-r)}$]—. This polymer is well folded in solution as happens with poly-**1**. In case of poly-(*R*)-**2**, two different scaffolds are obtained when the polymer is dissolved in chloroform and THF, where the polymer adopts a *c-c* (ω_1 c.a. 65-75°) and a *c-t* (ω_1 c.a. 155°) helical structure respectively (Figure 4a,b).

ECD studies show a chiral conflict between the two enantiomeric comonomers within the copolymer series in both solvents, $CHCl_3$ and THF. The lack of communication between the two enantiomeric monomers indicates the presence of a controlled number of reversals in the poly[(*R*)-**2**$_r$-co-(*S*)-**2**$_{(1-r)}$] copolymer series which can be tuned by varying the (*R*)-**2**/(*S*)-**2** ratio (Figure 4c,d).

PE studies were carried out for the different copolymers of the poly[(*R*)-**2**$_r$-co-(*S*)-**2**$_{(1-r)}$] copolymer series and monitored by ECD (Figure 4e,g). Similarly to the results obtained for the poly[(*R*)-**1**$_r$-co-(*S*)-**1**$_{(1-r)}$] copolymer series, a strong relationship is found between the copolymer photostability and the percentage of reversals —$t_{ECD50\%}$ or $t_{ECD20\%}$ *vs* percentage of reversals (*r*)— within the poly[(*R*)-**2**$_r$-co-(*S*)-**2**$_{(1-r)}$] copolymer series (Figure 4f,h), where the decay can be fitted to a first order reaction (2). Two different equations are obtained depending on the helical scaffold adopted by poly-**2**, a *cis-transoidal* helix in THF, and a more compressed *cis-cisoidal* structure in $CHCl_3$. This equation is different from the one obtained for the poly[(*R*)-**1**$_r$-co-(*S*)-**1**$_{(1-r)}$] copolymer series (3), because the elongation degree is different (ω_1 c.a. 145-150° for poly-**1** and ω_1 c.a. 70° for poly-**2** in $CHCl_3$ and c.a. 155-160° for poly-**2** in THF).

(*c-t*$_{155}$) $t_{ECD50\%}=132.3\cdot\exp^{(-0.009231\cdot\%r)}-69.53$ ($R^2=0.966$) (4)

(*c-t*$_{155}$) $t_{ECD20\%}=76.71\cdot\exp^{(-0.03066\cdot\%r)}+21.24$ ($R^2=0.986$) (4)

(*c-c*) $t_{ECD50\%}=15.62\cdot\exp^{(-0.04525\cdot\%r)}+5.512$ ($R^2=0.989$) (5)

(*c-c*) $t_{ECD20\%}=18.73\cdot\exp^{(-0.07467\cdot\%r)}+16.05$ ($R^2=0.984$) (5)

This fact indicates, as predicted, that the PE depends on the dynamic behavior of the polymer and on the secondary structure of the PPA.

Considering the library of PPAs with well-known secondary structure that we handle, we have postulated three different equations that will allow us predicting the percentage of reversals in PPAs with *c-c* (ω_1 ca. 60-80°, equation 3) or *c-t* helix scaffolds (ω_1 ca. 140-150° equation 4, ω_1 ca. 150-155° equation 5).

With this information on hand, we decided to analyze the percentages of reversals present in PPAs with known secondary structure that fit those values.

Thus, poly-(*S*)-**3**, that bears the *para*-ethynylanilide of (*S*)-mandelic acid as substituent and poly-(*R*)-**4**, that bears the *para*-ethynylanilide of (*S*)-α-methoxy-α-phenylacetic acid as substituent were chosen as examples of PPAs bearing a *c-c* scaffold to perform these studies. PE studies of these polymers monitored by ECD allowed us to extract their polymer photostability values ($t_{ECD50\%}$) —poly-(*S*)-**3**, $t_{ECD50\%}$= 21 min; poly-(*R*)-**4**, $t_{ECD50\%}$= 8.8 min—(Figure 4i), which are correlated with the percentage of reversals present in the helix scaffold by fitting them to equation 5. As a result, it was concluded that poly-(*S*)-**3** is fully folded in THF (X< 1%), while poly-(*R*)-**4** shows approximately a 34% along the helical scaffold when is dissolved in THF.

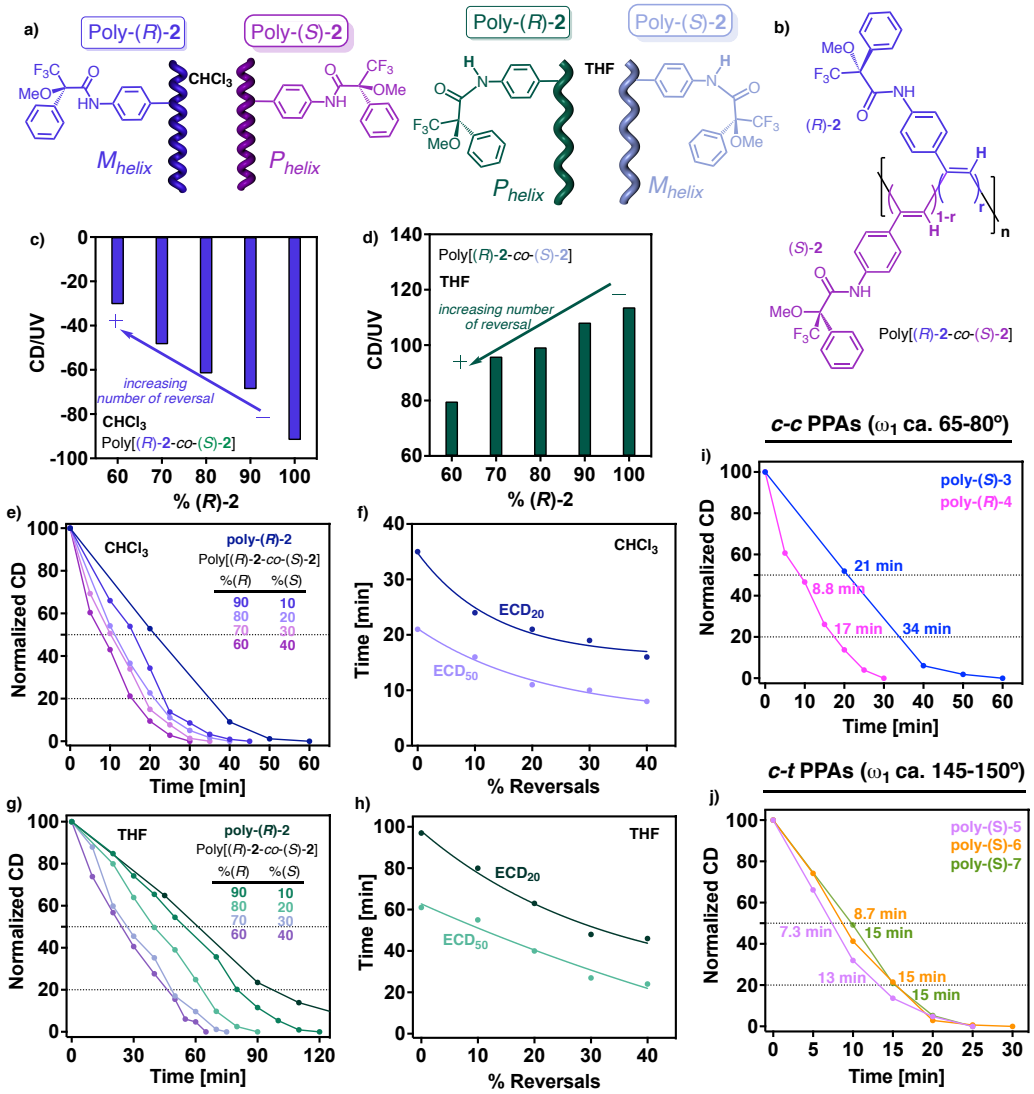

Figure 4. a) Chemical structure and helix sense/elongation representation of poly-(*R*)-**2** and poly-(*S*)-**2** in $CHCl_3$ and THF. b) Chemical structure of the copolymer poly[(*R*)-**2**-co-(*S*)-**2**]. c), d) Variation of the CD/UV signal vs percentage of (*R*)-**2** in the poly[(*R*)-**2**-co-(*S*)-**2**] series in $CHCl_3$ (CD@377nm) and THF (CD@378nm) respectively. e), g) Normalized CD signal decay vs. time for poly[(*R*)-**1**-co-(*S*)-**1**] series at different irradiation times under visible light in $CHCl_3$ (CD@377nm) and THF (CD@378nm) respectively. f), h) Time consumed for reach ECD signal 50 % and 20 % during the photochemical electrocyclization vs percentage of reversals in the poly[(*R*)-**1**-co-(*S*)-**1**] series in $CHCl_3$ (CD@377nm) and THF (CD@378nm) respectively. [poly[(*R*)-**2**-co-(*S*)-**2**]]= $9.00 \cdot 10^{-4}$ M. Normalized CD signal decay vs. time at different irradiation times under visible light for i) poly-(*S*)-**3** (CD@386nm) and poly-(*R*)-**4** (CD@383nm) and j) poly-(*S*)-**5** (CD@368nm), poly-(*S*)-**6** (CD@367nm) and poly-(*S*)-**7** (CD@368nm). [poly-(*S*)-**3**]= $1.19 \cdot 10^{-3}$ M, [poly-(*R*)-**4**]= $1.13 \cdot 10^{-3}$ M, [poly-(*S*)-**5**]= $1.30 \cdot 10^{-3}$ M, [poly-(*S*)-**6**]= $1.16 \cdot 10^{-3}$ M, [poly-(*S*)-**7**]= $9.76 \cdot 10^{-4}$ M.

Similarly at 20% of remaining ECD signal poly-(*S*)-**3**, $t_{ECD20\%}$= 34 min; poly-(*R*)-**4** $t_{ECD20\%}$= 17 min— and correlate them with the percentage of reversals present in the helix scaffold by fitting them to equation 5. As a result, poly-(*S*)-**3** is fully folded in THF (X< 1%), while poly-(*R*)-**4** shows approximately a 40% along the helix scaffold when is dissolved in THF.

Analogous studies were carried out for poly-(*S*)-**5**, poly-(*S*)-**6** and poly-(*S*)-**7**, three PPAs that bear the para-ethynylbenzamide of (*L*)-alanine methyl ester, (*L*)-valine methyl ester and (*L*)-phenylalanine methyl ester respectively (Figure 4j). These PPAs possess a *c-t* helix scaffold with ω_1 of ca. 148°. To determine the percentage of reversals in these polymers it is mandatory to apply equation (3). For these polymers PE studies show a fast isomerization of the polyene backbone that does not correspond to a fully folded helical scaffold. For poly-(*S*)-**5**, $t_{ECD50\%}$= 7.3 min, while for poly-(*S*)-**6**, $t_{ECD50\%}$= 8.7 min and for poly-(*S*)-**7**, $t_{ECD50\%}$= 10 min that correspond to helices with a 43%, 40% and 37% of reversals within the helix respectively. Similarly, at 20% of remaining ECD signal, poly-(*S*)-**5**, $t_{ECD20\%}$= 13 min, while for poly-(*S*)-**6**, $t_{ECD20\%}$= 15 min and poly-(*S*)-**7**, $t_{ECD20\%}$= 15 min that corresponds to helices with a 54%, 48% and 48% of reversals within the helix respectively. Furthermore, the good agreement between percentages obtained applying $t_{ECD50\%}$ or $t_{ECD20\%}$ evidence the robustness of the results.

Importantly, although these polymers are ECD active and show an intense ECD trace, the photochemical studies reveal a poorly folded structure that will badly affect to the potential applications of PPAs such as chiral ligands in asymmetric synthesis or chiral stationary phases in HPLC among others.

Finally, to cover the entire range of *c-t* PPAs we need prepare a *c-t* copolymer with (ω_1>160°; for ω_1 ca. 140-150° we propose equation 4 and for ω_1 ca. 150-155° the equation 5). Poly-(*R*)-**8** that bears the *meta*-ethynylbenzamide of (*R*)-phenylglycine methyl ester as pendant is constituted by an equilibrium of two *cis-transoidal* helices with different elongation (both P_{int}, ω_1 ca. 160° (CD@373nm) and 165° (CD@428nm). To explore the role of reversals on stretched *c-t* polymers, copolymer series containing the two enantiomers of monomer-**8** —poly[(*R*)-$\mathbf{8}_r$-co-(*S*)-$\mathbf{8}_{(1-r)}$]— was polymerized (Figure 5a,b). ECD studies for the 165° helix (CD@428nm) show a chiral conflict between the two enantiomeric comonomers (Figure 5c). Therefore, a controlled number of reversals is introduced again along the chain based on the mismatch of absolute configuration —*R/S*— present.

PE studies, monitored by ECD, for the different copolymers of poly[(*R*)-$\mathbf{8}_r$-co-(*S*)-$\mathbf{8}_{(1-r)}$] reveals a strong relationship between the copolymer photostability and the percentage of reversals (Figure 5d). Such as poly[(*R*)-$\mathbf{1}_r$-co-(*S*)-$\mathbf{1}_{(1-r)}$] and poly[(*R*)-$\mathbf{2}_r$-co-(*S*)-$\mathbf{2}_{(1-r)}$] series, the decay can be fitted to a first order reaction (6) (Figure 5e). Due to the presence of a mixtures of two helices, only the time at 20% of ECD signal was considered. Furthermore, for the dependence of the PE on the dynamic behavior, the effect of the reversals in the photostability is reduced as we increase ω_1 —elongation and dynamic behavior go oppositely in PPAs—.[33] Thus, representation t_r/t_i at ECD= 20% demonstrate that the

effect of the reversals in the photostability decrease as ω_1 increase (Figure 5f). Being t_r the ECD signal at 20% for the copolymer in a X %r and t_i the ECD signal at 20% for the corresponding homopolymer.

(c-t_{165}) $t_{ECD20\%}=40.8\cdot\exp^{(-0.04522\cdot\%r)}+178.5$ ($R^2=0.983$) (6)

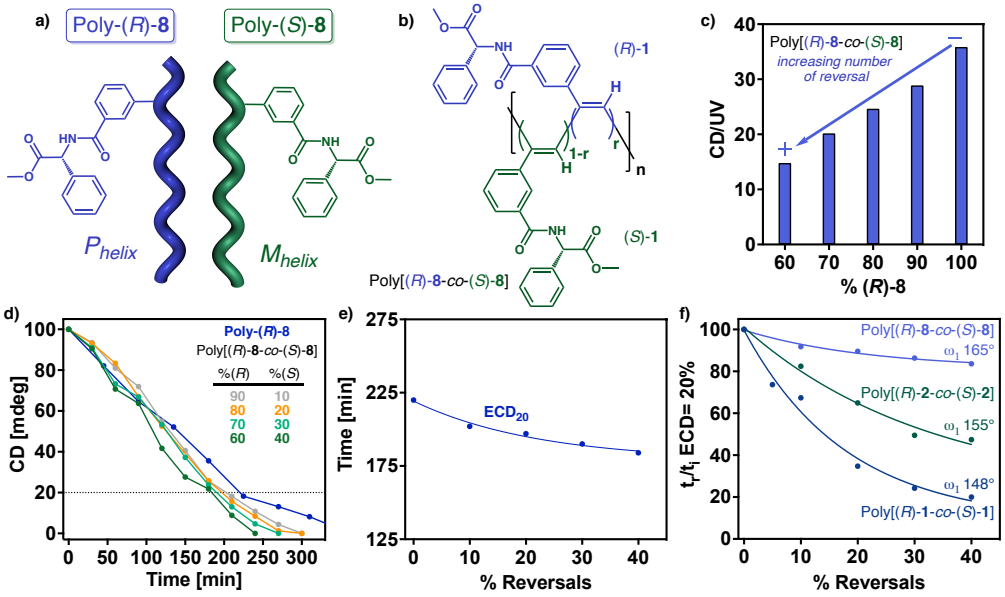

Figure 5. a) Chemical structure and helix sense representation of poly-(*R*)-**8** and poly-(*S*)-**8**. b) Chemical structure of the copolymer poly[(*R*)-**8**-co-(*S*)-**8**]. c) Variation of the CD/UV signal (CD@428nm) vs percentage of (*R*)-**8** in the poly[(*R*)-**8**-co-(*S*)-**8**] series. d) Normalized CD signal decay (CD@428nm) vs. time for poly[(*R*)-**8**-co-(*S*)-**8**] series at different irradiation times under visible light. e) Time consumed for reach ECD signal 20% during the photochemical electrocyclization vs percentage of reversals in the poly[(*R*)-**8**-co-(*S*)-**8**] series. f) Normalized time at ECD= 20% vs percentage of reversals. [poly[(*R*)-**1**-co-(*S*)-**1**]]= $1.02\cdot10^{-3}$ M, [poly[(*R*)-**2**-co-(*S*)-**2**]]= $9.00\cdot10^{-4}$ M, [poly[(*R*)-**8**-co-(*S*)-**8**]]= $1.02\cdot10^{-3}$ M.

3. Conclusion

In conclusion we have demonstrated that the PE of PPAs in solution can be used as a structural tool to determine their secondary structure of PPAs and the presence of reversals within the helical structure. PE of PPAs does not depends on the chemical structure of the pendant groups or the solvents used to do the studies, being the rate of the PE process affected only by the secondary structure of the PPA. Thus, while in *c-c* PPAs the PE is fast, in *c-t* PPAs the PE is slower, speed being the speed largely affected by temperature. Therefore, PE at different temperatures allow us to classify PPAs into *c-c* or *c-t* PPAs. Moreover, PE studies also allow obtaining the dihedral angle between conjugated double bonds in well folded polymers. However, if the polymers are not well folded, the presence of reversals along the helix affects largely the PE process, being this shortened in time. This relationship between the PE of PPAs and the presence of reversals along the

helix allowed us to generate an equation that predicts the number of reversals present in a PPA with a certain scaffold. To apply this equation, it is necessary to know if the polymer has *c-c* or *c-t* structure, which can be easily obtained from PE studies at different temperatures or by using DSC studies. In the case of *c-c* PPAs there is only one equation to determine the folding of PPAs, and in the case of *c-t* PPAs is necessary to have an approximated value for ω_1 to determine its folding degree. At this stage, there are three different equations for *c-t* PPAs; one for PPAs with ω_1 ca. 148°; a second one for PPAs with ω_1 ca. 155°, and a third one for PPAs with ω_1 ca. 165°.

These studies can be of great interest to the scientific community because they are dealing, for the first time, with the folding degree of PPAs in solution. In literature, dynamic helical polymers are used as chiral catalyst, chiral recognition agents and chiral stationary phases in HPLC. However, these polymers are applied without considering the polymer folding. By using this approximation, it is possible to determine if the polymer is well folded or not in solution, and therefore, to explain how the helical scaffold affects the applications of the polymer.

4. References

[1] E. Yashima, N. Ousaka, D. Taura, K. Shimomura, T. Ikai, K. Maeda, *Chem. Rev.,* **2016**, *116*, 13752-13990.

[2] K. Maeda, M. Nozaki, K. Hashimoto, K. Shimomura, D. Hirose, T. Nishimura, G. Watanabe, E. Yashima, *J. Am. Chem. Soc*., **2020**, *142*, 7668-7682.

[3] E. Yashima, K. Maeda, *Bull. Chem. Soc. Jpn.*, **2021**, *94*, 2637-2661.

[4] J. J. Tarrío, R. Rodríguez, B. Fernández, E. Quiñoá, F. Freire, *Angew. Chem. Int. Ed.,* **2022**, *61*, e202115070.

[5] X. Guan, S. Wang, G. Shi, J. Zhang, X. Wan, *Macromolecules*, **2021**, *54*, 4592-4600.

[6] K. Maeda, H. Mochizuki, M. Watanabe, E. Yashima, *J. Am. Chem. Soc*., **2006**, *128,* 7639-7650.

[7] S. Arias, F. Freire, E. Quiñoá, R. Riguera, *Polym. Chem*., **2015**, *6*, 4725-4733.

[8] T. Ikai, R. Ishidate, K. Inoue, K. Kaygisiz, K. Maeda, E. Yashima, *Macromolecules*, **2020**, *53*, 973-981.

[9] K. Maeda, N. Kamiya, E. Yashima, *Chem. Eur. J.,* **2004**, *10*, 4000-4010.

[10] K. Cobos, R. Rodriguez, O. Domarco, B. Fernández, E. Quiñoá, R. Riguera, F. Freire, *Macromolecules*, **2020**, *53*, 3182-3193.

[11] R. Rodríguez, E. Quiñoá, R. Riguera, F. Freire. *Small,* **2019**, *15*, 1805413.

[12] F. Ishiwari, K. Nakazono, Y. Koyama, T. Takata, *Angew. Chem. Int. Ed.,* **2017**, *56*, 14858-14862.

[13] R. Rodríguez, S. Arias, E. Quiñoá, R. Riguera, F. Freire, *Nanoscale*, **2017**, *9*, 17752-17757.

[14] N. Zhu, K. Nakazono, T. Takata, *Chem. Commun.,* **2016**, *52*, 3647-3649.

[15] M. Alzubi, S. Arias, R. Rodríguez, E. Quiñoá, R. Riguera, F. Freire, *Angew. Chem. Int. Ed.*, **2019**, *58*, 13365-13369.

[16] R. Rodríguez, E. Quiñoá, R. Riguera, F. Freire, *Chem. Mater.* **2018**, *30*, 2493-2497.

[17] T. Van Leeuwen, G. H. Heideman, D. Zhao, S. J. Wezenberg, B. L. Feringa. *Chem. Commun.* **2017**, *53*, 6393-6396.

[18] S. Arias, M. Núñez-Martínez, E. Quiñoá, R. Riguera, F. Freire. *Polym. Chem*., **2017**, *8*, 3740-3745.

[19] M. Alzubi, S. Arias, I. Louzao, E. Quiñoá, R. Riguera, F. Freire, *Chem. Commun*., **2017**, *53*, 8573-8576.

[20] S. Arias, J. Bergueiro, F. Freire, E. Quiñoá, R. Riguera, *Small*, **2016**, *12*, 238-244.

[21] K. Cobos, R. Rodríguez, E. Quiñoá, R. Riguera, F. Freire, *Angew. Chem. Int. Ed*. **2020**, *59*, 23724.

[22] M. Ando, R. Ishidate, T. Ikai, K. Maeda, E. Yashima, *J. Polym. Sci., Part A: Polym. Chem.* **2019**, *57*, 2481-2490.

[23] C. Zhang, Y. Qiu, S. Bo, F. Wang, Y. Wang, L. Liu, Y. Zhou, H. Niu, H Dong, T. Satoh, *J. Polym. Sci., Part A: Polym. Chem.* **2019**, *57*, 1024-1031.

[24] R. P. Megens, G. Roelfes, *Chem. Eur. J.* **2011**, *17*, 8514-8523.

[25] E. Anger, H. Iida, T. Yamaguchi, K. Hayashi, D. Kumano, J. Crassous, N. Vanthuyne, C. Roussel, E. Yashima, *Polym. Chem*. **2014**, *5*, 4909-4914.

[26] R. Ishidate, T. Sato, T. Ikai, S. Kanoh, E. Yashima, K. Maeda, *Polym. Chem.*, **2019**, *10*, 6260-6268.

[27] D. Hirose, A. Isobe, E. Quiñoá, F. Freire, K. Maeda, *J. Am. Chem. Soc.*, **2019**, *141*, 8592-8598.

[28] G. Wu, *Polym. Chem.*, **2022**, *13*, 3036-3047.

[29] M. G. Mayershofer, O. Nuyken, *J. Polym. Sci., Part A: Polym. Chem.***, 2005**, *43*, 5723–5747.

[30] M. Shiotsuki, F. Sanda, T. Masuda, *Polym. Chem.,* **2011**, *2*, 1044–1058.

[31] K. Echizen, T. Taniguchi, T. Nishimura, K. Maeda, *J. Am. Chem. Soc.*, **2021**, *143*, 3604-3612.

[32] R. Rodríguez, E. Suárez-Picado, E. Quiñoá, R. Riguera, F. Freire. *Angew. Chem. Int. Ed.,* **2020**, *59*, 8616-8622.

[33] R. Rodriguez, E. Quiñoá, R. Riguera, F. Freire, *J. Am. Chem. Soc.*, **2016**, *138*, 9620-9628.

[34] Tabei, J.; Shiotsuki, M.; Sanda, F.; Masuda, T. *Macromolecules,* **2005**, *38*, 9448-9454.

[35] T. Kaneko, Y. Umeda, T. Yamamoto, M. Tereguchi, T. Aoki, *Macromolecules,* **2005**, *38*, 9420-9426.

[36] F. Takei, H. Hayashi, K. Onitsuka, N. Kobayashi, S. Takahashi, *Angew. Chem. Int. Ed.,* **2001**, *40*, 4092-4094.

[37] B. Nieto-Ortega, R. Rodríguez, S. Medina, E. Quiñoá, R. Riguera, J. Casado, F. Freire, F. J. Ramírez, *J. Phys. Chem. Lett.*, **2018**, *9*, 2266-2270.

[38] H. Shirakawa, T. Ito, S. Ikeda, *Polym. J.* **1973**, *4,* 460-462.

[39] L. Palomo, R. Rodríguez, S. Medina, E. Quiñoá, J. Casado, F. Freire, F.J. Ramírez, *Angew. Chem. Int. Ed*., **2020**, *59*, 9080-9087.

[40] L. Liu, T. Namikoshi, Y. Zang, T. Aoki, S. Hadano, Y. Abe, I. Wasuzu, T. Tsutsuba, M. Teraguchi, T. Kaneko, *J. Am. Chem. Soc.***, 2013**, *135*, 602-605.

[41] J. Kumaki, *Polym. J.*, **2016**, *48*, 3-14.

[42] J. Kumaki, S.-I. Sakurai, E. Yashima, *Chem. Soc. Rev.*, **2009**, *38*, 737-746.

[43] S.-I. Sakurai, K. Okoshi, J. Kumaki, E. Yashima, *J. Am. Chem. Soc.,* **2006**, *128*, 5650-5651.

[44] K. Okoshi, S.-I. Sakurai, S. Ohsawa, J. Kumaki, E. Yashima, *Angew. Chem. Int. Ed.,* **2006**, *45*, 8173-8176.

[45] S.-I. Sakurai, K. Okoshi, J. Kumaki, E. Yashima, *Angew. Chem. Int. Ed.*, **2006**, *45*, 1245-1248.

[46] V. Percec, J. G. Rudick, M. Peterca, S. R. Staley, M. Wagner, M. Obata, C. M. Mitchell, W.-D. Cho, V. S. K. Balagurusamy, J. N. Lowe, M. Glodde, O. Weichold, K. J. Chung, N. Ghionni, S. N. Magonov, P. A. Heiney, *Chem. Eur. J.,* **2006**, *12*, 5731-5746.

[47] V. Percec, J. G. Rudick, M. Wagner, M. Obata, C. M. Mitchell, W.-D. Cho, S. N. Magonov, *Macromolecules,* **2006**, *39*, 7342-7351.

[48] J. G. Rudick and V. Percec, *Macromol. Chem. Phys.*, **2008**, *209,* 1759-1768.

[49] V. Percec, M. Obata, J. G. Rudick, B. B. De, M. Glodde, T. K. Bera, S. N. Magonov, V. S. K. Balagurusamy, P. A. Heiney, *J. Polym. Sci. Part A Polym. Chem.,* **2002**, *40*, 3509–3533.

[50] S. Leiras, F. Freire, J. M. Seco, E. Quiñoá, R. Riguera, *Chem. Sci.*, **2013**, *4*, 2735-2743.

[51] Z. Fernández, B. Fernández, E. Quiñoá, R. Riguera, F. Freire. *Chem. Sci.*, **2020**, *11*, 7182-7187.

[52] F. Rey-Tarrío, S. Guisán-Ceinos, J. M. Cuerva, D. Miguel, M. Ribagorda, E. Quiñoá, F. Freire, *Angew. Chem. Int. Ed.* **2022**, *61*, e202207623.

[53] F. Rey-Tarrío, R. Rodríguez, E. Quiñoá, R. Riguera, F. Freire, *Angew. Chem. Int. Ed*., **2021**, 60, 8095-8103.

[54] L. Liu, T. Namikoshi, Y. Zang, T. Aoki, S. Hadano, Y. Abe, I. Wasuzu, T. Tsutsuba, M. Teraguchi, T. Kaneko, *J. Am. Chem. Soc.*, **2013**, *135*, 602-605.

[55] Y. Tang, L. Liu, J. Suzuki, M. Teraguchi, T. Kaneko, T. Aoki, *Chirality*, **2022**, *34*, 450-461.

[56] S. -i. Sakurai, S. Ohsawa, K. Nagai, K. Okoshi, J. Kumaki, E. Yashima, *Angew. Chem. Int. Ed*., **2007**, 46, 7605-7608.

[57] R. Rodríguez, J. Ignés-Mullol, F. Sagués, E. Quiñoá, R. Riguera, F. Freire, *Nanoscale*, **2016**, *8*, 3362-3367.

Chapter V

Photostability and Dynamic Helical Behavior in Chiral Poly(phenylacetylene)s with a Preferred Screw-Sense

CHAPTER V: Photostability and Dynamic Helical Behavior in Chiral Poly(phenylacetylene)s with a Preferred Screw-Sense

Adapted from:

Francisco Rey-Tarrío, Santiago Guisán-Ceinos, Juan M. Cuerva, Delia Miguel, Maria Ribagorda, Emilio Quiñoá, and Félix Freire[a]

[*] F. Rey-Tarrío, E. Quiñoá, F. Freire

Centro Singular de Investigación en Química Biolóxica e Materiais Moleculares (CiQUS) and Departamento de Química Orgánica. Universidade de Santiago de Compostela, 15782, Santiago de Compostela (Spain)

Guisán-Ceinos ,M. Ribagorda

Departamento de Química Orgánica, Facultad de Ciencias. Universidad Autónoma de Madrid, 28049, Madrid (Spain)

J. M. Cuerva

Departamento de Química Orgánica, Facultad de Ciencias. Universidad de Granada (UGR), Unidad de Excelencia de Química Aplicada a la Biomedicina y Medioambiente (UEQ), 18071, Granada (Spain)

D. Miguel

Departamento de Fisicoquímica, Facultad de Farmacia. Universidad de Granada (UGR,UEQ), 18071, Granada (Spain)

M. Ribagorda

Institute for Advanced Research in Chemical Sciences (IAdChem). Universidad Autónoma de Madrid, 28049, Madrid (Spain)

Angew. Chem. Int. Ed. **2022**, *61*, e202207623.

Abstract

*Helical polymers such as poly(phenylacetylene)s (PPAs) are interesting materials due to the possibility of tuning their helical scaffold (sense and elongation) once they have been prepared and by the presence of external stimuli. The main limitation in the application of PPAs is their poor photostability. These polymers degrade under visible light exposure through a photochemical electrocyclization process. In this work, it was demonstrated, through a selected example, how the photochemical degradation in PPAs is directly related to their dynamic helical behavior. Thus, while PPAs with dynamic helical structures show poor photostability under UV-vis light exposure, poly-(R)-**1**, bearing an enantiopure sulfoxide group as pendant group and designed to have a quasi-static helical behavior, shows a large photostability due to the restricted conformational composition at the polyene backbone, needed to orient the conjugated double bonds prior to the photochemical electrocyclization process and the subsequent degradation of the material.*

1. Introduction

Dynamic helical polymers such as poly(phenylacetylene)s (PPAs) have attracted the attention of the scientific community due to their stimuli responsive properties.[1-12] Thus, modulation of either the helical sense[13-19] and/or elongation[20-28] of a PPA is possible by using different external stimuli such as metal ions,[13,29,31,32] chiral molecules,[33] temperature,[34-36] solvents,[37-41] or anions.[42-44] However, the industrial application of these polymers as chiral stationary phases,[45-46] chiral recognition reagents,[47-50] or as dynamic chiral ligands in asymmetric synthesis [51-52] is reduced due to their poor thermal or light exposure stability.[53-57]

On the other hand, static helical polymers, although they do not show stimuli-responsive properties, have important applications in fields such as chiral recognition, chiral stationary phases, or chiral catalysts among others,[1] due to the robustness and folding degree of the helical scaffold that is not perturbed by environmental conditions. A great challenge for the scientific community is to create dynamic or static helical polymers using the same polymeric material, where the advantages of both, dynamic and static helical polymers can be compared.

Recently, our group found that the stability of PPAs under light exposure is directly related to the elongation degree of the polyene backbone,[58] which is defined by the dihedral angle between conjugated double bonds (ω_1). Thus, compressed *cis-cisoidal* PPAs (ω_1<90°) show lower stability than extended *cis-transoidal* PPAs (ω_1>90°). This fact makes possible not only to distinguish between compressed and extended helical structures but also to estimate a value for ω_1 in a PPA with unknown secondary structure. In addition, these studies also revealed that in extended almost planar structures (ω_1>170°), the dynamic behavior of the PPAs is dramatically reduced due to their restricted conformational freedom at the pendant group caused by steric effects —e. g. ortho substituted PPAs—, resulting in a null isomerization of conjugated double bonds under light exposure.

In this work, we want to go a step forward and establish a relationship between the dynamic behavior of a PPA and its stability, which should be applied to all the PPA helical scaffolds and not only to the highly stretched ones (ω_1>170°). To do that, it is necessary to prepare a PPA that comprises two requirements: 1) a "quasi static" behavior and 2) a helical scaffold where the dihedral angle between conjugated double bonds is lower than 170° (ω_1<170°), scaffolds that are known to be effectively affected by light when the PPA is dynamic. In such system (PPA with quasi-static behavior and ω_1<170°), it should be

possible to determine if the dynamic helical character of the PPA affects to its stability under light exposure. To create a PPA that comprises these two features, it is necessary to make a rational monomer design. Thus, we envisioned monomer mono-(*R*)-**1** as a potential candidate to generate a PPA that adopts a helical scaffold with a quasi-static behavior (Figure 1a). This sulfynilarene was previously used as source of chirality in *ortho*-phenylene ethynylene (*o*-OPE) foldamers, allowing an efficient transfer of chirality to the helically folded *o*-OPE, leading to electronic circular dichroism (ECD), circularly polarized luminescence (CPL)- and vibrational circular dichroism (VCD)-active compounds.[59-61]

Based in our expertise in the field of helical polymers and sulfinyl arenes, we foresee that polymerization of *para*-sulfynilaryl acetylene monomer (*R*)-**1** will generate a PPA that comprises the desired requirements, helical structure with ω_1<170° and quasi-static behavior. The chiral sulfoxide group present in **1** is a medium size pendant group and presents the ability to favor a single conformation, thanks to the vicinal disposition of the methoxy group,[62] fact that should enhance its power as helical inductor and promote the formation of a helical scaffold with a ω_1<170°. Therefore, it is expected that the orientation of the chiral pendant group respect to the polyene along the helical scaffold will be the same, producing an effective transfer of chirality from the enantiopure sulfoxide used as pendant to the polyene backbone.

2. Results and Discussion

To test our hypothesis, monomer (*R*)-**1** was prepared accordingly to a previously reported method.[59,62] X-ray diffraction series (XRD) of mono-(*R*)-**1** crystals obtained from a chloroform solution showed the presence of a preferred conformer where the sulfoxide group is oriented towards the phenylacetylene group, placing the oxygen group oriented planar towards the H at *ortho* position of the aryl ring (O-S-C-C angle= 13°) (Figure 1b).[63]

Electronic Circular Dichroism studies of mono-(*R*)-**1** in different solvents reveal a restricted conformational composition, where the ECD trace is not affected by either the polarity or the donor character of the solvent (Figure 1d). Moreover, the *p*-tolyl group is arranged almost perpendicular to the plane formed by the phenylacetylene and the methoxy groups (C-C-S-C dihedral angle of 84°), avoiding the repulsions between methoxy and sulfoxide groups (Figure 1a), and generating a chiral distribution between planes, which results in a strong absorption on CD and UV-Vis around 330 nm (Figure 1c,d).

Theoretical ECD calculations, time-dependent density functional theory (TD-DFT) was used together with a rCAM-B3LYP density functional and 6-31G* basis set (TD-DFT(rCAM-B3LYP)/6-31G*), were performed on the molecular structure obtained from X-ray studies. The simulated ECD spectrum is in good agreement with the experimental one obtained in all the different solvents tested indicating that mono-(*R*)-**1** adopts, as expected, the same conformation in solution that in the solid state (Figure 1e).

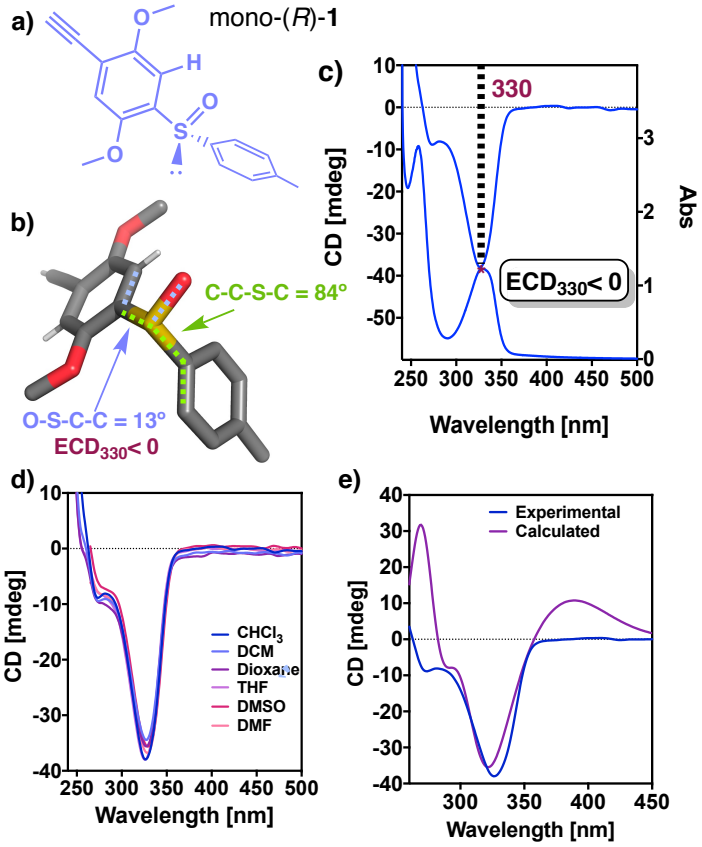

Figure 1. a) Chemical structure and b) X-Ray of mono-(*R*)-**1**. c) Experimental ECD and UV spectra of mono-(*R*)-1 in $CHCl_3$. [mono-(*R*)-1]= 0.3 mg/mL. d) Experimental ECD and UV spectra of mono-(*R*)-**1** in different solvents ([mono-(*R*)-**1**]= 0.3 mg/mL). e) Comparison of calculated and experimental ECD spectra of mono-(*R*)-**1** in $CHCl_3$.

Next, mono-(*R*)-**1** was polymerized using $[Rh(nbd)Cl]_2$ as catalyst (nbd= 2,5-norbornadiene), affording poly-(*R*)-**1** in good yield (66%, Figure 2) and with a high content of cis configuration of the double bonds as inferred from ^{1}H-NMR and Raman studies (see ESI for experimental details and characterization data). The number-average molecular weight (Mn= 88701) and distribution (Mw/Mn= 2.15) of the oligomers were determined by gel permeation chromatography (GPC) using THF as eluent with polystyrene standards as calibrants (see Supporting Information).

ECD and UV studies of poly-(*R*)-**1** were carried out in different solvents with different polarity and donor character to determine if poly-(*R*)-**1** adopts a helical structure with a preferred helical sense and tunable scaffold (Figure 2). In all solvents tested an ECD trace with and intense negative Cotton in the less energetic band indicates an *M* helical orientation of the polyene backbone (Figure 2b,c). Moreover, comparison of the mono-(*R*)-**1** and poly-(*R*)-**1** ECD and UV spectra show that the Cotton bands of the monomers are preserved in the PPA where two consecutive negative Cotton bands at ca. 260 and 310 nm are present. The hypsochromic shifting of the ECD band at 310 nm (330 in monomer) is due to the overlapping with other Cotton effects present in the polymer, such as the classical alternating -/+/- or +/-/+ Cotton bands usually found in PPAs.[64] Moreover, this overlapping of Cotton effect affects not only to the wavelength of the peaks but also to their intensity. In this case, the intensity of the Cotton bands related to the pendant group have similar intensity while in the monomer the UV band at 301 nm is four times the band at 260 nm.

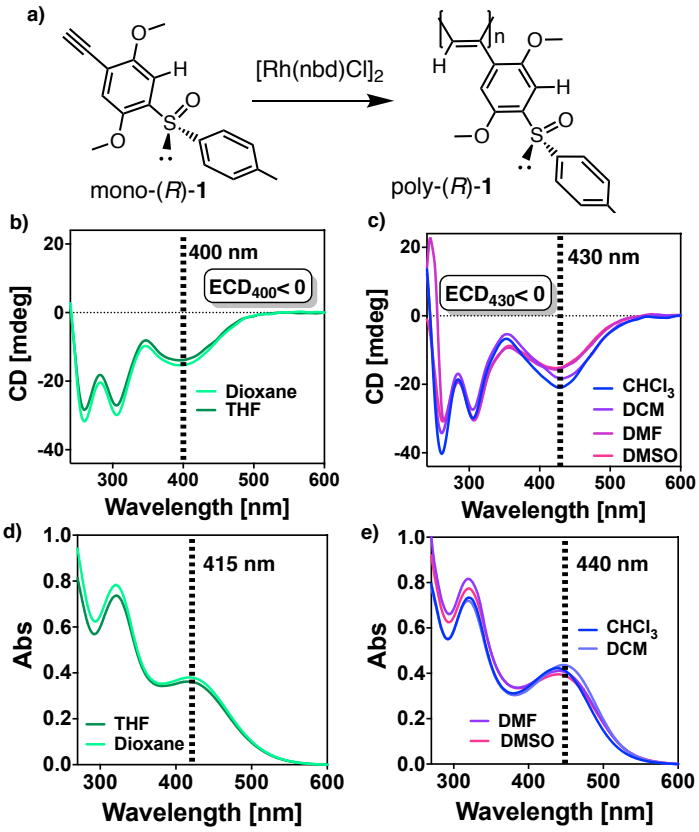

Figure 2. a) Polymerization scheme of mono-(*R*)-**1**. ECD spectra of poly-(*R*)-**1** in (b) dioxane and THF or in (c) DMF, DMSO, DCM and $CHCl_3$. UV-vis spectra of poly-(*R*)-**1** in (d) dioxane and THF or in (e) DMF, DMSO, DCM and $CHCl_3$. [poly-(*R*)-**1**]= 0.3 mg/mL.

Apart from these two bands, a new ECD/UV band appears at ca. 400 nm. ECD and UV-vis band appears at ca. 400 nm ECD and UV/Vis experiments show that this band suffers a

bathochromic shift of ca. 30 nm when is dissolved in DCM or $CHCl_3$ (430 nm) respect to the value obtained in THF or dioxane (400 nm) (Figure 2b,c). Therefore, the polymer adopts a more compressed helical scaffold ($ECD_{400} < 0$) in THF or Dioxane than when is dissolved in DCM, $CHCl_3$, DMF or DMSO ($ECD_{430} < 0$). Moreover, the absorbance of the yellowish polyene solution at wavelengths lower than 500 nm indicates that the poly(phenylacetylene) backbone does not adopt a highly extended, almost planar, helical scaffold, which usually shows a reddish color solution with a maximum of the polyene band at > 500 nm.[65,66]

To determine an approximated tridimensional structure for poly-(*R*)-**1** in $CHCl_3$ and THF, AFM studies were carried out. Thus, 2-D crystals of poly-(*R*)-**1** were prepared following of Yashima's protocol which consist in spin coat a dilute solution of the polymer onto a highly oriented pyrolytic graphite (HOPG) substrate and leave the sample under solvent atmosphere for 12 h.[66] As a result, well-ordered 2-D crystals of poly-(*R*)-**1** were obtained in both solvents, which allowed to obtain high-resolution AFM images for poly-(*R*)-**1** in $CHCl_3$ and THF. From these images is possible to extract important helical parameters such as the orientation of the helical structure described by the pendant groups or the helical pitch. In PPAs, the helical scaffold is defined by two coaxial helices. A helical structure is described by the polyene backbone, denoted as internal helix (H_{int}), whose helical sense can be determined by the sign of the Cotton bands associated to the polyene band — ECD < 0, M_{helix}; ECD > 0, P_{helix}—, and an external helix (H_{ext}) defined by the pendant groups whose orientation can be determined from AFM studies (Figure 3a,b).

As it was mentioned above, ECD studies showed that the internal helix of poly-(*R*)-**1** is oriented describing an *M* helix due to the presence of a negative Cotton band at ca. 400 nm in THF and at ca. 430 nm in $CHCl_3$. In addition, AFM images for poly-(*R*)-**1** in $CHCl_3$ revealed a right-handed orientation of the external helix, which is opposite to the orientation of the internal helix. These data correspond to a *cis-transoidal* polyene skeleton with ω_1>90°. With the aim of refining the helical scaffold adopted by poly-(*R*)-**1**, another helical parameter such as the helical pitch of ca. 5.1 nm, obtained from the AFM, was introduced into the modelling studies. The helical scaffold that satisfies the two structural data, ω_1>90° and helical pitch of ca. 5.1 nm, is a helix with ω_1=-165°.

Computational studies [TD-DFT(rCAM-B3LYP)/3-21G*] were performed on an *M* helix (n= 8) of poly-(*R*)-**1** —*cis-transoidal* skeleton (ω_1= -165°). In this model, the chiral moiety was introduced into the conformation obtained from X-ray studies. The simulated ECD spectrum is in good agreement with the one obtained experimentally, reproducing all the ECD bands and their relative intensity (Figure 3c).

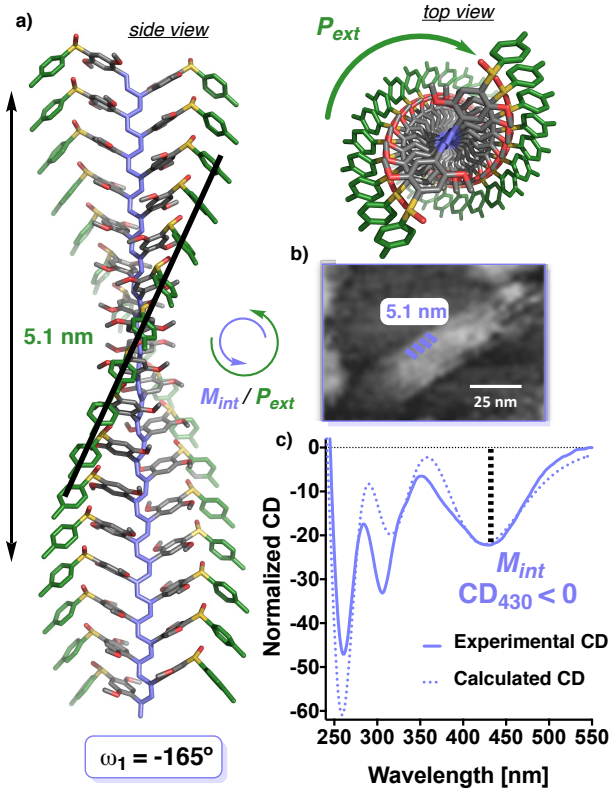

Figure 3. a) 3-D structure adopted by poly-(*R*)-**1** in $CHCl_3$. b) AFM image of a 2-D crystal of poly-(*R*)-**1** prepared in $CHCl_3$. c) Theoretical and experimental ECD spectra of poly-(*R*)-**1** (normalized at 430 nm). [poly-(*R*)-**1**]= 0.3 mg/mL.

On the other hand, AFM studies for poly-(*R*)-**1** in THF showed fiber like structures with a right-handed orientation of the external helix (Figure 4a). From these images it is not possible to extract helical parameters such as the helical pitch because individual helices are not visualized. Thus, to build up an approximated structure for poly-(*R*)-**1** in THF it was considered that the polyene scaffold is compressed when compared to the helix adopted in $CHCl_3$ (ω_1= -165°) due to the hypsochromic effect observed in the polyene band. Hence, molecular mechanics studies (MMFF94) were done to optimize the geometry of poly-(*R*)-**1** with ω_1< -165°, and where the calculated and the experimental ECD spectra show a good fit (Figure 4c). In this case, it was found that computational studies [TD-DFT(rCAM-B3LYP)/3-21G*] on an *M* helix (n= 8) of poly-(*R*)-**1** *cis-transoidal* skeleton, with a dihedral angle between conjugated double bonds of ω_1= -157°, produces a ECD trace that shows a good fit with the experimental one.

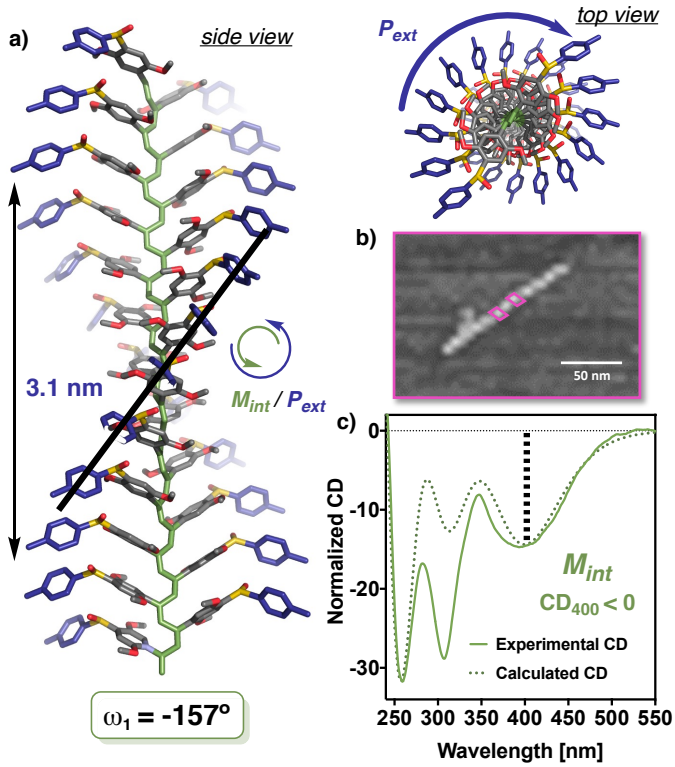

Figure 4. a) 3-D structure adopted by poly-(*R*)-**1** in THF. b) AFM image of a 2-D crystal of poly-(*R*)-**1** prepared in THF. c) Theoretical and experimental ECD spectra of poly-(*R*)-**1**. [poly-(*R*)-$\mathbf{1}_{(ECD)}$]= 0.3 mg/mL.

Finally, photostability studies were carried out for both, compressed, and stretched helical scaffolds (Figure 5a,b). As expected, the two helices show a strong photostability, inferred from ECD studies that show how the ECD traces remain almost unaltered even after 240 min of irradiation with visible light. This is attributed to the *quasi*-static behavior of the PPA and not to the electronic properties of the sulfoxide group. In literature, it is found that PPAs bearing a sulfoxide group at para position show a *cis*- to *trans*-isomerization of double bonds due to delocalization of radicals generated at the polyene, which can migrate to the sulfoxide group, producing the loss of its chirality.[30]

In addition, thermal stability studies of poly-(*R*)-**1** in $CHCl_3$ and THF reveal also the poor dynamic character of the PPA and its correlated high thermal stability (Figure 5c,d). In both solvents, the ECD trace obtained for poly-(*R*)-**1** is not affected by temperature changes, either by cooling down or heating up the cuvette containing a solution of the polymer. These results indicate that once the polymer is dissolved in a certain solvent, the helical folding is not perturbed by temperature changes.

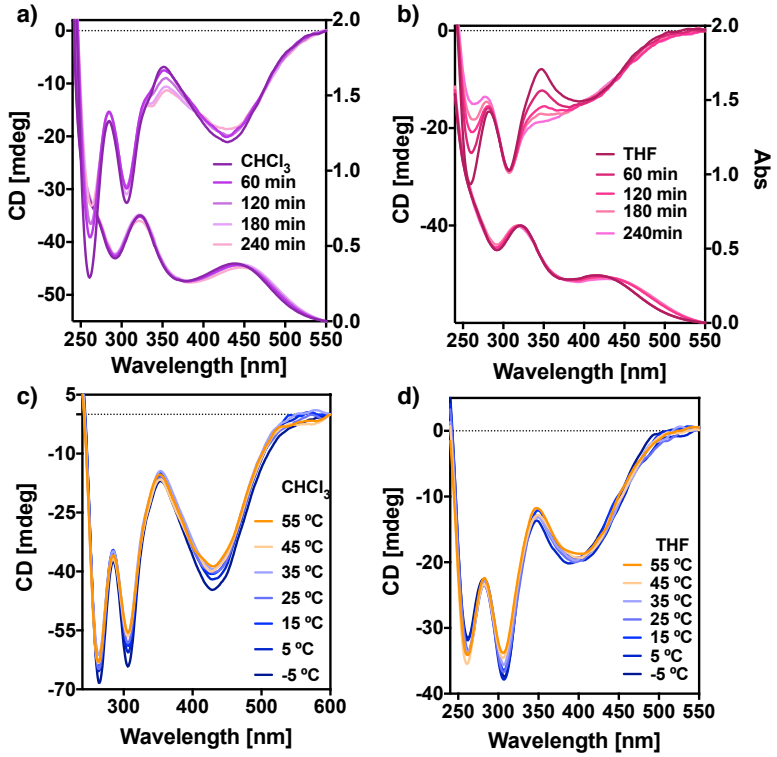

Figure 5. Photostability and thermal stability ECD studies of poly-(*R*)-**1** in a,c) $CHCl_3$ and b,d) THF. [poly-(*R*)-**1**]= 0.3 mg/mL; irradiation with visible light (350-550 nm).

3. Conclusion

In conclusion, it has been demonstrated through a rational design that photostability of PPAs is directly related to its dynamic behavior. Thus, those PPAs with a high dynamic behavior, whose helical sense or elongation can be altered by the presence of external stimuli are more prompt to degrade under light exposure due to photoisomerization of the double bonds that end up with a photochemical electrocyclization of the polyene backbone. On the other hand, PPAs with a restricted conformational composition and therefore a poor dynamic behavior shows a great photostability, being the helical scaffold not affected by irradiation with UV light. Therefore, dynamic behavior and photostability in PPAs are compromised, fact that is necessary to consider in the design and potential application of PPAs.

4. References

[1] E. Yashima, N. Ousaka, D. Taura, K. Shimomura, T. Ikai, K. Maeda, *Chem. Rev.*, **2016**, *116*, 13752-13990.

[2] E. Yashima, K. Maeda, H. Iida, Y. Furusho, K. Nagai, *Chem. Rev.*, **2009**, *109*, 6102-6211.

[3] T. Nakano, Y. Okamoto, *Chem. Rev.*, **2001**, *101*, 4013-4038.

[4] J. Tarrío, R. Rodríguez, B. Fernández, E. Quiñoá, F. Freire, *Angew. Chem. Int. Ed.*, **2022**, *134*, e202115070.

[5] E. Schwartz, M. Koepf, H. J. Kitto, R. J. M. Nolte, A. E. Rowan, *Polym. Chem.*, **2011**, *2*, 33-47.

[6] E. Yashima, K. Maeda, Y. Furusho, *Acc. Chem. Res.*, **2008**, *41*, 1166-1180.

[7] R. Sakai, E. B. Barasa, N. Sakai, S. -I. Sato, T. Satoh, T. Kakuchi, *Macromolecules*, **2012**, *45*, 8221-8227.

[8] E. Yashima, K. Maeda, *Macromolecules*, **2008**, *41*, 3-12.

[9] K. Maeda, E. Yashima, *Top. Curr. Chem.* **2006**, *265*, 47-88.

[10] R. Nonokawa, E. Yashima, *J. Am. Chem. Soc.*, **2003**, *125*, 1278-1283.

[11] E. Yashima, K. Maeda, Y. Okamoto, *Nature*, **1999**, *399*, 449-451.

[12] E. Yashima, K. Maeda, T. Matsushima, Y. Okamoto, *Chirality*, **1997**, *9*, 593-600.

[13] R. Rodríguez, E. Suárez-Picado, E. Quiñoá, R. Riguera, F. Freire, *Angew. Chem. Int. Ed.* **2020**, *59*, 8616-8622.

[14] F. Freire, J. M. Seco, E. Quiñoá, R. Riguera, *J. Am. Chem. Soc*., **2012**, *134*, 19374-19383.

[15] F. Ishiwari, K. Nakazono, Y. Koyama, T. Takata, *Angew. Chem. Int. Ed.,* **2017**, *56*, 14858-14862.

[16] R. Rodríguez, S. Arias, E. Quiñoá, R. Riguera, F. Freire, *Nanoscale*, **2017**, *9*, 17752-17757.

[17] N. Zhu, K. Nakazono, T. Takata, *Chem. Commun.,* **2016**, *52*, 3647-3649.

[18] S. Leiras, F. Freire, J. M. Seco, E. Quiñoá, R. Riguera, *Chem. Sci.*, **2013**, *4*, 2735-2743.

[19] K. Maeda, H. Mochizuki, M. Watanabe, E. Yashima, *J. Am. Chem. Soc*., **2006**, *128,* 7639-7650.

[20] K. Maeda, N. Kamiya, E. Yashima, *Chem. Eur. J.,* **2004**, *10*, 4000-4010.

[21] T. Ikai, R. Ishidate, K. Inoue, K. Kaygisiz, K. Maeda, E. Yashima, *Macromolecules*, **2020**, *53*, 973-981.

[22] M. Alzubi, S. Arias, R. Rodríguez, E. Quiñoá, R. Riguera, F. Freire, *Angew. Chem. Int. Ed.*, **2019**, *58*, 13365-13369.

[23] R. Rodríguez, E. Quiñoá, R. Riguera, F. Freire, *Chem. Mater.* **2018**, *30*, 2493-2497.

[24] T. Van Leeuwen, G. H. Heideman, D. Zhao, S. J. Wezenberg, B. L. Feringa, *Chem. Commun.* **2017**, *53*, 6393-6396.

[25] M. Alzubi, S. Arias, I. Louzao, E. Quiñoá, R. Riguera, F. Freire, *Chem. Commun*., **2017**, *53*, 8573-8576.

[26] S. Arias, F. Freire, E. Quiñoá, R. Riguera, *Polym. Chem*., **2015**, *6*, 4725-4733.

[27] F. Freire, J. M. Seco, E. Quiñoá, R. Riguera, *Angew. Chem. Int. Ed.*, **2011**, *50*, 11692-11696.

[28] I. Louzao, J. M. Seco, E. Quiñoá, R. Riguera*, Angew. Chem. Int. Ed.* **2010**, *49*, 1430-1433.

[29] S. Arias, J. Bergueiro, F. Freire, E. Quiñoá, R. Riguera, *Small*, **2016**, *12*, 238-244.

[30] K. Huang, S. Y. Mawatary, A. Miyasaka, Y. Sadahiro, M. Tabata, Y. Kashiwaya, *Polymer*, **2007**, *48*, 6366-6373.

[31] S. Arias, M. Núñez-Martínez, E. Quiñoá, R. Riguera, F. Freire *Polym. Chem.,* **2017**, 8, 3740-3745.

[32] M. Núñez-Martínez, S. Arias, E. Quiñoá, R. Riguera, F. Freire, *Chem. Mater.,* **2021**, *33*, 4805–481.

[33] K. Maeda, K. Morino, Y. Okamoto, T. Sato, E. Yashima, *J. Am. Chem. Soc.*, **2004**, *126*, 4329-4342.

[34] S. Li, K. Liu, G. Kuang, T. Masuda, A. Zhang, *Macromolecules*, **2014**, *47*, 3288-3296.

[35] S. Arias, F. Freire, M. Calderón, J. Bergueiro, *Angew. Chem. Int. Ed.*, **2017**, *129*, 11578-11583.

[36] F. Wang, C. Zhou, K. Liu, J. Yan, W. Li, T. Masuda, A. Zhang, *Macromolecules*, **2019**, *52*, 8631-8642.

[37] J. Bergueiro, M. Núñez-Martínez, S. Arias, E. Quiñoá, R. Riguera, F. Freire, *Nanoscale Horiz.,* **2020**, *5(3),* 495-500.

[38] R. Rodríguez, E. Suárez-Picado, E. Quiñoá, R. Riguera, F. Freire, *Angew. Chem. Int. Ed.*, **2020**, *132*, 8694-8700.

[39] K. Cobos, R. Rodriguez, O. Domarco, B. Fernandez, E. Quinoa, R. Riguera, R., F. Freire, *Macromolecules*, **2020**, *53*, 3182-3193.

[40] E. Suárez-Picado, E. Quiñoá, R. Riguera, F. Freire, *Angew. Chem. Int. Ed.*, **2020**, *59*, 4537-4543.

[41] M. Fukuda, R. Rodríguez, Z. Fernández, T. Nishimura, D. Hirose, G. Watanabe, E. Quiñoá, F. Freire, K. Maeda, *Chem. Comm*., **2019**, *55*, 7906-7909.

[42] K. Maeda, M. Ishikawa, E. Yashima, *J. Am. Chem. Soc.*, **2004**, *126*, 15161-15166.

[43] Y. Cao, L. Ren, Y. Zhang, X. Lu, X. Zhang, J. Yan, W. Li, T. Masuda, A. Zhang, *Macromolecules*, **2021**, 54, 7621-7631.

[44] S. Leiras, E. Suárez-Picado, E. Quiñoá, R. Riguera, F. Freire, *Giant*, **2021**, *7*, 100068.

[45] R. Ishidate, T. Sato, T. Ikai, S. Kanoh, E. Yashima, K. Maeda, *Polym. Chem.*, **2019**, *10*, 6260-6268.

[46] D. Hirose, A. Isobe, E. Quiñoá, F. Freire, K. Maeda, E. Yashima, K. Maeda, *J. Am. Chem. Soc.*, **2019**, *141*, 8592-8598.

[47] Y. Zhou, C. Zhang, Q. Geng, L. Liu, H. Dong, T. Satoh, Y. Okamoto, *Polym. J.*, **2017**, 131, 17-24.

[48] Y. Zhou, C. Zhang, Z. Zhou, R. Zhu, L. Liu, J. Bai, H. Dong, T. Satoh, Y. Okamoto, *Polym. Chem.,* **2019**, *10*, 4810-4817.

[49] M. Ando, R. Ishidate, T. Ikai, K. Maeda, E. Yashima, *J. Polym. Sci., Part A: Polym. Chem.* **2019**, *57*, 2481-2490

[50] C. Zhang, Y. Qiu, S. Bo, F. Wang, Y. Wang, L. Liu, Y. Zhou, H. Niu, H Dong, T. Satoh, *J. Polym. Sci., Part A: Polym. Chem.* **2019**, *57*, 1024-1031.

[51] Z. Tang, H. Iida, H. Y. Hu, E. Yashima, *ACS Macro Lett.,* **2012**, *1*, 261-265.

[52] H. Iida, Z. Tang, E. Yashima, *J. Polym. Sci. A: Polym. Chem.,* **2013**, *51*, 2869-2879.

[53] S. A. Karim, R. Nomura, T. Masuda, *J. Polym. Sci. Part. A: Polym. Chem.,* **2001**, *39*, 3130-3136.

[54] V. Percec, J. G. Rudick, P. Nombel, W. Buchowicz, *J. Polym. Sci., Part A: Polym. Chem.,* **2002**, *40*, 3212-3220.

[55] V. Percec, J. G. Rudick, *Macromolecules*, **2005**, *38*, 7241-7250.

[56] L. Liu, T. Namikoshi, Y. Zang, T. Aoki, S. Hadano, Y. Abe, I. Wasuzu, T. Tsutsuba, M. Teraguchi, T. Kaneko, *J. Am. Chem. Soc.*, **2013**, *135*, 602-605.

[57] Y. Tang, L. Liu, J. Suzuki, M. Teraguchi, T. Kaneko, T. Aoki, *Chirality*, **2022**, *34*, 450-461.

[58] F. Rey-Tarrío, R. Rodríguez, E. Quiñoá, R. Riguera, F. Freire, *Angew. Chem. Int. Ed.,* **2021**, *60*, 8095–8103.

[59] S. Resa, D. Miguel, S. Guisán-Ceinos, G. Mazzeo, D. Choquesillo-Lazarte, S. Abbate, L. Crovetto, D. J. Cárdenas, M. C. Carreño, M. Ribagorda, G. Longhi, A. J. Mota, L. Á. de Cienfuegos, J. M. Cuerva, *Chem. Eur. J.*, **2018**, *24*, 2653-2662.

[60] P. Reiné, A. M. Ortuño, S. Resa, L. Á. de Cienfuegos, V. Blanco, M. J. Ruedas-Rama, G. Mazzeo, S. Abbate, A. Lucotti, M. Tommasini, S. Guisán-Ceinos, M. Ribagorda, A. G. Campaña, A. Motta, G. Longhi, D. Miguel, J. M. Cuerva, *Chem. Comm.,* **2018**, *54*, 13985-13988.

[61] S. Resa, P. Reiné, L. Á. de Cienfuegos, S. Guisán-Ceinos, M. Ribagorda, G. Longhi, G. Mazzeo, S. Abbate, A. J. Mota, D. Miguel, J. M. Cuerva, *Org. Biomol. Chem.,* **2019**, *17*, 8425-8434.

[62] M. C. Carreño, I. García, I. Núñez, E. Merino, M. Ribagorda, S. Pieraccini, and G. P. Spada, *J. Am. Chem. Soc.* **2007**, *129*, 7089-7100.

[63] Deposition Number 2174549 contains the supplementary crystallographic data for this paper. These data are provided free of charge by the joint Cambridge Crystallographic DataCentre and Fachinformationszentrum Karlsruhe Access Structures service.

[64] V. Percec, M. Peterca, J. G. Rudick, E. Aqad, M. R. Imam, P. A. Heiney, *Chem. Eur. J.,* **2007**, *13*, 9572-9581.

[65] R. Rodríguez, E. Quiñoá, R. Riguera, F. Freire, *Small,* **2019**, *15*, 1805413.

[66] R. Rodríguez, E. Quiñoá, R. Riguera, F. Freire, *J. Am. Chem. Soc.*, **2016**, *138*, 9620-9628.

[67] J. Kumaki, S. I. Sakurai, E. Yashima, *Chem. Soc. Rev.*, **2009**, *38*, 737-746.

Chapter VI

Photostable Multi-Switches Based on Azo-Poly(phenylacetylene)s with Three Different Chiral Motifs ($Helix_{int}$/$Helix_{ext}$/$Helix_{Azo}$)

CHAPTER VI: Photostable Multi-Switches Based on Azo-Poly(phenylacetylene)s with Three Different Chiral Motifs ($Helix_{int}$/$Helix_{ext}$/$Helix_{Azo}$)

Abstract

Dynamic helical polymers have been extensively studied with different stimuli such as metals, solvents or temperature, among others. However, the use of light as stimulus was barely analyzed in these systems. Herein, two poly(phenylacetylene)s containing azobenzene groups were synthesized, the combination of both systems results in multi-switch materials that interact with light, temperature, solvents, acids, metals, etc. Furthermore, the interaction with the stimuli was analyzed from a conformational point of view. Demonstrating how switches are activated in the helical structure, and as remarkable goal, opening a new route to prepare for the first time, highly dynamic helical polymers with improved stability vs photochemical electrocyclization.

1. Introduction

Helices are structural motifs found in Nature that play an important role in the biological function of macromolecules such as peptides, proteins, DNA, or polysaccharides. This structure/function relationship led the scientific community to explore other non-natural system such as helical polymers (covalent and supramolecular)[1-7] looking for applications in catalysis,[8-10] chiral stationary phases[11-13] for HPLC or as stimuli-responsive materials[14-17] among others. Within the classical covalent helical polymers, dynamic helical polymers such as poly(phenylacetylene)s (PPAs), poly(acetylene)s, poly(methylmetacrylate)s (PMMAs), poly(isocyanate)s or poly(phenyl isocyanide)s play an important role due to the possibility of tuning their helical sense[18-21] and/or elongation[22-24] once they have been prepared. This phenomenon is not found in Nature, making this class of materials unique.

Different stimuli have been employed to perturb the helical scaffold of dynamic helical polymers such as chiral additives,[25] metal ions,[26-29] anions,[30-32] solvents,[33-36] pH,[37] or temperature.[38-40] Among them, light was scarcely employed as external stimulus. In literature there are just a few examples of dynamic helical polymers that interact with light.[41-43] One of these examples was developed by Prof. Feringa and coworkers who created a poly(isocyanate) functionalized at one end with a chiral light-driven rotary molecular motor which allows a fully reversible control of the preferred helical sense of the polymer backbone.[44] However, most of the examples found in literature are related to PMMAs that bear and azo group at the pendant that is placed in a remote position, separated from the backbone through an achiral and flexible alkyl chain.[45-49] In these polymers, a chiral arrangement of the azo groups can be induced by irradiating the polymer with circularly polarized light,[50-51] by using chiral solvents[52-54] or even by placing a chiral residue close to the backbone.[55] The stimuli responsiveness of these polymers is usually related to an ON/OFF switch of the supramolecular chiral rearrangement of the azo groups induced by light or temperature. Intriguingly, from these studies it is not possible to extract the role of the main chain during the chiral arrangement of the azo groups, determining therefore if it is folded into a helical scaffold or into a random coil structure.

In this work, we aim to prepare a multi-switch material that responds to the presence of different stimuli such as solvents, metal ions, temperature, and light. Moreover, our goal is also to explain from a structural and conformational point of view how the switches are activated ON and OFF by the presence/absence of the different stimuli added.

To do that, we will use as platform to perform our studies a family of helical polymers that has been used during the last years in our group, the PPAs. The first objective in this work is to design a monomer that comprise all requirements to behave as a multi-switch. Thus, we envisioned a phenylacetylene that bears the 4-benzamide of (*L*)-alanine and (*L*)-valine derivatized at the C-terminus with 4-aminoazobenzene —mono-(*L*)-**1** and mono-(*L*)-**2** respectively— (Figure 1a). Thus, in these monomers it is possible to play either with the *syn*/*anti* conformational composition between the two carbonyl groups of the amino acid moiety or with the *Z*/*E* orientation of the azo group. Interestingly, in literature there are just a few examples of PPAs derivatized with azo groups. These polymers are achiral, and the studies are limited to analyze their photostability and their liquid-crystalline properties.[41] However, no studies are found related to the helical sense or the screw sense induction in PPAs bearing azo groups as pendants. This fact is probably due to the poor photostability of the PPA polyene backbone, which is degraded under visible light.[56-58] In our opinion, PPAs derivatized with azo groups must be photostable, because the they should absorb the light avoiding the polyene photochemical electrocyclization.

2. Results and Discussion

Monomers mono-(*L*)-**1** and mono-(*L*)-**2** (Figure 1a) were prepared by coupling 4-aminoazobenzene to Fmoc-Ala-OH and Fmoc-Val-OH residues. Next, the Fmoc groups were deprotected with piperidine and the amino groups were coupled to 4-ethynylbenzoic acid to yield mono-(*L*)-**1** and mono-(*L*)-**2** (see SI for synthetic and characterization details). X-ray diffraction (XRD) studies on crystals of mono-(*L*)-**1** obtained from a $CHCl_3$ solution reveal the presence of a preferred *anti*-conformation of the carbonyl groups in combination with an *E* azobenzene isomer (Figure 1b).

UV-Vis studies of mono-(*L*)-**1** and mono-(*L*)-**2** show two intense bands at ca. 255 and 350 nm that correspond to the absorbance of the carbonyls (255 nm) and azo groups (255 and 350 nm)[59-61] (figure 1d). These groups are also active in the ECD spectrum indicating the presence of a preferred conformation at the pendant group (Figure 1c). Theoretical ECD calculations, time-dependent density functional theory (TD-DFT) together with a rCAM-B3LYP density functional and 6-31G* basis set (TD-DFT(rCAM-B3LYP)/6-31G*), were performed on the molecular structure obtained from X-ray studies after DFT optimization. The simulated ECD spectrum is in good agreement with the experimental one obtained in all the different solvents tested indicating that mono-(*L*)-**1** adopts, as expected, the same conformation in solution as in the solid state (Figure 1c).

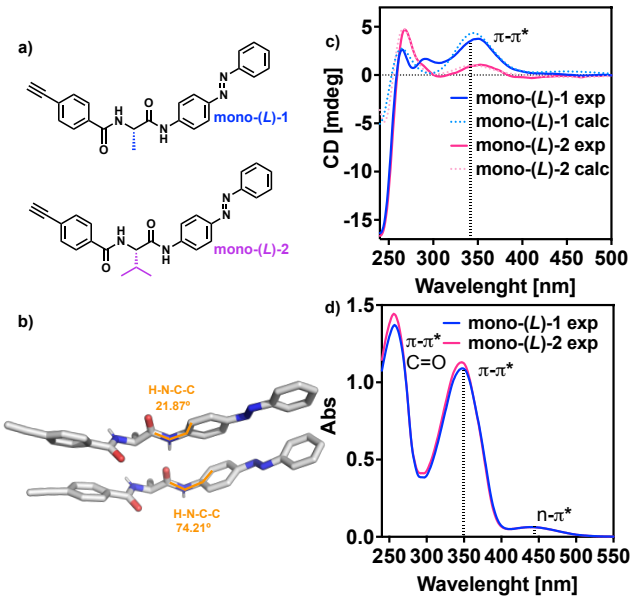

Figure 1. a) Structures of mono-(*L*)-**1** and mono-(*L*)-**2**. b) X-ray of mono-(*S*)-**1**. c) ECD and (d) UV-Vis of mono-(*L*)-**1** and mono-(*L*)-**2** in $CHCl_3$. [mono-(*L*)-**1**]= 0.2 mg/mL, [mono-(*L*)-**2**]= 0.2 mg/mL

Irradiation studies with UV light of 350 nm (see SI for details) promotes a fast *E* to *Z* isomerization of the azo group, which can be easily monitored by UV-Vis. A signal decay of the UV band at ca. 350 nm (π-π* transition band) accompanied with an increase of the UV bands at ca. 420 nm (n-π* transition band) and 258 nm (π-π* transition band) is observed after 20 min of light irradiation (350 nm), which indicates the *E* to *Z* isomerization of the azo group. This process can be reverted by irradiating the cuvette with a source of light of 420 nm (Figure 2).

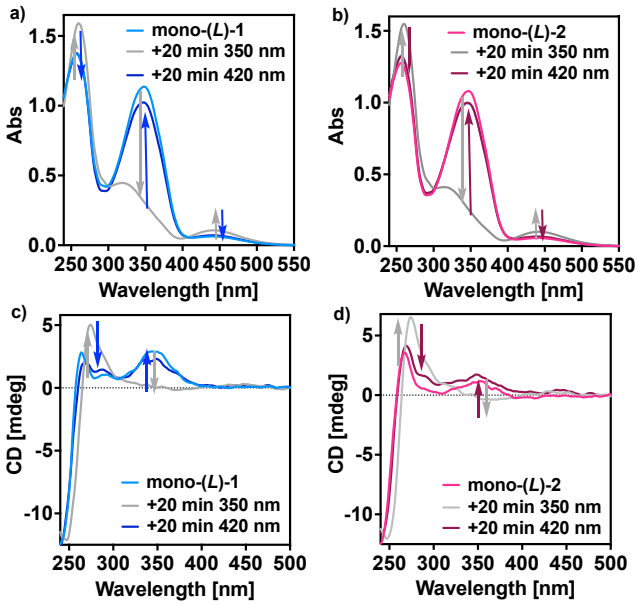

Figure 2. UV-vis and ECD spectra of a,c) mono-(*L*)-**1** and b,d) mono-(*L*)-**2** in $CHCl_3$ before and after irradiation with UV light (350 nm), followed by irradiation with UV-light (420 nm). [mono-(*L*)-**1**]= 0.2 mg/mL, [mono-(*L*)-**2**]= 0.2 mg/mL.

Next, monomers mono-(*L*)-**1** and mono-(*L*)-**2** were transformed into the corresponding polymers —poly-(*L*)-**1** and poly-(*L*)-**2**— using $[Rh(nbd)Cl]_2$ (nbd= 2,5-norbornadiene), as catalyst. This catalyst provides the polymers in high yield (>80%), low polydispersity and high *cis* content of double bonds (see SI for details).

ECD studies of poly-(*L*)-**1** and poly-(*L*)-**2** in DMF show the classical ECD traces of helical PPAs,[62-64] with three alternating Cotton bands, being the first one positive, which corresponds to a *P* orientation of the polyene backbone ($ECD_{370} > 0$; P_{helix}) (Figure 3a). The ECD traces obtained for poly-(*L*)-**1** and poly-(*L*)-**2** in DMF are similar to those observed previously for other benzamide PPAs derivatized with (*L*)-amino acids.[65-66] This fact indicates that the group used to cap the C-terminus of the amino acid (methanol, undecanol or 4-aminoazobenzene) does not affect the conformational composition of the pendant group in DMF, adopting in all cases *syn* conformation.

DSC studies show thermograms that correspond to *cis-transoidal* skeletons, similarly to those obtained for other PPAs bearing amino acids as pendant groups (see SI). With this information on hand, computational studies [TD-DFT-(rCAM-B3LYP)/3-21G*] were performed on a *P* helix (*n*= 8) of poly-(*L*)-**1** (ω_1= 148°). Interestingly, the array of azo groups along the helical scaffold makes not possible a supramolecular interaction between them, due to a large shifting between an Azo group and those located in upper and bottom positions (Figure 3b). UV-vis studies corroborate this hypothesis, because we could observe that the π-π* transition band of the azo group (ca. 355 nm) is not affected when shifting from the monomeric to the polymer structure, which indicates that the azo groups do not interact with each other along the polymer scaffold (Figure 3c).

Furthermore, VT-ECD studies for poly-(*L*)-**1** in DMF show an interesting phenomenon: while the ECD spectra and the helical scaffold remain stable up to 80°C, a helix inversion is produced when the solution is cooled at -10°C (Figure 3d). This fact indicates that poly-(*L*)-**1** works as chiroptical switch with temperature. On the contrary, in the case of poly-(*L*)-**2**, VT experiments showed the classical thermal behavior for helical PPAs, i.e., a better folding when the temperature decreases and a helix perturbation when the temperature increases (Figure 3e).

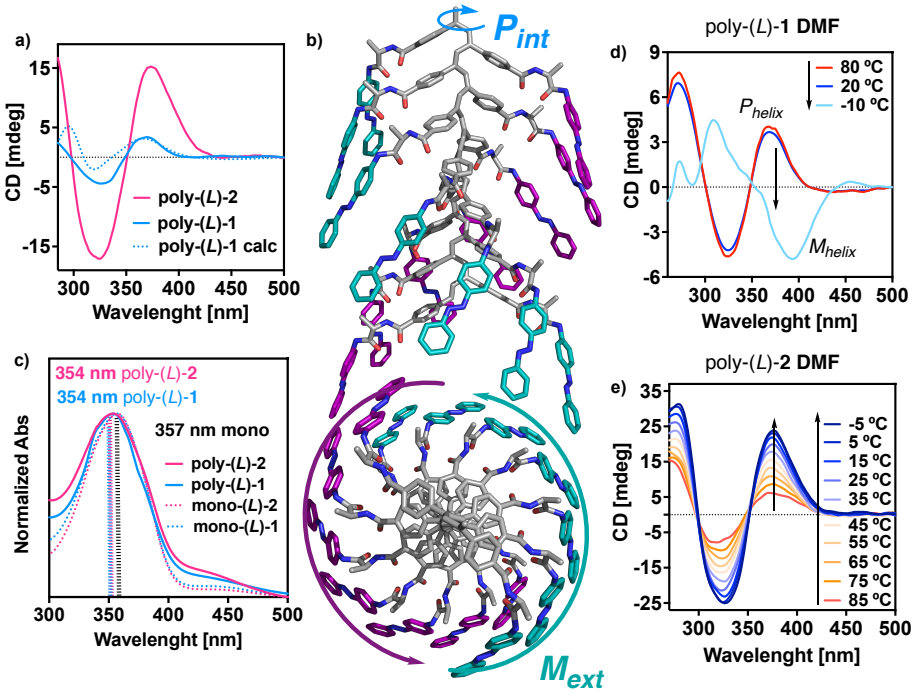

Figure 3. a) ECD spectra of poly-(*L*)-**1** and poly-(*L*)-**2** in DMF and comparison with the theoretical ECD spectrum obtained for poly-(*L*)-**1**. b) 3D model for poly-(*L*)-**1** (ω_1=148°, P_{helix}). c) UV-vis spectra of mono-(*L*)-**1**, mono-(*L*)-**2**, poly-(*L*)-**1** and poly-(*L*)-**2** in DMF. VT-ECD experiments of a DMF solution of d) poly-(*L*)-**1** and e) poly-(*L*)-**2**. [poly-(*L*)-**1**]= 0.3 mg/mL, [poly-(*L*)-**2**]= 0.3 mg/mL.

When these studies were carried out in a low-polar solvent such as $CHCl_3$, a completely different ECD pattern was obtained for both poly-(*L*)-**1** and poly-(*L*)-**2** (Figure 4a). In this case, a negative bisignate is observed at the π-π* transition band of the azo group (337 nm). This exciton coupling is produced due to cooperative dipole-dipole interactions between neighboring azo chromophores. At this point, the classical ECD pattern of a helical PPA is negligible, being just dominated by the chiral azo array.

Different structural studies were performed to determine the helical folding of poly-(*L*)-**1** and poly-(*L*)-**2** in $CHCl_3$. Thus, DSC studies shows a thermogram that corresponds to a *cis-cisoidal* polyene backbone (ω_1< 90°) (see SI). Moreover, 2D-crystals of poly-(*L*)-**1** could be obtained by spin coating a dilute $CHCl_3$ solution of poly-(*L*)-**1** onto highly oriented pyrolytic graphite (HOPG), which allowed us to perform AFM studies. High-resolution AFM images of these 2D-crystals were obtained and structural parameters such as the helical pitch (2.4 nm) or the orientation of the external helix (M_{ext}) could be extracted (Figure 4b).

From these studies, it was possible to model a *cis-cisoidal* PPA for poly-(*L*)-**1** that comprises all the structural requirements obtained from AFM and DSC (Figure 4c). In this structure, the pendant group was introduced in the conformation obtained from X-ray studies, an *antiperiplanar* orientation of the two carbonyl groups present in the pendant,

which is known from previous studies that is the preferred conformation for PPAs derivatized with amino acid groups in low-polar solvents. Also, the dihedral angle between conjugated double bonds has a value of ω_1= -70°, which shows an *M* orientation of the polyene backbone (M_{int}) and an *M* orientation of the pendant groups (M_{ext}). Moreover, the tilting degree between azo groups is negative (θ= -59°), producing an extra helical array of these groups at the periphery of the helix (M_{Azo}) responsible of the negative bisignate obtained at ca. 347 nm. As a result, a complex helical architecture with three different helical motifs is produced: *helix$_{int}$* defined by the polyene, *helix$_{ext}$* defined by the pendants, and *helix$_{Azo}$* described by the supramolecular azo array. In this case, a $M_{int}/M_{ext}/M_{Azo}$ are produced when poly-(*L*)-**1** and poly-(*L*)-**2** are dissolved in $CHCl_3$.

By looking at the UV-vis spectra of poly-(*L*)-**1** and poly-(*L*)-**2** in $CHCl_3$, it is possible to observe a hypsochromic shift of the π-π* transition band of the azo group from the monomeric form to the polymeric ones (Figure 4d). More precisely, for poly-(*L*)-**2** the UV band of the azo group is 20 nm blue shifted respect to mono-(*L*)-**2** — poly-(*L*)-**2** (331 nm); mono-(*L*)-**2** (353 nm)—, while in case of poly-(*L*)-**1** this UV band is 10 nm blue shifted respect to mono-(*L*)-**1** —poly-(*L*)-**1** (341 nm); mono-(*L*)-**1** (353 nm)—.

These polymers are completely solubilized in $CHCl_3$ as inferred from dynamic light scattering (DLS) studies, and therefore, the shifting of the UV-band is not related to an aggregation phenomenon. In this case, a chiral azo must be produced within a macromolecular dissolved helical polymer structure, which is the responsible of the blue shifting of the π-π* transition band. Moreover, the azo array in the macromolecular helical structure must resemble a supramolecular *H*-aggregate (θ< 54.7°) (Figure 4e). Otherwise, in case of resembling a supramolecular *J*-aggregate (θ< 54.7°), a red shifting should be observed when compared to the monomeric form.

Computational studies [TD-DFT-(rCAM-B3LYP)/3-21G*] were performed next on an $M_{int}/M_{ext}/M_{Azo}$ (*n*= 9) oligomer of poly-(*L*)-**1**, which possess a *cis-cisoidal* skeleton (ω_1= -70°, ω_2= 10°) and an *anti*-conformation at the pendant group (see SI for details). The theoretical ECD spectrum shows a good match with the experimental one, indicating that the proposed structure is in good agreement with the experimental one. As a result, we can conclude that in this case the ECD spectrum of the PPA becomes negligible, being just dominated by the azo array along the helical scaffold.

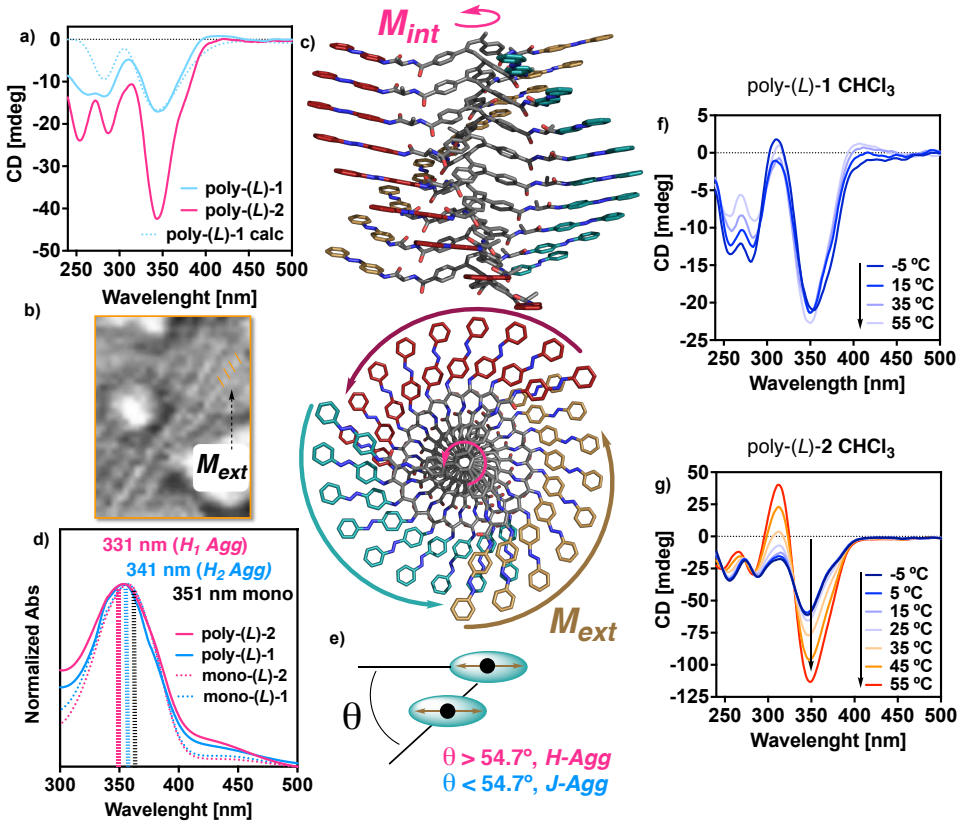

Figure 4. a) Comparison between the experimental ECD spectra of poly-(*L*)-**1** and poly-(*L*)-**2** in $CHCl_3$ and the theoretical [TD-DFT (CAM-B3LYP)/3-21G] ECD spectrum of poly-(*L*)-**1**. b) High resolution AFM images of poly-(*L*)-**1**. c) 3D model for poly-(*L*)-**1** (ω_1=-70°, M_{int}/M_{ext}). d) UV-vis spectra of poly-(*L*)-**1** and poly-(*L*)-**2** in $CHCl_3$. e) Illustration of the different intramolecular packing of azo groups found in macromolecularly dissolved poly-(*L*)-**1** and poly-(*L*)-**2**. VT-ECD experiments of a $CHCl_3$ solution of f) poly-(*L*)-**1** and g) poly-(*L*)-**2**. [poly-(*L*)-**1**]= 0.3 mg/mL, [poly-(*L*)-**2**]= 0.3 mg/mL.

VT-ECD studies for poly-(*L*)-**1** and poly-(*L*)-**2** in $CHCl_3$ reveal a large stability of these *H*-structures, where the helices do not suffer any variation in a temperature range from -5°C to 30°C. Interestingly, while in case of poly-(*L*)-**1** the *H*-helix is not affected by heating up to 55°C, in the case of poly-(*L*)-**2**, the *H*-helix improves its folding in more than 150% (Figure 4f,g). This fact indicates that the supramolecular interactions emerged between azo groups along a *H*-scaffold produce a large thermal stabilization of the helix.

Later, the stimuli-responsive properties of poly-(*L*)-**1** and poly-(*L*)-**2** dissolved in $CHCl_3$ were explored. Thus, different perchlorate metal salts dissolved in MeOH (10 mg/mL) were added to a $CHCl_3$ solution of poly-(*L*)-**1** and poly-(*L*)-**2** (0.3 mg/mL) in a 1.0/1.0 mol/mol ratio (Figure 5 for $Ba(ClO_4)_2$ and SI for other metals). As a result, while poly-(*L*)-**1** shows stimuli-responsive properties with metal ions (Figure 5a), poly-(*L*)-**2** does not (Figure 5d). This different behavior can be explained through the different folding degree of the two PPAs. Poly-(*L*)-**2** shows an ECD trace much higher in intensity, indicating a

better folding and therefore a more stable supramolecular array of the azo groups along the helix. While poly-(*L*)-**1**, for its poor azo array, presents an interesting stimuli-responsive behavior (Figure 5 and SI).

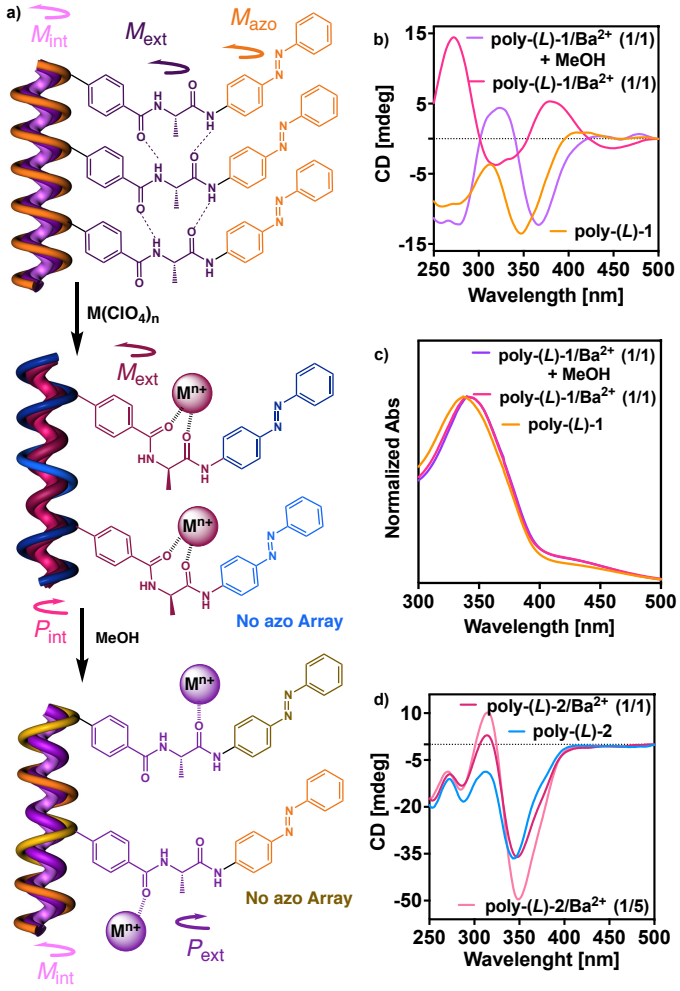

Figure 5. a) Graphical representation of the structural changes produced in poly-(*L*)-**1** by interaction with metal ions. b) Variation at the ECD and (c) UV-vis spectrum of poly-(*L*)-**1** after chelation with metal ions and further addition of methanol. d) Screw sense enhancement of poly-(*L*)-**2** after chelation with metal ions and further addition of methanol. [poly-(*L*)-**1**]= 0.3 mg/mL, [poly-(*L*)-**2**]= 0.3 mg/mL.

The addition of metal salts to form a poly-(*L*)-**1**/M^{n+} complex in 1.0/1.0 mol/mol ratio producess as expected the *anti* to *syn* conformational change at the pendant originating the ECD spectra found previously in polar solvents such as DMF, which favors the *anti*-conformation (Figure 5a). Interestingly, this conformational change at the pendant breaks the *H*-supramolecular array of the azo groups along the helix (*cis-cisoidal*, $M_{int}/M_{ext}/M_{Azo}$) and produces a helix inversion and stretching of the polyene backbone (*cis-transoidal*, P_{int}/M_{ext}), without any further organization of the azo groups (Figure 5b). In the UV-vis spectra a red-shift of the azo band is observed indicating the disruption of the *H*-supramolecular array (Figure 5c). Further additions of methanol increase the polarity of

the media and breaks the chelate to just coordinate the metal ion with the different carbonyl groups. As a result, a *syn* to *anti* conformational change is produced, and a helix inversion is obtained (Figure 5a-c). In this case, the helical scaffold remains *cis-transoidal*, where no supramolecular array of the azo groups is present. Therefore, poly-(*L*)-**1** can adopt three different helical scaffolds in $CHCl_3$ in the absence (*cis-cisoidal*, $M_{int}/M_{ext}/M_{Azo}$) and the presence of metal ions (*cis-transoidal*, P_{int}/M_{ext} and M_{int}/P_{ext}).

Next, we decided to play with the stimuli responsive properties of the azo group and check how its perturbation affects the helical structure of poly-(*L*)-**1** and poly-(*L*)-**2**. The first experiment was the protonation of the azo group by addition of TFA, HCl or HNO_3. The two nitrogen atoms of the azo group are basic and can be protonated by addition of acids.[67-68] Hence, to a $CHCl_3$ solution of poly-(*L*)-**1** and poly-(*L*)-**2** 17 μL of different acids were added over 1 mL of polymer solution. In all cases it was observed that the protonation of the azo group produces a large bathochromic shift of the π-π* transition band from 339 to 468 nm (see Figure 6 for poly-(*L*)-**1** and Si for poly-(*L*)-**2**), which is accompanied with a colorimetric change from yellow to orange (Figure 6 and SI). Interestingly, although the azo group is protonated, it is still ECD active, and an exciton coupling is produced due to cooperative dipole-dipole interactions between neighboring azo-H^+ chromophores. Therefore, the protonation of the azo group does not affect their chiral supramolecular array along the helix, although the exciton coupling suffers a bathochromic shifting which is accompanied with a colorimetric change. This process is reversible and can be easily reverted by adding a protic solvent such as MeOH that solvates the acid (Figure 6).

Finally, light irradiation studies were carried out to analyze how the *Z/E* configuration of the azo group affects the folding of poly-(*L*)-**1** and poly-(*L*)-**2.** Thus, different experiments were performed in the two different scaffolds adopted by poly-(*L*)-**1** and poly-(*L*)-**2**, the "classical" helix made by two coaxial helices (*helix$_{int}$*/*helix$_{ext}$*), and the triple helix (*helix$_{int}$*/*helix$_{ext}$*/*helix$_{azo}$*).

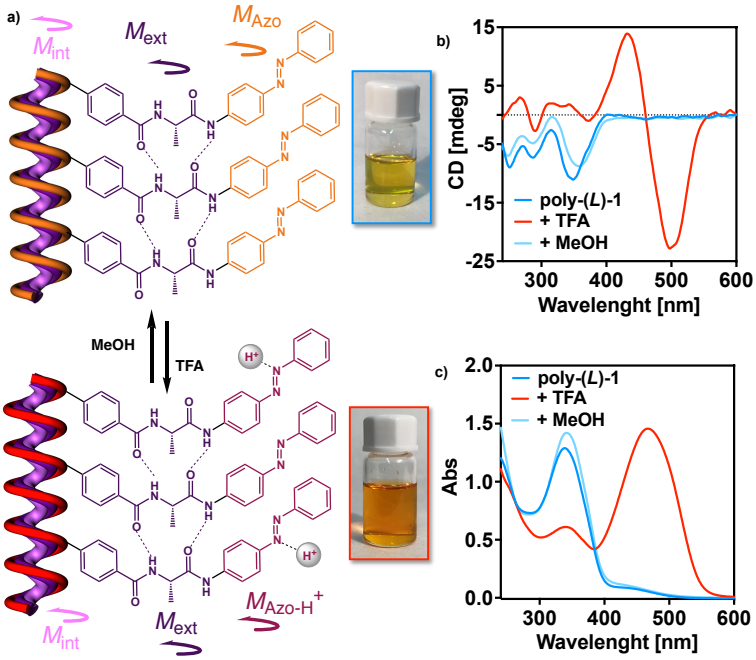

Figure 6. a) Schematic illustration of the reversible protonation equilibrium of the Azo groups in poly-(*L*)-**1**. Variations on the b) ECD and c) UV-vis spectrum of poly-(*L*)-**1** dissolved in $CHCl_3$ after protonation with TFA and further deprotonation with a protic solvent such as MeOH.

First, two different vials containing either a solution of poly-(*L*)-**1** and a solution of poly-(*L*)-**2** in DMF (classical, P_{int}/M_{ext}) were irradiated with visible light of 350 nm. It was observed that in both cases, the ECD decreases after light irradiation indicating that the *E* to *Z* isomerization of the azo groups affects the PPAs folding. Furthermore, while further irradiation with UV-vis light centered at 420 nm, which promotes the *Z* to *E* isomerization of the azo group, does not recover the starting ECD spectra, this recovery was achieved after thermal treatment (60°C) (Figure 8a,b). This different photophysical and thermal behavior is due to the different energies applied to the whole system. Thus, while light-irradiation affects only the conformational composition of the azo group, thermal treatment affects the conformational composition of the whole PPA (annealing).

Next, irradiation studies were carried out over two different vials containing either a solution of poly-(*L*)-**1** and a solution of poly-(*L*)-**2** in $CHCl_3$ (triple helix, $M_{int}/M_{ext}/M_{Azo}$). In both cases, irradiation with UV-vis light (350 nm) unfolds the PPA due to an *E* to *Z* isomerization of the azo group. Interestingly, while in poly-(*L*)-**1** an aggregate is formed after irradiation studies, in the case of poly-(*L*)-**2** the polymer remains completely soluble in $CHCl_3$. As a result, irradiation studies with UV-vis light (420 nm) to promote the *Z* to *E* isomerization of the azo group has no effect on the poly-(*L*)-**1** aggregates. In the case of poly-(*L*)-**2**, the PPA helix is recovered —M_{int}/M_{ext}— although the chiral azo supramolecular arrangement is not recovered. The return to the initial state is possible by using thermal

treatment (60°C), where the *Z* to *E* isomerization of the azo group produced by temperature is accompanied with a refolding of the triple helix (M_{int}/M_{ext}/ M_{Azo}).

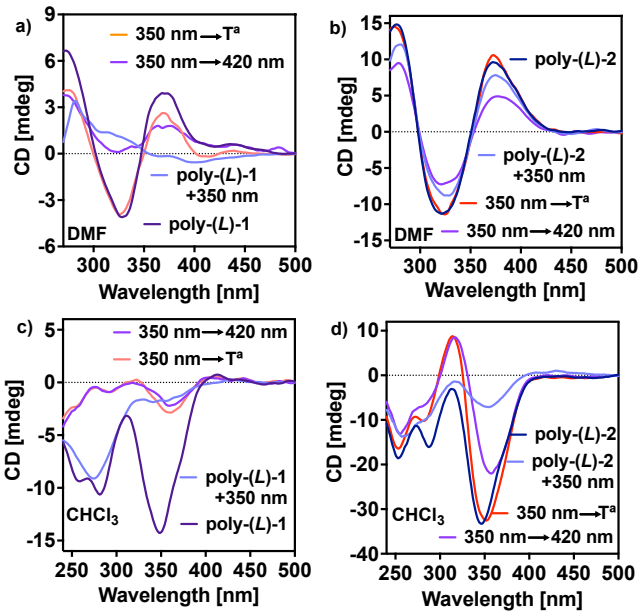

Figure 7. Variation on the ECD spectra of a DMF solution of a) poly-(*L*)-**1** and b) poly-(*L*)-**2** before and after irradiation with UV light (350 nm) followed by light irradiation with 420 nm light or thermal treatment (60°C). Variation on the ECD spectra of a $CHCl_3$ solution of c) poly-(*L*)-**1** and d) poly-(*L*)-**2** before and after irradiation with UV light (350 nm) followed by light irradiation with 420 nm and thermal treatment (60°C).

Considering that PPAs have low photostability and rapidly degrade under light exposure due to a photoisomerization of the double bonds that end up with a photochemical electrocyclization of the polyene backbone, we checked the photostability of poly-(*L*)-**1** and poly-(*L*)-**2** by irradiation with UV-vis light using a short pass filter of 550 nm, (see SI for more details). No degradation of poly-(*L*)-**1** and poly-(*L*)-**2** was observed indicating that the presence of a chromophore at the pendant results in a photostable material. This is due to the light absorbance by the azo group which avoid the light-polyene interaction and the corresponding polymer degradation.

3. Conclusion

The introduction of a photo-switchable group as substituent of a chiral pendant in a PPA improves the photostability of the material and provides additional stimuli-responsive properties. For instance, in this work, two different PPAs has been prepared bearing the benzamide of alanine [poly-(*L*)-**1**] and valine [poly-(*L*)-**2**] as pendants derivatized with 4-aminoazobenzene. These polymers are photostable and can be stored under light without being degraded. This fact is very important to improve the industrial applications of PPAs, because their poor photostability is a limiting factor in the commercial world.

It is also remarkable that the introduction of the Azo group does not affect to the stimuli-responsive properties of the amino acids, being poly-(*L*)-**1** and poly-(*L*)-**2** sensitive to solvents, temperature and metal ions, whose helical sense can be inverted, amplified, or zeroed out by these stimuli. Moreover, it was also found that depending on the helical scaffold adopted by the PPA —value of ω_1—, the azo units can form a chiral array generating a macromolecular scaffold consisting of three different chiral motifs: 1) the helix described by the polyene backbone (*helix$_{int}$*), 2) the helix described by the pendant groups (*helix$_{ext}$*) and 3) the helix described by the azo array (*helix$_{Azo}$*). When these three chiral motifs coexist within a PPA, its ECD spectra is dominated by the azo array. By playing with acids, light or temperature it is possible to modulate the UV-vis or ECD bands of the azo array (pH effect), and the scaffold between helices consisting on two coaxial helices ("*classical*" helix: *helix$_{int}$*/*helix$_{ext}$*) or a macromolecular structure with three coexisting chiral motifs (*helix$_{int}$*/*helix$_{ext}$*/ *helix$_{Azo}$*).

Therefore, these studies open a new horizon in the development of smart materials that can act as multi-switches. To do that it is necessary to introduce, in the monomer repeating unit, functional groups with different stimuli-responsive and self-assembling properties that allow to create novel architectures, stable under ambient conditions and with interesting multiswitch properties.

4. References

[1] V. Percec, Q. Xiao, *Bull. Chem. Soc. Jpn.*, **2021**, *94*, 900-928.

[2] E. Yashima, N. Ousaka, D. Taura, K. Shimomura, T. Ikai, K. Maeda, *Chem. Rev.*, **2016**, *116*, 13752-13990.

[3] Y. Dorca, E. E. Greciano, J. S. Valera, R. Gómez, L. Sánchez, *Chem. Eur. J.*, **2019**, *25*, 5848.

[4] E. Yashima, K. Maeda, H. Iida, Y. Furusho, K. Nagai, *Chem. Rev.*, **2009**, *109*, 6102-6211.

[5] Z. Fernández, B. Fernández, E. Quiñoá, F. Freire, *Angew. Chem. Int. Ed.*, **2021**, *60*, 9919-9924.

[6] E. Yashima, K. Maeda, *Bull. Chem. Soc. Jpn.*, **2021**, *94*, 2637-2661.

[7] J. J. Tarrío, R. Rodríguez, B. Fernández, E. Quiñoá, F. Freire, *Angew. Chem. Int. Ed.,* **2022**, *61*, e202115070.

[8] T. Yamamoto, R. Murakami, S. Komatsu, M. Suginome, *J. Am. Chem. Soc.*, **2018**, *140*, 3867-3870.

[9] C. Zhang, Y. Qiu, S. Bo, F. Wang, Y. Wang, L. Liu, Y. Zhou, H. Niu, H. Dong, T. Satoh, *J. Polym. Sci. Part A: Polym. Chem.*, **2019**, *57*, 1024-1031.

[10] Z. Tang, H. Iida, H. Y. Hu, E. Yashima, *ACS Macro Lett.*, **2012**, *1*, 261-265.

[11] R. Ishidate, T. Sato, T. Ikai, S. Kanoh, E. Yashima, K. Maeda, *Polym. Chem.*, **2019**, *10*, 6260-6268.

[12] D. Hirose, A. Isobe, E. Quiñoá, F. Freire, K. Maeda, *J. Am. Chem. Soc.*, **2019**, *141*, 8592-8598.

[13] G. Wu, *Polym. Chem.*, **2022**,*13*, 3036-3047.

[14] R. Rodríguez, E. Suárez-Picado, E. Quiñoá, R. Riguera, F. Freire, *Angew. Chem. Int. Ed.* **2020**, *59*, 8616-8622.

[15] F. Freire, J. M. Seco, E. Quiñoá, R. Riguera, *J. Am. Chem. Soc*., **2012**, *134*, 19374-19383.

[16] Q. Zhang, Y. Zhang, Y. Wan, W. Carvalho, L. Hu, M. J. Serpe, *Prog. Polym. Sci.*, **2021**, *116*, 101386.

[17] Y. He, S. Lin, J. Guo, Q. Li, *Aggregate*, **2021**, *2*, e141.

[18] X. Guan, S. Wang, G. Shi, J. Zhang, X. Wan, *Macromolecules*, **2021**, 54, 4592-4600.

[19] S. Leiras, F. Freire, J. M. Seco, E. Quiñoá, R. Riguera, *Chem. Sci.*, **2013**, *4*, 2735-2743.

[20] K. Maeda, H. Mochizuki, M. Watanabe, E. Yashima, *J. Am. Chem. Soc*., **2006**, *128,* 7639-7650.

[21] S. Arias, F. Freire, E. Quiñoá, R. Riguera, *Polym. Chem*., **2015**, *6*, 4725-4733.

[22] T. Ikai, R. Ishidate, K. Inoue, K. Kaygisiz, K. Maeda, E. Yashima, *Macromolecules*, **2020**, *53*, 973-981.

[23] K. Maeda, N. Kamiya, E. Yashima, *Chem. Eur. J.,* **2004**, *10*, 4000-4010.

[24] K. Cobos, R. Rodriguez, O. Domarco, B. Fernández, E. Quiñoá, R. Riguera, F. Freire, *Macromolecules*, **2020**, *53*, 3182-3193.

[25] K. Maeda, K. Morino, Y. Okamoto, T. Sato, E. Yashima, *J. Am. Chem. Soc.*, **2004**, *126*, 4329-4342.

[26] J. Bergueiro, M. Núñez-Martínez, S. Arias, E. Quiñoá, R. Riguera, R., F. Freire, Nanoscale Horiz., **2020**, *5*, 495-500.

[27] M. Núñez-Martínez, S. Arias, E. Quiñoá, R. Riguera, F. Freire, *Chem. Mater.,* **2021**, *33*, 4805–481.

[28] S. Arias, J. Bergueiro, F. Freire, E. Quiñoá, R. Riguera, *Small*, **2016**, *12*, 238-244.

[29] M. Núñez-Martínez, S. Arias, J. Bergueiro, E. Quiñoá, R. Riguera, F. Freire, *Macromol. Rapid Commun.*, **2022**, 43, 2100616.

[30] K. Maeda, M. Ishikawa, E. Yashima, *J. Am. Chem. Soc.*, **2004**, *126*, 15161-15166.

[31] Y. Cao, L. Ren, Y. Zhang, X. Lu, X. Zhang, J. Yan, W. Li, T. Masuda, A. Zhang, *Macromolecules*, **2021**, 54, 7621-7631.

[32] S. Leiras, E. Suárez-Picado, E. Quiñoá, R. Riguera, F. Freire, *Giant*, **2021**, *7*, 100068.

[33] Z. Fernández, B. Fernández, E. Quiñoá, F. Freire, *J. Am. Chem. Soc.*, **2021**, *143*, 20962-20969.

[34] E. Suárez-Picado, E. Quiñoá, R. Riguera, F. Freire, *Angew. Chem. Int. Ed.*, **2020**, *59*, 4537-4543.

[35] M. Fukuda, R. Rodríguez, Z. Fernández, T. Nishimura, D. Hirose, G. Watanabe, E. Quiñoá, F. Freire, K. Maeda, *Chem. Comm*., **2019**, *55*, 7906-7909.

[36] Y. Cui, Z. He, Y. Xu, Y. Su, L. Ding, Y. Li, *Chem. Eng. J.*, **2021**, *405*, 126608.

[37] Y. Zhao, X. Zhang, W. Li, A. Zhang, *Eur. Polym. J.*, **2019**, *118*, 275-279.

[38] Y. Gu, L. Liu, Y. Wang, C. Zhang, H. Dong, T. Aoki, *Macromolecules*, **2021**, *54*, 10216-10223.

[39] Y. Kotsuchibashi, *Polym. J.,* **2020***, 52*, 681–689.

[40] S. Arias, F. Freire, M. Calderón, J. Bergueiro, *Angew. Chem. Int. Ed.*, **2017**, 129, 11578-11583.

[41] A. Xiao, H. Zhao, Y. Gao, J. Tong, L. Shan, Y. Chen, S. Zhang, A. Qin, J. Z. Sun, B. Z. Tang, *Polymer*, **2011**, *52*, 5290-5301.

[42] M. Teraguchi, T. Masuda, *Macromolecules*, **2000**, *33*, 240-242.

[43] S. Jiang, Y. Zhao, L. Wang, L. Yin, Z. Zhang, J. Zhu, W. Zhang, X. Zhu, *Polym. Chem.*, **2015**, *6*, 4230-4239.

[44] D. Pijper, B. L. Feringa, *Angew. Chem. Int. Ed.*, **2007**, *46*, 3693-3696.

[45] J. del Barrio, R. M. Tejedor, L. Oriol, *Eur. Polym. J.*, **2012**, *48*, 384-390.

[46] X. Cheng, T. Miao, Y. Ma, X. Zhu, W. Zhang, X. Zhu, *Angew. Chem. Int. Ed.*, **2021**, *60*, 24430.

[47] X. Tong, L. Cui, Y. Zhao, *Macromolecules*, **2004**, *37*, 3101-3112.

[48] S. Huang, Y. Chen, S. Ma, H. Yu, *Angew. Chem. Int. Ed.*, **2018**, 57, 12524-12528.

[49] X. Cheng, T. Miao, L. Yin, Y. Ji, Y. Li, Z. Zhang, W. Zhang, X. Zhu, *Angew. Chem. Int. Ed.*, **2020**, *59*, 9669–9677.

[50] L. Wang, L. Yin, W. Zhang, X. Zhu, M. Fujiki, *J. Am. Chem. Soc*., **2017**, *139*, 13218-13226.

[51] S. Huang, H. Yu, Q. Li, *Adv. Sci.*, **2021**, *8*, 2002132.

[52] T. Miao, X. Cheng, H. Ma, Z. He, Z. Zhang, N. Zhou, W. Zhang, X. Zhu, *Angew. Chem. Int. Ed.*, **2021**, *60*, 18566-18571.

[53] L. Yin, Y. Zhao, M. Liu, N. Zhou, W. Zhang, X. Zhu, *Polym. Chem*., **2017**, *8*, 1906-1913.

[54] L. Yin, M. Liu, Y. Zhao, S. Zhang, W. Zhang, Z. Zhang, X. Zhu, *Polym. Chem.*, **2018**, *9*, 769-776.

[55] X. Cheng, T. Miao, Y. Qian, Z. Zhang, W. Zhang, X. Zhu, *Int. J. Mol. Sci.*, **2020**, *21*, 6186.

[56] L. Liu, T. Namikoshi, Y. Zang, T. Aoki, S. Hadano, Y. Abe, I. Wasuzu, T. Tsutsuba, M. Teraguchi, T. Kaneko, *J. Am. Chem. Soc.*, **2013**, *135*, 602-605.

[57] Y. Tang, L. Liu, J. Suzuki, M. Teraguchi, T. Kaneko, T. Aoki, *Chirality*, **2022**, *34*, 450-461.

[58] F. Rey-Tarrío, R. Rodríguez, E. Quiñoá, R. Riguera, F. Freire, *Angew. Chem. Int. Ed.,* **2021**, *60*, 8095–8103.

[59] M. Han, M. Hara, *J. Am. Chem. Soc.*, **2005**, *127*, 10951-10955.

[60] M. R. Han, Y. Hirayama, M. Hara, *Chem. Mater.*, **2006** *18*, 2784-2786.

[61] M. R. Han, D. Hashizume, M. Hara, *New J. Chem.*, **2007**, *31*, 1746-1750.

[62] S. Arias, R. Rodríguez, E. Quiñoá, R. Riguera, F. Freire, *J. Am. Chem. Soc.*, **2018**, *140*, 667-674.

[63] F. Freire, J. M. Seco, E. Quiñoá, R. Riguera, *Angew. Chem. Int. Ed.,* **2011**, *50*, 11692-11696.

[64] M. Alzubi, S. Arias, I. Louzao, E. Quiñoá, R. Riguera, F. Freire, *Chem. Commun.*, **2017**, *53*, 8573-8576.

[65] S. Arias, M. Núñez-Martínez, E. Quiñoá, R. Riguera, F. Freire, *Polym. Chem.*, **2017**, *8*, 3740-3745.

[66] R. Rodríguez, E. Quiñoá, R. Riguera, F. Freire, *J. Am. Chem. Soc.*, **2016**, 138, 9620-9628.

[67] M. A. Hoefnagel, A. Van Veen, B. M. Wepster, *Recl. Trav. Chim. Pays-Bas*, **1969**, *88*, 562-572.

[68] H. D. Bandara, S. C. Burdette, *Chem. Soc. Rev.*, **2012**, *41*, 1809-1825.

Chapter VII

Multi-Helical Materials by combining Metallo-Supramolecular and Covalent Helical Polymers: Five Axially Motifs within a Helical Polymer

Chapter VII

Multi-Helical Materials by combining Metallo-Supramolecular and Covalent Helical Polymers: Five Axially Motifs within a Helical Polymer

CHAPTER VII: Multi-Helical Materials by combining Metallo-Supramolecular and Covalent Helical Polymers: Five Axially Motifs within a Helical Polymer

Abstract

Supramolecular and covalent polymers share multiple structural effects such as communication mechanisms among monomer repeating units. These features are related to the axial helical structure found in both supramolecular and covalent helical materials. Herein, a multi-helical material combining information from both metallo-supramolecular polymers —bispyridyldichloride platinum(II) complex— and covalent helical polymers —poly(acetylene) (PA)—, is presented. In this case, the helical structure described by the polyene backbone (cis-cisoidal, cis-transoidal), orients the pendant groups in a fashion where a tilting degree emerges between a pendant and the upper and bottom ones at the helical crest. Thus, a chiral supramolecular array is produced in the spacer used to separate the polyene from the chiral residue, in this case, the bispyridyldichloride platinum(II) complex. As a result, a multi-helix material is formed by four different helices when the polyene skeleton adopts a cis-transoidal configuration, the two coaxial helices —internal (helix 1) and external (helix 2)— and the two helices described by the bispyridyldichloride Pt^{II} complexes axial array (helices 3 and 4), or made by five different helices when the polyene skeleton adopts a cis-cisoidal configuration, the two coaxial helices —internal (helix 1) and external (helix 2)— and the three helices described by the axial array of the bispyridyldichloride Pt^{II} complexes (helices 3, 4 and 5).

1. Introduction

During the last years, covalent and supramolecular helical polymers have attracted the attention of the scientific community inspired by the relation structure/function found in helical biomacromolecules such as peptides, proteins, DNA or polysaccharides.[1-12] Synthetic helical polymers, covalent and supramolecular, led to the formation of novel helical structures with new functionalities which can provide the material with interesting properties and functions not found in nature. These materials can be classified as either static or dynamic depending on the possibility of tuning the helical scaffold once have been obtained in the lab.[13-18] Thus, in dynamic helical polymers is possible to tame their helical sense (*P* or *M*), elongation (compressed/stretched) or aggregate shape (J-aggregate, H-aggregate, and so on) by the presence of different external stimuli (e.g., solvent, pH, temperature, metal ions, chiral additives, or light).[19-38] Interestingly, supramolecular, and covalent helical polymers share many features such as the communication mechanisms between monomer repeating units (Sergeants and Soldiers Effect,[39-43] Majority Rules,[44-46] Chiral Coalition,[47] Chiral Accord,[48] or Chiral Conflict).[49,50] This fact led to the formation of chiral materials that combine these two structural motifs, where supramolecular arrays of dendronized planar molecules or azo groups are found at the covalent helix periphery stabilizing the helix.[51-56] Recently, in our group we have prepared a poly[oligo(*p*-phenyleneethynylene)acetylene]s (POPEPAs) in which although the chiral center is placed at a remote position from the backbone, separated through a planar oligo(*p*-phenyleneethynylene) (OPE) spacer, a helix induction occurs due to the chiral arrangement of the achiral spacers, which is harvested by the polyene backbone.[57] Interestingly, depending on the stretching degree of the polyene backbone is possible to obtain either the classical helix for polyacetylenes with two coaxial helices, an internal helix (helix 1) described by the polyene, and an external helix (helix 2) described by the pendant groups, or a multi-helical scaffold where four different helices coexist in the helical material: the two coaxial helices —internal (helix 1) and external (helix 2)— and the two helices described by the OPE axial array (helices 3 and 4).

Herein we want to show that more multi-helical scaffolds can be obtained by a correct monomer design. In this case, we selected a metal containing monomer, consisting of an asymmetric bispyridyldichloride platinum(II) complex, functionalized at one edge with an alkyne group, needed to get the polyacetylene derivative by a polymerization reaction. On the other edge, a chiral group must be introduced to induce a screw sense in the helical polymer.

Supramolecular polymers (SPs) of transition metal complexes have recently gained considerable attention due to their versatile self-assembly behavior and outstanding photophysical properties.[58-62] A remarkable feature of self-assembled d^8 metal complexes is their ability to generate metal-metal contacts through the interaction of the filled metal —d_z^2—orbitals. During the last years, bispyridyldichloride Pt^{II} complexes with an extended aromatic surface have been used to prepare a large variety of supramolecular aggregates by different aggregation pathways.[63-68] In these aggregates, the metal containing monomers self-assemble through Pt···Pt, and π···π interactions, producing supramolecular stacks that resemble those observed in the supramolecular polymerization of OPEs. Hence, an asymmetric bispyridyldichloride platinum(II) complex should comprise all the requirements to generate a multi-helical scaffold.

2. Results and Discussion

To validate our hypothesis two pyridyl chiral ligands containing as chiral centers the *L*-valine and the *L*-alanine methyl ester were synthesized and complexed to a dichloride Pt^{II} center in combination with 4-ethynylpyridine, to obtain mono-(*S*)-**1** and mono-(*S*)-**2** respectively (See SI for synthesis and characterization of the complexes). Next, mono-(S)-**1** and mono-(*S*)-**2** were polymerized using $[Rh(nbd)Cl]_2$ as catalyst (nbd = 2,5-norbornadiene) to obtain poly-(*S*)-**1** and poly-(*S*)-**2**, in good yield and high content of *cis*-double bonds (Figure 1).

UV-vis studies for mono-(*S*)-**1** and mono-(*S*)-**2** show spectra with four bands between 350 and 250 nm. UV-vis theoretical calculations done for mono-(*S*)-**1** (time-dependent density functional theory (TD-DFT) together with a wB97XD density functional and LANL2DZ basis set (TD-DFT(wB97XD)/ LANL2DZ), were performed on the molecular structure obtained from X-ray studies after DFT optimization, see Si for details). Results allowed us to identify which fragments of mono-(*S*)-**1** are responsible of these absorption bands. Thus, the UV-band at higher wavelength —ca. 345 nm— corresponds to the core of the bispyridyldichloride Pt^{II} complexes, the band at ca. 305 nm corresponds to *para*-ethynylpyridyl complexed to the dichloride Pt^{II}, while the band at 280 nm is attributed to the *para*-pyridylbenzamide of (*L*)-Valine-methyl ester complexed to the dichloride Pt^{II}. Finally, the band at 250 nm is related to the benzamide group of the chiral moiety (See Figure 1c and SI).

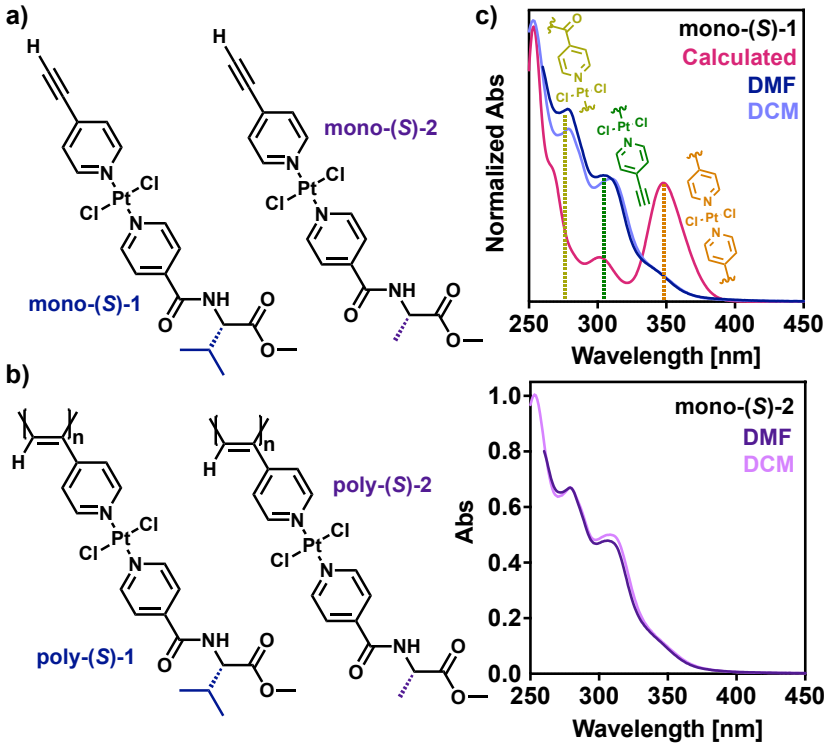

Figure 1. Chemical structure of (a) mono-(*S*)-**1** and mono-(*S*)-**2**. (b) Chemical structure of poly-(*S*)-**1** and poly-(*S*)-**2**. (c) UV-vis spectra of mono-(*S*)-**1** and mono-(*S*)-**2** dissolved in DCM and DMF. [mono-(*R*)-**1**]= 0.3 mg/mL, [mono-(*R*)-**2**]= 0.3 mg/mL.

Intriguingly, UV-vis studies for poly-(*S*)-**1** and poly-(*S*)-**2** show a very interesting phenomenon. Thus, while in low polar solvents such as THF or DCM, poly-(*S*)-**1** adopts a stretched helix (*cis-transoidal*), in polar solvents such as DMF, the polymer adopts a compressed scaffold (*cis-cisoidal*). This elongation change is explained by looking at the hypsochromic shift suffered by the polyene band, from 417 to 380 nm when passing from a DCM/THF solution towards a DMF one. In the case of poly-(*S*)-**2**, similar results are obtained in DMF, being not possible to solubilize it in THF or DCM (see SI for details). The compression of the polyene backbone is accompanied by a color change from yellow to translucent due to the lack of alternating double bonds conjugation of the polyene backbone (Figure 2a).

ECD studies of poly-(*S*)-**1** and poly-(*S*)-**2** in these solvents, show again an interesting effect. Thus, poly-(*S*)-**1** shows in THF or DCM a complex ECD spectra, with multiple bands in the 250-350 nm region (Figure 2b). On the contrary, in polar solvents such as DMF, the ECD spectrum is dominated by a strong bisignate in the 250-350 nm region of the ECD spectrum (Figure 2c). By looking carefully at the ECD spectrum in DMF of poly-(*S*)-**1**, is possible to observe that the first negative Cotton band, shows two minimums, one centered at 385 nm and the other at 355 nm, which corresponds to the polyene backbone

and the core of the bispyridyldichloride Pt^{II} complexes (see above). Moreover, a strong positive Cotton band is obtained at 302 nm, and a negative one at 280 nm, both also corresponding to the metal containing spacer. More precisely, the band at ca. 302 nm corresponds to *para*-ethynylpyridyl complexed to the dichloride Pt^{II}, while the band at 280 nm is attributed to the *para*-pyridylbenzamide of (*L*)-Valine-methyl ester complexed to the dichloride Pt^{II} as was observed above in the monomer calculations (Figure 1c).

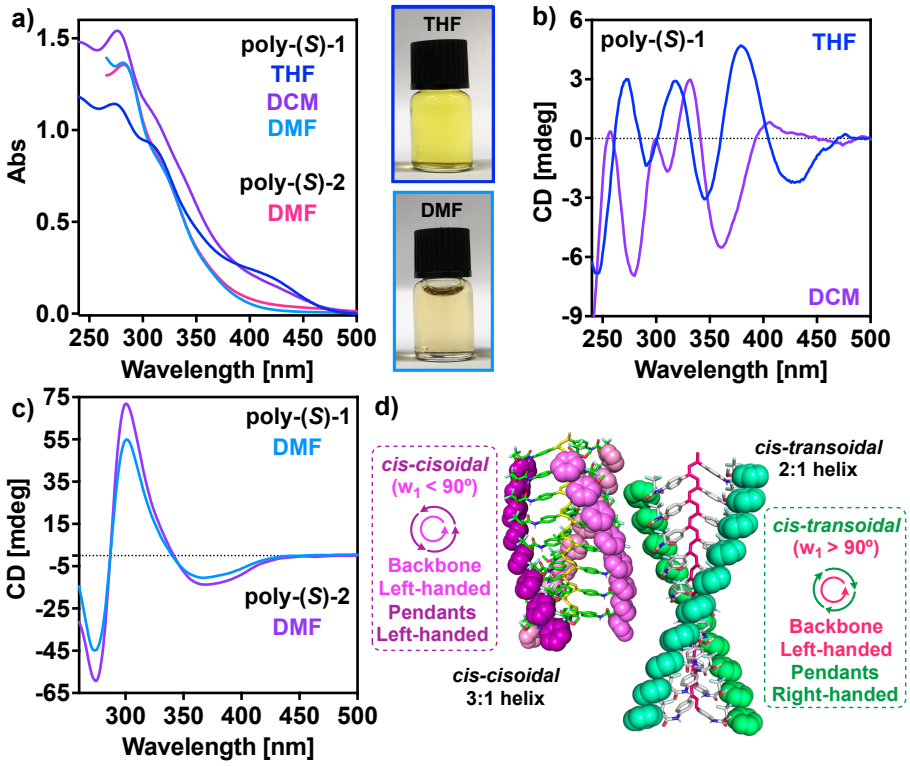

Figure 2. a) UV-vis spectra of poly-(*S*)-**1** in THF, DCM and DMF and poly-(*S*)-**2** in DMF. b) ECD spectra of poly-(*S*)-**1** in THF and DCM. c) ECD spectra of poly-(*S*)-**1** and poly-(*S*)-**2** in DMF. d) Schematic representation of the helical structure of PPA in a *cis-cisoidal* and a *cis-transoidal* conformation. [poly-(*R*)-**1**]= 0.6 mg/mL, [poly-(*R*)-**2**]= 0.6 mg/mL.

The complexity of the ECD spectrum obtained for poly-(*S*)-**1** in different solvents can be explained by combining the classical ECD spectrum of a PPA with three alternating Cotton bands, in this case -/+/-, with the ECD trace obtained by a chiral supramolecular orientation of the metal containing spacers within the helical scaffold. Thus, while in DMF, poly-(*S*)-**1**, adopts a compressed *cis-cisoidal* structure (ω_1< 90°), in DCM or THF an elongated *cis-transoidal* structure (ω_1> 90°) is adopted by the polyene backbone. As a result, two different architectures are obtained for poly-(*S*)-**1**, which have different structural properties. The *cis-cisoidal* helix in PPAs is made by two coaxial helices that rotate in the same direction (P_{int}/P_{ext} or M_{int}/M_{ext}), while the *cis-transoidal* helix rotates in opposite direction (P_{int}/M_{ext} or M_{int}/P_{ext}). Moreover, in the *cisoidal* scaffold, the helix

contains three residues per turn, generating a helix with three crests at the periphery. In the other case, the *transoidal* scaffold, the helix has two residues per turn, describing a helix with two crests (Figure 2d). Interestingly, by looking at the arrangement of the metal-containing spacers on the different crest of the *cis-cisoidal* and *cis-transoidal* helices, is possible to observe a novel helical arrangement of these achiral spacers within the helix crest whose sense will depend on the helical scaffold. Thus, in *cis-cisoidal* PPAs, the orientation of the achiral spacers within the helix crest has the same sense that the internal and external helices. As a result, a multi-helical structure with five structural motifs is generated —internal helix, external helix and three helices described by the arrangement of the metal containing spacers at the helix crest—.

From the literature, it is known that PPAs with a *P* orientation of the polyene backbone show an alternating ECD spectrum with three Cotton bands +/-/+, while those PPAs with an *M* orientation of the polyene backbone show the opposite orientation of the ECD bands -/+/-. To determine how affects the axially chiral orientation of the metal containing monomer, theoretical ECD studies were carried out in a supramolecular helical arrangement of an asymmetric bispyridyldichloride platinum(II) complex. Thus, the geometry of supramolecular trimers arranged as left-handed and right-handed helices were done using density functional theory (DFT) together with the rCAM-B3LYP functional and the LANL2DZ basis set. Over the optimized structures, theoretical ECD calculations, TD-DFT(CAM-B3LYP)/LANL2DZ, were performed obtaining a -/+ bisignate for the *M* helix, while a +/- bisignate was obtained for the *P* helix. Interestingly these two bands correspond with the core of the bispyridyldichloride Pt^{II} complex (350nm) and to the *para*-ethynylpyridyl complexed to the dichloride Pt^{II} (302nm) (Figure 3a).

Considering this result, if the polymer adopts a *cis-transoidal* scaffold with a preferred *P* orientation of the polyene backbone, the external helix and the axial array described by the metal containing spacer will rotate in opposite direction (*M* helix). Thus, while the polyene produces a +/-/+ ECD trace, the spacers axial array promotes a -/+ ECD with an opposite orientation to that described by the polyene. As a result, depending on the intensity and wavelength absorbance of the first and second ECD bands produced by the polyene backbone and the axial array of the metal containing spacer, a complex ECD spectra are obtained with multiple positive and negative ECD bands as observed in poly-(*S*)-**1** dissolved in DCM or THF (Figure 2b).

On the contrary, in a *cis-cisoidal* helix with a *P* orientation of the internal and the external helices, and a *P* orientation of the asymmetric bispyridyldichloride platinum(II) complexes used as spacers, the first and second cotton bands of the classical ECD spectrum (+/-/+), suffer an additive effect of the (+/-) bands obtained for the axial array of the spacers. As a result, an ECD spectrum with three alternating Cotton bands is obtained, where the second is very intense. In the case of a polymer adopting a *cis-cisoidal* structure with a preferred *M* screw sense of the polyene backbone the opposite -/+/- ECD trace must be obtained. This is what we observed for poly-(*S*)-**1** dissolved in DMF, an ECD trace with three alternating Cotton bands (-/+/-), showing the second and third band an abnormally large intense, confirming the additive effect by ECD theoretical calculations (TD-DFT(CAM-B3LYP)/LANL2DZ). Identical spectrum were obtained for poly-(*S*)-**2** dissolved in DMF (Figure 3b and SI).

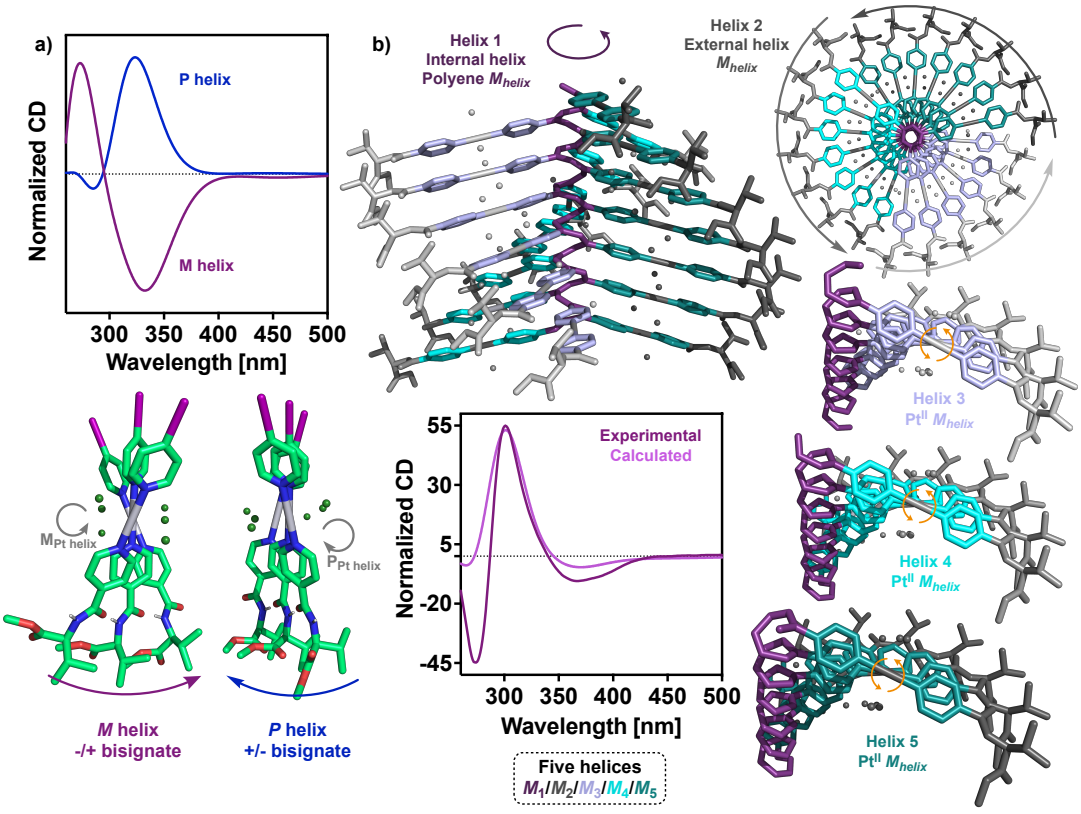

Figure 3. a) Representation of the calculated models for the assembly of three units of mono-(*S*)-**1** in a left-handed and a right-handed helix with the calculated ECD spectra. b) Illustration and ECD of the 3D model of a *c-c* helix of poly-(*S*)-**1** resulting in a multi-helical material composed of five helices. [poly-(*R*)-**1**]= 0.6 mg/mL.

3. Conclusion

In conclusion, we have demonstrated through two different examples —poly-(*S*)-**1** and poly-(*S*)-**2**— that it is possible to obtain a multi-helix material by linking a supramolecular helix, made by bispyridyldichloride Pt^{II} complexes, to a covalent helical polymer (PA). By looking at the structures generated by the two systems we envisioned that the two systems could fit into a multi-helical material. In this case and considering the tilting degree angle found in the supramolecular helices of bispyridyldichloride Pt^{II} complexes (Θ) close to 20°, we assumed that this axial array could fit either into *cis-cisoidal* and *cis-transoidal* polyacetylene scaffolds. As a result, a multi-helix material is prepared by stabilizing a metallo-supramolecular polymer in a covalent helix. A great example is poly-(*S*)-**1**, in this case when the polymer is dissolved in non-polar solvents adopts a *cis-transoidal* structure ($\omega_1 > 90°$), which shows a complex ECD spectrum due to the opposite ECD traces generated by the polyene backbone and the metallo-supramolecular array. In this chiral material, four different helices are found, the two coaxial helices —internal (helix 1) and external (helix 2)— and the three helices described by the bispyridyldichloride Pt^{II} complexes axial array (helices 3 and 4). These four helices are interconnected and, by identifying the orientation of one of them, it is possible to obtain the helical sense of the others. Therefore, two scenarios are possible: $M_1/P_3/P_4/P_2$ or $P_1/M_3/M_4/M_2$.

For its part, when the poly-(*S*)-**1** is dissolved in DMF, a *cis-cisoidal* scaffold is obtained ($\omega_1 > 90°$). In this case, an ECD trace with three alternating Cotton bands is obtained, like those found for classical PPAs. However, the relative intensity of the ECD bands is different, being here much more intense than the second one due to the ECD traces generated by the polyene backbone and the metallo-supramolecular array. In this chiral material, five different helices are found, the two coaxial helices —internal (helix 1) and external (helix 2)— and the three helices described by the bispyridyldichloride Pt^{II} complexes axial array (helices 3, 4 and 5). These four helices are interconnected and, by identifying the orientation of one of them, it is possible to obtain the helical sense of the others. Therefore, two scenarios are possible: $P_1/P_3/P_4/P_5/P_2$ or $P_1/M_3/M_4/M_5/M_2$. These results indicate that by a correct design is possible the stabilization of supramolecular helices in covalent polymers, opens a new horizon in the design of novel multi-helical materials. These structures that stabilize metallo-supramolecular polymers in covalent systems also allow the application of these materials in polar solvents which could not be accessed due to the difficulty of generating metal-containing supramolecular polymers in polar solvents.

4. References

[1] E. Yashima, N. Ousaka, D. Taura, K. Shimomura, T. Ikai, K. Maeda, *Chem. Rev.,* **2016**, *116*, 13752-13990.

[2] E. Yashima, K. Maeda, H. Iida, Y. Furusho, K. Nagai, *Chem. Rev.,* **2009**, *109*, 6102-6211.

[3] T. Nakano, Y. Okamoto, *Chem. Rev.*, **2001**, *101*, 4013-4038.

[4] J. Tarrío, R. Rodríguez, B. Fernández, E. Quiñoá, F. Freire, *Angew. Chem. Int. Ed.*, **2022**, *134*, e202115070.

[5] V. Percec, *Isr. J. Chem.*, **2020**, *60*, 48-66.

[6] E. Yashima, K. Maeda, Y. Furusho, *Acc. Chem. Res.,* **2008**, *41*, 1166-1180.

[7] S. Okuda, N. Ousaka, T. Iwata, R. Ishida, A. Urushima, N. Suzuki, S. Nagano, T. Ikai, E. Yashima, *J. Am. Chem. Soc.*, **2022**, *144*, 2775-2792.

[8] L. Brunsveld, B. J. B. Folmer, E. W. Meijer, R. P. Sijbesma, *Chem. Rev.*, **2001**, *101*, 4071-4098.

[9] T. F. A. de Greef, E. W. Meijer, *Nature*, **2008**, *453*, 171-173.

[10] V. Percec, Q. Xiao, *Bull. Chem. Soc. Jpn.*, **2021**, *94*, 900-928.

[11] T. Aida, E. W. Meijer, *Isr. J. Chem.,* **2020**, *60*, 33-47.

[12] Z. Fernández, B. Fernández, E. Quiñoá, F. Freire, *Angew. Chem. Int. Ed.* **2021**, *60*, 9919-9924.

[13] J. Liu, L. W. Y. Lam, B. Z. Tang, *Chem. Rev.*, **2009**, *109*, 5799-5867.

[14] E. Schwartz, M. Koepf, H. J. Kitto, R. J. Nolte, A. E. Rowan, *Polym. Chem.*, **2011**, *2*, 33-47.

[15] E. Anger, H. Iida, T. Yamaguchi, K. Hayashi, D. Kumano, J. Crassous, N. Vanthuyne, C. Roussel, E. Yashima, *Polym. Chem.*, **2014**, *5*, 4909-4914.

[16] T. Ikai, T. Kurake, S. Okuda, K. Maeda, E. Yashima, *Angew. Chem. Int. Ed.*, **2021**, *60*, 4625-4632.

[17] F. Rey-Tarrío, S. Guisán-Ceinos, J. M. Cuerva, D. Miguel, M. Ribagorda, E. Quiñoá, F. Freire, *Angew. Chem. Int. Ed.*, **2022**, *61*, e202207623.

[18] R. Rodriguez, E. Quiñoá, R. Riguera, F. Freire, *J. Am. Chem. Soc.*, **2016**, *138*, 9620-9628.

[19] X. Guan, S. Wang, G. Shi, J. Zhang, X. Wan, *Macromolecules*, **2021**, 54, 4592-4600.

[20] S. Leiras, F. Freire, J. M. Seco, E. Quiñoá, R. Riguera, *Chem. Sci.*, **2013**, *4*, 2735-2743.

[21] K. Maeda, H. Mochizuki, M. Watanabe, E. Yashima, *J. Am. Chem. Soc*., **2006**, *128,* 7639-7650.

[22] S. Arias, F. Freire, E. Quiñoá, R. Riguera, *Polym. Chem*., **2015**, *6*, 4725-4733.

[23] T. Ikai, R. Ishidate, K. Inoue, K. Kaygisiz, K. Maeda, E. Yashima, *Macromolecules*, **2020**, *53*, 973-981.

[24] K. Maeda, N. Kamiya, E. Yashima, *Chem. Eur. J.,* **2004**, *10*, 4000-4010.

[25] K. Cobos, R. Rodriguez, O. Domarco, B. Fernández, E. Quiñoá, R. Riguera, F. Freire, *Macromolecules*, **2020**, *53*, 3182-3193.

[26] T. van Leeuwen, G. H. Heideman, D. Zhao, S. J. Wezenberg, B. L. Feringa, ChemComm., **2017**, *53*, 6393-6396.

[27] E. Suárez-Picado, E. Quiñoá, R. Riguera, F. Freire, *Chem. Mater.*, **2018**, *30*, 6908-6914.

[28] M. Fukuda, R. Rodríguez, Z. Fernández, T. Nishimura, D. Hirose, G. Watanabe, E. Quiñoá, F. Freire, K. Maeda, ChemComm. **2019**, *55*, 7906-7909.

[29] J. Matern, k. k. Kartha, L. Sánchez, G. Fernández, *Chem. Sci.*, **2020**, *11*, 6780-6788.

[30] N. Sasaki, M. F. J. Mabesoone, J. Kikkawa, T. Fukui, N. Shioya, T. Shimoaka, T. Hasegawa, H. Takagi, R. Haruki, N. Shimizu, S. Adachi, E. W. Meijer, M. Takeuchi, K. Sugiyasu, *Nat. Commun.*, **2020**, *11*, 1-9.

[31] G. Ghosh, R. Barman, A. Mukherjee, U. Ghosh, S. Ghosh, G. Fernández, *Angew. Chem. Int. Ed.*, **2022**, *61*, e202113403.

[32] R. Rodríguez, R.; E. Quiñoá, R. Riguera, F. Freire, *Small*, **2019**, *15*, e1805413.

[33] Z. Fernández, B. Fernández, E. Quiñoá, R. Riguera, F. Freire, *Chem. Sci.*, **2020**, *11*, 7182-7187.

[34] R. Rodríguez, E. Suárez-Picado, E. Quiñoá, R. Riguera, F. Freire, *Angew. Chem. Int. Ed.*, **2020**, 59, 8616-8622.

[35] X. Yan, F. Wang, B. Zheng, F. Huang, *Chem. Soc. Rev.*, **2012**, 41, 6042-6065.

[36] X. Ma, H. Tian, *Acc. Chem. Res.*, **2014**, *47*, 1971-1981.

[37] R. Rodríguez, E. Quiñoá, R. Riguera, F. Freire, *Chem. Mater.*, **2018**, *30*, 2493-2497.

[38] S. Arias, F. Freire, M. Calderón, J. Bergueiro, Angew. Chem. Int. Ed. **2017**, *56*, 11420-11425.

[39] S. Arias, J. Bergueiro, F. Freire, E. Quiñoá, R. Riguera, *Small*, **2016**, *12*, 238-244.

[40] Y. Nagata, T. Nishikawa, M. Suginome, *ACS Macro Lett.*, **2016**, *5*, 519-522.

[41] M. M. J. Smulders, I. A. W. Filot, J. M. A. Leenders, P. van der Schoot, A. R. A. Palmans, A. P. H. J. Schenning, E. W. Meijer, *J. Am. Chem. Soc.*, **2010**, *132*, 611-619.

[42] B. Adelizzi, N. J. Van Zee, L. N. J. de Windt, A. R. A. Palmans, E. W. Meijer, J. *Am. Chem. Soc.*, **2019**, *141*, 6110-6121.

[43] G. Vantomme, G. M. ter Huurne, C. Kulkarni, H. M. M. ten Eikelder, A. M. Markvoort, A. R. A. Palmans, E. W. Meijer, *J. Am. Chem. Soc.*, **2019**, *141*, 18278-18285.

[44] Y. -Z. Ke, Y. Nagata, T. Yamada, M. Suginome, *Angew. Chem., Int. Ed.*, **2015**, *54*, 9333-9337.

[45] M. M. J. Smulders, P. J. M. Stals, T. Mes, T. F. E. Paffen, A. P. H. J. Schenning, A. R. A. Palmans, E. W. Meijer, *J. Am. Chem. Soc.,* **2010**, *132*, 620-626.

[46] J. van Gestel, A. R. A. Palmans, B. Titulaer, J. A. J. M. Vekemans, E. W. Meijer, *J. Am. Chem. Soc.*, **2005**, *127*, 5490-5494.

[47] K. Cobos, E. Quiñoá, R. Riguera, F. Freire, *J. Am. Chem. Soc.*, **2018**, *140*, 12239-12246.

[48] K. Cobos, R. Rodríguez, E. Quiñoá, R. Riguera, F. Freire, *Angew. Chem., Int. Ed.*, **2020**, *59*, 23724-23730.

[49] M. Alzubi, S. Arias, R. Rodríguez, E. Quiñoá, R. Riguera, F. Freire, *Angew. Chem., Int. Ed.*, **2019**, *58*, 13365-13369

[50] K. Tang, M. M. Green, K. S. Cheon, J. V. Selinger, B. A. Garetz, *J. Am. Chem. Soc.*, **2003**, *125*, 7313-7323.

[51] J. G. Rudick, V. Percec, *Acc. Chem. Res.*, **2008**, *41*, 1641-1652.

[52] J. del Barrio, R. M. Tejedor, L. Oriol, *Eur. Polym. J.*, **2012**, *48*, 384-390.

[53] X. Cheng, T. Miao, Y. Ma, X. Zhu, W. Zhang, X. Zhu, *Angew. Chem. Int. Ed.*, **2021**, *60*, 24430.

[54] X. Tong, L. Cui, Y. Zhao, *Macromolecules*, **2004**, *37*, 3101-3112.

[55] S. Huang, Y. Chen, S. Ma, H. Yu, *Angew. Chem. Int. Ed.*, **2018**, 57, 12524-12528.

[56] X. Cheng, T. Miao, L. Yin, Y. Ji, Y. Li, Z. Zhang, W. Zhang, X. Zhu, *Angew. Chem. Int. Ed.*, **2020**, *59*, 9669–9677.

[57] Z. Fernández, B. Fernández, E. Quiñoá, F. Freire, *J. Am. Chem. Soc.*, **2021**, *143*, 20962-20969.

[58] K. C. Bentz, S. M. Cohen, *Angew. Chem. Int. Ed.*, **2018**, *57*, 14992-15001.

[59] G. R. Whittell, M. D. Hager, U. S. Schubert, I. Manners, *Nat. Mater.*, **2011**, *10*, 176-188.

[60] A. Winter, U. S. Schubert, *Chem. Soc. Rev.*, **2016**, *45*, 5311-5357.

[61] J. Matern, Y. Dorca, L. Sánchez, G. Fernández, *Angew. Chem. Int. Ed.*, **2019**, *58*, 16730-16740.

[62] Y. Zhu, W. Zheng, W. Wang, H. B. Yang, *Chem. Soc. Rev.*, **2021**, *50*, 7395-7417.

[63] N. Bäumer, K. K. Kartha, S. Buss, J. P. Palakkal, C. A. Strassert, G. Fernández, *Org. Chem. Front.*, **2021**, *8*, 4138-4143.

[64] J. Matern, I. Maisuls, C. A. Strassert, G. Fernández, *Angew. Chem. Int. Ed.*, **2022**, *61*, e202208436.

[65] N. Bäumer, J. Matern, G. Fernández, *Chem. Sci.*, **2021**, *12*, 12248-12265.

[66] J. Matern, N. Bäumer, G. Fernández *J. Am. Chem. Soc.*, **2021**, *143*, 7164-7175.

[67] N. Bäumer, K. K. Kartha, S. Buss, I. Maisuls, J. P. Palakkal, C. A. Strassert, G. Fernández, *Chem. Sci.*, **2021**, *12*, 5236-5245.

[68] N. K. Allampally, M. J. Mayoral, S. Chansai, M. C. Lagunas, C. Hardacre, V. Stepanenko, R. Q. Albuquerque, G. Fernández, *Chem. Eur. J.*, **2016**, *22*, 7810-7816.

Chapter VIII

Metallo-Supramolecular Fibers from Phenylacetylene Monomers: Cation Induced Self-Assembly

CHAPTER VIII: Metallo-Supramolecular Fibers from Phenylacetylene Monomers: Cation Induced Self-Assembly

Abstract

An unprecedent route to obtain a new type of metallo-supramolecular fibers has been developed. The helical helices were obtained by mixing a phenylacetylene monomer with $AgClO_4$. The resulting complex self-assembles immediately, and the different monomer/silver(I) (mol/mol) ratios allowed the control of the morphology of the fibers from individual ones to tridimensional networks. Furthermore, controlling the added ratio of cosolvent, the helical assemblies can be transformed from solutions to gels.

1. Introduction

The development of supramolecular polymers has emerged in recent years as one of the most interesting fields in chemistry. These structures arise from the assembly of monomeric units through intermolecular non-covalent interactions.[1-6] Among them, some supramolecular polymers have attracted the attention of the scientific community due to the formation of helical assemblies[7,8] and the properties associated to this structural motif that have found applications in many scientific fields such as asymmetric synthesis,[9-12] circularly polarized light emissive materials[13,14] or sensing.[15,16] Relevant properties, associated to the helical structure, are the sergeants and soldiers effect,[17-19] majority rules[20-22] or chiral conflict effects,[23,24] where communication ocurrs between different building blocks forming the helix.

To generate these chiral supramolecular aggregates it is necessary to consider the driving force that will hold the building blocks together, which can be for instance, π-π interactions, found in chiral supramolecular aggregates made by perylenebisimides (PBI),[25-27] 1,3,5-tricarboxiamides (BTAs)[28,29] or oligo(phenyleneethynylene)s (OPEs).[30-33] Nevertheless, there is a wide range of alternatives such as those based on host-guest interactions[34-36] or metal-ligand coordination,[37,38] among others, which show a high number of potential applications in diodes,[39-41] photovoltaic cells,[42-44] luminescence,[45] etc. An interesting family of chiral aggregates are the metallo-supramolecular polymers, in which transition metals or lanthanides are combined to organic ligands to generate linear metallopolymers that fold into helical structures.[46-51] In other cases, a metal containing monomer[52] is used as a building block to self-assembly into a chiral aggregate through supramolecular interactions.[53] In such cases, it is necessary to prepare first the complex, which is further aggregated into supramolecular architectures.

Herein we want to use a metal containing monomer to generate a chiral supramolecular aggregate by a mix and shake procedure. Our goal is to mix a solution of an organic ligand with a solution of a metal ion to generate a metal containing monomer that spontaneously aggregates into a chiral fiber. To do that, we envisioned a phenylacetylene (PA) monomer complexed to a metal ion such as Ag(I). The PA monomer by itself does not have to show self-assembling properties, however, if a metal ion such as silver(I) is added, the cation will form a diacetylide-Ag^+ complex, where the metal is inserted into the triple bond of two phenylacetylene units, generating a linear structure, with the two PA ligands placed at 180° (Scheme 1). This linear and flat structure comprises all the requirements to

aggregate spontaneously into helical fibers. In literature, it is found the formation of PA-Ag(I)-PA complexes although their self-assembling properties have not been studied.[54-57]

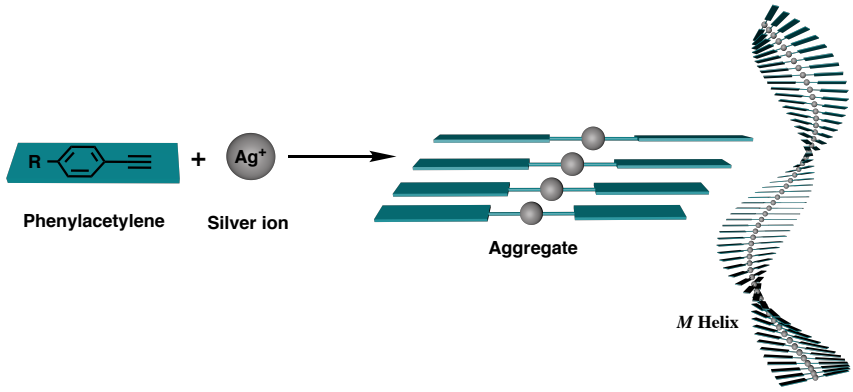

Scheme 1. Schematic illustration of spontaneous aggregation of PA-Ag(I)-PA complexes.

2. Results and Discussion

To test our hypothesis, a PA monomer bearing a chiral sulfoxide as pendant [(*R*)-**1**] was prepared (Figure 1b). This monomer does not show any aggregation tendency in different solvents such as $CHCl_3$, CH_2Cl_2 or CCl_4, neither at different concentrations nor temperatures.

Next, we analyzed formation of the complex by adding different equivalents of a methanolic solution of $AgClO_4$ (10.0 mg/mL) to a $CHCl_3$ solution of (*R*)-**1** in $CHCl_3$ [0.3 mg/mL ($9.98 \cdot 10^{-4}$ M)], generating several monomer/cation (mol/mol) ratios. This salt was chosen taking into account the non-coordinating behavior of the perchlorate anion, which can be considered inert.

UV-vis studies show a strong interaction between (*R*)-**1** and the silver ions by the presence of a new band at 380 nm (figure 1a), which corresponds to the formation of the double silver acetylide complex, confirmed by ^{1}H NMR and IR studies. Thus, while in the NMR spectra the alkyne proton disappears once the metal ion is added, in the IR spectrum an increase of the C≡C vibration signal is produced as result of the acetylide formation (See SI for details).

This metal containing monomer (*R*)-**1**—Ag^+—(*R*)-**1** complex is flat and should show a large aggregation tendency due to the formation of $Ag^+\cdots Ag^+$, $Ag^+\cdots\pi$ and $\pi\cdots\pi$ interactions (Figure 1c). ECD studies show, as expected, a -/+ bisignate centered at 380 nm indicating a chiral organization of the acetylide silver core in the aggregate ($ECD_{403} < 0$) describing an *M* helix (Figure 1b).

Combining the information obtained from UV-vis and ECD studies it suggests the formation of a *J* helical aggregate with a preferred *M* screw sense (Figure 1b).

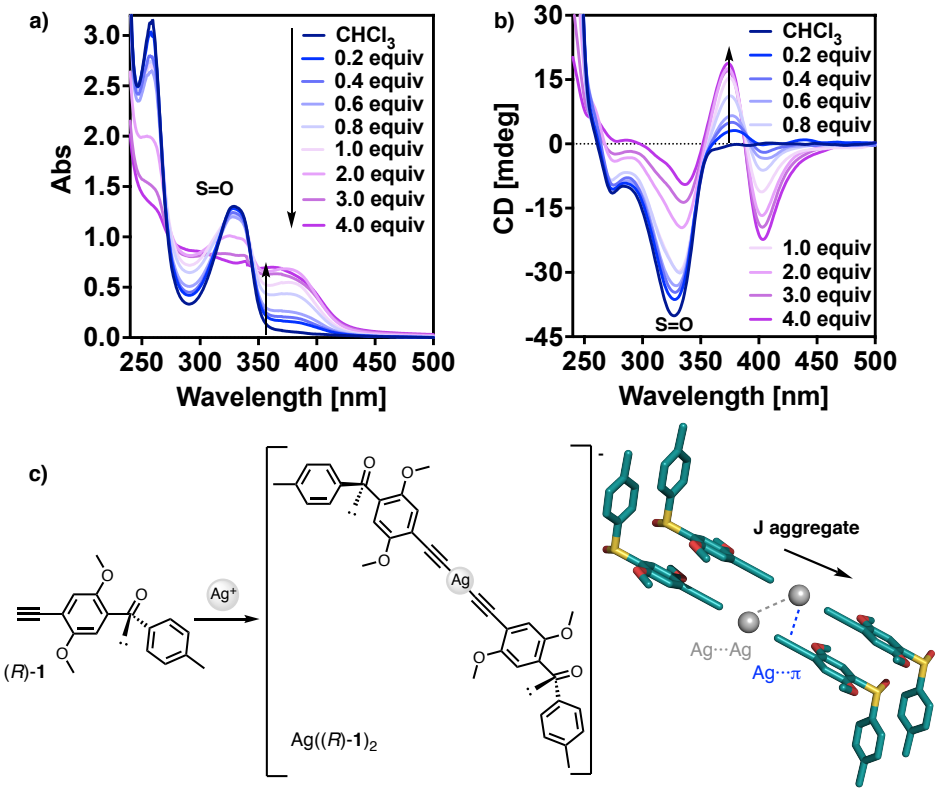

Figure 1. Experimental a) UV-Vis and b) ECD spectra of mono-(*R*)-**1** in $CHCl_3$ with addition of different equivalents of $AgClO_4$. c) (*R*)-**1** structure and proposed Ag[(R)-**1**]$_2$ structure and stacking. [(*R*)-**1**]= 0.3 mg/mL $CHCl_3$, [$AgClO_4$]= 10 mg/mL MeOH.

To analyze the formation of the aggregate, the degree of aggregation [$\alpha_{ECD(403nm)}$] was plotted vs the equivalents of $AgClO_4$ added to the (*R*)-**1** solution. By looking at the graph it is possible to observe a two-step process in the aggregation of the (*R*)-**1**/Ag^+ complex (Figure 2a). Thus, when the amount of the metal ion is low (< 1.8 equiv), a linear growth is observed that corresponds to the formation of the Ag((*R*)-**1**)$_2$ complex (Figure 2d). In this step, as the diacetylide/Ag^+ complex is formed, a helical *J* aggregate is generated by combination of the metallophilic $Ag^+\cdots Ag^+$, $Ag^+\cdots\pi$ and $\pi\cdots\pi$ interactions. SEM studies of the (*R*)-**1**/Ag^+ complex in a 1.0/0.6 mol/mol ratio shows a high degree of polymerization, with the presence of fibers that show regular lengths (2-8 μm) and widths (200-300 nm) and a preferred *M* screw sense (Figure 2b,c). Furthermore, AFM studies allow to determine a regular distance between the fiber groves, about 400 nm (see SI).

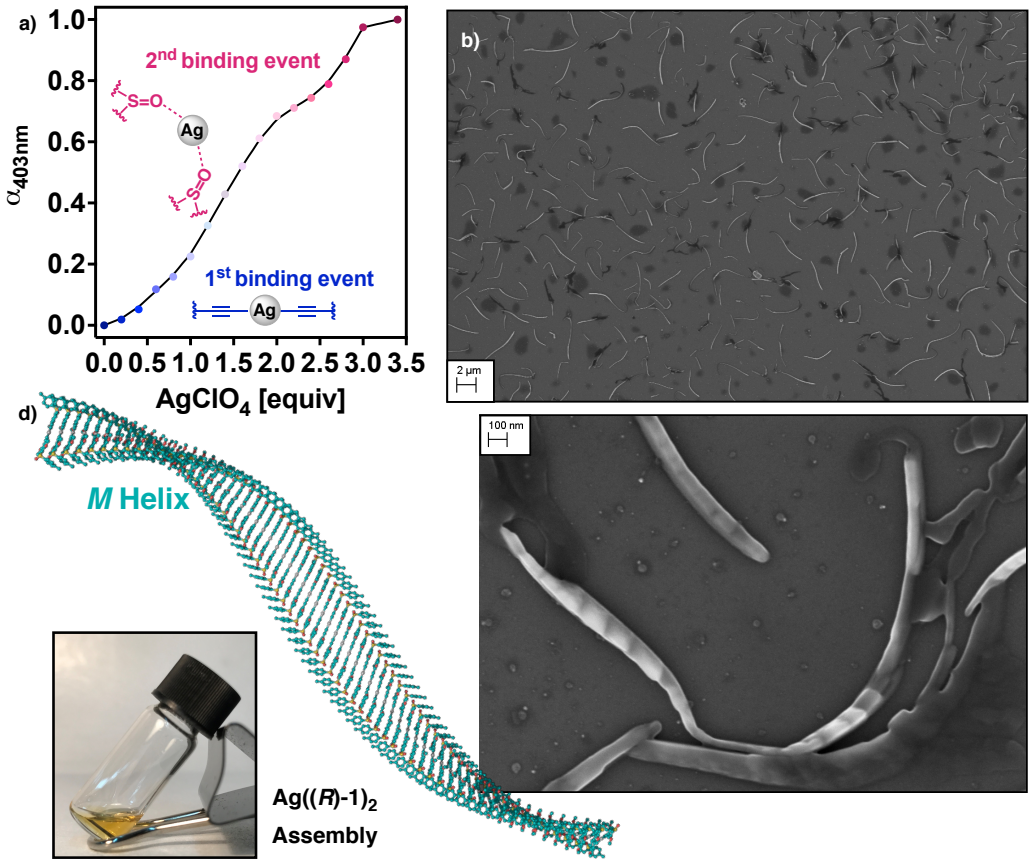

Figure 2. a) Representation of $\alpha_{ECD=403nm}$ vs silver equivalents added for mono-(*R*)-**1**. b, c) SEM microscope images for the 1.0/0.6 mol/mol (*R*)-**1**)/Ag relation. d) Schematic illustration of the linear growth of the (Ag((*R*)-**1**)$_2$ units and image of the solution with 1.0/0.5 mol/mol ratio. [(*R*)-**1**]= 0.3 mg/mL, [$AgClO_4$]= 10 mg/mL.

Interestingly, during this titration studies it is possible to observe a second process when the amount of the metal ion is higher than 1.8 equiv. SEM studies of the (*R*)-**1**/Ag^+ complex in 1.0/4.0 mol/mol ratio show how the fibers get longer and thicker when the amount of the metal ion is higher than 1.8 equiv. In this case, the cation also chelates the sulfoxide group of the PA.[58] This coordination is corroborated by UV-Vis studies, where the absorption band of the sulfoxide group centered at 329 nm decreases dramatically when the acetylene groups are saturated (Figure 1a). This coordination between the silver ion and the sulfoxide group allows the crosslinking of the fibers due to a double coordination of the metal ion to sulfoxide groups of different fibers. When the amount of metal ion is high, *i.e.*, 4.0 equiv, the (*R*)-**1**/Ag^+ complex evolves from fiber like aggregates to a gel structure (Figures 3a-c).

VT-ECD experiments of the fibers were performed of the complex with (*R*)-**1**/Ag^+ ratios of 1.0/0.8 mol/mol and 1.0/4.0 mol/mol. In these conditions, the crosslinking

ability of the cation, together with the $Ag^{+}\cdots Ag^{+}$, $Ag^{+}\cdots\pi$ and $\pi\cdots\pi$ interactions provide a high thermal stability to the material, not found in other OPE aggregates.

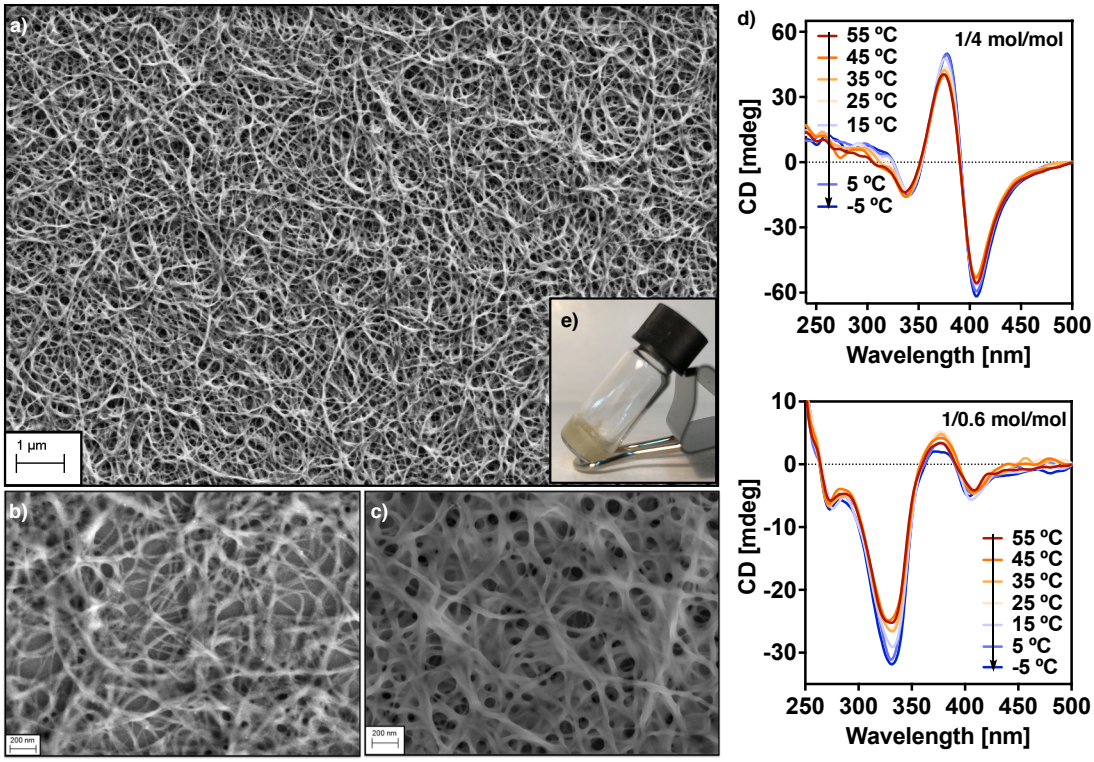

Figure 3. a), b), c) SEM images of 1.0/4.0 mol/mol (*R*)-**1**/Ag ratio ($AgClO_4$ from 10 mg/mL solution). d) VT-CD with a 1.0/4.0 and 1.0/0.5 mol/mol (*R*)-**1**/Ag ratio. e) Image of the gel obtained from (*R*)-**1** with a 1.0/4.0 mol/mol (*R*)-**1**/Ag ratio using a 50 mg/mL solution of $AgClO_4$. [(*R*)-**1**]= 0.3 mg/mL.

3. Conclusion

In conclusion, we have prepared a phenylacetylene derivative that bears a chiral sulfoxide group that forms a chiral supramolecular aggregate in $CHCl_3$ once silver perchlorate is added. In this system, the silver ion forms a linear and planar diacetylide/Ag^{+} complex (metal containing monomer) that self-assembles through supramolecular $Ag^{+}\cdots Ag^{+}$, $Ag^{+}\cdots\pi$ and $\pi\cdots\pi$ interactions generating a chiral *J* aggregate that evolves towards fibers or gel depending on the amount of the silver metal ion added. Thus, if the (*R*)-**1**/Ag^{+} complex is formed in a 1.0/<1.8 mol/mol ratio, a fiber like structure is obtained, while if a 1.0/>1.8 mol/mol ratio is employed, the fibers grow until reach a gel state. This result is produced by the coordination of the silver ion to the sulfoxide groups placed at the periphery of the fiber. This metal ion can act as crosslinking agent chelating more than one sulfoxide group, which results in the formation of bigger fibers or a gel. This fact provides a great thermal stability to these supramolecular aggregates, which remain unchanged even at 55°C in solution.

In our opinion, this mechanism to form *in situ* chiral supramolecular aggregates by spontaneous aggregation of metal containing monomers opens a new horizon in the preparation of stimuli responsive materials, because it is an inexpensive and greener process with potential applications in sensors, diodes, photovoltaic cells and so on.

4. References

[1] J. Matern, Z. Fernández, N. Bäumer, G. Fernandez, *Angew. Chem. Int. Ed.*, **2022**, *61*, e202203783.

[2] L. Brunsveld, B. J. B. Folmer, E. W. Meijer, R. P. Sijbesma, *Chem. Rev.*, **2001**, *101*, 4071-4098.

[3] T. F. de Greef, E. W. Meijer, *Nature*, **2008**, *453*, 171-173.

[4] T. Aida, E. W. Meijer, S. I. Stupp, *Science*, **2012**, *335*, 813-817.

[5] T. Aida, E. W. Meijer, *Isr. J. Chem.,* **2020**, *60*, 33-47.

[6] M. F. J. Mabesoone, A. R. A. Palmans, E. W. Meijer, *J. Am. Chem. Soc.*, **2020**, *42*, 19781-19798.

[7] Z. Fernández, B. Fernández, E. Quiñoá, F. Freire, *Angew. Chem. Int. Ed.*, **2021**, *60*, 9919-9924.

[8] L. N. J. de Windt, Z. Fernández, M. Fernández-Míguez, F. Freire, A. R. Palmans, *Chem. Eur. J.*, **2022**, *28*, e202103691.

[9] Y. Li, A. Hammoud, L. Bouteiller, M. Raynal, *J. Am. Chem. Soc.,* **2020**, *142*, 5676–5688.

[10] A. Desmarchelier, X. Caumes, M. Raynal, A. Vidal-Ferran, P. W. N. M. van Leeuwen, L. Bouteiller, *J. Am. Chem. Soc.*, **2016**, *138*, 4908–4916.

[11] E. Huerta, B. van Genabeek, B. A. G. Lamers, M. M. E. Koenigs, E. W. Meijer, A. R. A. Palmans, *Chem. Eur. J.,* **2015**, *21*, 3682–3690.

[12] M. Raynal, F. Portier, P. W. van Leeuwen, L. Bouteiller, *J. Am. Chem. Soc.*, **2013**, *135*, 17687–17690.

[13] T. Ikai, M. Okubo, Y. Wada, *J. Am. Chem. Soc.*, **2020**, *142*, 3254–3261.

[14] X. M. Chen, S. Zhang, X. Chen, Q. Li, *ChemPhotoChem*, **2022**, 6, e202100256.

[15] K. Salikolimi, V. K. Praveen, A. A. Sudhakar, K. Yamada, N. N. Horimoto, Y. Ishida, *Nat. Commun.*, **2020**, *11*, 1-12.

[16] S. Shanmugaraju, H. Jadhav, R. Karthik, P. S. Mukherjee, *RSC adv.*, **2013**, *3*, 4940-4950.

[17] K. Cobos, R. Rodríguez, E. Quiñoá, R. Riguera, F. Freire, *Angew. Chem. Int. Ed.*, **2020**, *59*, 23724-23730.

[18] A. Ajayaghosh, R. Varghese, S. J. George, C. Vijayakumar, *Angew. Chem. Int. Ed.*, **2006**, *45*, 1141-1144.

[19] J. S. Valera, R. Gómez, L. Sánchez, *Angew. Chem. Int. Ed.,* **2019**, *58*, 510-514.

[20] J. van Gestel, *Macromolecules*, **2004**, *37*, 3894-3898.

[21] X. Shang, I. Song, M. Han, J. H. Lee, H. Ohtsu, W. Choi, J. C. Kim, J. Ahn, S. K. Kwak, J. H. Oh, *Adv. Optical Mater.*, **2021**, *9*, 2001911.

[22] M. M. J. Smulders, P. J. M. Stals, T. Mes, T. F. E. Paffen, A. P. H. J. Schenning, A. R. A. Palmans, E. W. Meijer, *J. Am. Chem. Soc.,* **2010**, *132*, 620–626.

[23] M. Alzubi, S. Arias, R. Rodríguez, E. Quiñoá, R. Riguera, F. Freire, *Angew. Chem. Int. Ed.*, **2019**, *58*, 13365-13369.

[24] Y. Liu, C. Chen, T. Wang, M. Liu, *Langmuir*, **2016**, *32*, 322-328.

[25] M. Wehner, M. I. S. Röhr, M. Bühler, V. Stepanenko, W. Wagner, F. Würthner, *J. Am. Chem. Soc.,* **2019**, *141*, 14, 6092–6107.

[26] F. Würthner, C. R. Saha-Möller, B. Fimmel, S. Ogi, P. Leowanawat, D. Schmidt, *Chem. Rev.*, **2016**, *116*, 962-1052.

[27] S. Ogi, V. Stepanenko, K. Sugiyasu, M. Takeuchi, F. Würthner, *J. Am. Chem. Soc.*, **2015**, *137*, 3300-3307.

[28] E. Weyandt, G. M. Ter Huurne, G. Vantomme, A. J. Markvoort, A. R. Palmans, E. W. Meijer, *J. Am. Chem. Soc.*, **2020**, *142*, 6295-6303.

[29] M. M. J. Smulders, I. A. W. Filot, J. M. A. Leenders, P. van der Schoot, A. R. A. Palmans, A. P. H. J. Schenning, E. W. Meijer, *J. Am. Chem. Soc.*, **2010**, *132*, 611–619.

[30] M. Hifsudheen, R. K. Mishra, B. Vedhanarayanan, V. K. Praveen, A. Ajayaghosh, *Angew. Chem. Int. Ed.*, **2017**, *56*, 12634-12638.

[31] J. Buendia, J. Calbo, F. García, J. Aragó, P. M. Viruela, E. Orti, L. Sánchez, *ChemComm.*, **2016**, *52*, 6907-6910.

[31] F. García, P. A. Korevaar, A. Verlee, E. W. Meijer, A. R. Palmans, L. Sánchez, *ChemComm.*, **2013**, *49*, 8674-8676.

[32] J. Matern, K. K. Kartha, L. Sánchez, G. Fernández, *Chem. Sci.*, **2020**, *11*, 6780-6788.

[33] N. Bäumer, K. K. Kartha, S. Buss, I. Maisuls, J. P. Palakkal, C. A. Strassert, G. Fernández, *Chem. Sci.*, **2021**, *12*, 5236-5245.

[34] D. Xia, P. Wang, X. Ji, N. M. Khashab, J. L. Sessler, F. Huang, *Chem. Rev.*, **2020**, *120*, 6070-6123.

[35] S. Dong, B. Zheng, F. Wang, F. Huang, *Acc. Chem. Res.*, **2014**, *47*, 1982-1994.

[36] T. Xiao, L. Zhou, X. Q. Sun, F. Huang, C. Lin, L. Wang, *Chin. Chem. Lett.*, **2020**, *31*, 1-9.

[37] B. Li, T. He, Y. Fan, X. Yuan, H. Qiu, S. Yin, *ChemComm.*, **2019**, *55*, 8036-8059.

[38] B. Hosseinzadeh, M. Ahmadi, *Coord. Chem. Rev.*, **2022**, *471*, 214733.

[39] W. Zhou, Z. Wang, J. Zhang, S. Hu, Q. Xie, Z. Liu, A. Liang, *Dyes Pigm.*, **2020**, *172*, 107790.

[40] Y. Huang, S. Huang, X. Li, Z. Wang, J. Xu, Y. Pan, A. Liang, *J. Inorg. Organomet. Polym. Mater.*, **2022**, *32*, 1499-1505.

[41] L. Xu, X. Shen, Z. Zhou, T. He, J. Zhang, H. Qiu, M. L. Saha, S. Yin, P. J. Stang, *J. Am. Chem. Soc.*, **2018**, *140*, 16920-16924.

[42] A. Ghosh, S. Shankar, D. S. Philips, A. Ajayaghosh, *Mater. Today Chem.*, **2020**, *16*, 100242.

[43] H. Ouchi, T. Kizaki, M. Yamato, X. Lin, N. Hoshi, F. Silly, T. Kajitani, T. Fukushima, K. Nakayama, S. Yagai, *Chem. Sci.*, **2018**, *9*, 3638-3643.

[44] S. R. Jena, J. Choudhury, *Sol. Energy Mater Sol. Cells*, **2022**, *239*, 111660.

[45] J. Matern, I. Maisuls, C. A. Strassert, G. Fernandez, *Angew. Chem. Int. Ed.*, **2022**, *61*, e202208436

[46] K. C. Bentz, S. M. Cohen, *Angew. Chem. Int. Ed.*, **2018**, *57*, 14992-15001.

[47] N. Bäumer, K. K. Kartha, S. Buss, J. P. Palakkal, C. A. Strassert, G. Fernández, *Org. Chem. Front.*, **2021**, *8*, 4138-4143.

[48] G. R. Whittell, M. D. Hager, U. S. Schubert, I. Manners, *Nat. Mater.*, **2011**, *10*, 176-188.

[49] A. Winter, U. S. Schubert, *Chem. Soc. Rev.*, **2016**, *45*, 5311-5357.

[50] L. N. Neumann, E. Oveisi, A. Petzold, R. W. Style, T. Thurn-Albrecht, C. Weder, S. Schrettl, *Sci. Adv.*, **2021** 7, eabe4154.

[51] Y. Zhu, W. Zheng, W. Wang, H. B. Yang, *Chem. Soc. Rev.*, **2021**, *50*, 7395-7417.

[52] N. Bäumer, J. Matern, G. Fernández, *Chem. Sci.*, **2021**, *12*, 12248-12265.

[53] A. D. Pomogailo, V. S. Savost'yanov, Synthesis and polymerization of metal-containing monomers, *CRC Press*. **2018**

[54] R. Buschbeck, P. J. Low, H. Lang, *Coord. Chem. Rev.*, **2011**, *255*, 241-272.

[55] C. Brasse, P. R. Raithby, M. A. Rennie, C. A. Russell, A. Steiner, D. S. Wright, *Organometallics*, **1996**, *15*, 639-644.

[56] C. H. Shu, Y. He, R. X. Zhang, J. L. Chen, A. Wang, P. N. Liu, *J. Am. Chem. Soc.*, **2020**, *142*, 16579-16586.

[57] J. Liu, Q. Chen, K. Cai, J. Li, Y. Li, X. Yang, Y. Zhang, Y. Wang, H. Tang, D. Zhao, K. Wu, *Nat. Commun.*, **2019**, *10*, 1-10.

[58] J. Liu, Q. Chen, K. Cai, J. Li, Y. Li, X. Yang, Y. Zhang, Y. Wang, H. Tang, D. Zhao, K. Wu, *Nat. Commun.*, **2019**, *10*, 1-10.

Chapter IX

Resume

RESUME

Inspirándose na relación estrutura-función observada en diversas biomoléculas como as proteínas ou o ADN, a comunidade científica puxo o seu foco na preparación de novos materias sintéticos tratando de emular estas propiedades. De tal forma que, a investigación científica en materiais poliméricos non parou de crecer dende os seus inicios no século XIX, dando lugar na actualidade a unha ampla gama de polímeros helicoidais sintéticos cun sen fin de propiedades e aplicacións.

Nesta ampla liña de investigación, pódense diferenciar dous grandes grupos en base a forza principal que impulsa a súa formación e os estabiliza. Así, podemos atopar os polímeros helicoidais covalentes e supramoleculares, sendo os primeiros de natureza irreversible (unha vez xerados non se poden desensamblar as unidades monoméricas que os compoñen) mentres que os segundos pódense ensamblar e desensamblar repetidamente baixo condicións controladas. Pese a estas diferenzas, ambas clases de polímeros comparten moitas propiedades (amplificación da quiralidade, efecto sarxentos e soldados, regra do maioritario, acordo quiral, etc.).

No caso dos polímeros helicoidais covalentes, unha destacable familia deste grupo son os poli(acetilenos)s (PA) e dentro deles os poli(fenilacetileno)s (PPAs). Esta subfamilia, destaca polo seu gran carácter dinámico, podendo así modular a súa estrutura (elongación e sentido de xiro) mediante a aplicación dunha ampla gama de estímulos externos como son a temperatura, os ións metálicos, as propiedades do disolvente, o pH, etc.

Do mesmos xeito, no grupo dos polímeros helicoidales supramoleculares existen unha ampla variedade de subclases. Así, dentro desta inmensa familia, cabe destacar a especial relevancia que cobraron nos últimos anos os polímeros metalo-supramoleculares grazas a súa versatilidade e capacidade de xerar interaccións estabilizantes de tipo metal-metal ou metal-π entre outras.

Esta tese de doutoramento titulada “Fotoreactividade e Novos Deseños en Materiais Quirais Intelixentes” expón, o longo de seis proxectos experimentais, o estudo da fotoreactividade en polímeros helicoidais covalentes baseados en PPAs, a aplicación destes resultados no análise estrutural dos mesmos. Tamén se aborda a preparación e estudo de novos PPAs fotoestables e novos PPAs multi-resposta. Posteriormente, da combinación de polímeros helicoidais covalentes e supramoleculares, obtéñense e estúdanse novos materiais intelixentes multi-helicoidais mediante a combinación de PAs con centros metálicos para finalmente propoñer a obtención mediante novas rutas de materiais metalo-poliméricos baseados en estruturas supramoleculares.

Capítulo III. Electrociclización fotoquímica de poli(fenilacetileno)s: desenrolando hélices para dilucidar a súa estrutura 3D en disolución

Os PPAs helicoidais poden presentar unha estrutura *cis-cisoide* (ángulo entre dobres enlaces (ω_1) menor de 90°) ou *cis-transoide* (ω_1> 90°). Coñecer esta información e clave a fin de poder elucidar a estrutura secundaria para poder así controlar e modular as súas propiedades. Para este fin, xeralmente recurrese a combinación de diversas técnicas como a microscopía de forza atómica (AFM), a calorimetría diferencial de barrido (DSC) ou o dicroísmo circular (CD), entre outras técnicas coa fin de xerar un modelo que permita determinar a conformación *cis/trans* do material. Sen embargo, en ocasión a identificación e difícil pois as técnicas maís relevantes dan lugar a resultados imprecisos (DSC) ou ben a técnica e complexa e difícil de aplicar con éxito a tódolos casos (AFM).

Como alternativa a estes problemas, neste capítulo proponse unha nova metodoloxía para a elucidación da estrutura secundaria (*cis/trans*) de PPAs. Así, abordouse a relación entre a estrutura secundaria dos PPAs e a electrociclación fotoquímica dos mesmos. Esta reacción e un proceso en dúas etapas (electrociclación fotoquímica seguida dun proceso de aromatización), que da lugar a formación de bencenos 1,3,5-trisustituidos a partir do esqueleto poliénico.

Coa fin de establecer esta relación entre a fotoreactividade e a estrutura, abordouse a preparación dunha librería de PPAs cunha estrutura secundaria coñecida e implementouse un protocolo de irradiación para os mesmos que inclúe o seguimento do proceso mediante dicroísmo circular. Os datos resultantes combináronse coa información coñecida da estrutura destes materias dando lugar a unha ecuación que permite relacionar o tempo de vida media ($t_{1/2}$) da sinal vinílica de ECD durante a electrociclación fotoquímica co ángulo ω_1. Como resultado, dos datos cinéticos obtidos a partir dos estudos de dicroísmo circular e a ecuación proposta pode obterse un valor aproximado de ω_1 clasificando así o PPA en *cis-cisoide* (ω_1< 90°) ou *cis-transoide* (ω_1> 90°).

A validez desta metodoloxía foi confirmada cun total de seis PPAs e ata nove hélices diferentes. Confirmando así a independencia da reactividade da conexión do PPA (anilida ou benzamida), da substitución do anel aromático (*orto-*, *meta-* ou *para-*) e do residuo quiral presente no polímero. Ademais, os estudos demostraron que a metodoloxía permite o análise de casos complexos tales como a presencia de mesturas de hélices en equilibrio.

Capítulo IV. Reversións na hélice en poli(fenilacetileno)s: máis que motivos estruturais

As reversións en materiais helicoidais son puntos nos que o sentido de xiro predominante da hélice se inverte. Estes motivos estruturais diminúen o exceso do sentido de xiro predominante do polímero e dada a relación estrutura-función destes materiais poden ter grandes implicacións nas súas aplicacións. Sen embargo, non existen metodoloxías que permitan cuantificar as reversións presentes nun polímero helicoidal en disolución, e por tanto este factor tan importante non se esta avaliando correctamente a hora de implementar os PPAs para algunhas aplicacións onde a helicidade é clave (como pode ser a resolución de mesturas quirais). A presencia de reversións tan so se coñece grazas a súa identificación en fase sólida mediante AFM. Para tratar de analizar este motivo estrutural en disolución, valorouse o uso da electrociclación fotoquímica a fin de desenvolver unha metodoloxía que permite determinar as reversións en disolución.

Así, dada a gran sensibilidade mostrada pola reactividade fotoquímica dos PPAs buscouse dar un paso máis na utilización desta técnica. Para realizar isto, prepararónse unha ampla librería de PPAs e aplicouse a metodoloxía desenrolada no capítulo III para determinar a estrutura. Dada a presencia de reversións na hélice, os resultados obtidos estaban fora de valores aceptables para ambas conformacións (*cis-cisoide* e *cis-transoide*), o cal é indicativo da influencia das reversións na reactividade fotoquímica. Dende este punto, o primeiro paso foi propoñer unha metodoloxía que permita determinar si existen reversións ou non na hélice para saber si se pode aplicar a metodoloxía descrita no capítulo III.

Para este fin, realizáronse estudos de electrociclación fotoquímica a 4°C e a temperatura ambiente. En combinación, os tempos de reacción entre ambos casos mostráronse moi concluíntes a fin permitiron identificar a presencia ou non das reversións. Así, unha vez determinada a presencia dos mesmos, para a cuantificación do porcentaxe de reversións propuxéronse catro ecuacións en base o grado de elongación da hélice a analizar. Estas ecuacións desenroláronse a partir de catro PPAs con diferente grado de elongación, para os que se prepararon series de copolímeros enantioméricos en diferentes porcentaxes. En tódalas series estudadas existe un conflito quiral entre comonómeros co cal o porcentaxe de reversións presentes na hélice é coñecido, permitindo xerar as catro ecuacións (unha para *cis-cisoides* e *tres para cis-transoides*, en función do grado de elongación) que relacionan a caída da sinal de dicroísmo circular durante o proceso fotoquímico co porcentaxe de reversións.

Con estes datos, comprobáronse as ecuación mediante o análise o 50% e 20% da sinal de CD durante a electrociclación fotoquímica cunha serie de PPAs de características diferentes (*cis-cisoides*/*cis-transoides* e anilidas/benzamidas), confirmando así a boa relación entre os fenómenos de reversión da hélice e a fotoreactividade.

Capítulo V. Fotoestabilidade e comportamento helicoidal dinámico en poli(fenilacetileno)s quirais cun sentido de xiro preferido

En recentes estudos profundizouse na fotoreactividade dos PPAs, demostrando a dependencia da estabilidade destes materiais co grao de elongación e o dinamismo da hélice. A relevancia destes resultados basease en que, unha das grandes limitacións para a aplicación en entorno real dos PPAs e a súa escasa estabilidade a luz. Con toda esta información, e baseándose nos resultados obtidos nos capítulos anteriores, neste proxecto buscouse preparar un PPA fotoestable mediante a modificación do dinamismo e a elongación da hélice.

Para lograr este obxectivo, seleccionouse un sulfinilareno como grupo indutor da quiralidade da hélice, este presenta unha conformación ríxida coa fin de favorecer unha única conformación (evitando así a formación de reversións). Ademais, introducironse grupos metoxi no anel do PPA para promover a formación dunha hélice cun alto grao de elongación. Unha vez sintetizado, diversos estudios, principalmente CD, demostraron a gran rixidez e indución quiral que presenta o residuo quiral.

A continuación, procedeuse a polimerización do mesmo seguindo os procedementos clásicos de polimerización e purificación de PPAs. Tras isto, o primeiro paso foi a caracterización do mesmo, tal como esperabamos, como unha hélice *cis-transoide* cun alto grado de elongación. Para este fin, recorreuse a estudos de AFM en combinación con DSC e CD entre outras técnicas. Coa información resultante xerouse un modelo 3D que se confirmou mediante cálculos teóricos, logrando a identificación de dúas posibles hélices, en función da polaridade do medio, ambas con conformación *cis-transoide* e un alto grao de elongación (ω_1 de -157° e -165°). Estas estruturas foron sometidas posteriormente a estudios de reactividade fotoquímica baixo a metodoloxía desenrolada no capítulo III. Como resultado, o espectro de dicroísmo resulta case inalterado en ambos casos, non producíndose en ningún momento unha degradación da cadea poliénica grazas o alto grado de elongación e a rixidez da conformación helicoidal.

Chapter VI. Interruptores múltiples fotostables baseados en azo-poli(fenilacetileno)s con tres motivos quirais diferentes (***Hélice$_{int}$*/*Hélice$_{ext}$*/*Hélice$_{Azo}$***)

Na literatura apenas se atopan exemplos de polímeros helicoidais dinámicos que empreguen luz como estímulo externo, sendo a ampla maioría polimetilmetacrilatos. No caso concreto dos PPAs, non se reportou ningún exemplo, o cal probablemente se deba a que é amplamente coñecido que o esqueleto poliénico dos PPAs se degrada, de xeito irreversible, en presencia de luz.

Sen embargo, grazas os recentes avances na fotoreactividade de PPAs contamos con máis información a cerca deste proceso coa fin de poder controlalo ou ben tratar de evitalo. Como resultado, quixemos desenvolver novos PPAs que empreguen luz como un estímulo externo reversible, para realizar isto pensamos que a mellor opción pasaba pola introdución na hélice de grupos azobenzeno, xa que o seu equilibrio *E/Z* resulta facilmente modulable con luz. Ademais, dada o alto grao de dinamismo que posúen estes polímeros, a combinación de ambos materiais deu lugar a xeración de materiais multiresposta (sensibles a luz, temperatura, ácidos, polaridade do disolvente, metais, etc.).

Para levar isto a cabo, sintetizáronse unha parella de aminoácidos (*L*-Alanina e *L*-Valina) combinados cun grupo 4-aminoazobenceno e o resto fenilacetilénico. Tras a polimerización dos mesmos, os estudos en diferentes disolventes combinados coa información obtida a través de diversas técnicas demostraron o control da estrutura secundaria entre hélices *cis-transoide* e *cis-cisoide* en función da polaridade do medio. Ademais, revelouse que dependo da conformación da hélice os grupos azobenzeno poden ensamblarse de forma quiral arredor da hélice dando lugar a formación de triples hélices (hélice$_{int}$, correspondente o esqueleto poliénico; hélice$_{ext}$, correspondente os grupos colgantes e hélice$_{azo}$ debido o ensamblaxe quiral dos grupos azobenceno arredor da estrutura clásica composta pola hélice$_{int}$ e a hélice$_{ext}$).

Por outro lado, a resposta a metais, non se viu afectada pola introdución de grupos fotosensibles (podendo así controlar o equilibrio *ap/sp* entre grupos carbonilo). Mentres que nos casos nos que existe un apilamento supramolecular entre azos, o uso de estímulos como a luz, a temperatura ou a adición de ácidos si xera diferencias na resposta en presencia ou non de ensamblaxe entre grupos azobenceno, dando lugar a materiais multi-resposta. Ademais, cabe destacar que a resposta a luz non so é reversible grazas a presencia de grupos azobenzeno, sinon que o amplío espectro de absorción destes grupos fotomodulables evita a absorción de radiación polo esqueleto poliénico resultando en

materiais cunha alta fotoestabilidade fronte a degradación lumínica o mesmo tempo que cun gran dinamismo.

Chapter VII. Materiais multihelicoidais mediante a combinación de polímeros helicoidais covalentes e metalo-supramoleculares: cinco motivos axiais dentro dun polímero helicoidal

Os polímeros helicoidais —supramoleculais e covalentes— comparten moitas características en común (amplificación da quiralidade, efecto sarxento e soldado, inversión da helicidade, etc.). Como resultado destas similitudes a combinación de ambos materiales debería producir grandes sinerxías, dando lugar a novidosos materiais helicoidais con prometedoras propiedades.

En PPAs está descrito que a introdución de espazadores ríxidos entre o esqueleto poliénico e o residuo quiral, como as unidades de oligofenilenotinileno (OPEs), da lugar a indución da helicidade a través dun apilamento quiral entre os espazadores ríxidos. Este feito, permite a formación de materiais multi-helicoidais con formación de ata catro hélices dentro da mesma estrutura (resultado da combinación nunha estrutura *cis-transoide* das dúas hélices clásicas: interna e externa, xunto con outras dúas descritas polos espazadores). Inspirándonos neste resultado xunto co observado no capítulo anterior, onde xa se logrou a formación de hélices triples tanto en polímeros *cis-cisoide* coma *cis-transoide*, neste proxecto quíxose dar un paso máis e xerar a partir do mesmo material multi-hélices de maior complexidade.

Para lograr isto, combináronse complexos de bispiridildicloruro de platino (II) —moi empregados na xeración de estruturas supramoleculares— xunto con poliacetilenos (PA). Os monómeros resultantes sometéronse a estudos de UV-vis e cálculos teóricos coa fin de determinar que rexións da estrutura eran responsables das absorcións encontradas. No caso dos polímeros, da combinación destes datos xunto con estudos de CD, UV-vis e CD teórico demostrouse que a combinación da hélice supramolecular xerada polos complexos de Pt^{II} xunto coa hélice de PA resulta na formación de materiais multihelicoidais altamente dinámicos. Así, en función da polaridade do medio pódense obter polímeros *cis-cisoides* (hélice 3:1, e.g., DMF)), dando como resultado a formación de materiais cun total de cinco hélices ($hélice_{int}$, $hélice_{ext}$ e tres hélices correspondentes o ensamblaxe dos complexos de Pt^{II} a través de cada unha das hélices coaxiales que conforman a estrutura). Mentras que en conformación *cis-transoide* (hélice 2:1, e.g., DCM, THF), obtéñense un total de catro hélices ($hélice_{int}$, $hélice_{ext}$ e dúas hélices correspondentes o ensamblaxe dos complexos de Pt^{II}). Ademais, demostrouse que como na conformación *cisoide* as hélices interna e externa xiran no mesmo sentido mentras que na *transoide* o fan en sentidos opostos,

pódese determinar o sentido de xiro de tódalas hélices xa que as hélices descritas polos complexos de Pt^{II} adoptan o mesmo sentido helicoidal que a hélice externa.

Chapter VIII. Fibras metalo-supramoleculares a partir de monómeros de fenilacetileno: ensamblaxe inducido por catións

Os polímeros supramoleculares surxen do ensamblaxe non covalente de unidades monoméricas a través de interaccións non covalentes. Esta característica outórgalles un carácter reversible as macroestruturas xeradas que lles confire aplicacións únicas. Neste campo existen unha gran variedade de subclases así como posibles clasificacións, dentre todas estas posibilidades una subfamilia moi interesante son os polímeros metalo-supramoleculares. Nestos, a gran variedade de centros metálicos dispoñibles outorga unha enorme versatilidade a estes materiais.

Neste traballo, descríbese un novo proceso de obtención de fibras quirais mediante a mestura dun ión metálico (Ag^{I}) en combinación con un fenilacetileno quiral. De xeito individual, este ligando orgánica é incapaz de autoensamblarse por si mesmo, pero en combinación con catións de prata forma un complexo en relación 2:1 ligando/metal que autoensambla espontaneamente impulsado principalmente polas interaccións Ag···Ag e Ag···π. A través do espectro UV-vis o forte desprazamento o vermello indica a formación dun agregado J, ademais, os estudos de dicroísmo circular mostran a formación dun -/+ bisignato indicando o ensamblamento quiral das unidades. Ademais, dos estudos de dicroísmo circular pódese analizar o valor de α_{ECD} durante a formación do ensamblaxe, determinando que existen dúas etapas na formación das estruturas helicoidais. Así, mantendo unha baixa relación ligando/metal o crecemento da estrutura e principalmente lineal, dada a formación de acetiluros de prata lineais, tal como se observa das imaxes de AFM e SEM onde se poden identificar largas fibras individuais. Mentres, a altos ratios ligando/metal prodúcese unha interdixitación entre as diferentes fibras pola formación de interaccións entre grupos sulfoxidos, que dan lugar en condición adecuadas a unha estrutura tipo xel.

Por tanto, o longo dos seis capítulos experimentais aquí descritos pódese observar, tal como se plantexaba nos obxectivos iniciais a consecución en primeiro lugar dunha metodoloxía para discernir entre a estrutura helicoidal de PPAs (cis-cisoide ou cis-transoide) mediante o emprego dun total de 6 polímeros e 9 hélices (*c-c* e *c-t*, *c-t*, *c-c*, *c-t*, mixtura *c-c* e *c-t*, mixtura *c-t* e *c-t* e finalmente mixtura *c-c* e *c-t*) mediante reactividade fotoquímica baixo condicións controladas (disolución a 0.3 mg/mL e emprego de luz visible 350-550 nm). A partir deste resultado, e empregando o mesmo protocolo descrito para o anterior capítulo, realizouse o estudo de varias series de copolimeros derivadas de polifenilacetilenos (*c-t*, *c-c* e *c-t* e *c-t)*. Como resultado, logrouse un novidoso proceso para determinar a %r (porcentaxe de inversións da hélice) frente o tempo de irradiación. En ambos procesos, esta metodoloxía explota a utilización da reactividade do polieno conxugado (dobles enlaces consecutivos que soportan a helicidade da estrutura).

A continuación, os seguintes dous traballos son tamén unha continuación, logrando así unha linealidade experimental o longo da tese. Demostrouse en ambos, a través do emprego de novos materiais derivados de PPAs, que a incorporación de grupos azobenzeno no primeiro caso ou indutores quirais a partir de sulfoxidos no seguinte, da posibilidade do control da reactividade fotoquímica. Así, no primeiro caso, obtuveronse dous PPAs fotoestables, cun alto grado de dinamismo e resposta a unha gran variadede de estímulos: ácidos (TFA), metais (principalmente divalentes, M^{2+}), propiedades do disolvente (características de poder dador e polaridade) e un control da helicade mediante a irradiación do grupo azobenzeno controlando a conformación *cis* (350 nm) ou *trans* (420 nm). No segundo caso, o grupo sulfoxido (S=O), da lugar a un polímero cunha única conformación e por tanto este sistema semiestático logra unha gran estabilidade fotoquímica e o mesmo tempo a xeración de duas hélices c-t. En ambos casos, estes materiais tamén logran novas propiedades grazas a combinación de materiais.

Finalmente, nos dous últimos capítulos experimentais (VII e CVIII) adentrouse na preparación de metalo-polímeros. No primeiro caso, da combinación de polímeros covalentes e supramoleculares dando lugar a materiais multi-helicoidais M_1, M_2, M_3, M_4, M_5 para a hélice *c-c* e M_1, P_2, P_3, P_4, para a *c-t*. A último capítulo experimental, dun xeito similar logra hélices supramoleculares mediante o autoensamblaxe espontáneo a través da combinaci´n dun ligando orgánico e un centro metálico (relación mol/mol (*R*)-**1** frente a Ag entre 1.0/0 a 1.0/4.0).

Chapter X

Conclusions

CONCLUSIONS

In in this thesis was described the preparation, characterization and study of the properties of covalent and supramolecular helical polymers. In covalent helical polymers, a library of known and new poly(phenylacetylene)s (PPAs), a family of dynamic helical polymers, were prepared. Furthermore, in the field of supramolecular polymers a phenylacetylene monomer was combined with a metal ion to generate a helical metallopolymer.

Throughout the different chapters, the photoresponsiveness-structure relationship of the PPAs was evidenced, and with this information new material —covalent and supramolecular— was developed. Furthermore, the elucidation of these materials took on special relevance in this work. Considering this information, the main conclusions of each chapter was detailed below.

Chapter III. Photochemical Electrocyclization of Poly(phenylacetylene)s: Unwinding Helices to Elucidate their 3D-Structure in Solution

A novel approach to discerning the conformation of the double bonds (*cc/ct*) of a PPA has been demonstrated. Thus, through a good number of PPAs with different well-known helical structures —6 polymers, 9 helical scaffolds— was determine that visible light irradiation can be introduced as a powerful technique to determine the secondary structure of polyacetylenes. The basis of the method lies on the quite different rate observed for the photochemical electrocyclization depending on the scaffold (*cis-cisoidal*, *cis-transoidal*) of the helical polymer.

To perform these studies, vials containing a dilute solution of a PPA [(poly-(**1**-**6**)]= 2.1 mg/ 7 mL; c.a. $1 \cdot 10^{-3}$ M] was irradiated with visible light (ω_1> 350 nm) and the CD signal decay monitored versus time to afford the photochemical electrocyclization rate and the $t_{1/2}$ as the relevant parameters.

The results show that there is a direct relationship between the elongation of a PPA (ω_1) and its $t_{1/2}$. For instance, $t_{1/2}$= 26 min corresponds to a *cis-cisoidal* PPA with ω_1 c.a. 70°. such as poly-(*R*)-**1** ($CHCl_3$), poly-(*S*)-**3** or poly-(*S*)-**5** (helix 1). For their part, PPAs with more elongated chain (larger ω_1) show higher $t_{1/2}$ values —poly-(*R*)-**1** (THF) (ω_1= 155°, $t_{1/2}$= 78 min.); poly-(*R*)-**2** (ω_1= 148°, $t_{1/2}$= 63 min); poly-(*S*)-**4** (ω_1= 170°, $t_{1/2}$= 1513 min)—. The kinetic data for all the polymers used in this study, fit well into equation 2 that therefore can be used to predict the scaffold of a PPA (ω_1) from its $t_{1/2}$ kinetic value. The use of the visible light for the photochemical electrocyclization of PPAs as a tool to

determine their helical structure by using a $t_{1/2}$/ ω_1 relationship, is exceptionally important in this field because no other techniques can provide an approximated value for ω_1 in solution. This value is necessary to build up an approximated helical structure of the PPA, where important helical parameters such as relative helical sense of the internal and external helices of a PPA depends on this value —*cis-cisoidal* structures (ω_1< 90°) both helices rotate in the same direction, while in *cis-transoidal* scaffolds (ω_1< 90°) both helices rotate in opposite directions

Although the studies in this work are limited to PPAs substituted by amide groups (anilide, benzamide), no doubt similar investigations can be carried out with other PPAs that bear other connecting groups (ester, ether...). To do this, it will be essential to have a solid base of structural information on these polymers, including AFM images and theoretical calculations, in order to know if the results would be comparable to those of the anilide/benzamide PPAs.

Chapter IV. Helix Reversals in Poly(phenylacetylene)s: More than Structural Motifs

In this chapter, we have demonstrated that the PE of PPAs in solution can be used as a structural tool to determine their secondary structure of PPAs and the presence of reversals within the helical structure. PE of PPAs does not depends on the chemical structure of the pendant groups or the solvents used to do the studies, being the rate of the PE process affected only by the secondary structure of the PPA. Thus, while in *c-c* PPAs the PE is fast, in *c-t* PPAs the PE is slower, speed being the speed largely affected by temperature. Therefore, PE at different temperatures allow us to classify PPAs into *c-c* or *c-t* PPAs. Moreover, PE studies also allow obtaining the dihedral angle between conjugated double bonds in well folded polymers. However, if the polymers are not well folded, the presence of reversals along the helix affects largely the PE process, being this shortened in time. This relationship between the PE of PPAs and the presence of reversals along the helix allowed us to generate an equation that predicts the number of reversals present in a PPA with a certain scaffold. To apply this equation, it is necessary to know if the polymer has *c-c* or *c-t* structure, which can be easily obtained from PE studies at different temperatures or by using DSC studies. In the case of *c-c* PPAs there is only one equation to determine the folding of PPAs, and in the case of *c-t* PPAs is necessary to have an approximated value for ω_1 to determine its folding degree. At this stage, there are three different equations for *c-t* PPAs; one for PPAs with ω_1 ca. 148°; a second one for PPAs with ω_1 ca. 155°, and a third one for PPAs with ω_1 ca. 165°.

These studies can be of great interest to the scientific community because they are dealing, for the first time, with the folding degree of PPAs in solution. In literature, dynamic helical polymers are used as chiral catalyst, chiral recognition agents and chiral stationary phases in HPLC. However, these polymers are applied without considering the polymer folding. By using this approximation, it is possible to determine if the polymer is well folded or not in solution, and therefore, to explain how the helical scaffold affects the applications of the polymer.

Chapter V. Photostability and Dynamic Helical Behavior in Chiral Poly(phenylacetylene)s with a Preferred Screw-Sense

In conclusion, it has been demonstrated through a rational design that photostability of PPAs is directly related to its dynamic behavior. Thus, those PPAs with a high dynamic behavior, whose helical sense or elongation can be altered by the presence of external stimuli are more prompt to degrade under light exposure due to photoisomerization of the double bonds that end up with a photochemical electrocyclization of the polyene backbone. On the other hand, PPAs with a restricted conformational composition and therefore a poor dynamic behavior shows a great photostability, being the helical scaffold not affected by irradiation with UV light. Therefore, dynamic behavior and photostability in PPAs are compromised, fact that is necessary to consider in the design and potential application of PPAs.

Chapter VI. Photostable Multi-Switches Based on Azo-Poly(phenylacetylene)s with three different chiral motifs (*Helix*$_{int}$/*Helix*$_{ext}$/*Helix*$_{Azo}$)

The introduction of a photo-switchable group as substituent of a chiral pendant in a poly(phenylacetylene) improves the photostability of the material and provides additional stimuli-responsive properties. For instance, in this work, two different PPAs has been prepared bearing the benzamide of alanine [poly-(*L*)-**1**] and valine [poly-(*L*)-**2**] as pendants derivatized with 4-aminoazobenzene. These polymers are photostable and can be stored under light without being degraded. This fact is very important to improve the industrial applications of PPAs, because their poor photostability is a limiting factor in the commercial world.

It is also remarkable that the introduction of the Azo group does not affect to the stimuli-responsive properties of the amino acids, being poly-(*L*)-**1** and poly-(*L*)-**2** sensitive to solvents, temperature and metal ions, whose helical sense can be inverted, amplified, or zeroed out by these stimuli. Moreover, it was also found that depending on the helical

scaffold adopted by the PPA —value of ω_1—, the azo units can form a chiral array generating a macromolecular scaffold consisting of three different chiral motifs: 1) the helix described by the polyene backbone (*helix*$_{int}$), 2) the helix described by the pendant groups (*helix*$_{ext}$) and 3) the helix described by the azo array (*helix*$_{Azo}$). When these three chiral motifs coexist within a PPA, its ECD spectra is dominated by the azo array. By playing with acids, light or temperature it is possible to modulate the UV-vis or ECD bands of the azo array (pH effect), and the scaffold between helices consisting on two coaxial helices ("*classical*" helix: *helix*$_{int}$/*helix*$_{ext}$) or a macromolecular structure with three coexisting chiral motifs (*helix*$_{int}$/*helix*$_{ext}$/ *helix*$_{Azo}$).

Therefore, these studies open a new horizon in the development of smart materials that can act as multi-switches. To do that it is necessary to introduce, in the monomer repeating unit, functional groups with different stimuli-responsive and self-assembling properties that allow to create novel architectures, stable under ambient conditions and with interesting multiswitch properties.

Chapter VII. Multi-helical Materials by combining Metallo-Supramolecular and Covalent Helical Polymers: Five Axially Motifs within a Helical Polymer

In this chapter, we have demonstrated through two different examples —poly-(*S*)-**1** and poly-(*S*)-**2**— that it is possible to obtain a multi-helix material by linking a supramolecular helix, made by bispyridyldichloride Pt^{II} complexes, to a covalent helical polymer (PA). By looking at the structures generated by the two systems we envisioned that the two systems could fit into a multi-helical material. In this case and considering the tilting degree angle found in the supramolecular helices of bispyridyldichloride Pt^{II} complexes (Θ) close to 20°, we assumed that this axial array could fit either into *cis-cisoidal* and *cis-transoidal* polyacetylene scaffolds. As a result, a multi-helix material is prepared by stabilizing a metallo-supramolecular polymer in a covalent helix. A great example is poly-(*S*)-**1**, in this case when the polymer is dissolved in non-polar solvents adopts a *cis-transoidal* structure (ω_1> 90°), which shows a complex ECD spectrum due to the opposite ECD traces generated by the polyene backbone and the metallo-supramolecular array. In this chiral material, four different helices are found, the two coaxial helices —internal (helix 1) and external (helix 2)— and the three helices described by the bispyridyldichloride Pt^{II} complexes axial array (helices 3 and 4). These four helices are interconnected and, by identifying the orientation of one of them, it is possible to obtain the helical sense of the others. Therefore, two scenarios are possible: $M_1/P_3/P_4/P_2$ or $P_1/M_3/M_4/M_2$.

For its part, when the poly-(*S*)-**1** is dissolved in DMF, a *cis-cisoidal* scaffold is obtained (ω_1> 90°). In this case, an ECD trace with three alternating Cotton bands is obtained, like those found for classical PPAs. However, the relative intensity of the ECD bands is different, being here much more intense than the second one due to the ECD traces generated by the polyene backbone and the metallo-supramolecular array. In this chiral material, five different helices are found, the two coaxial helices —internal (helix 1) and external (helix 2)— and the three helices described by the bispyridyldichloride Pt^{II} complexes axial array (helices 3, 4 and 5). These four helices are interconnected and, by identifying the orientation of one of them, it is possible to obtain the helical sense of the others. Therefore, two scenarios are possible: $P_1/P_3/P_4/P_5/P_2$ or $P_1/M_3/M_4/M_5/M_2$. These results indicate that by a correct design is possible the stabilization of supramolecular helices in covalent polymers, opens a new horizon in the design of novel multi-helical materials. These structures that stabilize metallo-supramolecular polymers in covalent systems also allow the application of these materials in polar solvents which could not be accessed due to the difficulty of generating metal-containing supramolecular polymers in polar solvents.

Chapter VIII. Metallo-Supramolecular Fibers from Phenylacetylene Monomers: Cation Induced Self-Assembly

In conclusion, we have prepared a phenylacetylene derivative that bears a chiral sulfoxide group that forms a chiral supramolecular aggregate in $CHCl_3$ once silver perchlorate is added. In this system, the silver ion forms a linear and planar diacetylide/Ag^+ complex (metal containing monomer) that self-assembles through supramolecular $Ag^+\cdots Ag^+$, $Ag^+\cdots\pi$ and $\pi\cdots\pi$ interactions generating a chiral *J* aggregate that evolves towards fibers or gel depending on the amount of the silver metal ion added. Thus, if the (*R*)-**1**/Ag^+ complex is formed in a 1.0/<1.8 mol/mol ratio, a fiber like structure is obtained, while if a 1.0/>1.8 mol/mol ratio is employed, the fibers grow until reach a gel state. This result is produced by the coordination of the silver ion to the sulfoxide groups placed at the periphery of the fiber. This metal ion can act as crosslinking agent chelating more than one sulfoxide group, which results in the formation of bigger fibers or a gel. This fact provides a great thermal stability to these supramolecular aggregates, which remain unchanged even at 55°C in solution.

In our opinion, this mechanism to form *in situ* chiral supramolecular aggregates by spontaneous aggregation of metal containing monomers opens a new horizon in the preparation of stimuli responsive materials, because it is an inexpensive and greener process with potential applications in sensors, diodes, photovoltaic cells and so on.

Chapter XI

Experimental Sections and Methodology

Experimental Section Chapter III

1. Materials and methods

CD measurements were done in a Jasco-720. The amount of polymer used for CD measurements were 0.3 mg/mL in $CHCl_3$, THF and DMF.

UV spectra were registered in a Jasco V-630. The amount of polymer used for UV measurements were 0.3 mg/mL in $CHCl_3$, THF and DMF.

Irradiation experiments were done in an Asahi Spectra Xenon light model MAX-303. The light was filtered using a short pass filter / Vis 550 nm 25 dia.

Optical rotation was measured in a Jasco-P2000.

NMR experiments were measured in a Varian 300 operating at 300 MHz for proton NMR, 282 MHz for fluorine and 75 MHz for carbon. $CDCl_3$ signal (δ= 77.2ppm) or DMSO-d_6 (δ= 39.5 ppm) was used as standard for ^{1}H or ^{13}C experiments.

GPC studies were made in a Waters Alliance equipped with a Phenomenex GPC columns. The amount of polymer used for GPC measurements was 0.3 mg/mL in THF.

2. Synthesis of monomers

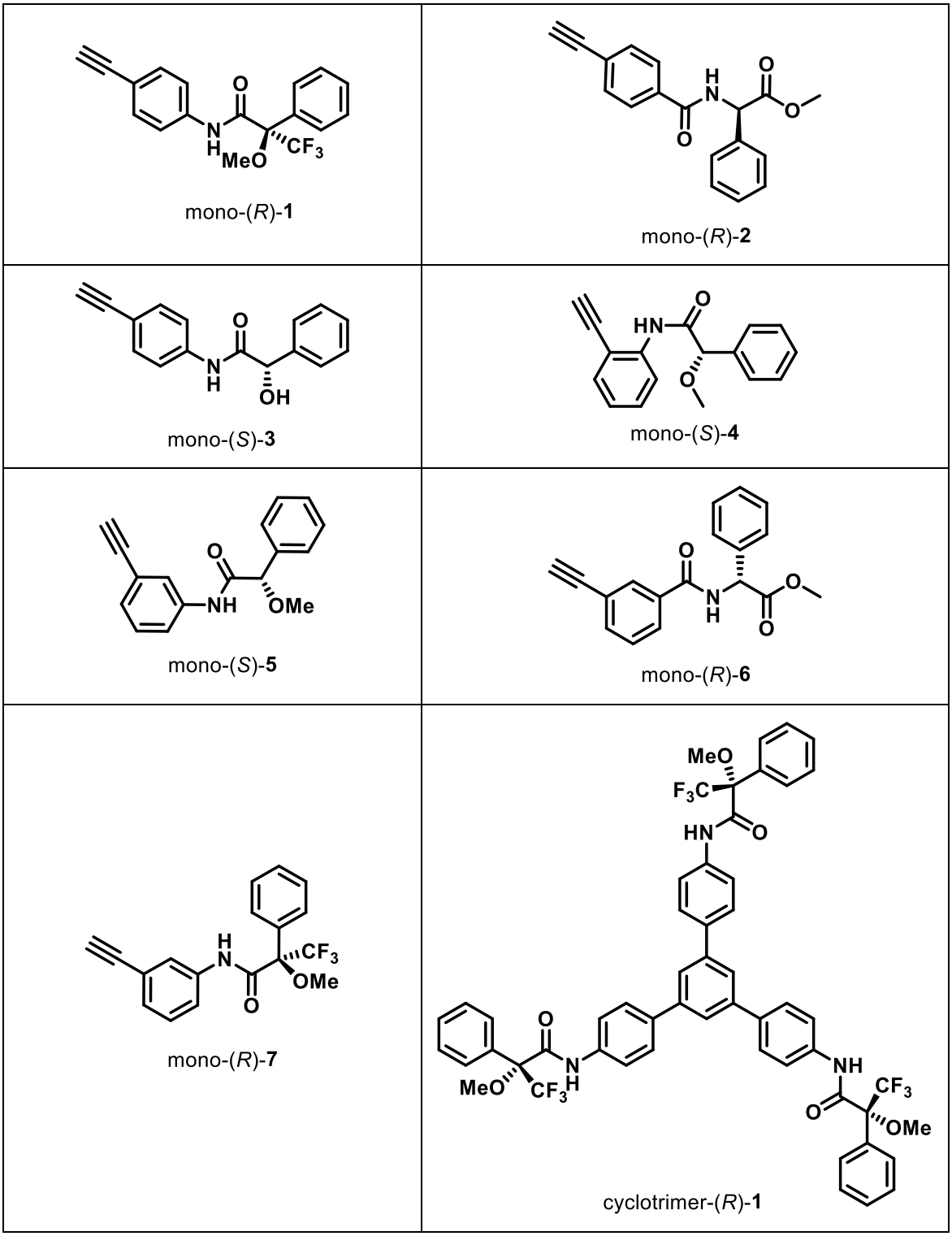

Figure S1. Compounds mono-(*R*)-**1**, mono-(*R*)-**2**, mono-(*S*)-**3**, mono-(*S*)-**4**, mono-(*S*)-**5**, mono-(*R*)-**6**, mono-(*R*)-**7** and cyclotrimer-(*R*)-**1** were prepared following the experimental procedure depicted below.

Mono-(*R*)-**1,** mono-(*R*)-**2** and mono-(*S*)-**3** were prepared according to Ref. **S1**, **S2** and **S3** respectively. Monomers (*S*)**-4**, (*S*)**-5** and (*R*)**-6** were prepared according to Ref. **S4**. For preparation of mono-(*R*)-**7** and cyclotrimer-(*R*)-**1** see experimental details below.

(*R*)-N-(4-ethynylphenyl)-3,3,3-trifluoro-2-methoxy-2-phenylpropanamide [mono-(*R*)-7]:

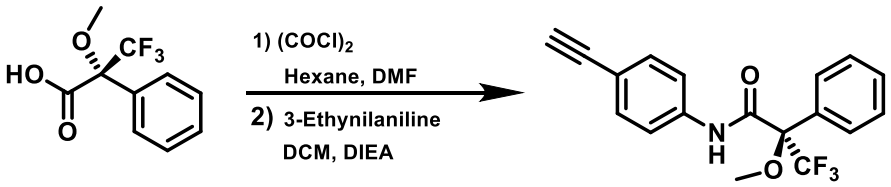

Oxalyl chloride (1.3 mL, 1.4 equiv) was added dropwise to a solution of (*R*)-α-methoxy- α-(trifluoromethyl)phenylacetic acid (0.50 g, 1.0 equiv) in dry hexane (10 mL) and DMF (150 μL, 1.0 equiv) at 0 °C under an Ar atm. After 4 h stirring at rt, the reaction mixture was filtered, and the solution obtained dried under vacuum to give the acetyl chloride. Then (*R*)-α-methoxy-α-(trifluoromethyl)phenylacetyl chloride obtained (0.54 g, 1.0 equiv), was dissolved in DCM (20.0 mL). Next, diisopropyltriethylamine (DIEA, 0.6 mL, 1.6 equiv) and 3-ethynilaniline (250.0 mg, 1.0 equiv) where added to the solution. The reaction mixture was stirred at rt overnight. The residue was diluted with DCM and the organic solution was washed with HCl 1M, saturated $NaHCO_3$ aq solution and saturated NaCl aq solution; then the organic layer was dried over anhydrous Na_2SO_4. After filtration, the solution was evaporated and the residue was chromatographed on silica gel with hexane-AcOEt (7/3, v/v) as eluent, obtaining 0.61 g of mono-(*R*)-**7** (85 % yield) of pure product.

$[\alpha]_D^{20}$ = +4.7 (c = 5.0 mg/mL, $CHCl_3$)

^{1}H NMR (300 MHz, $CHCl_3$) δ(ppm): 3.05 (s, 1H), 3.48 (s, 3H), 7.23-7.29 (m, 2H), 7.38- 7.44 (m, 3H), 7.53-7.61 (m, 3H), 7.73 (s, 1H) 8.60 (broad s, 1H)

^{19}F NMR (282.3 MHz, $CHCl_3$) δ (ppm): -68.6

^{13}C NMR (75 MHz, $CHCl_3$) δ (ppm): 55.3, 77.8, 82.8, 120.3, 121.8, 123.0, 123.3, 125.6, 127.7, 128.7, 128.8, 129.1, 129.8, 132.0, 136.8, 164.4.

HRMS (ESI) m/z calcd for $C_{18}H_{15}F_3NO_2$ $[M+H]^+$: 334.1010, found: 334.1052.

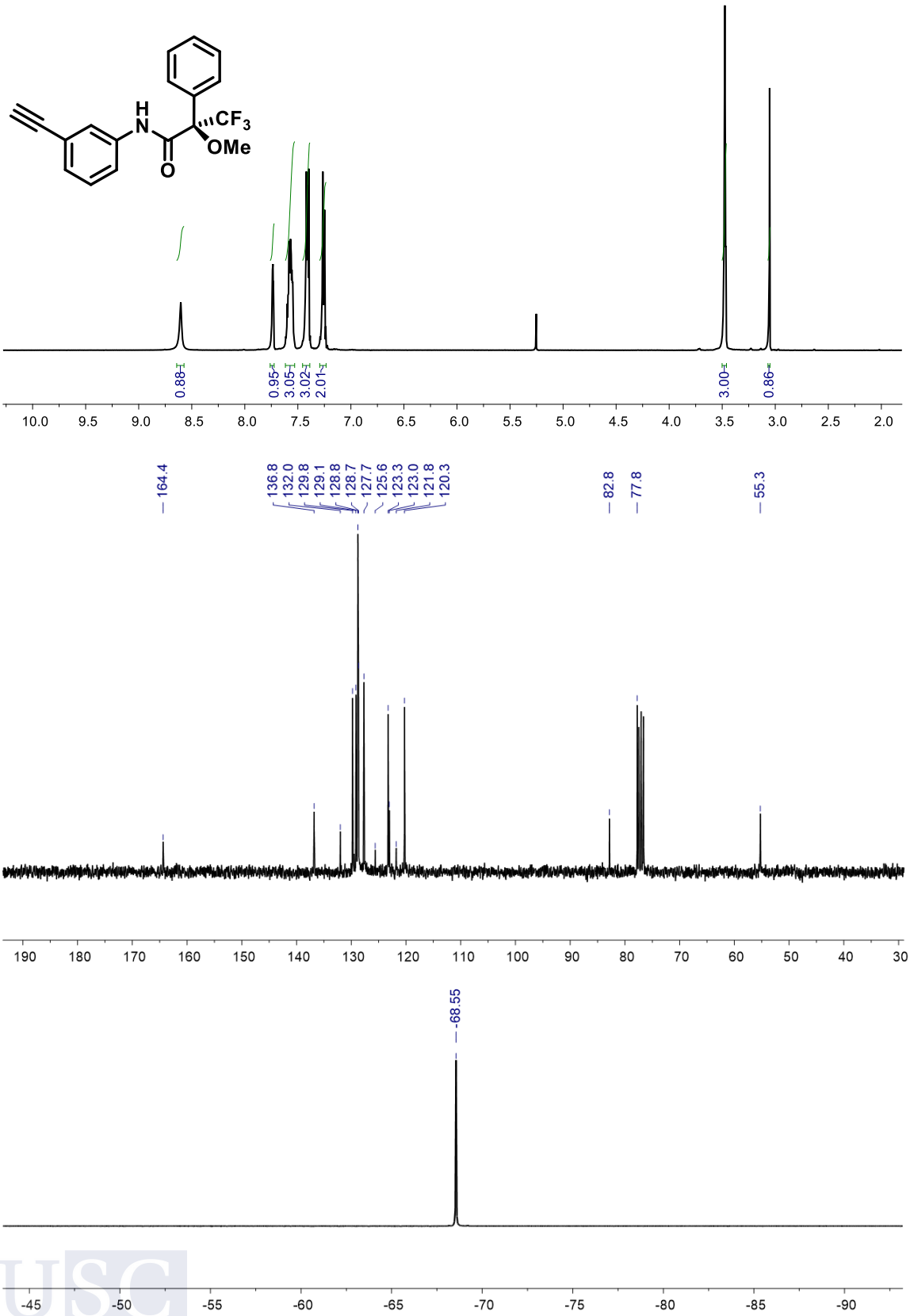

Figure S2. ^{1}H, ^{13}C and ^{19}F NMR spectra of mono-(*R*)-**7** ($CDCl_3$, 300, 75 and 282 MHz respectively).

1,3,5-tri-(*R*)-3,3,3-trifluoro-2-methoxy-N,2-diphenylpropanamidebenzene [cyclotrimer-(*R*)-1]:

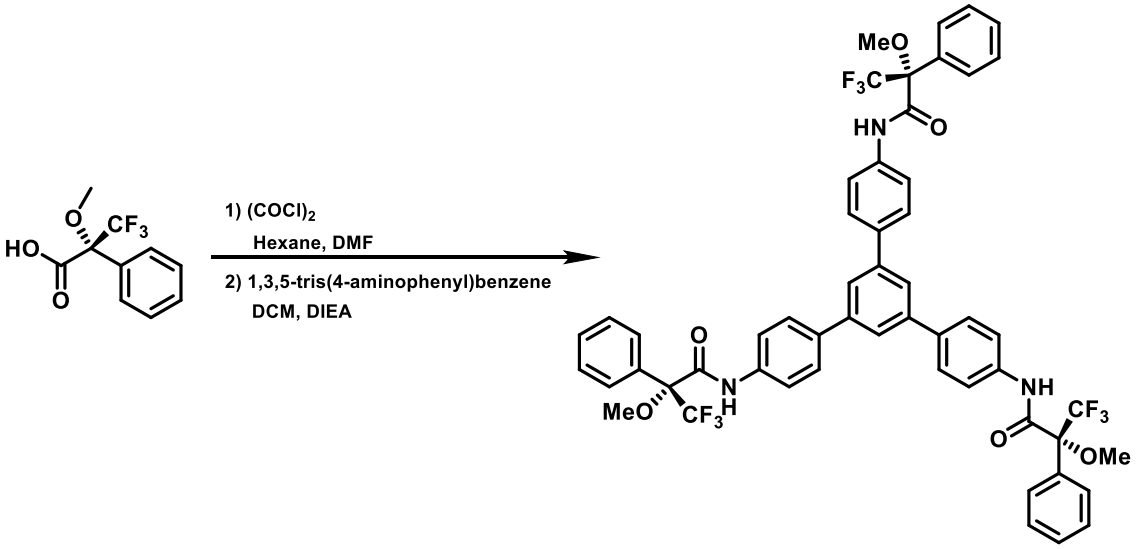

Oxalyl chloride (1.3 mL, 1.4 equiv) was added dropwise to a solution of (*R*)-α-methoxy- α-(trifluoromethyl)phenylacetic acid (0.50 g, 1.0 equiv) in dry hexane (10 mL) and DMF (150 μL, 1.0 equiv) at 0 °C under an Ar atm. The reaction was allowed to reach room temperature and stirred during 4h. Next, the reaction mixture was filtered, and dried under vacuum to yield corresponding the acetyl chloride derivative. Then, (*R*)-α-methoxy-α-(trifluoromethyl)phenylacetyl chloride (0.54 g, 1.0 equiv) was dissolved in DCM (20.0 mL) and diisopropyltriethylamine (DIEA, 0.6 mL, 1.6 equiv) and 1,3,5-tris(4-aminophenyl)benzene (250.0 mg, 0.33 equiv) where added to the solution. The reaction mixture was stirred at rt overnight. The residue was diluted with DCM and the organic solution was washed with HCl 1M, saturated $NaHCO_3$ aq solution and saturated NaCl aq solution, and then dried over anhydrous Na_2SO_4. After filtration, the solution was evaporated and the residue was chromatographed on silica gel with hexane-AcOEt (7/3, v/v) as eluent, obtaining 0.63 g of cyclotrimer-**1** (85 % yield) of pure product.

$[\alpha]_D^{20}$ = +304.77 (c = 10.0 mg/mL, $CHCl_3$)

^{1}H NMR (300 MHz, $CHCl_3$) δ(ppm): 3.53 (s, 9H), 7.39- 7.48 (m, 9H), 7.56-7.63 (m, 6H), 7.64-7.74 (m, 15H), 8.64 (s, 3H)

^{19}F NMR (282.3 MHz, $CHCl_3$) δ (ppm): -68.6

^{13}C NMR (75 MHz, $CHCl_3$) δ (ppm): 55.8, 120.7, 122.4, 125.1, 126.2, 128.3, 128.5, 129.3, 130.3, 132.7, 136.9, 138.2, 142.2, 164.9.

HRMS (ESI) m/z calcd for $C_{18}H_{15}F_3NO_2$ $[M+H]^+$: 1000.3008, found: 1000.2990

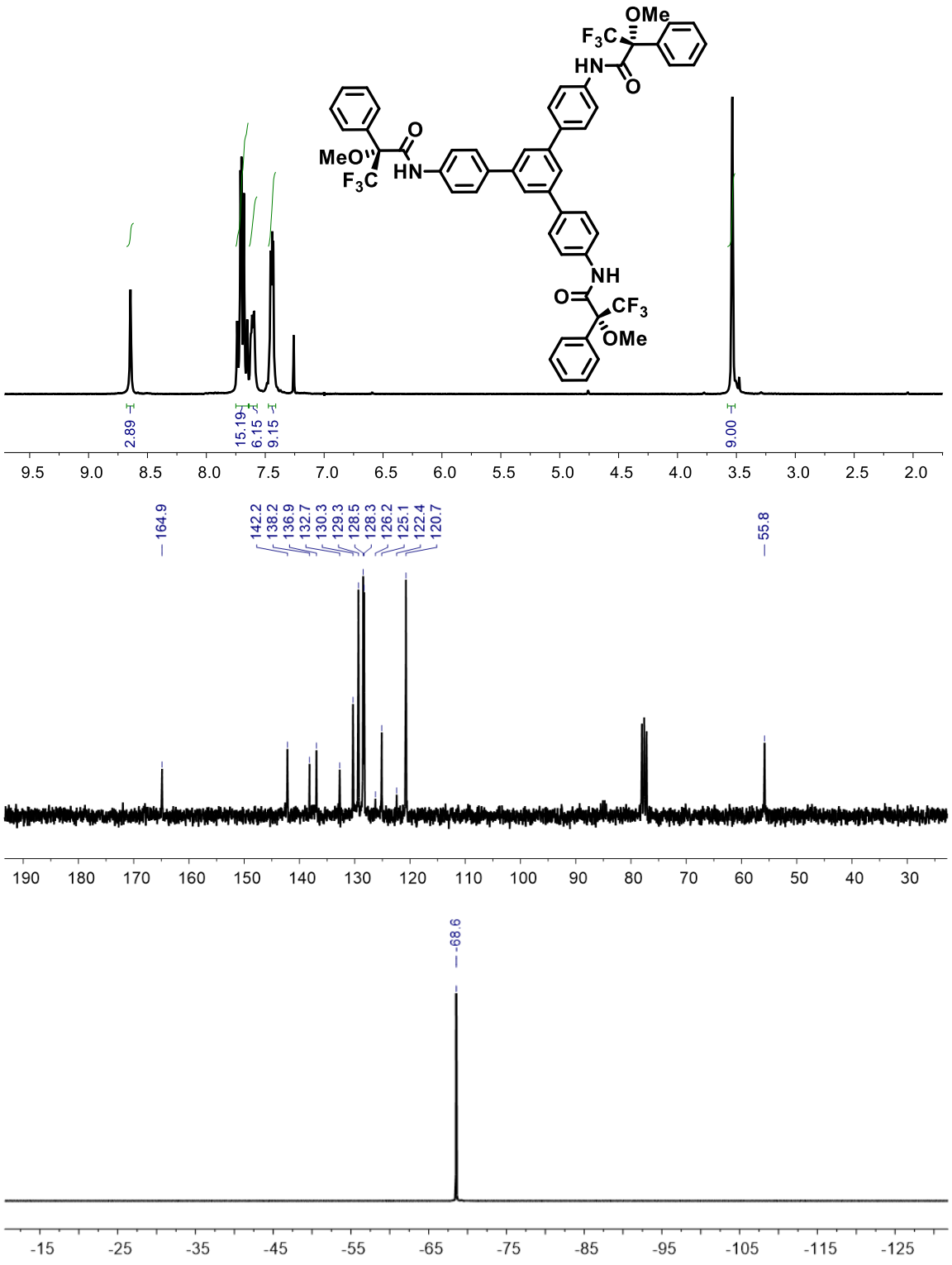

Figure S3. ^{1}H, ^{13}C and ^{19}F NMR spectra of cyclotrimer-(*R*)-**1** ($CDCl_3$, 300, 75 and 282 MHz respectively).

3. Synthesis of polymers

General procedure for polymerization

The reaction flask (sealed ampoule) was dried under vacuum and argon flushed for three times before monomer was added as a solid. Then, the flask was evacuated on a vacuum line and flushed with dry argon (three times). Dry THF was added with a syringe and the triethylamine dropwise. A solution of rhodium norbornadiene chloride dimer, $[Rh(nbd)Cl]_2$, in THF was added at 30 °C. The reaction mixture was stirring at 30 °C for 6 h. Then, the resulting polymer was diluted in CH_2Cl_2 and it was precipitated in a large amount of methanol, centrifuged (2 times), reprecipitated in hexane and centrifuged again.

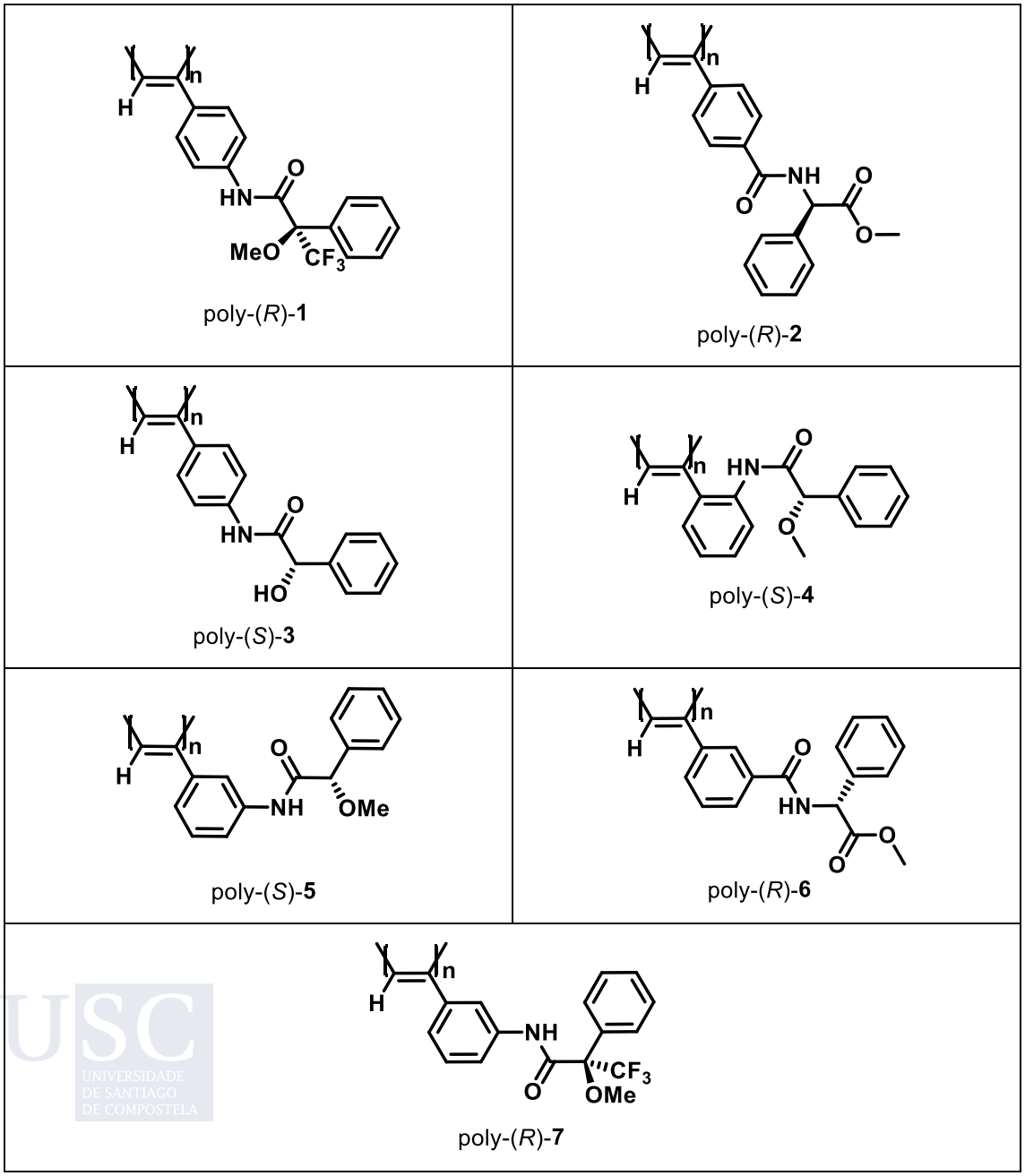

Figure S4. Structure of the polymers prepared in this work.

Table 1. Polymerization conditions of the corresponding polymers.

Polymer	Mass (mg)	THF (mL)	$[Rh(nbd)Cl]_2$ (mg)	EEt_3N ((µL)	Yield (%)
Poly-(*R*)-**1**	100	1.0	1.0	5	92
Poly-(*R*)-**2**	100	1.0	1.0	5	91
Poly-(*S*)-**3**	100	1.0	1.0	5	90
Poly-(*S*)-**4**	100	1.0	1.0	5	86
Poly-(*S*)-**5**	100	1.0	1.0	5	82
Poly-(*R*)- **6**	100	1.0	1.0	5	65
Poly-(*R*)-**7**	100	1.0	1.0	5	81

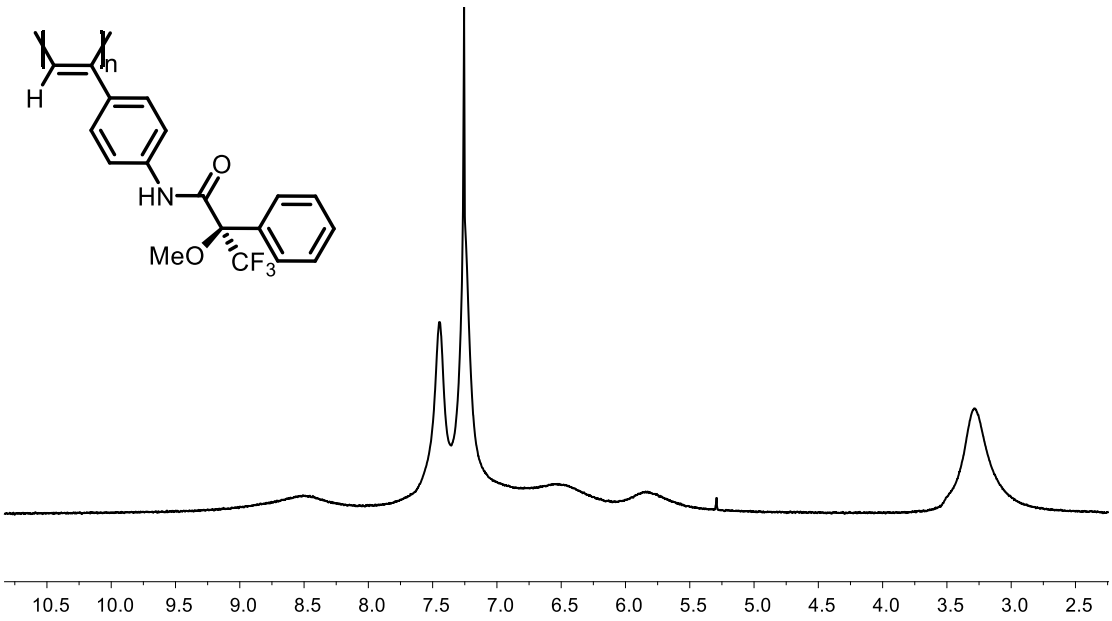

Figure S5. ^1H NMR spectra of poly-(*R*)-**1** ($CDCl_3$, 300 MHz).

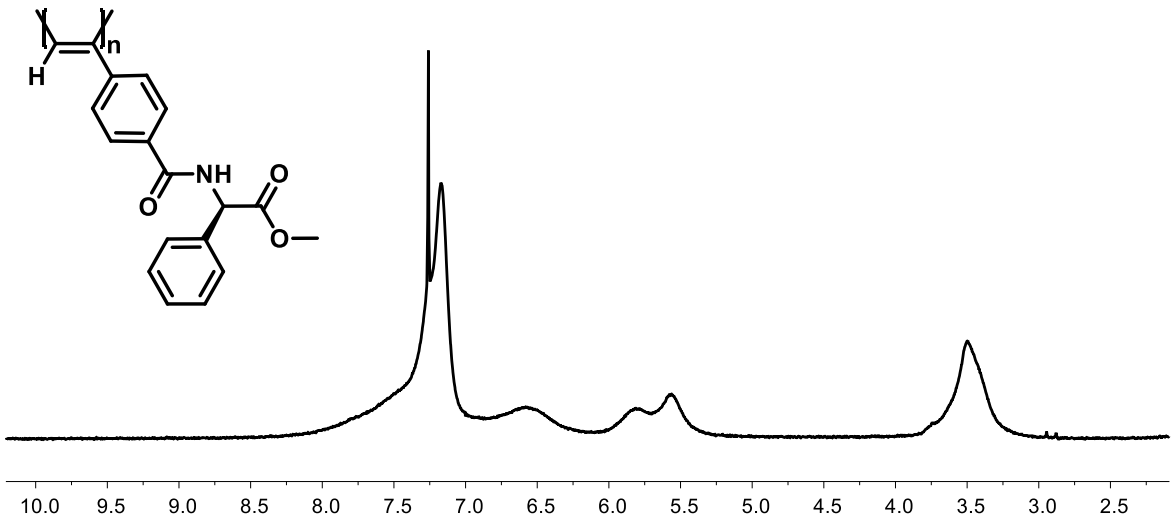

Figure S6. ^{1}H NMR spectra of poly-(*R*)-**2** ($CDCl_3$, 300 MHz).

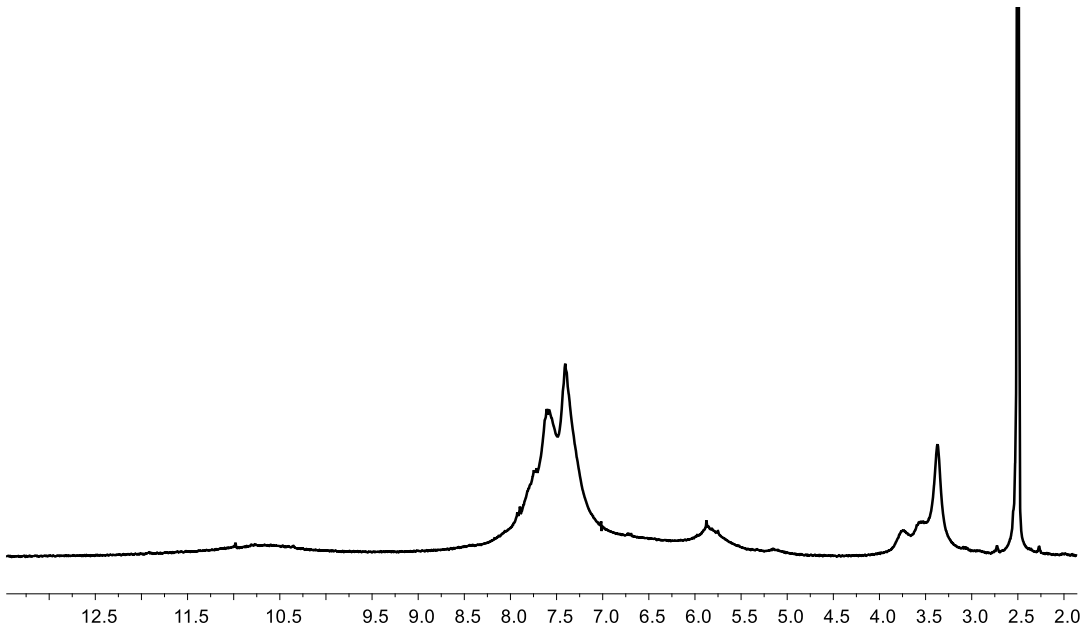

Figure S7. ^{1}H NMR spectra of poly-(*S*)-**3** (DMSO, 300 MHz).

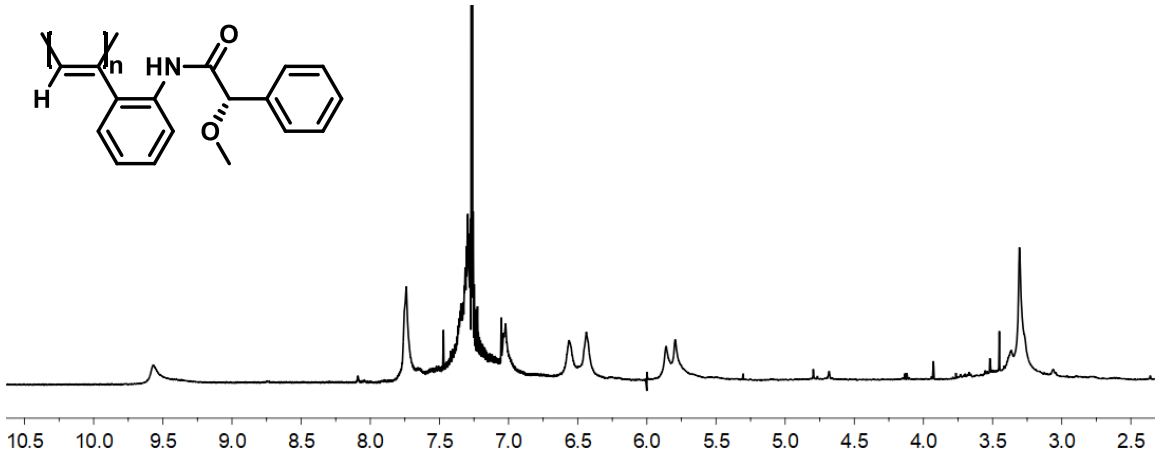

Figure S8. ^{1}H NMR spectra of poly-(*S*)-**4** ($CDCl_3$, 300 MHz).

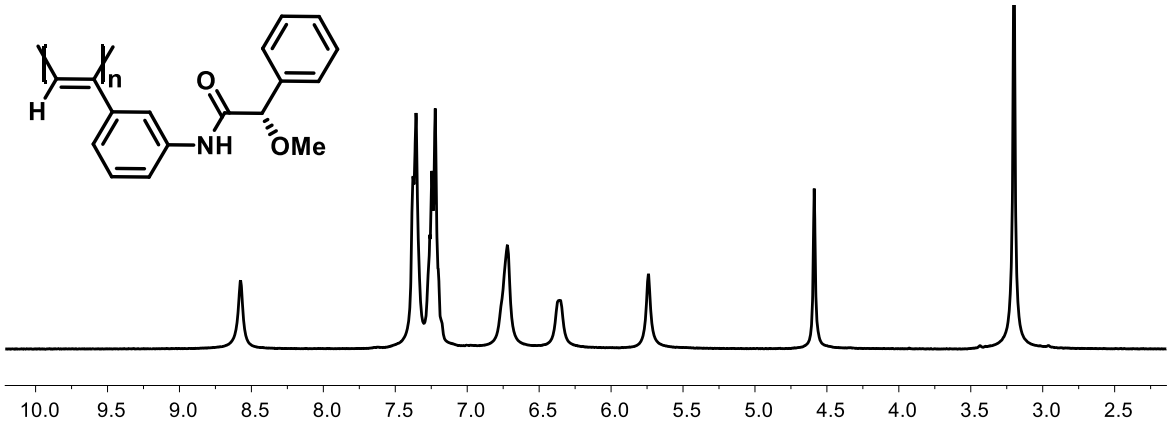

Figure S9. ^{1}H NMR spectra of poly-(*S*)-**5** ($CDCl_3$, 300 MHz).

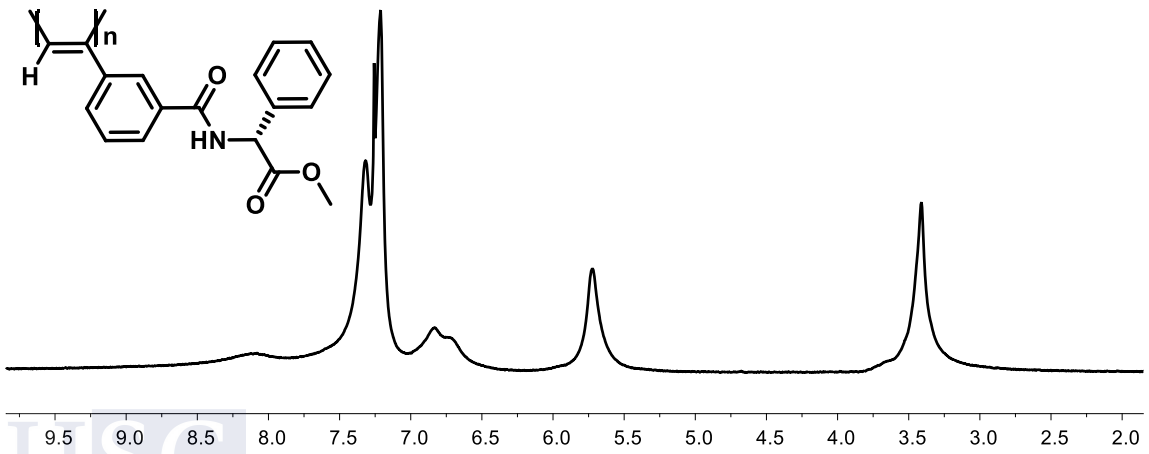

Figure S10. ^{1}H NMR spectra of poly-(*R*)-**6** ($CDCl_3$, 300 MHz).

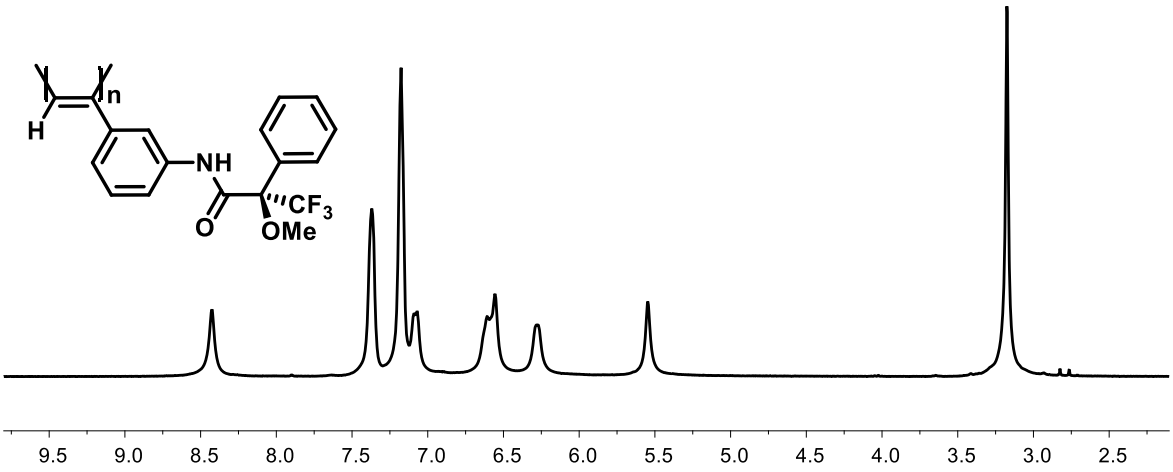

Figure S11. ^{1}H NMR spectra of poly-(*R*)-**7** ($CDCl_3$, 300 MHz).

4. General Protocol for PPA Irradiation

To perform the photochemical electrocyclization studies, we employed the methodology depicted in Scheme S1 (see below). 0.3 mg/mL solutions of the corresponding PPAs were prepared (Poly-**1**/**6**), potential acid traces present in $CHCl_3$ were removed by filtering the solvent through basic alumina. The solutions were deoxygenated prior to light irradiation by bubbling Ar for 5 min. 0.2 mL of purged solution of the corresponding polymer were transferred to a 1 mm cuvette to measure CD/UV-Vis spectra —being this spectrum t= 0 min of irradiation— and 7.0 mL of solution was transferred to a second flask under Ar atmosphere.

Irradiation experiments were performed using a collimator Lens (x1.0) of a MAX-303 (Asahi Spectra) equipped with a UV-VIS mirror module (300-600 nm) using a shortpass filter (VIS 550nm 25 dia.). After the 20 minutes required for the irradiation source stabilization, the light beam (with the intensity selected at 100%) was directly focused to the flask containing the 7.0 mL of purged polymer solution. The irradiation system was covered to avoid the incidence of any additional light. Following the abovementioned procedure, the polymer solutions were irradiated for the desired times, recording after each time the CD spectrum by transferring aliquots of 200 μL of polymer solution to a 1 mm cuvette, via syringe, keeping the system under an inert atmosphere and without interrupting the irradiation process.

For polymers measured on 10 mm cuvettes, the irradiation process is halted by closing the irradiation path of the light source. Next, 2.0 mL of the corresponding polymer solution was taken via syringe and CD/UV-Vis spectra were consequently measured. After measurement, the polymer solution is reintroduced into the flask where the irradiation process takes place, and the path light is open again.

Note that the time while the light source remains closed is not taken into consideration in the total time. Remarkably, without light irradiation the reaction stops immediately, and the obtained CD trace remains constant.

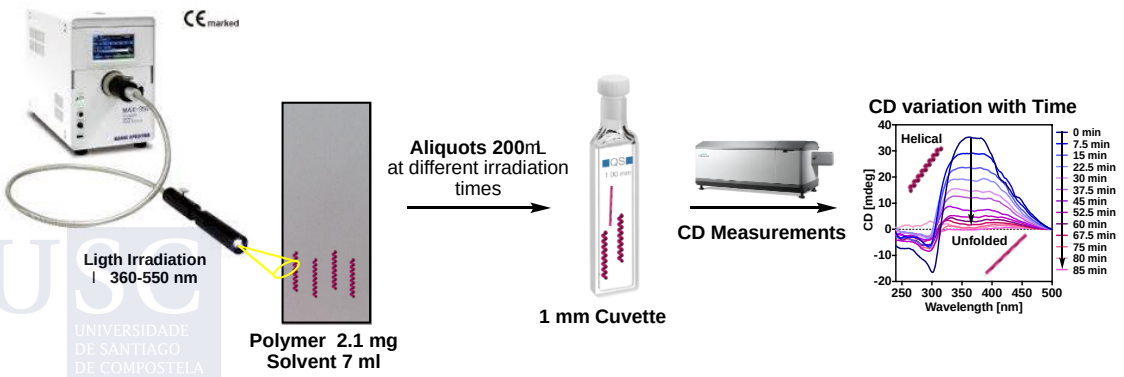

Scheme S1. Schematic illustration of the irradiation process to study the photochemical electrocyclization of PPAs.

5. Spectrum of the light filter

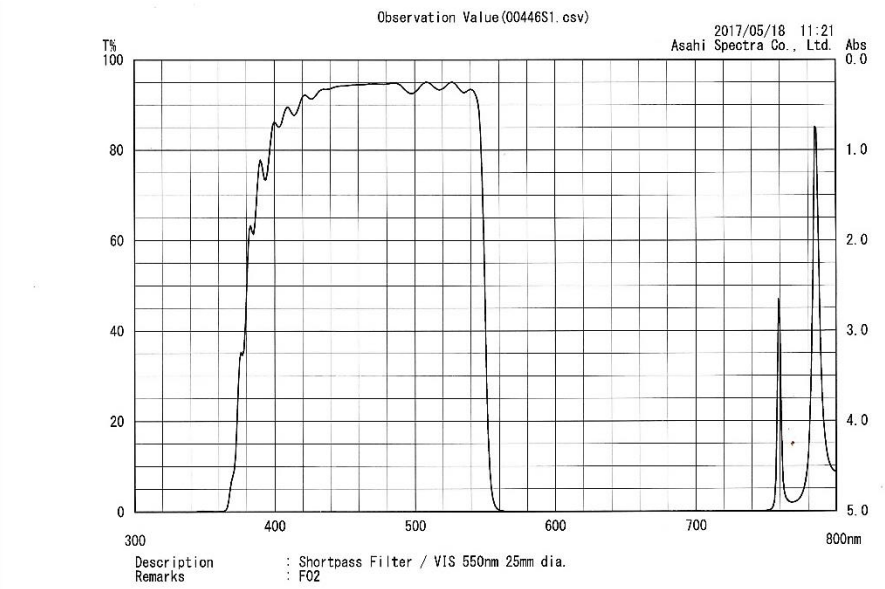

Image 1. Abs and T% spectrum of the short pass filter (VIS 550nm 25 dia.).

6. PPA photochemical electrocyclization: ECD Studies

Poly-(*R*)-1

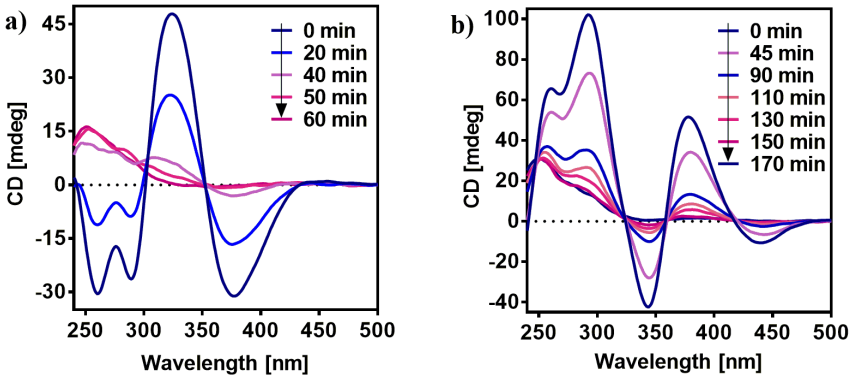

Figure S12. CD spectra in (a) $CHCl_3$ (b) THF of poly-(*R*)-**1** after irradiation under visible light in $CHCl_3$. The spectra were measured in a **1 mm quartz cuvette**. [poly-(*R*)-**1**]= $9.00 \cdot 10^{-4}$ M.

Poly-(*R*)-2

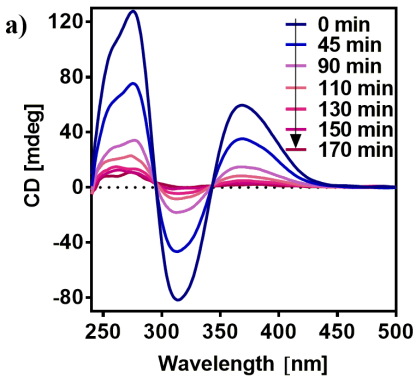

Figure S13. CD spectra of poly-(*R*)-**2** after irradiation under visible light in $CHCl_3$. The spectra were measured in a **1 mm quartz cuvette**. [poly-(*R*)-**2**]= $1.02 \cdot 10^{-3}$ M.

Poly-(*S*)-3

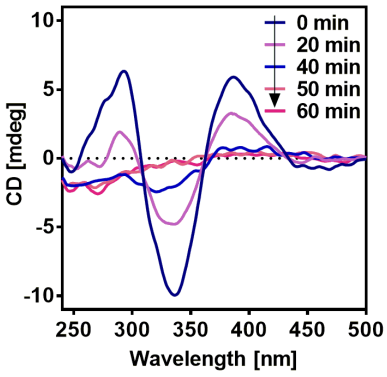

Figure S14. CD spectra of poly-(*S*)-**3** after irradiation under visible light in THF. The spectra were measured in a **1 mm quartz cuvette**. [poly-(*S*)-**3**]= $1.19 \cdot 10^{-3}$ M.

Poly-(*S*)-4

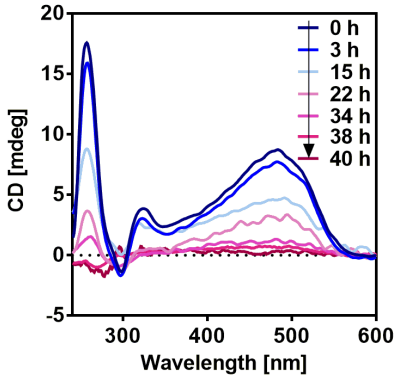

Figure S15. CD spectra of poly-(*S*)-**4** after irradiation under visible light in $CHCl_3$. The spectra were measured in a **1 mm quartz cuvette**. [poly-(*S*)-**4**]= $1.13 \cdot 10^{-3}$ M.

Poly-(*S*)-5

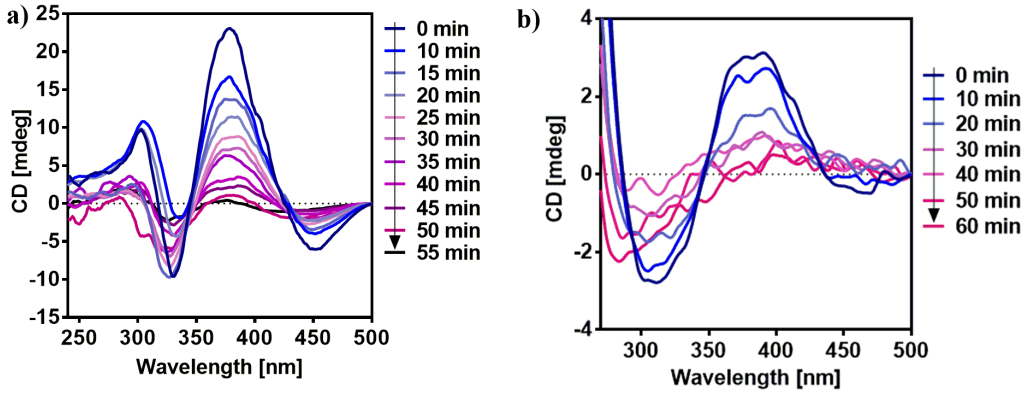

Figure S16. CD spectra of poly-(*S*)-**5** after irradiation under visible light in $CHCl_3$. The spectra were measured in a (a) **10 mm quartz cuvette** and (b) **1 mm quartz cuvette**. [poly-(*S*)-**5**]= $1.13 \cdot 10^{-3}$ M.

Poly-(*R*)-6

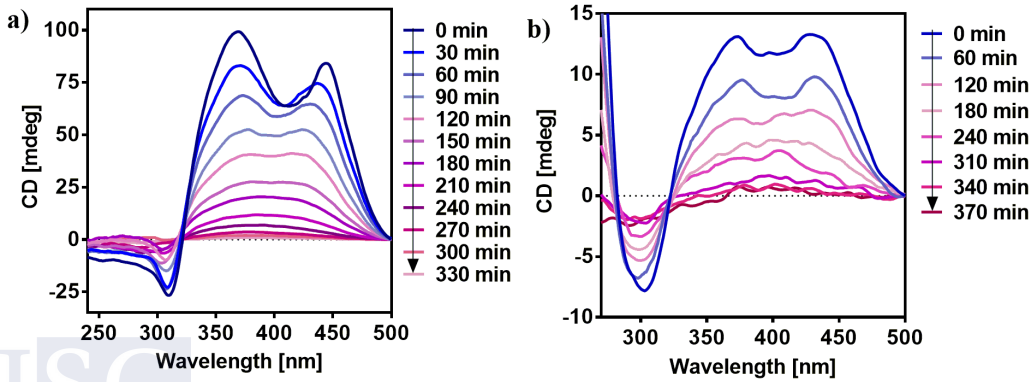

Figure S17. (a) CD spectra of poly-(*R*)-**6** after irradiation under visible light in $CHCl_3$. The spectra were measured in a (a) **10 mm quartz cuvette** and (b) **1 mm quartz cuvette**. [poly-(*R*)-**6**]= $1.02 \cdot 10^{-3}$ M.

Poly-(*R*)-7

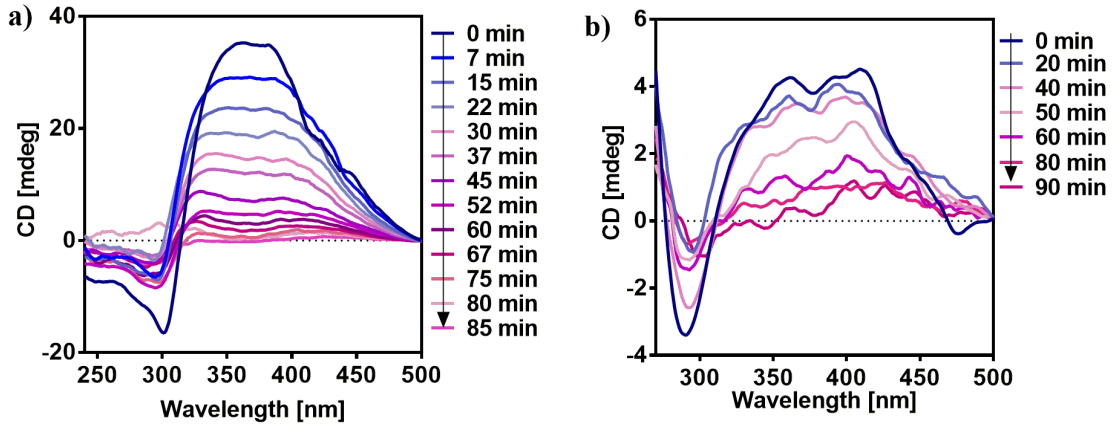

Figure S18. CD spectra of poly-(*R*)-**7** after irradiation under visible light in $CHCl_3$. The spectra were measured in a (a) **10 mm quartz cuvette** and (b) **1 mm quartz cuvette**. [poly-(*R*)-**7**]= $9.00 \cdot 10^{-4}$ M.

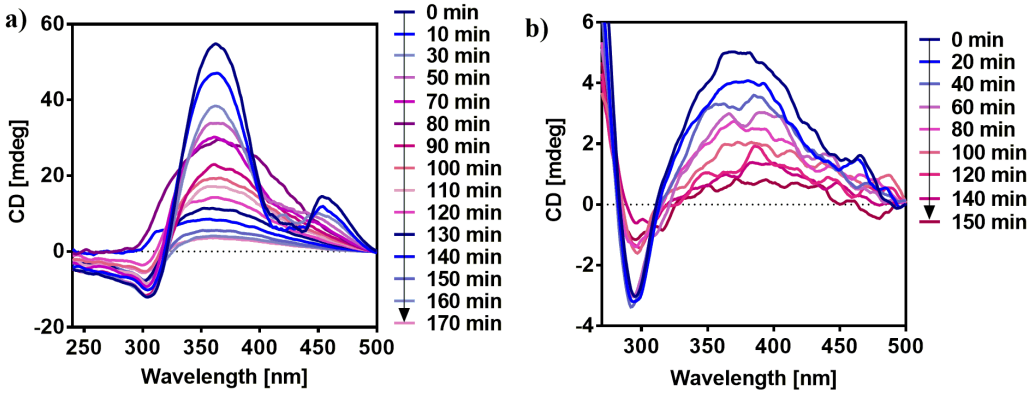

Figure S19. CD spectra of poly-(*R*)-**7** after irradiation under visible light in THF. The spectra were measured in a (a) **10 mm quartz cuvette** and (b) **1 mm quartz cuvette**. [poly-(*R*)-**7**]= $9.00 \cdot 10^{-4}$ M.

7. PPA photochemical electrocyclization: UV-Vis Studies

Poly-(*R*)-1

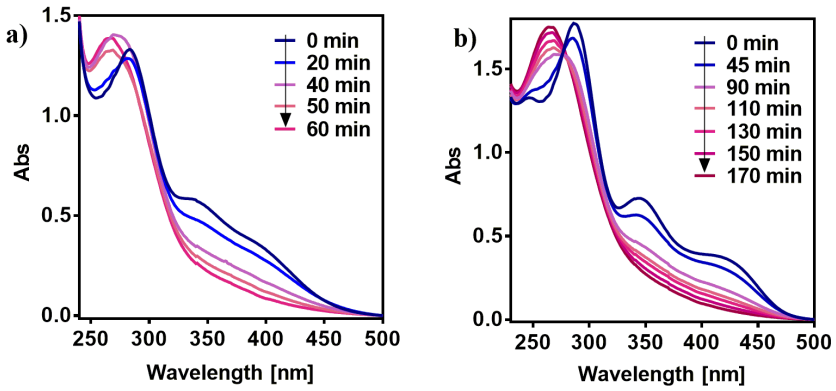

Figure S20. UV spectra in (a) $CHCl_3$ (b) THF of poly-(*R*)-**1** after irradiation under visible light in $CHCl_3$. The spectra were measured in a **1 mm cuvette**. [poly-(*R*)-**1**]= $9.00 \cdot 10^{-4}$ M.

Poly-(*R*)-2

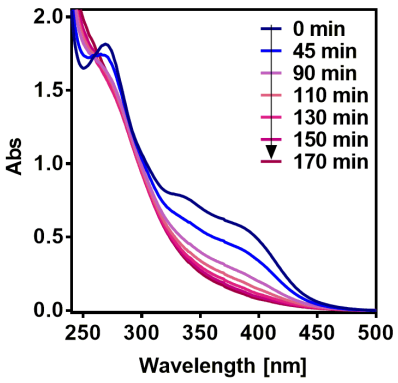

Figure S21. UV spectra of poly-(*R*)-**2** after irradiation under visible light in $CHCl_3$. The spectra were measured in a **1 mm cuvette**. [poly-(*R*)-**2**]= $1.02 \cdot 10^{-3}$ M.

Poly-(*S*)-3

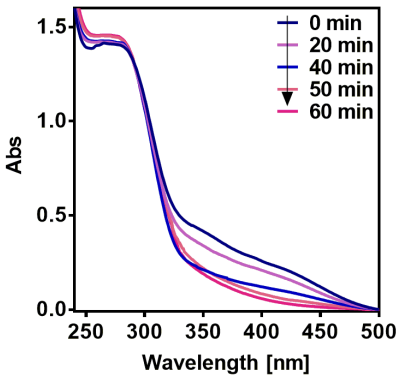

Figure S22. UV spectra of poly-(*S*)-**3** after irradiation under visible light in THF. The spectra were measured in a **1 mm cuvette**. [poly-(*S*)-**3**]= $1.19 \cdot 10^{-3}$ M.

Poly-(*S*)-4

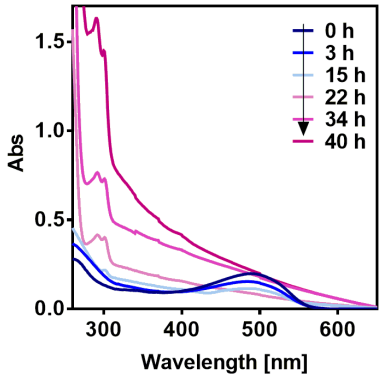

Figure S23. UV spectra of poly-(*S*)-**4** after irradiation under visible light in $CHCl_3$. The spectra were measured in a **1 mm cuvette**. [poly-(*S*)-**4**]= $1.13 \cdot 10^{-3}$ M.

Poly-(*S*)-5

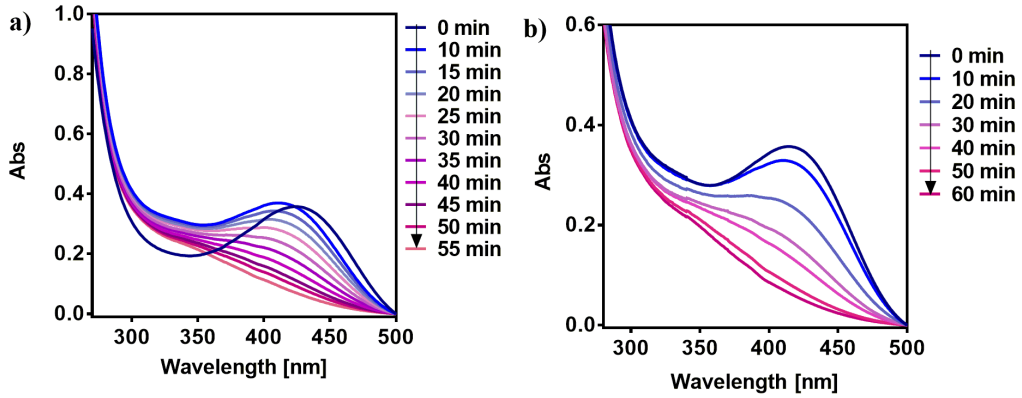

Figure S24. UV spectra of poly-(*S*)-**5** under irradiation visible light in $CHCl_3$ in two different modes: (a) start/stop UV-vis light irradiation during the UV-measurement and (b) continuous irradiation. The spectra were measured in a **1 mm cuvette**. [poly-(*S*)-**5**]= $1.13 \cdot 10^{-3}$ M.

Poly-(*R*)-6

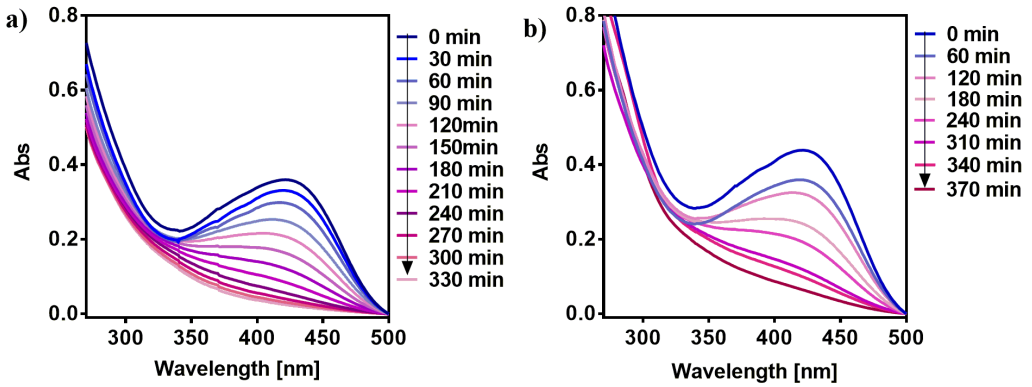

Figure S25. UV spectra of poly-(*R*)-**6** under irradiation visible light in $CHCl_3$ in two different modes: (a) start/stop UV-vis light irradiation during the UV-measurement and (b) continuous irradiation. The spectra were measured in a **1 mm cuvette**. [poly-(*R*)-**6**]= $1.02 \cdot 10^{-3}$ M.

Poly-(*R*)-7

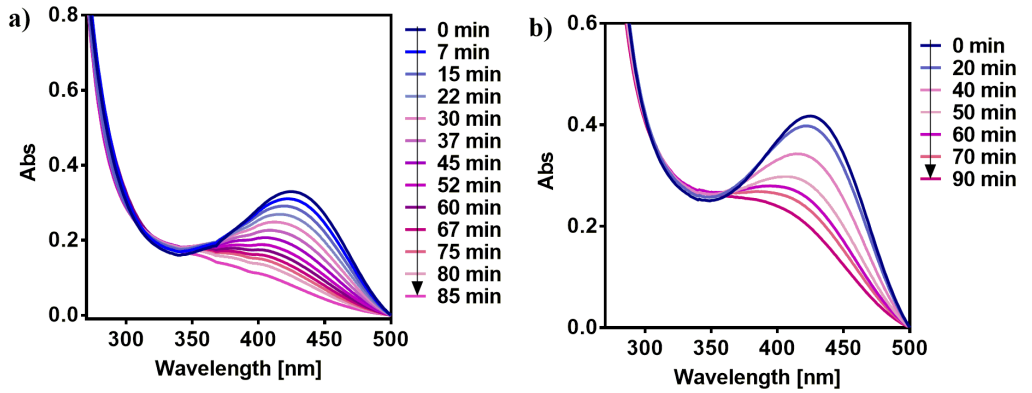

Figure S26. UV spectra of poly-(*R*)-**7** under irradiation visible light in $CHCl_3$ in two different modes: (a) start/stop UV-vis light irradiation during the UV-measurement and (b) continuous irradiation. The spectra were measured in a **1 mm cuvette.** [poly-(*R*)-**7**]= $9.00 \cdot 10^{-4}$ M.

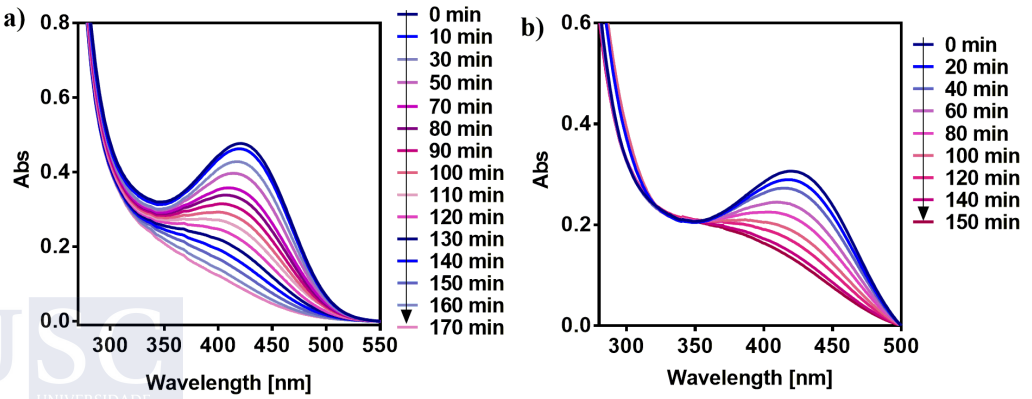

Figure S27. (a) CD and (b) UV spectra of poly-(*R*)-**7** under irradiation visible light in THF in two different modes: (a) start/stop UV-vis light irradiation during the UV-measurement and (b) continuous irradiation. The spectra were measured in a **1 mm cuvette**. [poly-(*R*)-**7**]= $9.00 \cdot 10^{-4}$ M.

8. Extra irradiation studies after PPA photochemical electrocyclization

Mass spectrometry of poly-(*R*)-1 after irradiation during 6h

The photochemical electrocyclization process (null CD) for poly-(*R*)-**1** in $CHCl_3$ was reached in 60 min of irradiation. However, by MS-ESI studies it was determined that at least five extra hours are needed to detect the formation of the correspond cyclic trimer due to the aromatic photocyclic reaction.

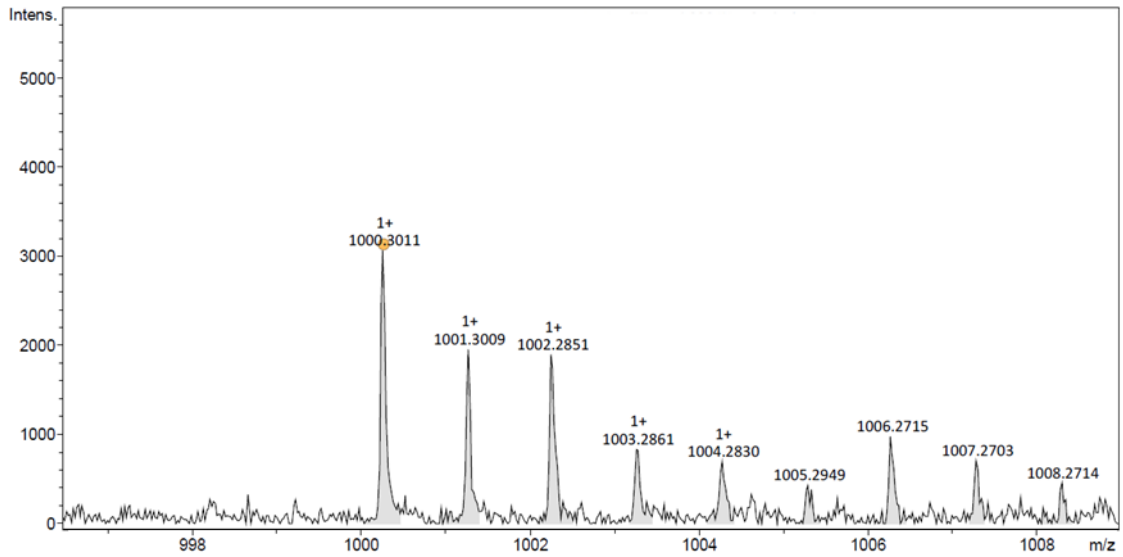

Figure S28. ESI-MS spectrum of poly-(*R*)-**1** after irradiation under visible light. HRMS (ESI) m/z= 1000.3011 correspond to the 1,3,5-trisubstituted benzene formed from poly-(*R*)-**1**. HRMS (ESI) m/z calcd for $C_{54}H_{42}F_9N_3O_6$ $[M+H]^+$: 1000.3008, found: 1000.3011.

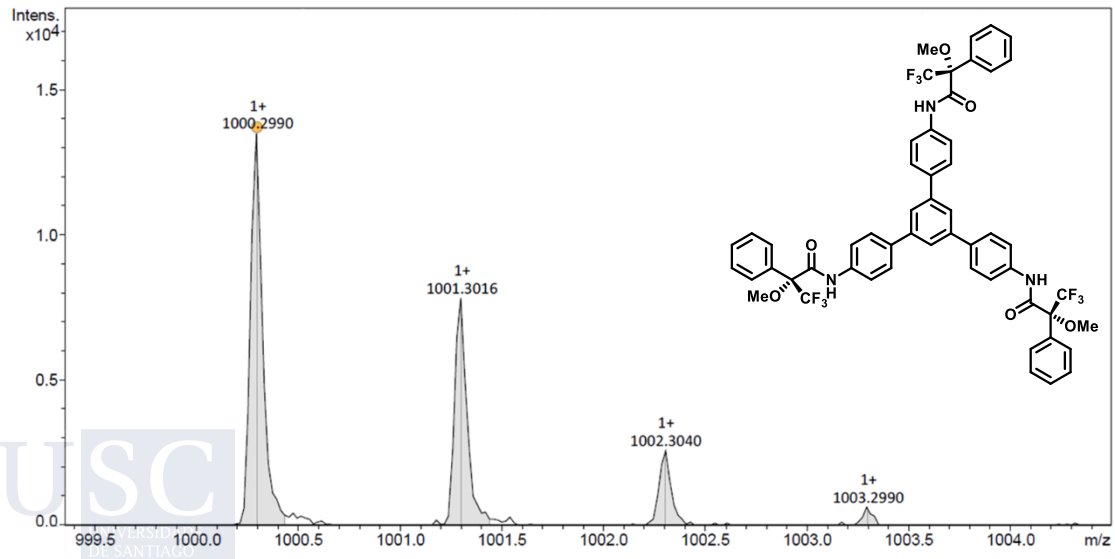

Figure S29. ESI-MS spectrum of cyclotrimer-**1**. HRMS (ESI) m/z calcd for $C_{54}H_{42}F_9N_3O_6$ $[M+H]^+$: 1000.3008, found: 1000.2990.

Polymer size effects

Two batches of poly-(*R*)-**1** was polymerized to get long and short chains of polymer (Figure S30c) to study the effect of the chain length in the photochemical electrocyclization process. Both batches of poly-(*R*)-**1** were irradiated in solution of $CHCl_3$ (Figures S30a and 30b) applying the standard methodology described in this work. The results show that, independently of the chain length, the values gotten were similar for the two PPAs (figure S30d).

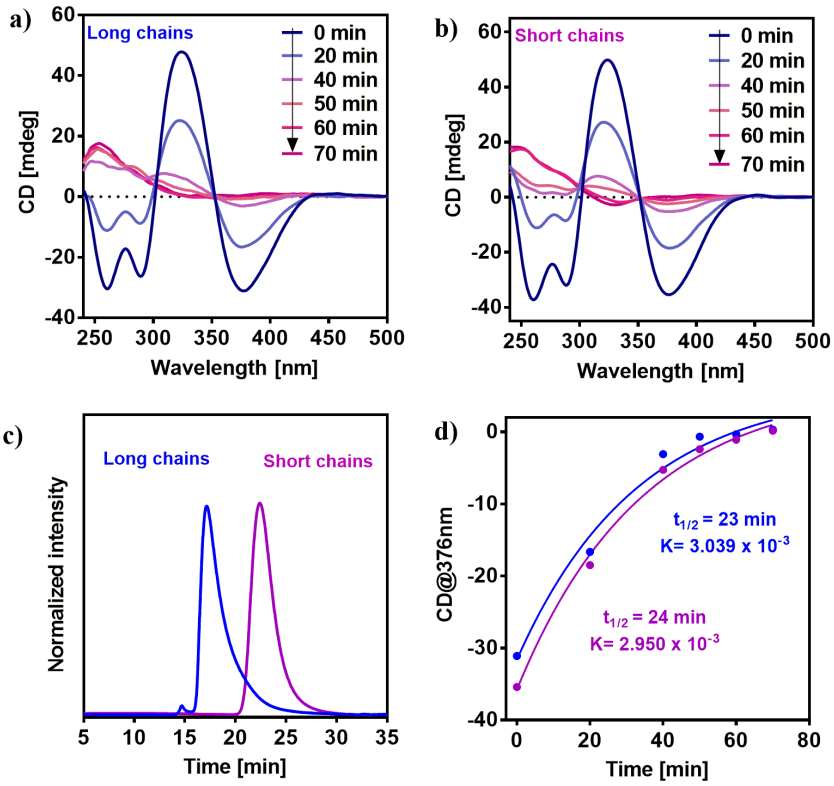

Figure S30. CD spectra of poly-(*R*)-**1** at different times of irradiation for (a) long chains and (b) short chains of polymer, the spectra were measured in a **1 mm cuvette**. (c) GPC chromatograms of the two poly-(*R*)-**1** chain lengths. (d) First order reaction fit obtained for the CD signal decay *vs* time for the two chain lengths.

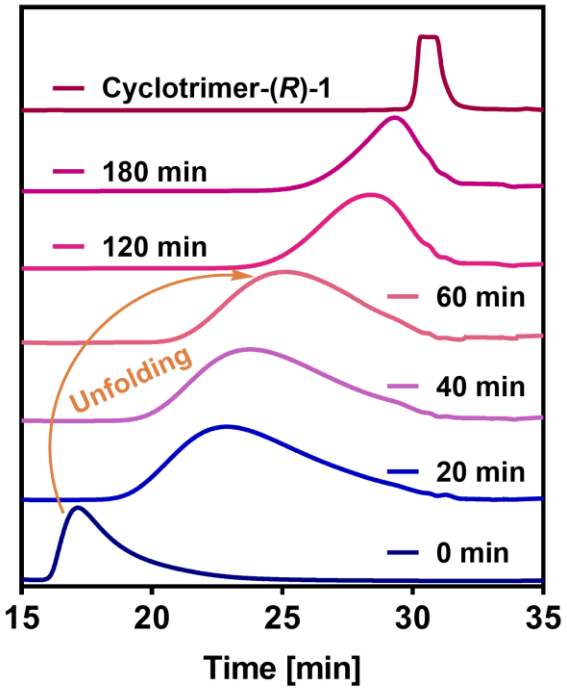

Figure S31. Comparison of GPC chromatograms of poly-(*R*)-**1** after irradiation under visible light in $CHCl_3$ at different times and the synthesized cyclotrimer-(*R*)-**1**.

9. ECD signal decay studies at different wavelengths for poly-(*S*)-5 and poly-(*R*)-6

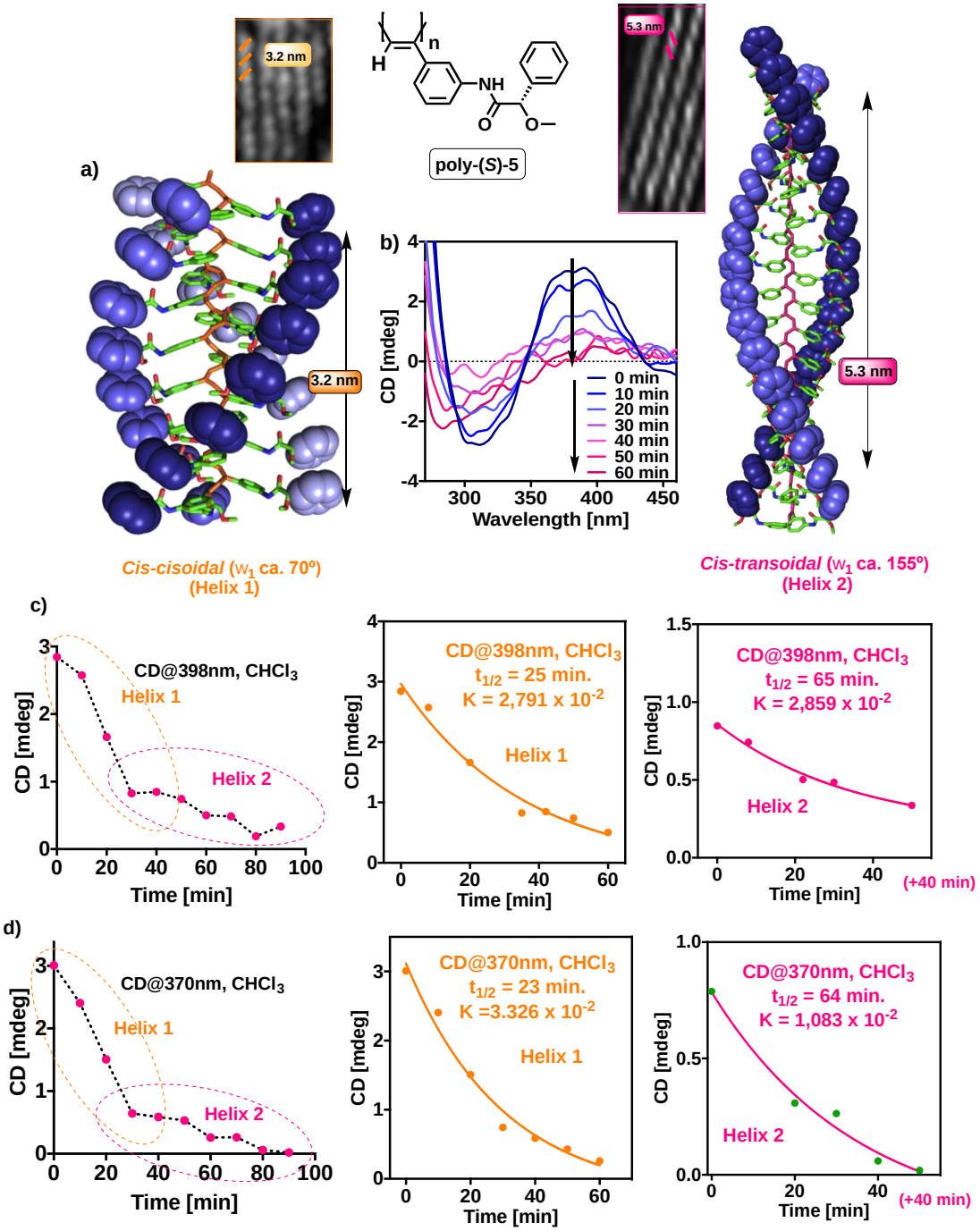

Figure S32. (a) Chemical structure and representative *cis-cisoidal* and *cis-transoidal* helical scaffolds adopted by poly-(*S*)-**5**. (b) CD spectra of poly-(*S*)-**5** at different times of irradiation under visible light. ECD signal decay at (c) 398 and (d) 370 nm *vs* time for poly-(*S*)-**5** after irradiation with visible light. [poly-(*S*)-**5**]= $1.13 \cdot 10^{-3}$ M, $CHCl_3$. The spectra were measured in a **1 mm cuvette**.

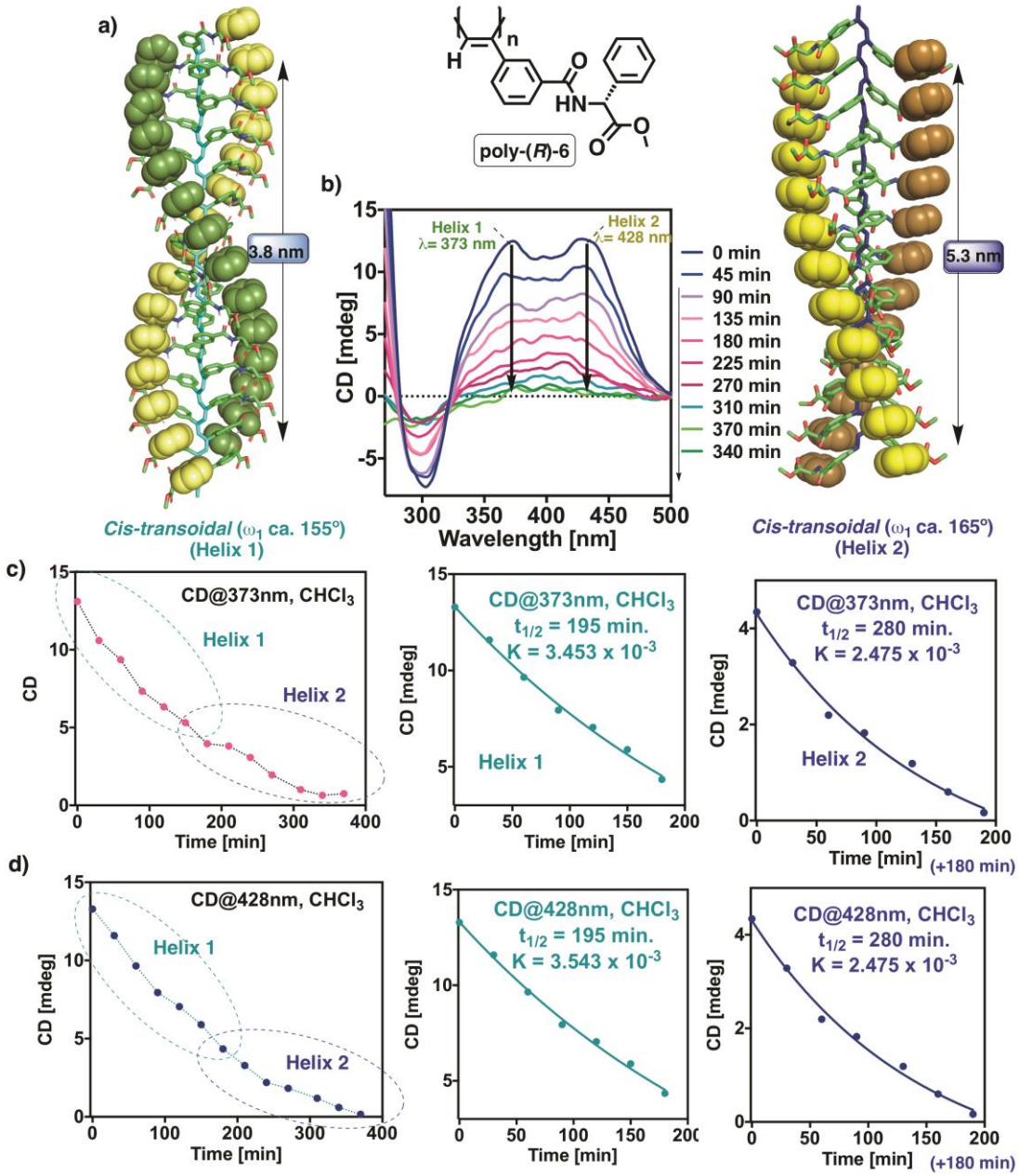

Figure S33. (a) Chemical structure and representative *cis-cisoidal* and *cis-transoidal* helical scaffolds adopted by poly-(*R*)-**6**. (b) CD spectra of poly-(*R*)-**6** at different times of irradiation under visible light. ECD signal decay at (c) 373 and (d) 428 nm *vs* time for poly-(*R*)-**6** after irradiation with visible light. [poly-(*R*)-**6**]= $1.02 \cdot 10^{-3}$ M, $CHCl_3$. The spectra were measured in a **1 mm cuvette**.

10. Comparison of ECD signal decay studies measured in a 1 and 10 mm cuvettes

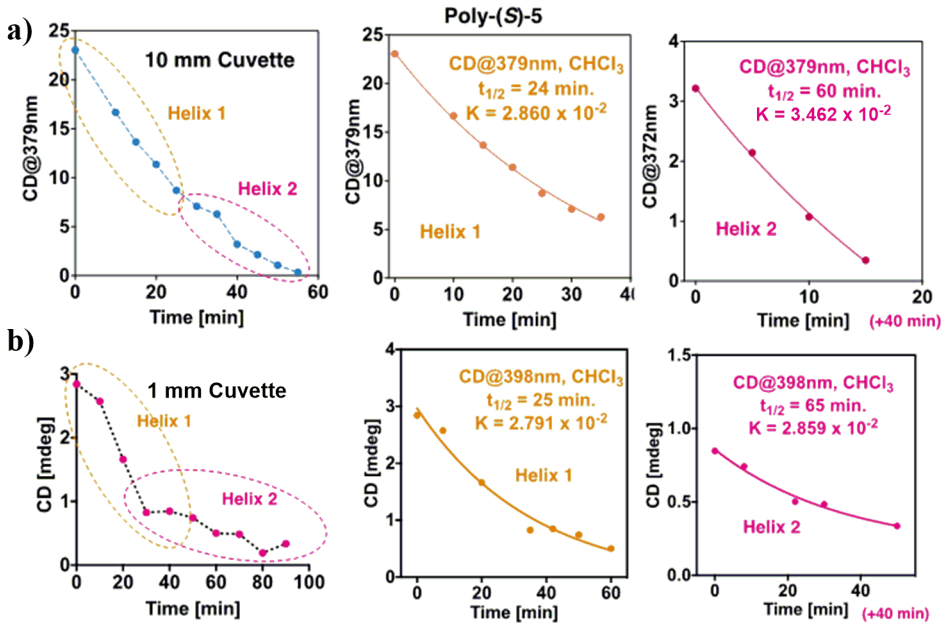

Figure S34. (a) **10 mm cuvette** (379 nm) and (b) **1 mm Cuvette** (398 nm), CD *vs* time for poly-(*S*)-**5** after irradiation with visible light. [poly-(*S*)-**5**]= $1.13 \cdot 10^{-3}$ M, $CHCl_3$.

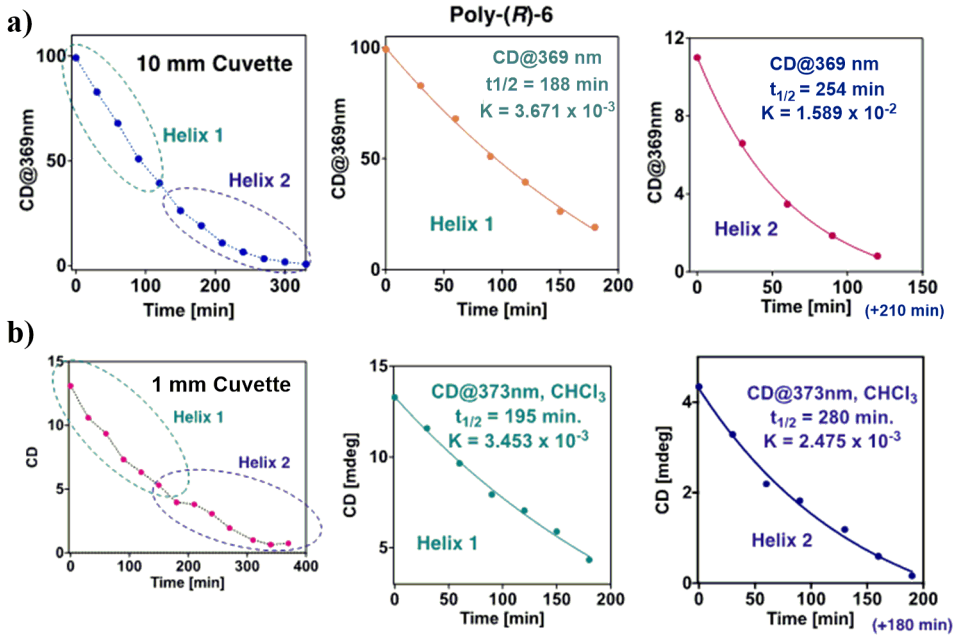

Figure S35. (a) **10 mm cuvette** (369 nm) and (b) **1 mm Cuvette** (373 nm), CD *vs* time for poly-(*R*)-**6** after irradiation with visible light. [poly-(*R*)-**6**]= $1.02 \cdot 10^{-3}$ M, $CHCl_3$.

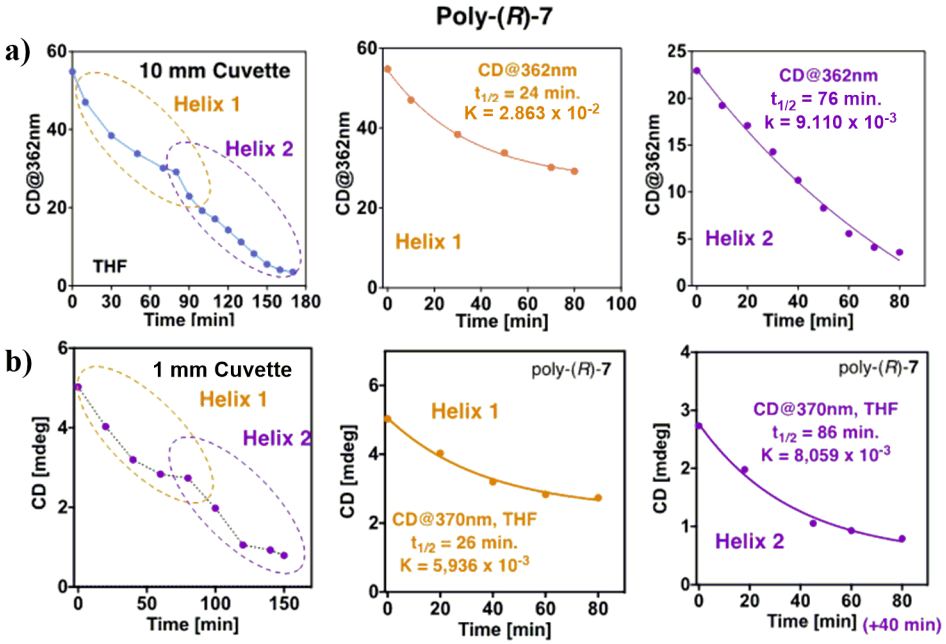

Figure S36. (a) **10 mm cuvette** (362 nm) and (b) **1 mm Cuvette** (370 nm), CD *vs* time for poly-(*R*)-**7** after irradiation with visible light. [poly-(*R*)-**7**]= $9.00 \cdot 10^{-4}$ M, THF.

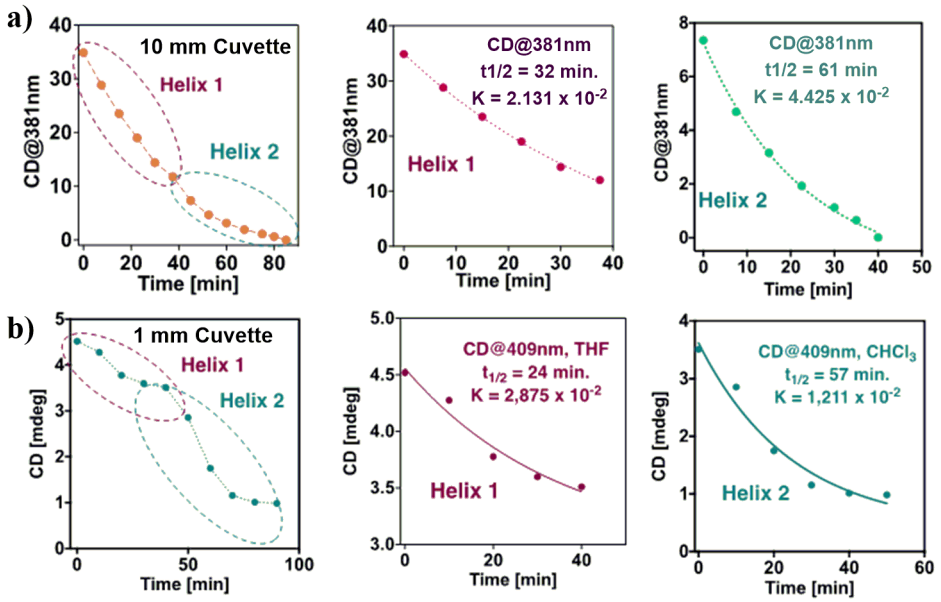

Figure S37. (a) **10 mm cuvette** (381 nm) and (b) **1 mm Cuvette** (409 nm), CD *vs* time for poly-(*R*)-**7** after irradiation with visible light. [poly-(*R*)-**7**]= $9.00 \cdot 10^{-4}$ M, $CHCl_3$.

11. UV kinetic studies of photochemical electrocyclization

First order reaction fit was applied to the abs signal decay *vs* time obtained for the UV studies of PPAs. However, due to residual absorptions of the polymer, the UV signal does not correlate with the equation, because rearomatization with chain cleavage does not yet take place. This fact makes that is not possible to stablish a correlation between the variation on the Abs value with time during the photochemical electrocyclization process (figure S38).

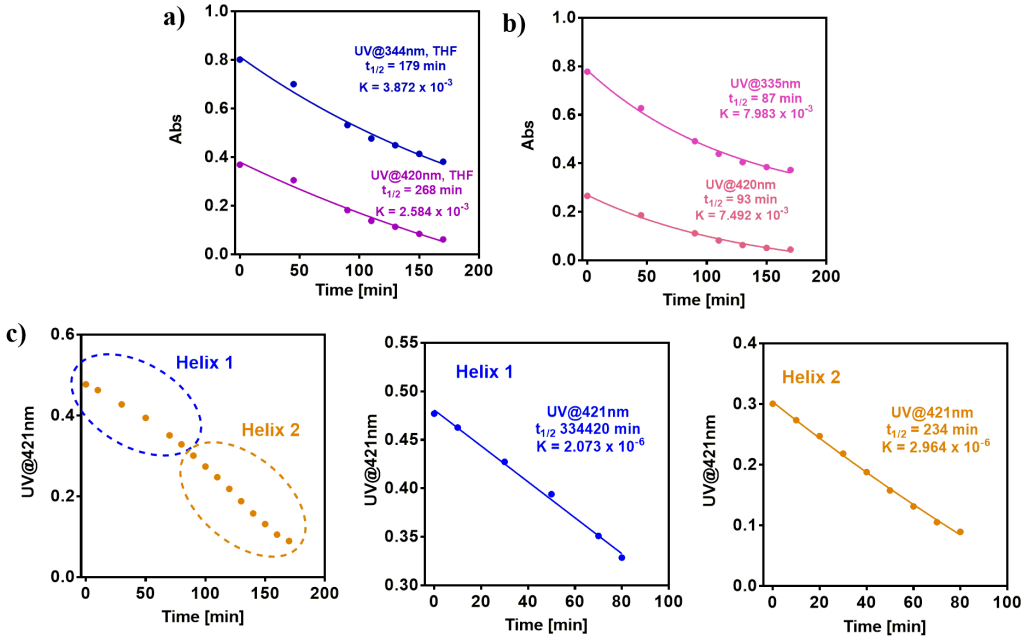

Figure S38. UV signal decay *vs* time for (a) poly-(*R*)-**1** in THF, (b) poly-(*R*)-**2** in $CHCl_3$ and (c) poly-(*R*)-**7** in THF. The spectra were measured in a **1 mm cuvette**.

12. Supporting References

S1. S. Leiras, F. Freire, J. M. Seco, E. Quiñoá, R. Riguera, *Chem. Sci.*, **2013**, *4*, 2735-2743.

S2. I. Louzao, J. M. Seco, E. Quiñoá, R. Riguera, *Angew. Chem. Int., Ed.,* **2010**, *49*, 1430-1433.

S3. K. Cobos, R. Rodríguez, O. Domarco, B. Fernández, E. Quiñoá, R. Riguera, F. Freire, *Macromolecules*, **2020**, *53,* 3182-3193.

S4. R. Rodríguez, E. Quiñoá, R. Riguera, F. Freire, *J. Am. Chem. Soc.*, **2016**, *138*, 9620-9628.

Experimental Section Chapter IV

1. Materials and methods

CD measurements were done in a Jasco-720. The amount of polymer used for CD measurements were 0.3 mg/mL in $CHCl_3$ and THF.

UV spectra were registered in a Jasco V-630. The amount of polymer used for UV measurements were 0.3 mg/mL in $CHCl_3$ and THF.

Irradiation experiments were done in an Asahi Spectra Xenon light model MAX-303. The light was filtered using a shortpass filter / Vis 550 nm 25 dia.

Optical rotation was measured in a Jasco-P2000.

NMR experiments were measured in a Varian 300 operating at 300 MHz for proton NMR and 75 MHz for carbon. $CDCl_3$ signal (δ= 77.2ppm) or DMSO-d_6 (δ= 39.5 ppm) was used as standard for ^{1}H or ^{13}C experiments.

2. General Protocol for PPA Irradiation

Irradiation experiments were performed using a collimator Lens (x1.0) of a MAX-303 (Asahi Spectra) equipped with a UV-VIS mirror module (300-600 nm) and a shortpass filter (VIS 550nm 25 dia.) applying the general protocol for PPA irradiation described in the reference **S8** for measures in a 1 mm cuvette.

3. Synthesis of Monomer

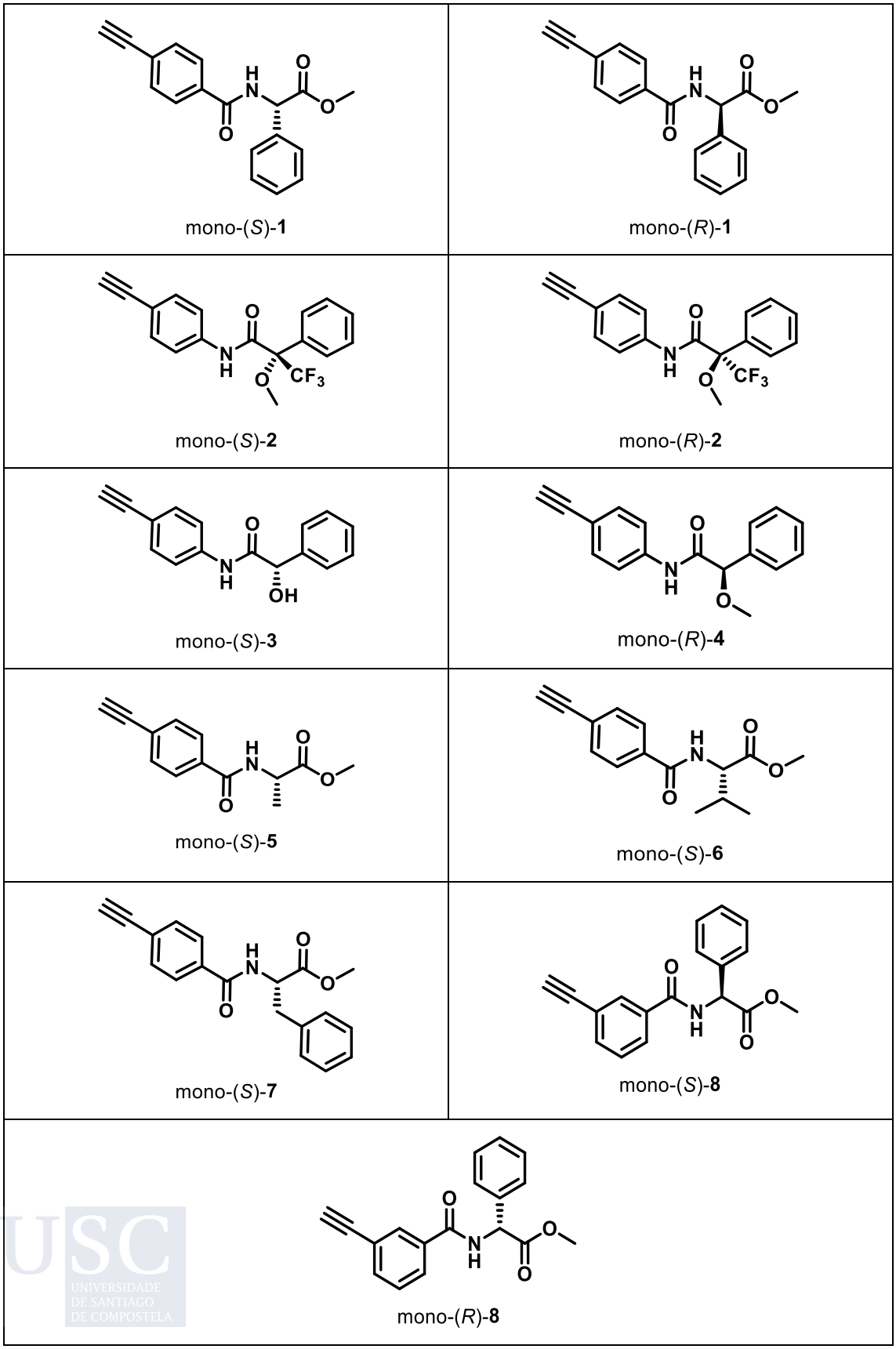

Figure S1. Structure of the monomers synthesized.

Mono-**1** and mono-**2** was prepared according to references **S1** and **S2** respectively; mono-(*S*)-**3** and mono-(*R*)-**4** was prepared according to reference **S3**; mono-(*S*)-**5**, mono-(*S*)-**6** and mono-(*S*)-**7** was prepared according to references **S4**, **S5** and **S6** respectively and mono-**9** was prepared according to reference **S7**.

4. Synthesis of homopolymers

General procedure for polymerization

The reaction flask (sealed ampoule) was dried under vacuum and argon flushed for three times before monomer was added as a solid. Then, the flask was evacuated on a vacuum line and flushed with dry argon (three times). Dry THF was added with a syringe and the triethylamine dropwise. A solution of rhodium norbornadiene chloride dimer, $[Rh(nbd)Cl]_2$, in THF was added at 30 °C. The reaction mixture was stirring at 30 °C for 6 h. Then, the resulting polymer was diluted in CH_2Cl_2 and it was precipitated in a large amount of methanol, centrifuged (2 times), reprecipitated in hexane and centrifuged again. As exception, in the centrifugation of poly-(*S*)-**3**, it is used a mixture MeOH:Ether (10:90) instead pure methanol.

Table 1. Polymerization conditions of the corresponding homopolymers.

Polymer	Mass (mg)	THF (mL)	$[Rh(nbd)Cl]_2$ (mg)	ET_3N (μL)	Yield (%)
Poly-(S)-**1**	75	1.0	1.0	5	89
Poly-(*R*)-**1**	75	1.0	1.0	5	90
Poly-(S)-**2**	75	1.0	1.0	5	88
Poly-(S)-**2**	75	1.0	1.0	5	87
Poly-(S)-**3**	75	1.0	1.0	5	84
Poly-(*R*)-**4**	75	1.0	1.0	5	92
Poly-(*S*)-**5**	75	1.0	1.0	5	88
Poly-(*S*)-**6**	75	1.0	1.0	5	88
Poly-(*S*)-**7**	75	1.0	1.0	5	87
Poly-(*S*)-**8**	75	1.0	1.0	5	86
Poly-(*R*)-**8**	75	1.0	1.0	5	87

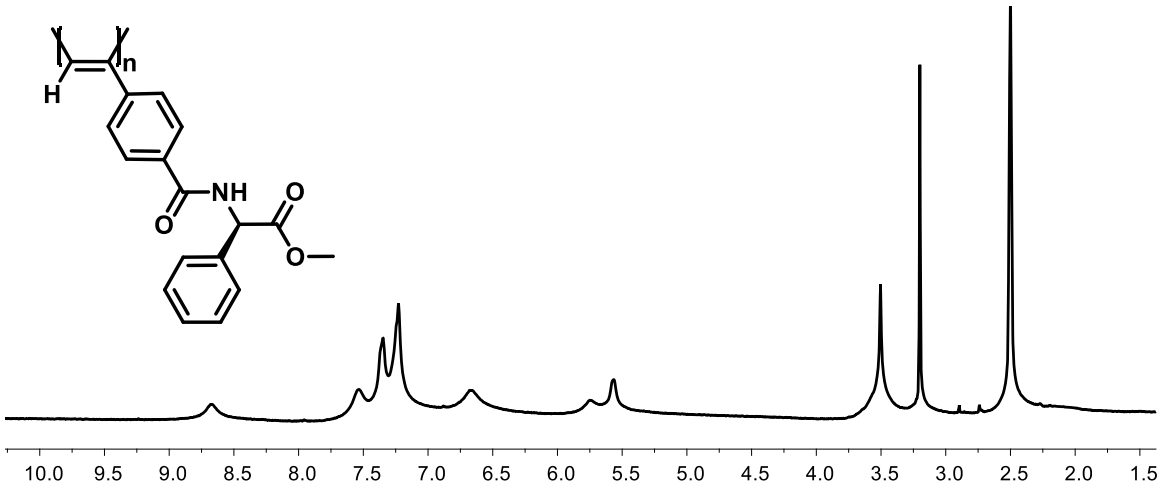

Figure S2. ^{1}H NMR spectra of poly-(*R*)-**1** (DMSO, 300 MHz).

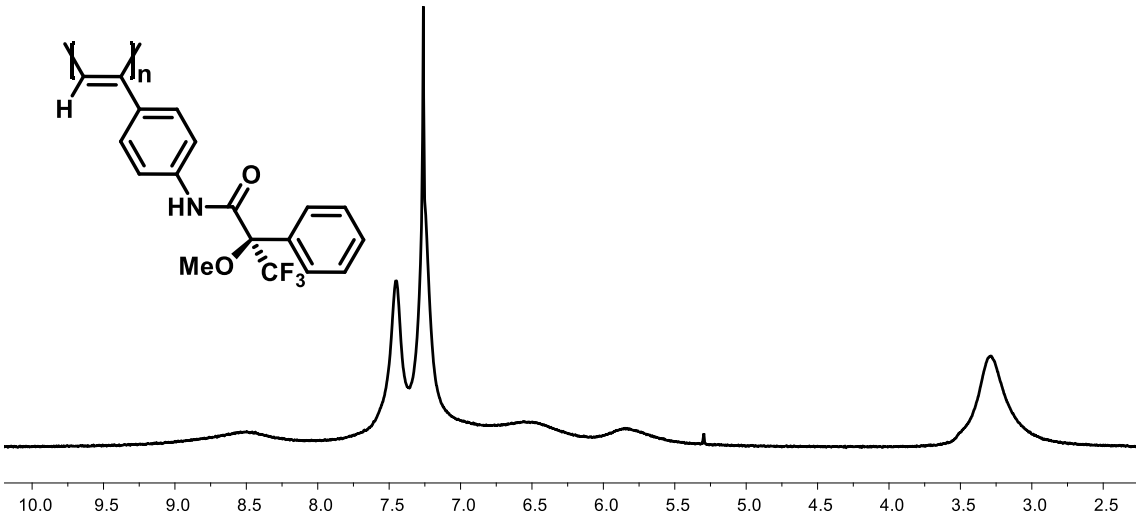

Figure S3. ^{1}H NMR spectra of poly-(*R*)-**2** ($CDCl_3$, 300 MHz).

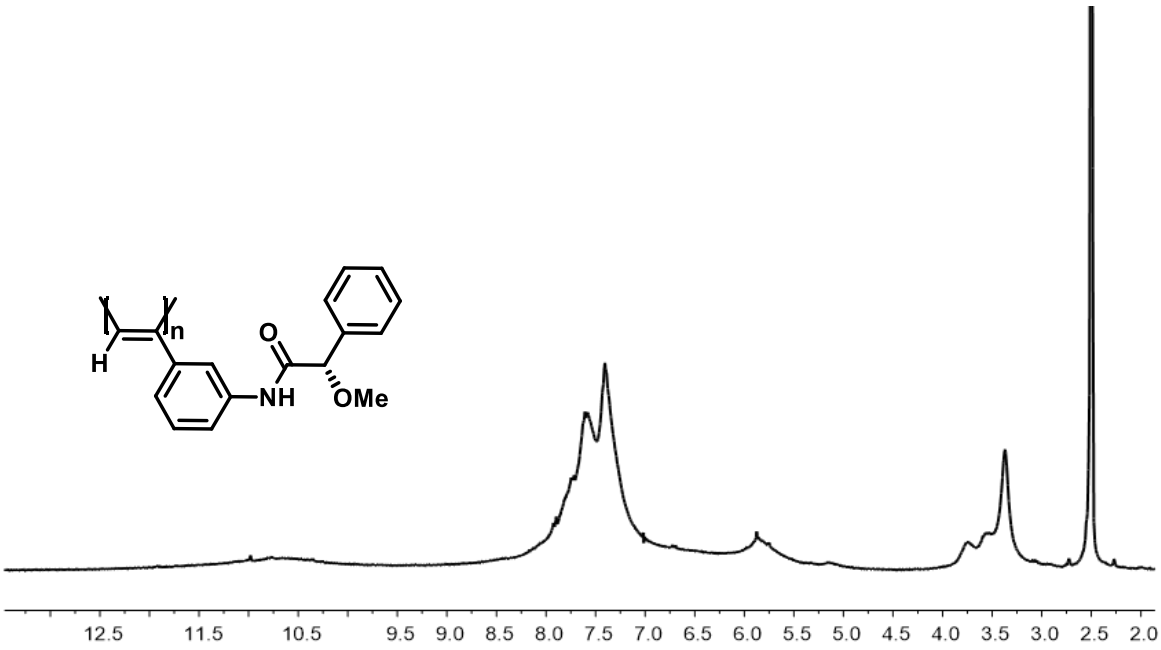

Figure S4. ^{1}H NMR spectra of poly-(*S*)-**3** (DMSO, 300 Mhz).

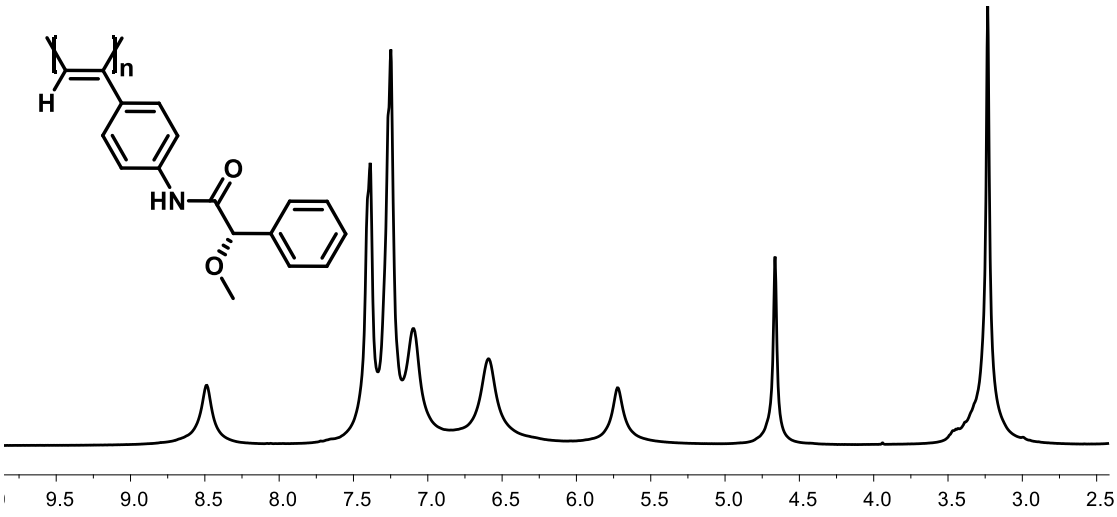

Figure S5. ^{1}H NMR spectra of poly-(*R*)-**4** ($CDCl_3$, 300 MHz).

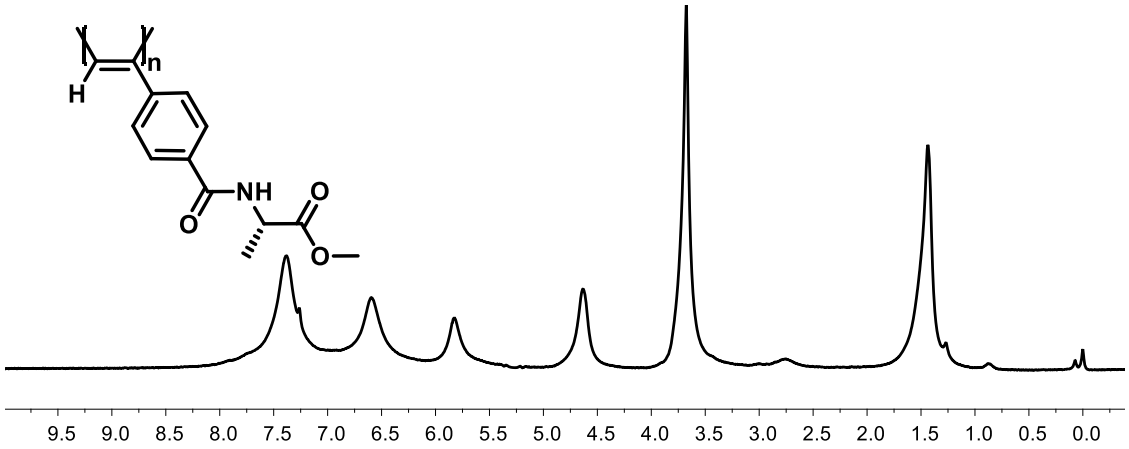

Figure S6. ^{1}H NMR spectra of poly-(*S*)-**5** ($CDCl_3$, 300 MHz).

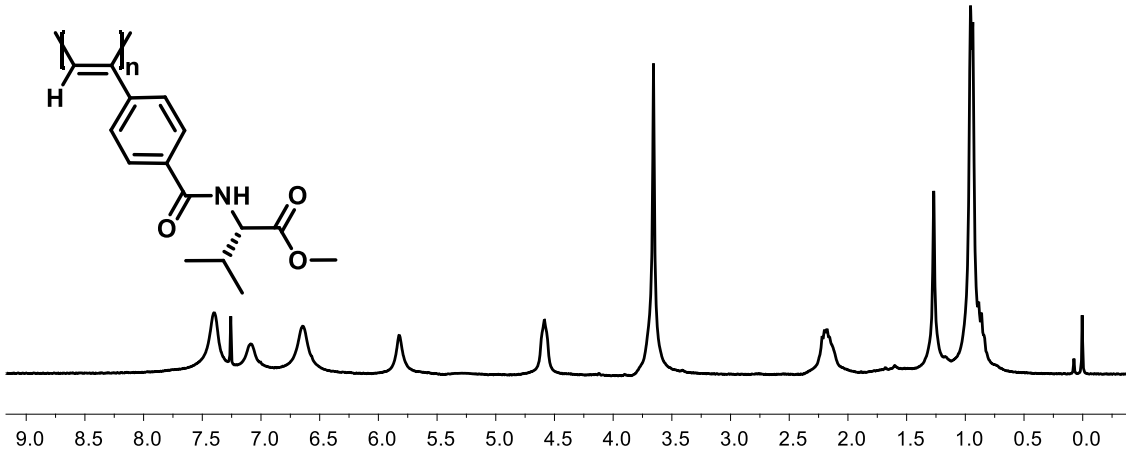

Figure S7. ^{1}H NMR spectra of poly-(*S*)-**6** ($CDCl_3$, 300 MHz).

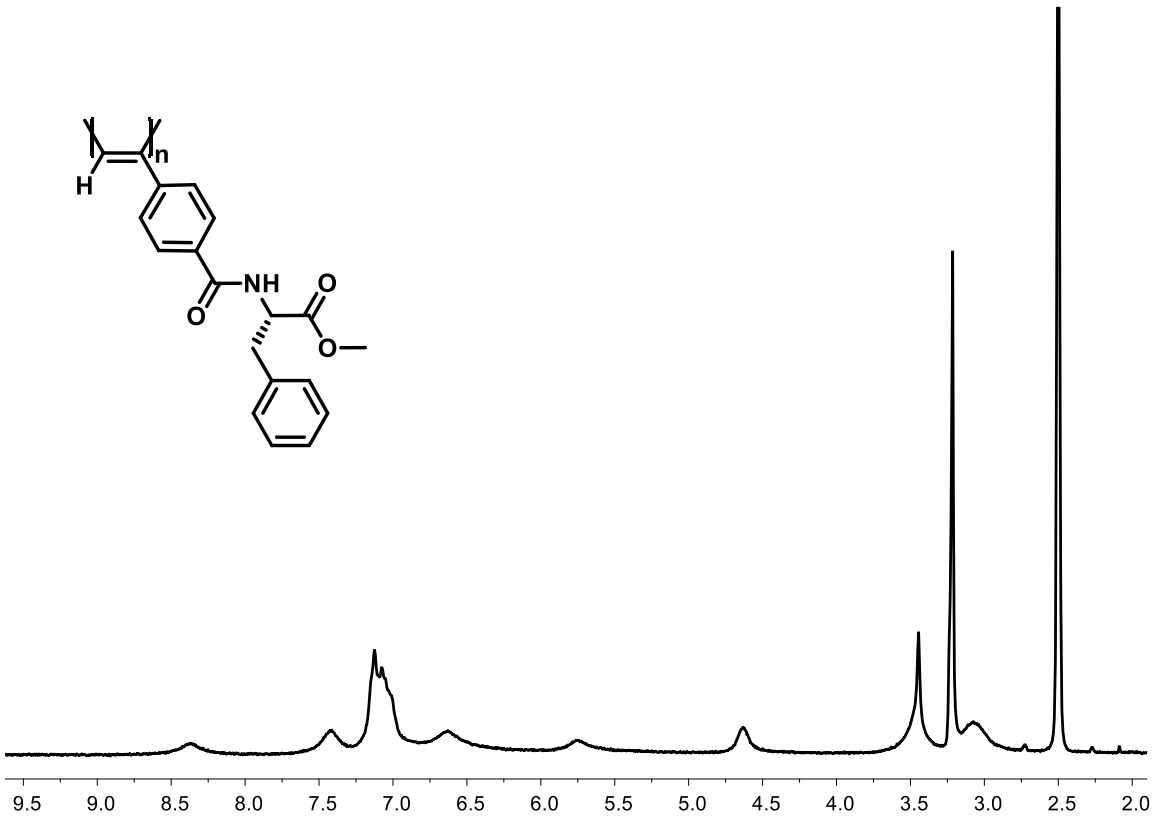

Figure S8. ^{1}H NMR spectra of poly-(*S*)-**7** (DMSO, 300 MHz).

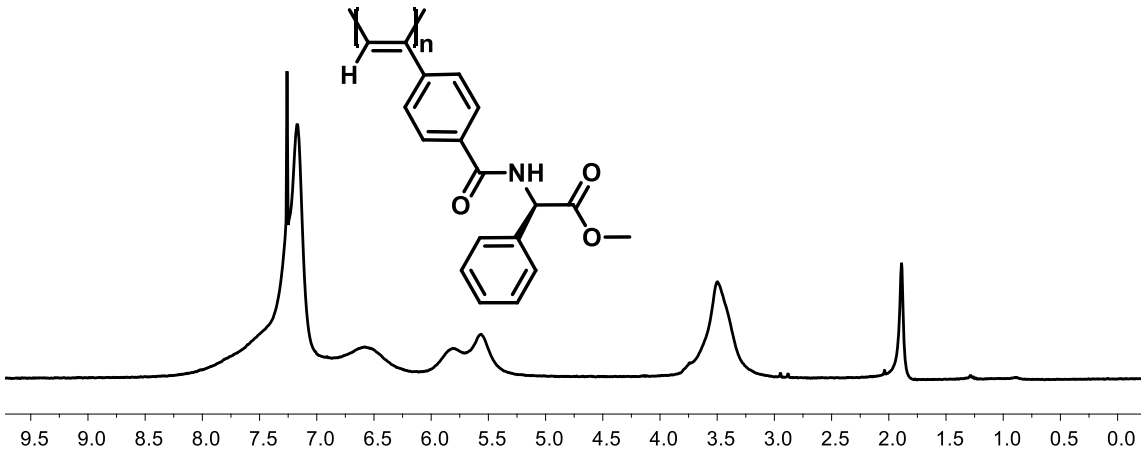

Figure S9. ^{1}H NMR spectra of poly-(*R*)-**8** ($CDCl_3$, 300 MHz).

Synthesis of copolymers

Following the general procedure for homopolymers polymerization copolymers were prepared according to the amounts of monomers indicated for each case in the next tables.

Synthesis of the copolymers of the poly[(*R*)-**1**$_r$-co-(*S*)-**1**$_{(1-r)}$] series

Table 2. Polymerization conditions for poly[(*R*)-**1**$_r$-co-(*S*)-**1**$_{(1-r)}$] series.

Copolymer	M-(*R*)-1 (mg)	M-(*R*)-1 (mmol)	M-(*S*)-1 (mg)	M-(*S*)-1 (mmol)	$[Rh(nbd)Cl]_2$ (mg)	ET_3N (μL)	Yield (%)
poly[(*R*)-**1**$_{0.95}$-co-(*S*)-**1**$_{0.05}$]	83.6	0.285	4.4	0.015	1.3	5	90
poly[(*R*)-**1**$_{0.9}$-co-(*S*)-**1**$_{0.1}$]	79.2	0.270	8.8	0.030	1.3	5	88
poly[(*R*)-**1**$_{0.8}$-co-(*S*)-**1**$_{0.2}$]	74.8	0.255	13.2	0.045	1.3	5	89
poly[(*R*)-**1**$_{0.7}$-co-(*S*)-**1**$_{0.3}$]	70.4	0.240	17.6	0.060	1.3	5	89
poly[(*R*)-**1**$_{0.6}$-co-(*S*)-**1**$_{0.4}$]	52.8	0.180	35.2	0.120	1.3	5	87

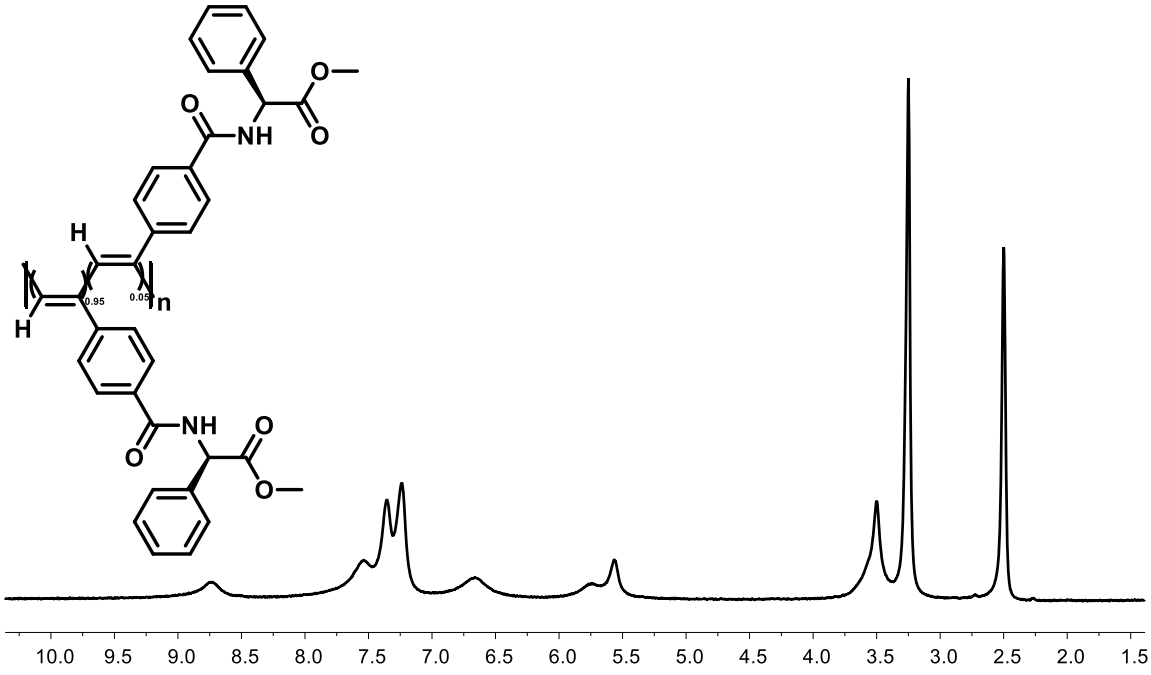

Figure S10. ^1H NMR spectra of poly[(*R*)-**1**$_{0.95}$-co-(*S*)-**1**$_{0.05}$] (DMSO, 300 MHz).

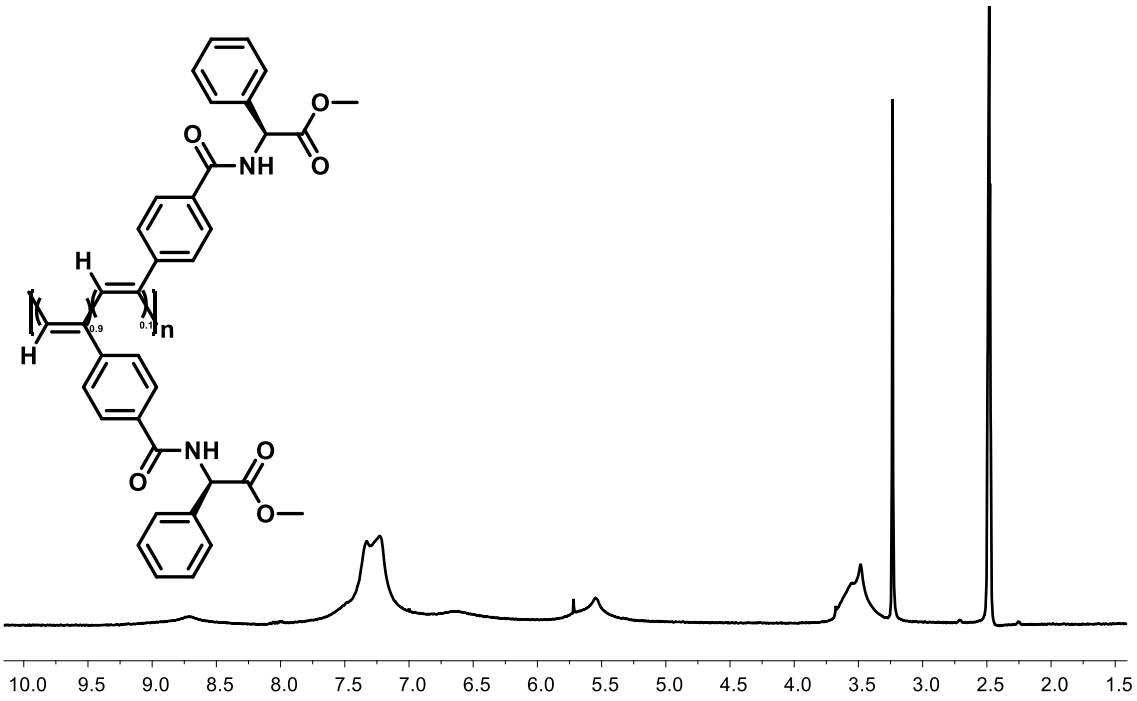

Figure S11. ^{1}H NMR spectra of poly[(*R*)-**1**$_{0.9}$-co-(*S*)-**1**$_{0.1}$] (DMSO, 300 MHz).

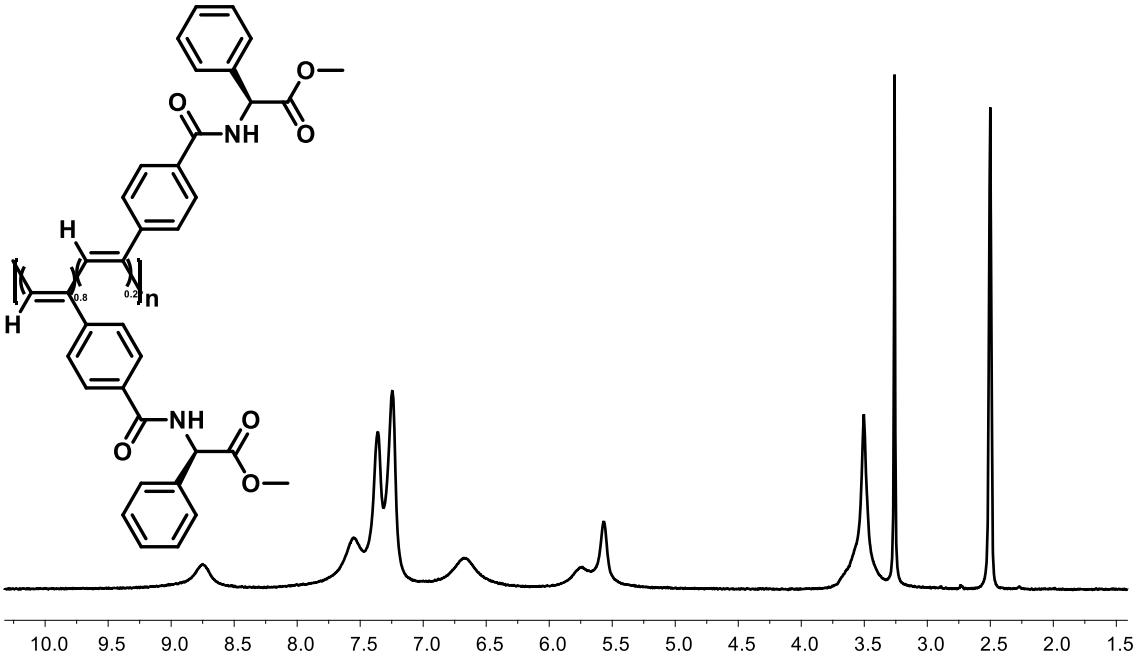

Figure S12. ^{1}H NMR spectra of poly[(*R*)-**1**$_{0.8}$-co-(*S*)-**1**$_{0.2}$] (DMSO, 300 MHz).

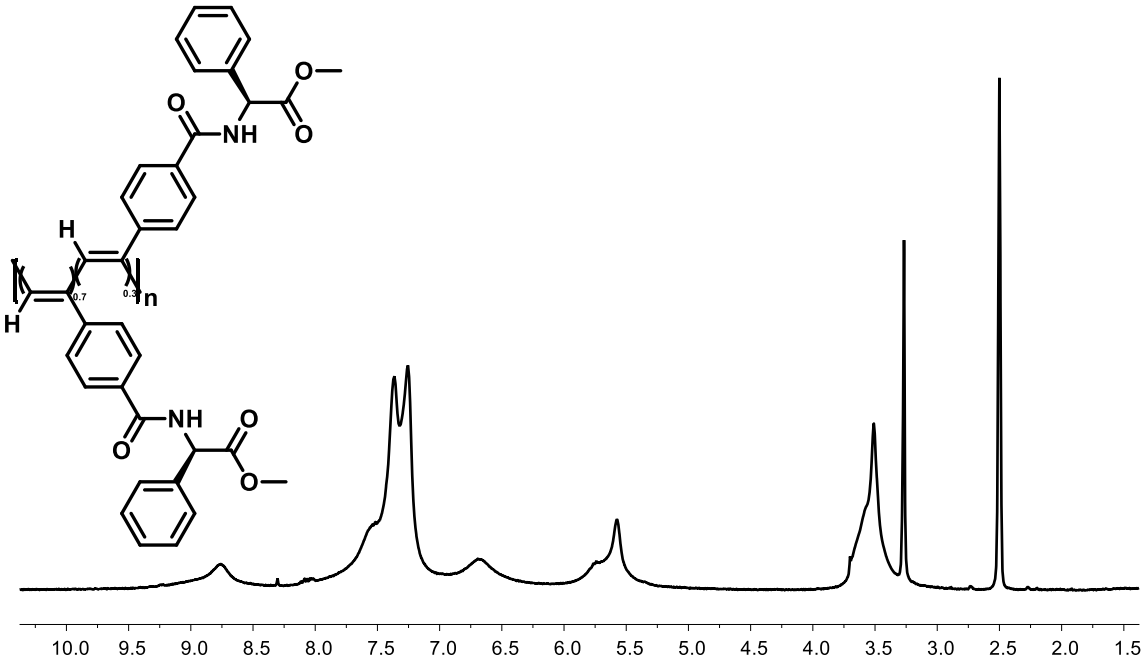

Figure S13. ^{1}H NMR spectra of poly[(*R*)-**1**$_{0.7}$-co-(*S*)-**1**$_{0.3}$] (DMSO, 300 MHz).

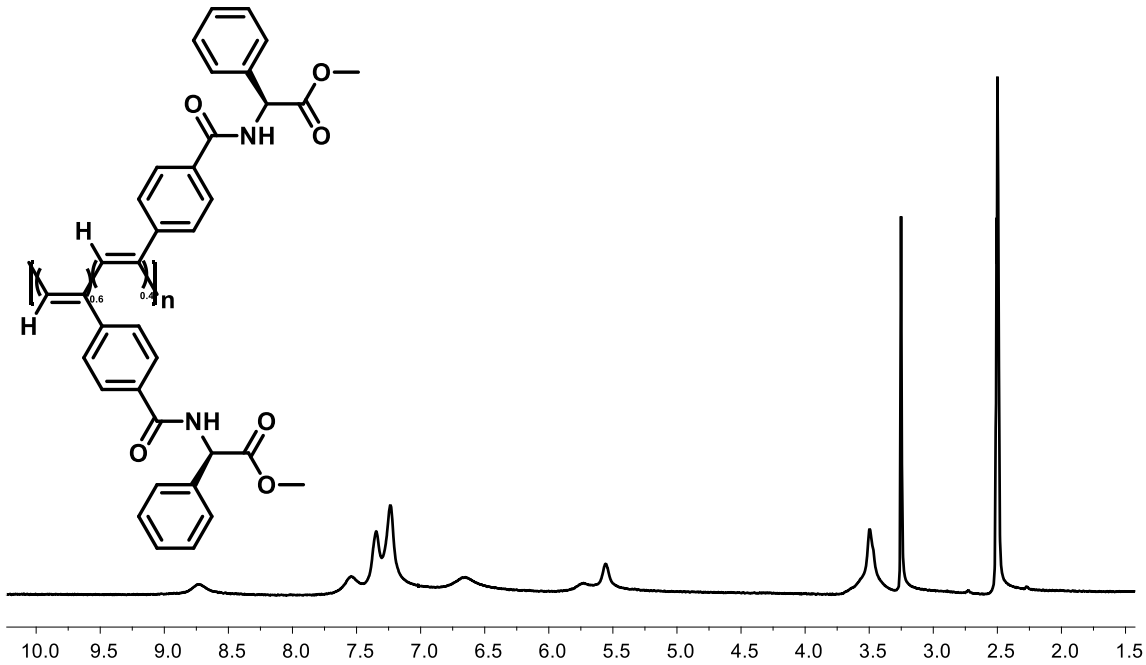

Figure S14. ^{1}H NMR spectra of poly[(*R*)-**1**$_{0.6}$-co-(*S*)-**1**$_{0.4}$] (DMSO, 300 MHz).

Synthesis of the copolymers of the poly[(*R*)-**2**$_r$-co-(*S*)-**2**$_{(1-r)}$] series

Table 3. Polymerization conditions for poly[(*R*)-**2**$_r$-co-(*S*)-**2**$_{(1-r)}$] series.

Copolymer	M-(*R*)-2 (mg)	M-(*R*)-2 (mmol)	M-(*S*)-2 (mg)	M-(*S*)-2 (mmol)	$[Rh(nbd)Cl]_2$ (mg)	ET_3N (μL)	Yield (%)
poly[(*R*)-**2**$_{0.9}$-co-(*S*)-**2**$_{0.1}$]	90.0	0.270	10.0	0.030	1.3	5	91
poly[(*R*)-**2**$_{0.8}$-co-(*S*)-**2**$_{0.2}$]	80.0	0.240	20.0	0.060	1.3	5	90
poly[(*R*)-**2**$_{0.7}$-co-(*S*)-**2**$_{0.3}$]	70.0	0.210	30.0	0.090	1.3	5	88
poly[(*R*)-**2**$_{0.6}$-co-(*S*)-**2**$_{0.4}$]	60.0	0.180	40.0	0.120	1.3	5	88

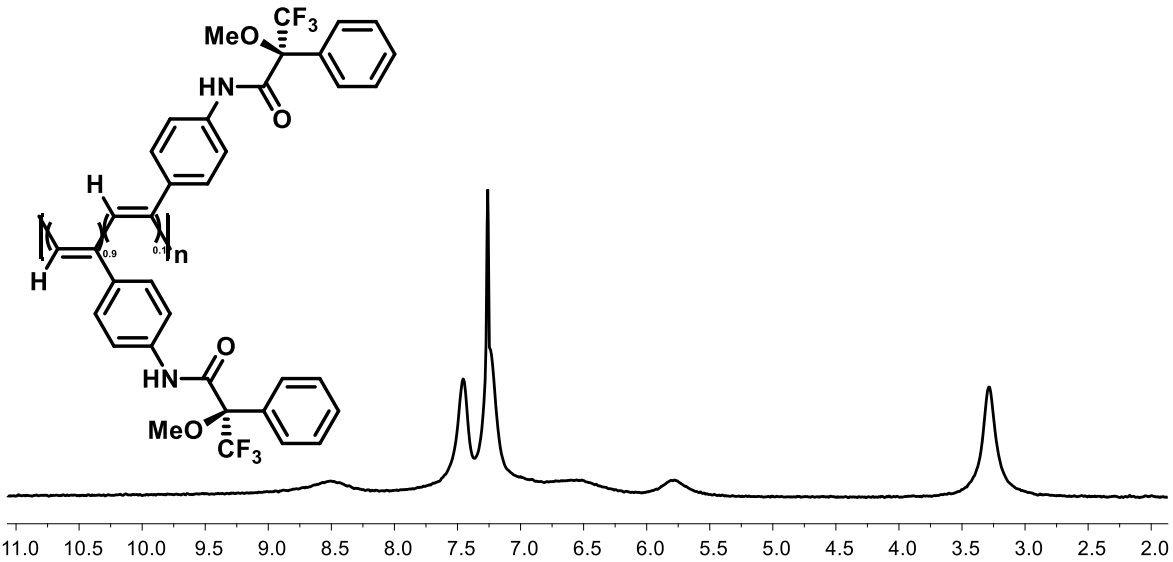

Figure S15. ^1H NMR spectra of poly[(*R*)-**2**$_{0.9}$-co-(*S*)-**2**$_{0.1}$] ($CDCl_3$, 300 MHz).

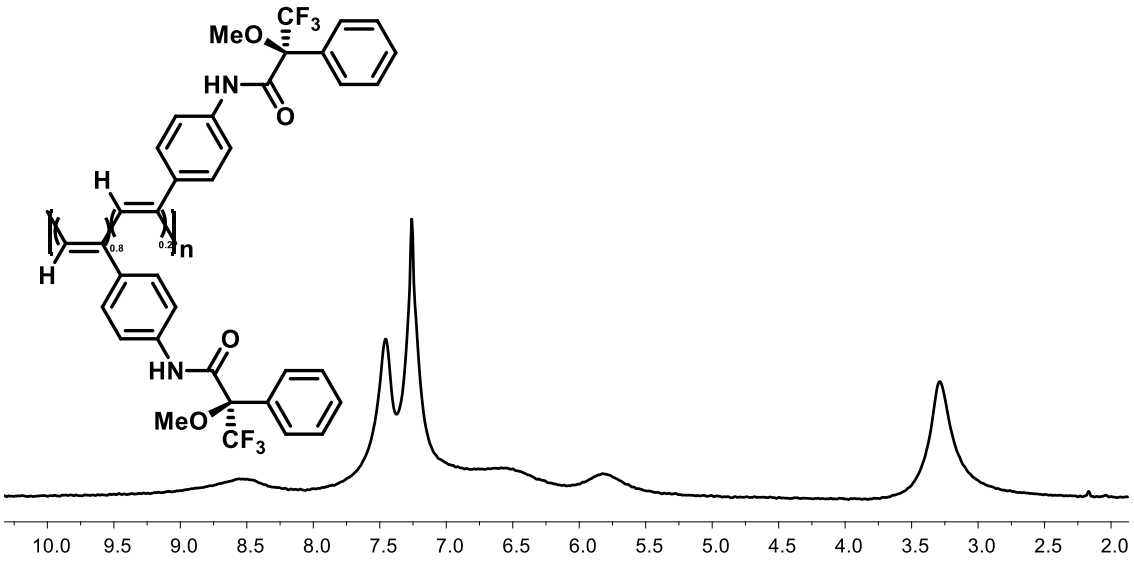

Figure S16. ^{1}H NMR spectra of poly[(*R*)-**2**$_{0.8}$-co-(*S*)-**2**$_{0.2}$] ($CDCl_3$, 300 MHz).

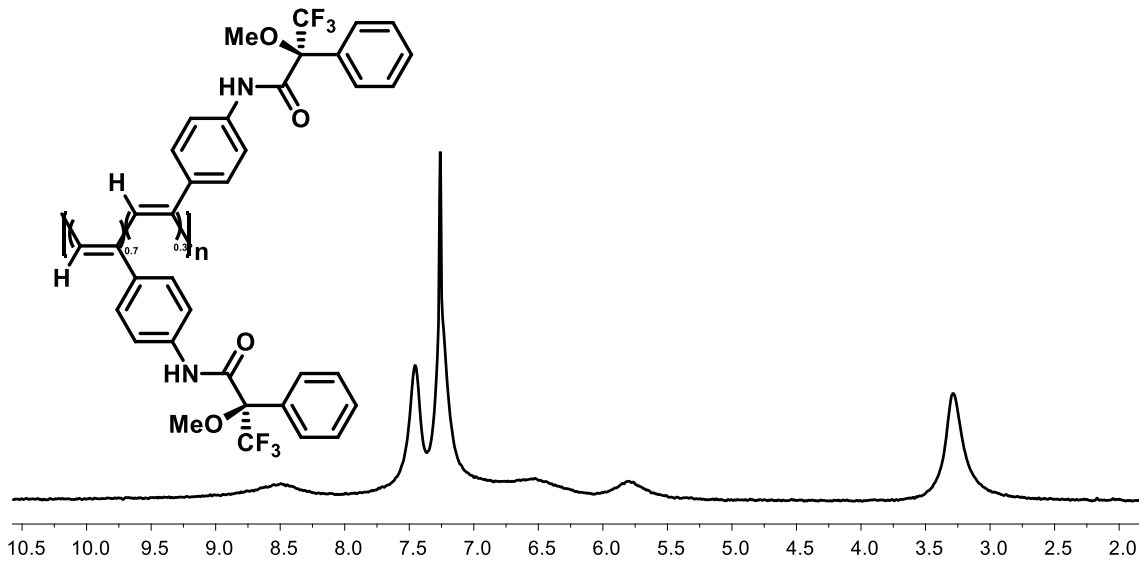

Figure S17. ^{1}H NMR spectra of poly[(*R*)-**2**$_{0.7}$-co-(*S*)-**2**$_{0.3}$] ($CDCl_3$, 300 MHz).

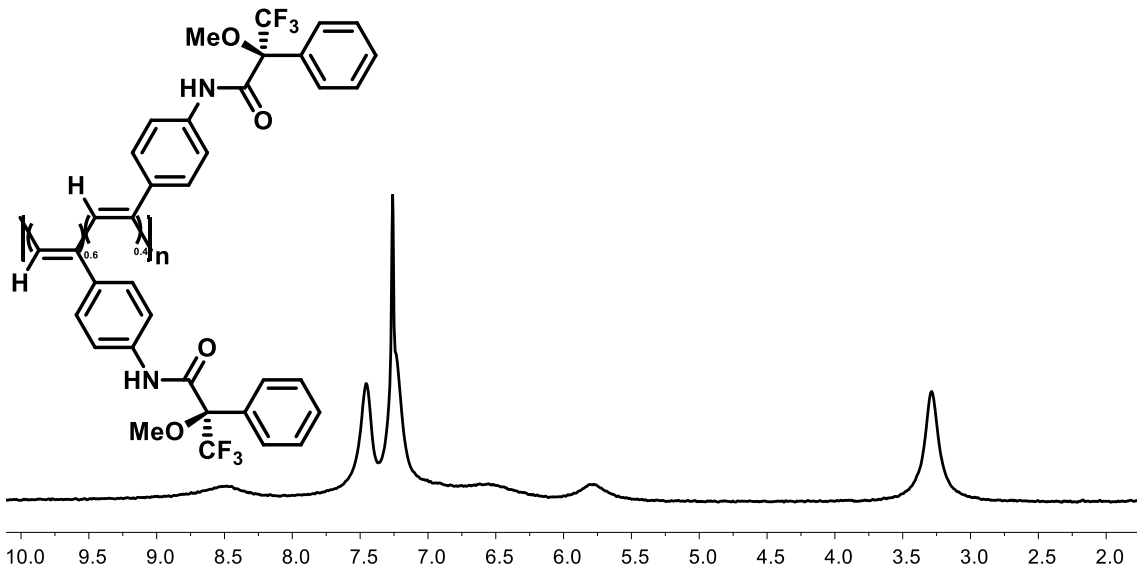

Figure S18. ^{1}H NMR spectra of poly[(*R*)-**2**$_{0.6}$-co-(*S*)-**2**$_{0.4}$] ($CDCl_3$, 300 MHz).

Synthesis of the copolymers of poly[(*R*)-**8**$_r$-co-(*S*)-**8**$_{(1-r)}$] series

Table 4. Polymerization conditions for poly[(*R*)-**8**$_r$-co-(*S*)-**8**$_{(1-r)}$] series.

Copolymer	M-(*R*)-8 (mg)	M-(*R*)-8 (mmol)	M-(*S*)-8 (mg)	M-(*S*)-8 (mmol)	$[Rh(nbd)Cl]_2$ (mg)	ET_3N (μL)	Yield (%)
poly[(*R*)-**8**$_{0.9}$-co-(*S*)-**8**$_{0.1}$]	79.2	0.270	8.8	0.030	1.3	5	85
poly[(*R*)-**8**$_{0.8}$-co-(*S*)-**8**$_{0.2}$]	74.8	0.255	13.2	0.045	1.3	5	84
poly[(*R*)-**8**$_{0.7}$-co-(*S*)-**8**$_{0.3}$]	70.4	0.240	17.6	0.060	1.3	5	84
poly[(*R*)-**8**$_{0.6}$-co-(*S*)-**8**$_{0.4}$]	52.8	0.180	35.2	0.120	1.3	5	82

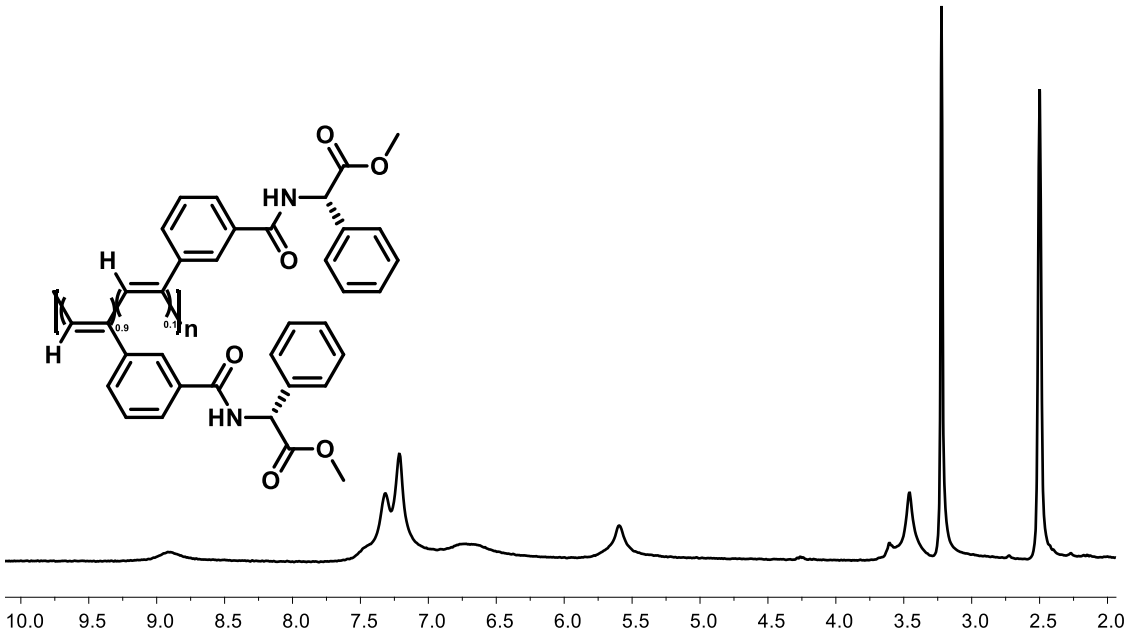

Figure S19. ^{1}H NMR spectra of poly[(*R*)-**8**$_{0.9}$-co-(*S*)-**8**$_{0.1}$] (DMSO, 300 MHz).

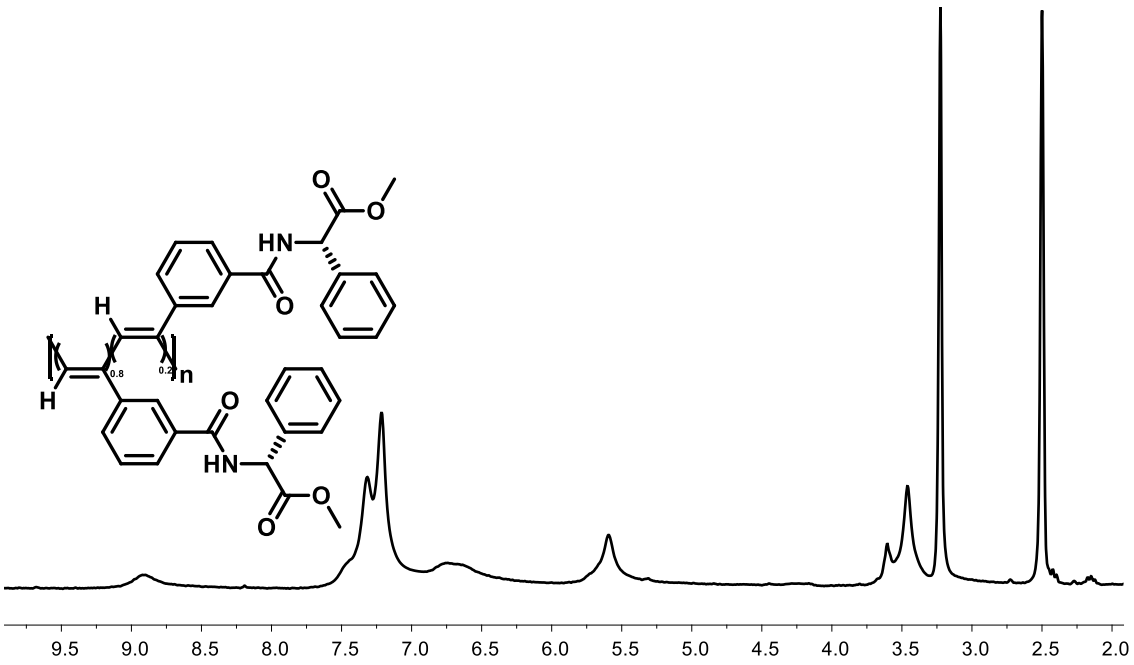

Figure S20. ^{1}H NMR spectra of poly[(*R*)-**8**$_{0.8}$-co-(*S*)-**8**$_{0.2}$] (DMSO, 300 MHz).

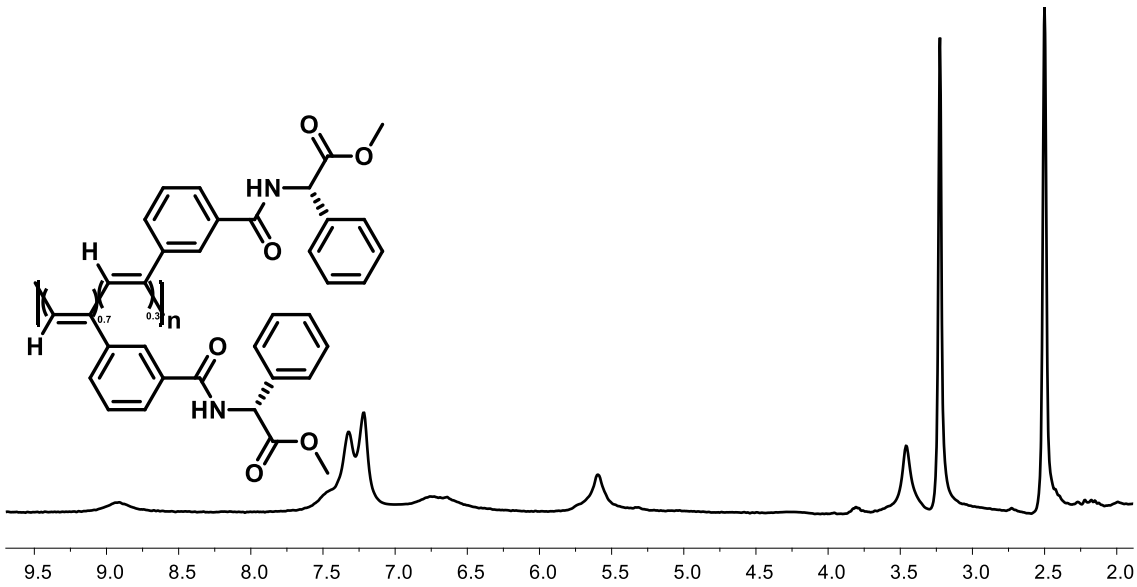

Figure S21. ^{1}H NMR spectra of poly[(*R*)-**8**$_{0.7}$-co-(*S*)-**8**$_{0.3}$] (DMSO, 300 MHz).

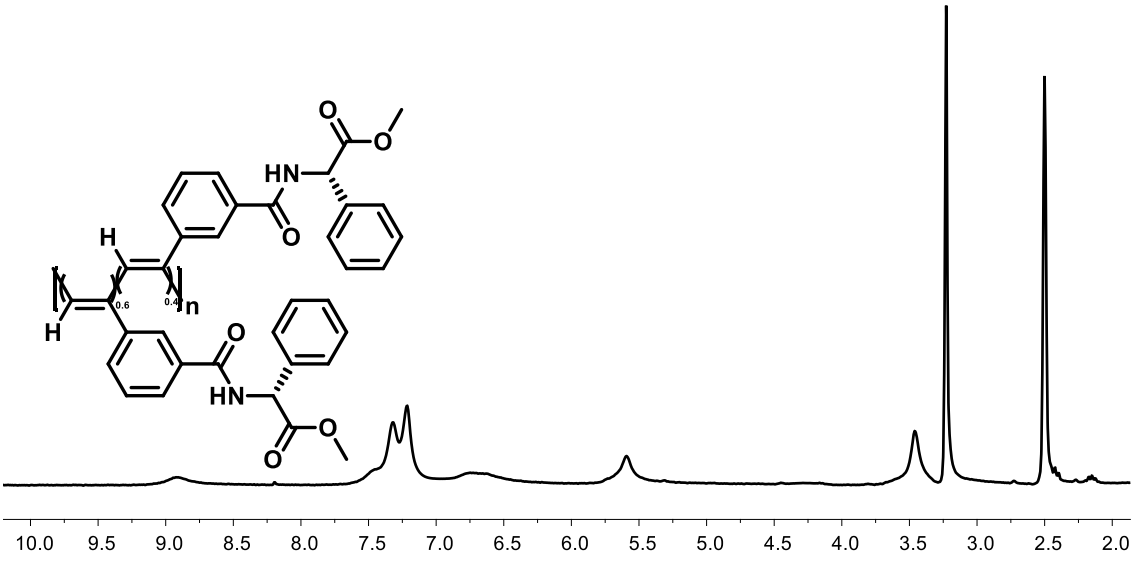

Figure S22. ^{1}H NMR spectra of poly[(*R*)-**8**$_{0.6}$-co-(*S*)-**8**$_{0.4}$] (DMSO, 300 MHz).

5. CD and UV irradiation studies

Homopolymers

Poly-(*R*)-1

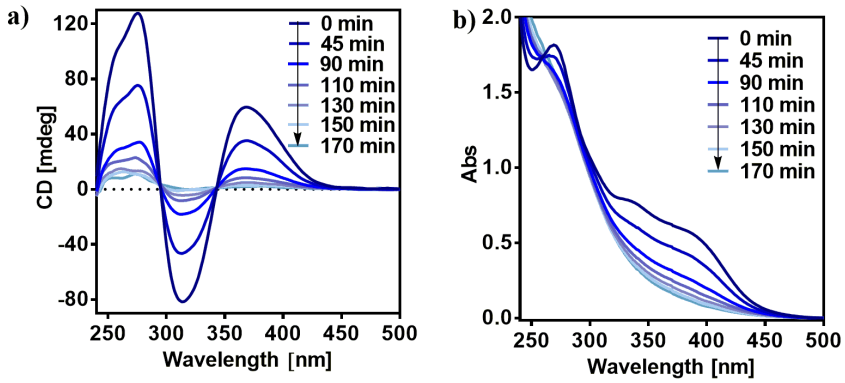

Figure S23. (a) CD and (b) UV spectra of poly-(*R*)-**1** in $CHCl_3$ after irradiation under visible light. [poly-(*R*)-**1**]= $1.02 \cdot 10^{-3}$ M.

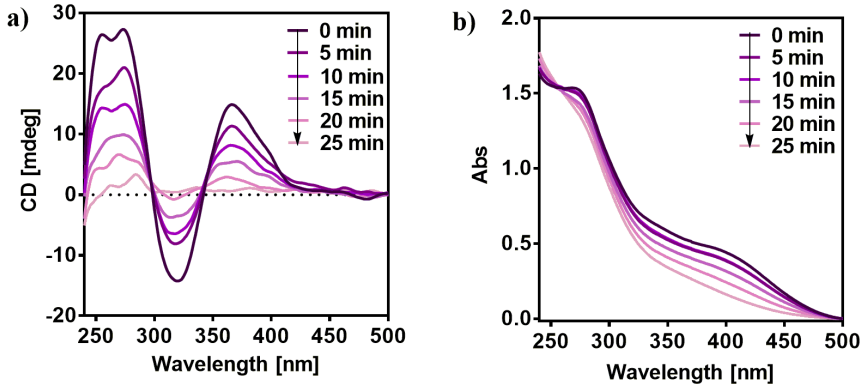

Figure S24. (a) CD and (b) UV spectra of poly-(*R*)-**1** in THF after irradiation under visible light. [poly-(*R*)-**1**]= $1.02 \cdot 10^{-3}$ M.

Poly-(*R*)-2

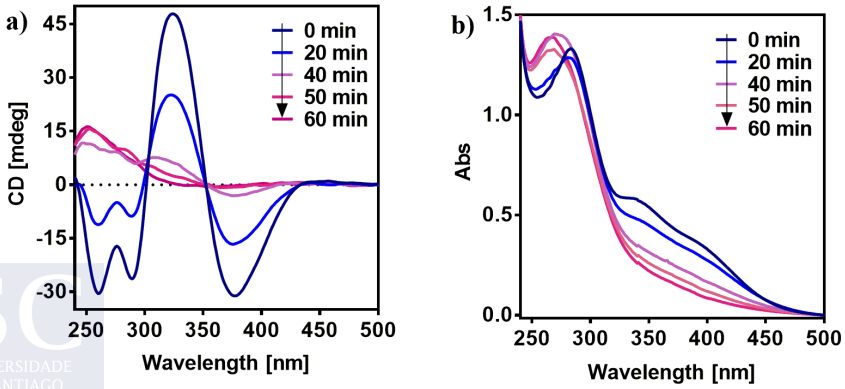

Figure S25. (a) CD and (b) UV spectra poly-(*R*)-**2** in $CHCl_3$ after irradiation under visible light. [poly-(*R*)-**2**]= $9.00 \cdot 10^{-4}$ M.

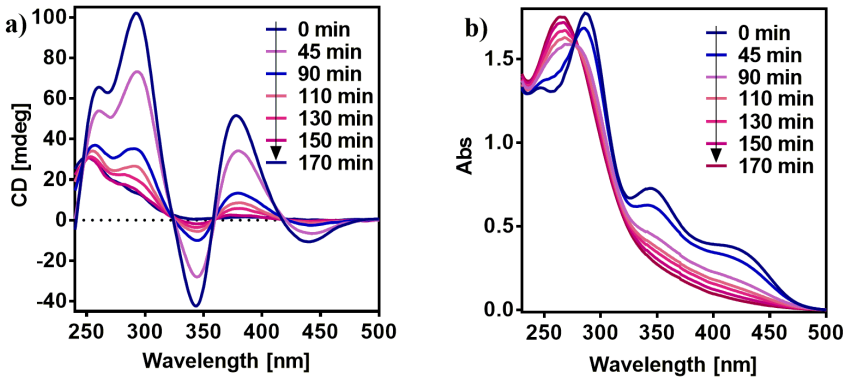

Figure S26. (a) CD and (b) UV spectra poly-(*R*)-**2** in THF after irradiation under visible light. [poly-(*R*)-**2**]= $9.00 \cdot 10^{-4}$ M.

Poly-(*S*)-3

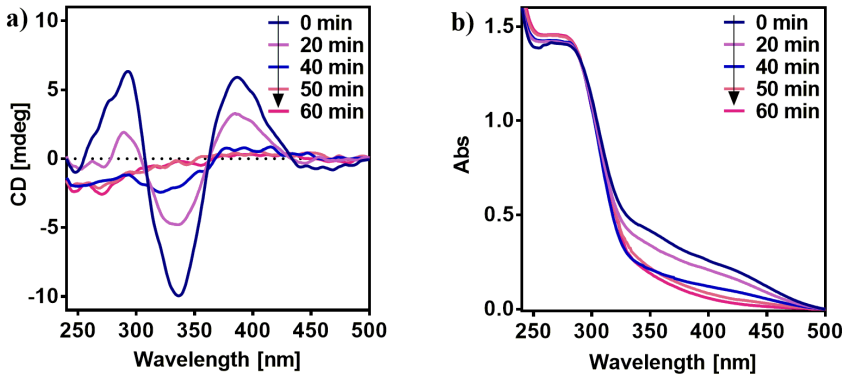

Figure S27. (a) CD and (b) UV spectra of poly-(*S*)-**3** in THF after irradiation under visible light. [poly-(*S*)-**3**]= $1.19 \cdot 10^{-3}$ M.

Poly-(*R*)-4

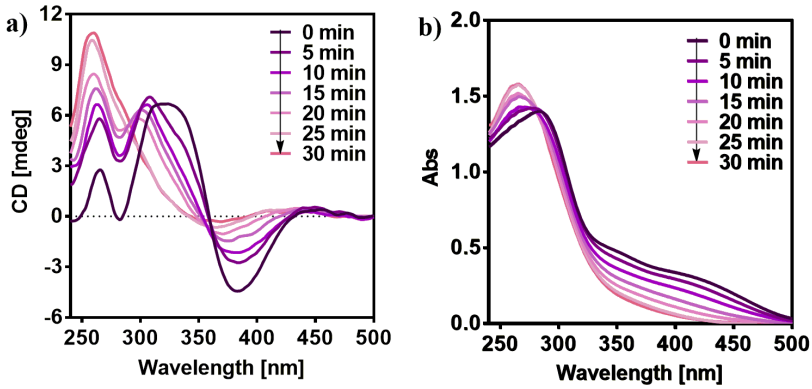

Figure S28. (a) CD and (b) UV spectra of poly-(*R*)-**4** in $CHCl_3$ after irradiation under visible light. [poly-(*R*)-**4**]= $1.13 \cdot 10^{-3}$ M.

Poly-(*S*)-5

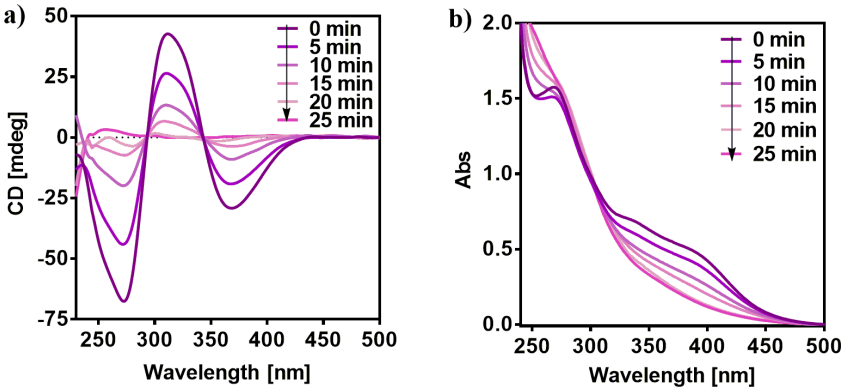

Figure S29. (a) CD and (b) UV spectra of poly-(*S*)-**6** in $CHCl_3$ after irradiation under visible light. [poly-(*S*)-**5**]= $1.30 \cdot 10^{-3}$ M.

Poly-(*S*)-6

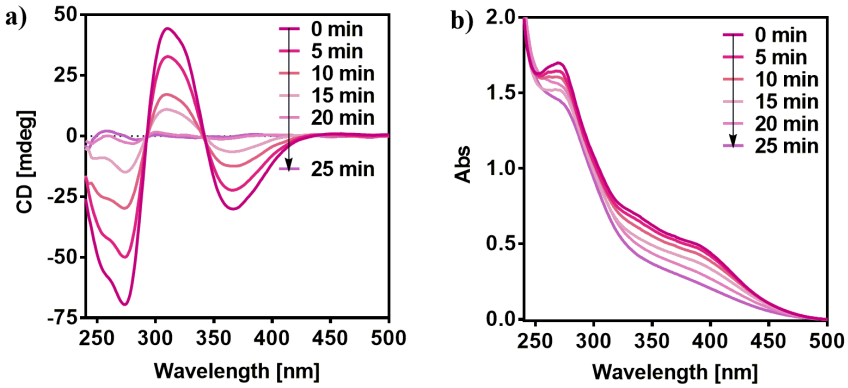

Figure S30. (a) CD and (b) UV spectra of poly-(*S*)-**7** in $CHCl_3$ after irradiation under visible light. [poly-(*S*)-**6**]= $1.16 \cdot 10^{-3}$ M.

Poly-(*S*)-7

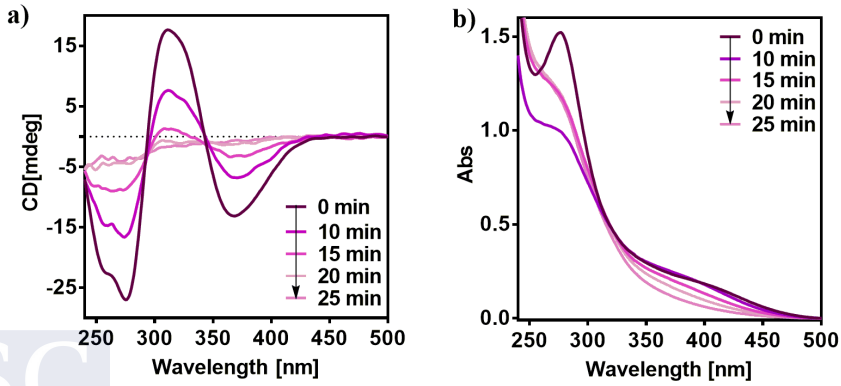

Figure S31. (a) CD and (b) UV spectra of poly-(*S*)-**8** in $CHCl_3$ after irradiation under visible light. [poly-(*S*)-**7**]= $9.76 \cdot 10^{-4}$ M.

Poly-(*R*)-8

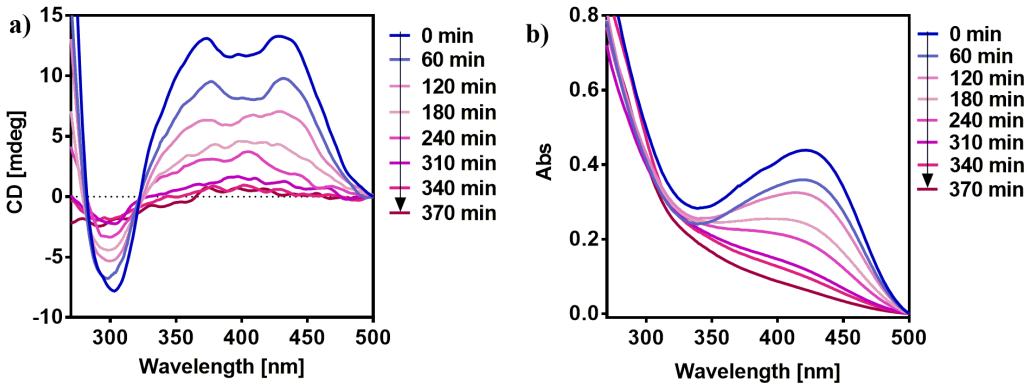

Figure S32. (a) CD and (b) UV spectra of poly-(*R*)-**9** in $CHCl_3$ after irradiation under visible light. [poly-(*R*)-**8**]= $1.02 \cdot 10^{-3}$ M.

Low temperature studies (4 °C)

Low temperature studies were performed introducing the light source (Asahi Spectra Xenon light model MAX-303) and solutions in a cold room stabilized at 4 °C. After 30 minutes to stabilize the temperature of the introduced material, irradiation experiments were carried out following the general protocol for PPA irradiation.

Poly-(*R*)-1

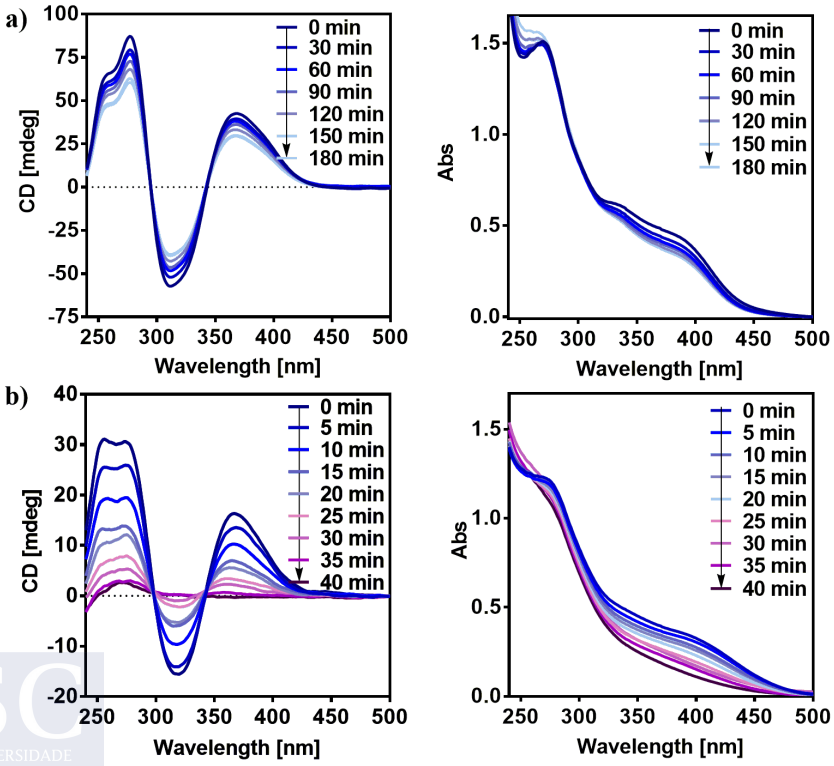

Figure S33. (a) CD and UV spectra of poly-(*R*)-**1** after irradiation under visible light at 4 °C in a) $CHCl_3$ and b) THF. [poly-(*R*)-**1**]= $1.02 \cdot 10^{-3}$ M.

Poly-(*R*)-2

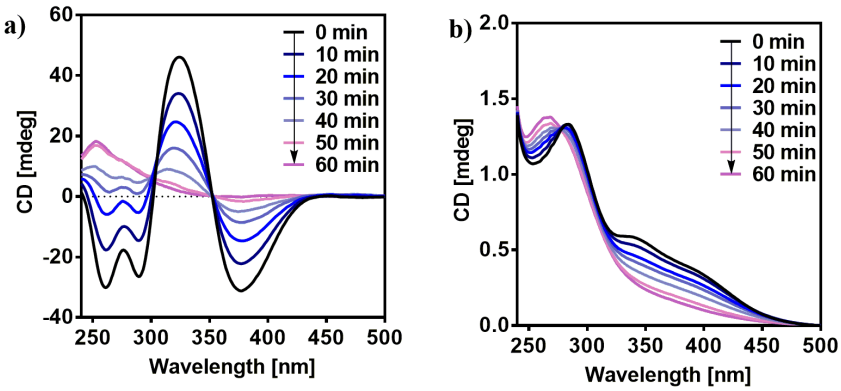

Figure S34. (a) CD and (b) UV spectra poly-(*R*)-**2** in $CHCl_3$ after irradiation under visible light at 4 °C. [poly-(*R*)-**2**]= $9.00 \cdot 10^{-4}$ M.

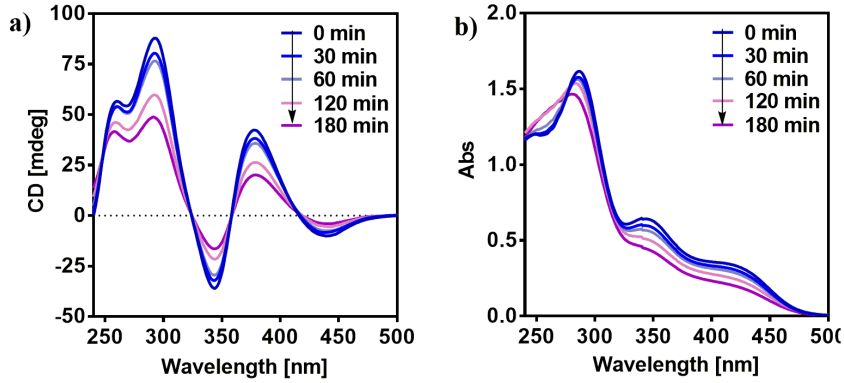

Figure S35. (a) CD and (b) UV spectra poly-(*R*)-**2** in THF after irradiation under visible light at 4 °C. [poly-(*R*)-**2**]= $9.00 \cdot 10^{-4}$ M.

Poly-(*S*)-3

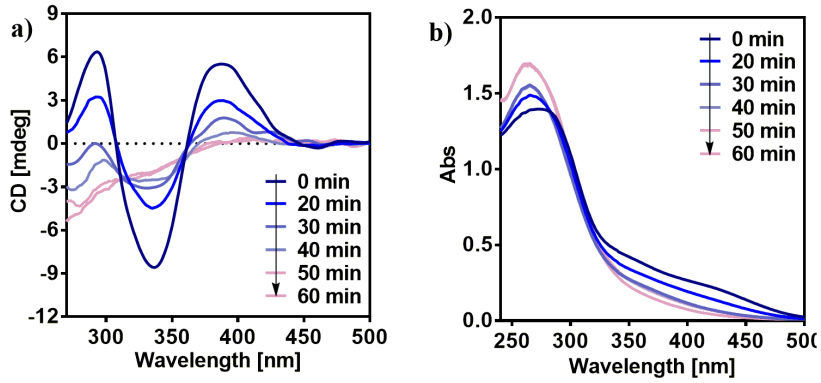

Figure S36. (a) CD and (b) UV spectra of poly-(*S*)-**3** in THF after irradiation under visible light at 4 °C. [poly-(*S*)-**3**]= $1.19 \cdot 10^{-3}$ M.

Poly-(*R*)-4

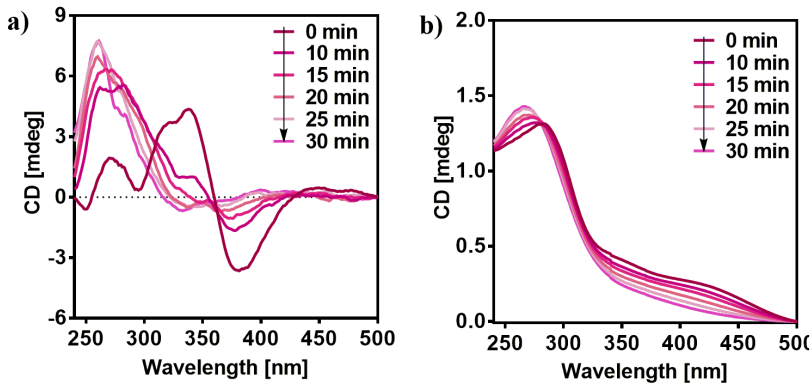

Figure S37. (a) CD and (b) UV spectra of poly-(*S*)-**5** in THF after irradiation under visible light at 4 °C. [poly-(*R*)-**4**]= $1.13 \cdot 10^{-3}$ M.

Poly-(*S*)-5

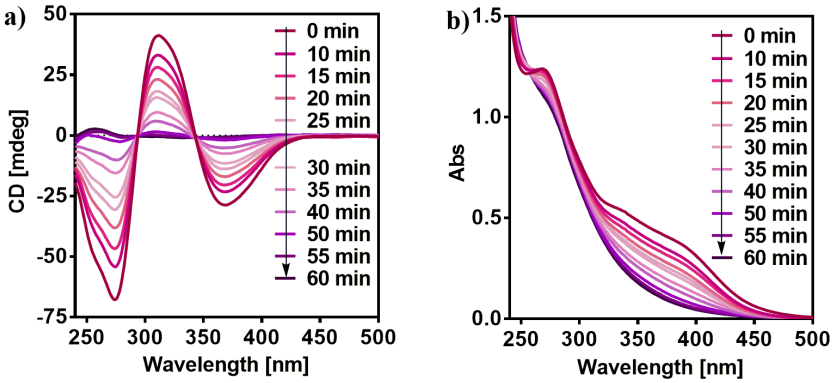

Figure S38. (a) CD and (b) UV spectra of poly-(*S*)-**6** in $CHCl_3$ after irradiation under visible light at 4 °C. [poly-(*S*)-**5**]= $1.30 \cdot 10^{-3}$ M.

Poly-(*S*)-6

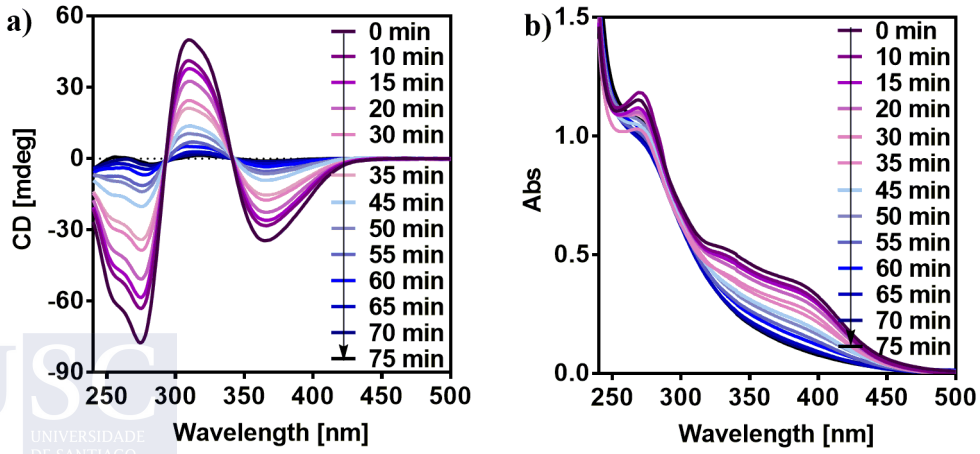

Figure S39. (a) CD and (b) UV spectra of poly-(*S*)-**7** in $CHCl_3$ after irradiation under visible light at 4 °C. [poly-(*S*)-**6**]= $1.16 \cdot 10^{-3}$ M.

Poly-(*S*)-7

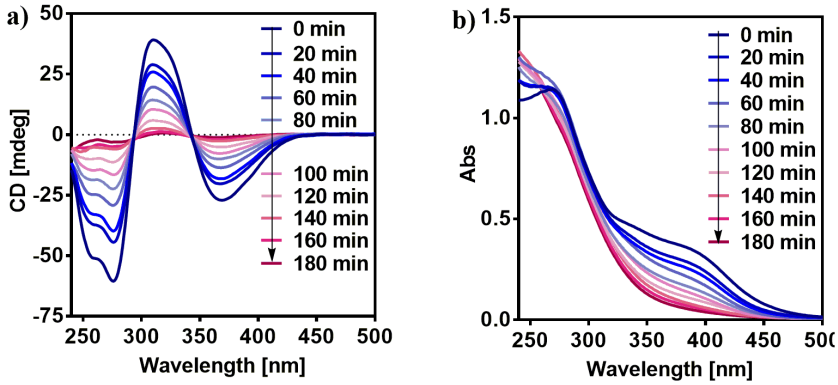

Figure S40. (a) CD and (b) UV spectra of poly-(*S*)-**8** in $CHCl_3$ after irradiation under visible light at 4 °C. [poly-(*S*)-**7**]= $9.76 \cdot 10^{-4}$ M.

Copolymers

Poly[(*R*)-1_r-co-(*S*)-$1_{(1-r)}$] series

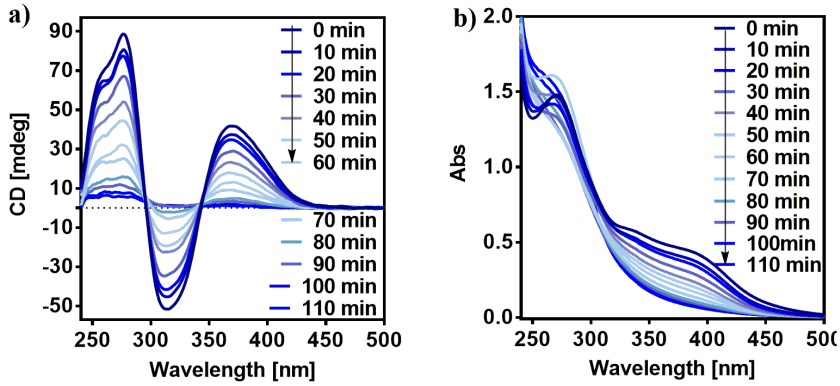

Figure S41. (a) CD and (b) UV spectra of poly[(*R*)-$\mathbf{1}_{0.95}$-co-(*S*)-$\mathbf{1}_{0.05}$] in $CHCl_3$ after irradiation under visible light. [poly[(*R*)-$\mathbf{1}_{0.95}$-co-(*S*)-$\mathbf{1}_{0.05}$]]= $1.02 \cdot 10^{-3}$ M.

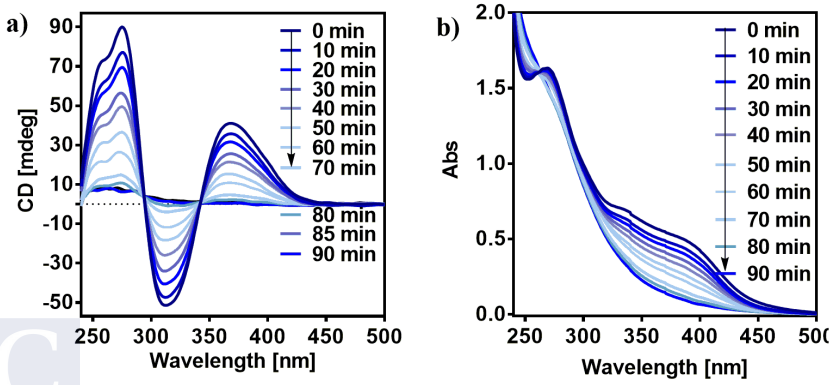

Figure S42. (a) CD and (b) UV spectra of poly[(*R*)-$\mathbf{1}_{0.9}$-co-(*S*)-$\mathbf{1}_{0.1}$] in $CHCl_3$ after irradiation under visible light. [poly[(*R*)-$\mathbf{1}_{0.9}$-co-(*S*)-$\mathbf{1}_{0.1}$]]= $1.02 \cdot 10^{-3}$ M.

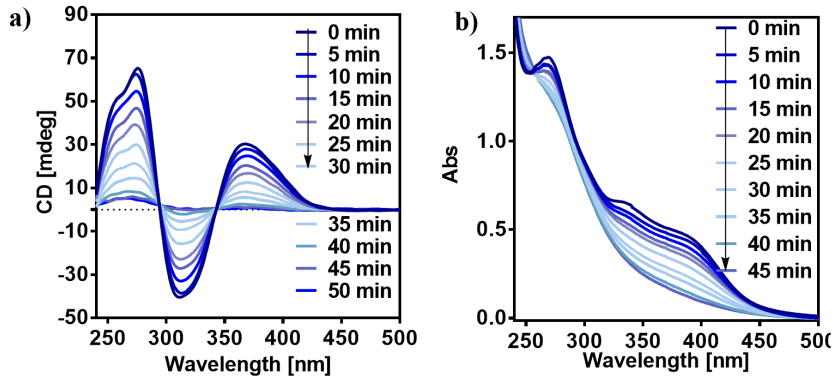

Figure S43. (a) CD and (b) UV spectra of poly[(*R*)-**1**$_{0.8}$-co-(*S*)-**1**$_{0.2}$] in $CHCl_3$ after irradiation under visible light. [poly[(*R*)-**1**$_{0.8}$-co-(*S*)-**1**$_{0.2}$]]= $1.02 \cdot 10^{-3}$ M.

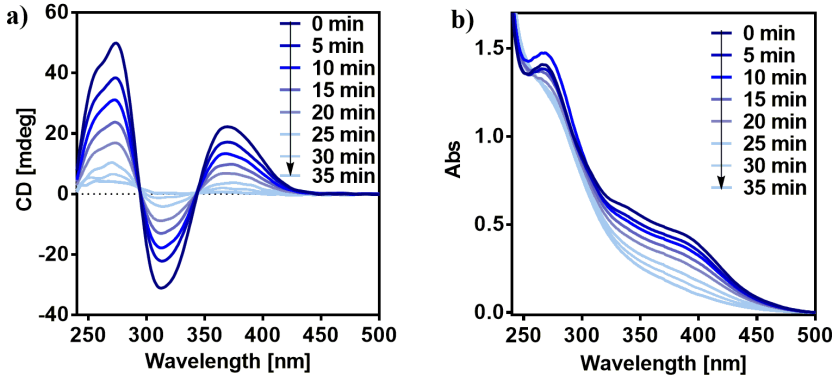

Figure S44. (a) CD and (b) UV spectra of poly[(*R*)-**1**$_{0.7}$-co-(*S*)-**1**$_{0.3}$] in $CHCl_3$ after irradiation under visible light. [poly[(*R*)-**1**$_{0.7}$-co-(*S*)-**1**$_{0.3}$]]= $1.02 \cdot 10^{-3}$ M.

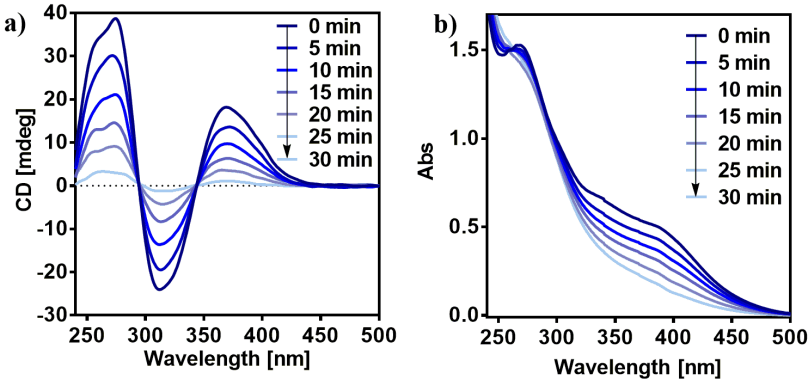

Figure S45. (a) CD and (b) UV spectra of poly[(*R*)-**1**$_{0.6}$-co-(*S*)-**1**$_{0.4}$] in $CHCl_3$ after irradiation under visible light. [poly[(*R*)-**1**$_{0.6}$-co-(*S*)-**1**$_{0.4}$]]= $1.02 \cdot 10^{-3}$ M.

Poly[(*R*)-2$_r$-co-(*S*)-2$_{(1-r)}$] series

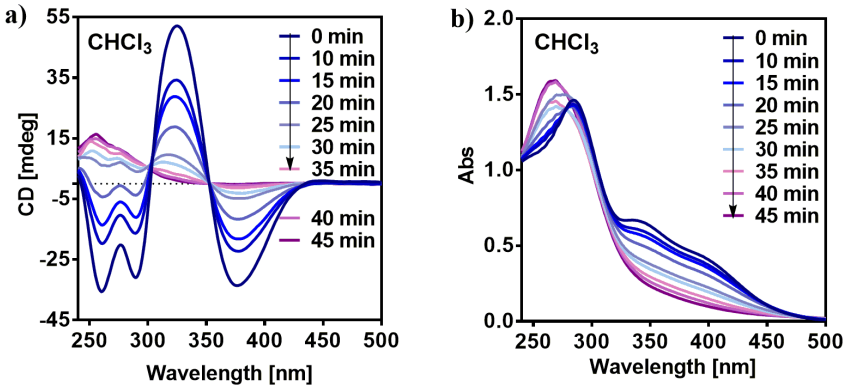

Figure S46. (a) CD and (b) UV spectra of poly[(*R*)-**2**$_{0.9}$-co-(*S*)-**2**$_{0.1}$] in $CHCl_3$ after irradiation under visible light. [poly[(*R*)-**2**$_{0.9}$-co-(*S*)-**2**$_{0.1}$]]= $9.00 \cdot 10^{-4}$ M.

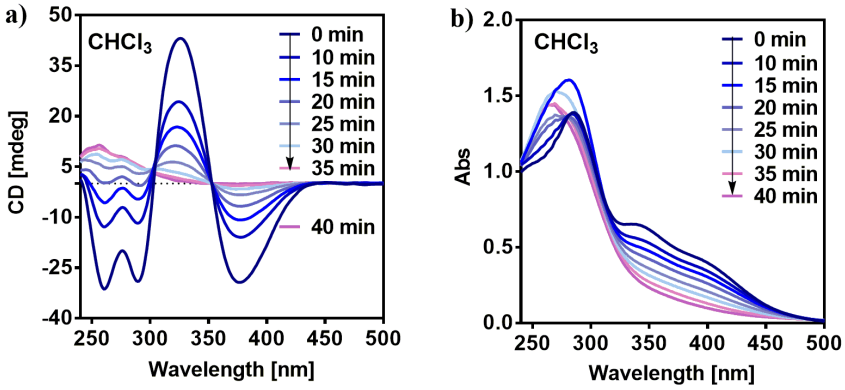

Figure S47. (a) CD and (b) UV spectra of poly[(*R*)-**2**$_{0.8}$-co-(*S*)-**2**$_{0.2}$] in $CHCl_3$ after irradiation under visible light. [poly[(*R*)-**2**$_{0.8}$-co-(*S*)-**2**$_{0.2}$]]= $9.00 \cdot 10^{-4}$ M.

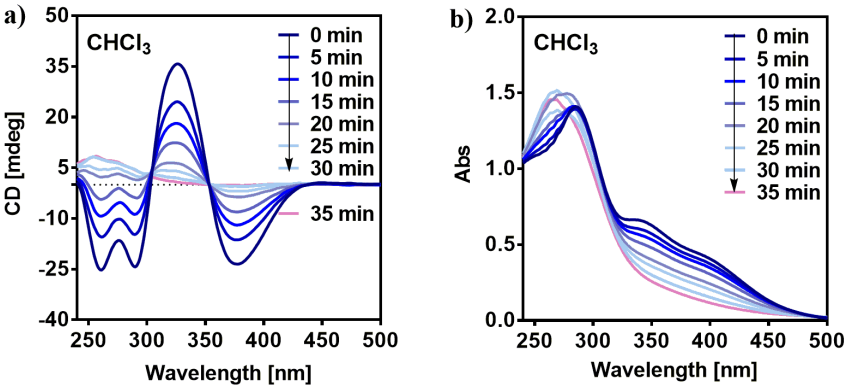

Figure S48. (a) CD and (b) UV spectra of poly[(*R*)-**2**$_{0.7}$-co-(*S*)-**2**$_{0.3}$] in $CHCl_3$ after irradiation under visible light. [poly[(*R*)-**2**$_{0.7}$-co-(*S*)-**2**$_{0.3}$]]= $9.00 \cdot 10^{-4}$ M.

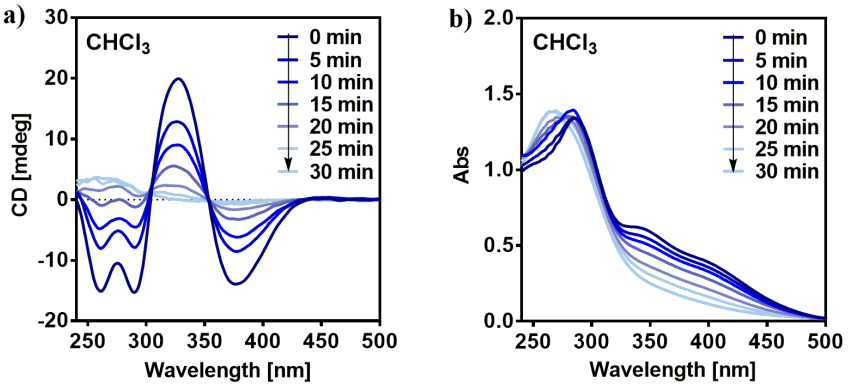

Figure S49. (a) CD and (b) UV spectra of poly[(*R*)-**2**$_{0.6}$-co-(*S*)-**2**$_{0.4}$] in $CHCl_3$ after irradiation under visible light. [poly[(*R*)-**2**$_{0.6}$-co-(*S*)-**2**$_{0.4}$]]= $9.00 \cdot 10^{-4}$ M.

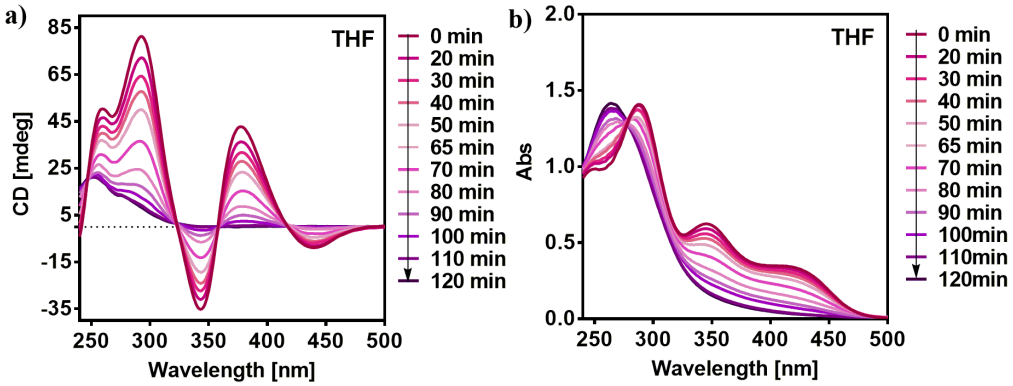

Figure S50. (a) CD and (b) UV spectra of poly[(*R*)-**2**$_{0.9}$-co-(*S*)-**2**$_{0.1}$] in THF after irradiation under visible light. [poly[(*R*)-**2**$_{0.9}$-co-(*S*)-**2**$_{0.1}$]]= $9.00 \cdot 10^{-4}$ M.

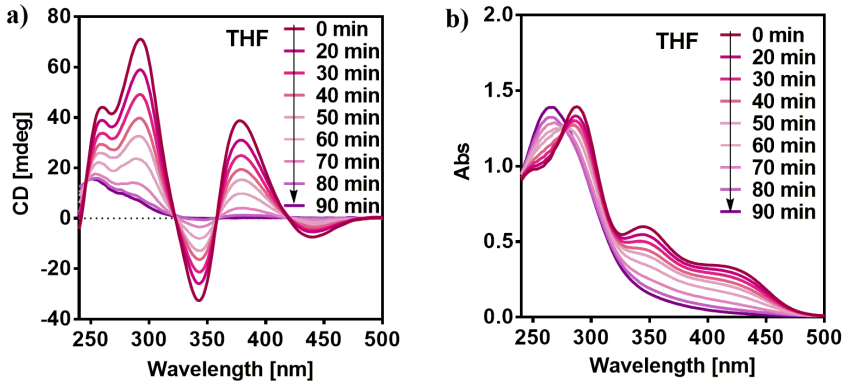

Figure S51. (a) CD and (b) UV spectra of poly[(*R*)-**2**$_{0.8}$-co-(*S*)-**2**$_{0.2}$] in THF after irradiation under visible light. [poly[(*R*)-**2**$_{0.8}$-co-(*S*)-**2**$_{0.2}$]]= $9.00 \cdot 10^{-4}$ M.

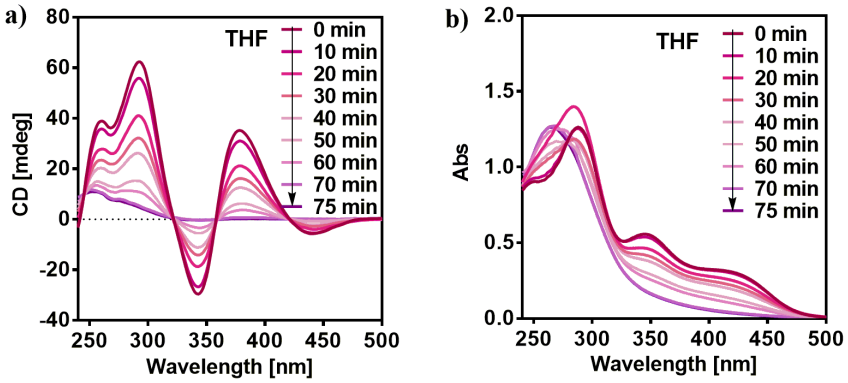

Figure S52. (a) CD and (b) UV spectra of poly[(*R*)-**2**$_{0.7}$-co-(*S*)-**2**$_{0.3}$] in THF after irradiation under visible light. [poly[(*R*)-**2**$_{0.7}$-co-(*S*)-**2**$_{0.3}$]]= $9.00 \cdot 10^{-4}$ M.

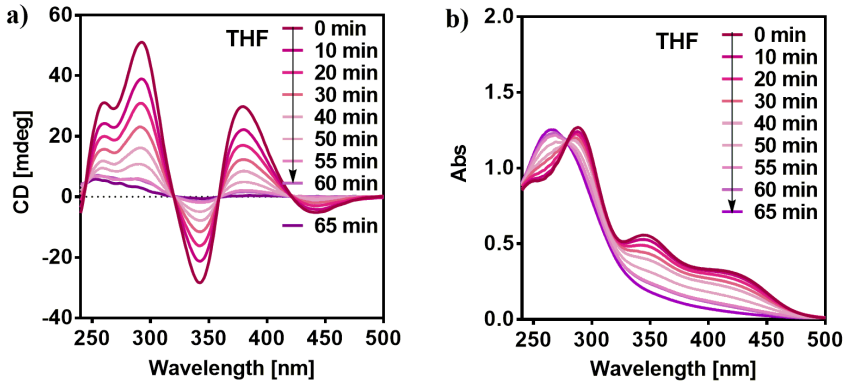

Figure S53. (a) CD and (b) UV spectra of poly[(*R*)-**2**$_{0.6}$-co-(*S*)-**2**$_{0.4}$] in THF after irradiation under visible light. [poly[(*R*)-**2**$_{0.6}$-co-(*S*)-**2**$_{0.4}$]]= $9.00 \cdot 10^{-4}$ M.

Poly[(*R*)-8$_r$-co-(*S*)-8$_{(1-r)}$] series

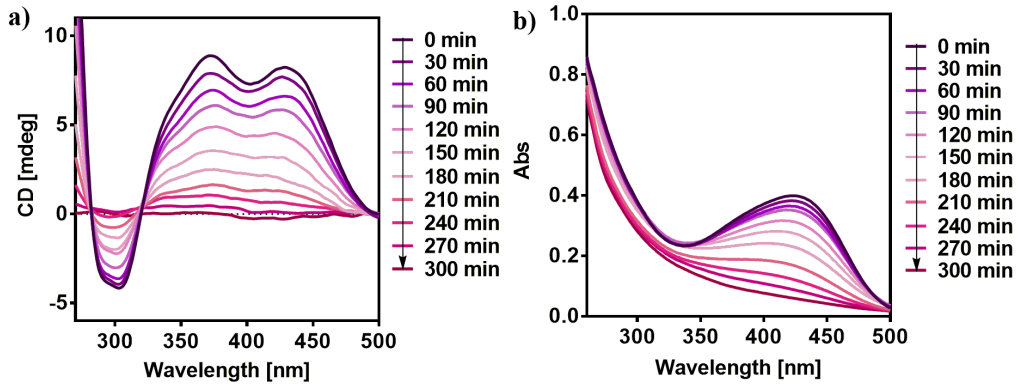

Figure S54. (a) CD and (b) UV spectra of poly[(*R*)-**2**$_{0.9}$-co-(*S*)-**2**$_{0.1}$] in $CHCl_3$ after irradiation under visible light. [poly[(*R*)-**8**$_{0.9}$-co-(*S*)-**8**$_{0.1}$]]= $1.02 \cdot 10^{-3}$ M.

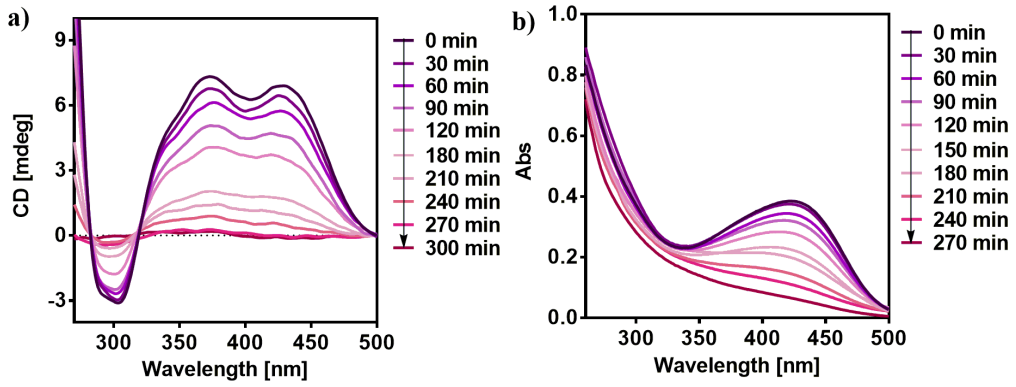

Figure S55. (a) CD and (b) UV spectra of poly[(*R*)-**2**$_{0.8}$-co-(*S*)-**2**$_{0.2}$] in $CHCl_3$ after irradiation under visible light. [poly[(*R*)-**8**$_{0.8}$-co-(*S*)-**8**$_{0.2}$]]= $1.02 \cdot 10^{-3}$ M.

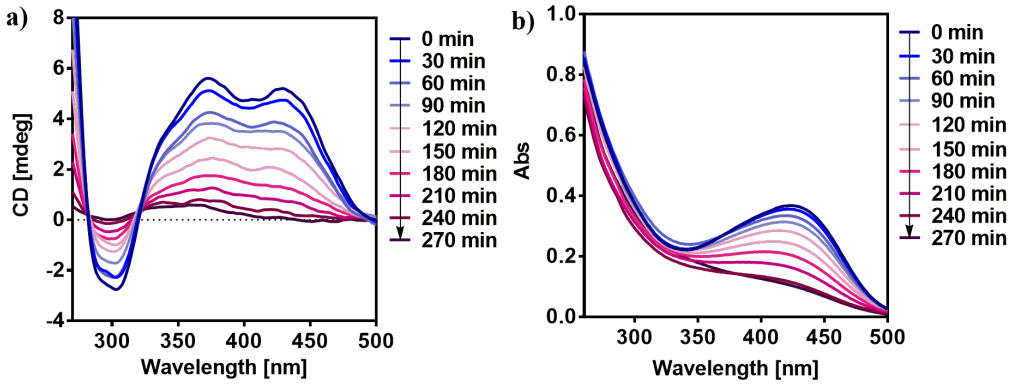

Figure S56. (a) CD and (b) UV spectra of poly[(*R*)-**2**$_{0.7}$-co-(*S*)-**2**$_{0.3}$] in $CHCl_3$ after irradiation under visible light. [poly[(*R*)-**8**$_{0.7}$-co-(*S*)-**8**$_{0.3}$]]= $1.02 \cdot 10^{-3}$ M.

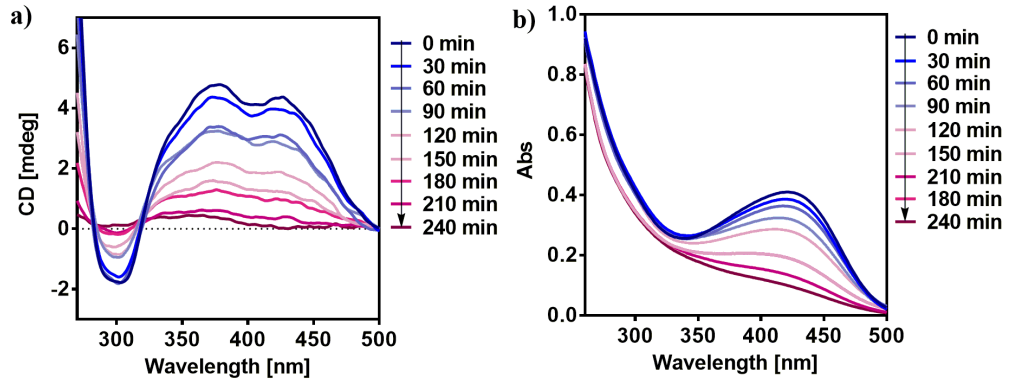

Figure S57. (a) CD and (b) UV spectra of poly[(*R*)-**2**$_{0.6}$-co-(*S*)-**2**$_{0.4}$] in $CHCl_3$ after irradiation under visible light. [poly[(*R*)-**8**$_{0.6}$-co-(*S*)-**8**$_{0.4}$]]= $1.02 \cdot 10^{-3}$ M.

6. Supporting References

S1. I. Louzao, J. M. Seco, E. Quiñoá, R. Riguera, *Angew. Chem. Int. Ed.* **2010**, *49*, 1430-1433.

S2. S. Leiras, F. Freire, J. M. Seco, E. Quiñoá, R. Riguera, *Chem. Sci.*, **2013**, *4*, 2735-2743.

S3. K. Cobos, R. Rodríguez, E. Quiñoá, R. Riguera, F. Freire, *Angew. Chem. Int. Ed.* **2020**, *59*, 23724-23730.

S4. S. Arias, M. Núñez-Martínez, E. Quiñoá, R. Riguera, F. Freire, *Polym. Chem.* **2017**, *8*, 3740-3745.

S5. S. Arias, R. Rodríguez, E. Quiñoá, R. Riguera, F. Freire, *J. Am. Chem. Soc.*, **2018**, *140*, 667-674.

S6. M. Alzubi, S. Arias, I. Louzao, E. Quiñoá, R. Riguera, F. Freire, *ChemComm*, **2017**, *53*, 8573-8576.

S7. R. Rodríguez, E. Quiñoá, R. Riguera, F. Freire, F., *J. Am. Chem. Soc.*, **2016**, *138*, 9620-9628.

S8. F. Rey-Tarrío, R. Rodríguez, E. Quiñoá, R. Riguera, F. Freire, *Angew. Chem. Int. Ed.*, **2021** *60*, 8095-8103.

Experimental Section Chapter V

1. Materials and methods

ECD measurements were done in a Jasco-720 and VT-ECD measurements in a Jasco-1100 with a 1 mm quartz cuvette. The amount of polymer used for ECD and VT-ECD measurements was 0.3 mg/mL.

UV spectra were registered in a Jasco V-630 with a 1 mm quartz cuvette. The amount of polymer used for UV measurements was 0.3 mg/mL.

Optical rotation was measured in a Jasco-P2000.

NMR experiments were measured in a Varian 300 operating at 300 MHz for proton NMR and 75 MHz for carbon. $CDCl_3$ signal (δ= 77.2ppm) was used as standard for ^{1}H or ^{13}C experiments.

Crystallographic data was obtained with a Bruker D8 Venture.

ATR/FT-IR spectra were recorded in a Perkin Elmer FT-IR ATR Spectrum Two

Raman spectra were done in a Renishaw confocal Raman spectrometer (Invia Reflex model), equipped with two lasers (diode laser 785 nm and Ar laser 514 nm).

Vibrational CD (VCD) experiments were measured in a 150 μm BaF_2 cell with a JASCO FVS-6000 spectrometer. The amount of polymer used was 50 mg/mL in $CDCl_3$ and d^8-THF.

GPC studies were carried out in a Waters Alliance 2695 HPLC with a UV-2489 detector (Waters) and three Phenomenex GPC columns. The amount of polymer used for GPC measurements was 0.3 mg/mL.

DSC traces were obtained in a DSC Q200 Tzero Technology (TA Instruments, New Castle, UK), equipped with a refrigerated cooling system RCS90 (TA Instruments, New Castle, UK), using a Tzero low-mass aluminum pan.

TGA traces were obtained in a TGA Q5000 (TA Instruments, New Castle, UK) using a platinum pan.

AFM measurements were performed in a MultiMode V Scanning Probe Microscope (Veeco Instruments) in air at rt with standard silicon cantilevers and supersharp cantilevers in tapping mode using 12 μm and 1 μm scanners Nanoscope processing software and WSxM 4.0 Beta 1.0 [4] (Nanotec Electronica, S.L.) were used for image analysis. All measurements were performed at CACTI (Vigo University, Spain).

Irradiation experiments were done in an Asahi Spectra Xenon light model MAX-303.

2. Synthesis of Monomer

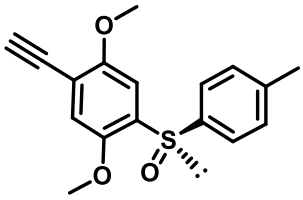

mono-(*R*)-**1**

mono-(*R*)-**1** was prepared according to the procedure described in the Reference **S1.**

$[\alpha]_D^{20}$ = -2.3820 (c = 5.0 mg/mL, $CHCl_3$)

^{1}H NMR (300 MHz, $CDCl_3$) δ(ppm): 2.35 (s, 3H), 3.36 (s, 1H), 3.71 (s, 3H), 3.96 (s, 3H), 6.92 (s, 1H), 7.12-7.23 (d, 2H) 7.47-7.58 (m, 3H)

^{13}C NMR (75 MHz, $CDCl_3$) δ (ppm): 21.6, 56.5, 57.0, 79.6, 83.0, 107.1, 114.2, 117.1, 125.7, 130.0, 135.8, 141.9, 142.3, 149.1, 156.3.

HRMS (ESI) m/z calcd for $C_{17}H_{17}O_3S$ $[M+H]^+$: 301.0898, found: 301.0896

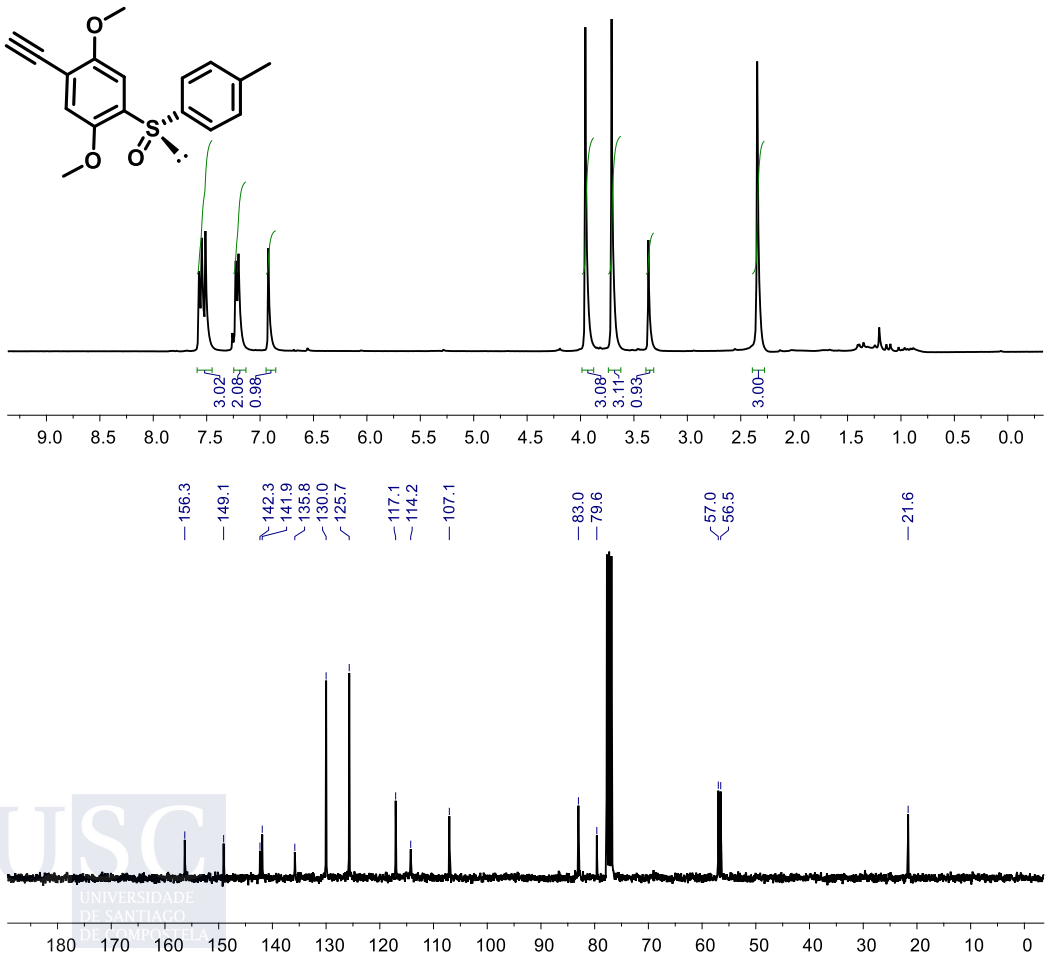

Figure S1. ^{1}H and ^{13}C NMR spectra of mono-(*R*)-**1** ($CDCl_3$, 300 and 75 MHz respectively).

3. Synthesis of Polymer

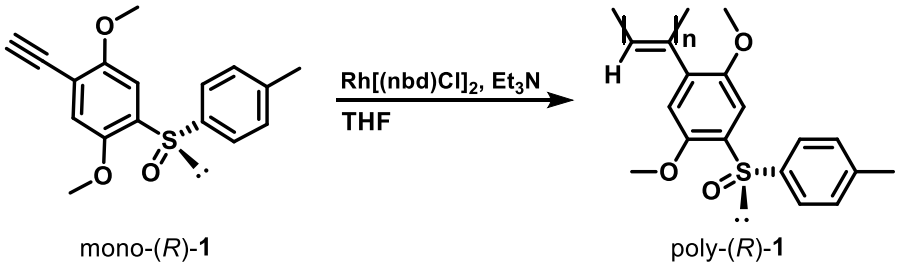

The reaction flask (sealed ampoule) was dried under vacuum and argon flushed for three times before monomer was added as a solid (80 mg, 0.27 mmol). Dry THF (0.5 mL) was added with a syringe. A solution of rhodium norbornadiene chloride dimer, $[Rh(nbd)Cl]_2$, (1.23 mg) and ET_3N (7.1 μL) in dry THF (0.1 mL) was added at 50 °C. The reaction mixture was stirring at 50 °C for 12 h. Then, the resulting polymer was diluted in CH_2Cl_2 and it was precipitated in a large amount of methanol:diethyl ether (2:8), centrifuged (2 times), reprecipitated in hexane and centrifuged again obtaining 53 mg of poly-(*R*)-**1** (66 %).

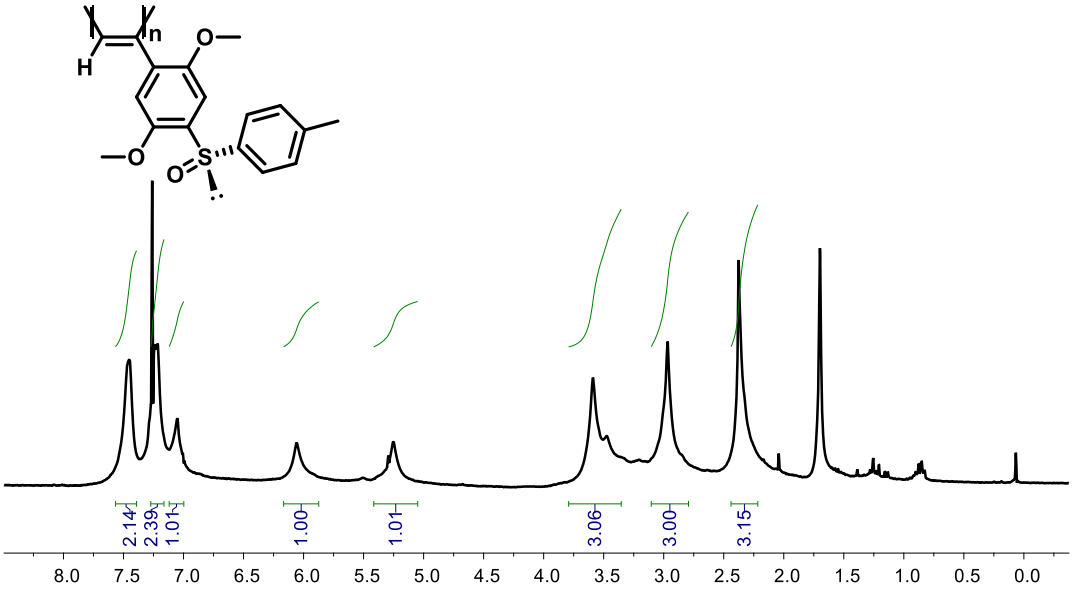

Figure S2. ^1H NMR spectra of poly-(*R*)-**1** ($CHCl_3$, 300 MHz).

4. General Protocol for PPA Irradiation

Poly-(*R*)-**1** was solubilized at room temperature by stirring in the correspondent solvent for prepare a solution of 2.1 mg in 7 mL. After this, irradiation experiments were performed using a collimator Lens (x1.0) of a MAX-303 (Asahi Spectra) equipped with a UV-VIS mirror module (300-600 nm) and a shortpass filter (VIS 550nm 25 dia.) applying the general protocol for PPA irradiation described in the reference S2 for measures in a 1 mm cuvette.

5. Crystallographic Data

For X-ray analysis, crystals of mono-(*R*)-**1** was grown by slow evaporation from a $CHCl_3$ solution. The obtained crystal was collected in a total of 4451 frames for 3.51 hours. The frames were integrated with the Bruker SAINT software package using a narrow-frame algorithm. The integration of the data using a triclinic unit cell yielded a total of 32926 reflections to a maximum θ angle of 28.35° (0.75 Å resolution), of which 3514 were independent (average redundancy 9.370, completeness = 99.8 %, R_{int} = 6.69%, R_{sig} = 3.30 %) and 3292 (93.68 %) were greater than 2σ (F2). The final cell constants are a = 5.5842(4) Å, b = 6.8897(4) Å, c = 9.4917(6) Å, α = 93.865(3)°, β = 92.971(3)°, γ = 94.308(3)°, volume = 362.72(4) $Å^3$, that are based upon the refinement of the XYZ-centroids of 9896 reflections above 20 σ(I) with 5.945° < 2θ < 56.66°. Data were corrected for absorption effects using the Multi-Scan method (SADABS). The ratio of minimum to maximum apparent transmission was 0.870. The calculated minimum and maximum transmission coefficients (based on crystal size) are 0.9470 and 0.9620.

The structure was solved and refined using the Bruker SHELXTL Software Package, using the space group P 1, with Z = 1 for the formula unit, $C_{17}H_{16}O_3S$. The final anisotropic full-matrix least-squares refinement on F2 with 193 variables converged at R1 = 3.35 %, for the observed data and wR2 = 8.65 % for all data. The goodness-of-fit was 1.038. The largest peak in the final difference electron density synthesis was 0.423 e-/$Å^3$ and the largest hole was -0.243 e-/$Å^3$ with an RMS deviation of 0.053 e-/$Å^3$. On the basis of the final model, the calculated density was 1.375 g/cm^3 and F(000), 158 e-.

6. Spectroscopy Studies

Raman

Samples was prepared by drop casting 0.5 mg/mL solutions of poly-(*R*)-**1** in $CHCl_3$ and THF over a microscope slide. After solvent evaporation, the spectra were recovered in a Renishaw confocal Raman spectrometer.

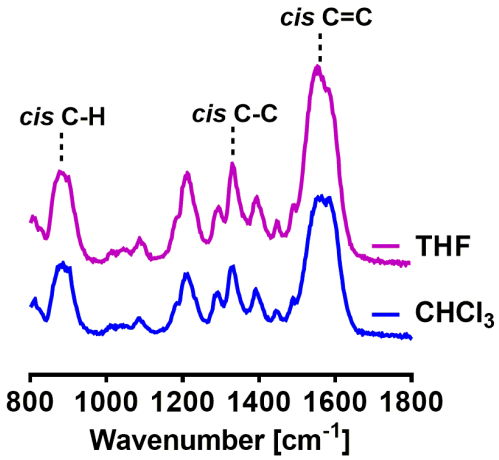

Figure S3. (a) Raman spectra of poly-(*R*)-**1** in compressed ($CHCl_3$) and stretched (THF) helices.

ATR/FT-IR

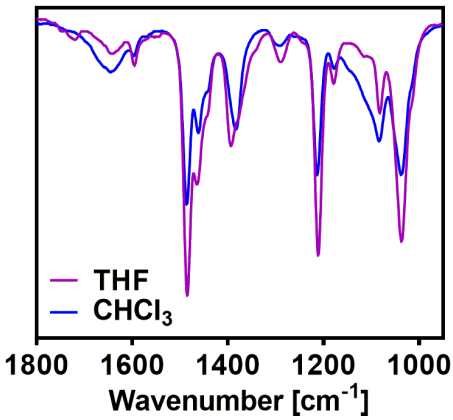

Figure S4. (a) ATR/FT-IR spectra of poly-(*R*)-**1** in compressed ($CHCl_3$) and stretched (THF) helices.

7. Thermal Studies

DSC studies

A polymer sample, pre-dried in the correspondent solvent, was introduced in an aluminum pan and heated from 40 °C to 350 °C with a heating rate of 10 °C/min (Figure S5). The thermograms of the polymers show traces of a *cis-transoidal* backbone, where two exothermal peaks corresponding to the *c-t* to *c-c* and the *c-c* to *t-t* were observed. The exothermal peak corresponding to *c-t* to *c-c* transition show strong variations in intensity and broad of the peak in comparison with the standard PPAs for the stiffness of the polymer.

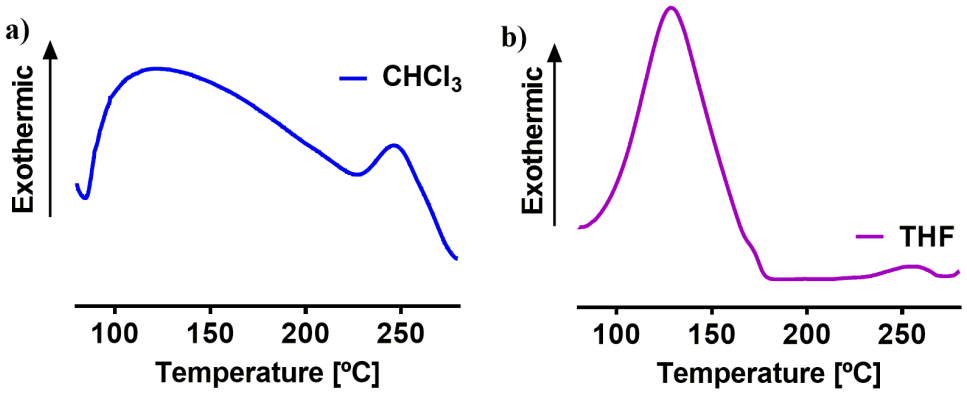

Figure S5. DSC thermograms of a polymer sample dried in (a) $CHCl_3$ and (b) THF of poly-(*R*)-**1**.

TGA studies

A solid polymer sample was remained under vacuum for 12 hours. After this, was introduced in a platinum pan and heated from 40 °C to 800 °C with a heating rate of 10 °C/min (Figure S6).

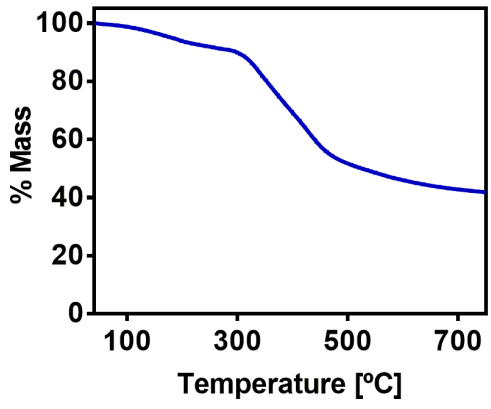

Figure S6. TGA thermogram of poly-(*R*)-**1**.

8. GPC Studies

GPC results were obtained in an Aliance 2695 HPLC with a UV-2489 detector (Waters). The samples were eluted in THF by three Phenogel columns connected to each other with stationary phases of 103, 104 and 105 Armstrong and packed with a solid support of a cross-linked styrene and p-divinylbenzene copolymer. For GPC data of poly-(*R*)-**1** see the table below.

Mn (Daltons)	**Mw** (Daltons)	**Mp** (Daltons)	**Mz** (Daltons)	**Mw/Mn**
88701	191229	160973	37351	2.15

9. AFM Studies

Monolayers was prepared from 0.1 mg/mL solutions in $CHCl_3$ and THF spin-coated over HOPG and kept under the corresponding solvent vapor 12 hours. After this, AFM measurements were performed at CACTI (Vigo University, Spain) in a MultiMode V Scanning Probe Microscope (Veeco Instruments) in air and room temperature. Also, Standard silicon cantilevers and supersharp cantilevers in tapping mode was selected using 12 μm and 1 μm scanners. Nanoscope processing software and WSxM 4.0 Beta 1.0 (Nanotec Electronica, S.L.) were used for image analysis.

Stretched helix ($CHCl_3$)

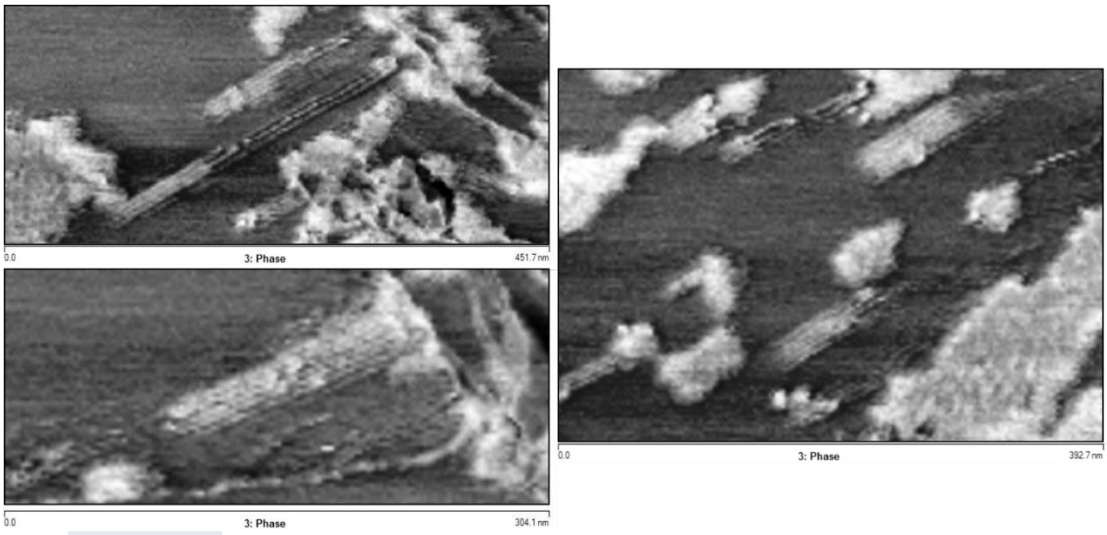

Figure S7. AFM images of stretched helical monolayers of poly-(*R*)-**1** from $CHCl_3$ solution.

Compressed helix (THF)

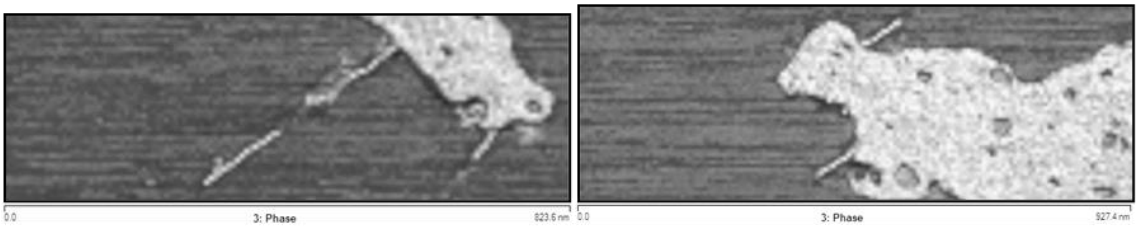

Figure S8. AFM images of helical monolayers of poly-(*R*)-**1** from THF solution.

10. Monomer calculations

Calculated ECD spectra reveals a S_0 to S_1 transition experimentally absent. As result, S_0 to S_7 transition is bathochromically displaced of its expected maximum (this displacement is negligible due to the lambda factor applied as result of the difference between the theoretical and experimental wavelengths). Finally, last ECD signal (experimentally around 275 nm) corresponds mainly to S_0 to S_{17} transition.

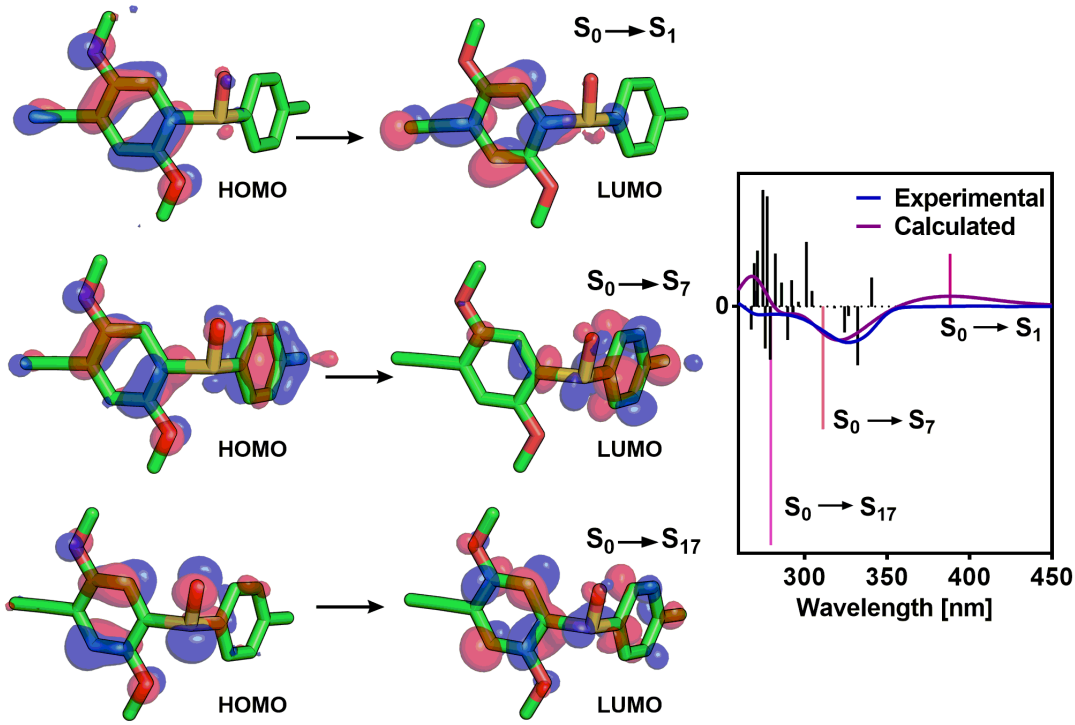

Figure S9. Main HOMO and LUMO of the transition assign to each calculated natural transition orbitals (NTO).

11. VT-ECD Experiments

Variable temperature circular dichroism (VT-ECD) experiments were measured in a 1 mm quartz cell in a Jasco-1100. The amount of sample used was 0.3 mg/mL in the solvents analysed.

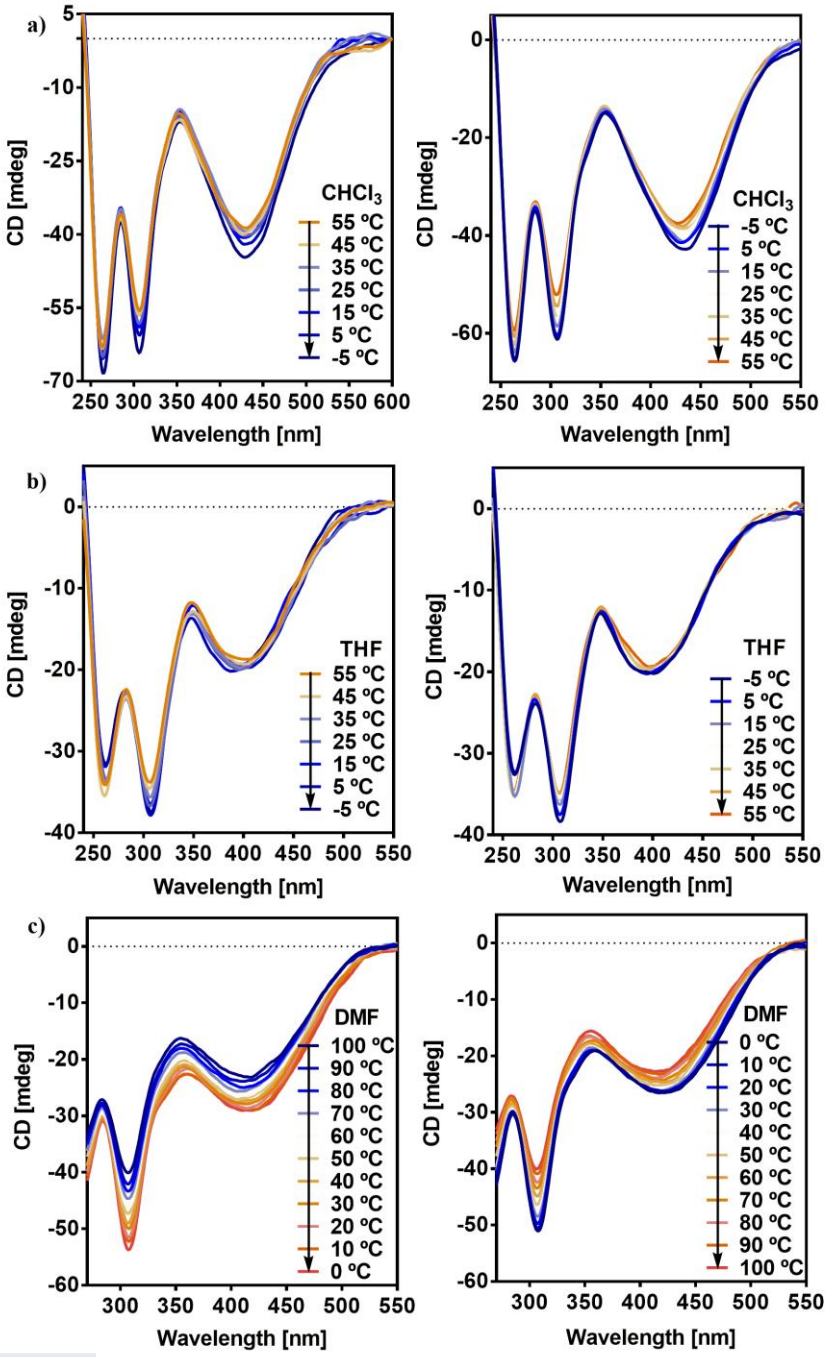

Figure S10. Heating/cooling ECD curves of poly-(*R*)-**1** in (a) $CHCl_3$, (b) THF and (c) DMF.

12. ECD and UV Experiments

ECD and UV experiments were measured in a 1 mm quartz cell in a Jasco-720 and a Jasco V-630 respectively. The amount of sample used was 0.3 mg/mL in the solvents analysed.

Poly-(*R*)-1

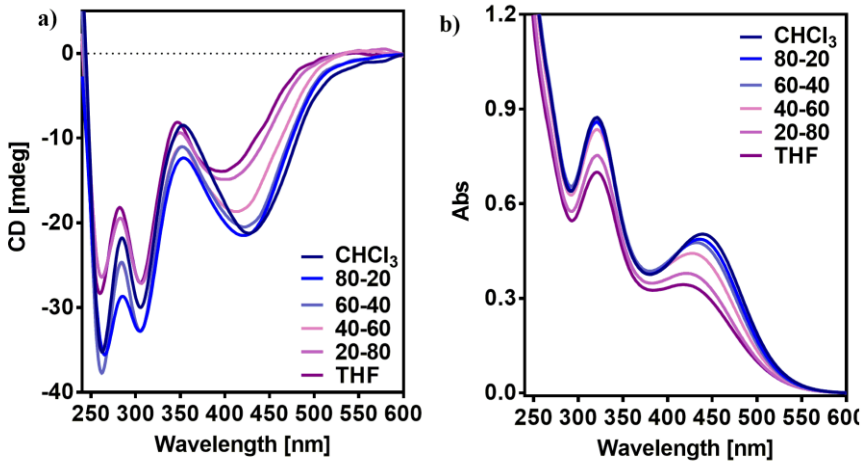

Figure S11. Mixture of poly-(*R*)-**1** at 0.3 mg/mL in different percentages of $CHCl_3$ and THF monitored by (a) ECD and (b) UV spectra.

m-(*R*)-1

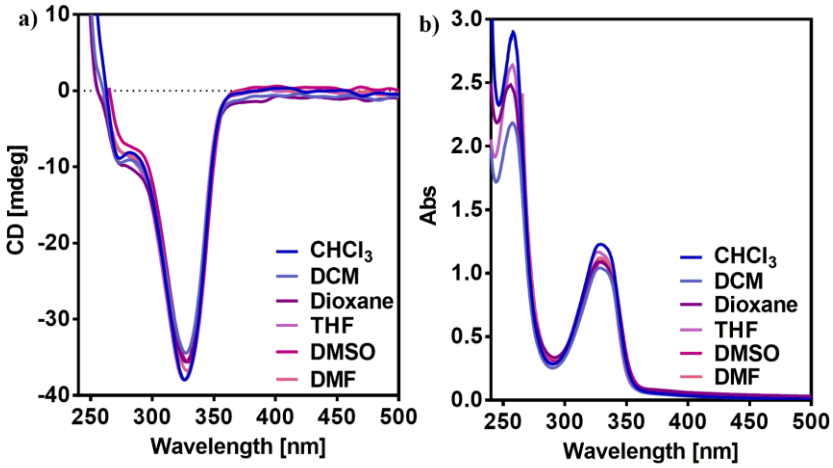

Figure S12. Mono-(*R*)-**1** at 0.3 mg/mL in different solvents monitored by (a) ECD and (b) UV spectra.

13. Enantiomeric Studies

Using the same protocol described for preparation of poly-(*R*)-**1**, its enantiomer (poly-(*S*)-**1**) was polymerized in a 63 % of yield. Appling the same experimental conditions, mono-(*S*)-**1** and poly-(*S*)-**1** was submitted to ECD and UV experiments to confirm that their chirality transfers properties can promote the formation of its corresponding right-handed helices instead the left-handed observed in poly-(*R*)-**1**.

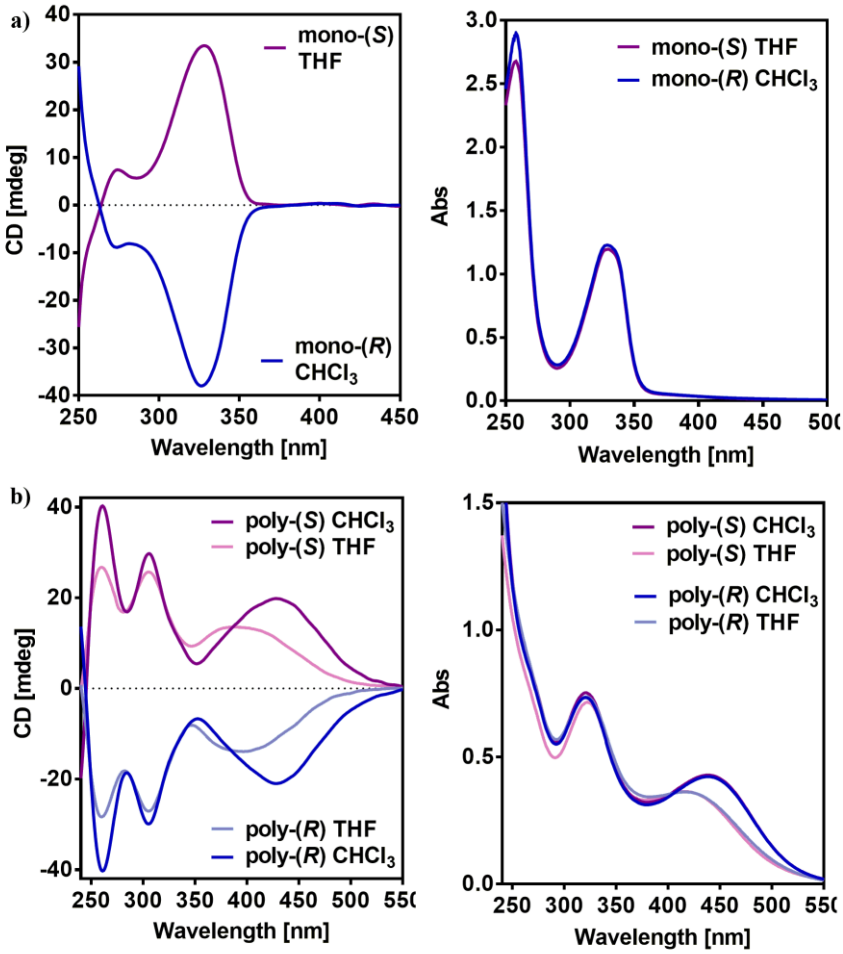

Figure S13. ECD and UV comparison between (a) m-(*R*)-**1** and m-(*S*)-**1** and (b) poly-(*R*)-**1** and poly-(*S*)-**1**.

14. Computational Details

Considering the difficulties to carry out theoretical calculations on large polymers, we apply the methodology reported in the reference S3. Thus, oligomers constituted by 8 monomer repeating units was build using Spartan 18. The generated structure was adjusted according to the information obtained from several techniques such as Raman, IR, ECD and AFM. Moreover, this experimentally supported structure was refined through Molecular Mechanics (MMFF94) before being submitted for ECD calculations. Finally, the time-dependent density functional theory (TD-DFT, Ref. S4) was used together with the rCAM-B3LYP density functional (Ref. S5) and the 3-21G* basis set (Ref. S6). We included 100 excitation energies in the calculation for the stretched scaffold ($CHCl_3$) and 110 excitation energies for the compressed scaffold (THF). The resulting ECD spectrums were selected with a full width at half height (FWHM) of 0.4 eV. Moreover, we evaluated a correction factor for lambda as the difference between the theoretical and experimental wavelengths, and we shifted the rest of the theoretical spectra accordingly. In a similar way, the intensity, was rescaled for the theoretical values to get the experimental intensity at the first Cotton effect band.

For monomer calculations, optimization of the geometry was applied using the density functional theory (DFT) together with the rCAM-B3LYP functional and the 6-31G* basis set. Thus, the theorical ECD spectrum was calculated since the optimized geometry using the time-dependent density functional theory (TD-DFT) together the rCAM-B3LYP density functional and the 6-31G* basis set. The resulting ECD spectrum was selected with a full width at half height (FWHM) of 0.45 eV. Moreover, we evaluated a correction factor for lambda as the difference between the theoretical and experimental wavelengths, and we shifted the rest of the theoretical spectrum accordingly. Similarly, the ECD intensity was rescaled in the theoretical values.

15. Supporting References

S1. P. Reiné, A. M. Ortuño, S. Resa, L. Á. de Cienfuegos, V. Blanco, M. J. Ruedas-Rama, G. Mazzeo, S. Abbate, A. Lucotti, M. Tommasini, S. Guisán-Ceinos, M. Ribagorda, A. G. Campaña, A. Mota, G. Longhi, D. Miguel, J. M. Cuerva, *ChemComm.*, **2018**, *54*, 13985-13988.

S2. F. Rey-Tarrío, R. Rodríguez, E. Quiñoá, R. Riguera, F. Freire, *Angew. Chem. Int. Ed.* **2020**, *60*, 8095-8103.

S3. B. Fernández, R. Rodríguez, A. Rizzo, E. Quiñoá, R. Riguera, F. Freire, *Angew. Chem. Int. Ed.* **2018**, *57*, 3666-3670.

S4. E. Runge, E. K. U. Gross, *Phys. Rev. Lett.* **1984**, *52*, 997-1000.

S5. A. J. Cohen, P. Mori-Sánchez, W. Yang, *J. Chem. Phys.* **2007**, *126*, 191109.

S6. J. S. Binkley, J. A. Pople, W. J. Hehre, *J. Am. Chem. Soc.* **1980**, 102, 939- 947.

Experimental Section Chapter VI

1. Materials and methods

CD measurements were done in a Jasco-720 with a 1 mm quartz cuvette. The amount of polymer used for CD measurements was 0.3 mg/mL.

UV spectra were registered in a Jasco V-630 with a 1 mm quartz cuvette. The amount of polymer used for UV measurements was 0.3 mg/mL.

Optical rotation was measured in a Jasco-P2000.

NMR experiments were measured in a Varian 300 operating at 300 MHz for proton NMR and 75 MHz for carbon. $CDCl_3$ signal (δ= 77.2ppm) or DMSO-d_6 (δ= 39.5 ppm) was used as standard for ^{1}H or ^{13}C experiments.

Crystallographic data was obtained with a Bruker D8 Venture.

Raman spectra were done in a Renishaw confocal Raman spectrometer (Invia Reflex model), equipped with two lasers (diode laser 785 nm and Ar laser 514 nm).

ATR/FT-IR spectra were recorded in a Perkin Elmer FT-IR ATR Spectrum Two.

DSC traces were obtained in a DSC Q200 Tzero Technology (TA Instruments, New Castle, UK), equipped with a refrigerated cooling system RCS90 (TA Instruments, New Castle, UK), using a Tzero low-mass aluminium pan.

TGA traces were obtained in a TGA Q5000 (TA Instruments, New Castle, UK) using a platinum pan.

AFM measurements were performed in a MultiMode V Scanning Probe Microscope (Veeco Instruments) in air at rt with standard silicon cantilevers and supersharp cantilevers in tapping mode using 12 μm and 1 μm scanners Nanoscope S4 processing software and WSxM 4.0 Beta 1.0 [4] (Nanotec Electronica, S.L.) were used for image analysis. All measurements were performed at CACTI (Vigo University, Spain).

Irradiation experiments were done in an Asahi Spectra Xenon light model MAX-303.

DLS studies were performed on a Nano-ZS 90 (Malvern) equipped with a He-Ne laser (l= 633 nm), under scattering angle of 173° and a sample concentration of 0.3 mg/mL.

2. Synthesis of Monomers

(*S*,*E*)-2-amino-N-(4-(phenyldiazenyl)phenyl)propanamide:

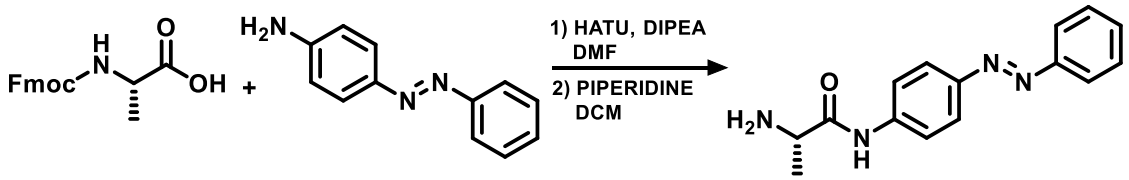

Fmoc-*L*-alanine (1000 mg, 1 equiv), N-[(Dimethylamino)-1H-1,2,3-triazolo-[4,5-b]pyridin-1-ylmethylene]-N-methylmethanaminium hexafluorophosphate N-oxide (HATU, 1342 mg, 1.1 equiv) and diisopropyltriethylamine (DIPEA, 0.61 mL, 1.1 equiv) were dissolved in 20 mL of DMF under Ar. The mixture was stirred for 15 min to activate the acid. Then, 4-aminoazobenzene was added (697 mg, 1.1 equiv), and the reaction mixture was stirred overnight. The organic layer was washed three times with HCl 1M and a saturated solution of $NaHCO_3$. The combined organic layers were dried over anhydrous Na_2SO_4, filtered and the solvent was evaporated at reduced pressure. The crude of the reaction was dissolved in DCM (50 mL) and 10 mL of piperidine was added and the mixture was stirred 15 min. After removing the solvent, the crude product was chromatographed on silica gel (40-63 mesh) with hexane/ethyl acetate (60:40) as eluent obtaining, after solvent removal, an orange solid (749 mg, 87% of yield).

^{1}H NMR (300 MHz, $CDCl_3$) δ(ppm): 1.23 (s, 3H), 3.48 (S, 1H) 7.50-7.64 (m, 4H), 7.82-7.97 (m, 7H).

^{13}C NMR (75 MHz, $CDCl_3$) δ (ppm): 26.5, 56.4, 124.5, 127.5, 128.9, 134.6, 136.2, 147.3, 152.7, 157.2, 180.7.

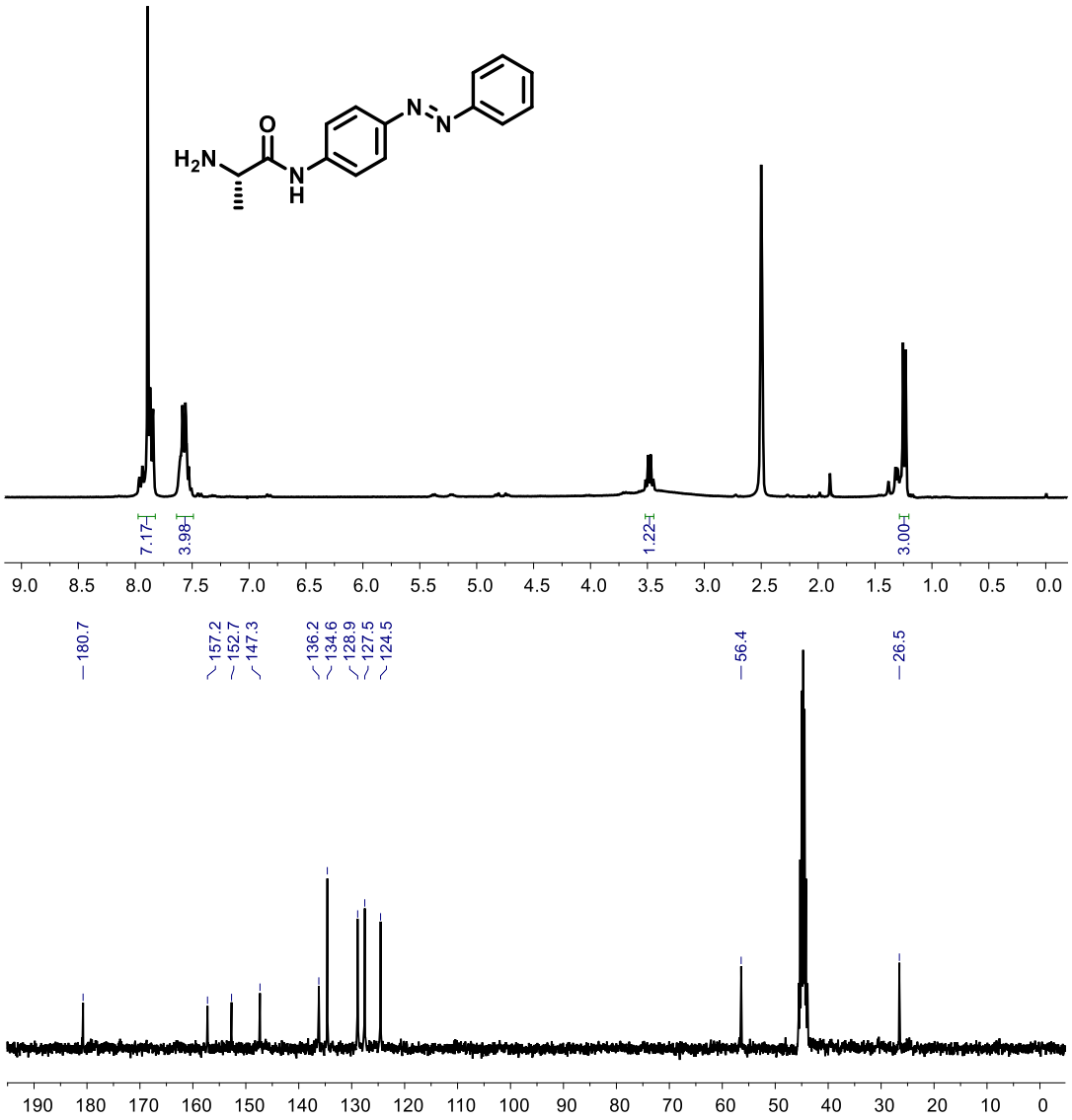

Figure S1. ^{1}H and ^{13}C NMR spectra of (*S,E*)-2-amino-N-(4-(phenyldiazenyl)phenyl)propanamide (DMSO, 300 and 75 MHz respectively).

(*S,E*)-4-ethynyl-N-(1-oxo-1-((4-(phenyldiazenyl)phenyl)amino)propan-2-yl)benzamide [mono-(*L*)-1):

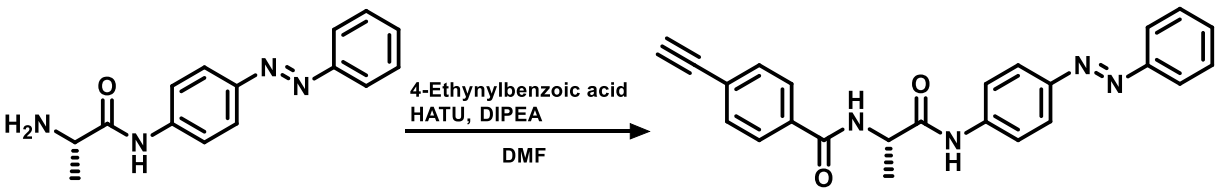

mono-(*S*)-1

4-ethynylbenzoic acid (449 mg, 1.1 equiv), N-[(Dimethylamino)-1H-1,2,3-triazolo-[4,5-b]pyridin-1-ylmethylene]-N-methylmethanaminium hexafluorophosphate N-oxide (HATU, 1168 mg, 1.1 equiv) and diisopropyltriethylamine (DIPEA, 0.54 mL, 1.1 equiv) were dissolved in 20 mL of DMF under Ar. The mixture was stirred for 15 min to activate the acid. Then, (*S,E*)-2-amino-N-(4-(phenyldiazenyl)phenyl)propanamide was added (749 mg, 1 equiv), and the reaction mixture was stirred overnight. The organic layers were washed three times with HCl 1M and a saturated solution of $NaHCO_3$. After removing the solvent, the crude product was chromatographed on silica gel (40-63 mesh) with hexane/ethyl acetate (70:30) as eluent obtaining, after solvent removal, an orange solid (884 mg, 80% of yield).

$[\alpha]_D^{20}$ = -3.6800 (c = 1.0 mg/mL, $CHCl_3$)

^{1}H NMR (300 MHz, $CDCl_3$) δ(ppm): 1.47 (s, 3H), 4.38 (s, 1H), 4.64 (quint, 1H), 7.51-7.61 (m, 5H), 7.84-7.97 (m, 8H), 8.82 (d, 1H), 10.46 (s, 1H).

^{13}C NMR (75 MHz, $CDCl_3$) δ (ppm): 22.7, 55.4, 88.1, 124.7, 127.5, 128.9, 129.8, 133.1, 134.6, 136.2, 136.8, 139.1, 147.4, 152.7, 157.2, 170.8, 177.1.

HRMS (ESI) m/z calcd for $C_{24}H_{21}N_4O_2$ $[M+H]^+$: 397.1654, found: 397.1659

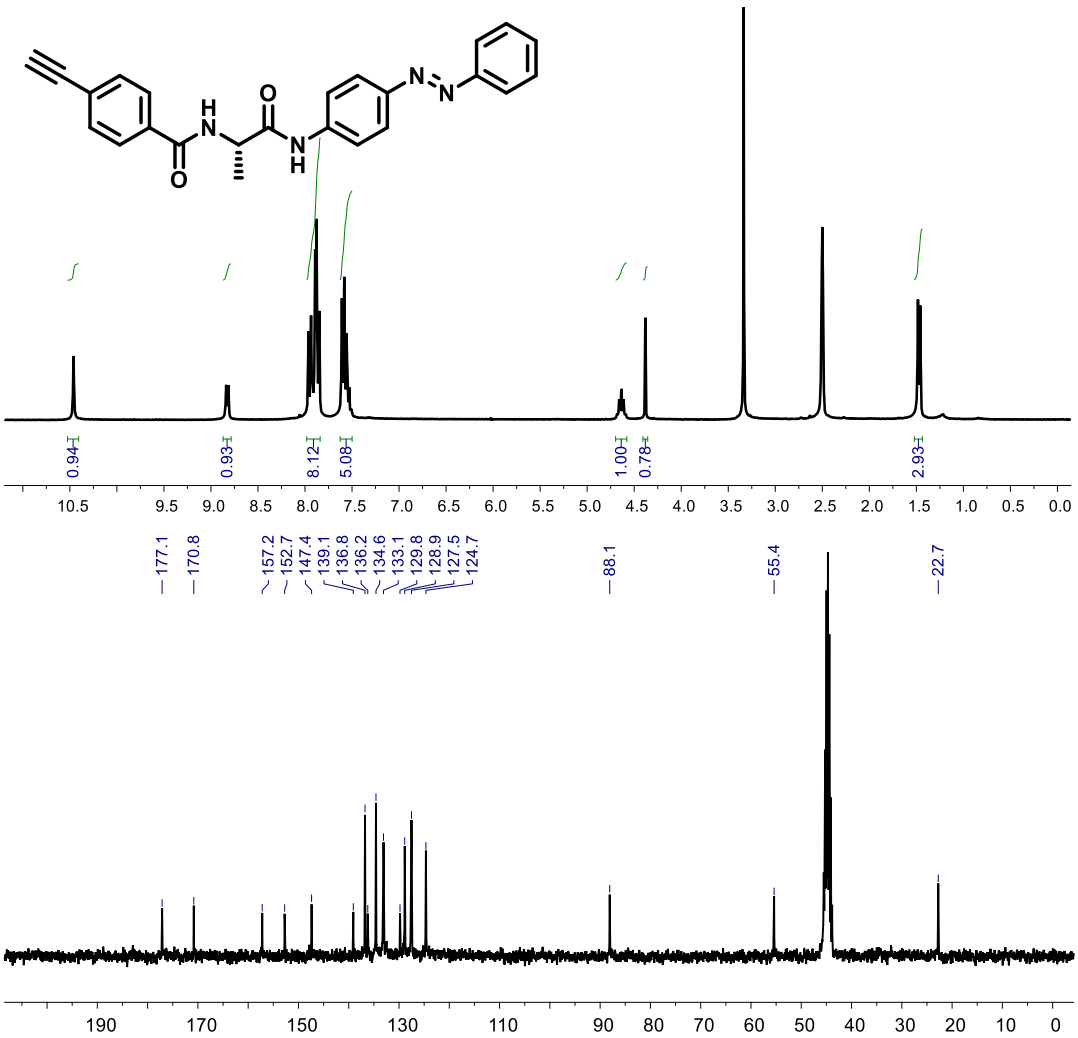

Figure S2. ^{1}H and ^{13}C NMR spectra of mono-(*L*)-**1** (DMSO, 300 and 75 MHz respectively).

(*S,E*)-2-amino-3-methyl-N-(4-(phenyldiazenyl)phenyl)butanamide:

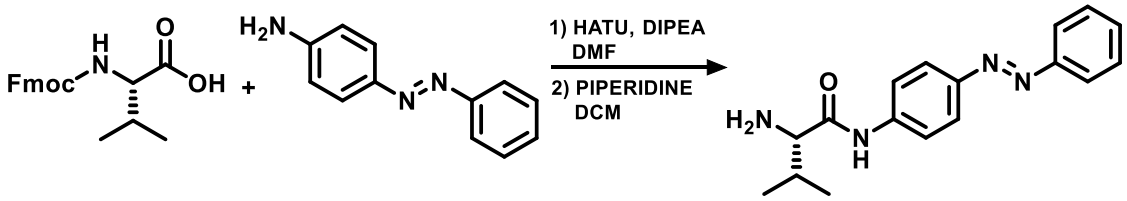

Fmoc-*L*-valine (500 mg, 1 equiv), N-[(Dimethylamino)-1H-1,2,3-triazolo-[4,5-b]pyridin-1-ylmethylene]-N-methylmethanaminium hexafluorophosphate N-oxide (HATU, 616 mg, 1.1 equiv) and diisopropyltriethylamine (DIPEA, 0.28 mL, 1.1 equiv) were dissolved in 10 mL of DMF under Ar. The mixture was stirred for 15 min to activate the acid. Then, 4-aminoazobenzene was added (319 mg, 1.1 equiv), and the reaction mixture was stirred overnight. The organic layer was washed three times with HCl 1M and a saturated solution of $NaHCO_3$. The combined organic layers were dried over anhydrous Na_2SO_4, filtered and the solvent was evaporated at reduced pressure. The crude of the reaction was dissolved in DCM (25 mL) and 5 mL of piperidine was added and the mixture was stirred 15 min. After removing the solvent, the crude product was chromatographed on silica gel (40-63 mesh) with hexane/ethyl acetate (60:40) as eluent obtaining, after solvent removal, an orange solid (319 mg, 73% of yield).

^{1}H NMR (300 MHz, $CDCl_3$) δ(ppm): 0.88 (d, 3H), 1.04 (d, 3H), 1.66 (s, 2H), 2.39-2.53 (m, 1H), 3.38 (d, 1H), 7.40-7.55 (m, 3H), 7.77 (d, 1H), 7.86-7.97 (m, 4H), 9.78 (s, 1H).

^{13}C NMR (75 MHz, $CDCl_3$) δ (ppm): 16.0, 19.8, 30.7, 60.5, 119.4, 122.7, 124.0, 129.0, 130.7, 148.8, 152.7, 172.9.

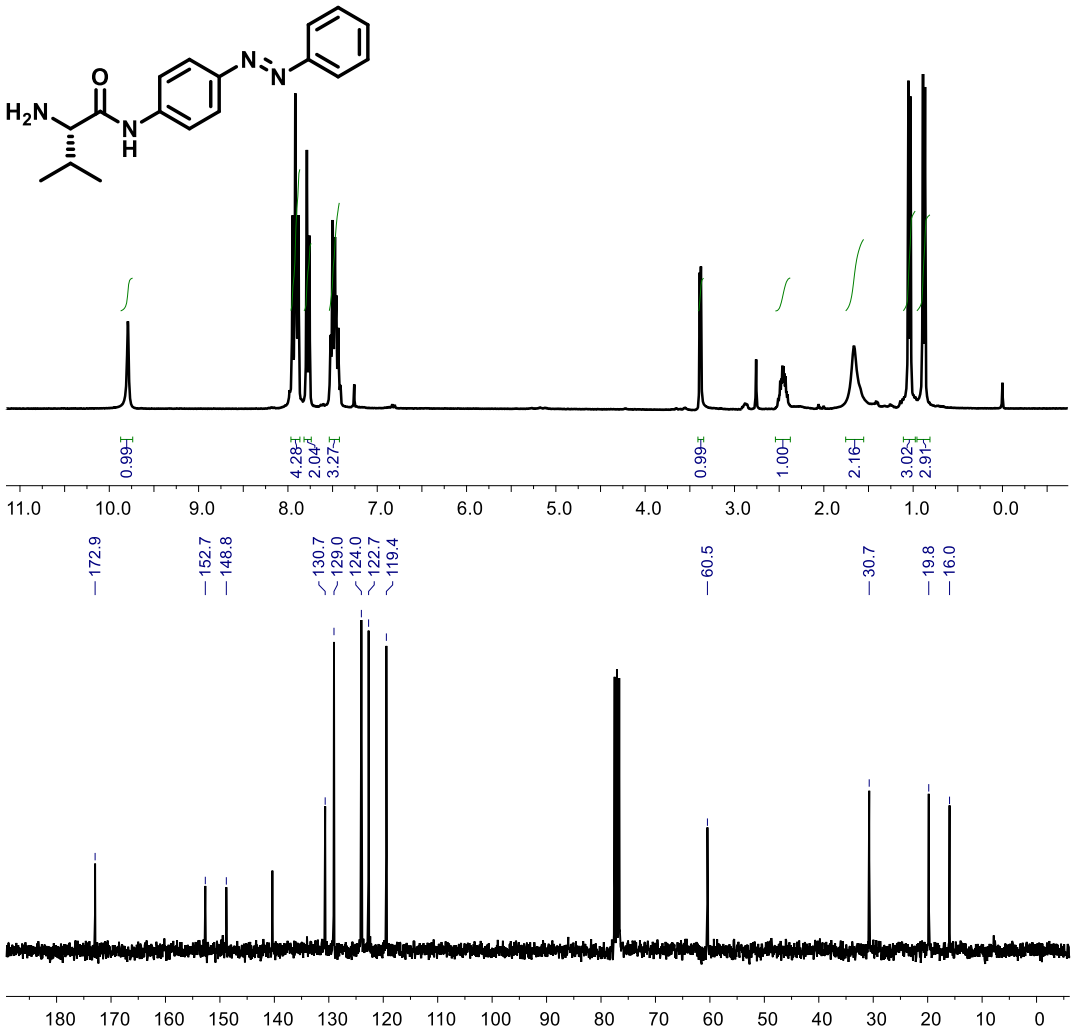

Figure S3. ^{1}H and ^{13}C NMR spectra of (*S,E*)-2-amino-3-methyl-N-(4-(phenyldiazenyl)phenyl)butanamide ($CDCl_3$, 300 and 75 MHz respectively).

(*S,E*)-4-ethynyl-N-(3-methyl-1-oxo-1-((4-(phenyldiazenyl)phenyl)amino)butan-2-yl)benzamide [mono-(*L*)-2):

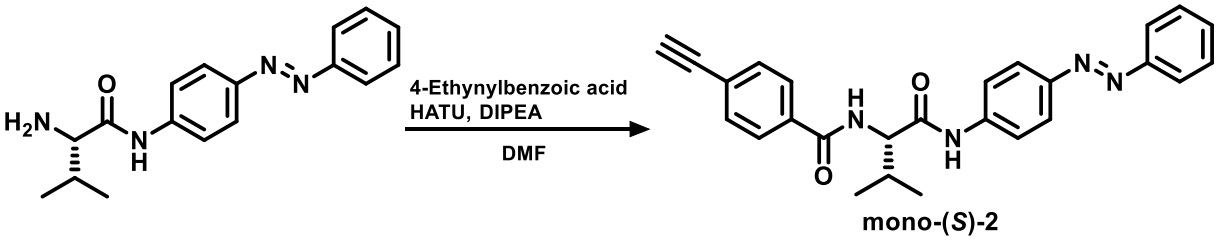

4-ethynylbenzoic acid (173 mg, 1.1 equiv), N-[(Dimethylamino)-1H-1,2,3-triazolo-[4,5-b]pyridin-1-ylmethylene]-N-methylmethanaminium hexafluorophosphate N-oxide (HATU, 450 mg, 1.1 equiv) and diisopropyltriethylamine (DIPEA, 0.21 mL, 1.1 equiv) were dissolved in 10 mL of DMF under Ar. The mixture was stirred for 15 min to activate the acid. Then, (*S,E*)-2-amino-3-methyl-N-(4-(phenyldiazenyl)phenyl)butanamide was added (319 mg, 1 equiv), and the reaction mixture was stirred overnight. The organic layers were washed three times with HCl 1M and a saturated solution of $NaHCO_3$. After removing the solvent, the crude product was chromatographed on silica gel (40-63 mesh) with hexane/ethyl acetate (70:30) as eluent obtaining, after solvent removal, an orange solid (311 mg, 68 % of yield).

$[\alpha]_D^{20}$ = 3.66 (c = 1.0 mg/mL, $CHCl_3$)

^{1}H NMR (300 MHz, $CDCl_3$) δ(ppm): 1.02 (t, 6H), 4.38 (s, 1H), 4.45 (t, 1H), 7.48-7.61 (m, 5H), 7.83-7.97 (m, 8H), 8.70 (d, 1H), 10.58 (s, 1H).

^{13}C NMR (75 MHz, $CDCl_3$) δ (ppm): 19.7, 30.4, 60.9, 83.2, 83.3, 120.0, 122.8, 124.2, 125.0, 128.4, 129.8, 131.5, 132.0, 134.5, 142.3, 148.1, 152.4, 166.5, 171.4.

HRMS (ESI) m/z calcd for $C_{26}H_{25}N_4O_2$ $[M+H]^+$: 425.1977, found: 425.1972

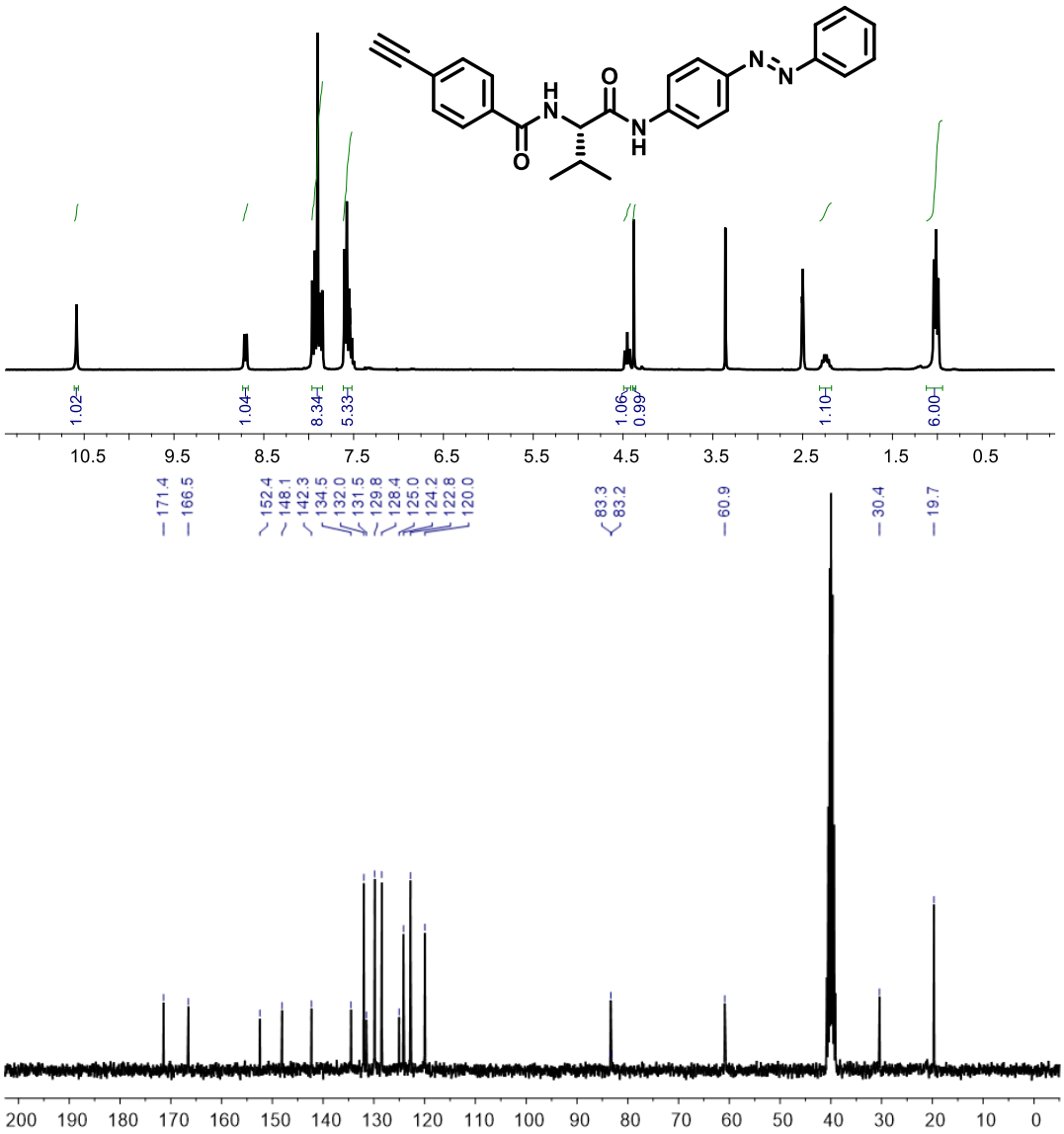

Figure S4. ^{1}H and ^{13}C NMR spectra of mono-(*L*)-**2** (DMSO, 300 and 75 MHz respectively).

3. General Procedure for Polymerization

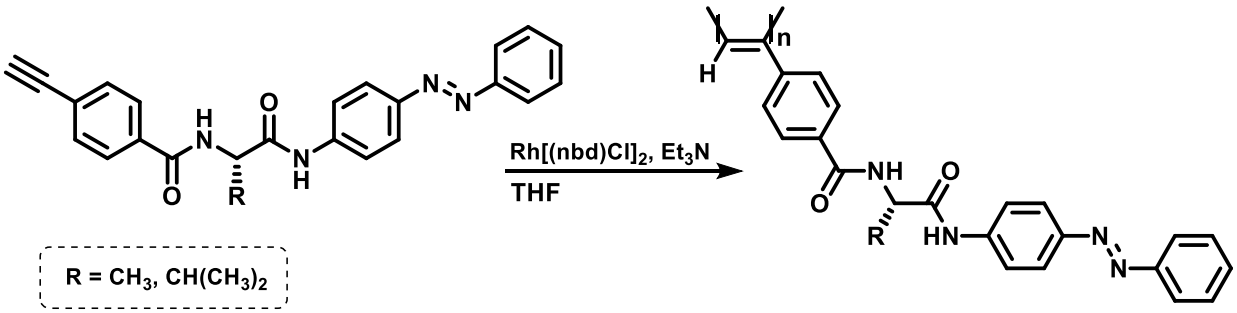

Figure S5. Schematic illustration of polymerization conditions

The reaction flask (sealed ampoule) was dried under vacuum and argon flushed for three times before monomer was added as a solid. Then, the flask was evacuated on a vacuum line and flushed with dry argon (three times). Dry THF was added with a syringe and the triethylamine dropwise. A solution of rhodium norbornadiene chloride dimer, $[Rh(nbd)Cl]_2$, in THF was added at 30 °C. The reaction mixture was stirring at 30 °C for 12 h. Then, the resulting polymer was diluted in CH_2Cl_2 and it was precipitated in a large amount of methanol, centrifuged (2 times), reprecipitated in hexane and centrifuged again.

Table 1. Polymerization conditions of the corresponding polymers.

Polymer	Mass (mg)	THF (mL)	$[Rh(nbd)Cl]_2$ (mg)	ET_3N (µL)	Yield (%)
Poly-(*L*)-**1**	100	2	1.5	5	86
Poly-(*L*)-**2**	100	2	1.5	5	85

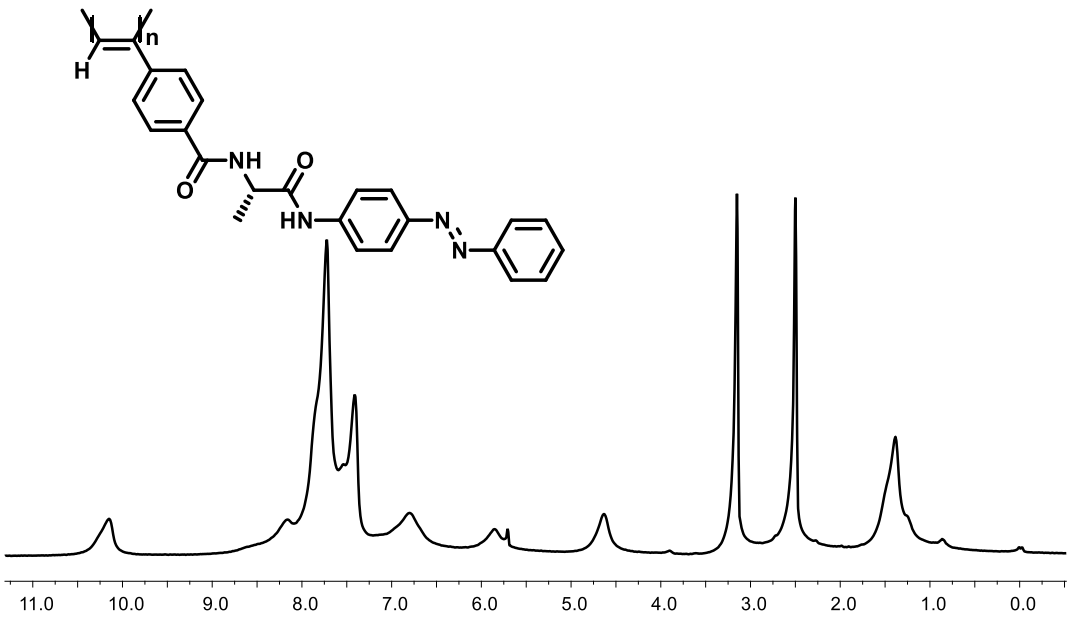

Figure S6. ^{1}H NMR spectra of poly-(*L*)-**1** (DMSO, 300 MHz).

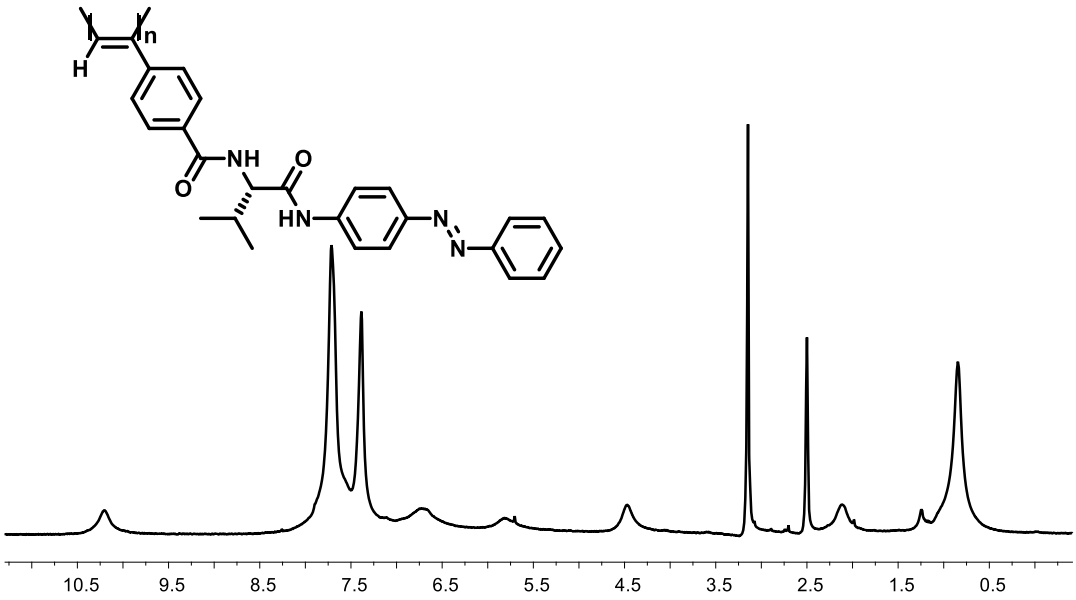

Figure S7. ^{1}H NMR spectra of poly-(*L*)-**2** (DMSO, 300 MHz).

4. Protocols for Light Irradiation

Irradiation experiments was performed using a collimator Lens (x1.0) of a MAX-303 (Asahi Spectra) equipped with a UV-VIS mirror module (300-600 nm). Two experimental conditions were employed depending on the reactivity depending on the reactivity sought.

For the polyene backbone reactivity experiments, a short pass filter was employed (VIS 550 nm 25 dia.). Experimental details for these conditions were described in the SI of the reference **S1**.

To induce the photoisomerization of azobenzene groups two high transmission Bandpass filters was employed (350 and 420 nm with 25 dia.). After stabilizing the irradiation source (20 min), a flask containing 3 mL of the corresponding polymer (0.3 mg/mL) was directly focused with the light beam and covered to avoid the incidence of additional light. To monitor the isomerization process, at the desired time, aliquots of 250 μL of the irradiated polymer solution was transferred to a 1 mm cuvette to measure CD and UV spectra.

5. Crystallographic Data

For X-ray analysis, crystals of mono-(*L*)-**1** was grown by slow evaporation from a $CHCl_3$ solution. The obtained crystal was collected in a total of 4393 frames for 39.87 hours. The frames were integrated with the Bruker SAINT software package using a narrow-frame algorithm. The integration of the data using a triclinic unit cell yielded a total of 34697 reflections to a maximum θ angle of 74.49° (0.80 Å resolution), of which 7909 were independent (average redundancy 4.387, completeness = 99.7%, Rint = 5.90%, Rsig = 4.52%) and 6808 (86.08%) were greater than 2σ(F2). The final cell constants of a = 6.2789(2) Å, b = 7.5997(2) Å, c = 21.2345(6) Å, α = 83.772(2)°, β = 87.258(2)°, γ = 86.945(2)°, volume = 1004.95(5) $Å^3$, are based upon the refinement of the XYZ-centroids of 1882 reflections above 20 σ(I) with 8.385° < 2θ < 156.6°. Data were corrected for absorption effects using the Multi-Scan method (SADABS). The ratio of minimum to maximum apparent transmission was 0.893. The calculated minimum and maximum transmission coefficients (based on crystal size) are 0.8893 and 0.9860.

The structure was solved and refined using the Bruker SHELXTL Software Package, using the space group P 1, with Z = 1 for the formula unit, $C_{46}H_{34}N_{10}O_4$. The final anisotropic full-matrix least-squares refinement on F2 with 555 variables converged at R1 = 4.28%, for the observed data and wR2 = 11.49% for all data. The goodness-of-fit was 1.046. The largest peak in the final difference electron density synthesis was 0.377 e-/$Å^3$ and the largest hole was -0.184 e-/$Å^3$ with an RMS deviation of 0.040 e-/$Å^3$. On the basis of the final model, the calculated density was 1.307 g/cm^3 and F(000), 412 e-.

6. Thermal Studies

DSC studies

Samples of both polymers were dissolved in the corresponding solvent ($CHCl_3$, THF and DMF) to induce the associated scaffold. After this, solvents were concentrated, and samples were dried at vacuum for 12 hours. Next, the solids were then placed in an aluminum pan and heated from 50 °C to 350 °C with a heating rate of 5 °C/min. Thermograms of both polymers associated to $CHCl_3$ solutions indicate a *cis-cisoidal* polyene backbone (Figure S8a), one exothermic peak (*c-c* to *t-t*). In the other hand, thermograms corresponding to THF and DMF samples (Figure S8b) reveal another exothermic, corresponding to *c-t* to *c-c* isomerization, indicating that in these solvents starting materials adopt a *cis-transoidal* polyene backbone.

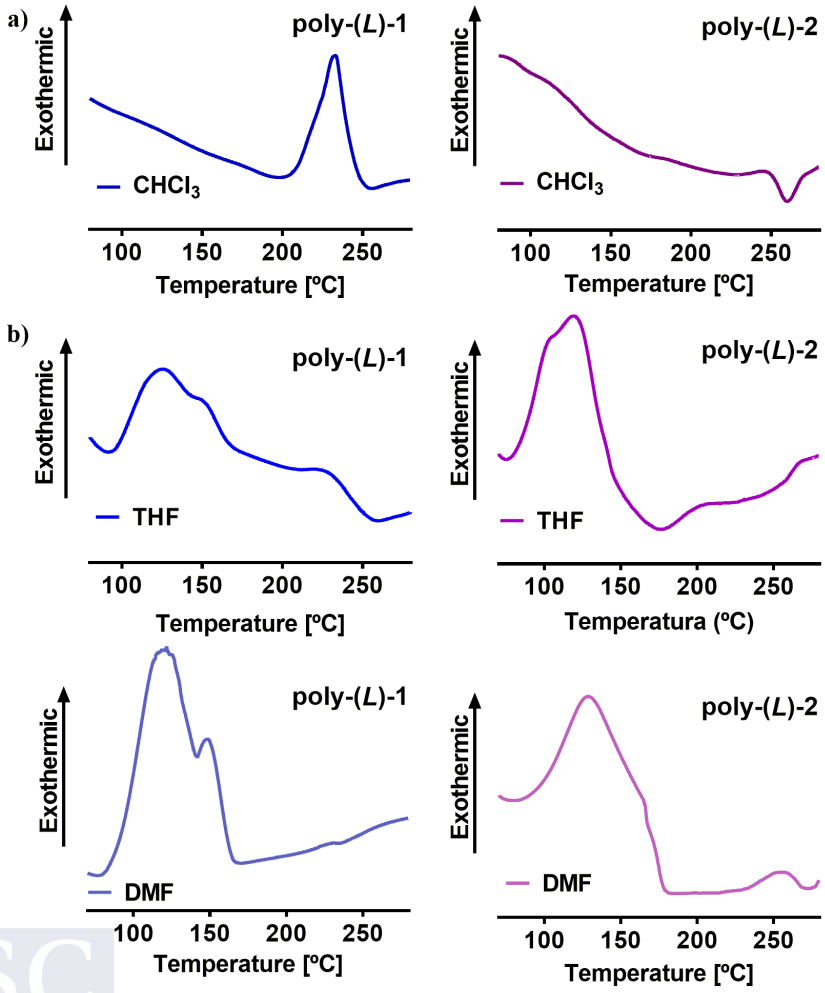

Figure S8. DSC thermograms of both polymer in a) *cis-cisoidal* and b) *cis-transoidal* conformations.

TGA studies

Solid samples of both polymers were kept under vacuum for 12 hours, after this time samples were introduced in a platinum pan and heating since 50 °C to 800 °C with a heating rate of 10°C/min.

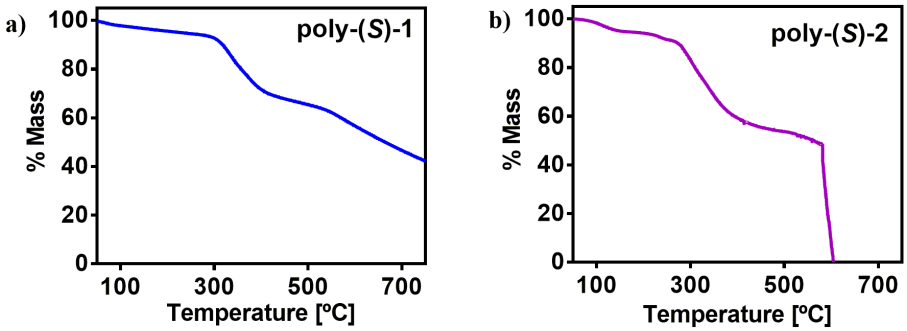

Figure S9. TGA thermograms of a) poly-(*L*)-**1** and b) poly-(*L*)-**2.**

7. Spectroscopy Studies

Raman

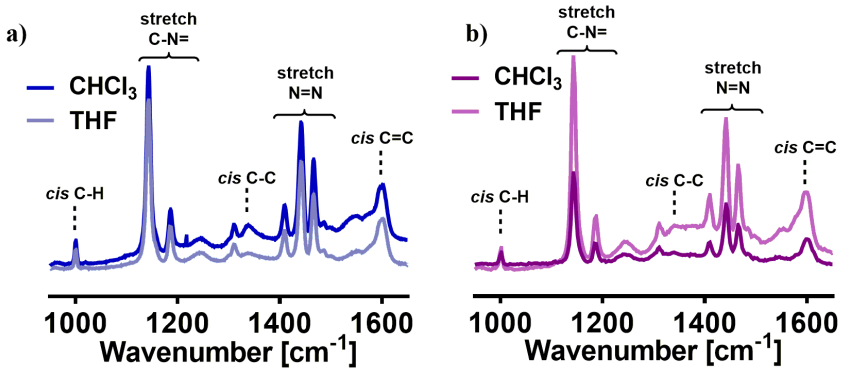

Figure S10. Raman spectra in $CHCl_3$ and THF (*c-c* and *c-t* scaffolds respectively) of (a) poly-(*L*)-**1** and b) poly-(*L*)-**2**.

ATR/FT-IR

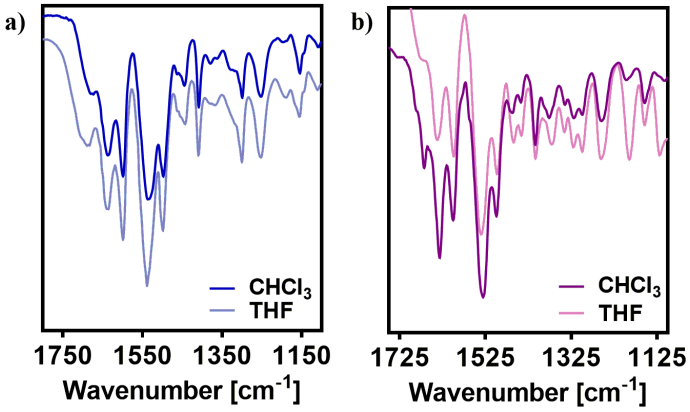

Figure S11. IR spectra in $CHCl_3$ and THF of (a) poly-(*L*)-**1** and b) poly-(*L*)-**2**.

8. AFM Studies

Monolayer was prepared from 0.1 mg/mL solution of poly-(*L*)-**1** in $CHCl_3$, spin-coated over HOPG and kept under the corresponding solvent vapor 24 hours. After this, AFM measurements were performed at CACTI (Vigo University, Spain) in a MultiMode V Scanning Probe Microscope (Veeco Instruments) in air and room temperature. Also, Standard silicon cantilevers and supersharp cantilevers in tapping mode was selected using 12 µm and 1 µm scanners. Nanoscope processing software and WSxM 4.0 Beta 1.0 (Nanotec Electronica, S.L.) were used for image analysis.

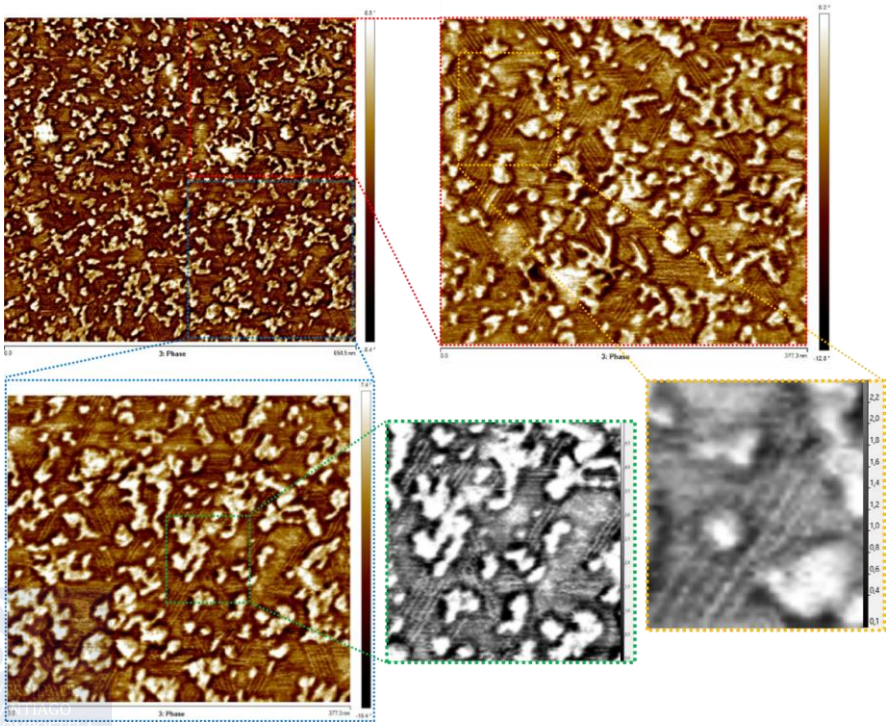

Figure S12. AFM images of left-handed helical monolayers of poly-(*L*)-**1** prepared from a 0.1 mg/mL solution in $CHCl_3$ over HOPG by spin-coating.

9. VT-CD Experiments

VT-CD experiments were measured in a Jasco-1100 using a 1 mm quartz cuvette with polymer solutions of 0.3 mg/mL.

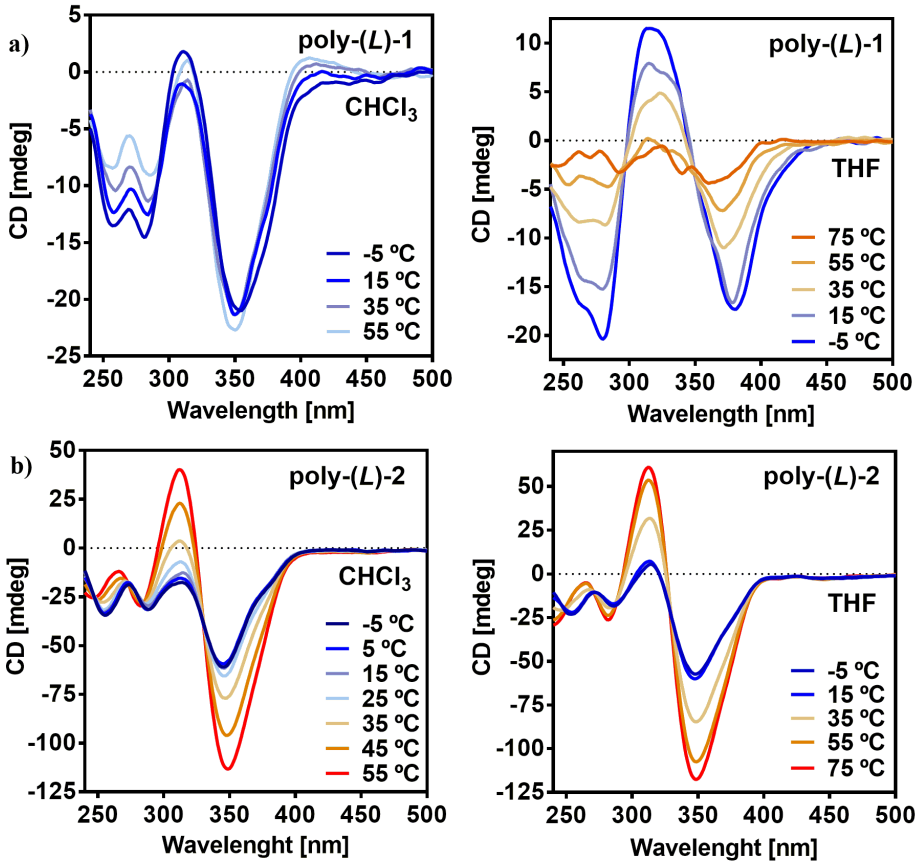

Figure S13. VT-CD spectra of a) poly-(*L*)-**1** and b) poly-(*L*)-**2** in $CHCl_3$ and THF. [poly-(*L*)-**1**]= 0.3 mg/mL,[poly-(*L*)-**2**]= 0.3 mg/mL.

10. Responsive to Metal Cations

CD and UV measurements were performed in a Jasco 720 and a Jasco V-630 respectively, using a 1 mm quartz cuvette with polymer solutions of 0.3 mg/mL. Metal ions was prepared as solutions in MeOH of 10 mg/mL and the corresponding amount was drop over 1 mL of polymer solution.

Poly-(*L*)-1

Perchlorate salts of Ba^{2+}, Mn^{2+} and Ca^{2+} can reach the helical inversion by chelation of both carbonyl groups inducing a *sp* conformation. Furthermore, subsequent addition of MeOH increase the polarity of the media, breaking the chelate and recovering the *ap* conformation.

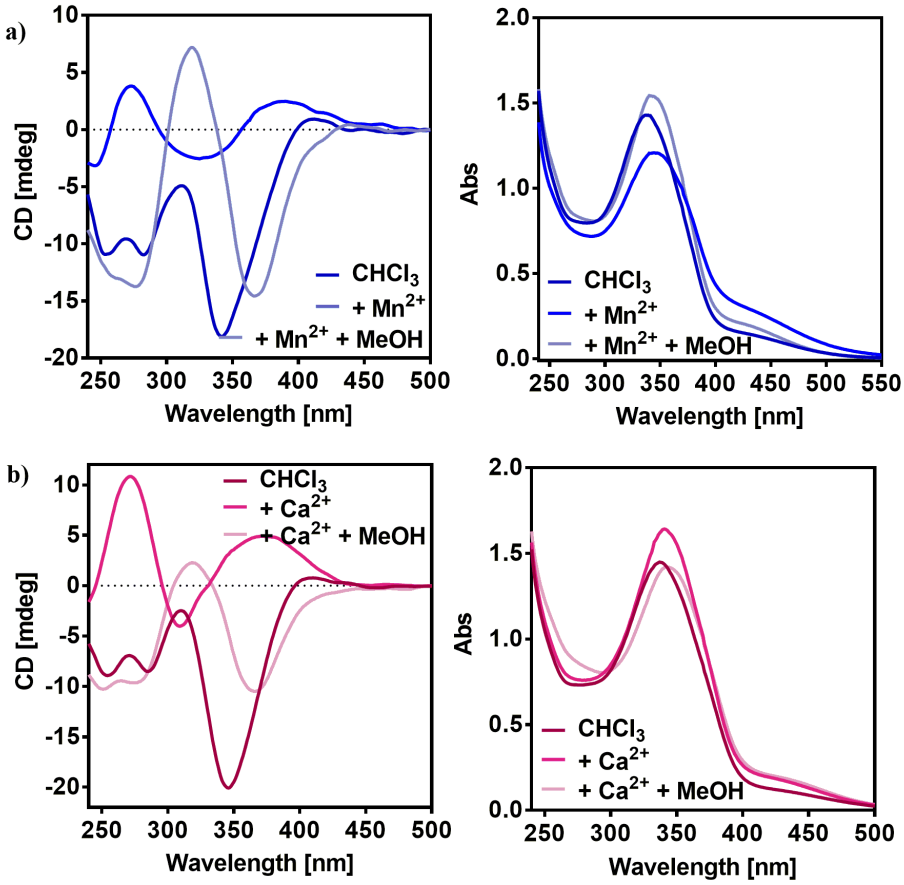

Figure S14. CD and UV spectra of poly-(*L*)-**1** in $CHCl_3$ and with consecutives additions of metal ion and methanol. a) 0.8 equiv of $Mn(ClO_4)_2$ and b) 2 equiv of $Ca(ClO_4)_2$. [poly-(*L*)-**1**]= 0.3 mg/mL.

Poly-(*L*)-2

For poly-(*L*)-**2**, addition of metal cations, or just MeOH, improve the folding of the azobenzene groups.

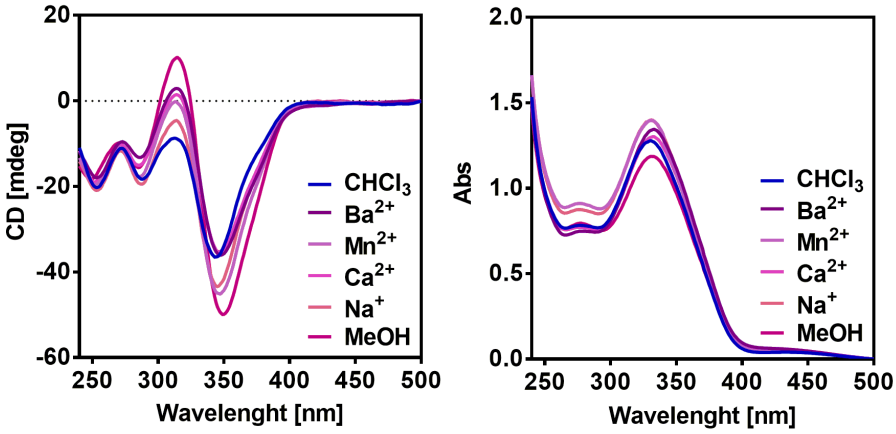

Figure S15. CD and UV spectra of poly-(*L*)-**2** in $CHCl_3$ and with addition of 1 equiv of $Ba(ClO_4)_2$, $Mn(ClO_4)2$, $Ca(ClO_4)_2$, $NaClO_4$ and MeOH. [poly-(*L*)-**2**]= 0.3 mg/mL.

11. IR studies with Metal Cations

To confirm the chelation of the metal cations, IR studies were performed in a Perkin Elmer FT-IR ATR Spectrum Two. Thus, for poly-(*L*)-**1** the inversion of the helical sense associated to the *anti* to *syn* change conformation as result of the chelation of divalent metal cations is confirmed by the shift of the carbonyls vibration (highlighting the variation on the carbonyl initially at 1680 cm^{-1}).

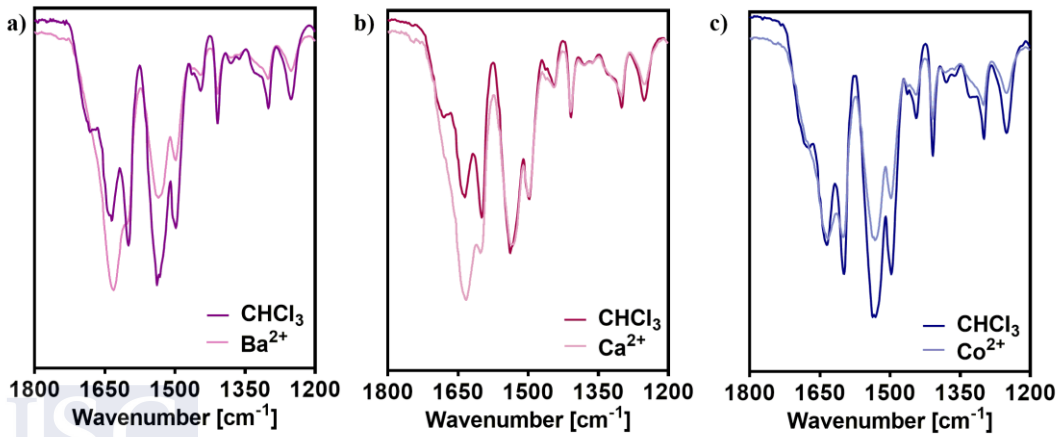

Figure S16. IR spectra of poly-(*L*)-**1** in $CHCl_3$ and with additions of a) $Ba(ClO_4)_2$, b) $Ca(ClO_4)_2$ and c) $Co(ClO_4)_2$.

12. Acids Reactivity

CD and UV measurements were performed in a Jasco 720 and a Jasco V-630 respectively, using a 1 mm quartz cuvette with polymer solutions of 0.3 mg/mL. The solutions were prepared adding the corresponding amount of acid solution to 1 mL solution of polymer and stirred few seconds. TFA was found as the more interesting case because preserve the helicity of the azobenzenes during the protonation. Moreover, for the other acids tested (Figure S19), in the case of poly-(*L*)-**2**, with addition of HCl, is possible discern in the ECD pattern the formation of the cotton associated with protonated azobenzenes oriented around 500 nm, but with less intensity that for TFA.

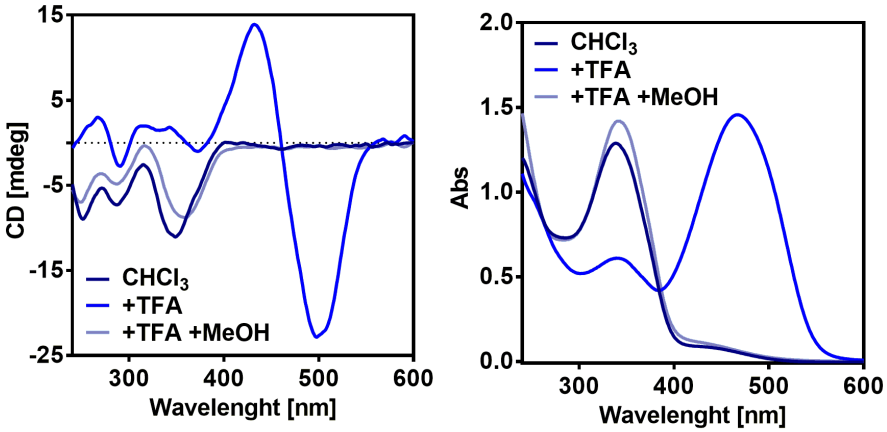

Figure S17. CD and UV spectra in $CHCl_3$ of poly-(*L*)-**1** with addition of 24 µL of TFA and 40 µL of MeOH. The addition of acid was over 1 mL of polymer solution. [poly-(*L*)-**1**]= 0.3 mg/mL.

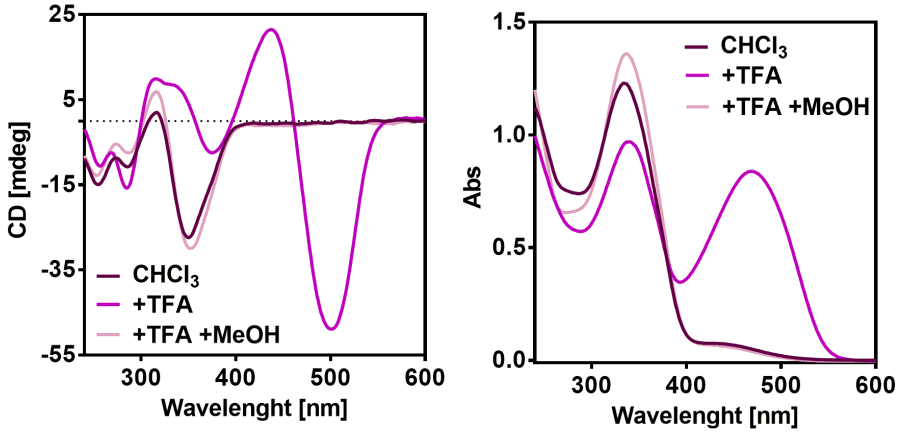

Figure S18. CD and UV spectra in $CHCl_3$ of poly-(*L*)-**2** with addition of 24 µL of TFA and 20 µL of MeOH. The addition of acid was over 1 mL of polymer solution. [poly-(*L*)-**2**]= 0.3 mg/mL.

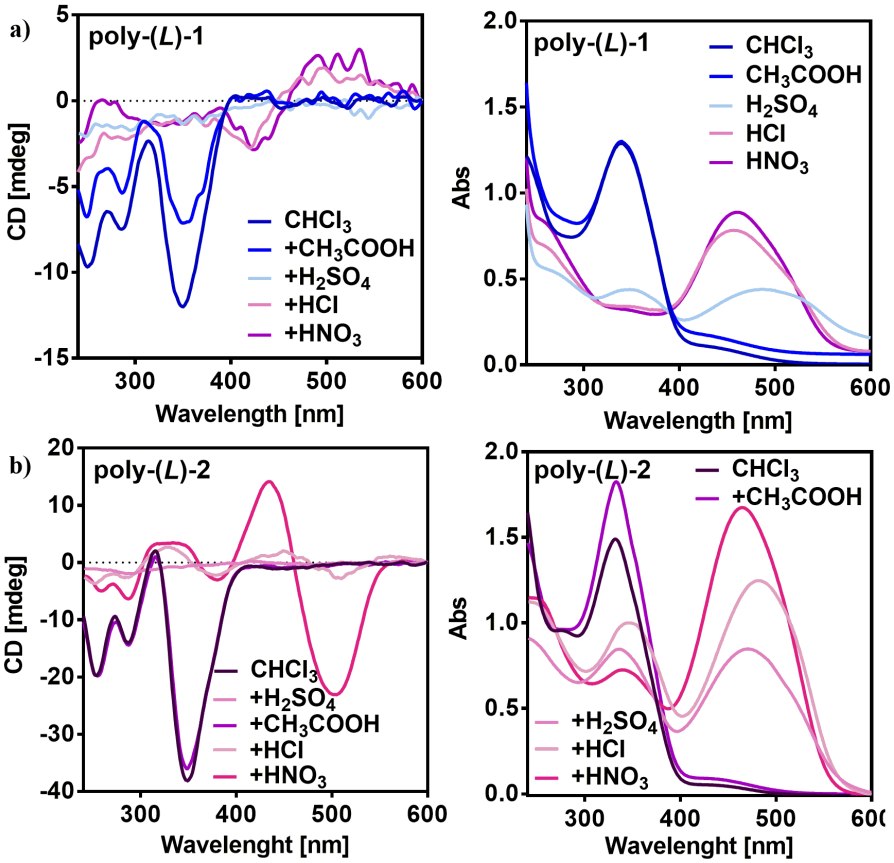

Figure S19. CD and UV spectra in $CHCl_3$ with addition of several acids (17 µL in each case) for a) poly-(*L*)-**1** and b) poly-(*L*)-**2**. In all cases, the addition of acids was over 1 mL of polymer solution. [poly-(*L*)-**1**]= 0.3 mg/mL, [poly-(*L*)-**2**]= 0.3 mg/mL.

13. *E/Z* Photochemical and Thermal Studies

For both polymers, the *E* to *Z* isomerization was carried out irradiating with a 350 nm light (See section "protocols for light irradiation" for more details). Consecutive *Z* to *E* isomerization was promoted by 420 nm light under same conditions or by temperature (heating polymer solutions at 60 °C and extracting aliquots at desired time to monitor CD and UV). Furthermore, for poly-(*L*)-**1** in $CHCl_3$, DLS studies were performed to confirm the formation of aggregates.

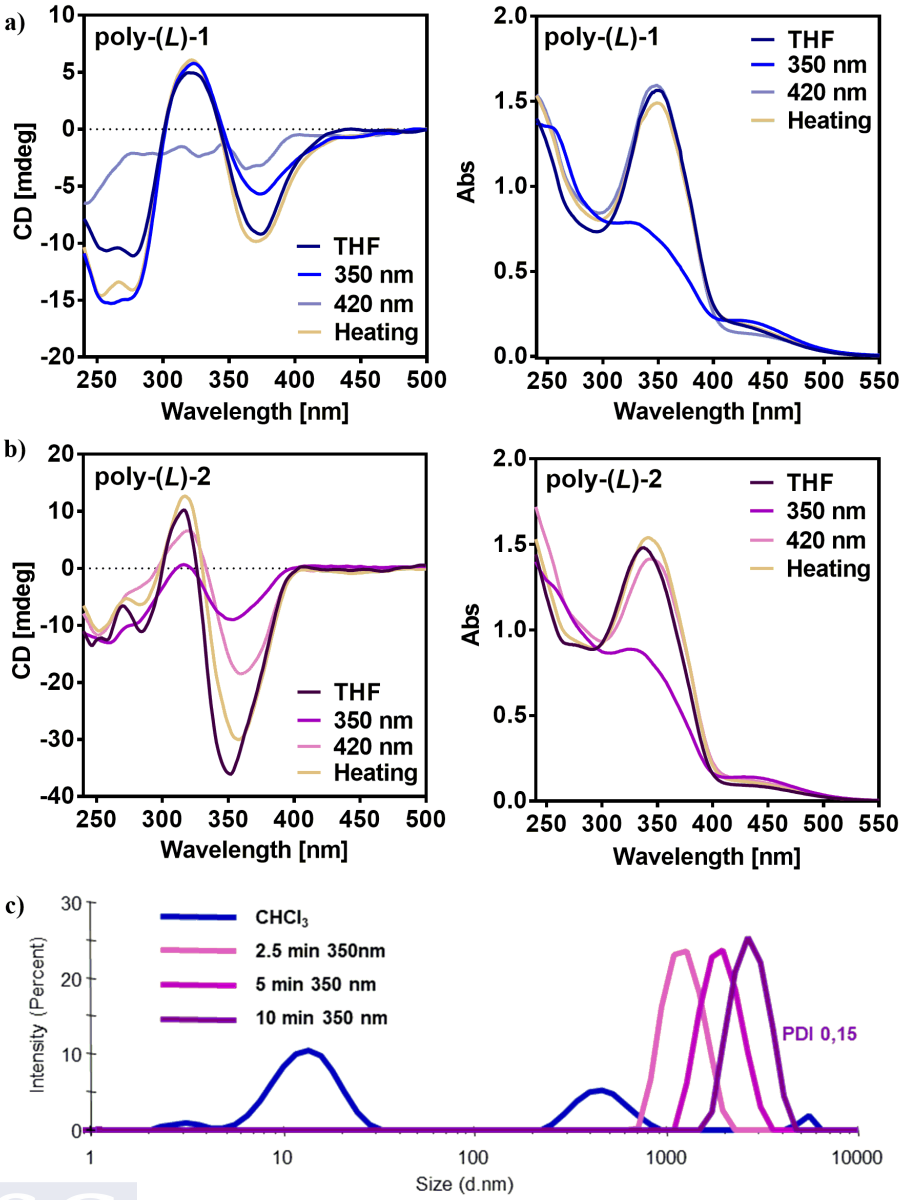

Figure S20. CD and UV spectra in THF of a) poly-(*L*)-**1** (350 nm light= 10 min, 420 nm light= 20 min and heating= 2 hours) and b) poly-(*L*)-**2** (350 nm light= 30 min, 420 nm light= 20 min and heating= 2.5 hours). c) DLS studies for poly-(*L*)-**1** in $CHCl_3$. [poly-(*L*)-**1**]= 0.3 mg/mL, [poly-(*L*)-**2**]= 0.3 mg/mL.

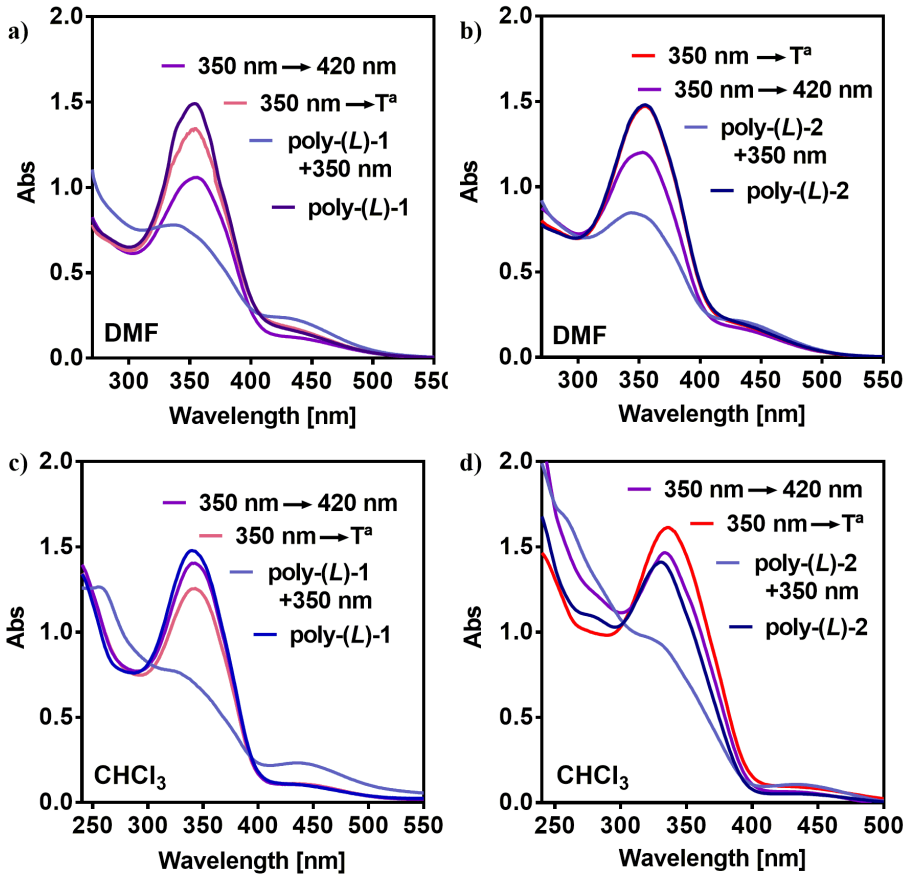

Figure S21. UV spectra in DMF of a) poly-(*L*)-**1** (350 nm light= 20 min, 420 nm light= 30 min and heating= 3 hours) and b) poly-(*L*)-**2** (350 nm light= 30 min, 420 nm light= 20 min and heating= 30 min). UV-Vis spectra in $CHCl_3$ of c) poly-(*L*)-**1** (350 nm light= 10 min, 420 nm light= 30 min and heating= 2 hours) and d) poly-(*L*)-**2** (350 nm light= 20 min, 420 nm light= 20 min and heating= 90 min). [poly-(*L*)-**1**]= 0.3 mg/mL, [poly-(*L*)-**2**]= 0.3 mg/mL.

14. Photochemical Stability

Stability of the polyene backbone of PPAs was evaluated using a short pass filter (VIS 550 nm 25 dia.) in a MAX-303 (Asahi Spectra). See section "protocols for light irradiation" for experimental details. Variations in the ECD and UV SPECTRA as result of irradiation for these azo-PPAs are far from the described photochemical electrocyclization process (See reference S1). Thus, UV-Vis spectra remain almost unchanged and ECD spectra for poly-(*L*)-**2** show an unfolding of the azobenzenes since the triple to a double helix (Figure S25). For poly-(*L*)-**1** (Figure S26) show a decrease of the ECD signal, leaving in the case of the starting double helix (Figure S25b) to a null ECD spectra.

Poly-(*L*)-2

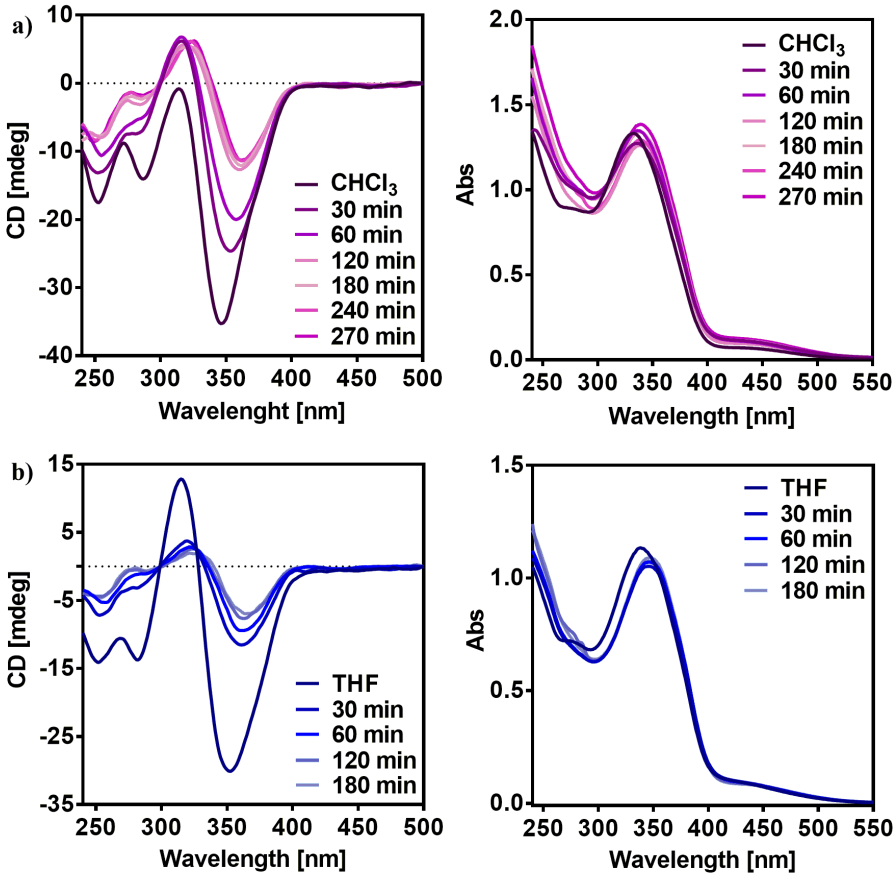

Figure S22. CD and UV spectra of poly-(*L*)-**2** under irradiation with UV-Visible light in a) $CHCl_3$ and b) THF. [poly-(*L*)-**2**]= 0.3 mg/mL.

Poly-(*L*)-1

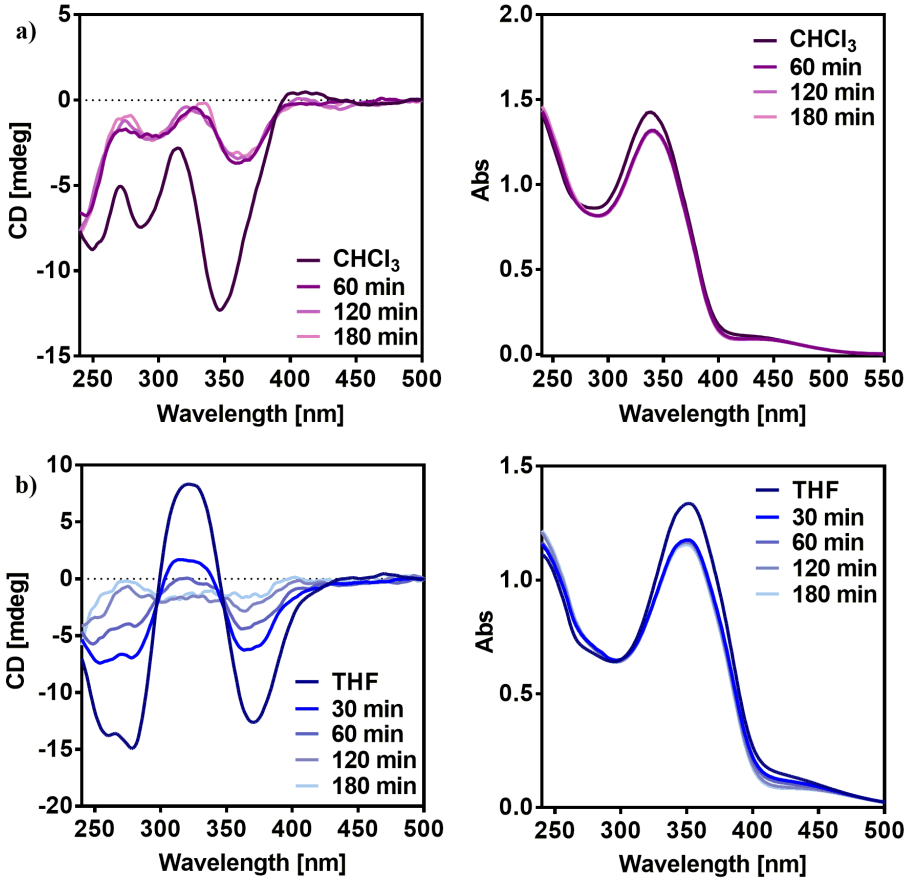

Figure S23. CD and UV spectra of poly-(*L*)-**1** under irradiation with UV-Visible light in a) $CHCl_3$ and b) THF. [poly-(*L*)-**1**]= 0.3 mg/mL.

15. Monomer calculations

Calculated ECD spectra in $CHCl_3$ reveals that S_0 to S_2 transition correspond to the azobenzene group in both monomers.

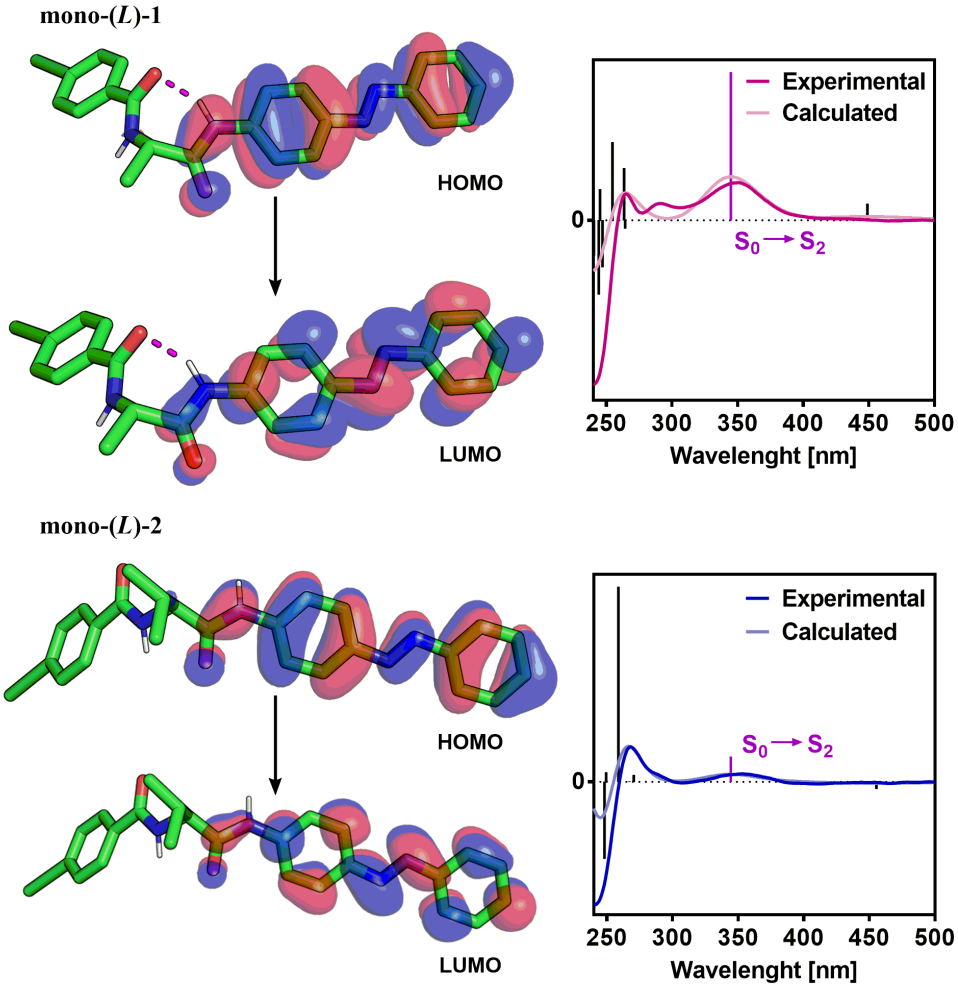

Figure S24. HOMO and LUMO of the S_0 to S_2 transition for both monomers assigned to each calculated natural bond orbitals (NBO).

16. Computational Details

Considering the difficulties to carry out theoretical calculations on large polymers, we apply the methodology reported in the reference **S2**. Thus, oligomers constituted by 9 and 8 monomer repeating units, for the *c*-*c* and *c*-*t* scaffolds respectively, was build using Spartan 18. The generated structure was adjusted according to the information obtained from several techniques such as Raman, IR, CD and AFM. Moreover, this experimentally supported structure was refined through Molecular Mechanics (MMFF94) before being submitted for ECD calculations. Finally, the time-dependent density functional theory (TD-DFT, Ref. **S3**) was used together with the rCAM-B3LYP density functional (Ref. **S4**) and the 3-21G basis set (Ref. **S5**). We included 90 excitation energies in the calculation for the compressed *c*-*c* scaffold ($CHCl_3$) of poly-(*L*)-**1**. The resulting ECD spectrum were selected with a full width at half height (FWHM) of 0.37 eV. In the case of the *c*-*t* scaffold (DMF), we included 80 excitation energies in the calculation. The resulting ECD spectrum were selected with a full width at half height (FWHM) of 0.20 eV. Moreover, we evaluated a correction factor for lambda as the difference between the theoretical and experimental wavelengths, and we shifted the rest of the theoretical spectra accordingly. In a similar way, the intensity, was rescaled for the theoretical values to get the experimental intensity at the first Cotton effect band.

For monomer calculations, optimization of the geometry was applied using the density functional theory (DFT) together with the rCAM-B3LYP functional and the 6-31G* basis set. Thus, the theorical ECD spectrum was calculated since the optimized geometry using the time-dependent density functional theory (TD-DFT) together the rCAM-B3LYP density functional and the 6-31G* basis set. The resulting ECD spectrum was selected with a full width at half height (FWHM) of 0.25 eV. Moreover, for mono-(*L*)-**2** we evaluated a correction factor for lambda as the difference between the theoretical and experimental wavelengths, and we shifted the rest of the theoretical spectrum accordingly. Similarly, the ECD intensity was rescaled in the theoretical values for both monomers.

17. Supporting References

S1. F. Rey-Tarrío, R. Rodríguez, E. Quiñoá, R. Riguera, F. Freire*, Angew. Chem. Int. Ed.*, **2021**, *60*, 8095-8103.

S2. B. Fernández, R. Rodríguez, A. Rizzo, E. Quiñoá, R. Riguera, F. Freire, *Angew. Chem. Int. Ed.* **2018**, *57*, 3666-3670.

S3. E. Runge, E. K. U. Gross, *Phys. Rev. Lett.* **1984**, *52*, 997-1000.

S4. A. J. Cohen, P. Mori-Sánchez, W. Yang, *J. Chem. Phys.* **2007**, *126*, 191109.

S5. J. S. Binkley, J. A. Pople, W. J. Hehre, *J. Am. Chem. Soc.* **1980**, 102, 939- 947.

Experimental Section Chapter VII

1. Materials and methods

CD measurements were done in a Jasco-720 and VT-CD measurements in a Jasco-1500 with a 1 mm quartz cuvette. The amount of polymer used for CD and VT-CD measurements was 0.6 mg/mL.

UV spectra were registered in a Jasco V-750 with a 1 mm quartz cuvette. The amount of polymer used for UV measurements was 0.6 mg/mL.

Optical rotation was measured in a Jasco-P2000.

Mass spectra were obtained on an HP 5988A spectrometer (Hewlett-Packard, Palo Alto, CA, USA).

Elemental analyses were recovered in a Foss-Heraeus CHNO-Rapid analyzer.

NMR experiments were measured in a Varian 300 (1H: 300 MHz) or a Bruker Avance II 400 (1H: 400 MHz; 13C: 101 MHz; 19F: 376.4 MHz). Solid NMR experiments were measured in a Bruker NEO 750 using a 1.3 mm rotor.

IR measurements were carried out using a JASCO-FTIR-6800.

Raman spectra were done in a Renishaw confocal Raman spectrometer (Invia Reflex model), equipped with two lasers (diode laser 785 nm and Ar laser 514 nm).

DSC traces were obtained in a DSC Q200 Tzero Technology (TA Instruments, New Castle, UK), equipped with a refrigerated cooling system RCS90 (TA Instruments, New Castle, UK), using a Tzero low-mass aluminium pan.

TGA traces were obtained in a TGA Q5000 (TA Instruments, New Castle, UK) using a platinum pan.

2. Structures of the synthesized compounds

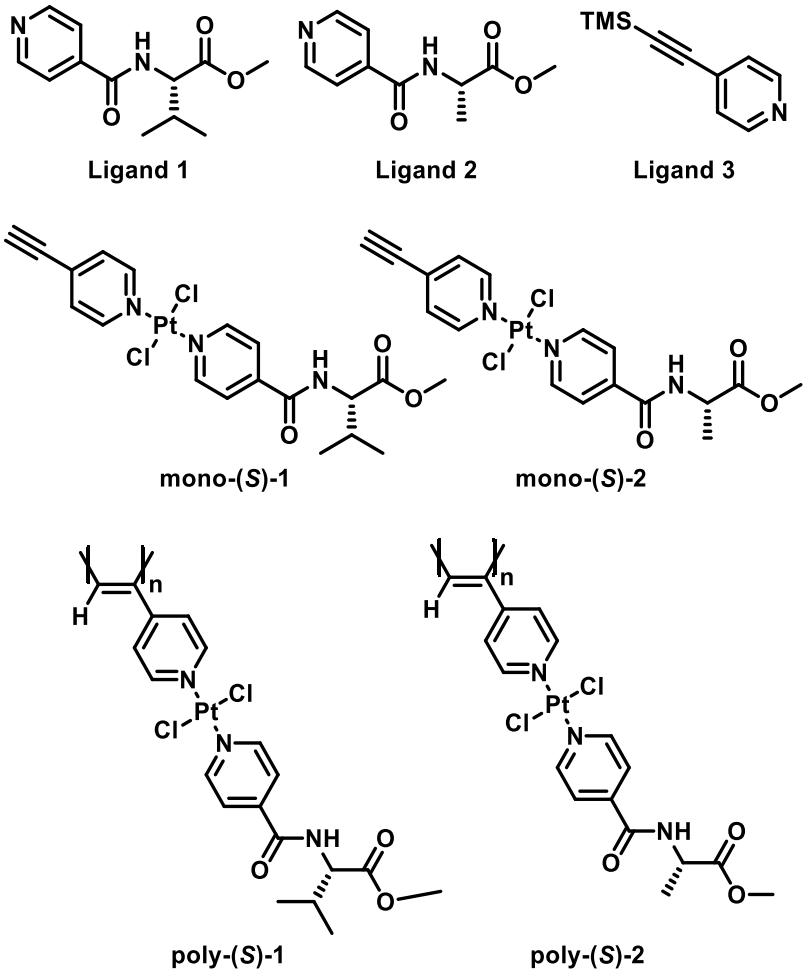

Figure S1. Structures of the synthesized compounds.

3. Synthesis of Ligands

Methyl isonicotinoyl-L-valinate [Ligand 1]

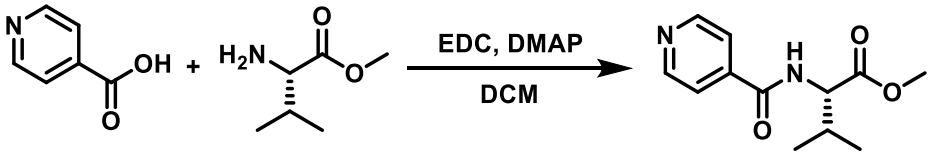

Isonicotinic acid (441 mg, 1.20 equiv.), 1-ethyl-3-(3-dimethylaminopropyl)carbodiimide (EDC, 686 mg, 1.20 equiv.), 1-hydroxybenzotriazole (HOBt, 484 mg, 1.20 equiv.) and 4-dimethylaminopyridine (DMAP, 437 mg, 1.20 equiv.) were dissolved in 30 mL of dry CH_2Cl_2. After 15 minutes, time needed to activate the acid, *L*-valine methyl ester (500 mg, 1.00 equiv.) was added and the mixture was stirred overnight. The organic layer was washed three times with HCl 1M and a saturated solution of $NaHCO_3$. The combined organic layers were dried over anhydrous Na_2SO_4, filtered and evaporated at reduced pressure. The crude product was chromatographed on silica gel with pentane/ethyl acetate (70:30) as eluent (388 mg, 55 % of yield).

^{1}H NMR (400 MHz, $CDCl_3$) δ_H (ppm): 0.89 (t, 6H), 2.16 (sextet, 1H), 3.67 (s, 1H), 4.64 (q, 1H), 7.21 (d, 1H), 7.54 (d, 2H), 8.59 (d, 2H).

^{13}C NMR (101 MHz, $CDCl_3$) δ_c (ppm): 18.1, 19.0, 31.3, 52.3, 57.7, 121.1, 141.2, 150.4, 165.6, 172.3.

HRMS (ESI-MS) m/z calcd for $C_{12}H_{16}N_2O_3Na^+$ $[M+Na]^+$: 259.1053, found: 259.1051.

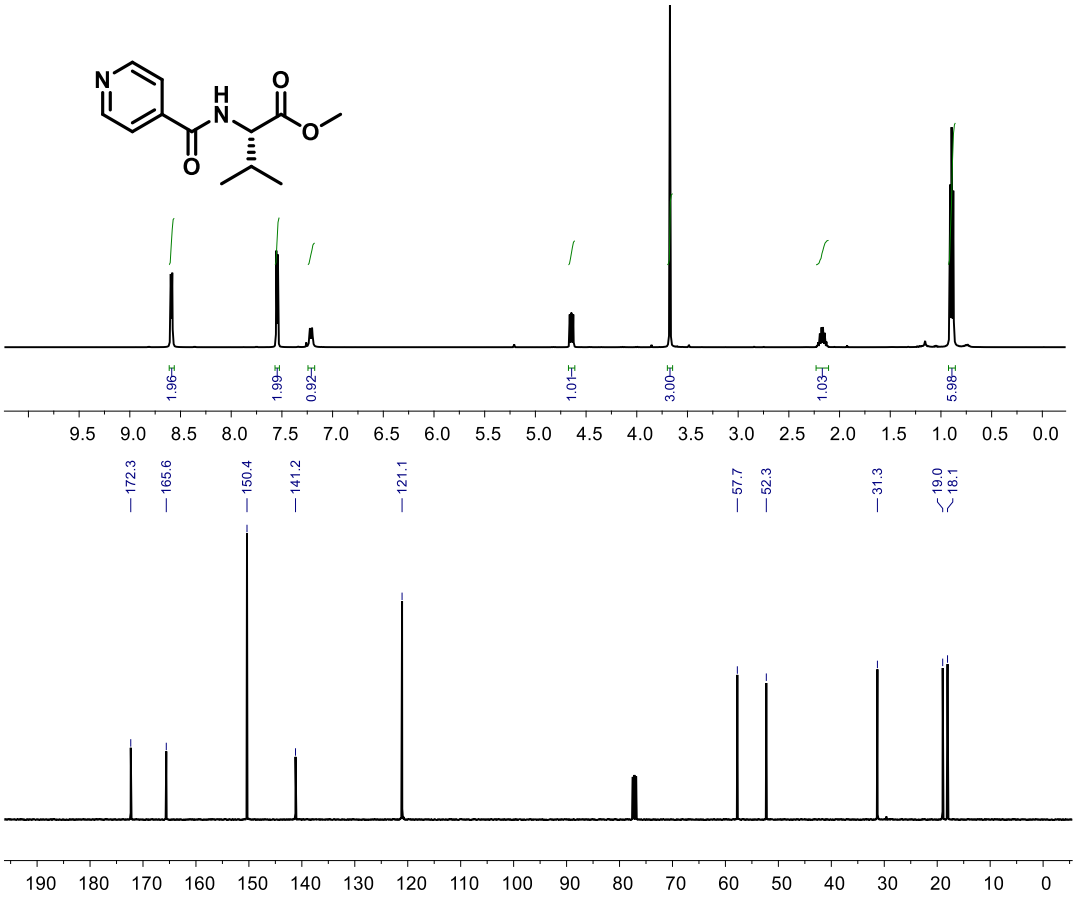

Figure S2. ^{1}H and ^{13}C NMR spectra of the ligand **1** ($CDCl_3$, 400 and 101 MHz respectively).

Methyl isonicotinoyl-*L*-alaninate [Ligand 2]

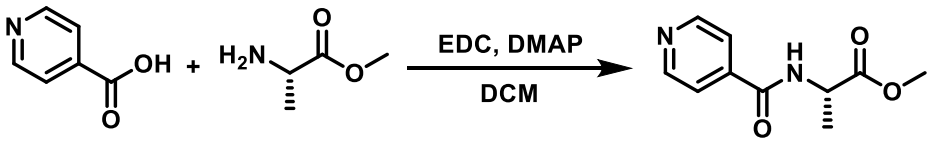

Isonicotinic acid (529 mg, 1.20 equiv.), 1-ethyl-3-(3-dimethylaminopropyl)carbodiimide (EDC, 824 mg, 1.20 equiv.), 1-hydroxybenzotriazole (HOBt, 581 mg, 1.20 equiv.) and 4-dimethylaminopyridine (DMAP, 525 mg, 1.20 equiv.) were dissolved in 30 mL of dry CH_2Cl_2. After 15 minutes, time needed to activate the acid, *L*-alanine methyl ester (500 mg, 1.00 equiv.) was added and the mixture was stirred overnight. The organic layer was washed three times with HCl 1M and a saturated solution of $NaHCO_3$. The combined organic layers were dried over anhydrous Na_2SO_4, filtered and evaporated at reduced pressure. The crude product was chromatographed on silica gel with pentane/ethyl acetate (70:30) as eluent (395 mg, 53 % of yield).

^{1}H NMR (400 MHz, $CDCl_3$) δ_H (ppm): 1.51 (d, 3H), 3.79 (s, 1H), 4.79 (quint, 1H), 7.52 (d, 1H), 7.66 (d, 2H), 8.68 (d, 2H).

^{13}C NMR (101 MHz, $CDCl_3$) δ_c (ppm): 18.3, 48.9, 52.9, 121.4, 141.3, 150.6, 165.4, 173.6.

HRMS (ESI-MS) m/z calcd for $C_{10}H_{12}N_2O_3Na^+$ $[M+Na]^+$: 231.0740, found: 231.0735.

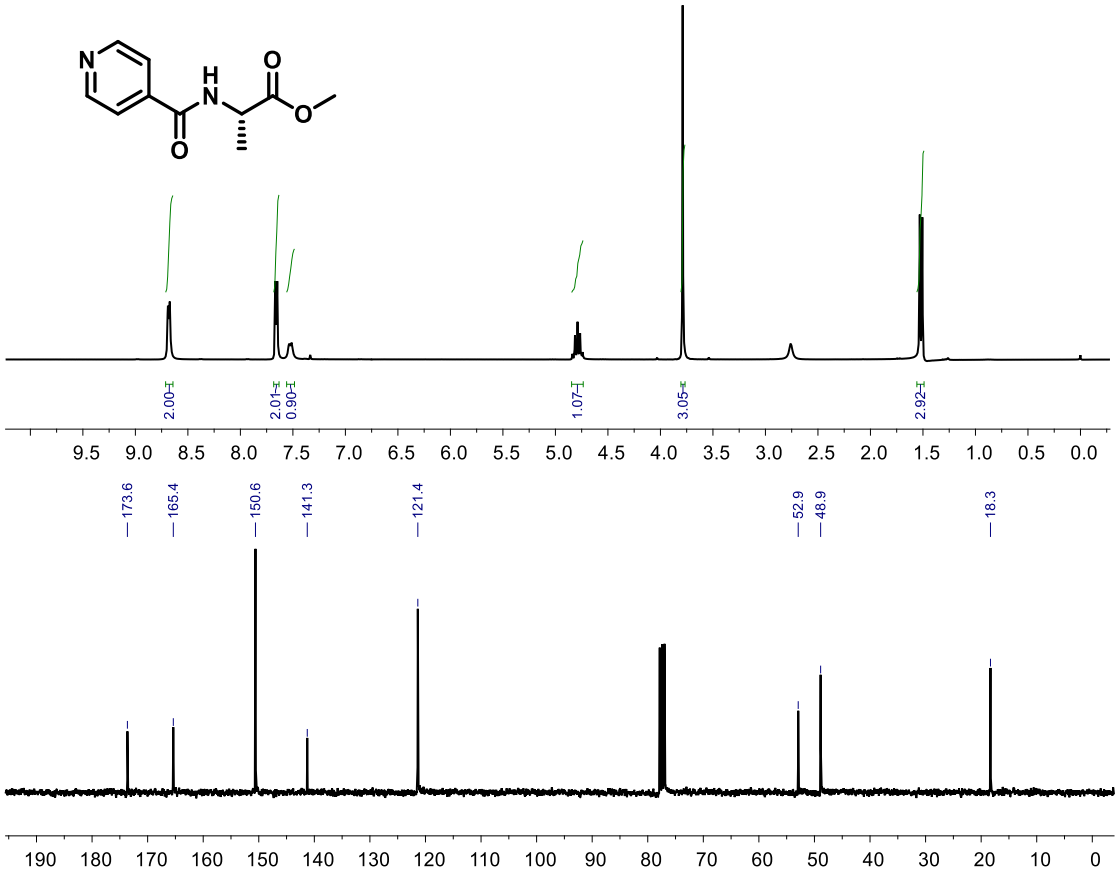

Figure S3. ^{1}H and ^{13}C NMR spectra of the ligand **2** ($CDCl_3$, 400 and 101 MHz respectively).

4-((trimethylsilyl) ethynyl)pyridine [Ligand 3]

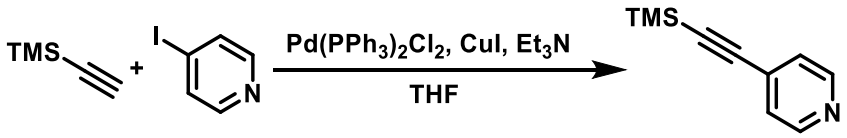

4-Iodopyridine (500 mg, 1.00 equiv.), bis(triphenylphosphine)palladium (II) dichloride ($Pd(PPh_3)_2Cl_2$, 6.85 mg, 0.04 equiv.), triphenylphosphine (10.2 mg, 0.016 equiv.) and copper iodide (CuI, 11.1 mg, 0.024 equiv.) were dissolved in dry THF (20 mL). Next, triethylamine (Et_3N, 10 mL) and ethynyltrimethylsilane (359 mg, , 1.5 equiv.) were added and the mixture was stirred for two hours. After removing the solvent, the crude product was chromatographed on silica gel with pentane/ethyl acetate (80:20) as eluent obtaining, after solvent removal, an oil (368 g, 86 % of yield).

^{1}H NMR (400 MHz, $CDCl_3$) δ_H (ppm): 0 (s, 9H), 7.01 (d, 2H), 8.28 (d, 2H).

^{13}C NMR (101 MHz, $CDCl_3$) δ_C (ppm): 0, 100.1, 102.4, 126, 131.4, 150.0.

HRMS (GC-EI-MS) m/z calcd for $C_{10}H_{13}NSi$ $[M+H]^+$: 175.31, found: 175.13.

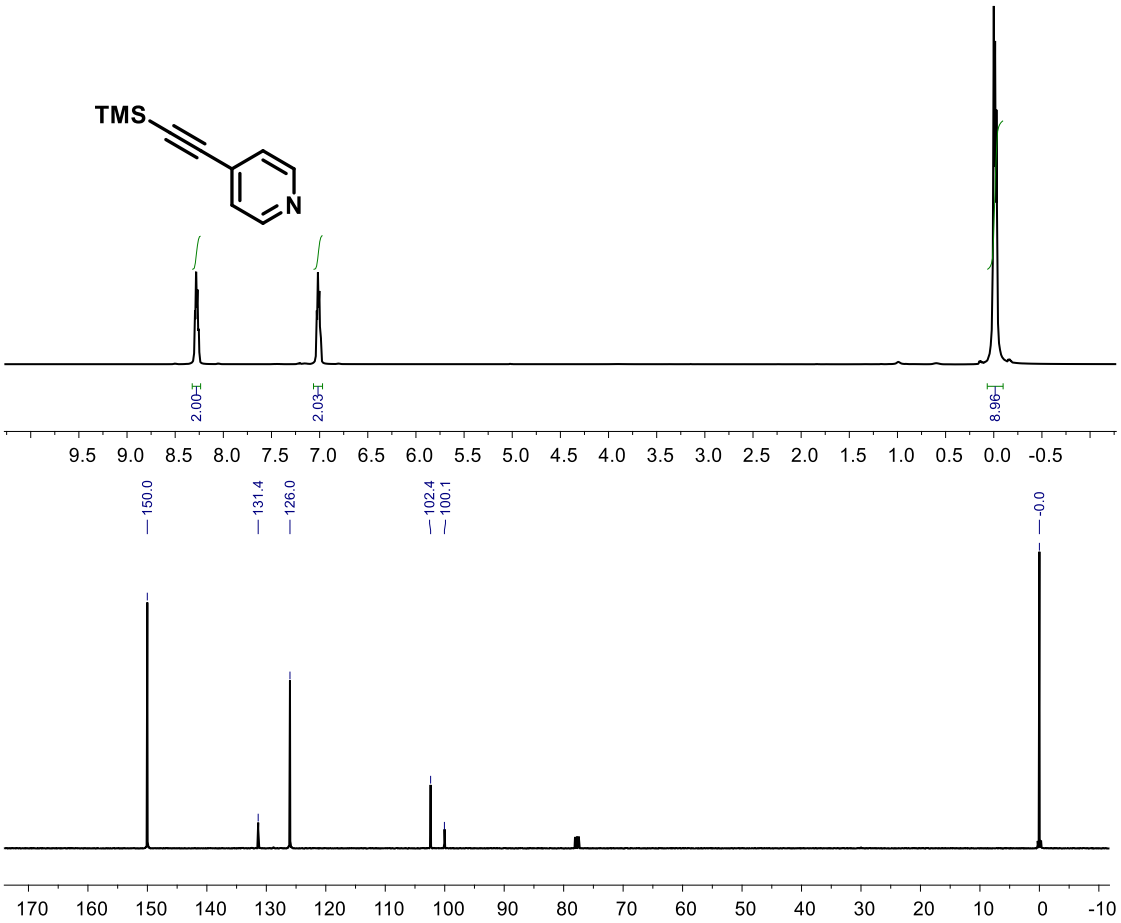

Figure S4. ^{1}H and ^{13}C NMR spectra of the ligand **3** ($CDCl_3$, 400 and 101 MHz respectively).

4. General protocol for complexation and deprotection of monomers

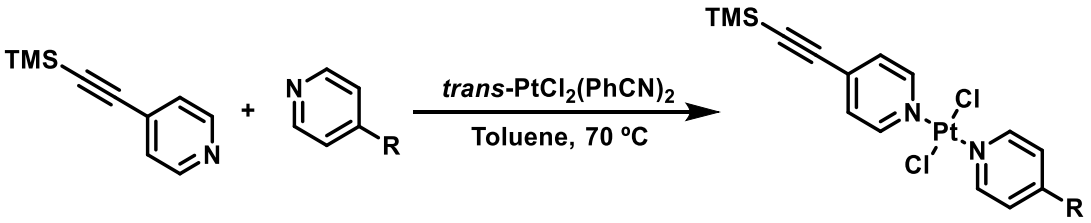

Ligand **3** (1.7 equiv.), *trans*-$PtCl_2(PhCN)_2$ (1.35 equiv.) and the corresponding ligand **1** or **2** (1 equiv.) were placed in a pressure tube and were subjected to five vacuum/Ar cycles. Subsequently, dry and degassed toluene were added and the mixture was heated to 70 °C and stirred at this temperature for one week. After evaporating the solvent, the crude was chromatographed on silica gel with pentane/ethyl acetate (80:20) as eluent.

Ligands	**Ligand 4** (mg)	**Ligand X** (mg)	***trans*-$PtCl_2(PhCN)_2$** (mg)	**Toluene** (mL)	**Yield** (%)
3 and **1**	126.1	100	269.8	4	38.1
3 and **2**	171.7	120	367.4	4	36.1

Table S1. Complexation conditions of the different ligands (**X** = **1** or **2** for ligand-**1** and ligand-**2** respectively).

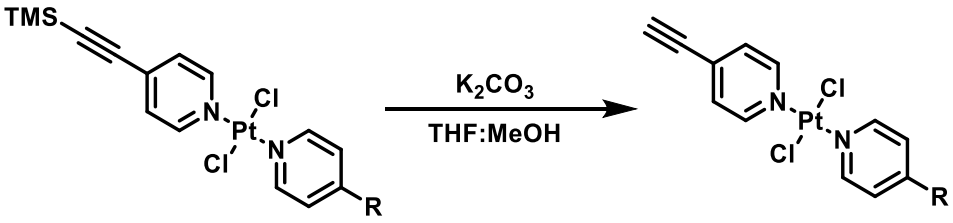

The corresponding protected monomer was dissolved in a mixture of THF:MeOH (3:1). Next K_2CO_3 was added (1.20 equiv.) and the reaction was stirred at r.t. for 1 hour. The crude was chromatographed on silica gel with pentane/ethyl acetate (60:40) as eluent.

	TMS-mono-(*S*)-X (mg)	**K_2CO_3** (mg)	**THF** (mL)	**MeOH** (mL)	**Yield** (%)
mono-(*S*)-1	164	40.1	9	3	95.1
mono-(*S*)-2	130	33.2	9	3	96.2

Table S2. Deprotection conditions of the different ligands (**X** = **1** or **2** for TMS-mono-(*S*)-**1** and TMS-mono-(*S*)-**2** respectively).

mono-(*S*)-1

^{1}H NMR (400 MHz, $CDCl_3$) δ_H (ppm): 0.98 (t, 3H), 2.28 (m, 1H), 3.53 (s, 1H), 3.79 (s, 1H), 4.71 (dd, 1H), 6.81 (d, 1H), 7.34 (d, 2H), 7.65 (d, 2H), 8.88 (d, 2H), 9.04 (d, 2H).

^{13}C NMR (101 MHz, $CDCl_3$) δ_c (ppm): 18.0, 19.0, 31.5, 52.6, 57.9, 79.4, 86.2, 122.8, 127.7, 133.2, 142.9, 153.4, 154.4, 163.4, 172.0.

HRMS (ESI-MS) m/z calcd for $C_{19}H_{21}Cl_2N_3O_3PtNa^+$ $[M+Na]^+$: 627.0500, found: 627.0508.

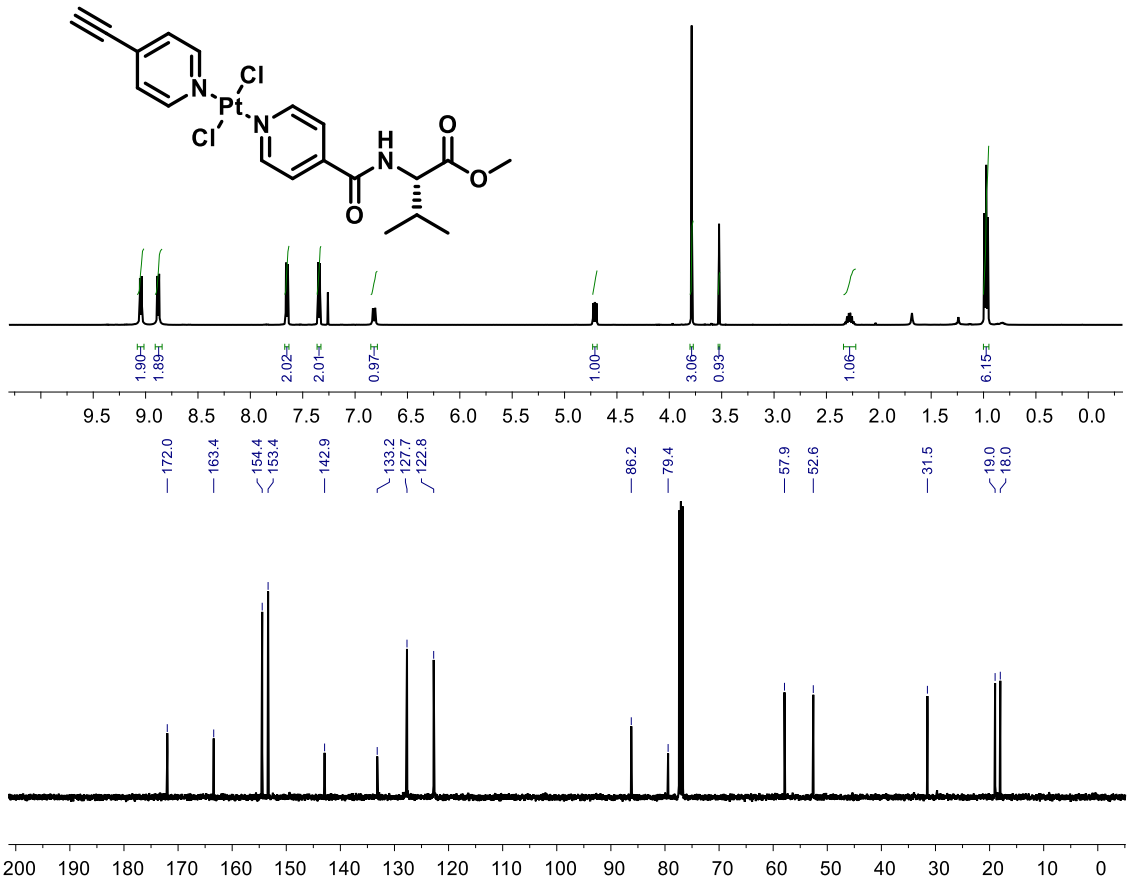

Figure S5. ^{1}H and ^{13}C NMR spectra of mono-(*S*)-**1** ($CDCl_3$, 400 and 101 MHz respectively).

mono-(*S*)-2

^{1}H NMR (400 MHz, $CDCl_3$) δ_H (ppm): 1.51 (d, 3H), 3.53 (s, 1H), 3.80 (s, 3H), 4.73 (quint, 1H), 7.10 (d, 1H), 7.34 (d, 2H), 7.63 (d, 2H), 8.87 (d, 2H), 9.02 (d, 2H).

^{13}C NMR (101 MHz, $CDCl_3$) δ_c (ppm): 18.1, 48.9, 52.9, 79.4, 86.3, 122.8, 127.7, 133.2, 142.6, 153.4, 154.4, 162.9, 173.0.

HRMS (ESI-MS) m/z calcd for $C_{17}H_{17}Cl_2N_3O_3PtNa^+$ $[M+Na]^+$: 600.3142, found: 600.0172.

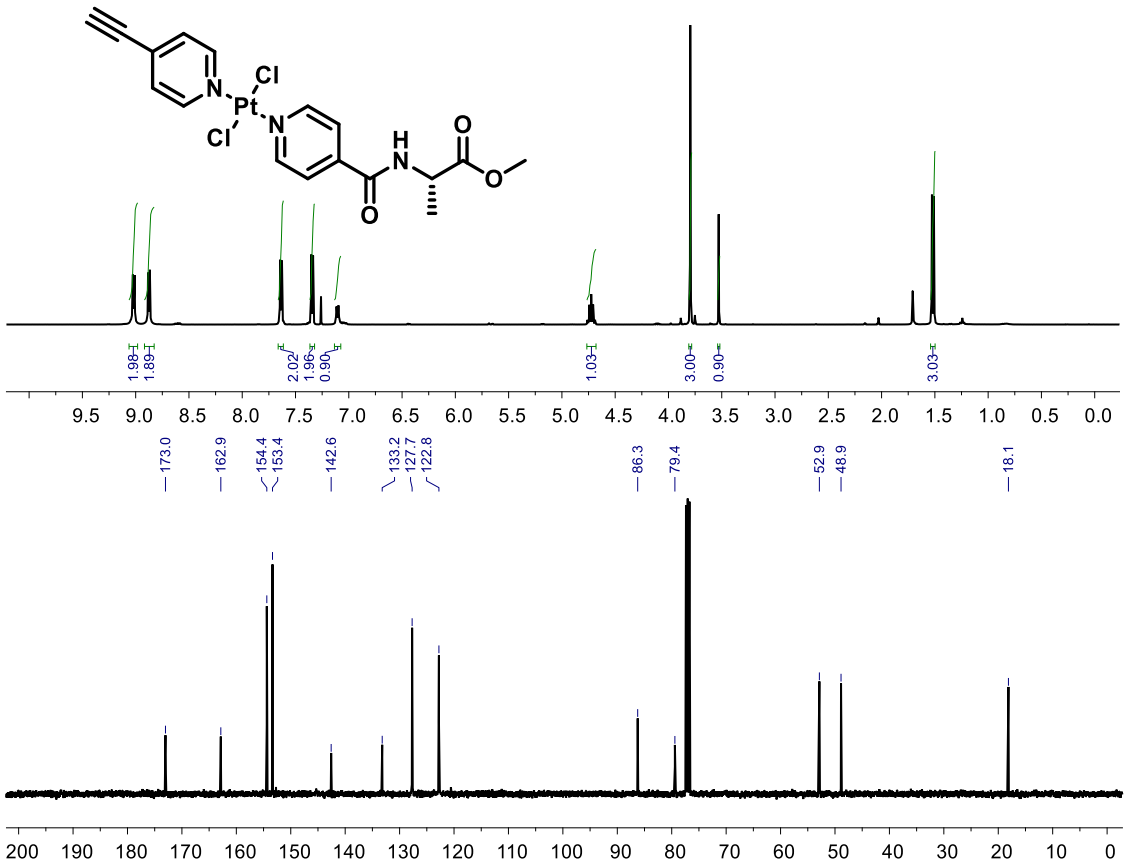

Figure S6. ^{1}H and ^{13}C NMR spectra of mono-(*S*)-**2** ($CDCl_3$, 400 and 101 MHz respectively).

5. Synthesis of Polymers

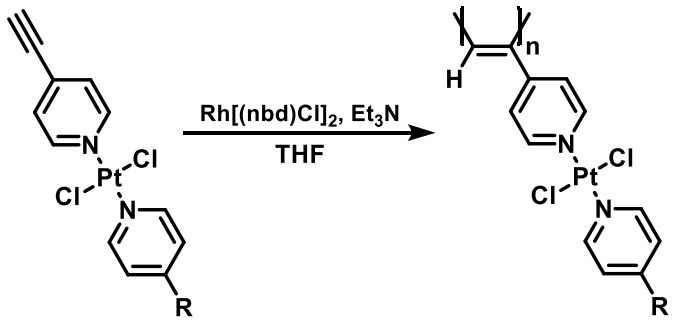

The reaction flask (sealed ampoule) was dried under vacuum and argon flushed for three times before monomer was added as a solid. Dry THF was added with a syringe. Next, a solution of rhodium norbornadiene chloride dimer, $[Rh(nbd)Cl]_2$, and ET_3N in dry THF was added to the reaction that is under stirring at 30 °C. After 6 hours, the resulting polymer was diluted in CH_2Cl_2 and it was precipitated in methanol and centrifuged (2 times), reprecipitated in hexane and centrifuged again.

Ligands	**mono-(*S*)-X** (mg)	**THF** (mL)	**[Rh(nbd)Cl]2** (mg)	**ET_3N** (µL)	**Yield** (%)
poly-(*S*)-1	75	0.25	1.2	5.0	95.1
poly-(*S*)-2	75	0.26	1.2	5	96.2

Table S3. Polymerization conditions of the different polymers (**X** = **1** or **2** for mono-(*S*)-**1** and mono-(*S*)-**2** respectively).

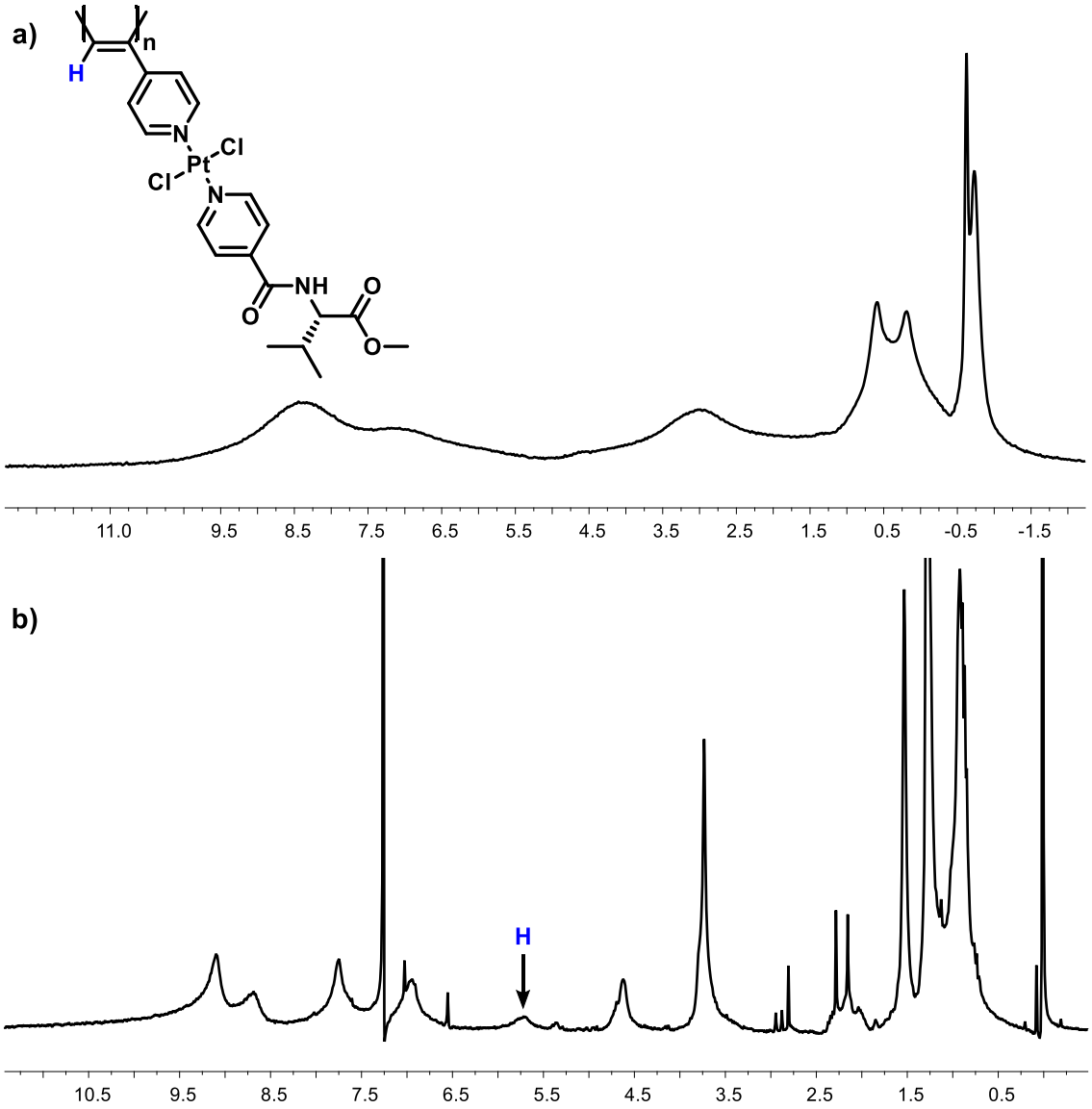

Figure S7. ^{1}H NMR spectra of poly-(*S*)-**1** as a) solid sample, ^{1}H spectra NEO-750 MHz with a 1.3 mm rotor and b) in $CDCl_3$, 400 MHz.

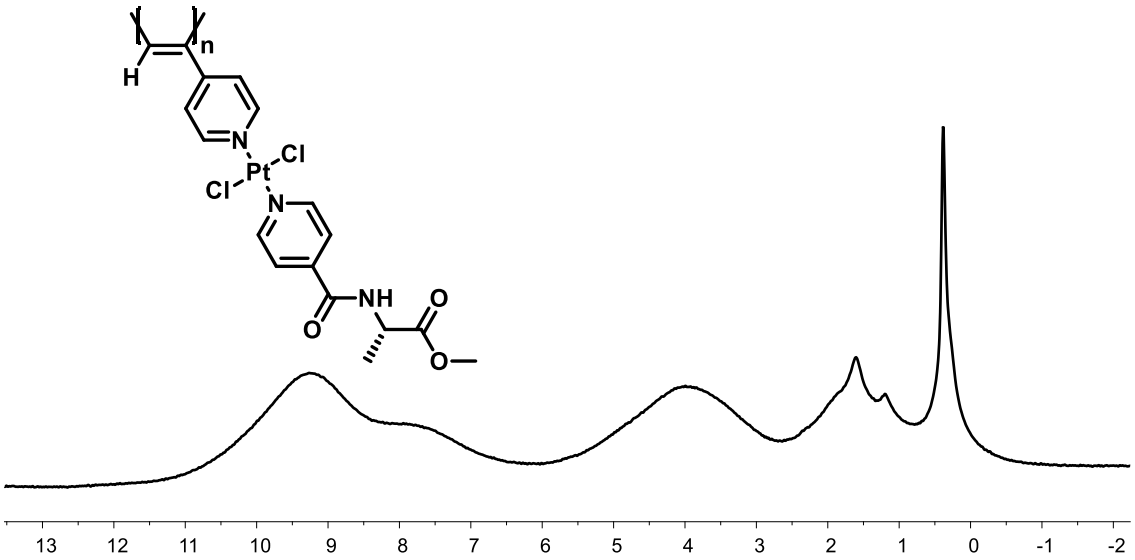

Figure S8. ^{1}H spectra of poly-(*S*)-**2** (Solid sample, NEO-750 MHz with a 1.3 mm rotor).

6. Elemental Analysis

A solid sample (5 mg) of the corresponding monomer was remained under vacuum for 24 hours before being submitted to elemental analysis.

	C (%)	H (%)	N (%)
	Estimated/measured	**Estimated/measured**	**Estimated/measured**
mono-(*S*)-1	37.70/38.11	3.50/3.72	6.94/6.69
mono-(*S*)-2	35.37/36.78	2.97/3.49	7.28/6.69

Table S4. Tabulated results of elemental analysis for the different monomers analysed.

7. Spectroscopy Studies

Raman

Samples was prepared by drop casting 0.5 mg/mL solutions of the corresponding polymer over a microscope slide. After solvent evaporation, the spectra were recovered in a Renishaw confocal Raman spectrometer. For DMF solutions, sample were deposited with the microscope slide at 175 °C.

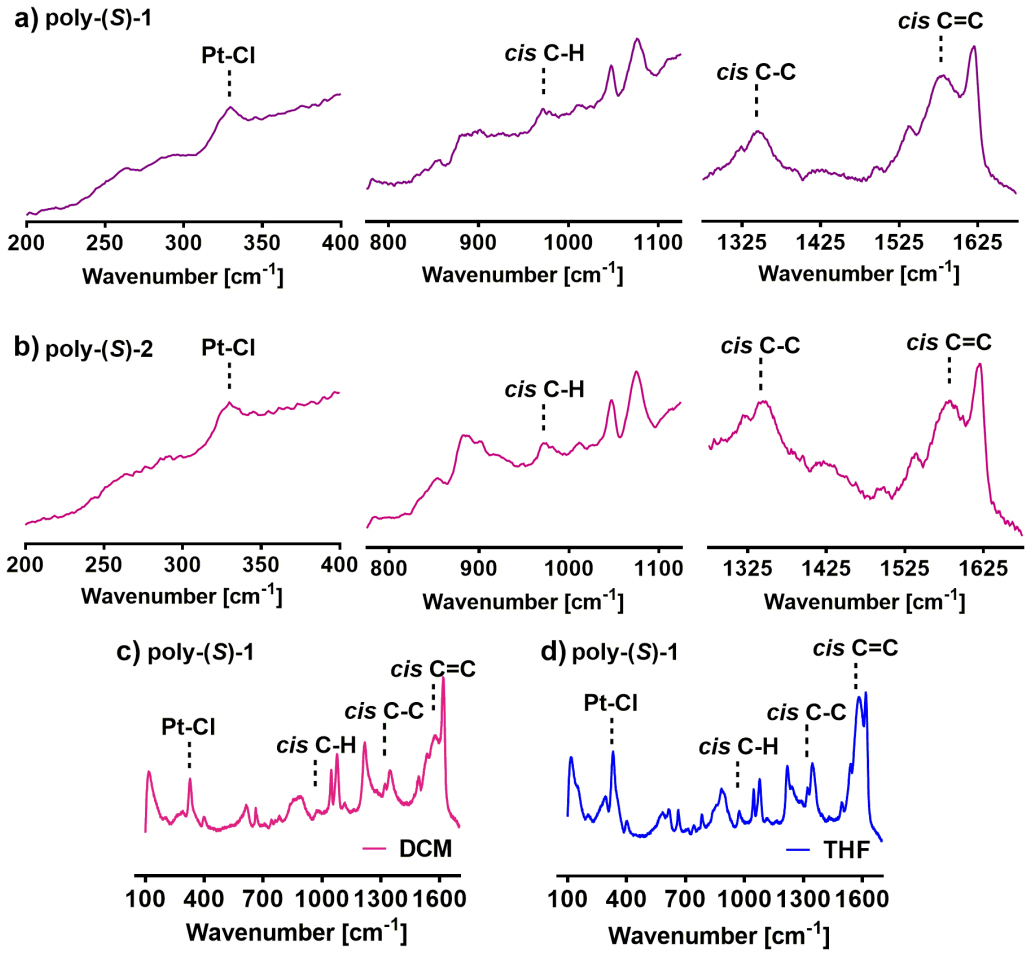

Figure S9. Raman spectra in DMF of a) poly-(*S*)-**1** and b) poly-(*S*)-**2**. Raman spectra of poly-(*S*)-**1** in c) DCM and d) THF.

ATR/FT-IR

Solid IR spectra were recovered to confirm the polymerization of the monomers as result of the dissaperence of the C≡C vibration around 2150 cm^{-1}.

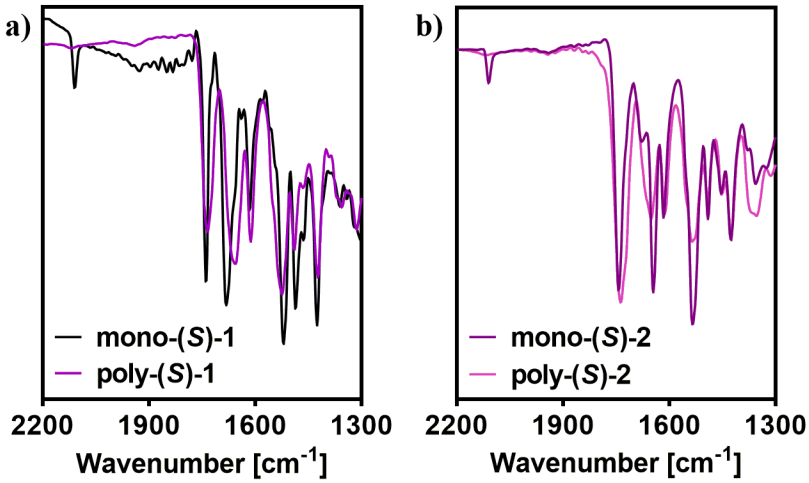

Figure S10. ATR/FT-IR spectra of a) mono-(*S*)-**1** and poly-(*S*)-**1** and b) mono-(*S*)-**2** and poly-(*S*)-**2**.

8. Thermal Studies

TGA studies

Solid polymer sample were remained under vacuum for 12 hours. After this time, were introduced in a platinum pan and heated from 40 °C to 800 °C with a heating rate of 10 °C/min.

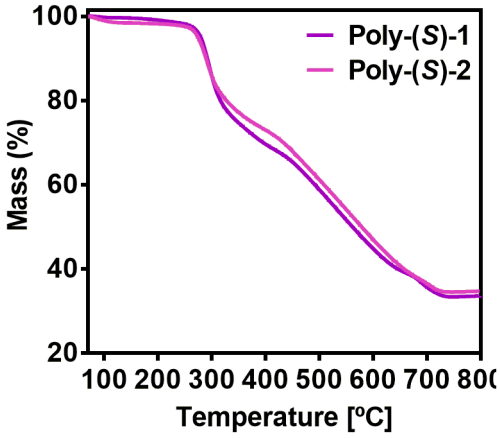

Figure S11. TGA thermograms of a) poly-(*S*)-**1** and b) poly-(*S*)-**2**.

DSC studies

A polymer sample, pre-dried, was introduced in an aluminum pan and heated from 60 °C to 350 °C with a heating rate of 5 °C/min. To compare all polymers in same conditions, DSC thermograms was performed immediately after polymerization (see section synthesis of polymers for details). Thus, the results for poly-(*S*)-**1** and poly-(*S*)-**2** show thermograms of the polymers shows a clear transition for the *c-c* to *t-t* transformation. However, despite the stiffness generated by the bispyridyldichloride platinum(II) complexes, the *c-t* to *c-c* transition is weak. For poly-(*S*)-**1**, the thermogram was also get after dissolving in DCM and evaporating the solvent. This thermogram was compared with the one obtained in DMF, due to the formation of a *c-c* scaffold in this solvent, the peak associated to *the c-t* to *c-c* transition disappear. Also, a new and broad exothermic peak appear between 120-260 °C, probably as result of the strong supramolecular assembly between the bispyridyldichloride platinum(II) groups.

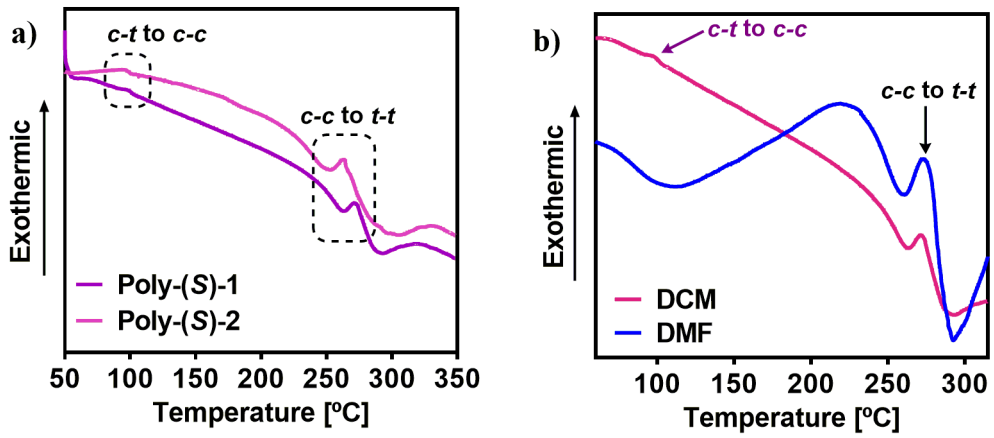

Figure S12. DSC thermograms of a) the three polymers after the polymerization and b) poly-(*S*)-**1** in DCM and DMF scaffolds.

9. VT-CD Experiments

Variable temperature circular dichroism (VT-CD) experiments were measured in a 1 mm quartz cell in a Jasco-1500 with a sample concentration of 0.6 mg/mL.

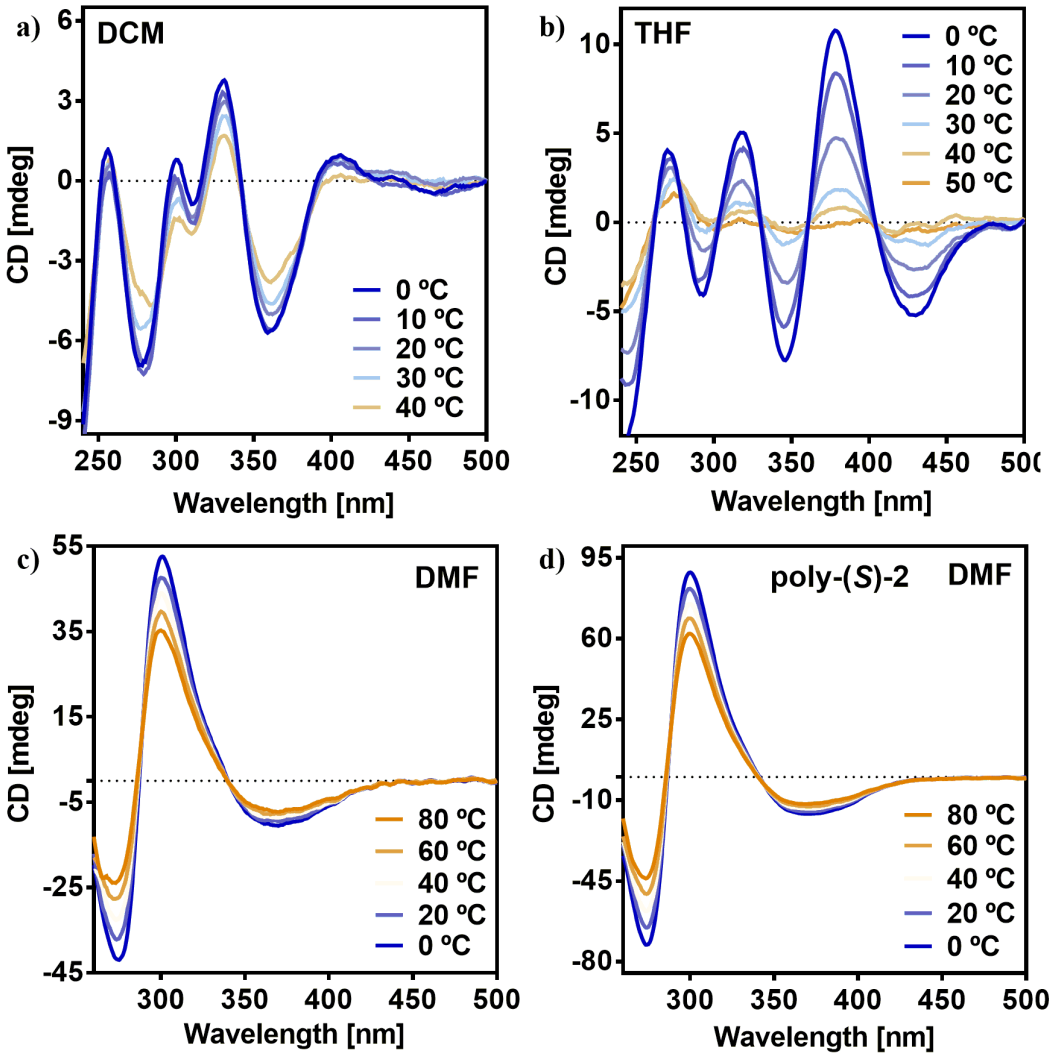

Figure S13. VT-CD spectra of poly-(*S*)-**1** in a) DCM, b) THF, c) DMF and d) poly-(*S*)-**2** in DMF. [poly-(*R*)-**1**]= 0.6 mg/mL, [poly-(*R*)-**2**]= 0.6 mg/mL.

10. Spatial distribution of bispyridyldichloride platinum(II) groups in a *cis-cisoidal/cis-transoidal* helix

Before submitting theoretical calculations, we build 3D models of the bispyridyldichloride platinum(II) complexes in a *cis-cisoidal* and a *cis-transoidal* helix. Thus, we can observe that the orientation of chloride groups and even the w_1 angle (relative orientation of the bispyridyldichloride platinum(II) toward the polyene) is influenced by the steric hindrance generated between upper and lower groups in the helix. As a result, the sign of these angles must be reverse with the inversion of the helical sense of the helix. The resulting 3D model submitted for theoretical calculations are agree with these assumptions and the resulted conformations and ECD/UV-vis calculated spectra confirms this idea.

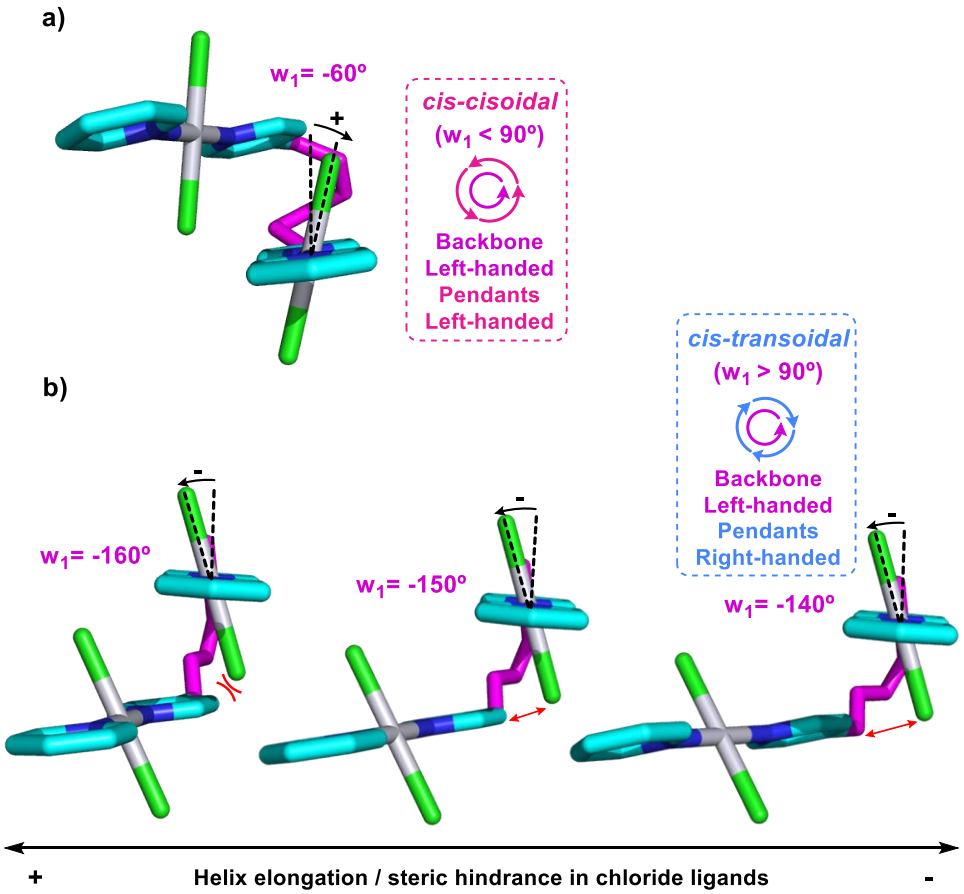

Figure S14. 3D model representing the spatial distribution of bispyridyldichloride platinum(II) groups in a a) *cis-cisoidal* helix and b) *cis-transoidal* helix.

11. UV-Vis Monomer calculations

Calculated UV-Vis spectra, after geometry optimization, allows identify the UV-vis absorptions. Thus, UV-band at higher wavelength —ca. 345 nm— corresponds to the core of the bispyridyldichloride PtII complexes (S_0 to S_9 and S_0 to S_{11}), the band at ca. 305 nm corresponds to *para*-ethynylpyridyl complexed to the dichloride Pt^{II} (S_0 to S_{26}), while the band at 280 nm is attributed to the para-pyridylbenzamide of (*L*)-Valine-methyl ester complexed to the dichloride Pt^{II} (S_0 to S_{44}). Finally, the band at 250 nm is related to the benzamide group of the chiral moiety (mainly S_0 to S_{65}).

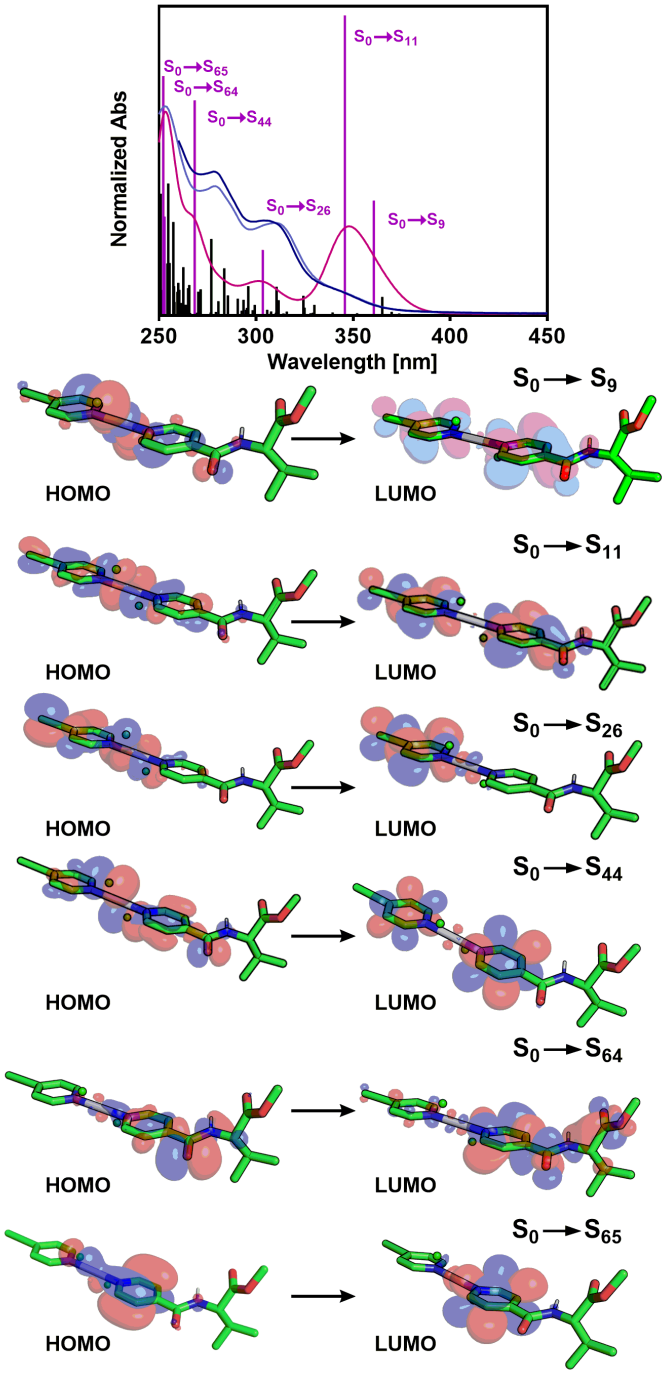

Figure S15. Main HOMO-LUMO transitions assigned to each calculated natural transition orbitals (NTO).

12. Computational Details

Considering the difficulties to carry out theoretical calculations on large polymers, we apply the methodology reported in the reference S2. Thus, oligomers constituted by 9 monomer repeating units was build using Spartan 18. The generated structure was adjusted according to the information obtained from several techniques such as Raman, IR, CD, UV-vis and the geometry calculated for the monomeric stacks in a left-handed helix. Finally, the time-dependent density functional theory (TD-DFT, Ref. S3) was used together with the rCAM-B3LYP density functional (Ref. S4) and the LANL2DZ basis set (Ref. S5). We included 180 excitation energies in the calculation for the scaffold. The resulting ECD spectrums were selected with a full width at half height (FWHM) of 0.33 eV. Moreover, we evaluated a correction factor for lambda as the difference between the theoretical and experimental wavelengths, and we shifted the rest of the theoretical spectra accordingly. In a similar way, the intensity was rescaled for the theoretical values.

For monomer calculations, individual monomer units were optimized in both geometries (to achieve the final left and right-handed orientation) using the density functional theory (DFT) together with the rCAM-B3LYP functional and the LANL2DZ basis set. The resulting geometries were used to build and stack three monomeric units, which were optimized again using the same parameters. Thus, the theorical ECD spectra were calculated since the optimized geometry of both stacks using the time-dependent density functional theory (TD-DFT) together the rCAM-B3LYP density functional and the LANL2DZ basis set. The resulting ECD spectrum was selected with a full width at half height (FWHM) of 0.33 eV. Moreover, the theorical UV-vis spectrum of the monomer was calculated from the previously optimized geometry for one monomeric unit using the time-dependent density functional theory (TD-DFT) together the wB97XD density functional and the LANL2DZ basis set. The resulting UV-vis spectrum was selected with a full width at half height (FWHM) of 0.2 eV. Also, we evaluated a correction factor for lambda as the difference between the theoretical and experimental wavelengths, and we shifted the rest of the theoretical spectrum accordingly. This correction factor was also applied to the ECD calculated of the monomeric stacks.

13. Supporting References

S1. F. Rey-Tarrío, R. Rodríguez, E. Quiñoá, R. Riguera, F. Freire, *Angew. Chem. Int. Ed.* **2020**, *60*, 8095-8103.

S2. B. Fernández, R. Rodríguez, A. Rizzo, E. Quiñoá, R. Riguera, F. Freire, *Angew. Chem. Int. Ed.* **2018**, *57*, 3666-3670.

S3. E. Runge, E. K. U. Gross, *Phys. Rev. Lett.* **1984**, *52*, 997-1000.

S4. A. J. Cohen, P. Mori-Sánchez, W. Yang, *J. Chem. Phys.* **2007**, *126*, 191109.

S5. P. J. Hay, W. R. Wadt, *J. Chem. Phys.*, **1985**, *82*, 270-283.

Experimental Section Chapter VIII

1. Materials and methods

CD measurements were done in a Jasco-720 and VT-CD measurements in a Jasco-1100 with a 1 mm quartz cuvette. Sample concentration for CD and VT-CD measurements was 0.3 mg/mL.

UV spectra were registered in a Jasco V-630 with a 1 mm quartz cuvette. Sample concentration for UV measurements was 0.3 mg/mL.

Optical rotation was measured in a Jasco-P2000.

NMR experiments were measured in a Varian 300 operating at 300 MHz for proton NMR and 75 MHz for carbon. $CDCl_3$ signal (δ= 77.2 ppm) was used as standard for ^{1}H or ^{13}C experiments.

ATR/FT-IR spectra were recorded in a Perkin Elmer FT-IR ATR Spectrum Two

AFM measurements were performed in a MultiMode V Scanning Probe Microscope (Veeco Instruments) in air at rt with standard silicon cantilevers and supersharp cantilevers in tapping mode using 12 μm and 1 μm scanners Nanoscope processing software and WSxM 4.0 Beta 1.0 [4] (Nanotec Electronica, S.L.) were used for image analysis. This measurements were performed at CACTI (Vigo University, Spain).

SEM images were recovered with a ZEISS FESEM ULTRA Plus. A drop of polymer solution of 0.3 mg/mL in $CHCl_3$, with the respective equivalents of silver perchlorate solution, was settled on a silicon wafer chip and allowed to dry at rt for 12 h.

Viscoelastic behavior were evaluated at 20°C in a Rheolyst AR-1000N rheometer (TA Instruments, New Castle, UK) equipped with an AR2500 data analyzer, and fitted with a Peltier plate. The storage (G') and the loss (G'') moduli were recorded using a cone-plate geometry (diameter 4 cm, angle 2°).

2. Analysis of the Supramolecular Polymerization

Time-dependent changes in the helical assembly of $(Ag((R)\text{-}\mathbf{1})_2$ $\alpha_{ECD=403nm}$ was calculated from the ECD intensity at λ= 403 nm using the following equation:

$$\alpha_{ECD=403nm} = \frac{ECD_{403nm}(equiv) - ECD_{403nm}(fully\ monomeric)}{ECD_{403nm}(fully\ aggregated) - ECD_{403nm}(fully\ monomeric)}$$

where ECD_{403nm}(equiv) is the ECD intensity at a given equivalents (equiv) and ECD_{403nm}(fully aggregated) and ECD_{403nm}(fully monomeric) are the ECD intensities of the purely aggregated state (equivalents that reach the maximum ECD signal at 403 nm) and monomeric state (0 equivalents) respectively.

3. Synthesis of Monomer

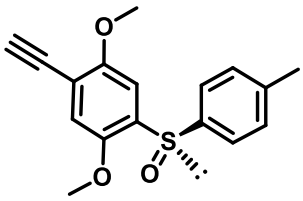

(*R*)-**1**

(*R*)-**1** was prepared according to the procedure described in the Reference **S1.**

$[\alpha]_D^{20}$ = -2.3820 (c = 5.0 mg/mL, $CHCl_3$)

^{1}H NMR (300 MHz, $CDCl_3$) δ(ppm): 2.35 (s, 3H), 3.36 (s, 1H), 3.71 (s, 3H), 3.96 (s, 3H), 6.92 (s, 1H), 7.12-7.23 (d, 2H) 7.47-7.58 (m, 3H)

^{13}C NMR (75 MHz, $CDCl_3$) δ (ppm): 21.6, 56.5, 57.0, 79.6, 83.0, 107.1, 114.2, 117.1, 125.7, 130.0, 135.8, 141.9, 142.3, 149.1, 156.3.

HRMS (ESI) m/z calcd for $C_{17}H_{17}O_3S$ $[M+H]^+$: 301.0898, found: 301.0896

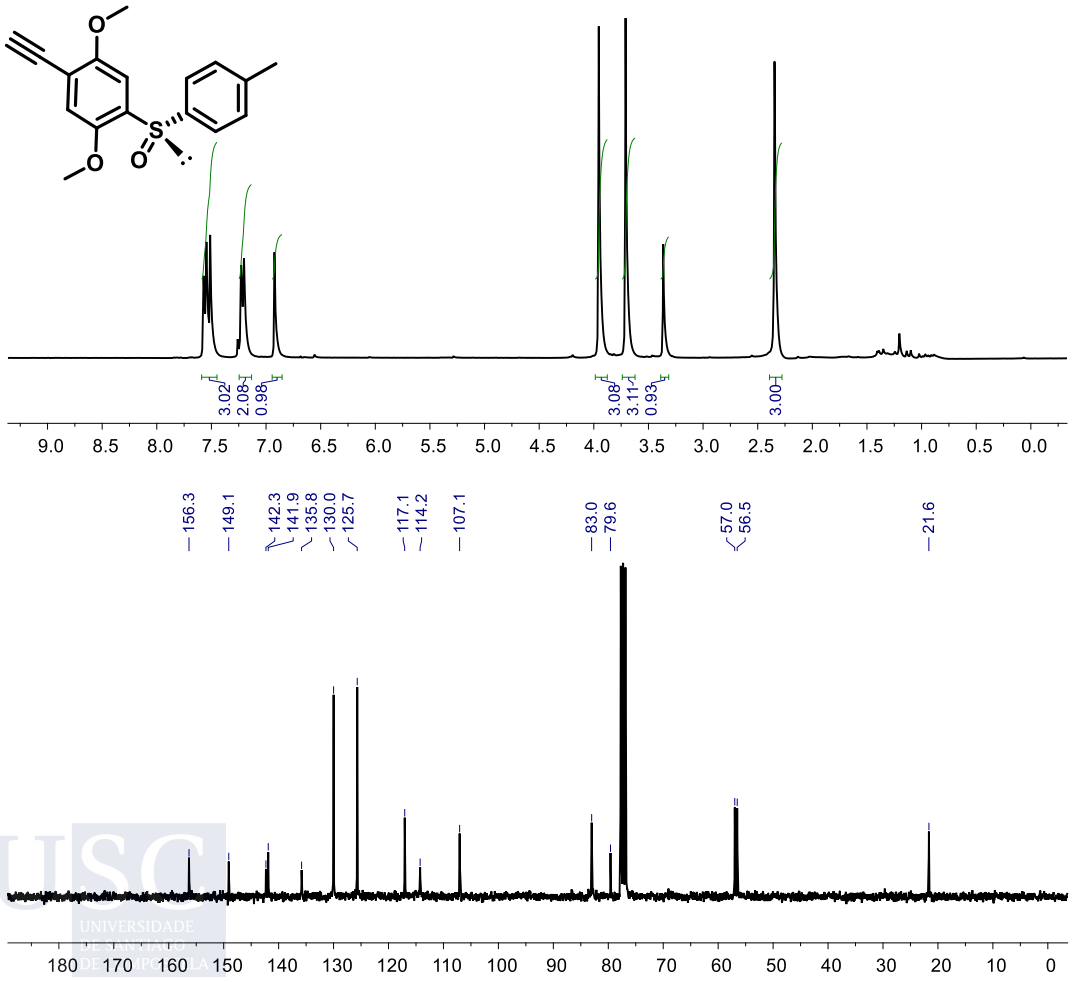

Figure S1. ^{1}H and ^{13}C NMR spectra of (*R*)-**1** ($CDCl_3$, 300 and 75 MHz respectively).

4. Synthesis of Protected Acetylene Monomer

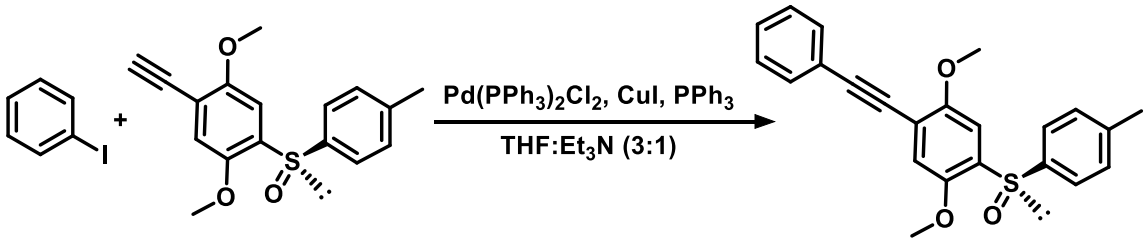

(*R*)-**1** Ph-(*R*)-**1**

Iodobenzene (102 mg, 1.50 equiv), bis(triphenylphosphine)palladium(II) dichloride ($Pd(PPh_3)_2Cl_2$, 1.40 mg, 0.004 equiv), triphenylphosphine (PPh_3, 2.02 mg, 0.016 equiv) and copper iodide (CuI, 2.29 mg, 0.024 equiv) were dissolved in dry THF (12 mL). Next, triethylamine (Et_3N, 4 mL) and (*R*)-**1** (100 mg, 1 equiv) were added and the mixture was stirred for two hours. After removing the solvent, the crude product was chromatographed on silica gel (40-63 mesh) with hexane/ethyl acetate (80:20) as eluent (112 mg, 86% of yield).

$[\alpha]_D^{20}$ = -511.25 (c = 5.0 mg/mL, $CHCl_3$)

^{1}H NMR (300 MHz, $CDCl_3$) δ(ppm): 2.35 (s, 3H), 3.73 (s, 3H), 3.97 (s, 3H), 6.97 (s, 1H), 7.21 (s, 1H), 7.24 (s, 1H), 7.30-7.35 (d, 3H), 7.51-7.61 (m, 5H).

^{13}C NMR (75 MHz, $CDCl_3$) δ (ppm): 21.4, 56.2, 56.7, 57.0, 85.0, 95.2, 106.6, 115.3, 116.1, 123.0, 125.4, 128.3, 128.5, 129.7, 131.7, 134.4, 141.6, 142.0, 148.8, 155.3.

HRMS (ESI) m/z calcd for $C_{24}H_{20}O_3S$ $[M+H]^+$: 377.1211, found: 377.1205.

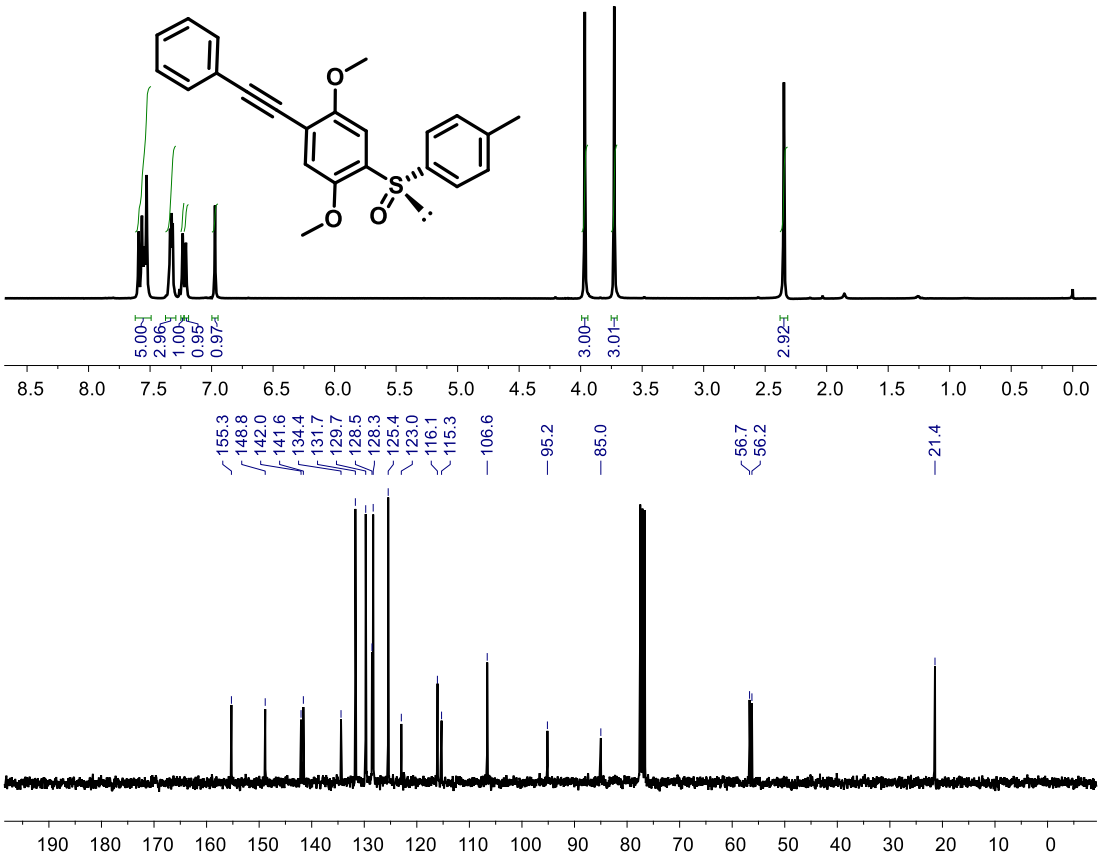

Figure S2. ^{1}H and ^{13}C NMR spectra of Ph-(*R*)-**1** ($CDCl_3$, 300 and 75 MHz respectively).

5. CD and UV studies

(*R*)-**1** was dissolved in several solvents at 0.3 mg/mL to evaluate its CD and UV-Vis spectra in each case. The results were similar in all cases, a similar ECD and UV spectra and good solubility independently of the solvent properties (with exception of MCH in that (*R*)-**1** is insoluble). Furthermore, no aggregation tendency was observed.

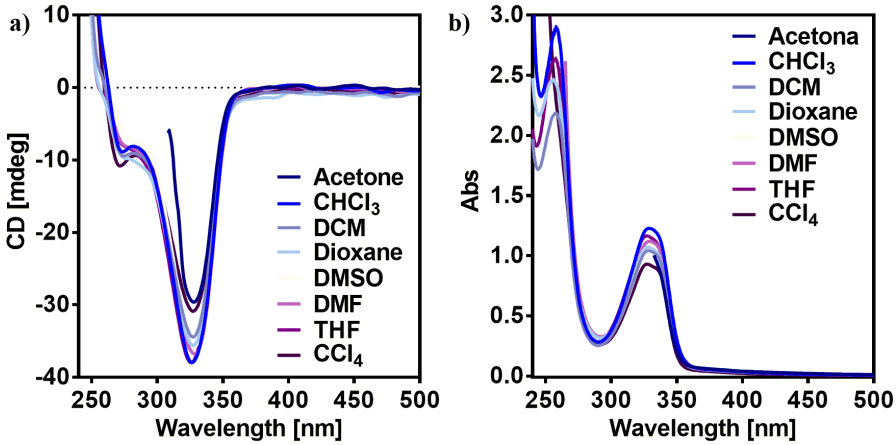

Figure S3. a) ECD and b) UV-Vis spectra of (*R*)-**1** in several solvents. [(*R*)-**1**]= 0.3 mg/mL.

From among these solvents, we evaluate for the less donor/polar their interaction in presence of $AgClO_4$, prepared as MeOH solution of 10 mg/mL.

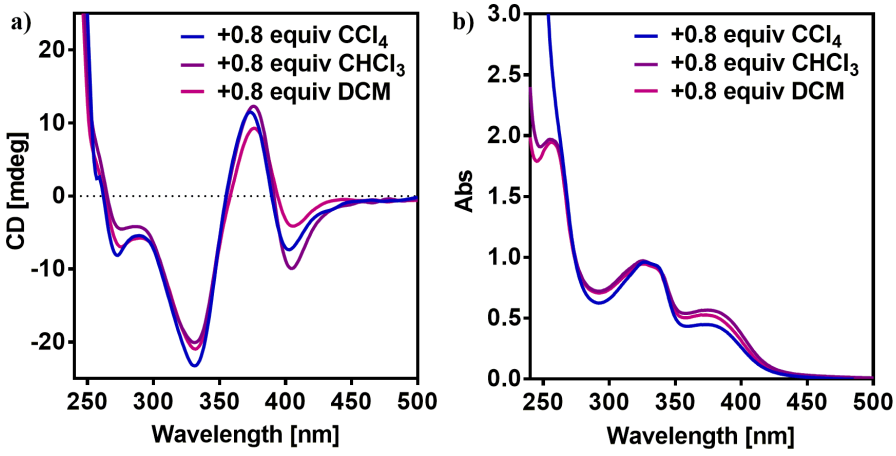

Figure S4. a) ECD and b) UV-Vis spectra of (*R*)-**1** in different solvents with 0.8 equivalents of $AgClO_4$. [(*R*)-**1**]= 0.3 mg/mL.

Furthermore, due to the need to use a more donor/polar solvent to solubilize silver cations, we evaluate the binding competition of the cosolvent and its influence on the aggregation process. Thus, using THF (Figure S5a) instead MeOH (Figure S5b) a poor agregation and stability is found.

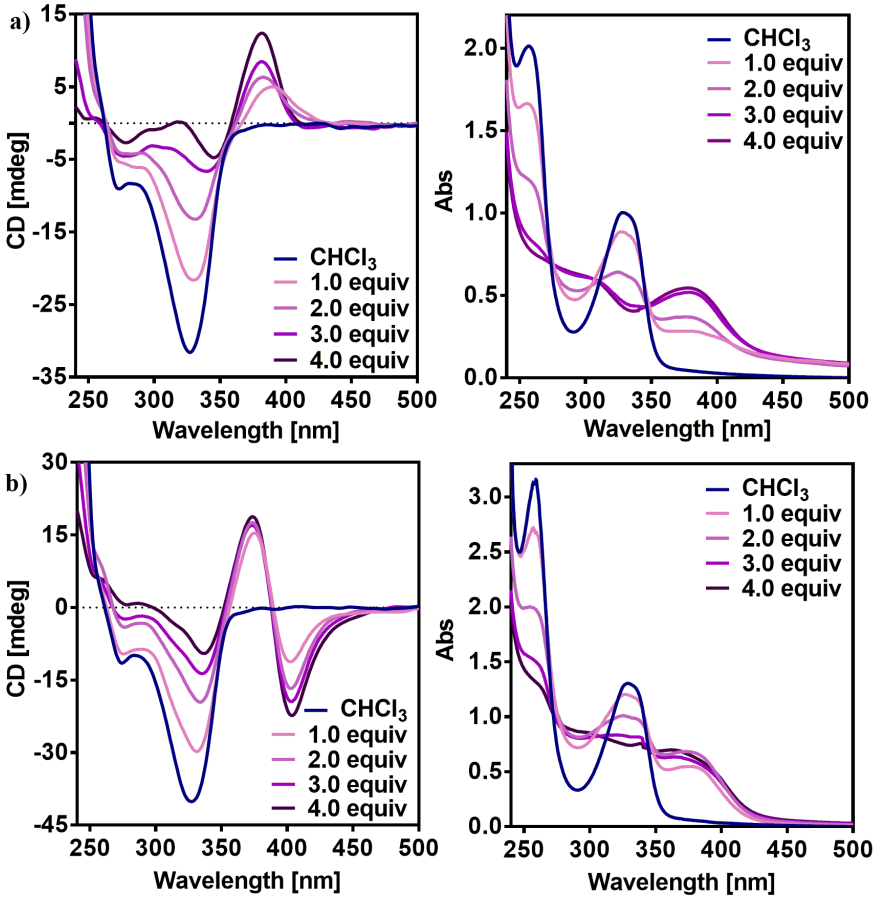

Figure S5. ECD and UV-Vis spectra of (*R*)-**1** titration with $AgClO_4$ (10 mg/mL) in a) THF and b) MeOH. [(*R*)-**1**]= 0.3 mg/mL.

6. Determination of the binding via terminal acetylene

NMR experiments

(*R*)-**1** was dissolved in $CDCl_3$ (6.5 mg/mL) and separate in two NMR tubes. For the first, only MeOD was injected while in the second the MeOD injected contains 0.8 equiv of $AgClO_4$ (1/0.8 mol/mol ((*R*)-**1**)/Ag relation, metal cation solution is 100 mg/mL instead 10 mg/mL due to the necesarry of reduce the intensity of the emerging peak of the MeOH contained in the MeOD). As result of the increased concentration of both solutions, we can no evaluate NMR at larger equivalents of silver (I) due to the gel formation and solvent residual peaks intensity.

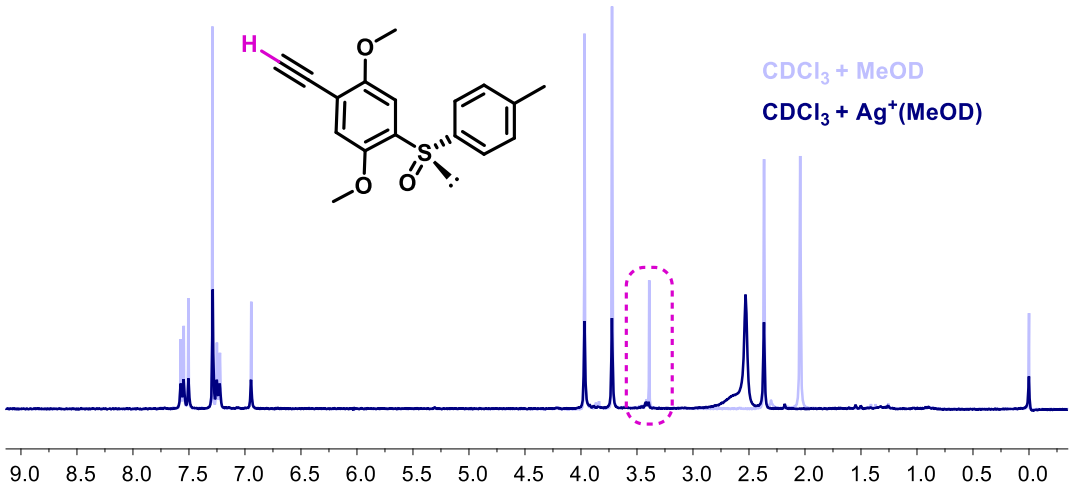

Figure S6. ^{1}H NMR spectra of (*R*)-**1** in $CDCl_3$ with addition of a) MeOD and b) 0.8 equivalents of $AgClO_4$ in MeOD.

To discard completely the possibility of η2-coordination instead terminal insertion we synthesized a derivative of (*R*)-**1** incorporating a phenyl group (Ph-(*R*)-**1**), that favoring the η2-coordination, instead the terminal H. In this case, silver (I) titration (MeOH, 10 mg/mL) don't reveal formation of any state of aggregation.

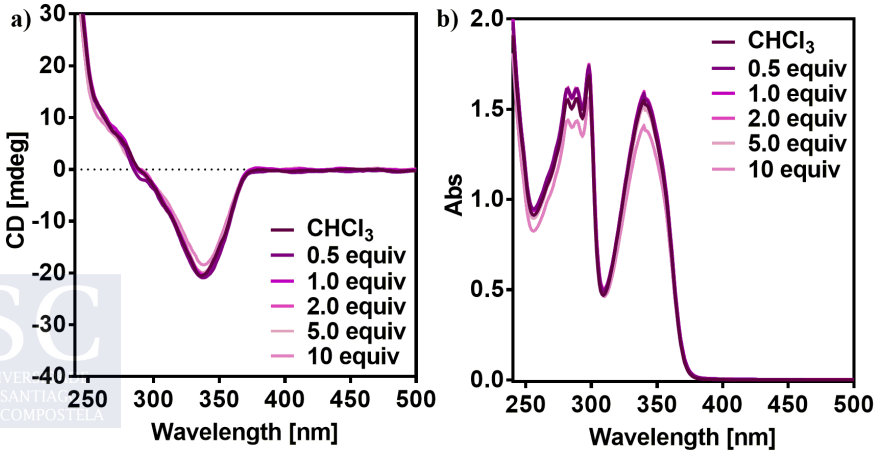

Figure S7. a) ECD and b) UV-Vis spectra of Ph-(*R*)-**1** titration with $AgClO_4$. [(*R*)-**1**]= 0.3 mg/mL.

Furthermore, IR studies reveals as the weak C≡C vibration emerge with the silver titration around 2000 cm^{-1} (Figure S8a). Also, was observed that methoxy groups remain almost unchanged whereas the S=O vibration cannot be analyzed due to the overlapping with the perchlorate salt signal around 1100 cm^{-1} (Figure S8b). The titration was performed over a 0.3 mg/mL solution of (*R*)-**1** in $CHCl_3$ with a 10 mg/mL solution of Ag (I) in MeOH.

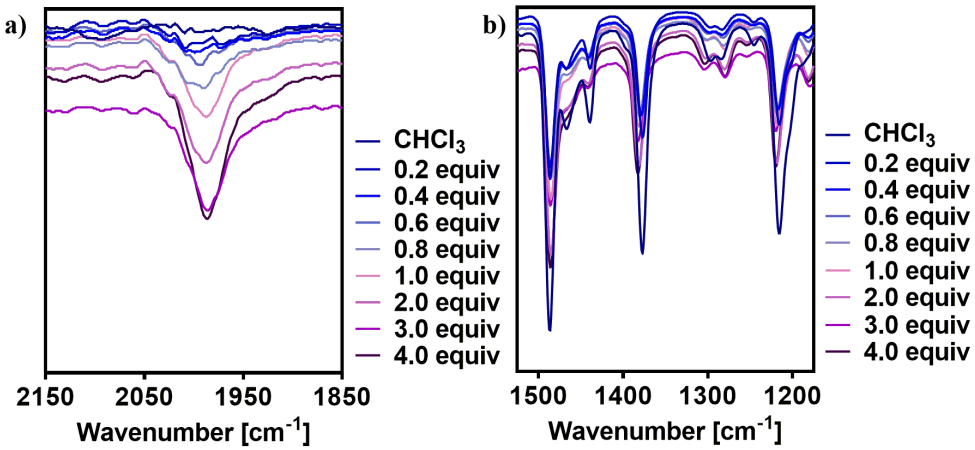

Figure S8. IR spectra of (*R*)-**1** with different equivalents of silver (I) cations. a) C≡C vibration and b) methoxy groups vibrations.

7. Enantiomeric Studies

Appling the same conditions described for (*R*)-**1**, its enantiomer (*S*) was prepared. Furthermore, applying the same measurement conditions, (*S*)-**1** was submitted to ECD and UV experiments to confirm the generation of aggregates with opposite helical sense.

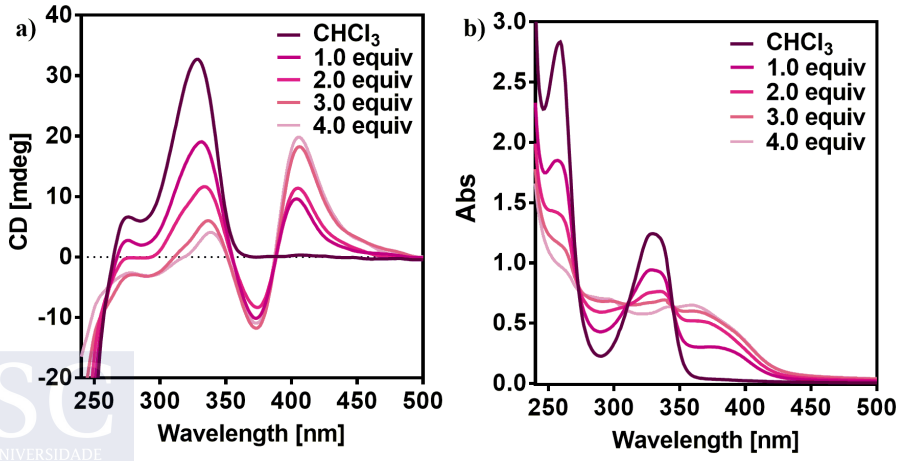

Figure S9. a) ECD and b) UV-Vis spectra of (*S*)-**1** (0.3 mg/mL) with addition of different equivalents of $AgClO_4$ solution (10 mg/mL). [(*R*)-**1**]= 0.3 mg/mL.

8. Assembly of Ag((*R*)-1)$_2$ units

Due to the steric hindrance generated by the rigid sulfinyl groups in both ends, cannot be possible overlap Ag((*R*)-**1**)$_2$ units without displacement one unit respect the other (Figure 10a). Furthermore, trying to fit both sulfoxide groups to the same side, the steric hindrance blocks both the H and J aggregate possibilities.

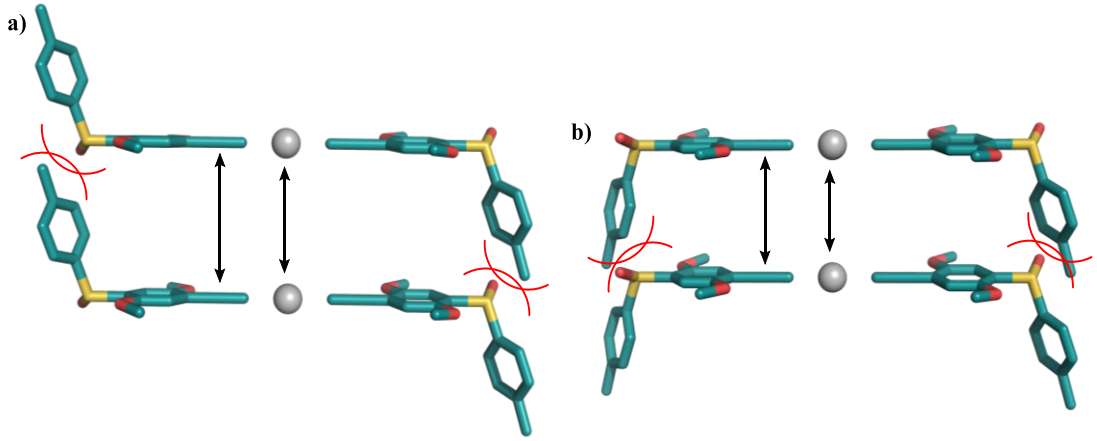

Figure S10. Schematic illustration of some possibilities for structural assembly of Ag((*R*)-**1**)$_2$ units.

9. AFM Studies

A solution of (*R*)-**1** in $CHCl_3$ (0.3 mg/mL) was prepared and 0.6 equiv of $AgClO_4$ dissolved in MeOH (10 mg/mL) was added and the mixture stirred few seconds. The resulting mixture was deposited over a silicon wafer chip and allowed to dry at rt for 12 h before performing measures. The AFM images reveal a regular distance between groves around 400 nm for the size of fibers obtained with this monomer-metal relationship.

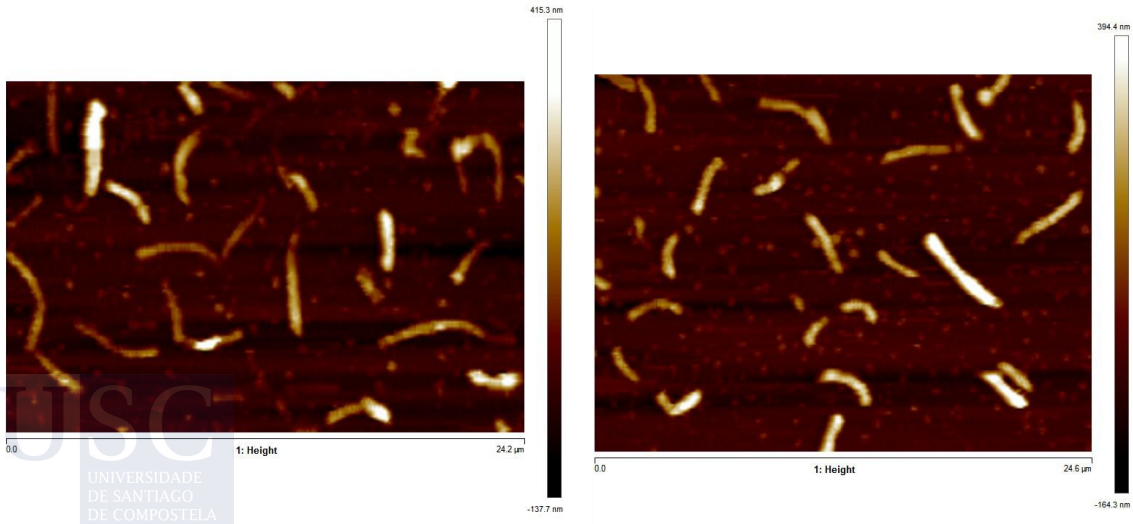

Figure S11. AFM images for a 1/0.6 mol/mol ((*R*)-**1**)/Ag relation.

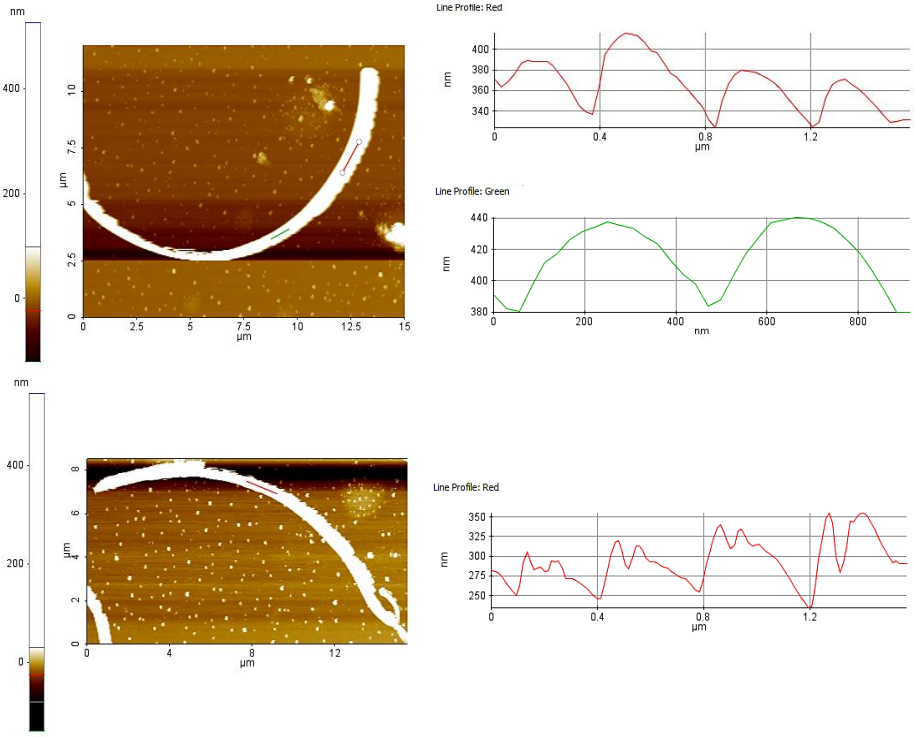

Figure S11. AFM images for a 1/0.6 mol/mol ((*R*)-**1**)/Ag relation showing distance between groves.

10. Rheological Studies

For rheological studies, a solution of (*R*)-**1** (0.3 mg/mL in $CHCl_3$) was prepared and 4 equiv of Ag ClO_4 (50 mg/mL in MeOH) was injected. The gelation is instant and the sample was analyzed in a a Rheolyst AR-1000N rheometer (TA Instruments, New Castle, UK) equipped with an AR2500 data analyzer, and fitted with a Peltier plate. The storage (G') and the loss (G'') moduli were recorded using a cone-plate geometry (diameter 4 cm, angle 2°).

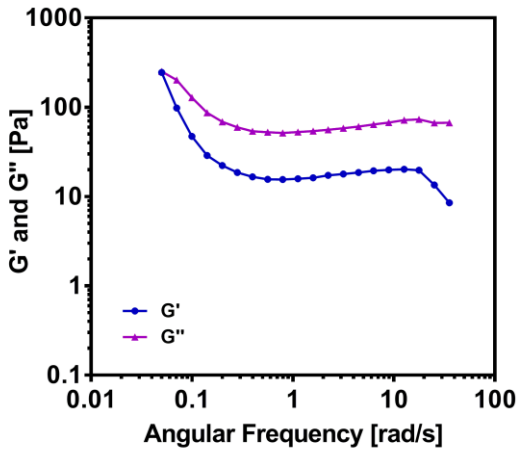

Figure S12. Rheological studies for a 1/4 mol/mol ((*R*)-**1**)/Ag relation. [(*R*)-**1**]= 0.3 mg/mL, [$AgClO_4$]= 50 mg/mL.

11. Supporting References

S1. P. Reiné, A. M. Ortuño, S. Resa, L. Á. de Cienfuegos, V. Blanco, M. J. Ruedas-Rama, G. Mazzeo, S. Abbate, A. Lucotti, M. Tommasini, S. Guisán-Ceinos, M. Ribagorda, A. G. Campaña, A. Mota, G. Longhi, D. Miguel, J. M. Cuerva, *ChemComm.*, **2018**, *54*, 13985-13988.

Helical polymers, covalent and supramolecular, have attracted the attention of the scientific community for the relation structure/function found in helical biomacromolecules such as peptides, proteins, or DNA, among others. Inspired by these works, in this thesis photochemical properties of several synthetic helical polymers from poly(phenylacetylene)s were studied, and the results were applied to elucidate its secondary structure. Furthermore, new helical systems, covalent and supramolecular, were prepared and studied, resulting in novel multi-responsive and multi-helical materials.